Transport signatures of higher-order topology in bismuth nanostructures

Alexandre Bernard

▶ To cite this version:

Alexandre Bernard. Transport signatures of higher-order topology in bismuth nanostructures. Quantum Physics [quant-ph]. Université Paris-Saclay, 2022. English. NNT : 2022UPASP140 . tel-04165403

HAL Id: tel-04165403
https://theses.hal.science/tel-04165403v1

Submitted on 19 Jul 2023

THESE DE DOCTORAT

NNT : 2022UPASP140

Transport signatures of higher-order topology in bismuth nanostructures

Signatures de topologie d'ordre supérieur dans des nanostructures de bismuth par mesures de transport

Thèse de doctorat de l'université Paris-Saclay

École doctorale n° 564 : physique en Île-de-France (PIF)
Spécialité de doctorat : Physique
Graduate School : Physique. Référent : Faculté des sciences d'Orsay

Thèse préparée dans l'unité de recherche **Laboratoire de Physique des Solides (Université Paris-Saclay, CNRS)**, sous la direction de **Sophie GUÉRON**, directrice de recherche, et le co-encadrement de **Hélène BOUCHIAT**, directrice de recherche

Thèse soutenue à Paris-Saclay, le 08 décembre 2022, par

Alexandre BERNARD

Composition du jury

Hugues POTHIER Directeur de recherche, CEA, Université Paris-Saclay	Président
Floriana LOMBARDI Professeure, Chalmers University of Technology	Rapporteur & examinatrice
Christian SCHÖNENBERGER Professeur, University of Basel	Rapporteur & examinateur
Julia MEYER Professeure des université, CEA, Université Grenoble-Alpes	Examinatrice
Sophie GUÉRON Directrice de recherche, LPS, Université Paris-Saclay	Directrice de thèse

université
PARIS-SACLAY

ÉCOLE DOCTORALE
Physique en
Île-de-France (PIF)

Titre : Signatures de topologie d'ordre supérieur dans des nanostructures de bismuth par mesures de transport...

Mots clés : isolant topologique, transport, jonction Josephson, Bismuth, nanofils

Résumé : Les isolants topologiques (TI) sont caractérisés par la présence d'états conducteurs topologiquement protégés sur leurs bords bien que leur cœur soit isolant. Le caractère topologique offre une robustesse unique, avec une conduction balistique qui n'est pas affectée par un faible désordre non-magnétique, dans la limite d'électrons n'interagissant pas entre eux. Combiné à de la supraconductivité, un TI peut héberger des quasi-particules exotiques appelées états liés de Majorana, qui présentent un comportement anyonique et constituent la base des architectures de calcul quantique topologique. En 2017, des travaux théoriques ont conduit à la découverte d'une nouvelle classe de TI : les isolants topologiques d'ordre supérieur (HOTI). Les isolants topologiques du second ordre (SOTI) sont des HOTI qui ont des états de bord protégés une dimension inférieure à leurs homologues standard du premier ordre, c'est-à-dire des états de charnière unidimensionnels (1d) pour un SOTI tridimensionnel (3d). En 2018, le bismuth monocristallin 3d pure fut le premier matériau SOTI (et HOTI) découvert. Il a été démontré théoriquement et expérimentalement qu'il possède des états balistiques 1d sur certaines de ses charnières. La théorie prédit également que ces états devraient être hélicoïdaux, avec des électrons de spin opposé se propageant dans des directions opposées. Cependant, la physique des états électroniques du bismuth est complexe et produit de nombreux effets qui dépendent de la géométrie du système, le principal problème étant que le cœur et les surfaces du bismuth ne sont pas isolantes, ce qui tend à masquer les effets dus au petit nombre des états charnières. Ma thèse de doctorat vise à explorer davantage la nature topologique des monocristaux de bismuth avec des expériences de transport dans des nanostructures de bismuth à basse température, détectant les états charnières hélicoïdaux topologiquement protégés prédis pour les SOTIs. Dans une première série d'expériences, nous avons mesuré le supercourant maximal que des segments de nanofils de bismuth à contacts supraconducteurs, formant des jonctions Josephson, peuvent supporter avant de devenir résistifs. Ce courant critique est affecté par des interférences à l'intérieur du nanofil : une phase quantique est associée à chaque état porteur de supercourant, qui change dans un champ magnétique via les effets orbitaux et Zeeman. Ce changement de phase génère des figures d'interférence du courant critique en fonction du champ magnétique, qui peuvent être utilisées pour déduire ce qu'il se passe dans le nanofil. Dans une deuxième série d'expériences, nous avons mesuré la statistique du courant critique d'un nano-anneau de bismuth avec des contacts supraconducteurs. Nous avons constaté qu'une telle jonction forme un dispositif d'interférence quantique supraconducteur (SQUID) intrinsèque, montrant un courant critique moyen périodique en champ magnétique avec une forme en dents de scie, persistant jusqu'à des valeurs de champ élevées. Ce comportement a confirmé la présence d'états charnières balistiques 1d. De plus, la mesure de la distribution complète du courant critique a révélé l'existence de régions de champ avec deux ou même trois valeurs de courant critique différentes. Nous associons ces supercourants à trois états/configurations supraconducteurs différents, correspondant à deux états charnières hélicoïdaux soit dans leur premier état excité, soit dans leur état fondamental, soit l'un dans son état excité et l'autre dans son état fondamental. Grâce à ces deux séries d'expériences, nous rapportons des signatures que le bismuth monocristallin 3d héberge des états hélicoïdaux 1d, comme prédit pour les SOTIs. Mon travail de thèse a aussi produit des résultats préliminaires sur un sujet émergent, l'anisotropie magnéto-chirale (MCA), qui est une autre manifestation du couplage entre le spin et l'impulsion des états électroniques.

université
PARIS-SACLAY

ÉCOLE DOCTORALE
Physique en
Île-de-France (PIF)

Title : Transport signatures of higher-order topology in bismuth nanostructures..........................

Keywords : topological insulator, transport, Josephson junction, bismuth, nanowires

Abstract : Topological Insulators (TI) are characterized by topologically-protected conducting states on their boundaries even though their bulk is insulating. The topological character provides a unique robustness, with ballistic conduction unaffected by weak non-magnetic disorder, in the limit of non-interacting electrons. When combined with superconductivity, TI can host exotic quasi-particles called Majorana bound states that exhibit anyonic physics and constitute the basis of topological quantum computation schemes. In 2017, theoretical works led to the discovery of a new class of topological insulators : higher-order topological insulators (HOTI). Second-order topological insulators (SOTI) are HOTI that feature protected edge states one dimension lower than their standard first-order counterparts, that is one-dimensional (1d) hinge states for a three-dimensional (3d) SOTI. In 2018, pristine 3d single-crystal bismuth was the first SOTI (and HOTI) material discovered. It was shown theoretically and experimentally that it has 1d ballistic states on some of its hinges. The theory also predicts that these states should be helical, with opposite-spin electrons propagating in opposite directions. However, the physics of the electronic states of bismuth is complex and produces many effects that depend on the geometry of the system, the main issue being that the bulk and surfaces of bismuth are not insulating, which tends to mask effects due to the small number of hinge states. My PhD thesis aims at exploring further the topological nature of bismuth single-crystals with low-temperature transport experiments in bismuth nanostructures, detecting the topologically-protected helical hinge states expected in SOTIs. In a first series of experiments, we measured the maximum supercurrent that segments of bismuth nanowires with superconducting contacts, forming Josephson junctions, can carry before switching to a resistive state. This switching current is affected by interference inside the nanowire : a quantum phase is associated to each supercurrent carrying state, which changes in a magnetic field via orbital and Zeeman effects. This change in phase results in interference patterns of the switching current versus magnetic field, which can be used to infer what is happening in the nanowire. In a second series of experiments, we measured the statistics of the switching current of a crystalline bismuth nanoring with superconducting contacts. We found that such a junction forms an intrinsic Superconducting Quantum Interference Device (SQUID), demonstrating an average switching current periodic in magnetic field with a sawtooth shape, persisting up to high field values. This behavior confirmed the presence of ballistic 1d hinge states. Moreover, the measurement of the full switching current distribution revealed the existence of field regions with two or even three different switching current values. We associate these supercurrents to three different superconducting states/configurations, corresponding to two helical hinge state either both in their first excited state, both in their ground state, or one in its excited state and the other in its ground state. Thanks to these two series of experiments, we report signatures that 3d crystalline bismuth hosts helical 1d states, as predicted for SOTI. My PhD work also produced preliminary results on an emerging topic, Magneto-Chiral Anisotropy (MCA), which is another manifestation of the coupling between the electronic state's spin and momentum.

Acknowledgments

Ces quelques paragraphes, les derniers que j'inscris dans ce manuscrit, marquent la fin d'une belle aventure intellectuelle et humaine, et le début d'une autre que j'espère aussi enrichissante. Durant ces années au Laboratoire de Physique des Solides, dans l'équipe de physique mésoscopique, j'ai eu la chance d'apprendre et d'expérimenter de nombreux aspects de la recherche. Avec les équipements du laboratoire, et parfois ceux d'autres laboratoires voisins, j'ai pu m'essayer à de multiples méthodes de nanofabrication d'échantillons. Pour nos expériences, j'ai aussi pu travailler avec de petits réfrigérateurs à dilution wet artisanaux ainsi que des dry plus imposants et "industriels". De plus, cette thèse exploratoire sur le bismuth associé à de la supraconductivité de proximité m'a permis de découvrir et de réfléchir à de nombreux concepts de la physique. La complexité du matériau, que nous avons tenté de dompter par différentes méthodes de mesure, explique en grande partie la taille de ce manuscrit, avec un long chapitre théorique et des chapitres entiers en annexes, ainsi que les difficultés que j'ai eues pour finir ma thèse. Durant ma thèse, la compréhension des données d'une de nos expériences a exigé un investissement en temps important, et a été l'occasion de rédiger un long article en collaboration avec des théoriciens internationaux. Enfin, d'un point de vue communication, j'ai pu présenter nos travaux de recherche à de multiples reprises durant divers événements, et j'ai eu l'opportunité de faire de la divulgation scientifique pour une audience plus large durant ma mission pour SIRTEQ.

Si ma thèse a pu bien se dérouler, ce n'est bien sûr pas uniquement grâce à des équipements et des livres de physique. Non. Pour cela, je dois avant tout remercier tous mes collègues qui ont fait du laboratoire un lieu où la recherche progresse et de manière agréable. En particulier, j'ai eu le privilège (et peut-être un peu le fardeau) d'avoir des encadrantes de thèse qui, au delà de leur compétence scientifique et de leur sympathie, n'étaient jamais très loin et qui pouvaient répondre à mes interrogations très rapidement.

Un grand merci donc à mes deux encadrantes de thèse avec qui j'ai tellement appris ! Merci à Sophie, ma directrice de thèse, qui est toujours encourageante même dans les moments où on pourrait s'attendre au contraire. Elle nous rappelle régulièrement que reprendre calmement un raisonnement à sa base permet bien souvent de clarifier les idées prises dans la turpitude de la recherche. Côté expériences, le principe de fonctionnement des mesures et les différents instruments utilisés n'ont pas de secret pour Sophie, et j'ai pu compter sur elle à de nombreuses occasions, tout comme le font les autres étudiants ! Sophie, merci aussi énormément pour tout le travail que tu as fait sur l'article, où à un moment tu as délibérément pris une grande partie de la charge de travail pour m'en libérer ! Un grand merci aussi à Hélène, directrice du groupe et ma co-encadrante de thèse, qui après lui avoir posé une question sur un détail qui clochait pendant mon stage, m'a proposé de venir faire ma thèse avec Sophie et elle. Sous ses airs parfois un peu rudes, Hélène fait preuve d'une humanité rare et est toujours prête à aider son prochain. Malgré ses diverses responsabilités, elle veut toujours être au courant de toutes les expériences en cours dans le groupe et y contribuer. Merci aussi de m'avoir soutenu durant ma difficile rédaction, ainsi que pour l'aide précieuse pour mon déménagement !

Un grand merci également aux autres membres de l'équipe MESO sans qui ma thèse aurait été impossible et moins agréable : Richard, Sandrine, Alexei, Alik, Miguel. En particulier, je remercie Meydi qui a partagé son bureau avec moi. Ca a été l'occasion pour moi de lui poser régulièrement des questions très conceptuelles à 19h, qui nous entrainaient dans une discussion presque métaphysique jusqu'à bien après la patrouille du gardien. Merci aussi à la nouvelle génération avec qui j'ai pu discuter, parfois boire, ou même danser : Xavier, Ziwei, Jorge, Victor, Diana, Taro, Jules, Matthieu, Kamila, Lucas, Léo, Noémie, Brendan, Alex, Aymeric, Antoine, Ansgar, Pierre, Maxime, Raphaëlle, Anil, et tous ceux que je n'ai pas cités. Je n'oublie pas les autres membres du LPS pour leur aide : Véronique Thieulart, Jean-Pierre Dalac, Raphaël Weil, Sophie Tourlet, Ciham Zaaboul-Aliane, Pouneh Milanian, Marie-France Mariotto, Marino Marsi. Je remercie aussi

Marco Aprili et François Boulogne, qui ont accepté d'être mon tuteur scientifique et mon parrain de thèse, respectivement. Merci aussi à Véronique Terras pour sa compréhension pour cette rédaction difficile.

I would also like to thank a lot Russell Deacon, Koji Ishibashi, and all the people of the Advanced Device Laboratory of RIKEN laboratory, for their invitation to come work with them during two weeks in Japan. Even though the experiments were not successful, my experience in Japan was very nice, thanks to Russell that welcomed me very well. I also thank the members of the jury that took time to review my (lengthy) PhD thesis manuscript and to participate to my PhD defense : Hugues Pothier, Floriana Lombardi, Christian Schönenberger, and Julia Meyer. At last, thanks to the many other physicists we exchanged with during my PhD, and especially the co-authors of the article resulting from our experiments. With Yuval Oreg, Felix von Oppen and Yang Peng, we met every week for online brainstorms during the first covid-19 lock-down to understand our data and elaborate the theoretical model. Our article, that was published recently, went to multiple stages during its long writing process, progressively and collectively refining our model and the text associated to it to propose a consistent interpretation of various features seen in the data. This work was my first time writing a scientific article, and was a great learning experience.

Enfin, entre le(s) confinement(s) et l'épreuve de la rédaction du manuscrit de thèse qui s'est éternisé, les dernières années ont été plutôt solitaires et le nombre de mes sorties limitées. Dans ce contexte, le fait d'avoir un environnement de travail rassurant et une famille soudée est primordial et cela m'a permis de tenir le coup mentalement. Donc je voudrais conclure cette partie en remerciant ma famille pour leur soutient indéfectible. Merci infiniment.

Table of contents

Synthèse en français

Depuis leur découverte il y a une quinzaine d'années, les isolants topologiques (TI) ont suscité un grand intérêt de la part de la communauté scientifique. Ces nouvelles " phases " de la matière se distinguent par des propriétés quantifiées robustes, associées à la topologie de la phase quantique de leurs états quantiques dans le coeur du matériau. Elles sont caractérisées par la présence d'états conducteurs topologiquement protégés à leurs frontières, tandis que leur coeur est isolant. Les TI impliquent des notions de physique générale comme la courbure de Berry, des phénomènes de physique quantique profonde tels que les fermions de Majorana, la physique anyonique et l'anomalie de parité, ainsi que des applications très pratiques comme des processus de transduction plus efficaces et une protection topologique contre les perturbations.

Très récemment, en 2017, de nouveaux travaux théoriques ont conduit à la découverte d'une nouvelle classe d'isolants topologiques : les isolants topologiques d'ordre supérieur (HOTI). Les isolants topologiques du second ordre (SOTI) présentent des états de bord protégés une dimension plus basse que leurs homologues standard du premier ordre. En 2018, le bismuth monocristallin pure fut le premier matériau SOTI (et le premier HOTI) découvert. Il a été démontré théoriquement et expérimentalement qu'il possède des états 1d sur certaines de ses charnières. La théorie prédit également que ces états devraient être hélicoïdaux, et que leur hélicité dépendrait de l'orientation des surfaces donnant lieu aux charnières. Cependant, la physique des états électroniques du bismuth est très complexe et produit de nombreux effets qui dépendent de la géométrie du système, le principal problème étant que le coeur et les surfaces du bismuth ne sont pas isolants, ce qui tend à masquer les effets dus au petit nombre d'états charnières.

Ma thèse de doctorat est la troisième à traiter du bismuth. Les premiers échantillons et mesures de transport avec des nanofils de bismuth connectés à des contacts supraconducteurs ont été réalisés au cours de la première [1]. La seconde thèse a montré l'existence d'états balistiques 1d conducteurs aux charnières de tels échantillons [2]. Le travail expérimental de ma thèse confirme les observations précédentes et approfondit le caractère hélicoïdal et la protection topologique de ces états charnières.

Au cours de ma thèse, nous avons également exploré un nouveau sujet pour le groupe, à savoir l'anisotropie magnéto-chirale (MCA). Pour les matériaux à fort couplage spin-orbite, présentant un verrouillage spin-impulsion, le courant et le champ magnétique sont liés par le spin via le couplage Zeeman. Cela donne lieu à des anisotropies des propriétés de transport, à la fois dans les états résistif et supraconducteur, en fonction de la géométrie de l'échantillon ainsi que de l'angle relatif entre le vecteur courant et le vecteur champ magnétique. Il s'agit d'un sujet intéressant qui commence à être étudié par la communauté scientifique.

Je me suis concentré sur trois aspects de la réponse de transport des nanofils monocristallins de bismuth :
- la mesure et l'analyse des motifs résultant de l'interférence entre les différents états d'Andreev dans les jonctions Josephson à base de nanofils de bismuth
- la mesure et l'analyse de la dynamique de bascule des états d'Andreev dans une jonction Josephson à base de bismuth et de nanofils, hors de son état supraconducteur de proximité
- la recherche de l'anisotropie magnéto-chirale induite par le spin-orbite à travers des nanofils de bismuth et des jonctions Josephson à base de bismuth et de nanofils, à la fois dans les états résistif et supraconducteur

Commençons par justifier brièvement nos choix d'échantillons de bismuth et de dispositifs de mesure. En effectuant nos mesures à basse température, certains aspects des objets de taille microscopique peuvent entrer dans un régime de cohérence quantique, où la phase quantique se manifeste à l'échelle microscopique, ce qui est l'objectif de la physique mésoscopique. En fabriquant des nanofils de Bi d'une taille de $\simeq 100nm$ et d'une longueur de $> 1,4\mu m$, nous réduisons le nombre d'états de coeur et de surface. En induisant de la supraconductivité à l'intérieur de nos nanofils de Bi résistifs grâce à la proximité de contacts supraconducteurs, nous créons des jonctions Josephson à base de bismuth. Cela diminue encore les contributions relatives des états diffusifs de coeur et de surface par rapport aux états balistiques de charnière topologiquement protégés, et nous permet également de faire interférer des supercourants. En mesurant la réponse en transport en fonction de l'intensité et de l'orientation du champ magnétique, nous sommes en mesure d'estimer l'effet du déphasage orbital, de la différence de phase supraconductrice et du couplage Zeeman, bien qu'ils puissent être difficiles à démêler.

Dans le reste de cette introduction, je résume les principaux résultats sur les états charnières hélicoïdaux 1d topologiquement protégés obtenus au cours de ma thèse de doctorat.

Interférence d'états charnières balistiques 1d

L'interférence entre les supercourants portés par différents états charnières balistiques 1d dans les jonctions Josephson à base de nanofils de bismuth a déjà été rapportée dans deux travaux de thèse antérieurs dans le groupe [1, 2]. Elle consiste à mesurer le supercourant maximal qu'un segment de nanofil de bismuth avec des contacts supraconducteurs peut transporter avant de devenir résistif. Ce courant de bascule est affecté par l'interférence des supercourants à l'intérieur du nanofil. Une phase quantique est associée à chaque état porteur de supercourant, et un champ magnétique peut les déphaser les uns par rapport aux autres via des effets orbitaux et Zeeman. Ce déphasage donne lieu à des motifs d'interférence du courant de bascule en fonction du champ magnétique, qui peuvent être utilisés pour déduire ce qui se passe dans le nanofil.

Durant mon doctorat, nous avons mené une analyse minutieuse de plusieurs jonctions Josephson à base de nanofils de bismuth. Nous avons confirmé l'existence de trois échelles de champ correspondant à un déphasage orbital entre des états balistiques 1d séparés dans l'espace à des champs faibles, à un déphasage orbital au sein d'états étroits individuels à des champs importants, et à un déphasage orbital et Zeeman à des champs intermédiaires, voir Fig.1. Ce travail confirme la présence d'états balistiques 1d dans les nanofils de bismuth, en accord avec la théorie des isolants topologiques d'ordre supérieur.

Allant au-delà des travaux de mes prédécesseurs, nous avons étendu notre analyse des figures d'interférence pour inclure les inductances auto-induites et cinétiques ainsi que les effets Josephson anormaux. Nous avons mesuré un effet de diode Josephson dans tous nos échantillons, avec des effets de déphasage à champ magnétique nul dans la plupart d'entre eux, qui peut être expliqué par la présence d'inductances cinétiques de $\sim 200pH$. Alternativement, ce décalage pourrait être produit par un effet Josephson anormal induit par le spin-orbite, où le supercourant induit un champ magnétique effectif de $\sim 100G.\mu A^{-1}$. De plus, nous avons révélé que les variations des motifs de courant de bascule en fonction de l'orientation du champ magnétique ne pouvaient pas être expliquées par un simple déphasage orbital entre des états situés dans un seul plan. De plus, nous avons trouvé un profil transverse de densité de courant anisotrope pour les états charnières 1d. L'analyse complète est faite dans le chapitre 3.

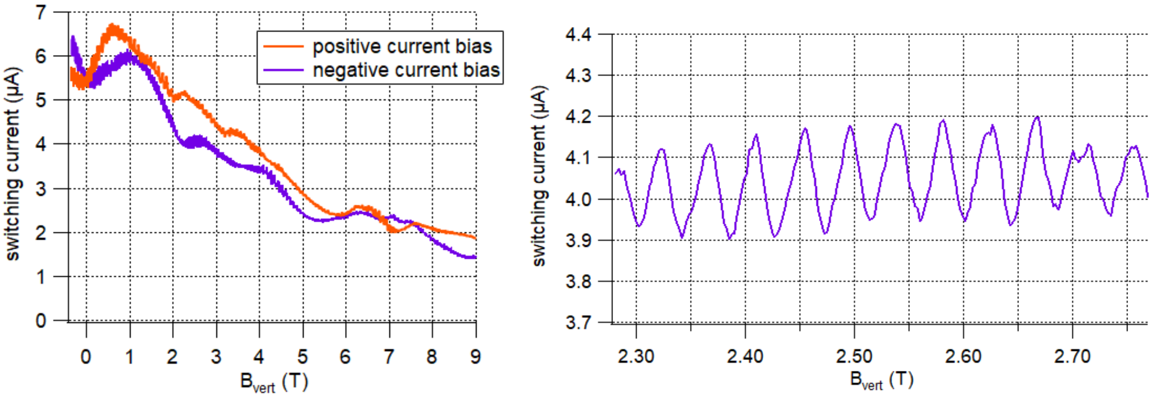

(a) (b)

Figure 1 – Courant de bascule moyen de la jonction Josephson à base de nanofil de bismuth Bi$_{12}^{wire}$ en fonction du champ magnétique vertical perpendiculaire au fil, pour une polarisation en courant positive (ligne continue orange) et négative (ligne continue violette). (a) Entre $-0.3T$ et $9T$. (b) Zoom sur une gamme de $0.45T$.

Dynamique de bascule d'états d'Andreev hélicoïdaux spatialement séparés

La mesure du courant de bascule en fonction du champ magnétique hors-plan d'une jonction Josephson constituée de deux branches d'un nano-anneau de bismuth, voir Fig.2a, formant un dispositif d'interférence quantique supraconducteur (SQUID) DC intrinsèque, a révélé des comportements très intéressants. Tout d'abord, l'observation d'un signal en dents de scie périodique en flux magnétique $\Phi = B.S = \Phi_0 = h/(2e)$ dans la surface S du nano-anneau a montré que l'échantillon se comporte comme un SQUID DC asymétrique intrinsèque donnant la relation courant-phase (CPR) de la branche la plus faible, voir Fig.2b. Cette CPR en dents de scie dans une longue jonction, survivant jusqu'à $7T$, confirme la présence d'états balistiques 1d, comme rapporté précédemment dans des montages similaires dans [3, 2, 4].

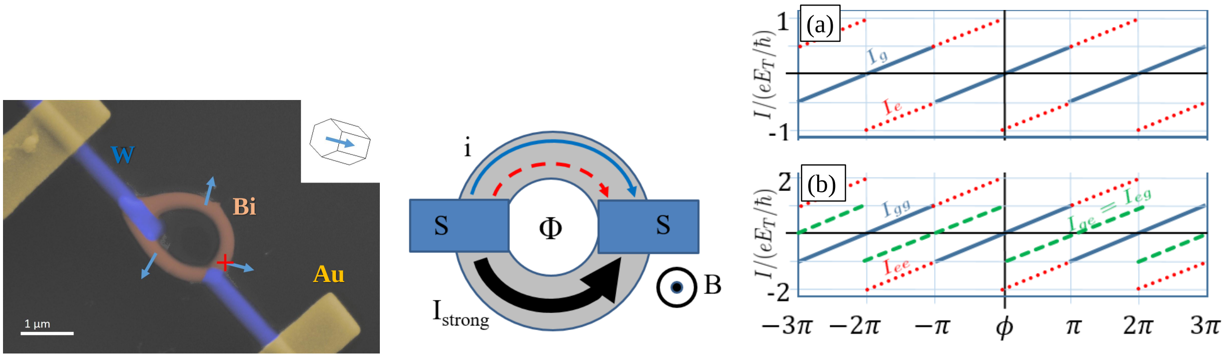

(a) (b) (c)

Figure 2 – (a) Image au microscope électronique à balayage avec fausses couleurs de l'échantillon Bi^{ring}. Il s'agit d'un nano-anneau de Bi (marron) avec des contacts supraconducteurs composés de W (bleu) et des fils d'Au (jaune). (b) Schéma simplifié du nano-anneau de bismuth connecté à deux contacts supraconducteurs (S), constituant un SQUID DC asymétrique intrinsèque avec deux états charnières hélicoïdaux dans la branche faible. (c) Supercourant de la branche faible en fonction de la configuration d'occupation de la ou des charnières. E_T est l'énergie de Thouless. En haut : une charnière dans son état fondamental (I_g) ou excité (I_e). En bas : deux charnières à l'état fondamental (g) ou excité (e).

En allant plus loin, au lieu de regarder uniquement le courant de bascule moyen sur des centaines d'événements de bascule, nous avons mesuré sa distribution complète, voir Fig.3. Cela a révélé deux choses importantes.

1) Premièrement, il existe deux valeurs distinctes de courant de bascule pour des valeurs de champ magnétique correspondant à une différence de phase supraconductrice π à travers la jonction balistique (branche faible). Nous l'interprétons comme une preuve supplémentaire d'un croisement parfait des états liés d'Andreev, attendu pour les états topologiquement protégés. À proximité de π, la jonction peut être dans deux états différents, transportant des supercourants opposés.

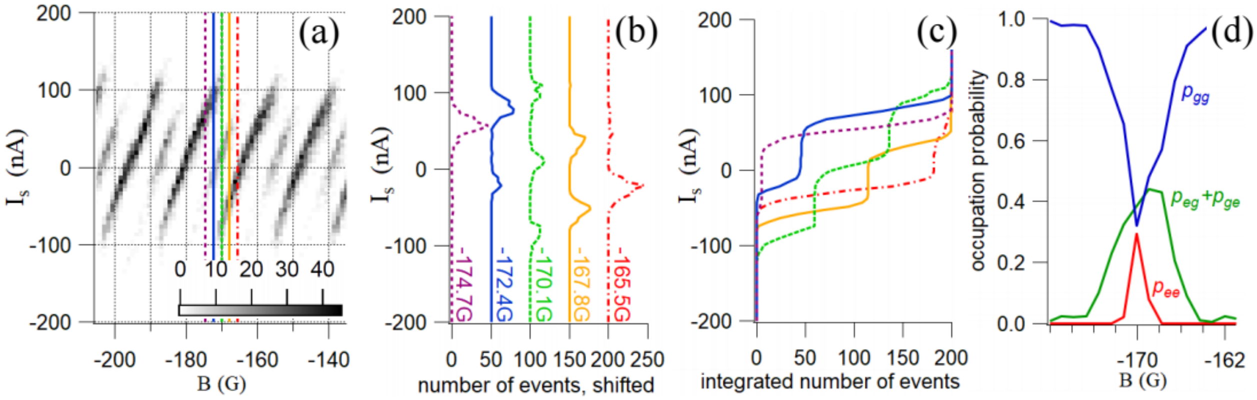

Figure 3 – Distributions de courant de bascule (histogrammes), en fonction du champ magnétique hors-plan, de la jonction Josephson formée par un nano-anneau de bismuth, avec une rampe de polarisation en courant à un fréquence de $17Hz$. (a) Histogrammes de courant de bascule sur quatre périodes de flux autour de $-170G$. Le nombre d'événements de bascule est codé en nuances de gris. La ligne de base du courant a été supprimé avec un polynôme du premier degré. (b) Histogrammes aux champs magnétiques autour du saut à $-170G$ où $\phi = \pi$, voir les lignes colorées correspondantes en (a). Les courbes sont décalées pour plus de clarté. (c) Histogrammes intégrés près du saut à $-170G$. (d) Variation en champ de la probabilité d'occupation de trois états d'Andreev porteurs de supercourants, correspondant respectivement aux deux charnières dans l'état fondamental (p_{gg}, courbe bleue), aux deux charnières dans l'état excité (p_{ee}, courbe rouge), et à une charnière dans l'état fondamental et l'autre dans l'état excité ($p_{eg} + p_{ge}$, courbe verte).

2) Deuxièmement, il existe une troisième valeur intermédiaire de courant de bascule visible sur une région étendue autour de π, voir Fig.3. Nous l'expliquons par la présence de deux sous-jonctions longues balistiques identiques en parallèle, correspondant à deux états charnières balistiques d'Andreev. Lorsque les deux sous-jonctions sont dans leur état fondamental, le courant est juste doublé. Cependant, lorsque l'une est excitée et l'autre non, la somme des deux est une dent de scie décalée, voir Fig.2c. Cette situation est plus susceptible de se produire près de π, où les états excité et fondamental sont proches en énergie.

Pour un état-charnière supraconducteur topologique, l'état lié d'Andreev est hélical et non dégénéré en spin, et il doit prendre ou céder une quasiparticule à son environnement pour effectuer la transition entre son état fondamental et son état excité. Nous avons trouvé de longs temps de transition uni-état-charnière de $\tau_{qp} \simeq 10ms$, correspondant à l'empoisonnement d'une seule quasiparticule dans la spectroscopie micro-onde des jonctions Josephson. Cette valeur est plutôt longue par rapport à la valeur moyenne trouvée dans la littérature. En revanche, le temps de transition inter-état-charnières s'est révélé extrêmement long par rapport à la littérature, avec $\tau_p \simeq 2ms \gg 1\mu s$. Ce processus correspond à une relaxation (ou excitation) simultanée de deux état-charnières par échange de paires de quasiparticules avec l'environnement. Pour une jonction conventionnelle, dans laquelle les deux hélicités ne sont pas séparées spatialement, ce processus est très facile, car la jonction peut simplement échanger une paire de quasiparticules avec le condensat de paires de Cooper, ce qui donne des temps de transition $\sim 1\mu s$. Cependant, pour une paire d'état-charnière d'Andreev hélicoïdaux, leur séparation spatiale, plus grande que la longueur de cohérence supraconductrice, réduit considérablement cette possibilité. Nous l'interprétons comme une preuve solide que les état-charnières ne sont pas seulement balistiques, mais aussi non dégénérés en spin (hélicoïdaux), comme prévu pour un isolant topologique de second ordre.

Ce travail a été réalisé en collaboration avec les théoriciens Dr. Yang Peng, Prof. Yuval Oreg et Prof. Felix von Oppen. Il a donné lieu à un article, qui vient d'être publié dans Nature Physics [5]. L'analyse complète est disponible dans le chapitre 4.

Organisation du manuscrit

Le manuscrit de ma thèse est organisé de la manière suivante :
- Le premier chapitre introduit toutes les idées théoriques utiles à la compréhension du travail de ma thèse. Ce chapitre peut être sauté si on le souhaite, et les parties pertinentes peuvent être lu lorsqu'on y fait référence dans un autre chapitre.
- Le deuxième chapitre décrit les procédés et techniques utilisés pour réaliser les échantillons et les expériences.
- Le troisième chapitre présente la mesure et l'analyse des motifs résultant de l'interférence entre les différents états d'Andreev dans les jonctions Josephson à base de nanofils de bismuth.
- Le quatrième chapitre présente la mesure et l'analyse de la dynamique du courant de bascule des états d'Andreev dans une jonction Josephson formée par un nano-anneau de bismuth, hors de son état supraconducteur induit par effet de proximité.
- Le cinquième chapitre conclut ce manuscrit et aborde les développements futurs.

Les résultats sur la MCA sont présentés séparément dans les annexes. Dans l'annexe 6.7, nous discutons de la théorie de la MCA, impliquant les effets Edelstein. Dans l'annexe 6.2, nous étudions les différentes sources d'asymétrie (telles que les inductances) et leur dépendance vis-à-vis de divers paramètres. Nous montrons qu'il est difficile, mais pas impossible, de séparer la MCA des autres sources d'asymétrie. Dans l'annexe 6.9.1, nous présentons nos mesures d'un champ magnétique effectif $B_{eff} = \beta_N I$ dans de longs nanofils de bismuth avec des contacts résistifs à $\simeq 100mK$, que nous associons à la MCA. Dans l'annexe 6.12, nous montrons nos mesures de $B_{eff} = \beta_N I$ dans l'état résistif et de $B_{eff} = \beta_S I$ dans l'état supraconducteur d'une jonction Josephson à base de nanofils de bismuth en-dessous et au-dessus de sa température critique. Toujours en annexe, nous fournissons plus de détails sur des points spécifiques de fabrication, de mesure et de calcul.

Summary in english

Since their discovery approximately fifteen years ago, Topological Insulators (TI) have attracted a lot of interest from the scientific community. These new « phases » of matter distinguish themselves by robust quantized properties, associated to the topology of the quantum phase of their quantum states in the bulk of the material. They are characterized by the presence of topologically-protected conducting states on their boundaries even though their bulk is insulating. TI feature general physics notions like the Berry curvature, deep quantum physics phenomenon such as Majorana fermions, anyonic physics and parity anomaly, as well as very practical applications like more efficient transduction processes and topological protection against perturbations.

Very recently, in 2017, new theoretical works led to the discovery of a new class of topological insulators : higher-order topological insulators (HOTI). Second-order topological insulators (SOTI) display protected edge states one dimension lower than their standard first-order counterparts. In 2018, pristine single-crystal bismuth was the first SOTI material (and first HOTI) discovered. It was shown theoretically and experimentally that it has 1d states on some of its hinges. The theory also predicts that they should be helical, and that their helicity would depend on the orientation of the surfaces giving rise to the hinges. However, the physics of the electronic states of bismuth is very complex and produces many effects that depends on the geometry of the system, the main issue being that the bulk and surfaces of bismuth are not insulating, which tend to mask effects due to the small number of hinge states.

My PhD thesis is the third to deal with bismuth. The first samples and transport measurements with bismuth nanowires connected to superconducting contacts were realized during the first one [1]. The second PhD thesis showed the existence of ballistic 1d conducting states at hinges of such samples [2]. The experimental work of my PhD confirms the previous observations and further probe the helical character and the topological protection of these hinge states.

During my PhD, we also explored a new topic for the group, which is Magneto-Chiral Anisotropy (MCA). For materials with high spin-orbit coupling, exhibiting spin-momentum locking, the current and the magnetic field are related by the spin via Zeeman coupling. It yields anisotropies of transport properties, in both the resistive and the superconducting states, depending on the geometry of the sample as well as the relative angle between the current vector and the magnetic field vector. This is an interesting topic that begins to be investigated by the scientific community.

I have focused on three aspects of the transport response of bismuth single-crystal nanowires :

- the measurement and analysis of patterns resulting from the interference between the various Andreev states in bismuth-nanowire-based Josephson junctions
- the measurement and analysis of the switching dynamics of Andreev states in a bismuth-nanoring-based Josephson junction, out of its proximity-induced superconducting state
- the search of spin-orbit-induced Magneto-Chiral Anisotropy through bismuth nanowires and bismuth-nanowire-based Josephson junctions, both in the resistive and superconducting states

Let us first briefly justify our choices of bismuth sample and measurement setups. By performing our measurements at low temperature, some aspects of microscopic-size objects can enter a quantum-coherent regime, where the quantum phase manifests itself on the microscopic scale, which is the focus of mesoscopic physics. By making Bi nanowires $\simeq 100nm$ large and $> 1.4\mu m$ long, we reduce the number of bulk and surface states. By inducing superconductivity inside our resistive Bi nanowires thanks to the proximity of superconducting contacts, we create bismuth-based Josephson junctions. This further decreases the relative contributions of the diffusive bulk and surface states compared to the ballistic topologically-protected hinge states, and we also allow for supercurrent interference. By measuring the transport response as a function of magnetic field intensity and orientation, we are able to measure the effect of orbital dephasing, superconducting phase difference, and Zeeman spin-field coupling, although they may be hard to disentangle.

In the remaining of this introduction, I summarize the main results on the topologically protected 1d helical hinge states obtained during my PhD.

1d ballistic hinge states interference

The interference between supercurrents carried by different 1d ballistic hinge states in bismuth-nanowire-based Josephson junctions was already reported in two previous PhD works in the group [1, 2]. It consist in measuring the maximum supercurrent that a segment of bismuth nanowire with superconducting contacts can carry before becoming resistive. This switching current is affected by the supercurrents interference inside the nanowire. A quantum phase is associated to each supercurrent carrying state, and a magnetic field can dephase them via orbital and Zeeman effects. This dephasing results in switching current versus magnetic field interference patterns, which can be used to infer what is happening in the nanowire.

During my PhD, we led a careful analysis of multiple bismuth-nanowire-based Josephson junctions. We confirmed three field scales corresponding to orbital dephasing between spatially separated 1d ballistic states at small fields, to orbital dephasing within individual narrow states at large fields, and to both orbital and Zeeman dephasing at intermediate fields, see Fig.4. This work confirms the presence of 1d ballistic states in bismuth nanowires, consistent with the higher-order topology picture.

Going beyond the work of my predecessors, we extended our analysis of the interference patterns to include self and kinetic inductances as well as anomalous Josephson effects. We measured a Josephson diode effect in all our samples, with dephasing effects at zero magnetic field in most of them, that can be explained by the presence of kinetic inductances of $\sim 200pH$. Alternatively, this shift could be produced by spin-orbit-induced anomalous Josephson effect, where the supercurrent induces an effective magnetic field of $\sim 100G.\mu A^{-1}$. In addition, we revealed that the variations of the magnetic field patterns as a function of magnetic field orientation could not be explained by simple orbital dephasing between states embedded in a single plane. Moreover, we found an anisotropic transverse current density profile for the 1d hinge states. The full analysis is done in chapter 3.

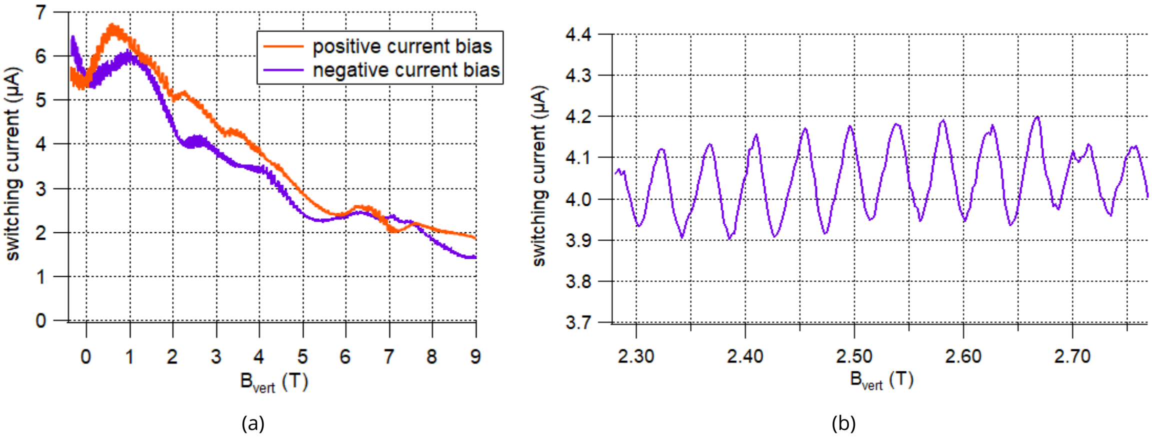

(a)

(b)

Figure 4 – Average switching current of bismuth-nanowire-based Josephson junction Bi$_{12}^{wire}$ as a function of vertical magnetic field perpendicular to the wire, for positive (orange solid line) and negative (purple solid line) current bias. (a) Between $-0.3T$ and $9T$. (b) Zoom over a $0.45T$ range.

Switching dynamics of spatially separated helical Andreev states

The measurement of the switching current versus out-of-plane magnetic field pattern of a Josephson junction made of two branches of a bismuth nanoring, see Fig.5a, forming an intrinsic DC Superconducting Quantum Interference Device (SQUID), revealed very interesting behaviors. First, the observation of a sawtooth signal periodic in magnetic flux $\Phi = B.S = \Phi_0 = h/(2e)$ in the surface S of the nanoring showed that the sample behaves as an intrinsic asymmetric DC SQUID yielding the Current-Phase Relation (CPR) of the weakest branch, see Fig.5b. This sawtooth CPR in a long junction, surviving up to $7T$, confirms the presence of 1d ballistic states, as reported previously in similar setups in [3, 2, 4].

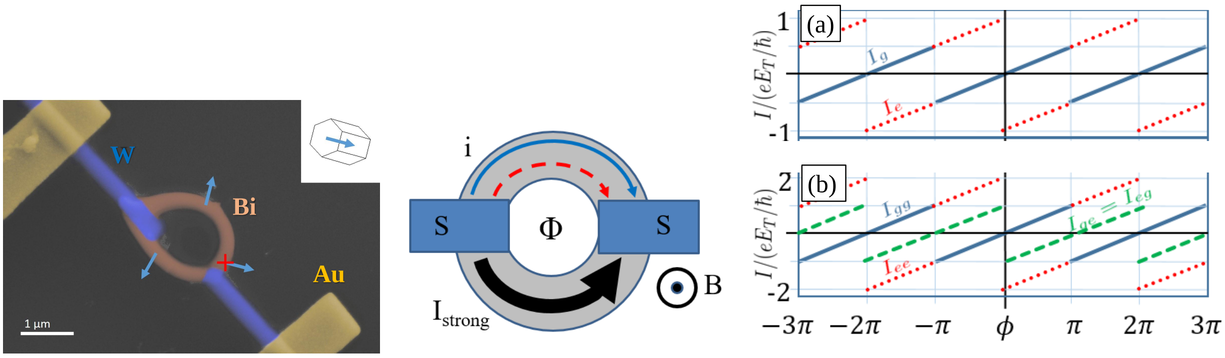

(a) (b) (c)

Figure 5 – (a) Scanning-electron-microscope image with false colors of the Bi^{ring} sample. It is a Bi ring (brown) with superconducting W compound contacts (blue) and Au leads (yellow). (b) Simplified sketch of the bismuth nanoring connected to two superconducting contacts (S), constituting an intrinsic asymmetric DC SQUID with two helical hinge states in the weak branch. (c) Supercurrent of the weak branch depending on the occupation configuration of the hinge(s). E_T is the Thouless energy. Top : one hinge in its ground (I_g) or excited (I_e) state. Bottom : two hinges in ground (g) or excited (e) states.

Going further, instead of looking only at the average switching current over hundreds of switching events, we measured its full distribution, see Fig.6. It revealed two major things.

1) First, there are two distinct switching current values for magnetic field values corresponding to a superconducting phase difference π across the (weak branch) ballistic junction. We interpret it as further proof of a perfect crossing of Andreev bound states, expected for topologically-protected states. Close to π, the junction can be in two different states, carrying opposite supercurrents.

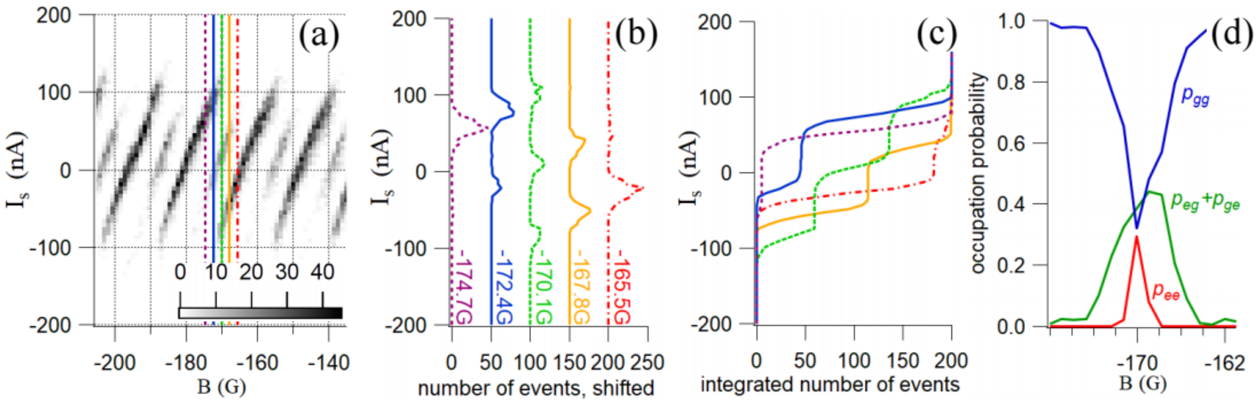

Figure 6 – Switching current distributions (histograms) as a function of out-of-plane magnetic field of the bismuth-nanoring based Josephson junction, with a $17Hz$ current bias ramp frequencies. (a) Switching current histograms over four flux periods around $-170G$. The number of switching events is coded in shades of grey. The background has been removed with a first order polynomial. (b) Histograms at magnetic fields around the jump at $-170G$ where $\phi = \pi$, see the corresponding colored lines in (a). Curves are shifted for clarity. (c) Integrated histograms close to the jump at $-170G$. (d) Field-dependence of the occupation probability of three supercurrent-carrying Andreev states, corresponding respectively to both hinges in the ground state (p_{gg}, blue curve), both hinges in the excited state (p_{ee},red curve), and one hinge in the ground state and the other in the excited state ($p_{eg} + p_{ge}$, green curve).

2) Second, there is a third, intermediate switching current value visible on an extended region around π, see Fig.6. We explain it by the presence of two identical long ballistic subjunctions in parallel, corresponding to two ballistic Andreev hinge states. When both subjunctions are in their ground state, the current is just doubled. When one is excited and the other is not however, the sum of the two is a shifted sawtooth, see Fig.5c. This situation is more likely to happen near π, where excited and ground states are close in energy.

For a topological superconducting hinge states, the Andreev bound state is helical and non-spin-degenerate, and it needs to absorb or release one quasiparticle with its environment to make the transition between its ground and excited state. We found long single-hinge-transition times of $\tau_{qp} \simeq 10ms$, corresponding to single-quasiparticle poisoning in Josephson junction microwave spectroscopy. This value is rather long compared to the average value found in the literature. In contrast, the inter-hinge-transition time was found to be extremely long compared to the literature, with $\tau_p \simeq 2ms \gg 1\mu s$. This process corresponds to simultaneous relaxation (or excitation) of the two hinges by exchange of pairs of quasiparticle with the environment. For a conventional junction, in which both helicities are not spatially separated, this process is very easy, as the junction can just exchange a pair of quasiparticles with the Cooper pair condensate, yielding transition times $\sim 1\mu s$. For a pair of helical Andreev hinge states however, their spatial separation, larger the superconducting coherence length, greatly reduces this possibility. We interpret it as a strong proof that the hinge states are not only ballistic, but also non-spin-degenerate (helical), as predicted for a second-order topological insulator.

This work was realized in collaboration with the theoreticians Dr. Yang Peng, Prof. Yuval Oreg and Prof. Felix von Oppen. It gave rise to an article, just published in Nature Physics [5]. The full analysis is available in chapter 4.

Outline

My thesis manuscript is organized as follows :
- The first chapter introduces all the theoretical ideas useful to the understanding of the work of my PhD. This chapter can be skipped if desired, and the relevant parts can be red when referred to by another chapter.
- The second chapter describes the processes and techniques used to realize the samples and the experiments.
- The third chapter presents the measurement and analysis of patterns resulting from the interference between the various Andreev states in bismuth-nanowire-based Josephson junctions.
- The fourth chapter presents the measurement and analysis of the switching current dynamics of Andreev states in a bismuth-nanoring-based Josephson junction, out of its proximity-induced superconducting state.
- The fifth chapter concludes this manuscript and discuss future developments.

The results on MCA are presented separately in the appendix. In appendix 6.7, we discuss the theory of MCA, involving the Edelstein effects. In appendix 6.2, we study the different sources of asymmetry (such as inductances) and their dependence on various parameters. We show that it is hard, although not impossible, to disentangle MCA from the other sources of asymmetry. In appendix 6.9.1, we present our measurements of an effective magnetic field $B_{eff} = \beta_N I$ in long bismuth nanowires with resistive contacts at $\simeq 100mK$, that we associate to MCA. In appendix 6.12, we show our measurements of $B_{eff} = \beta_N I$ in the resistive state and $B_{eff} = \beta_S I$ in the superconducting state of a bismuth-nanowire-based Josephson junction below and above its critical temperature. Still in the appendix, we provide more details on specific fabrication, measurement, and calculation points.

1 - Useful theoretical ideas

This theoretical chapter contains general ideas useful to understand the experiments done during my PhD. Some elements presented in this chapter result from considerable efforts and time investments during the course of my PhD, in order to clarify concepts that are relevant for the experiments we did during my PhD, but also other present and future experiments in the group.

First, we introduce spin-orbit coupling, fundamental element of time-reversal-symmetric topological insulators, and source of Magneto-Chiral Anisotropy. Second, we review the known transport properties of bismuth single-crystal in its bulk form as well as in finite-size nanostructures, and discuss its topological properties. Third, we give the basic ideas to understand how a supercurrent flows in a non-superconducting material by superconducting proximity effect, introducing the important Current-Phase Relations. We also introduce the concept of parity-protection specific to topological helical junctions. After that, we present the different types of experiments that can give (partial) access to the Current-Phase Relation(s) of the junction, probing the type of transport in the junction. Then, we develop in four sections the expected behavior of a junction with multiple conduction channels, exhibiting supercurrent interference with orbital and Zeeman-induced dephasing processes. Lastly, we present the theoretical models used to analyze the dynamics of the switching current in a conventional (spin-degenerate) Josephson junction, that we later adapt to model our experiment on topological (helical) hinge states of our bismuth-based Josephson junction.

To complete the theoretical analysis, appendix 6.1 provides an introduction to topological insulators, appendix 6.2 details the various sources of inductance and their respective behaviors, and appendix 6.7 properly introduce the spin-orbit-induced Mangeto-Chiral Anisotropy in both the resistive and superconducting states, necessary to understand the experiments reported in appendix 6.9 and 6.12.

If the reader is familiar with the theoretical aspects just mentioned, he can skip this chapter, and come back to the relevant parts when referred to in the experimental chapters 2, 3 and 4.

1.1 . Spin-orbit coupling

This section is dedicated to spin-orbit coupling (SOC). SOC couples the orbital degrees of freedom to the spin degree of freedom. It has important consequences on the band structure, lifting the spin-degeneracy when inversion symmetry is broken. Materials with SOC can exhibit non-trivial Fermi surface spin-textures, yielding spin-momentum locking, which is a key ingredient to spin-orbit-induced Magneto-Chiral Anisotropy arising from the Edelstein effect. The spin-momentum locking can be exploited for spintronics device. Moreover, the SOC term partially breaks time-reversal symmetry, which is a crucial element for time-reversal symmetric TI. This section introduces SOC and the spin-orbit-induced spin-texture. The Edelstein effects and some of their consequences are discussed in appendix 6.7.

1.1.1 . General form

Spin-orbit coupling (SOC) can be understood as a relativistic effect : an electron moving at a speed $\boldsymbol{v}$ in an electrostatic potential $-\boldsymbol{\nabla} V = -e\boldsymbol{E}$ experiences an additionnal magnetic field $\boldsymbol{B} = -\frac{1}{c^2}\boldsymbol{v} \times \boldsymbol{E}$, and its spin couples with this field with an interaction energy $-\mu_B \boldsymbol{B} \cdot \boldsymbol{\sigma}$. This leads to an additonnal term in the hamiltonian [6] (include the $1/2$ factor from Thomas precession) :

$$H_{SO} = \frac{\hbar}{4mc^2} \boldsymbol{\sigma} \cdot (\boldsymbol{\nabla} V \times \boldsymbol{v}) \tag{1.1}$$

with $\boldsymbol{\sigma} = (\sigma_x, \sigma_y, \sigma_z)$ and $\sigma_{x,y,z}$ are the 2x2 Pauli matrices.

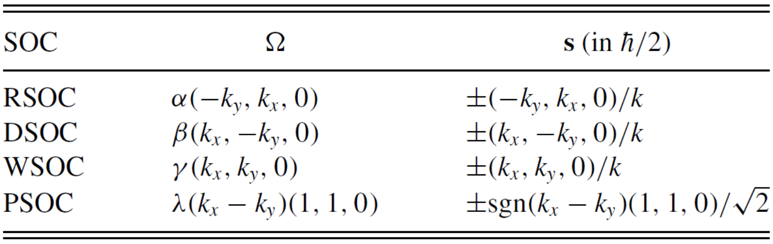

SOC	Ω	$\mathbf{s}$ (in $\hbar/2$)
RSOC	$\alpha(-k_y, k_x, 0)$	$\pm(-k_y, k_x, 0)/k$
DSOC	$\beta(k_x, -k_y, 0)$	$\pm(k_x, -k_y, 0)/k$
WSOC	$\gamma(k_x, k_y, 0)$	$\pm(k_x, k_y, 0)/k$
PSOC	$\lambda(k_x - k_y)(1, 1, 0)$	$\pm\mathrm{sgn}(k_x - k_y)(1, 1, 0)/\sqrt{2}$

Figure 1.1 – Spin-orbit field $\boldsymbol{\Omega}(\boldsymbol{k})$ and the related spin texture $\boldsymbol{s}(\boldsymbol{k})$ for Rashba (RSOC, parameter α), Dresselhaus (DSOC, parameter β), Weyl (WSOC, parameter γ) and persistent-spin-texture (PSOC, parameter λ). From [8].

The translation of this spin-orbit coupling in materials depends on their local crystallographic structure and their symmetries. We cite Rashba in 2006 [7] :

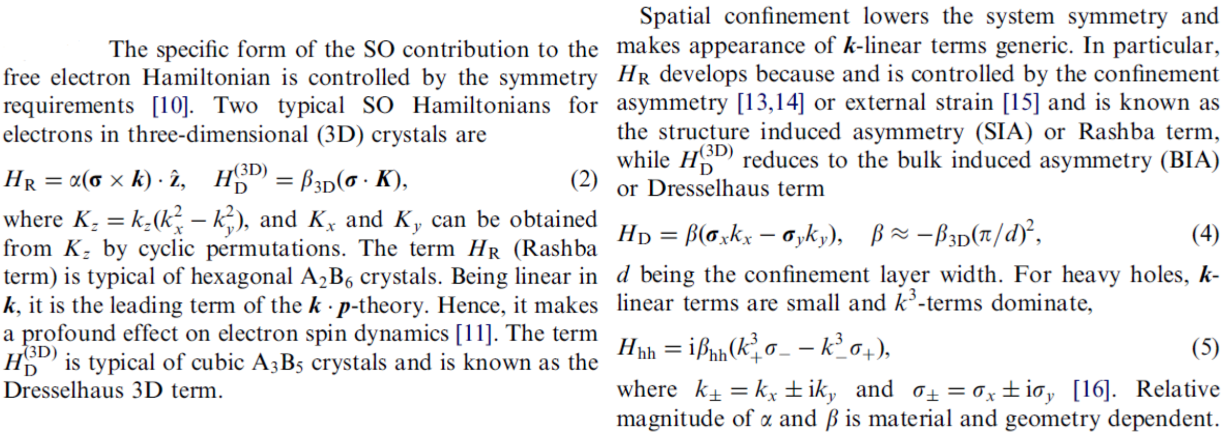

> The specific form of the SO contribution to the free electron Hamiltonian is controlled by the symmetry requirements [10]. Two typical SO Hamiltonians for electrons in three-dimensional (3D) crystals are
>
> $$H_\mathrm{R} = \alpha(\boldsymbol{\sigma}\times\boldsymbol{k})\cdot\hat{\boldsymbol{z}},\quad H_\mathrm{D}^{(3\mathrm{D})} = \beta_{3\mathrm{D}}(\boldsymbol{\sigma}\cdot\boldsymbol{K}), \tag{2}$$
>
> where $K_z = k_z(k_x^2 - k_y^2)$, and K_x and K_y can be obtained from K_z by cyclic permutations. The term H_R (Rashba term) is typical of hexagonal A$_2$B$_6$ crystals. Being linear in $\boldsymbol{k}$, it is the leading term of the $\boldsymbol{k}\cdot\boldsymbol{p}$-theory. Hence, it makes a profound effect on electron spin dynamics [11]. The term $H_\mathrm{D}^{(3\mathrm{D})}$ is typical of cubic A$_3$B$_5$ crystals and is known as the Dresselhaus 3D term.
>
> Spatial confinement lowers the system symmetry and makes appearance of $\boldsymbol{k}$-linear terms generic. In particular, H_R develops because and is controlled by the confinement asymmetry [13,14] or external strain [15] and is known as the structure induced asymmetry (SIA) or Rashba term, while $H_\mathrm{D}^{(3\mathrm{D})}$ reduces to the bulk induced asymmetry (BIA) or Dresselhaus term
>
> $$H_\mathrm{D} = \beta(\boldsymbol{\sigma}_x k_x - \boldsymbol{\sigma}_y k_y),\quad \beta \approx -\beta_{3\mathrm{D}}(\pi/d)^2, \tag{4}$$
>
> d being the confinement layer width. For heavy holes, $\boldsymbol{k}$-linear terms are small and k^3-terms dominate,
>
> $$H_\mathrm{hh} = \mathrm{i}\beta_\mathrm{hh}(k_+^3\sigma_- - k_-^3\sigma_+), \tag{5}$$
>
> where $k_\pm = k_x \pm \mathrm{i}k_y$ and $\sigma_\pm = \sigma_x \pm \mathrm{i}\sigma_y$ [16]. Relative magnitude of α and β is material and geometry dependent.

In [8], considering only SOC up to the first order in k , they analyze the influence of Rashba, Dresselhaus, Weyl and persistent-spin-texture SOC. They write :

$$\hat{H} = \frac{\hbar^2\boldsymbol{k}^2}{2m} + \boldsymbol{\Omega}(\boldsymbol{k})\cdot\boldsymbol{\sigma} \tag{1.2}$$

with $\boldsymbol{k} = (k_x, k_y)$ the wavevector in an orthonormal basis, $\boldsymbol{\Omega} = (\Omega_x, \Omega_y, \Omega_z)$ the spin-orbit field defined in $\boldsymbol{k}$-space as shown in Tab.1.1. This model does not include anisotropic bands ($m_x = m_y = m$) or anisotropic SOC parameters ($\alpha_x = \alpha_y = \alpha$, etc.).

For every spin-orbit field $\boldsymbol{\Omega}(\boldsymbol{k})$, the SOC $\boldsymbol{\Omega}(\boldsymbol{k})\cdot\boldsymbol{\sigma}$ breaks the spin degeneracy of the $\frac{\hbar^2\boldsymbol{k}^2}{2m}$ band, and split it into two spin-polarized bands, such that the expectation value of the spin operator $\boldsymbol{s}(\boldsymbol{k}) = \frac{\hbar}{2}\langle\boldsymbol{\sigma}\rangle$ is parallel to $\boldsymbol{\Omega}(\boldsymbol{k})$ (see Tab.1.1). This gives rise to a non-trivial spin-texture associated to the electrons close to the Fermi lines (2d equivalent of the Fermi surface of 3d materials).

It relates the electron wavevector $\boldsymbol{k}$ to its spin $\boldsymbol{s}(\boldsymbol{k})$ and is the origin of various interesting phenomenons, at the heart of the spintronics field, among others. We will exploit the Edelstein effect to measure the current-induced spin polarization in the non-linear transport responses of our bismuth samples (see appendix 6.7.3).

Notice that the SOC term $\boldsymbol{\Omega}(\boldsymbol{k})\cdot\boldsymbol{\sigma}$ is time-reversal-symmetric, as $\boldsymbol{\Omega}(-\boldsymbol{k})\cdot(-\boldsymbol{\sigma}) = -\boldsymbol{\Omega}(\boldsymbol{k})\cdot(-\boldsymbol{\sigma}) = \boldsymbol{\Omega}(\boldsymbol{k})\cdot\boldsymbol{\sigma}$. However, at a given $\boldsymbol{k}$, the SOC term breaks time-reversal-symmetry just like a Zeeman coupling term $-g\mu_B\boldsymbol{B}_{SO}\cdot\boldsymbol{\sigma}$ would do, with $B_{SO}(\boldsymbol{k}) = -\frac{\boldsymbol{\Omega}(\boldsymbol{k})}{g\mu_B}$ the spin-orbit Zeeman field. At the opposite wavevector $\boldsymbol{k}' = -\boldsymbol{k}$, $B_{SO}(\boldsymbol{k}') = -B_{SO}(\boldsymbol{k})$. This allows for a very special type of solid-state materials : time-reversal-invariant topological insulators (TI). This is discussed in appendix 6.1.

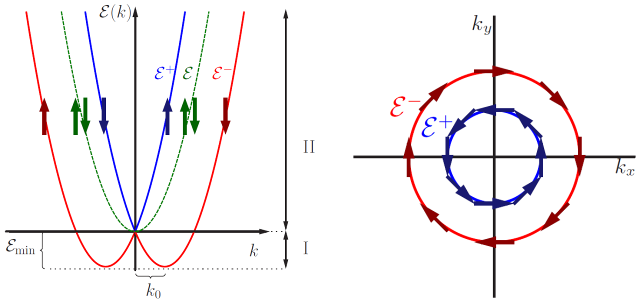

(a) (b)

Figure protected by copyright

See original publication
or ask for complete version

(c)

Figure protected by copyright

See original publication
or ask for complete version

(d)

Figure 1.2 – Splitting of energy bands due to spin-orbit coupling. (a) Energy spectrum of a 2DEG with Rashba SOC (solid lines) for one direction in $\boldsymbol{k}$-space. Blue and red represent the $+$ and $-$ branches from $\mathcal{E}_{\pm}(\boldsymbol{k}) = \frac{\hbar^2\boldsymbol{k}^2}{2m} \pm \alpha k$, respectively. $\mathcal{E}_{min} = -\alpha^2 m/(2\hbar^2)$ and $k_0 = \pm\alpha m/\hbar^2$. For comparison, the free electron parabola without SOC is shown (dashed line). The arrows indicate the spin expectation values with respect to a quantization axis perpendicular to $\boldsymbol{k}$. (b) Fermi lines ($\mathcal{E}_F > 0$) with corresponding spin expectation values (arrows). From [10]. (c) and (d) : sketches of the Fermi lines (solid lines) and associated spin expectation value $\boldsymbol{s}(\boldsymbol{k})$ (arrows) at $\mathcal{E}_F > 0$ for Dresselhaus SOC (c) and Weyl SOC (d). The red and blue lines correspond to the $\mathcal{E}_+$ and $\mathcal{E}_-$ branches, respectivelly. From [8].

1.1.2 . Spin-textures

In this subsection, we will study the influence of the various types of SOC on the band structure and on the Fermi lines. We will show that it gives rise to a spin-texture and spin-momentum locking. Let us first consider the influence of Rashba SOC ($\beta = \gamma = \lambda = 0$) on a 2d free electron gas (2DEG). It corresponds to an isotropic surface with a quadratic dispersion relation and where the inversion is broken locally in the z direction (perpendicular to the surface) only and uniformly everywhere in the surface. This is the main contribution to SOC in the surfaces of centrosymmetric non-magnetic materials. Following Edelstein [9] and [10], the hamiltonian writes :

$$\hat{H} = \frac{\hbar^2\boldsymbol{k}^2}{2m} + \alpha(k_x\sigma_y - k_y\sigma_x) \tag{1.3}$$

The eigenvalues are :

$$\mathcal{E}_{\pm}(\boldsymbol{k}) = \frac{\hbar^2\boldsymbol{k}^2}{2m} \pm \alpha k$$

.
The Rashba SOC splits the energy parabola of free electrons into two parabolas shifted by $\mathcal{E}_{min} = -\alpha^2 m/(2\hbar^2)$ and $k_0 = \pm\alpha m/\hbar^2$, as shown in Fig.1.2a. The spin expectation values $\boldsymbol{s}(\boldsymbol{k})$ on the Fermi lines are perpendicular to $\boldsymbol{k}$. We distinguish two energy regions : region I for $\mathcal{E} < 0$ and region II for $\mathcal{E} > 0$. The Fermi lines and their spin texture are different whether the Fermi energy $\mathcal{E}_F$ lies in region I or II. In region II, it forms concentric circle with the opposite spin textures but identical group velocities.In region I, its the opposite, with identical spin textures but opposite group velocities. The Fermi lines and their spin texture are shown in Fig.1.2b for $\mathcal{E}_F > 0$.

This analysis can be carried out for the different types of SOC [8], as shown in Figs.1.2c and 1.2d. We define the angle ϕ_k such that $\boldsymbol{k} = (k_x, k_y) = (k\cos\phi_k, k\sin\phi_k)$ and the angle ϕ_s such that $\boldsymbol{s}(\boldsymbol{k}) = (s_x, s_y) = (s\cos\phi_s, s\sin\phi_s)$. We see that the rotation of the spin expectation value differs for different type of SOC. We can define a spin-momentum angle : $\Delta\phi(\boldsymbol{k}) = \phi_s(\boldsymbol{k}) - \phi_k(\boldsymbol{k})$. For Rashba SOC, $\boldsymbol{s}(\boldsymbol{k})$ rotates with $\boldsymbol{k}$ following $\phi_s = \phi_k \pm \pi/2$, where $\pm$ depends on the energy branch, and $\boldsymbol{s}(\boldsymbol{k}) \perp \boldsymbol{k}$ on the Fermi lines ($\Delta\phi(\boldsymbol{k}) = \pm\pi/2$ constant), see Fig.1.2a. For Dresselhaus SOC, it rotates the opposite way $\phi_s = -\phi_k + \pi/2 \mp \pi/2$, and $\Delta\phi(\boldsymbol{k}) = -2\phi_k + \pi/2 \mp \pi/2$ explores all possible values for Fermi lines enclosing

Figure protected by copyright

See original publication
or ask for complete version

(a)

Figure protected by copyright

See original publication
or ask for complete version

(b)

Figure protected by copyright

See original publication
or ask for complete version

(c)

Figure 1.3 – Band structure (a) and corresponding horizontal slice (b) corresponding to an hamiltonian with isotropic Rashba SOC but anisotropic masses $m_x = 0.5 m_y$. (c) Fermi lines and spin-texture for a system with C_{3v} symmetry and an hexagonal warping term. From [10].

$\boldsymbol{k} = \boldsymbol{0}$ (making two full rotations for $\phi_k : 0 \longrightarrow 2\pi$), see Fig.1.2c. For Weyl SOC, $\phi_s = \phi_k + \pi/2 \mp \pi/2$ and $\boldsymbol{s}(\boldsymbol{k}) \parallel \boldsymbol{k}$ ($\Delta\phi(\boldsymbol{k}) = \pi/2 \mp \pi/2$ constant), see Fig.1.2d.

The analysis we presented so far only accounts for isotropic band structures ($m_x = m_y = m$ in the kinetic term without SOC) and isotropic SOC parameters ($\alpha_x = \alpha_y = \alpha$, etc.), which only is an approximation for certain real systems. In the case of bismuth crystal, there are strong anisotropies in the surface states, see part 1.2.2. In [10], they study the modifications of the band structure in the cases of anisotropic bands or SOC parameters for Rashba SOC. They write, for a system with a C_{2v} symmetry like the (110) surface of an fcc crystal :

$$\hat{H} = \frac{\hbar^2 k_x^2}{2m_x} + \frac{\hbar^2 k_y^2}{2m_y} + \alpha_x k_x \sigma_y - \alpha_y k_y \sigma_x \tag{1.4}$$

Fig.1.3a and 1.3b shows the band structure and a slice in the case $m_x = 0.5 m_y$ and $\alpha_x = \alpha_y$. We see that the Fermi lines can change drastically depending on $\mathcal{E}_F$.

For a system with C_{3v} symmetry, such as the (111) surface of fcc crystals and all the graphene-alike material, they write :

$$\hat{H} = \frac{\hbar^2 k^2}{2m} + \alpha(k_x \sigma_y - k_y \sigma_x) + \Lambda(k_+^3 + k_-^3)\sigma_z \tag{1.5}$$

with $k_\pm = k_x \pm i k_y$, and where one miror plane was chosen to be along $\hat{y}$. The $\Lambda \neq 0$ terms, referred as hexagonal warping, appears when there is a structural in-plane asymmetry, like a buckled structure. The spin texture is illustrated in Fig.1.3c. It ressemble the spin-texture of Bi(111) surface states, although with notable differences, see part 1.2.2, and could impact some of its transport properties like the magneto-chiral anisotropy.

1.1.3 . Bismuth inversion-symmetric unit cells

In the previous subsection, we introduced the lifting of the spin degeneracy and the generation of spin-textures for inversion-breaking unit cells.

But in the case of bismuth crystal, its bulk unit cell is centro-symmetric, implying $\mathcal{E}_{-\boldsymbol{k}s} = \mathcal{E}_{\boldsymbol{k}s}$ for the energy bands. Furthermore, it is time-reversal symmetric, implying $\mathcal{E}_{-\boldsymbol{k}s} = \mathcal{E}_{\boldsymbol{k}\bar{s}}$, where $\bar{s}$ is the spin opposite to s. Combining the two yields, for centro-symmetric bulk crystals :

$$\mathcal{E}_{\boldsymbol{k}s} = \mathcal{E}_{\boldsymbol{k}\bar{s}} \tag{1.6}$$

and the bands are spin-degenerate.

In such a case, does SOC have any influence on centro-symmetric bulk crystals ? The answer is yes. On the scales of the atoms, there still exists local potential gradients. It scales with the atomic number Z as Z^4. Because bismuth is the heaviest stable element with $Z = 83$, between lead ($Z = 82$) and polonium

($Z = 84$), SOC greatly influences its bulk and surfaces band structure. For this reason, bismuth is widely used for 3d materials that benefit from high SOC, such as the 3d topological insulators Bi_2Se_3, Bi_2Te_3, $BaBiO_3$, $Bi_{1-x}Sb_x$, BiTeI, $(Bi_{1-x}Sb_x)_2Te_3$. Just above bismuth in the periodic table is antimony, with $Z = 51$. The only thing that differs Sb from Bi crystals is the strength of the SOC [11]. The SOC in Bi crystal is also responsible for its topological character, see part 1.2.4. One can dope it with Sb, making $Bi_{1-x}Sb_x$, to change its band structure enough to transform it into a strong topological insulator. Moreover, the surfaces states of bismuth show large spin-plitting that influence its transport properties and can be exploited for spintronics, see next subsection.

1.2 . The case of bismuth single-crystal

Elemental Bi is the heaviest stable element with $Z = 83$, between lead ($Z = 82$) and polonium ($Z = 84$), which makes it ideal for synthesizing materials with strong spin-orbit coupling (scaling as Z^4), of great interest to build topological insulators or spintronic devices, see part 1.1 and appendix 6.1.

Bismuth single-crystal is one of the most studied material and is yet not fully understood. It was the material where were first discovered diamagnetism, the Seebeck effect, the Nernst effect, Shunikov-de Haas oscillations, and de Haas-van Alphen oscillations [12]. Very recently, it was proposed and demonstrated that single-crystal Bi is the first 3d higher order topological insulator discovered [13].

This PhD work contributes to the scientific effort on this topic, by measuring proximity induced superconducting current through $\simeq 100nm$ wide bismuth single-crystal nanowires. As we discuss in the following, the nanowire geometry allows us to reduce the contribution of bulk and surface states to conduction, enhancing the relative contribution of the topologically protected 1d helical hinge states. We present here several characteristics of bismuth single-crystal structure, starting with bulk, following by surfaces, and finishing with the topological nature of nanoscopic bismuth single-crystal structures (such as nanowires) and their conducting modes.

1.2.1 . Bulk bismuth

Elemental bismuth belongs to the group V elements, just beneath Sb in the periodic table of elements, with s^2p^3 outer shell electronic structure. At the pressures and temperatures used in our experiments ($P < 1.1bar$, $T < 320K$), bismuth crystallizes in a rhombohedral structure with space group $R\bar{3}m$ and an angle of $57.35°$. It is close to a fcc structure, with every other atom slightly shifted from its fcc position, see Fig.1.4a. It results in two Bi atoms per unit cell, with a total of 10 orbitals (two of which being at much lower energy and very far away from the Fermi energy), and a semi-metallic behavior [12]. The crystal has three-fold rotational symmetry (C_3) with respect to the trigonal axis, and inversion symmetry.

One-body clean bulk Bi calculations show no indirect gap at the Fermi energy, and a semi-metallic band structure with three skewed-ellipsoidal electron pockets at L points and one ellipsoidal hole pocket at the T point, strongly anisotropic, see Figs.1.4b and 1.4c. For numerical values of bulk band structure, we refer to the article from Liu and Allen [14], where the authors use a sp^3 tight-binding model to third nearest neighbors designed to match the state-of-the-art experimental data of 1995. The direct band gap at the L points (below E_F) is as small as $\simeq 14meV$, with $E_F \simeq 27meV$ above the bottom of the conduction band. The dispersion relation is Dirac-like, and yields very high g-factor $g \sim 1000$ [12]. The effective electron mass is very small and anisotropic, with $m_e < 0.26m_0$ along the bisectrix axis and $m_e \lesssim 0.0026$ along the trigonal axis. The direct band gap at the T point is about $\simeq 370meV$, with $E_F \simeq 11meV$ bellow the top of the valence band. The effective hole mass is $m_h \lesssim 0.068m_0$ along the bisectrix axis and $m_h = 0.6 - 0.7m_0$ along the trigonal axis.

These pockets yield an average Fermi velocity of $\langle v_F \rangle \simeq 6 \times 10^5 m.s^{-1}$, low electrons and hole densities

$n \simeq p \simeq 3 \times 10^{17} cm^{-3}$, as well as long Fermi wavelength of typical value $\lambda_F \simeq 50nm$. The long λ_F is responsible for quantum size effects arising from quantum confinement, yielding semi-metal to semi-conductor transitions in Bi thin film and nanowires of dimensions $d \simeq 30nm \sim \lambda_F$ [15, 16].

These small gaps at L-points require careful consideration on both the theoretical and experimental sides, as they are responsible for important responses (with inter-band effects such as magnetization and topological phases) of the system and can be affected by the lack of computational precision, or by additional effects deviating from the idealized system (such as quantum size effects or strain). Such issues are discussed in part 1.2.4, related to the topological nature of small bismuth structures.

In the next subsections, we extend our analysis to finite size bismuth single-crystal, showing metallic spin-split surface states, as well as spin-split propagating 1d edge states. We discuss more in depth the works done on Bi(111) bilayer(s) and surface defects, as it is a precursor of the discovery of higher order topology in bismuth.

Figure protected by copyright

See original publication
or ask for complete version

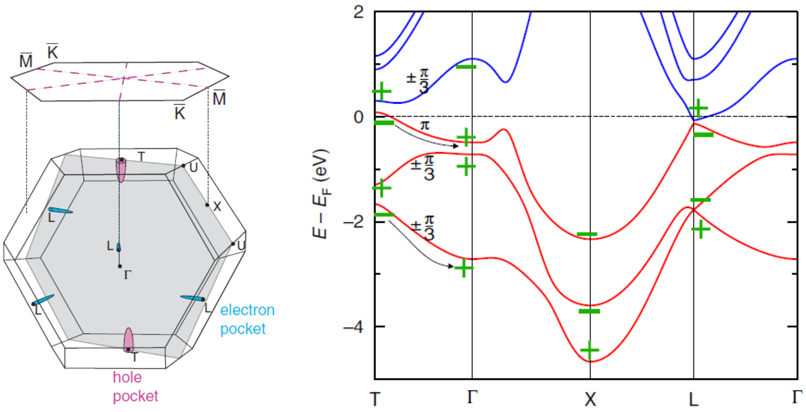

(a) (b) (c)

Figure 1.4 – Bulk structure of Bi in real-space and in reciprocal space, and spectrum. (a) Left : rhombohedral unit cell (dashed green lines) together with the hexagonal unit cell (dashed pink lines). Not all the atoms are shown. Blue and red mark the two atoms in the rhombohedral unit cell. The solid green and pink lines are the vectors spanning the rhombohedral and hexagonal lattice, respectively. The three cartesian axes are : bisectrix (C_1,y), binary (C_2,x) and trigonal (C_3, z). Right : illustration of the pseudocubic character of the structure together with the rhombohedral unit cell. From [17]. (b) Bulk Brillouin zone of Bi and projection on the (111) surface. The Fermi surface is sketched (not to scale) with electron pockets at L-points in blue and hole pockets at T-point in red. The $\Gamma - T$ line corresponds to the C_3 axis and the [111] direction in real space. From [17]. (c) Band structure of bismuth with inversion eigenvalues (green) and C_3 eigenvalues on the $\Gamma - T$ line (black). E_F denotes the Fermi energy. Black arrows indicate the two valence bands contributing to the C_3-eigenvalue -graded band inversion. From [13].

1.2.2 . Surfaces of bismuth single-crystal

Regardless of its topological nature, all surfaces of thick bismuth single-crystals are metallic, with higher density of states than the bulk ($n \simeq 3 \times 10^{13} cm^{-2}$ at point $\bar{\Gamma}$), and lower Fermi velocity (smaller by a factor ~ 10 in Bi(111) surface states on the hole pockets) [17]. They host propagating spin-splitted surface states, as demonstrated by Spin and Angle Resolved Photo-Emission Spectroscopy ((S)ARPES). Indeed, surfaces break inversion symmetry, allowing for SOC splitting of the bands, resulting in spin-textured Fermi surfaces (see part 1.1). What distinguish trivial from topological insulators is that, for first order 3d topological insulators, these surface states are guaranteed to exist and cannot be gaped out by time-reversal symmetric perturbations without closing a bulk gap.

The crystal surfaces are indexed by three numbers m, n, o, as (mno), which correspond to the surface plane which is perpendicular to the reciprocal lattice vector with coefficients (m, n, o), using the rhombohedral real-space lattice vectors depicted as green lines in Fig.1.4a (see [17] for more).

Each atom has three equidistant nearest neighbors $(4.54\mathring{A})$, other three equidistant next-nearest neighbors being slightly further away $(4.72\mathring{A})$. This results in buckled bilayers of atoms with surfaces oriented in the (111) direction, in which each atom is covalently bonded to its three nearest neighbors, forming a buckled hexagonal structure, see Fig.1.4a right and Fig.1.5a. The next nearest neighbors are in the adjacent bilayers and the bonding within each BL is much stronger than the van der Waals inter-bilayer bonding [18, 17]. The distance between two bilayers is $\simeq 0.39nm$. With this type of bonding, we see that only an infinite (111) surface would exhibit no dangling bonds. This bilayer structure plays a crucial role in the discussion of 1d (edge) states, as a bismuth bilayer is a QSHI [19, 20].

In this subsection, we focus on surface states of thick bismuth single-crystal with three orientations : Bi(111), Bi(110), and Bi(100), as reviewed in [17]. Their related real-space crystal structures, projection of bulk states in reciprocal space, and experimental probes of their Fermi surfaces are shown in Figs.1.5, 1.6, and 1.7. For Bi(111), the projection of bulk states on the 2d surface is illustrated in Fig.1.4b, and Fig.1.5c shows additional spin information obtained by SARPES.

The spin textures of Bi(110) [21, 22] and Bi(111) [23, 24, 25, 26] has been studied by SARPES, and shows large spin-splitting due to high SOC. In [27, 28], the spin-splitting of (111) surface states at $\bar{\Gamma}$ is found to have Rashba-like SOC with large parameter $\alpha \simeq 0.56eV.\mathring{A}$, wavevector offset $k_0 \simeq 0.05\mathring{A}^{-1}$, and energy offset $\mathcal{E}_{min} \simeq 14meV$, see part 1.1.2 for the meaning of these values. In [25, 26] however, in addition to the strongly anisotropic Fermi surface, the authors find large deviations from the Rashba SOC, with spin-polarization alternating between in- and out-of-plane perpendicular to the wavevector.

Figure protected by copyright

See original publication
or ask for complete version

(a)

Figure protected by copyright

See original publication
or ask for complete version

(b)

Figure protected by copyright

See original publication
or ask for complete version

(c)

Figure 1.5 – Bi(111) surface. (a) Truncated-bulk structure of Bi(111). The dark solid lines indicate covalent bonds between the atoms within the bilayers. Top : top view of the first three atomic layers. Each layer consists of a two-dimensional trigonal lattice. The mirror planes of the structure are shown as dashed lines. Bottom : side view of the first four layers along a mirror plane. From [17]. (b) Photoemission intensity at the Fermi level of the (111) surface of a thick cleaved Bi single-crystal. k_x and k_y are the parallel components of the electron momentum along the $\bar{\Gamma}\breve{}\bar{M}$ and $\bar{\Gamma}\breve{}\bar{K}$ direction, respectively. From [29]. (c) Spin-split band dispersion of the 7 BL Bi(111) films obtained from SARPES overlapped on the dispersion obtained by non-spin-resolved ARPES. The spin-up (-down) components are shown by the solid triangle pointing up (empty triangles facing down) and the magnitude of the spin polarization is shown by the size of the markers. The non-polarized states are shown by open circles. The spin orientation is in-plane and perpendicular to the wavevector. From [24].

According to [22], the surface states of Bi(111) and Bi(110) are well confined to the vicinity of the surface, over $\lesssim 10$ bilayers, whereas the Bi(100) surface state penetrates deeper in the bulk, over more than 22 bilayers [30]. Many later works however, suggest a much larger penetration depth for (111) surface states, leading to hybridization between top and bottom surface states for thin Bi(111) films. It is found to be ~ 80 bilayers for [31, 32] (experimental), ~ 200 bilayers for [33] (theoretical), and up to ~ 1000 bilayers for [34] (theoretical). This penetration depth is important when discussing quantum size effects, particularly

Figure protected by copyright

See original publication
or ask for complete version

(a)

Figure protected by copyright

See original publication
or ask for complete version

(b)

Figure protected by copyright

See original publication
or ask for complete version

(c)

Figure 1.6 – Bi(110) surface. (a) Truncated-bulk structure of Bi(110). The dark solid lines indicate covalent bonds between the atoms within the bilayers. Top : top view of the first two atomic layers. The single mirror plane of the structure is shown as dashed line. Bottom left and right : side views of the first eight layers (four double layers) perpendicular and parallel to the mirror plane, respectively. Dashed lines on the first layer atoms indicate dangling bonds. (b) Bulk Brillouin zone of Bi and projection on the (110) surface. The elements of the bulk Fermi surface are indicated but not to scale. (c) Photoemission intensity at the Fermi energy of the (110) surface of a thick mechanically polished Bi single-crystal (cleaned by cycles of Ar and Ne sputtering and annealing). From [17].

Figure protected by copyright

See original publication
or ask for complete version

(a)

Figure protected by copyright

See original publication
or ask for complete version

(b)

Figure protected by copyright

See original publication
or ask for complete version

(c)

Figure 1.7 – Bi(100) surface. (a) Truncated-bulk structure of Bi(100). The dark solid lines indicate covalent bonds between the atoms within the bilayers. Top : top view of the first four atomic layers. The single mirror plane of the structure is shown as dashed line. Bottom : side view of the first four layers parallel to the mirror plane. Dashed lines on the first layer atoms indicate dangling bonds. (b) Bulk Brillouin zone of Bi and projection onto the (100) surface. The elements of the bulk Fermi surface are indicated, but not to scale. (c) Normalized photoemission intensity at the Fermi level of the (100) surface of a thick mechanically polished Bi single-crystal (cleaned by cycles of Ar and Ne sputtering and annealing). Black corresponds to high intensity. The solid line is the Brillouin zone boundary. From [17].

when trying to deduce the topology of bulk Bi from the surface states of thin Bi films.

The surfaces states dominate transport in nanostructures, as discussed in the next subsection. Their spin-texture, exhibiting spin-momentum locking, may be the main cause of Magneto-Chiral Anisotropy in both the resistive and superconducting states, see appendix 6.7 for more details.

1.2.3 . Bismuth nanowires

Single-crystal bismuth makes for very interesting nanowires, with its exceptional semi-metallic band structure, exhibiting very small gaps and effective carrier masses. Its large λ_F is predicted to drive semi-metal to semiconductor transitions in circular nanowires with diameters between $40nm$ and $55nm$, for nanowire axes oriented along the binary and trigonal axes, respectively [16]. Nanowires have been first studied for their thermoelectricity, exploiting the Seebeck effect [35]. The large spin-splitting of surface states due to SOC may also have applications in spintronics, exploiting the spin-Hall and Edelstein effects, see appendix 6.7.1.

The transition was found to happen for diameters $\lesssim 40nm$ [36, 37], where the transport via the surface states completely dominates over the gaped bulk states. For diameters $\lesssim 150nm$ already, the confinement of bulk states becomes important [38] and transport changes to surface conduction [2, 39]. Additionally, surface state also experience quantum size effect ($\lambda_F^S \sim 4nm$), and certain surface states may hybridize, changing the surface carrier densities and velocities, as mentioned in the end of the previous subsection.

In addition to its exceptional spectral properties, bismuth single-crystal is a higher order topological insulator, as discussed in the next subsection. There is an issue however, that is that it is not an insulator to begin with, but a semi-metal. This issue is discussed in the next subsection, but we state here that it leads to an experimental limitation for transport measurements : the topological hinge states signature of its HOTI character represent only a small contribution to transport, in parallel with surface and bulk states conduction.

During this PhD, we used bismuth nanowires of transverse dimensions between 100 and $300nm$ to enhance the relative contribution of topological hinge states to transport, see part 2 for the sample fabrication. To further reduce the contribution from diffusive surface states, we induced superconducting correlations in the nanowire by proximity effect with superconducting contacts, see part 1.3.5 for the theoretical aspect. This method has proved successful in the past, see [40, 3, 2, 4].

1.2.4 . Higher-order Topology in bismuth

In this subsection, we review theoretical predictions and experimental measurements involving the topological character of bismuth single-crystal. For an in depth discussion on Quantum Spin-Hall Insulators (QSHI), 3d (first-order) Topological Insulators (TI), and Higher-Order Topological Insulators (HOTI), see appendix 6.1.

On top of its exceptional spectrum properties, bismuth single-crystal has a rich Berry curvature phenomenology. The 2d bilayer of Bi was predicted to be a QSHI, hosting one helical pair of states on its edges [19, 20] (see Fig.1.8a), with a QSHI phase surviving up to eight bilayers [41, 42] in parallel with surface states [22] (see Figs.1.8b and 1.8c). On the other hand, 3d bulk was predicted to be a topologically trivial semi-metal [43]. However, the topological nature of bulk bismuth depends critically on the states at the L-points that show a small gap. If the gap at L-points is inverted, for example by alloying with the strong topological insulator Sb with the same structure, bulk bismuth-antimony alloy becomes a strong topological insulator with non-vanishing weak topological indices (1 ;111) [43].

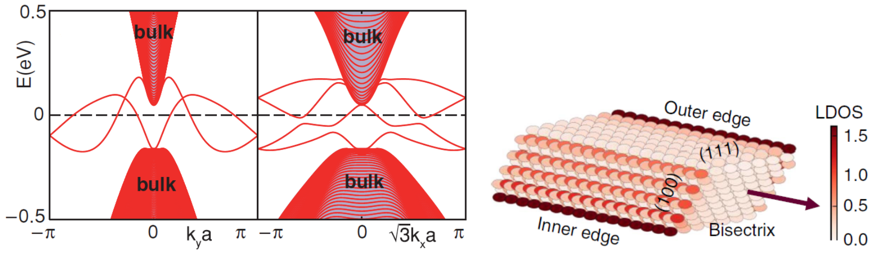

Figure protected by copyright

See original publication
or ask for complete version

(a) (b) (c)

Figure 1.8 – Theoretical predictions of propagating hinge states in Bi(111). (a) Left and right : energy bands of a Bi(111) zigzag- and armchair-edge bilayer ribbons, respectively, with a width of 20 unit cells, calculated from a refined tight-binding model. Both types of ribbon show one Kramers pair of edge states connecting the bulk valence band to the bulk conduction band, consistent with its QSHI character. From [20]. (b) and (c) : local density of states and spectrum, respectively, of a Bi nanowire obtained by stacking 5 Bi(111) zigzag-edge bilayers ribbons that are 7 atoms wide, calculated from the Liu-Allen tight-binding model [14]. κ_{loc} in (c) is a measure of the transverse spatial extension of the state. The bright yellow points correspond to hinge states, see LDOS in (b). From [2, 3].

To deduce the topological nature of Bi single-crystal, one experimental solution is to look for topologically protected boundary states, that is 1d helical edge states for small 2d bilayer stacks, or 2d helical surfaces states for 3d bulk bismuth. However, due to the finite size effects discussed in the previous paragraph and at the end of part 1.2.2, the topological nature of bismuth single-crystal is still controversial, as shown in the discussions surrounding Bi(111) films [18, 44]. One the one hand the calculated spectrums of Bi(111) films depend on the model and computational technique that are used, and on the other hand the experiments performed on films are hard to extrapolate to bismuth 2d bilayer stacks or 3d bulk. The spectrum of Bi(111) films has been reported to depends on thickness [22, 41, 42, 33, 31, 32, 34], strain [45], terminations [46], and top and bottom surfaces symmetry [44].

Several experiments on small bilayer structures on Bi(111) surfaces clearly shown the existence of propagating 1d edge states. It was first argued that a quantized $2e^2/h$ conductance plateau found in STM originates from edge conduction over a Bi bilayer stuck to the Bi(111) surface and to the STM tip [47]. Soon after, STM measurements on Bi(111) bilayer islands on top of (thick) Bi(111) surfaces (see Fig.1.9a for illustration) revealed edge states with a inverse square-root dependence on energy on one type of zigzag edges (parallel to a $\bar{\Gamma} - \bar{K}$ direction) typical of 1d states [48]. This work also shows strongly suppressed backscattering from the quasiparticle interference pattern of the LDOS. Moreover, the same 1d edge states behavior was observed on a two-bilayers hexagonal dip, see Fig.1.9c. These observations were later confirmed by STM measurement by [49] (underlying film thickness $d \simeq 96$ bilayers), [50] ($d \geq 15$ bilayers) and [51] ($d \leq 9$ bilayers), and by SARPES measurements by [52]. In [52], the authors found on Bi(111) surface ($d \simeq 15$ bilayers) with triangular bilayer islands (see Fig.1.9a) 1d dispersive states corresponding to zigzag edge states along $\bar{\Gamma} - \bar{K}$ directions (independent of film thickness), with parameters $k_0 = 0.17\mathring{A}^{-1}$, $\mathcal{E}_{min} = 68meV$, $\alpha = 0.80eV.\mathring{A}$, $m^* = 1.62m_0$ (see Fig.1.9b), and spin polarization perpendicular to the edge with equal in-plane and out-of-plane components. In [53], the authors measured signatures of Majorana zero-modes on a hinge of Bi proximitized by superconducting Nb and magnetic Fe, which constitute a first necessary step toward topological quantum computation.

Figure protected by copyright

See original publication
or ask for complete version

(a)

Figure protected by copyright

See original publication
or ask for complete version

(b)

Figure protected by copyright

See original publication
or ask for complete version

(c)

Figure 1.9 – Experimental data showing propagating 1d states along zigzag-edges of few-bilayers structures on a Bi(111) surface. (a) Atomic force microscope image of a Bi(111) thin film ($d = 15$ bilayers) featuring bilayer islands with zigzag-edges parallel to the $\bar{\Gamma} - \bar{K}$ direction. From [52]. (b) Second derivative of ARPES intensity near E_F along the $\bar{\Gamma} - \bar{K}$ direction, compared with a calculated band dispersion (pink solid lines) for the edge state of a bilayer island such as shown in (a), with Rashba SOC parameters $k_0 = 0.17\mathring{A}^{-1}$, $\mathcal{E}_{min} = 68meV$, $\alpha = 0.80eV.\mathring{A}$, $m^* = 1.62m_0$. From [52]. (c) Topography close to the hexagonal diatomic depression on a Bi(111) surface of a Bi single-crystal, false-coloured with differential conductance at $E = 183meV$, obtained with a scanning tunneling microscope. High conductance (red) is observed at every other edge of a hexagonal pit-like defect. From [48].

Our group took a different approach, making single-crystal bismuth nanowires of length $> 1.5\mu m$ and transverse sizes $< 300nm$, and measuring transport properties in its proximity-induced superconducting state (see chapter 2 for the fabrication methods and results). The nanowires are deposited on substrates with a thick amorphous layer of insulating oxide, such that it rules out all suspected effects involving interaction with the underlying Bi substrate in the Bi(111) surface discussions. The study of their switching currents as a function of magnetic field and superconducting phase difference revealed ballistic 1d conduction path along their hinges [40, 3, 2] (see Fig.1.10), consistent with the observations of QSHI-like, edge-dependent states reported earlier. Later ac susceptibility measurements showed absorption peaks at the Andreev level crossings, whose temperature and frequency dependencies point to protected topological crossings [4].

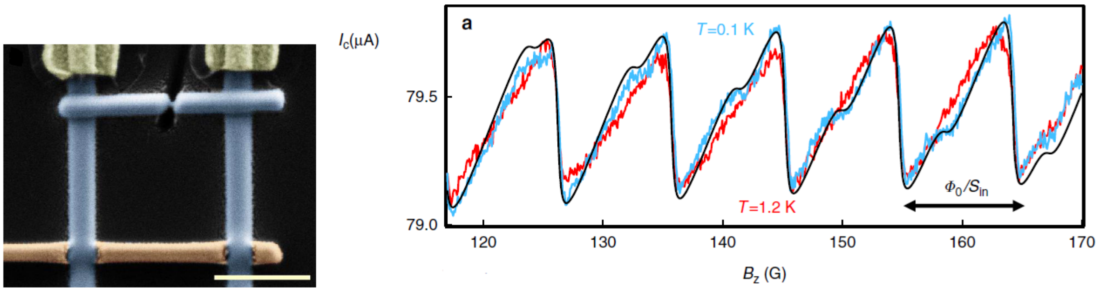

(a)

(b)

Figure 1.10 – Experimental data showing propagating narrow ballistic states along sides of a single-crystal Bi nanowire with (111) top surface, connected to superconducting contacts, forming a long Josephson junction. (a) Scanning electron microscope image with false colors of the Bi nanowire (brown), with superconducting disordered W compound contacts (blue) and Au leads (yellow). The scale bar is $1\mu m$ long. The weak link (top) in parallel with the Bi nanowire form an asymmetric DC SQUID whose switching current yields the current-phase relation of the Bi nanowire Josephson junction, with the superconducting phase difference controled by the magnetic flux inside the SQUID surface (see later discussions in part 1.5.3). (b) Switching current I_c of the asymmetric DC SQUID hosting a Bi nanowire junction as a function of out-of-plane magnetic field B_z. It shows two superimposed sawtooth with periods close to $9.5G$ but differing by 10%, corresponding to long ballistic supercurrent-carrying states on the opposite sides of the nanowire.

Additionally, let us mention that other bismuth surfaces may exhibit non-trivial topological properties. According to [20] calculations, Bi(110) 2-monolayer is a trivial insulator, but is a QSHI with a huge $\simeq 90\ meV$ gap according to [54] calculations and STM measurements of [55]. Magnetoresistance measurements of [110] nanoribbons (in hexagonal basis) of thickness $30-120nm$ show surface states with Berry curvature consistent with topological surface states. SARPES on Bi(114) surface shows 1d spin-plit propagating states along the $\bar{\Gamma}-\bar{X}$ direction [56], the (114) surface corresponding to alternating edges of tilted (111) bilayers. Lastly, STM measurements performed on Bi(110) surface ($d > 30$ bilayers) step edges also showed the presence of 1d states at particular edges [57].

In 2018, thanks to a newly developed topological classification (see appendix 6.1.5 for more details), bulk bismuth single-crystal was classified as a second-order topological insulator [13], a sub-class of higher-order topological insulator (HOTI). It features two band inversions, whose presence is not captured by the first-order topological index, which is only sensitive to the parity of band inversions. Bismuth crystal has inversion symmetry and C_3 symmetry with respect to its trigonal [111] axis (rhombohedral notation). It has eight time-reversal invariant momenta (TRIM(s)) noted $Y \in \Gamma, T, X_i, L_i$, with $i = 1, 2, 3$, see Fig.1.4b.

The bulk states for each band i and at each TRIM Y can be labeled by their C_3 and inversion operator eigenvalues, indicated as $\rho_{i,Y} = \pi$ or $\pm\frac{\pi}{3}$ and $\xi_{i,Y} = +$ or $-$ in Fig.1.4c, respectively. The inversion operation always relates states at TRIM to themselves, while C_3 operation relates states at different TRIMs for L-points and X-points. For inversion symmetric crystals, a topological index $\nu_Y = \prod_{i\in occ} \xi_{i,Y}$ can be defined [58], the so-called Fu-Kane index, where the product is over the occupied bands. In [13], the authors further define C_3 subspaces topological index $\nu_Y^{(\pi)}$ and $\nu_Y^{(\pm\pi/3)}$, where the product is restricted to the states with $\rho_{i,Y} = \pi$ and $\pm\frac{\pi}{3}$ eigenvalues, respectively. By C_3 symmetry, a band inversion affects equally all topological index of C_3 related TRIMs, such that $\nu_{X_1} = \nu_{X_2} = \nu_{X_3}$ and $\nu_{L_1} = \nu_{L_2} = \nu_{L_3}$, but also their C_3 subspaces topological index, such that a single band inversion translates into one band inversion in the π-subspace and a double (which equals no) band inversion in the $\pm\frac{\pi}{3}$-subspace.

The Fu-Kane first-order strong topological index is given by $\nu = \nu_\Gamma \nu_T \nu_{L_1} \nu_{L_2} \nu_{L_3} \nu_{X_1} \nu_{X_2} \nu_{X_3} = \nu_\Gamma \nu_T \nu_{L_1} \nu_{X_1} = (+1)(-1)^2(-1)^2(-1)^2 = +1$ (see Fig.1.4c), indicating no guaranteed topologically-protected surface states. Nonetheless, the topological index, counting the parity of the number of band inversions, can be evaluated within each C_3-subspace by :

$$\nu^{(\pi)} = \nu_\Gamma^{(\pi)} \nu_T^{(\pi)} \nu_{X_1} \nu_{L_1} \quad \text{and} \quad \nu^{(\pm\pi/3)} = \nu_\Gamma^{(\pm\pi/3)} \nu_T^{(\pm\pi/3)} \tag{1.7}$$

According to this analysis, we can distinguish three cases :
- for $\nu = \nu^{(\pi)} \nu^{(\pm\pi/3)} = -1$, the material is a strong ($\mathbb{Z}_2$) topological insulator with an odd number of band inversions
- for $\nu = \nu^{(\pi)} \nu^{(\pm\pi/3)} = +1$ and $\nu^{(\pi)} = \nu^{(\pm\pi/3)} = +1$, the material is a trivial insulator with no odd number of band inversions
- for $\nu = \nu^{(\pi)} \nu^{(\pm\pi/3)} = +1$ and $\nu^{(\pi)} = \nu^{(\pm\pi/3)} = -1$, the material is a HOTI with odd numbers of band inversions within each C_3-subspaces

Looking at the C_3 eigenvalues on the $\Gamma - T$ line in Fig.1.4c together with the inversion eigenvalues, we get :
- $\nu^{(\pm\pi/3)} = \nu_\Gamma^{(\pm\pi/3)} \nu_T^{(\pm\pi/3)} = [(+1)(+1)][(-1)(+1)] = -1$
- $\nu^{(\pi)} = \nu_\Gamma^{(\pi)} \nu_T^{(\pi)} \nu_{X_1} \nu_{L_1} = (+1)(-1)[(-1)^2(+1)][(-1)^2(+1)] = -1$

We thus conclude that bulk bismuth single-crystal is a HOTI. This double band inversion, one in each subspace, yields topologically protected propagating 1d helical states located at hinges preserving the C_3 symmetry of the crystal, as illustrated in Fig.1.11, see appendix 6.1.5 for a more detailed discussion on HOTIs. Moreover, the stability of the hinge states are not limited to symmetry-preserving surface perturbations (C_3, inversion, and time-reversal), but are also locally stable when the spatial symmetries are broken, as long as time-reversal symmetry is preserved. Citing [13], "The only way to remove it is to annihilate it with another Kramers pair coming from another hinge, which cannot be achieved with just a small perturbation. The higher-order hinge modes of a three-dimensional HOTI are therefore just as stable as the edge modes of a first-order TRS topological insulator in two dimensions.".

The second-order topological character of bulk bismuth successfully accounts for the previously mentioned reported experimental results, and clarify part of the controversy. For completeness, let us mention here two caveats to this interpretation. First, bulk bismuth is not an insulator to begin with. This does not hinder the definition of topological index, as it is always possible to continuously deform the band structure of bismuth enough to make it an insulator, without closing (and inverting) any gap. Alternatively, one can think of the last argument as a k-dependent E_F, such that E_F always lies in a band gap (that is why we included the three lower energy band also at T and L-points in the topological index calculations). However, the presence of trivial bulk and surface states in parallel with the topological hinge states may be detrimental to its topological protection. [59] suggests that localized modes can exist in HOTIs even in the absence of a bulk bandgap. Second, a recent STM work on a screw-dislocation defect on top of a thick Bi(111) surface suggests that bulk bismuth is a strong topological insulator with non-vanishing weak topological index, just like Sb [60]. Their analysis is based on a higher confidence in strain-induced transition calculations than in strain-less bulk calculations.

The results presented in chapter 3 confirm the previous measurement of ballistic hinge states, while the analysis in chapter 4 provides a new type of evidence for topologically protected hinge states, based on parity-protection.

Figure protected by copyright

See original publication
or ask for complete version

(a)

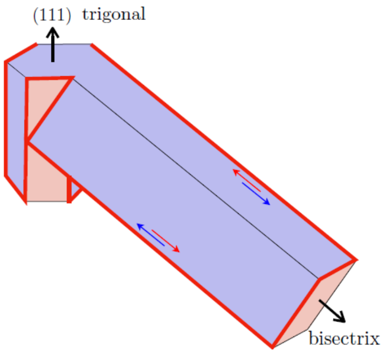

(b)

Figure protected by copyright

See original publication
or ask for complete version

(c)

Figure 1.11 – Theoretical predictions for a HOTI with C_3, inversion, and time-reversal symmetries. (a) Schematic of the hinge states of a hexagonally shaped HOTI oriented along the trigonal [111] axis, with C_3 and inversion symmetry (such as bismuth). Red lines represent a single one-dimensional Kramers pair of gapless protected (helical) modes. In the Dirac picture of a HOTI surface, red and blue surfaces correspond to opposite signs of the unique TRS surface mass term. From [13]. (b) Same as (a), with parallelogrammatic cross-section in relation to the bismuth nanowire with top surface perpendicular to the trigonal [111] axis examined in [3], see Figs.1.10 and 1.8b. From [13]. (c) Tight-binding simulation of a system with identical C_3 and inversion symmetries, and identical topological indices, showing 1d protected helical mode on its hinges.

1.3 . Superconducting proximity effect

In our work, we are interested in introducing superconducting correlations in our crystalline bismuth samples. We contact our samples with a tungsten compound BCS superconductor, thread a current through the superconductor-bismuth-superconductor structure thus formed, and measure the effects of a phase difference between the two superconductors on one hand, and of a magnetic field on the other hand. Such structures with a material sandwiched by two superconductors are called Josephson junctions. In the following, we introduce the key ideas to understand the physics of Josephson junctions.

After a brief tour of the main models used to describe the superconducting phase, we introduce the theoretical concepts necessary to grasp how the Current-Phase Relation (CPR) emerges from Andreev reflections.

We show that the supercurrent induced by the superconducting correlations exhibits a reduced contribution of diffusive states compared to ballistic states, which is interesting in our context of metallic diffusive surface states in parallel with the 1d helical hinge states in our bismuth nanowires. Moreover, we demonstrate that the CPR is a very good tool to distinguish various modes of transport, in particular transport through topological 1d helical edges (or hinges) showing a protected ballistic behavior. Lastly, we discuss the effects of Zeeman interaction in Josephson junction with and without spin-orbit coupling.

1.3.1 . Intrinsic s-wave superconductivity

During my PhD, we used superconductors with low critical temperature which are well described by the Bardeen-Cooper-Schriffer (BCS) model. In this model, for a temperature lower than the critical temperature T_c ($T_c \sim 1K$), the interaction between electrons of opposite momentum becomes attractive, mediated by phonons, promoting pairing between electrons, refereed as Cooper pairs. The pairing is the same, irrespective of the momentum direction, favoring s-wave Cooper pairs. Because electrons are fermions, the amplitude of the state describing electrons must change sign under the exchange of two of them. Thus, it is the spin part of the state that must change sign, which is only true for singlet spin state

$S=0: |\psi_{spin}\rangle = (|\uparrow\downarrow\rangle - |\downarrow\uparrow\rangle)/\sqrt{2}$. Forming pairs of electrons with opposite spin and momentum, the pairs can condense into a single macroscopic quantum state of lower energy described by $|\psi|e^{i\theta}$. It has a quantum phase θ that enforces coherence on macroscopic scales, allowing for quantum interference effects on large scales. We introduce briefly here three useful models that treat superconductivity on different levels.

The London model

In a phase coherent homogeneous perfect conductor, the carrier's quantum phase θ obey the relations of the London model [61, 62] :

$$-\hbar\frac{\partial\theta}{\partial t} = \frac{1}{2n}\Lambda\vec{J_S}^{\,2} + qV + \chi \;\; \text{is the energy} - \text{phase relation} \tag{1.8}$$

$$q\Lambda\vec{J_S} = \hbar\vec{\nabla}\varphi \;\; \text{is the current} - \text{phase relation} \tag{1.9}$$

$$\text{with} \;\; \vec{\nabla}\varphi = \left(\vec{\nabla}\theta - \frac{q}{\hbar}\vec{A}\right) \;\; \text{the gauge invariant phase gradient} \tag{1.10}$$

with $\vec{J_S}$ the (super)current density, $n \propto |\psi|^2$ the carriers density, q the carriers charge, m^* the carriers mass, $\Lambda = m^*/(nq^2)$ the London parameter, and $qV + \chi$ the electrochemical potential. The London model can be used to describe time-dependent situations in homogeneous superconductors under electric and magnetic fields. However, it fails to describe inhomogeneous situations. In part 1.5, we will use this model to derive the constraint on the superconducting phase in the presence of magnetic field in Superconducting Quantum Interference Devices.

The Ginzburg-Landau model

In 1950, Ginzburg and Landau proposed a phenomenological theory of superconductivity, in terms of modulus and gradient of the order parameter $\psi = |\psi|e^{i\theta}$ [63]. Like the Landau theory of phase transitions, it relies on an expansion of the free energy density in the order parameter ψ, close to the critical temperature T_c. For a 3d electron gas, it takes the form :

$$F_S = F_N + \alpha|\psi|^2 + \beta|\psi|^4 + \frac{1}{2m^*}\left|-i\hbar\boldsymbol{\nabla}\psi(\boldsymbol{r}) - q\boldsymbol{A}(\boldsymbol{r})\psi(\boldsymbol{r})\right|^2 + \frac{(\boldsymbol{b}(\boldsymbol{r}) - \boldsymbol{B}_{ext})^2}{2\mu_0} \tag{1.11}$$

where $\boldsymbol{b}(\boldsymbol{r})$ is the local flux density and $\boldsymbol{B}_{ext}$ is the spatially homogeneous applied magnetic field. Upon minimization, it yields the first and second Ginzburg-Landau equations :

$$\frac{1}{2m^*}\left(-i\hbar\boldsymbol{\nabla} - q\boldsymbol{A}(\boldsymbol{r})\right)^2\psi(\boldsymbol{r}) + \alpha\psi(\boldsymbol{r}) + \frac{1}{2}\beta|\psi(\boldsymbol{r})|^2\psi(\boldsymbol{r}) = 0 \tag{1.12}$$

$$\boldsymbol{J}_S = -i\frac{q\hbar}{2m^*}(\psi^*\boldsymbol{\nabla}\psi - \psi\boldsymbol{\nabla}\psi^*) - \frac{q^2}{m^*}|\psi(\boldsymbol{r})|^2\boldsymbol{A}(\boldsymbol{r}) \tag{1.13}$$

In 1959, it was shown that this model was consistent with the BCS microscopic theory for temperatures close to T_c [64]. The current-phase relation Eq.(1.9) of the London model can be derived from Eq.(1.13) of the Ginzburg-Landau model for $|\psi(\boldsymbol{r})|^2 = n$ constant. It is very useful to describe inhomogeneous situations, to discuss the influence of the symmetries of a material on its superconductivity, and its phase diagram. However, it fails to describe situations where the specific spectrum of the material matters (like in Josephson junctions), as well as time-dependent situations.

The Bogoliubov-de Gennes model

De Gennes proposed a model that extends the microscopic BCS model for the ground state to excited states thanks to Bogoliubov-Valatin transformations [65]. It extends the Hilbert space by adding new degrees of freedom for holes (Nambu space), allowing for electron-hole superpositions, needed to describe proximity induced superconductivity in non-superconducting materials, where the superconducting order parameters vanishes. From the Bogoliubov-de Gennes hamiltonian, one can express the problem in terms of propagators, which is adapted to deal with disorder.

In this model, the hamiltonian writes :

$$\mathcal{H} = \int d\boldsymbol{r}\Psi^\dagger(\boldsymbol{r})\mathcal{H}_{BdG}(\boldsymbol{r})\Psi(\boldsymbol{r}) \quad \text{with spinor} \quad \Psi(\boldsymbol{r}) = \begin{pmatrix} \psi_\uparrow(\boldsymbol{r}) \\ \psi_\downarrow^\dagger(\boldsymbol{r}) \end{pmatrix} \tag{1.14}$$

where $\psi_\uparrow(\boldsymbol{r})$ is the annihilation operator of an electron with spin ↑ at position $\boldsymbol{r}$, and $\psi_\downarrow^\dagger(\boldsymbol{r})$ is the creation operator of an electron with spin ↓ at position $\boldsymbol{r}$. With such hamiltonian, one can find eigenstates of the Bogoliubov-de Gennes hamiltonian $\mathcal{H}_{BdG}$:

$$\mathcal{H}_{BdG}(\boldsymbol{r}) \begin{pmatrix} u_n(\boldsymbol{r}) \\ v_n(\boldsymbol{r}) \end{pmatrix} = E_n \begin{pmatrix} u_n(\boldsymbol{r}) \\ v_n(\boldsymbol{r}) \end{pmatrix} \tag{1.15}$$

with

$$\mathcal{H}_{BdG} = \begin{pmatrix} \frac{(-i\hbar\boldsymbol{\nabla_r}-q\boldsymbol{A}(\boldsymbol{r}))^2}{2m^*} + V(\boldsymbol{r}) - \mu & \Delta(\boldsymbol{r}) \\ \Delta^*(\boldsymbol{r}) & -\left[\frac{(-i\hbar\boldsymbol{\nabla_r}-q\boldsymbol{A}(\boldsymbol{r}))^2}{2m^*} + V(\boldsymbol{r}) - \mu\right] \end{pmatrix} \tag{1.16}$$

$\mathcal{H}$ can then be rewritten in terms of eigenstates of $\mathcal{H}_{BdG}$, with "Bogoliubon" operators $\gamma_n(\boldsymbol{r}) = u_n^*(\boldsymbol{r})\psi_\uparrow(\boldsymbol{r}) + v_n^*(\boldsymbol{r})\psi_\downarrow^\dagger(\boldsymbol{r})$. These operators describe excitations that are superpositions of an electron and a hole. Applying such an operator on a state $|\phi\rangle$, adds a Bogoliubon to $|\phi\rangle$, changes its fermion parity and requires the absorption or the release of an electron. Note that the vacuum of Bogoliubons is not the vacuum of electrons and is far from being the ground state [66].

1.3.2 . Josephson tunnel junction and Josephson equations

To illustrate how Josephson junctions behave, we start by the simple case of an insulating barrier, referred as an S/I/S-junction. The junction is sketched in Fig.1.12, with $\psi_1 = \sqrt{n_1}e^{i\theta_1}$ and $\psi_2 = \sqrt{n_2}e^{i\theta_2}$ describing the left and right superconductors, respectively.

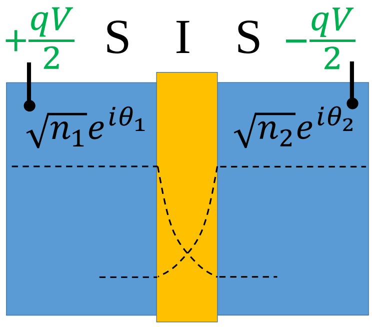

Figure 1.12 – Sketch of a superconductor-insulator-superconductor junction. The left (right) superconductor state is described by $\psi_1 = \sqrt{n_1}e^{i\theta_1}$ ($\psi_2 = \sqrt{n_2}e^{i\theta_2}$). The dashed black lines represent $|\psi_{1,2}|$ across the junction. A potential energy difference of qV is applied between the two superconductors.

If the insulating barrier is not too long or has a barrier potential not too high, there can be an appreciable interpenetration of the superconducting states, that we note K. Following [67], we describe the evolution of the system as :

$$i\hbar\frac{\partial\psi_1}{\partial t} = \frac{qV}{2}\psi_1 + K\psi_2$$
$$i\hbar\frac{\partial\psi_2}{\partial t} = -\frac{qV}{2}\psi_2 + K\psi_1$$

where we added a potential energy difference of qV between the two superconductors. Solving this set of coupled equations for $\sqrt{n_{1,2}}$ and $\theta_{1,2}$, and taking $n_1 = n_2 = n$, we get :

$$J = q\frac{\partial n_1}{\partial t} = -q\frac{\partial n_2}{\partial t} = \frac{2qK}{\hbar}n\sin(\Delta\theta) \tag{1.17}$$

$$\frac{\partial\Delta\theta}{\partial t} = \frac{\partial\theta_2}{\partial t} - \frac{\partial\theta_1}{\partial t} = \frac{qV}{\hbar} \tag{1.18}$$

with $\Delta\theta = \theta_2 - \theta_1$ the superconducting phase difference between the two superconductors. J is the current flowing from superconductor 2 to 1. Eq.(1.17) and (1.18) are the first and second Josephson relations. Similar to Eq.(1.9), J depends on the phase of the superconductors, but as $\sin(\Delta\theta)$ instead of $\vec{\nabla}\theta$. A finite dissipationless (super)current flows between the superconductors if $\Delta\theta \neq 0 \ mod \ \pi$. Eq.(1.18) is the energy-phase relation Eq.(1.8) with just the potential energy qV. For a constant qV, $\Delta\theta$ oscillates with a frequency $f = \frac{qV}{\hbar}$. This effect is used for metrologic voltage standard, relating time to voltage, see part 1.5.4. For a BCS superconductor, $q = -2e$.

1.3.3 . Andreev reflection and Andreev Bound States

In proximity to a normal conductor, the superconducting correlations can propagate in the normal conductor via a process called Andreev reflection. Let us consider the 1d situation depicted in Fig.1.13, with an interface normal conductor-superconductor (NS) with an incident electron with wavevector $k_e = k_F + q$ and spin $\uparrow$. Considering an electron of energy $\mathcal{E}_F + \epsilon < \Delta$, it can't propagate alone in the superconductor and must find a partner with (near) opposite wavevector $k_h = -k_F + q$ and spin to form a Cooper pair with momentum q. This is realized by taking another electron from the normal conductor Fermi sea at energy $-\epsilon$, effectively reflecting as a hole $k_h \downarrow$. This phenomenon is called Andreev reflection. In the reflection process, assuming $\Delta \ll \mathcal{E}_F$, the reflected hole is dephased by $\theta_2 - \arccos(\epsilon/\Delta)$. Considering the reversed process on the normal conductor-superconductor interface at the other end of the normal conductor, bound states can be formed, called Andreev Bound State (ABS). To form such an ABS, the accumulated phase along the full cycle must be a multiple of 2π. For this 1d problem, it writes :

$$(k_e - k_h)L - 2\arccos(\epsilon_n/\Delta) + \theta_1 - \theta_2 = 2\pi n \Longleftrightarrow \frac{2L}{\hbar v_F}\epsilon_n - 2\arccos(\epsilon_n/\Delta) + \theta_1 - \theta_2 = 2\pi n \tag{1.19}$$

with $(k_e - k_h)L$ the phase caused by the propagation through the junction of length L, v_F the Fermi velocity, and ϵ_n the ABS energy corresponding to n. The different regimes are discussed in the next subsections.

The Andreev bound states come in pairs : for every ABS at energy ϵ_n, there exists a complementary (particle-hole symmetric) ABS at $-\epsilon_n$ where the role of the electrons and holes are exchanged. From the ABS, we can construct multiple many-particles states that can be represented with respect to the vacuum of Bogoliubov quasiparticles (1-particle picture) or to the BCS ground state (excitation picture), as illustrated in Fig.1.14. The resulting states feature different numbers of quasiparticles, spin properties, and carry different supercurrents, depending on the occupation configuration. For example, one can induce photo-assisted transitions between states of identical parity of the number of quasiparticles only (e.g. from even to even), but this kind of experiment can be poisoned by the states of the other parity if one quasiparticle enters or leaves the junction. This idea is discussed more in depth in part 1.10 where we examine the dynamics of a Josephson junction, used in chapter 4 to analyze our experiment.

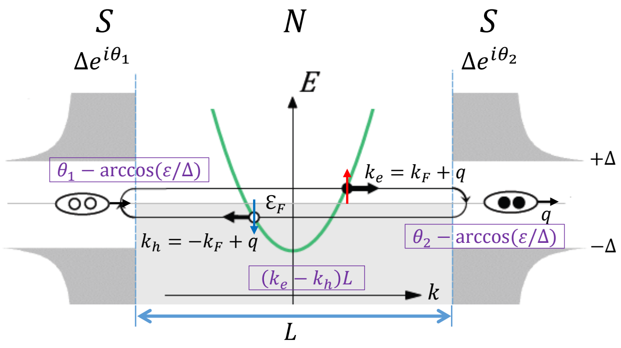

Figure 1.13 – Sketch illustrating Andreev reflection and Andreev Bound State processes in a normal conductor of length L sandwiched by two s-wave superconductors with phases $\theta_{1,2}$ and identical superconducting gap Δ. The picture is limited to a single transverse mode (channel) with quadratic dispersion relation. An electron $k_e = k_F + q \uparrow$ is Andreev reflected into a hole $k_h = -k_F + q \downarrow$ with an extra phase $\theta_2 - \arccos(\epsilon/\Delta)$, transferring a Cooper pair with wavevector q into the right hand superconductor. The hole propagates through the normal conductor, accumulating a phase $-k_h L$, and is reflected back into an electron by the inverse process. If the accumulated phase through the full cycle is a multiple of 2π, it forms an Andreev Bound State. Adapted from [68].

1.3.4 . Short and long ballistic junctions

Looking at Eq.(1.19), one can identify two limits. For short junctions, we can neglect the dephasing term $\frac{2L}{\hbar v_F}\epsilon_n$ due to the propagation of electrons and holes differing by an energy ϵ_n. It gives $-2\arccos(\epsilon_0/\Delta) + \theta_1 - \theta_2 = 0$ and :

$$\epsilon_0 = \Delta \cos\left(\frac{\varphi}{2}\right) \tag{1.20}$$

with $\varphi = \theta_2 - \theta_1$ the superconducting phase difference between the two superconductors. The resulting ABS spectrum is illustrated in Fig.1.15a. The particle-hole symmetric ABS has an energy $-\Delta\cos(\varphi/2)$, and they exchange roles at $\varphi = \pi$. At $\varphi = 0$, there is a Δ energy difference between the ground state and the first excited state.

In the other limit of long junctions, the term $\frac{2L}{\hbar v_F}\epsilon_n$ induces important phase shifts even for low ϵ_n, yielding multiple solutions with different $n \neq 0$. This results in many ABS, with ABS with energies close to $\epsilon_n \simeq 0$ almost linear in φ, whereas $\epsilon_n \simeq \Delta$ ABS show an important curvature, see Fig.1.15b. Two neighboring ABS are separated by an energy $\sim \frac{\hbar v_F}{2L}$. The ground state results from the occupation of all the ABS with $\epsilon_n < 0$. At $\varphi = 0$, the energy difference between the ground state and the first excited state is $\frac{\hbar v_F}{4L}$.

The distinction between short and long junction limit can be expressed in terms of the Thouless energy $E_T^b = \frac{\hbar v_F}{L}$ for ballistic junctions, where $E_T^b \gg \Delta$ ($E_T^b \ll \Delta$) corresponds to the short (long) junction regime. One can also express it in terms of a superconducting coherence length ξ_S^b such that $\Delta = E_T^b = \frac{\hbar v_F}{\xi_S^b}$, yielding $\xi_S^b = \frac{\hbar v_F}{\Delta}$, with v_F is a characteristic of the normal conductor and Δ a characteristic of the superconductor.

1.3.5 . Junctions with disorder

In the presence of impurities or imperfect interfaces, there is a finite probability for the electron and hole states to scatter. Let us first consider a set of four modes, indexed by $1, 2, 3, 4$. In a time-reversal symmetric and spin-independent normal conductor, for every mode with wavevector k_1 and spin s_1, there exist three other modes with $-k_2 = k_3 = -k_4 = k_1$ and $-s_2 = -s_3 = s_4 = s_1$, as illustrated in Fig.1.16a. A TRS scatterer can't change the spin of the scattered mode, and thus can only couple modes with non-orthogonal spins (e.g. not $\langle\uparrow|\downarrow\rangle = 0$). It can couple modes $1-4$ and $2-3$, as illustrated in Fig.1.16b. These couplings

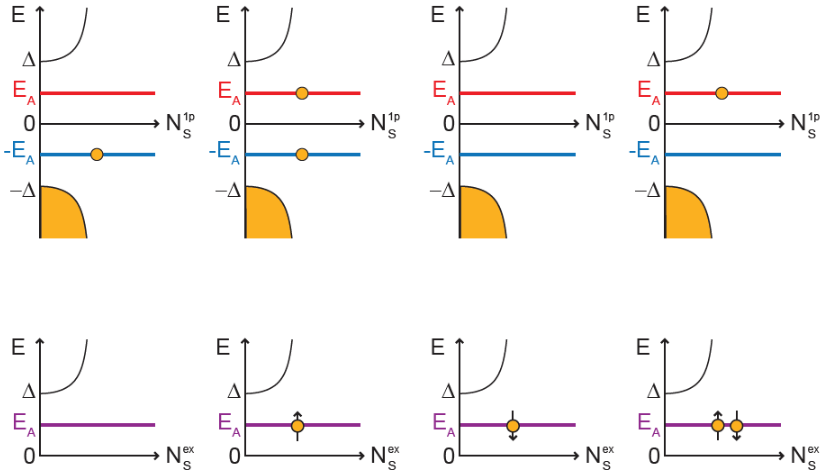

Figure 1.14 – Density of states with in-gap Andreev Bound States for a given superconducting phase difference φ. For spin-degenerate materials, the same spectrum exists for opposite spins. Top : 1-particle picture. Bottom : excitation picture. Left : ground-state with all the negative energy 1-particle states occupied. It is spinless and is populated by an even number of quasiparticles. Its energy varies with φ. Center left : first excited state. It requires the addition of an extra quasiparticle. It has a positive spin and an odd number of quasiparticles. Its energy is independent of φ. Center right : other first excited state, with a negative spin. Right : second excited state. It is spinless and is populated by an even number of quasiparticles. Its energy varies with φ. From [66].

induce avoided crossings at $\varphi = 0, \pi \ mod \ 2\pi$ in the ABS spectrum, and change the properties of the junction. Fig.1.17a shows the ABS spectrum of a short junction with an interface of imperfect transmission $\tau < 1$. Fig.1.17b shows the ABS spectrum of a long diffusive junction with a large number of channels and a large on-site potential disorder, see [70].

In long junctions, there is a very interesting additional effect caused by the superconducting correlations. The diffusive channels correspond to longer trajectories through the junction. This affects the geometric phase accumulated by ABS (see Eq.(1.19)), and thus changes their Thouless energy and their supercurrent compared to straight trajectories. For a junction of length L, ballistic channels propagate through the junction in a time $\tau_b = L/v_F$, contrasting with $\tau_d = L^2/D$ for diffusive channels, with $D = v_F l_e/m$ the diffusion coefficient, m being the effective dimensionality of the diffusion process. For diffusive junctions, the Thouless energy writes $E_T^d = \hbar D/L^2$. For long diffusive junctions, the energy (mini)gap between the ground state and the first excited state is $\simeq 3.1 E_T^d$, as can be seen in Fig.1.17b.

In the resistive state, the contribution of diffusive channels to conductance is reduced by a factor $\sim l_e/L$ by modes mixing from scattering [6]. In long Josephson junctions, the phase coherence between electrons and holes introduced by the superconducting correlations further reduce their contribution by a factor $\tau_b/\tau_d \sim l_e/L$, written more explicitly in the next subsection. This is a one advantage of introducing superconductivity by proximity effect in bismuth-based junctions, to reduce the contribution of surface channels that aren't topologically protected.

1.3.6 . Current-Phase Relations

From the ABS spectrum, one can compute the Current-Phase Relation (CPR) using the following formula [69] :

$$I(\varphi) = -\sum_n f_{FD}(\epsilon_n/(k_B T)) \frac{\partial \epsilon_n}{\partial \Phi} = -\frac{2\pi}{\Phi_0} \sum_n f_{FD}(\epsilon_n/(k_B T)) \frac{\partial \epsilon_n}{\partial \varphi} \tag{1.21}$$

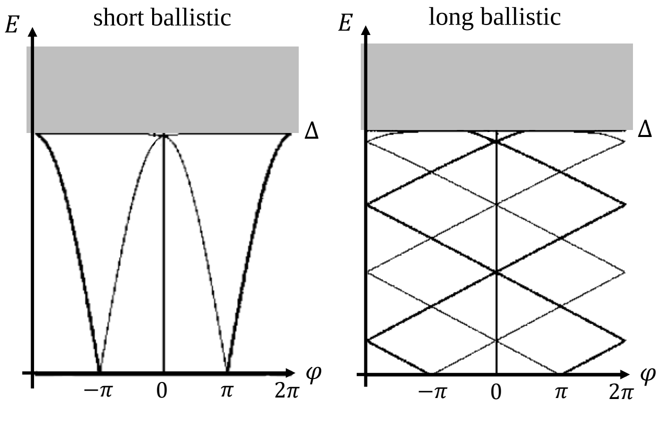

(a) (b)

Figure 1.15 – Positive energy Andreev bound state 1-particle spectrums of a short ballistic junction (a) and a long ballistic junction (b). The spectrums are spin degenerate in the absence of spin-dependent interactions. Adapted from [69].

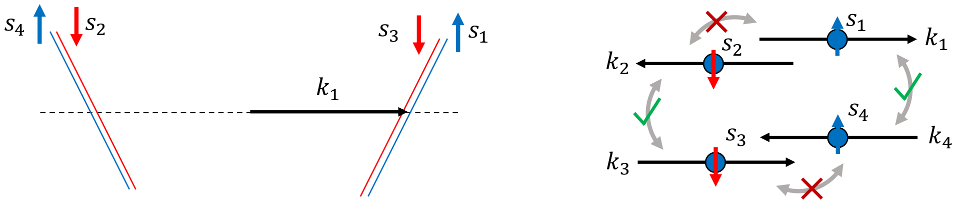

(a) (b)

Figure 1.16 – In a time-reversal symmetric and spin-independent normal conductor, for every mode 1 with wavevector k_1 and spin s_1, there exist three other modes $2, 3, 4$ with $-k_2 = k_3 = -k_4 = k_1$ and $-s_2 = -s_3 = s_4 = s_1$, illustrated in (a). A TRS scatterer can only couple modes $1-4$ and $2-3$ with identical spins, as illustrated in (b).

with $f_{FD}(x) = 1/(1+e^x)$ the Fermi-Dirac distribution, T the temperature, and k_B the Boltzmann constant. $\Phi_0 = h/2e$ is the superconducting quantum of flux, corresponding to the flux Φ needed for a junction in a superconducting ring (AC SQUID, see part $1.5.1$) to increase the superconducting phase difference φ by 2π.

The ABS spectrum depends on the characteristics of the junction, as identified in the previous parts. The corresponding CPR are plotted in Figs.1.18a and 1.18b for short and long junctions, respectively. We see that scattering results in a smoothing of the current discontinuity at $\varphi \simeq \pi \ mod \ 2\pi$ and a reduction of the maximum supercurrent. The maximum supercurrent is referred as the critical current. When both time-reversal symmetry and inversion symmetry are broken, the maximum supercurrent that can flow in one direction (say, $I_c^+ = \max_\varphi[I(\varphi)]$) can be different from the maximum supercurrent that can flow in the other direction (say, $I_c^- = |\min_\varphi[I(\varphi)]|$).

The expressions of the critical currents for various types of junctions are shown in Tab.1.1 [71]. The total current is the sum over M_{eff} effective channels in the resistive state, with $M_{eff} = M$ the number of modes in the ballistic case, and $M_{eff} \sim M\frac{l_e}{L}$ in the diffusive case. L is the junction length and l_e the elastic mean free path. We also display the critical current per effective channel M_{eff} in the resistive state, that is the contribution of the superconducting correlations to the current. We confirm that in long junctions, for a "pristine" number of mode M, the contribution of diffusive states compared to ballistic

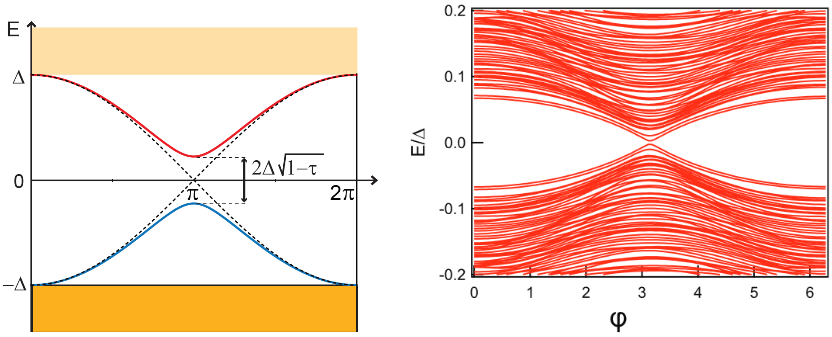

(a) (b)

Figure 1.17 – Andreev bound state 1-particle spectrums. (a) Short junction with an interface of imperfect transmission $\tau < 1$. From [66]. (b) Long diffusive junction with a high number of channels and a large on-site potential disorder. From [70].

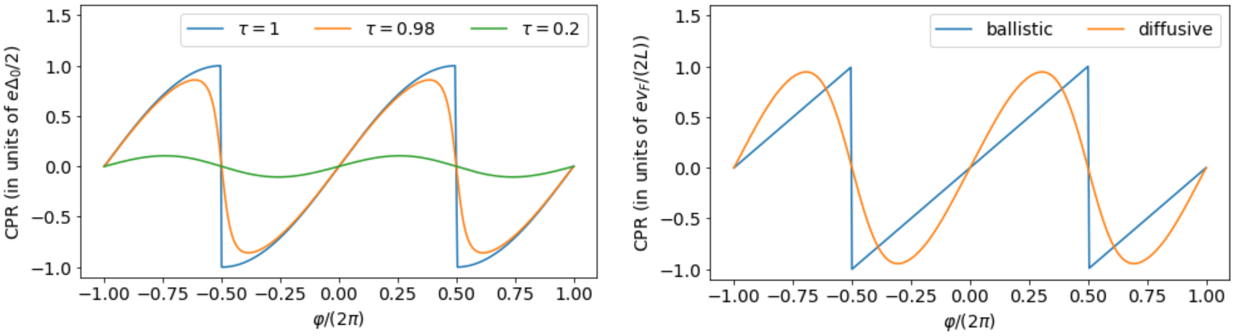

(a) (b)

Figure 1.18 – (a) CPR of short junctions with various transmission coefficients τ. (b) CPR of long junctions in the diffusive limit (gold line, normalized to $ev_F/(2L)$) and the ballistic limit (blue line).

states is $I_c^d/I_c^b \sim \frac{l_e^2}{L^2}$, with a factor l_e/L coming from the superconducting correlations between electrons and holes.

When the junction can't be considered in the short junction limit, the states with energy $|\epsilon| \gtrsim \Delta$ contribute to the CPR and must be taken into account, as their energies vary with the superconducting phase difference. In the presence of finite momentum pairing, the continuum yields an additional constant supercurrent [72, 73], as discussed in part 1.4.3.

1.3.7 . Voltage jump eR_NI_c

Let us consider the measurement of the critical current I_c of a Josephson junction, where we ramp the current I through the junction and we measure the voltage V across the junction. At $I = I_c - \varepsilon$, with $0 < \varepsilon << I_c$, the junction is superconducting and $V = 0$. At $I = I_c + \delta$, the junction becomes resistive and follows Ohm's law with a voltage $R_N(I_c + \varepsilon) \simeq R_NI_c$, yielding a voltage jump $\delta V \simeq R_NI_c$. But δV also corresponds to the voltage needed to carry more current than what dissipationless transport through ABS can offer, so we can guess that it relates to the gap in the spectrum, Δ for short junctions and E_T for long junctions. And indeed, there exist such relations for the various junction types.

For a short junction, $eR_NI_c = \alpha\Delta$ with $\alpha = \pi$ for a ballistic junction, $\alpha = \pi/2$ for a tunnel junction ($\tau \ll 1$), and $\alpha = 2.07$ for a diffusive junction [71]. $eR_NI_c = \pi E_T^b$ for a long ballistic junction, and

	ballistic short	ballistic long	diffusive short	diffusive long
I_c	$M_{eff}\frac{\pi\Delta}{\Phi_0} = M\frac{e\Delta}{\hbar}$	$M_{eff}\frac{\pi E_T^b}{\Phi_0} = M\frac{ev_F}{L}$	$M_{eff}\frac{2.07\Delta}{\Phi_0} = M\frac{l_e}{L}\frac{e4.14\Delta}{h}$	$M_{eff}\frac{10.8E_T^d}{\Phi_0} = M\frac{l_e}{L}\frac{e10.8v_F l_e}{\pi m L^2}$
I_c/M_{eff}	$\frac{e\Delta}{\hbar}$	$\frac{ev_F}{L}$	$\frac{e4.14\Delta}{h}$	$\frac{e10.8v_F l_e}{\pi m L^2}$

Table 1.1 – Critical current of a Josephson junction with various characteristics. M_{eff} is the effective number of channels in the resistive state, with $M_{eff} = M$ the number of modes in the ballistic case, and $M_{eff} \sim M\frac{l_e}{L}$ in the diffusive case. Δ is the superconducting gap, $\Phi_0 = h/(2e)$ the superconducting quantum of flux, E_T the Thouless energy, v_F the Fermi velocity, L the junction length, l_e the elastic mean free path, and m the effective dimensionality of the modes that diffuse.

$eR_N I_c \simeq 10.8E_T^d$ for a long diffusive junction. In theory, one can deduce the type of junction from the measurement of $R_N I_c$.

In reality however, this analysis faces several obstacles. On the one hand, the $R_N I_c$ analysis can suffer from the existence of multiple types of conduction channels, especially in the presence of ballistic and diffusive channels in long junctions, as the relative contribution of ballistic and diffusive channels are different depending on whether the junction is in its resistive state or in its superconducting state. On the other hand, one must note that the measured value of R_N can be larger than the resistance of the proximitized conductor part of the Josephson junction, if more elements become resistive when the Josephson junction switches to its resistive state. This is expected for the W contacts that are in series with the Josephson junction and can switch simultaneously because of the heat generated by the dissipation from the Josephson junction in its resistive state, especially for high values of I_c. If only the Josephson junction switches, one expect another jump in the resistance at higher current, when the superconducting contacts become resistive. But we have not systematically exposed the samples to high current by fear of damaging them. This cascade effect can be avoided by measuring the resistance dV/dI as a function of temperature with a small I_{AC} and no I_{DC}, rather than dV/dI as a function of I_{DC} with constant temperature. This reduces the current going through the junction, lowering the heating when the junctions is dissipative, thus reducing the cascade effect. Lastly, the measured $R_N I_c$ is also affected by the quality of the interfaces.

In our samples, considering the short junction limit, the short ballistic case is the most relevant because the intrinsic superconducting (Cooper-pairs) coherence length ξ_S^W of the W contacts is very short compared to the length of the normal conductor L ($L \gg \xi_S^W$, no Cooper-pair tunneling), and because the elastic mean free path length and the diffusive superconducting (Andreev-pairs) coherence length have similar values ($l_e \simeq \xi_S^d \simeq 200\ nm$, leaving not much room for the short diffusive limit). So, considering a short ballistic junction, $eR_N I_c = \pi\Delta \simeq 3.8\ meV$ taking a $T_c \simeq 6\ K$ for the W contacts.

1.3.8 . Superconducting proximity effect with spin-orbit coupling

spin-orbit coupling introduces a coupling between the orbital and the spin degrees of freedom. It lifts the spin degeneracy of the bands of the material and leads to Fermi surface spin-texture, see part 1.1. In superconductors with SOC, because of this spin-texture, the superconducting correlations produce a pairing with a finite triplet-state component. With a Zeeman energy, this can lead to finite momentum pairing and anomalous Josephson effect, that can also affect the CPR of Josephson junctions with SOC even though the superconductor has no SOC, yielding φ_0-junctions [74, 73]. This effect is exploited in the experiment presented in appendix 6.12, and discussed as a possible scenario to explain shifts in switching current patterns in part 3.5. In long Josephson junctions with multiple modes, SOC induces a lift of the spin degeneracy of the ABS, allowing for inter-manipulation of the orbital and spin degrees of freedom [75, 74, 76, 77, 68].

In topological insulators with 1d helical modes, superconducting correlations induce a special type of protection that forbids coupling between the ground state and the first excited state of the topological junction at $\varphi = \pi \ mod \ 2\pi$, called parity conservation. This protection leads to gapless states with specific noise signatures [78, 4], to 4π-Josephson effect [79, 80], to ballistic transport with specific transport signatures [40, 1, 3, 2].

In chapter 3, we demonstrate clear ballistic transport in all the sample we measured. In addition to the effects described above, we demonstrate in chapter 4 that the relaxation dynamics is affected by the spatial separation between Andreev modes of opposite helicities. This last result has motivated the writing of an article in collaboration with theoreticians (Y. Peng, Y. Oreg, F. von Oppen), and was just published in Nature Physics [5].

In the next subsection, we discuss the phase shifts that can be produced in the CPR in the presence of a Zeeman energy, including the anomalous Josephson effect in junctions with SOC.

1.3.9 . Zeeman-induced effects : π and φ_0-junctions

In this subsection, we discuss the effects of a Zeeman energy on Josephson junctions with and without SOC, and relate it to the π-junction and φ_0-junction behaviors, respectively. Both effects introduce phase shifts in the ABS spectrum and the CPR that are relevant and has been observed in our experiments.

Let us first consider the effect of a Zeeman energy on a superconductor without SOC, that can be implemented in S/F/S junctions or in S/N/S junctions with external magnetic field. Zeeman energy induces shifts of the Fermi surface and can lead to various phases with finite momentum pairing. For materials without SOC, it splits the spin degeneracy of the bands, shifting each band in energy, and shifting the Fermi surface accordingly. The Cooper pair (and ABS, by Andreev reflection) is formed by electrons of opposite spins, but Zeeman interaction splits the spins in momentum, resulting in a finite momentum pairing $\delta k = 2k_F(E_Z)$ for an $(+k_F \uparrow, -k_F \downarrow)$ pair, where $k_F(E_Z)$ denotes the relation between Fermi momentum and the Zeeman energy E_Z, as illustrated in Fig.1.19b. This effect is responsible for π-shifts in the CPR of S/F/S junctions [81] or S/N/S junctions with external magnetic field [74, 73], that depend on the magnitude of the Zeeman energy. The π-junction behavior is illustrated by the ABS spectrum in Fig.1.20a.

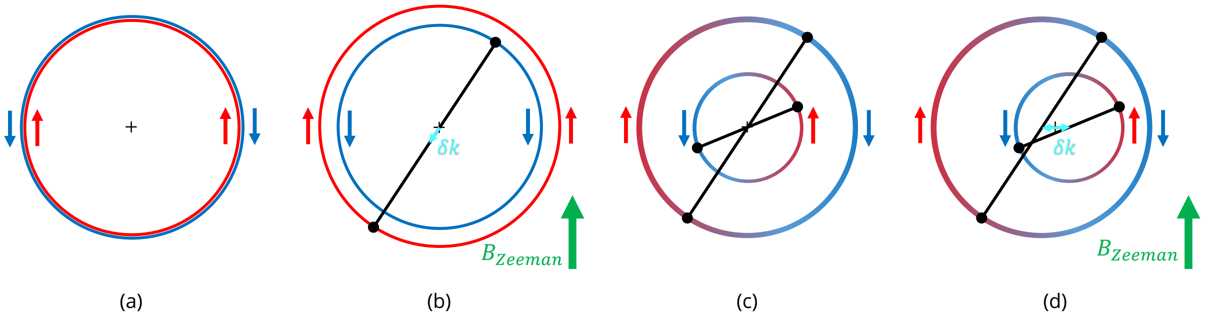

Figure 1.19 – Fermi surfaces (or rather lines) of a material (here a 2d electron gas) with different parameters, illustrating Zeeman-induced finite-momentum pairing. The colors and arrows indicate the expectation value of the spin along the in-plane "up" direction. The lines connecting two black dots represent the pairing induced by superconducting correlations. (a) Without SOC, without Zeeman energy E_Z. (b) Without SOC, with Zeeman energy $E_Z = -g_{eff}\mu_B \boldsymbol{B}_{Zeeman} \cdot \boldsymbol{s}$. (c) With Rashba SOC, without Zeeman energy. (d) With Rashba SOC, with Zeeman energy $E_Z = -g_{eff}\mu_B \boldsymbol{B}_{Zeeman} \cdot \boldsymbol{s}$ corresponding to an in-plane magnetic field $\boldsymbol{B}_{Zeeman}$.

Considering now the Fermi surface of a junction with SOC, we see that the bands are spin-splited even without Zeeman energy, the spin-orbit field $\boldsymbol{\Omega}(\boldsymbol{k})$ acting as a $\boldsymbol{k}$-dependent magnetic field, but still respecting TRS with $\boldsymbol{\Omega}(-\boldsymbol{k}) = -\boldsymbol{\Omega}(\boldsymbol{k})$, see part 1.1. Focusing on 2d systems with Rashba SOC, the Fermi surface is composed of two concentric circles with opposite spin-textures, see Fig.1.19c. Introducing a Zeeman interaction shifts the two circles in opposite directions, perpendicular to the in-plane magnetic field direction, see Fig.1.19d. Like the case without SOC, Zeeman energy induces a finite-momentum pairing δk between electrons of (near) opposite spins. However, we see that this finite momentum is less symmetric, breaking the isotropy, and yields different compensation mechanisms. It yields $\delta k \sim 2E_Z\alpha/v_F^2$ at low magnetic field, and $\delta k \sim 2E_Z/v_F$ at high magnetic field [82].

This finite-momentum pairing induces anomalous Josephson effects, with a phase shift φ_0 in the Josephson junction CPR, and in some cases an asymmetric critical current $I_c^{+,-}$ depending on the sign of the bias current. Various analysis have been done in ballistic [83, 84, 73] and diffusive [85, 82] homogeneous superconductor and weak links, as well as in ballistic [73, 86] and diffusive [87, 88] SNS junctions with SOC. The φ_0-junction behavior is illustrated by the ABS spectrum in Fig.1.20b. The anomalous Josephson effects are discussed more in depth in appendix 6.7.5.

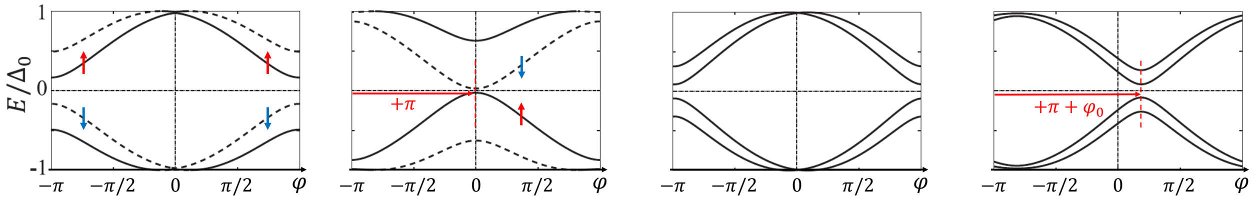

(a) (b) (c) (d)

Figure 1.20 – 1-particle ABS spectrum of a short junction with different parameters, illustrating π-junction and φ_0-junction behaviors. Up and down arrows indicate the spin polarization of the ABS. (a) Without SOC, with low Zeeman energy $E_Z \ll E_T^b$. (b) Without SOC, with high Zeeman energy $E_Z \sim E_T^b$. There is a shift of π compared to the case without Zeeman energy, inducing a π shift in the CPR. (c) With Rashba SOC with energy $E_{so} = \alpha k_0$ such that $k_0/k_F = 0.15$, with low Zeeman energy $E_Z \ll E_T^b$. (d) With Rashba SOC with $k_0/k_F = 0.15$, with high Zeeman energy $E_Z \sim E_T^b$. There is a shift of $\pi + \varphi_0$ compared to the Zeeman-free case, inducing a $\pi + \varphi_0$ shift in the CPR. For higher values of SOC α, the φ_0 shift is noticeable even for low Zeeman field $E_Z \ll E_T^b$ and shows a φ_0 shift only. Adapted from [74].

1.4 . Superconducting proximity effect in topological materials

In the limit of extreme spin-momentum locking, we find materials with helical band structure, in which there exists only one circle in the Fermi surface, and the direction of propagation is univoquelly tied to a spin direction. This type of conduction is found at the boundaries of time-reversal-symmetric topological materials, such as the helical edge states of 2DTI, the helical surface states of 3DTI (with a single massless Dirac cone), and the helical hinge states of 3D SOTI.

In the following subsections, we discuss the effects of proximity-induced superconductivity in the boundary states of TI.

1.4.1 . Helical states coupled to a superconductor

First, let us introduce unconventional superconductors, with an effective pairing potential deviating from the conventional singlet-s-wave pairing. In this type of systems, theoretical works have predicted the emergence of exotic excitations : Majorana Bound States (MBS) [89, 90, 91]. In this context, Majorana fermions are equal superpositions of electrons and holes and are their own antiparticle. Because they exist in delocalized pairs, they are protected against local perturbations, as long as pair members stay away from their partners. Moreover, they are degenerate and pinned at zero energy. Their degeneracy and protection make them very interesting candidates for quantum computing. Indeed, they exhibit anyonic behavior and can be "braided" to realize robust quantum computing operations. This is the foundation of a very rich domain of condensed matter physics : topological quantum computing [92].

Further theoretical investigations found that unconventional superconductivity can be achieved by coupling materials with helical states to conventional s-wave superconductors by proximity effect [93]. In 2008, Fu and Kane proposed a model for proximitized surfaces of 3DTI realizing a 2d $p_x + ip_y$ superconductor with Majorana Bound States (MBS) at vortices [94, 95]. In 2010, Oreg, Refael and von Oppen introduced a recipe to make a 1d spinless p_x-wave superconductor, realizing a Kitaev chain model [90] with MBS at the extremities, turning a quasi-1d nanowire with strong spin-orbit coupling (like InAs or InSb) to a 1d helical conductor thanks to a Zeeman field parallel to the nanowire [96, 97, 98].

In our situations, we are particularly interested in the effect of conventional s-wave contacts inducing superconducting correlations in a 1d helical state by proximity effect. Similar to [96], an s-wave superconductor covering the helical mode of a QSHI or a SOTI realizes an effective p_x-wave topological superconductor. If one removes the superconductor from a small part of the helical mode, it realizes a Josephson junction which is similar to coupled MBS at the ends of a Kitaev chain in its topological phase [78, 99], as discussed in the next subsection.

1.4.2 . Parity protection and fermion parity anomaly

a) Majorana Bound States of a Kitaev chain

Let us now provide some physical insights by deriving the CPR of a short 1d helical junction from the MBS of a topological Kitaev chain. Following Kitaev [90], considering a Kitaev chain without on-site energy and with equal superconducting and hopping coupling magnitude $w = \Delta$, the system has two degenerate ground states featuring MBS, noted $|\psi_0\rangle$ and $|\psi_1\rangle$. The Majorana operators are expressed as :

$$c_{2j-1} = a_j + a_j^\dagger \quad \text{and} \quad c_{2j} = -i(a_j - a_j^\dagger) \tag{1.22}$$

with two Majorana operators $(c_{2j-1} + ic_{2j})/2 = a_j$ on one site j forming a conventional fermion annihilation operator a_j. We have $c_{2j-1}^\dagger = c_{2j-1}$ and $c_{2j}^\dagger = c_{2j}$.

The parity operator, counting the number of fermions involved in a given state, modulo 2, is written $\mathcal{P} = -\prod_j ic_{2j-1}c_{2j}$. The two degenerate ground states can be written as eigenstates of the operator $\mathcal{V} = -ic_1c_{2L}$ as it only involves end Majorana operators that are decoupled from the bulk, yielding :

$$-ic_1c_{2L}|\psi_0\rangle = |\psi_0\rangle \quad \text{and} \quad -ic_1c_{2L}|\psi_1\rangle = -|\psi_1\rangle \tag{1.23}$$

c_1 and c_{2L} are Majorana operators of the first site $j = 1$ and the last site $j = L$ of the chain, respectively.

The parity operator, counting every site, can distinguish between the two states, with $\mathcal{P}|\psi_0\rangle = |\psi_0\rangle$ and $\mathcal{P}|\psi_1\rangle = -|\psi_1\rangle$. In other words, the two ground states have different fermion parities. The adiabatic change of the superconducting phase of the Kitaev chain by 2π is equivalent to applying the operator $-ic_1c_{2L}$ (up to a sign), which is equivalent to transfer one electron between the ends of the chain ($-ic_1c_{2L} = -ic_1^\dagger c_{2L}$).

b) Short 1d helical topological Josephson junction

What happens when we introduce a coupling between the MBS of the two ends, with a superconducting phase difference φ?

Such a coupling can be realized in an ring geometry, with a magnetic field inducing a flux Φ in the surface of the ring and a dephasing $\varphi = 2\pi\frac{2e}{h}\Phi$, as illustrated in Fig.1.21a. The coupling term can be expressed as

$-ite^{i\varphi/2}c_1c_{2L} + c.c. = -i2t\cos(\varphi/2)c_1c_{2L}$ [90, 78, 100], with $t \in \mathbb{R}^{+,*}$ the coupling strength. We notice that it is just $2t\cos(\varphi/2)\mathcal{V}$, implying that the previous degenerate ground states $|\psi_{0,1}\rangle$, eigenstates of $\mathcal{V}$ with different parities, are now eigenstates of the coupled system with opposite energies.

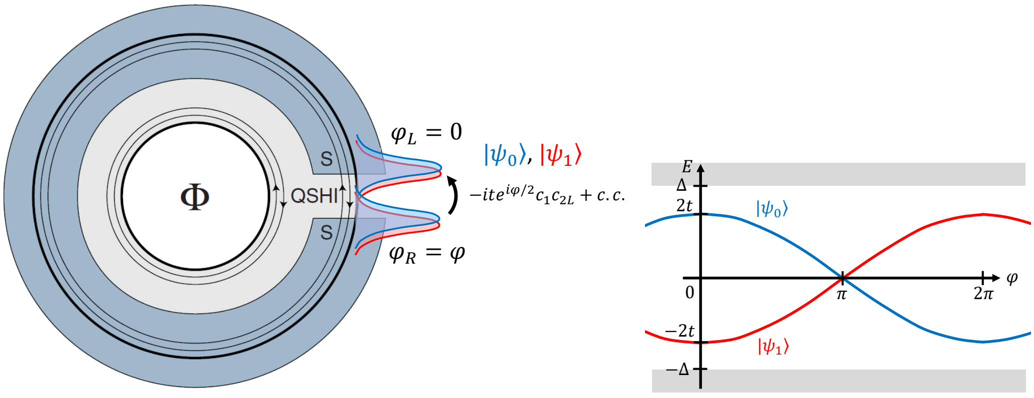

(a) (b)

Figure 1.21 – Josephson junction with a single helical pair of modes, based on one helical edge of a QSHI partially covered with an s-wave superconductor. A magnetic flux Φ induces a superconducting phase difference φ between the two sides of the junction. The junction couples the zero-energy MBS with a term $-i2t\cos(\varphi/2)c_1c_{2L}$, which is the product of a parity-sensitive operator $-ic_1c_{2L}$ and a phase-sensitive coupling $2t\cos(\varphi/2)$, shifting the two degenerate ground states of different parities $|\psi_{0,1}\rangle$ by opposite energies. (a) Sketch of the idealized experiment. Adapted from [78]. (b) Corresponding spectrum as a function of $\varphi = 2\pi\Phi/(h/(2e))$.

Thus, we write :

$$\mathcal{H}\,|\psi_0\rangle = 2t\cos(\varphi/2)\,|\psi_0\rangle \quad \text{and} \quad \mathcal{P}\,|\psi_0\rangle = +1\,|\psi_0\rangle \quad (\text{even}) \tag{1.24}$$

$$\mathcal{H}\,|\psi_1\rangle = -2t\cos(\varphi/2)\,|\psi_1\rangle \quad \text{and} \quad \mathcal{P}\,|\psi_1\rangle = -1\,|\psi_1\rangle \quad (\text{odd}) \tag{1.25}$$

The resulting spectrum is sketched in Fig.1.21b. Notice here that the spectrum is not a 1-particle spectrum nor a excitation spectrum. To get the energy of a state, one can only "occupy" one of the two conjugate states. For $\varphi = 0$, the ground state is $|\psi_1\rangle$ with an energy lowered by $-2t$ and an odd parity. For $\varphi = 2\pi$, the ground state is $|\psi_0\rangle$ with an energy lowered by $-2t$ and an even parity. Contrasting with the non-topological situation, the ground states at $\varphi = 0$ and $\varphi = 2\pi$ differs by their parity, even though the spectrum looks the same.

At $\varphi = \pi$, the two states are degenerate. Because they have different parities, no parity conserving process can couple them and open a gap. Furthermore, to hybridize the two states, one needs a *phase coherent* parity switching process. A short Josephson junction with the 1d helical edge state of a QSHI as a conductor results in the same spectrum as a ballistic short junction, but with a crossing at $E = 0$ and $\varphi = \pi$ that is protected by parity-conservation.

Another consequence of this parity difference is that, after a cycle $\varphi \longrightarrow \varphi + 2\pi$, the system needs to acquire or eject an electron to return to its ground state. If the system is designed to avoid such a parity "poisoning", e.g. if the measurement is done fast enough, one can measure a 4π-periodicity instead of the conventional 2π-periodicity. This 4π-periodicity can be understood as the transfer of a single electron between the two ends of the junction after a 2π cycle of φ, yielding $\Phi_0 = h/e$ instead of $h/(2e)$ [91, 101].

As illustrated in Fig.1.21a, discussed in [78], and tested in e.g. [53], the Kitaev chain do not only model systems based on InAs or InSb nanowires with a Zeeman field parallel to the nanowire [96, 97, 98], but also the helical edge states of QSHI with proximity-induced s-wave superconducting pairing correlations. Thus, the results we just discussed on a looped Kitaev chain can be applied to the short 1d helical topological Josephson junction (and the hinge states of Bi).

c) Fermion parity anomaly

The breaking of the 2π-periodicity is referred as "fermion parity anomaly" [78]. Considering the Josephson junction made from a 1d helical state on one edge of a QSHI, like illustrated in Fig.1.21a, and with a magnetic flux Φ controlling its φ, its local hamiltonian can be written $H_{loc}(\Phi)$. This hamiltonian is periodic in $\Phi_0 = \frac{h}{2e}$, $H_{loc}(\Phi) = H_{loc}(\Phi + \Phi_0)$, but its eigenstates are not, differing by their fermion parity, as discussed above! This anomaly is a consequence of the topological nature of the QSHI. The global hamiltonian of the system, including both edges, is not Φ_0-periodic but $2\Phi_0$-periodic : $H_{glob}(\Phi) = H_{glob}(\Phi + 2\Phi_0) = H_{glob}(\Phi + \frac{h}{e})$. Indeed, when a flux Φ_0 is inserted, the QSHI transfer one fermion from one edge to the other through its bulk, which is a property of TI called spectral flow (see appendix 6.1 for details). The global system only comes back to its initial hamiltonian when a pair of fermions has been transferred by this process, corresponding to a flux $2\Phi_0 = \frac{h}{e}$.

d) Conventional versus topological Josephson junctions

To understand better the difference between conventional and topological 2d Josephson junctions, we first consider a junction with both edge states of a QSHI conducting the supercurrent, as illustrated in Fig.1.22c. Such a system has two 1d helical junctions exhibiting the fermion-parity-protection introduced above.

However, after an increase of 2π of the superconducting phase difference $\varphi \longrightarrow \varphi + 2\pi$, the ground state of both 1d helical junctions changes parity, resulting in an overall unchanged parity of the system. If the two helical junctions are closer than the coherence length of the superconductor, they can both change their parity by breaking (or condensing into) a Cooper pair, impeding the parity-protection of their ABS level crossing at $\varphi = \pi$. If the two helical junctions are closer than their Fermi wavelength, they also can both change their parity by exchanging a fermion by tunneling.

In QSHI junctions, the two 1d helical junctions are spatially separated and can exhibit parity-protection. In conventional junctions however, there is no such spatial separation between helical pairs of channels, resulting in no parity-protection. This argumentation is illustrated in Fig.1.22.

In a helical junction, a bad interface reduces the supercurrent by reducing the coupling parameter t, whereas it opens a gap at $E = 0$ in a conventional junction. For a potential barrier of transmission coefficient T, the energy levels for the two types of junction writes [91] :

$$\varepsilon(\varphi) = \pm\Delta\sqrt{1 - T\sin^2(\phi/2)} \quad \text{for a conventional junction} \tag{1.26}$$

$$\varepsilon(\varphi) = \pm\Delta\sqrt{T}\cos(\phi/2) \quad \text{for a helical junction} \tag{1.27}$$

e) Long 1d helical topological Josephson junction

For long 1d topological junctions, additional ABS can form [78]. The parity of the ground and the first excited states remains different, and exchange roles at $\varphi = \pi \ mod\ 2\pi$, similar to short topological junctions. This situation has been examined by [78] and [102]. In Fig.1.23a, we illustrate the key idea developed in

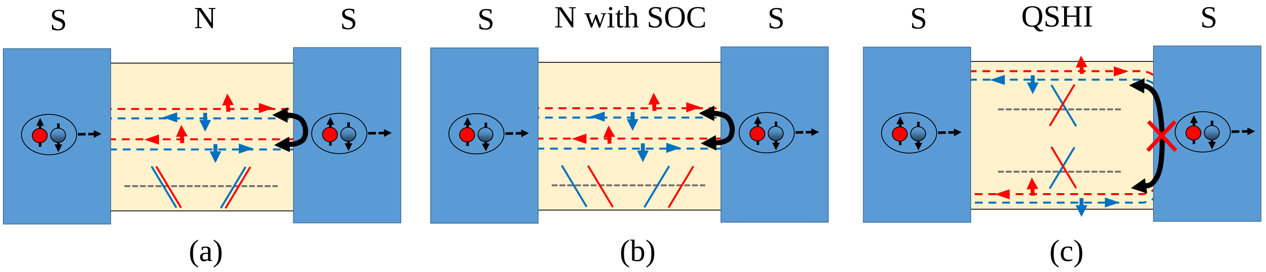

(a) (b) (c)

Figure 1.22 – Illustration of superconducting proximity effect in conventional conductors without SOC (a), in conductors with SOC (b), and in QSHI (c). The superconducting contacts (S) are represented in light blue. The conductor (N or QSHI) is represented in light yellow. Dashed blue and red lines represent trajectories of spin down and up electrons (and holes) in the conductor, respectively. The dashed grey line together with the solid blue and red lines illustrate the spectrum corresponding to the conducting states in the conductor, with blue (red) lines for spin down (up) electrons or holes. The transmission of Cooper pairs through the conductor is realized via helical Andreev states. The black double-arrow shows the coupling between the two helical Andreev states, that may be finite in the presence of scattering on impurities or interfaces. (a) Conventional conductor without SOC. The Andreev states are spin-degenerate and can couple, opening a gap, in case of scattering. (b) Conductor with SOC. The spin-degeneracy of the Andreev states is lifted, but they still coexist locally with Andreev states of opposite spin. In case of scattering, Andreev states of opposite spin can couple, opening a gap. (c) QSHI. The spin-degeneracy of the Andreev states is completely lifted, yielding helical Andreev states. The helical Andreev state of positive (negative) helicity carry Cooper pairs on, say, the top (bottom) edge of the conductor. Because there exists Andreev state(s) of only one helicity at a given edge, no scattering is possible. More rigorously, conduction through helical Andreev edge states is protected by parity against the opening of a gap.

[102], where the authors draw a parallel between the current circulating in a coherent ring of perimeter L in the normal state and the supercurrent circulating in a 1d helical junction of length $L/2$. The many-body spectrum corresponding to states with different parities is displayed in Fig.1.23b. From their work, we can define parity as the parity of the number of fermions below the Fermi energy at $\varphi = 0$, see Fig.1.23 caption.

In Fig.1.24, we present ABS spectrum in the 1-particle picture (with a special rule for occupation configurations), the many-body states energies, and the corresponding supercurrents of an intermediate-length 1d helical junction as a function of superconducting phase difference ϕ. The many-body spectrum exhibits level crossings at integer multiples of π. The crossings at odd multiples (full-line circles) are protected by fermion parity conservation, while those at even multiples (dashed circles) require TRS.

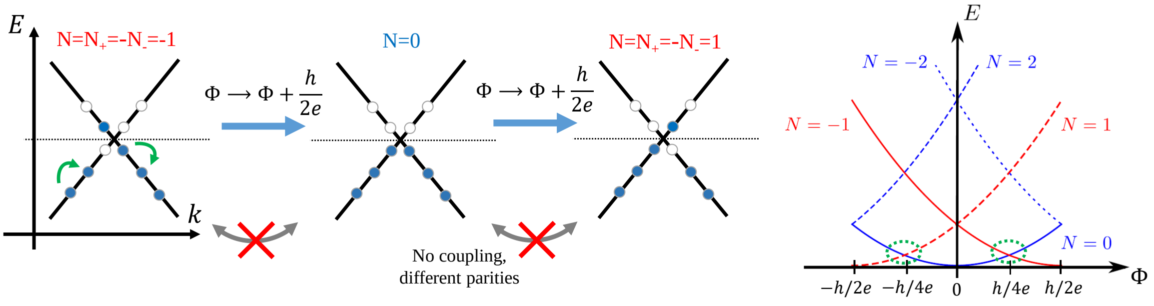

(a) (b)

Figure 1.23 – Many-body states and energies of a 1d helical junction of length $L/2$, similar to a coherent ring of perimeter L with a single pair of helical modes. (a) Three different many-body states changing with Φ. The periodic boundary conditions, together with a magnetic flux Φ in the surface of the ring, yield a quantization of the wavevector k that is related to Φ. In a normal coherent conductor, every quantized states move to its neighbor when Φ changes by h/e adiabatically. In a 1d helical junction of length $L/2$, the same process is realized when $\Phi \longrightarrow \Phi + h/2e$ (green arrows). The central cone represents the ground state at $\Phi = 0$, with $N = 0$ electron-hole excitation. The left cone state, with $N = -1$ at $\Phi = 0$, transforms into the ground state at $\Phi = h/2e$. In the process, the number of fermions under the Fermi energy changes by 1. One can distinguish the left cone state and the central state by the parity of the number of fermions under the Fermi energy. At $\Phi = h/4e$, the two states are degenerate and can't couple to each other because of their different parities. (b) Spectrum corresponding to many-body states with different numbers N (of electron-hole excitations at $\Phi = 0$), as a function of magnetic flux Φ through the ring. The parity-protected crossing are highlighted by the dashed green ellipsoids. Adapted from [102].

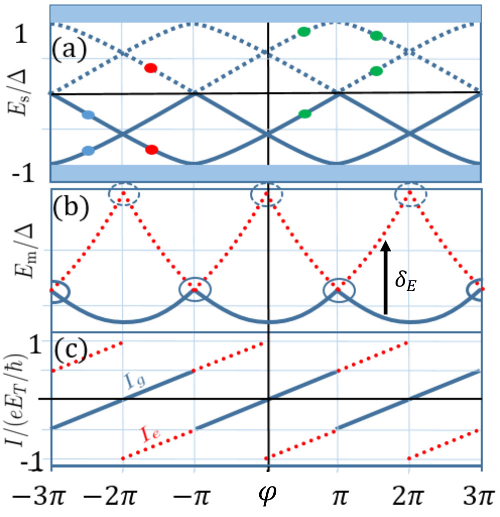

Figure 1.24 – ABS spectrum and supercurrent of an intermediate-length 1d helical junction as a function of superconducting phase difference ϕ. (a) Andreev spectrum of single-particle (Bogoliubov-de Gennes) excitations E_s. In the ground state, the two negative-energy states are occupied (blue circles). The lowest positive-energy state is occupied in the first excited state (and thus the corresponding negative-energy state empty, see red circles). Higher-energy excited states are indicated by green circles (but not included in our theoretical model). (b) Andreev spectrum of corresponding many body states E_m, including the ground state $E_g(\phi)$ (solid blue line) and the first excited state $E_e(\phi)$ (dashed red line). The excitation energy $\delta_E(\phi) = E_e(\phi) - E_g(\phi)$ is indicated by an arrow. (c) Corresponding supercurrents $I_g(\phi)$ in the ground state (solid blue line) and $I_e(\phi)$ in the first excited state (dashed red line).

1.4.3 . Zeeman-induced effects on a 1d helical Josephson junction

Depending on the orientation of the magnetic field, the Zeeman interaction have different effects on the spectrum of a 1d helical Josephson junction. If the magnetic field is perpendicular to the spin quantization axis of the helical modes, it opens gaps and can localize MBS at the limits of the superconducting region [78]. However, the crossing at $E = 0$ and $\varphi = \pi \ mod \ 2\pi$ remains protected by parity. If the magnetic field is aligned with the spin quantization axis, the ABS of opposite spin polarizations are simply shifted by opposite energies, and it exhibits anomalous Josephson effects [73].

In [73], the authors analyze the effect of such magnetic field aligned with the spin quantization axis of a 1d helical Josephson junction. They calculated the CPR for short and long junctions. The Zeeman energy $h = g_{eff}\mu_B B_{||}/2$ enters the ABS phase condition following :

$$\frac{2L(\epsilon_n + h)}{\hbar v_F} - 2\arccos(\frac{\epsilon_n + h}{\Delta}) = \varphi + 2\pi n \tag{1.28}$$

For a short junction :

$$I(\varphi) = \frac{eh}{\pi} - \frac{e\Delta_0}{2\hbar}\sin\frac{\varphi}{2}.\mathrm{sgn}\left[\sin\left(\frac{\varphi - 2\arccos(h/\Delta_0)}{2}\right)\right] \tag{1.29}$$

The first term induces a current shift and is due to the impact of finite momentum pairing on the bulk, as discussed in part 1.3.8. The second term is the usual CPR of a short junction, but with a phase shift $2\arccos(h/\Delta_0)$ of the discontinuity due to the Zeeman energy shift. CPR with various h/Δ_0 are displayed in Fig.1.25a. It can even induce a chiral spin-polarized 1d state for specific values of either only Zeeman splitting or by Zeeman splitting combined with bias current [103].

For a long junction :

$$I(\varphi) = \frac{ev_F}{2\pi L}\left[\varphi + \varphi_h - 2\pi Int\left(\frac{\varphi + \varphi_h}{2\pi}\right)\right] \quad \text{with} \quad \varphi_h = \frac{2L}{\hbar v_F}h + 2\arcsin(h/\Delta_0) \tag{1.30}$$

For long junctions, the CPR is simply shifted in phase by $\varphi_h = \frac{2L}{\hbar v_F}h + 2\arcsin(h/\Delta_0)$. The first term in φ_h is the Zeeman-induced dephasing between up and down spin along the junction of length L. The second term is the contribution from the bulk.

As discussed in part 1.3.8, the phase shifts and anomalous Josephson effects shown here are not specific to 1d helical junctions, and similar effects (albeit different formulas) can arise in junctions with SOC. Thus, this is not an unequivocal signature of conduction through TI.

For both short and long junctions, the current decreases for $h/\Delta_0 > 1$ and the discontinuity disappear, signaling the transition to a topologically trivial state. Lastly, they found that a Zeeman energy $h_\perp$, with a magnetic field perpendicular to the spin quantization axis, breaks the topological phase and opens a gap for $h_\perp > \sqrt{\Delta_{prox}^2 + \mu^2}$.

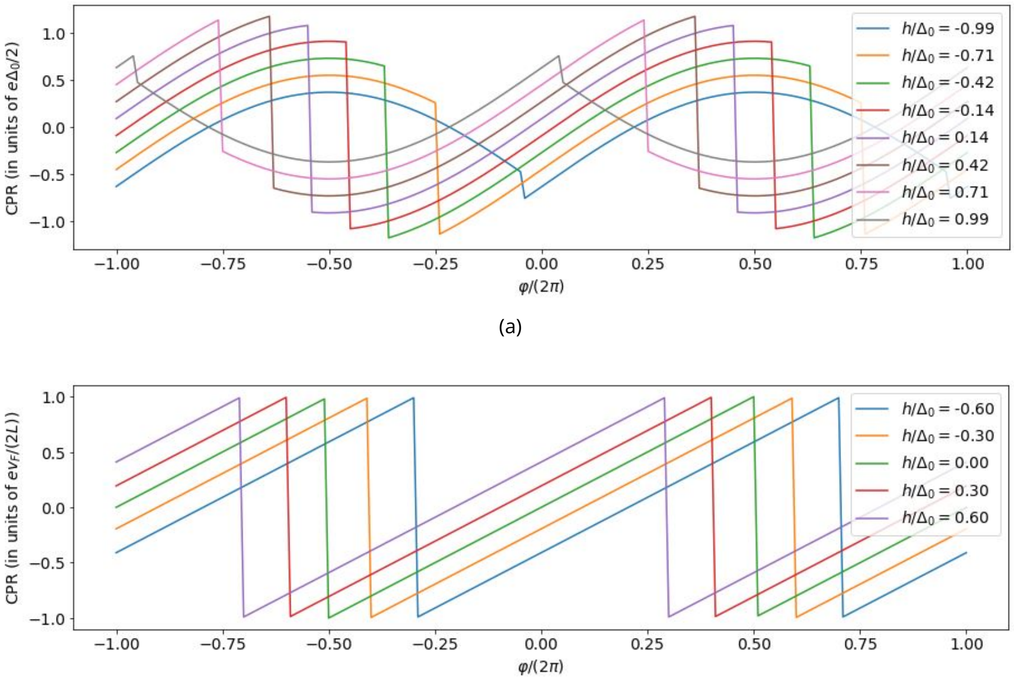

(a)

(b)

Figure 1.25 – (a) CPR of short topological junctions with various Zeeman energies. (b) CPR of long topological junctions with various Zeeman energies.

1.5 . Supercurrent measurements

We saw in the previous sections that the supercurrents, and especially the Current-Phase Relations are a good tool to probe the nature of the superconducting junction. In this section, we introduce the main types of measurements used to probe transport in Josephson junctions.

1.5.1 . AC SQUID

To probe the CPR of a Josephson junction, a first way is to embed it into a superconducting loop and rely on the quantization of flux of fully phase coherent quantum systems. When an external flux Φ is threaded through such a system, it creates an Aharonov-Bohm phase along the loop, and the system adapts its phase such that the total accumulated phase along the loop is a multiple of 2π, or equivalently that the internal flux is a multiple of the quantum of flux $\Phi_0 = h/(2e)$ (h/e if the charge carriers are individual electrons or if the effective phase periodicity of the system is 4π).

This setup is sketched in Fig. 1.26a and is called an "AC SQUID" device (or rf-SQUID), SQUID standing for Superconducting Quantum Interference Device. Following the method used in [62], let us consider the gauge dependent phase along the closed path represented by the black solid line in Fig.1.26a. It can be decomposed into two part : a path C_S from point L to point R going deep inside the superconductor, and a path C_J from point R to point L through the Josephson junction.

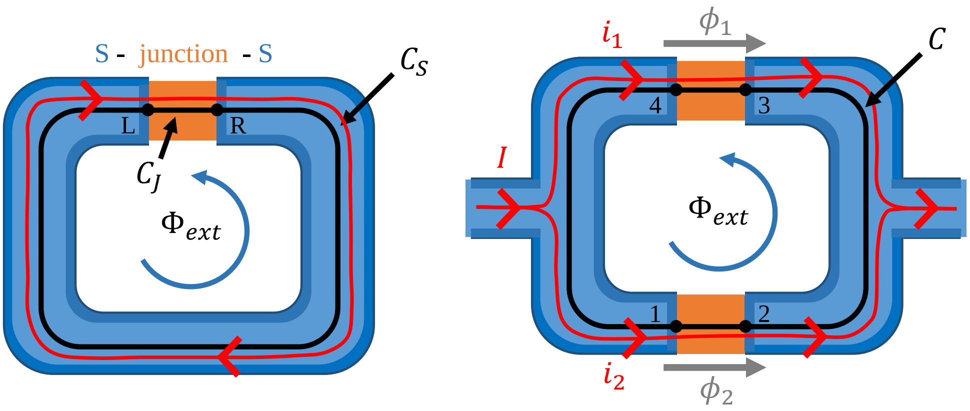

(a) (b)

Figure 1.26 – Sketches of Superconducting QUantum Interference Devices (SQUID). The superconductor leads are represented in blue, and the non-superconducting junction(s) in orange. The screening surface supercurrent is showed as a dark blue region. Applying a magnetic field B out of the plane of the SQUID generate a flux $\Phi_{ext} = B.S$ through the surface S inside the close path $C_S + C_J$ (black solid line). The red solid lines with arrows show the net supercurrent circulating through the device. (a) Sketch of a AC SQUID device. (b) Sketch of a DC SQUID device.

Let us recall that the supercurrent in any phase-coherent system can be written as (see part 1.3.1) :

$$q\Lambda\vec{J_S} = \hbar\vec{\nabla}\varphi \quad \text{with} \quad \vec{\nabla}\varphi = \left(\vec{\nabla}\theta - \frac{q}{\hbar}\vec{A}\right) \quad \text{the gauge invariant phase gradient} \tag{1.31}$$

with θ the gauge dependent phase, $n \propto |\psi|^2$ the carriers' density, q the carriers' charge, m^* the carriers' mass, $\Lambda = m^*/(nq^2)$ the London parameter. We then write the gauge dependent phase constraint for this closed path :

$$\oint_{C_J+C_S} \vec{\nabla}\theta.\vec{dl} = \int_{C_J} \vec{\nabla}\theta.\vec{dl} + \int_{C_S} \vec{\nabla}\theta.\vec{dl} = 0 \tag{1.32}$$

For the path C_S inside the superconductor,
$\int_{C_S} \vec{\nabla}\theta.\vec{dl} = \frac{q}{\hbar}\int_{C_S} \Lambda\vec{J_S}.\vec{dl} + \frac{q}{\hbar}\int_{C_S} \vec{A}.\vec{dl} = \frac{2\pi}{\Phi_0}\int_{C_S} \Lambda\vec{J_S}.\vec{dl} + \frac{2\pi}{\Phi_0}\int_{C_S} \vec{A}.\vec{dl}$

For the path C_J inside the Josephson junction, written as a function of the gauge invariant phase and not the supercurrent density,
$\int_{C_J} \vec{\nabla}\theta.\vec{dl} = \varphi(L) - \varphi(R) + \frac{2\pi}{\Phi_0}\int_{C_J} \vec{A}.\vec{dl}$
This relation does not involve the London model, and rely only on the U(1) gauge symmetry. As such, it is expected to hold for any type of junction that preserves phase coherence.

Thus, we can write :

$$(1.32) \Longleftrightarrow \varphi(R) - \varphi(L) = \frac{2\pi}{\Phi_0}\int_{C_S} \Lambda\vec{J_S}.\vec{dl} + \frac{2\pi}{\Phi_0}\int_{C_S} \vec{A}.\vec{dl} + \frac{2\pi}{\Phi_0}\int_{C_J} \vec{A}.\vec{dl} = \frac{2\pi}{\Phi_0}\int_{C_S} \Lambda\vec{J_S}.\vec{dl} + \frac{2\pi\Phi_{ext}}{\Phi_0}$$

To minimize its free energy, the superconductor cancels out the internal magnetic field by producing screening currents. This gives rise to a "skin" effect with screening currents on a layer of typical size $\lambda_L \sim 100nm$ at the surface of the superconductor, represented with a dark blue color in Fig.1.26a Deep inside the superconductor, $\vec{J_S} = 0$, so the remaining term $\int_{C_S} \Lambda\vec{J_S}.\vec{dl}$ is dominated by what happens at the interface. If the device is symmetric, or using a junction geometry that move the screening current region away from the junction interface, one can obtain $\int_{C_S} \Lambda\vec{J_S}.\vec{dl} \simeq 0$. The red solid line with arrows merely represents the net supercurrent in the loop for a positive magnetic field.

We write :

$$\varphi(R) - \varphi(L) \simeq \frac{2\pi\Phi_{ext}}{\Phi_0} \tag{1.33}$$

with $\Phi_0 = h/q = h/(2e)$, $q = 2e$ in superconductors.

We see that the relation (1.33) relate the gauge invariant phase difference across the junction to the magnetic flux through the loop. *Thus this AC SQUID device allow to control the phase difference with the magnetic field.*

This device has a major flaw however, it needs a way to measure the supercurrent circulating through the annulus. One way is to measure the magnetic field induced by the supercurrent flowing through the annulus, that leaks outside the device and can be probed with devices that are very sensitive to the neighboring field, such as a Hall bar [104] or detector based on giant magnetoresistance [105]. Another way is to couple it to a resonator and track the change of resonance frequencies as well as resonances quality factors as a function of the magnetic field [4, 76, 106].

1.5.2 . Switching current

The switching current measurement is the simplest of all to realize, but may be the hardest of all to interpret. It consists in threading a current through the junction, and measure at what current value the junction becomes resistive, developing a finite voltage. It yields the maximum supercurrent that can be supported by the junction with its present constraints. For idealized junctions, the superconducting phase difference φ across the junction adapts to the supercurrent according to the inverse CPR, and the switching current is equal to the critical current. For real junctions, φ may deviate from the inverse CPR, and the switching is stochastic, as discussed in part 1.10. As we introduced in parts 1.5.1, 1.3.8, 1.4.3 and further develop in parts 1.6, 1.7, 1.8 1.9, the evolution of the switching current of a single junction with magnetic field magnitude and orientation is affected by orbital dephasing and Zeeman coupling, giving insights on the distribution and type of states carrying the supercurrent.

1.5.3 . Asymmetric DC SQUID

A second way to probe the CPR of a Josephson junction is to use a known junction, called the reference junction ($I_{ref}(\phi_2)$), that fixes the phase by fixing its current. Putting in parallel the unknown junction ($I_u(\phi_1)$) that share the same superconducting leads, the two junctions have the same phase difference $\phi_1 = \phi_2$. Threading a magnetic flux inside the surface defined by the two junctions dephases their superconducting phase difference $\phi_{1,2}$, allowing to control the phase difference ϕ_1 of the unknown junction. Let us discuss this setup more rigorously.

We introduce the so-called "DC SQUID" device, sketch in Fig. 1.26b. Applying the same reasoning as for the AC SQUID, we have :

$$\oint_C \vec{\nabla}\theta.\vec{dl} = \int_1^2 \vec{\nabla}\theta.\vec{dl} + \int_2^3 \vec{\nabla}\theta.\vec{dl} + \int_3^4 \vec{\nabla}\theta.\vec{dl} \int_4^1 \vec{\nabla}\theta.\vec{dl} = 0 \tag{1.34}$$

with
$\int_1^2 \vec{\nabla}\theta.\vec{dl} = \phi_2 + \frac{2\pi}{\Phi_0}\int_1^2 \vec{A}.\vec{dl}$
$\int_3^4 \vec{\nabla}\theta.\vec{dl} = -\phi_1 + \frac{2\pi}{\Phi_0}\int_3^4 \vec{A}.\vec{dl}$
$\int_2^3 \vec{\nabla}\theta.\vec{dl} = \frac{2\pi}{\Phi_0}\int_2^3 \Lambda\vec{J_S}.\vec{dl} + \frac{2\pi}{\Phi_0}\int_2^3 \vec{A}.\vec{dl}$
$\int_4^1 \vec{\nabla}\theta.\vec{dl} = \frac{2\pi}{\Phi_0}\int_4^1 \Lambda\vec{J_S}.\vec{dl} + \frac{2\pi}{\Phi_0}\int_4^1 \vec{A}.\vec{dl}$

$$(1.34) \Longleftrightarrow \phi_1 - \phi_2 = \frac{2\pi\Phi_{ext}}{\Phi_0} + \frac{2\pi}{\Phi_0}\int_2^3 \Lambda\vec{J_S}.\vec{dl} + \frac{2\pi}{\Phi_0}\int_4^1 \Lambda\vec{J_S}.\vec{dl}$$

Thus

$$(1.34) \Longleftrightarrow \phi_1 - \phi_2 \simeq \frac{2\pi\Phi_{ext}}{\Phi_0}$$

Writing $i_1(\phi_1)$ the CPR of the top junction, $i_2(\phi_2)$ the CPR of the bottom junction, the total supercurrent I is :

$$I(\phi_1, \phi_2) = i_1(\phi_1) + i_2(\phi_2) = i_1(\phi_2 + \frac{2\pi\Phi_{ext}}{\Phi_0}) + i_2(\phi_2) = i_1(\phi_2 + \frac{2\pi B.S}{\Phi_0}) + i_2(\phi_2) = I(B, \phi_2) \quad (1.35)$$

with S the surface inside the loop C.

Now taking $i_1 = I_u$ and $i_2 = I_{ref}$, with $I_{c,ref} \gg I_{c,u}$, we get :

$$I_c(B) = \max_{\phi_2} I(B, \phi_2) = I(B, \phi_2^{max}) \simeq I_u(\phi_2^{max} + \frac{2\pi B.S}{\Phi_0}) + I_{c,ref} \quad (1.36)$$

with $I_{c,ref} = \max_{\phi_2}[I_{ref}(\phi_2)] = I_{ref}(\phi_2^{max})$ and ϕ_2^{max} known or not known, with a magnetic field dependence only on $I_u(\phi_2^{max} + \frac{2\pi B.S}{\Phi_0})$.

This asymmetric DC SQUID setup provides a way to probe the CPR of an unknown junction by measuring the total critical current variations as a function of magnetic field $I_c(B)$.

Here, we introduced the asymmetric DC SQUID as a way of measuring the CPR of an unknown junction, but it can be used to get some informations on the CPR of the junctions even in a more symmetric situation. This idea is developed in part. 1.6. Another benefit of the study of DC SQUID is that it is the building block of the theory of extended multichannel junctions, where different supercurrent paths inside a single junction can experience an orbital dephasing and give rise to interference patterns, just like the DC SQUID device.

1.5.4 . Dynamical Josephson effects

The second Josephson relation (Eqs.(1.18) or (1.8)) relates the evolution of the superconducting phase φ to the electrostatic energy V :

$$\hbar \frac{\partial \varphi}{\partial t} = 2eV \quad (1.37)$$

One can exploit this relation in two ways.

Let us consider a combination of DC and AC voltage $V(t) = V_{AC} \cos \omega t + V_{DC}$, φ writes $\varphi(t) = \varphi_0 + \frac{2eV_{DC}}{\hbar} t + \frac{2eV_{AC}}{\hbar\omega} \sin \omega t$. Decomposing the CPR in its harmonic content indexed by n and injecting the expression of $\varphi(t)$, we get :

$$\begin{aligned} I(t) &= \sum_n I_{c,n} \sin\left(n\left(\varphi_0 + \frac{2eV_{DC}}{\hbar} t + \frac{2eV_{AC}}{\hbar\omega} \sin \omega t\right) + \varphi_n\right) \\ &= \sum_n \sum_m (-1)^m I_{c,n} J_m\left(n\frac{2eV_{AC}}{\hbar\omega}\right) \sin\left(n\varphi_0 + \varphi_n + \left(n\frac{2eV_{DC}}{\hbar} - m\omega\right) t\right) \end{aligned} \quad (1.38)$$

where is included the time independent φ_n to account for anomalous Josephson effect. $J_m(x)$ is the m-th Bessel function.

First, biasing the junction with a DC voltage $V_{DC} \neq 0$ and $V_{AC} = 0$ produces an alternating supercurrent which period depends on the periodicity (harmonic content) of the CPR. This process is called by the AC Josephson effect. A conventional 2π-periodic CPR yields a current oscillating at $f_J = \frac{2eV_{DC}}{h} \Longrightarrow f_J/V_{DC} \simeq 484THz.V^{-1}$. For topologically-protected junctions, it features a doubling of the periodicity, the so-called 4π-Josephson effect, or equivalently a halving of the frequency $f_J/2$. One can detect these high-frequency current with adapted instruments.

Second, using an AC voltage $V_{AC} \neq 0$, one can induce quantized V_{DC} voltage plateaus with DC currents. Looking at Eq.(1.38), we see that we can obtain a DC current for $\left(n\frac{2eV_{DC}}{\hbar} - m\omega\right) = 0 \Longleftrightarrow V_{DC} = \frac{m}{n}\frac{\hbar\omega}{2e}$, with $m \in \mathbb{Z}$ the index of the Bessel development and n the index of the harmonic of the CPR. For a sinusoidal CPR with $I_{c,1} \neq 0$ and $I_{c,n\neq 1} = 0$, there is voltage plateaus every $\frac{\hbar\omega}{2e}$: $V_{DC} = m\frac{\hbar\omega}{2e}$. They are called Shapiro steps. CPR with higher harmonics n leads to intermediate steps. For a 4π-periodic junction, there is an additional contribution to the CPR in $\sin(\varphi/2)$, yielding $n = 1/2 \implies V_{DC} = 2m\frac{\hbar\omega}{2e}$, with stronger even m plateaus. This doubling effect is discussed in more details in [101].

During my PhD, I was invited to a two weeks trip to Advanced Device Laboratory, RIKEN, Wako, Japan to work with Russell S. Deacon in the team of Koji Ishibashi. I came with several bismuth-based Josephson junctions adapted for high frequency measurements. We tried to measure the 4π-periodicity both with missing odd Shapiro steps [79] and half-frequency Josephson emission [80], but the average switching current $\langle I_s \rangle$ of the junctions were too high for the measurement apparatus bandwidth f_{BW} ($\langle I_s \rangle \gtrsim 2\mu A \implies R\langle I_s \rangle > \frac{hf_{BW}}{4e} \simeq 10\mu V$).

1.6 . Critical current of a two-channel junction

In the previous sections, we studied various CPR and experimental methods to probe them. These CPR involve a single conducting channel, and possibly other degenerate channels that can couple together in the presence of a scatterer. In real junctions, it is very rare to have such single conducting channel, and we need to consider multi-channels junctions. In this subsection, we will first study the two channels case and the effects of magnetic flux and Zeeman interaction. To compute the critical currents and extract the individual phase differences of the superconducting channels, I created a simple python program that samples all phase configurations and looks for the one that maximize the total supercurrent while satisfying the total phase constrains.

1.6.1 . Two long ballistic channels

Let us start with a junction with two channels, labeled by 1 and 2. If the supercurrent through the junction is carried by these two channels only, the total supercurrent is :

$$I = i_1(\phi_1) + i_2(\phi_2) \tag{1.39}$$

with $i_1(\phi_1)$ the CPR for the path 1 with phase difference ϕ_1, and $i_2(\phi_2)$ the CPR for the path 2 with phase difference ϕ_2.

Just like in our analysis of the DC SQUID, the two paths can be abstractly joined inside the superconductor to form a closed loop, and define a surface S and a magnetic flux $\Phi = B.S$, that will give rise to a phase difference $2\pi\Phi/\Phi_0$, such that :

$$I(B, \phi_2) = i_1(\phi_2 + \frac{2\pi B.S}{\Phi_0}) + i_2(\phi_2) \tag{1.40}$$

and the critical current is $I_c(B) = \max_{\phi_2} I(B, \phi_2)$.

This method can be generalized to more than two channels, and can take into account the specific geometrical constraints by choosing the set of valid paths.

To illustrate the behavior of the two channels junctions with assumption that are relevant to the systems we are studying, let us look at the case of two long ballistic channels. They display sawtooth CPR that are linear $i_{1,2}(\phi_{1,2}) = i_{c1,c2}\mathrm{Saw}(\phi_{1,2}) = i_{c1,c2}\left(\frac{\phi_{1,2}}{\pi} - Int(\frac{\phi_{1,2}+\pi}{2\pi})\right)$, see Fig.1.18b. We can write :

$$I = i_{c1}\mathrm{Saw}(\phi_1) + i_{c2}\mathrm{Saw}(\phi_2), \tag{1.41}$$

where i_{c1} and i_{c2} are the critical currents of the two branches, and the superconducting phase differences at these two branches satisfy

$$\phi_1 - \phi_2 = \Phi, \tag{1.42}$$

with $\Phi = 2\pi\Phi/\Phi_0$. The critical current is obtained by maximizing the total current in Eq. (6.15) given the constraint specified by Eq. (6.16).

This problem can be solved analytically. Defining $\Delta\phi^+ = 2\pi\frac{i_{c1}}{i_{c1}+i_{c2}}$ and $\Delta\phi^- = 2\pi\frac{i_{c2}}{i_{c1}+i_{c2}}$, we can write the critical current as :

$$I_c(\Phi) = \begin{cases} i_{c1} + i_{c2} - i_{c2}\frac{\Phi}{\pi} & \Phi \geq 0 \\ i_{c1} + i_{c2} + i_{c1}\frac{\Phi}{\pi} & \Phi \leq 0 \end{cases} \tag{1.43}$$

The range of validity of this formula over a phase of 2π is given by :

$$-\Delta\phi^- \leq \Phi \leq \Delta\phi^+ \tag{1.44}$$

If Φ is outside this interval, then the critical current can be obtained by applying periodic property $I_c(\Phi) = I_c(\Phi + 2\pi)$.

The modulation amplitude is :

$$\Delta I_c = \frac{2 i_{c1} i_{c2}}{i_{c1} + i_{c2}} \tag{1.45}$$

In Fig.1.27, we show computation of the critical current as a function of magnetic field $I_c(\Phi = B.S)$ for symmetric and asymmetric critical currents (Fig.1.27a), and extract the individual phase differences $\phi_{1,2}$ of the superconducting channels. We see various behaviors that we investigate in the following.

We notice in Fig.1.27a that in the case of symmetric channels with identical $i_{c1} = i_{c2}$ (blue line), the supercurrent never goes to zero, that is $\Delta I_c/I_c^{\max} = 1/2$. Looking at the phases variations in Fig. 1.27b, we see a very peculiar behavior. Over one period, the phase ϕ_1 of channel 1 increases linearly from $\phi_1 = 0$ to π when the "flux phase" Φ increases from $\Phi = -\pi$ to 0 $(+2\pi n)$, and then stays constant at $\phi_1 = \pi$ for $\Phi = 0$ to π $(+2\pi n)$. Meanwhile, the phase ϕ_2 of channel 2 has a complementary behavior, following Eq. 6.16 phase constraint. It makes it clear that the junction changes its behavior at $\Phi = 0 + 2\pi n$ and $\Phi = \pi + 2\pi n$.

For asymmetric channels with different critical currents $i_{c1} \neq i_{c2}$, see Fig.1.27a orange line, we see that the modulation is reduced, and an asymmetry $I_c(\Phi) \neq I_c(-\Phi)$ developed, yielding skewed triangular periodic modulations. Looking at the individual phases of the two junctions in this configuration, Fig.1.27c, we identify similarities and differences with the symmetric case Fig.1.27b. It also displays plateaus at $\phi_{1,2} = \pi$, but whose extension is different for ϕ_1 and ϕ_2. Moreover, the range of variation of the phases are different, with ϕ_1 exploring a much wider range a phase than ϕ_2.

The critical current of this junction, behaving like a DC SQUID, can be understood by answering the following three questions :
- What is the maximum critical current and the corresponding flux ?
- What is the behavior close to the maximum critical current ?
- At what flux the junction can find another configuration for the phases $\phi_{1,2}$ such that the total maximum current is higher ?

In the situations studied here, the maximum of $I_c(\Phi)$ is at $\Phi = 0$. Let us consider the addition of a small positive flux for a junction at its maximum I_c : $\Phi = 0 + \varepsilon_0$ $(0 < \varepsilon_0 \ll \pi)$. Because of the constraint Eq.(6.16), such a flux imposes $\phi_1 - \phi_2 = \varepsilon_0$. To accommodate to this flux, either ϕ_1 must increase or ϕ_2 must decrease.

But at $\Phi = 0$, the channel 1 was already at its maximum current configuration $i_1(\phi_1 = \pi) = i_c$, and increasing its phase would mean to go above $\phi_1 = \pi$ and end up with a negative supercurrent $i_1(\pi + \varepsilon_0) = i_1(\pi + \varepsilon_0 - 2\pi) = i_1(-\pi + \varepsilon_0) = i_1(-(\pi - \varepsilon_0)) = -i_1(\pi - \varepsilon_0)$, that would lower the total current by $\sim 2i_{c1}$.

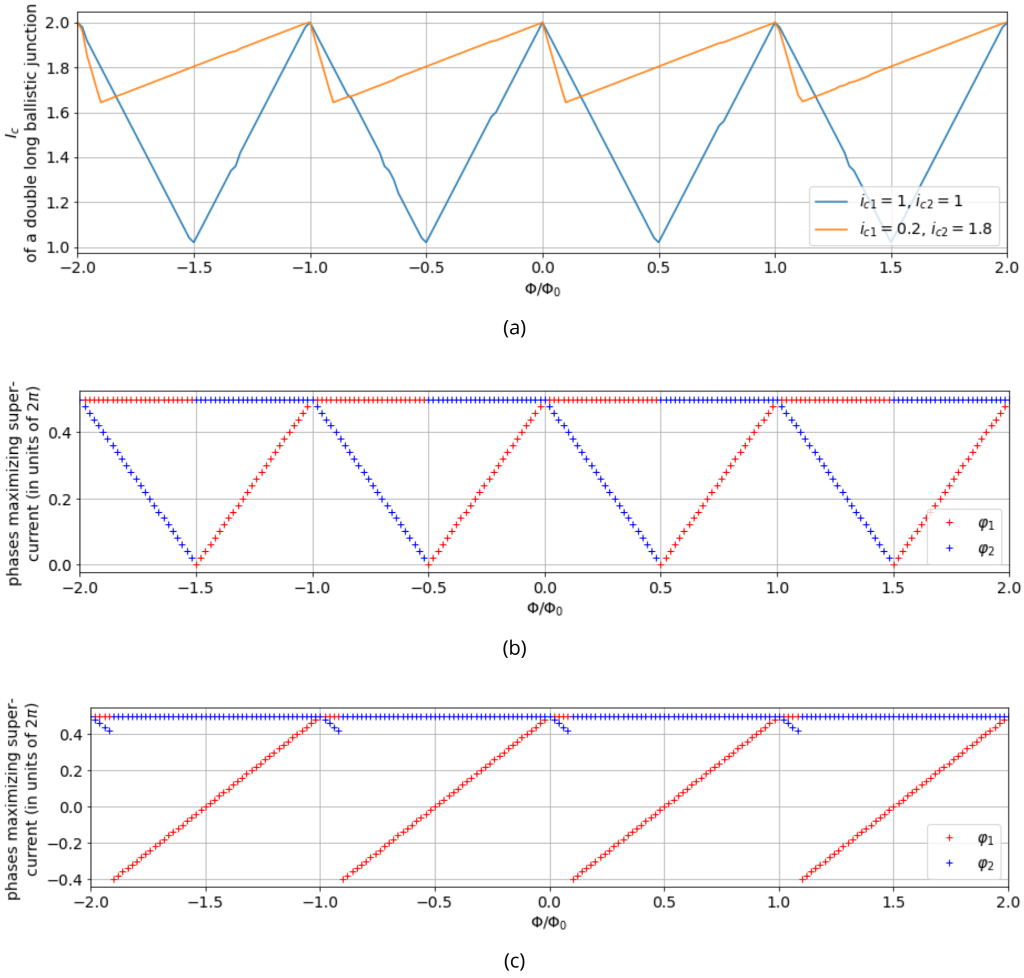

(a)

(b)

(c)

Figure 1.27 – (a) Critical current as a function of applied magnetic field for a junction featuring two long ballistic subjunctions, forming a DC SQUID. (b),(c) Corresponding phase differences of both junctions when $I = I_c$ in the symmetric case and in the asymmetric case, respectively.

On the other hand, decreasing ϕ_2 results in $i_2(\phi_2 = \pi - \varepsilon_0) = \frac{i_{c2}}{\pi}(\pi - \varepsilon_0)$, with a loss of total current $\delta i_2 = i_{c2} - i_2(\phi_2 = \pi - \varepsilon_0) = \frac{i_{c2}}{\pi}\varepsilon_0 \ll 2i_{c1}$. We conclude that at $\Phi = 0 + \varepsilon$, the phase of channel 2 varies to absorb the change of phase produced by the magnetic flux, and the phase of channel 1 stays at $\phi_1 = \pi$, just like what we see in the computed data. Applying the same reasoning for $\Phi = 0 - \varepsilon$, we conclude that ϕ_1 must decrease and $\phi_2 = \pi$.

However, with increasing Φ, there is a point where changing i_1 by $\delta i_1 = i_{c1} - i_1(\phi_1 = \pi + \Phi)$ and setting i_2 to its maximum value i_{c2} results in a higher total current. This condition writes :

$$\delta i_1 < \delta i_2 \Longleftrightarrow i_{c1} - i_1(\phi_1 = \pi + \Phi) < i_{c2} - i_2(\phi_2 = \pi - \Phi) \tag{1.46}$$

For the symmetric case, this condition is fulfilled when $\Phi/\Phi_0 > \pi$. At this value of flux, $\phi_1 - \phi_2 = \pi$, and one junction carries no current while the other carries its maximum current, yielding $I_c = i_{c1}(= i_{c2})$. This contrast with the usual pattern of symmetric DC SQUID with tunnel junctions, as discussed after. For the asymmetric case, Fig.1.28 shows the total current when either one phase vary or the other, and the critical current is the maximum over the two situations. We see that with its lower critical current $i_{c1} \ll i_{c2}$, varying the phase of junction 1 is the less "costly" in current for most of the flux values. Hence, except for the small range of flux where i_2 varies, the modulation of the critical current with flux reflects the CPR

$i_1(\phi_1)$ of junction 1, where only the part of its CPR with the lowest current is missing. This explains the behaviors observed in Fig.1.27. The total range of phase explored by ϕ_1 is $\pi\left(1+\frac{i_{c2}-i_{c1}}{i_{c1}+i_{c2}}\right)$, and by ϕ_2 is $\pi\left(1-\frac{i_{c2}-i_{c1}}{i_{c1}+i_{c2}}\right)$.

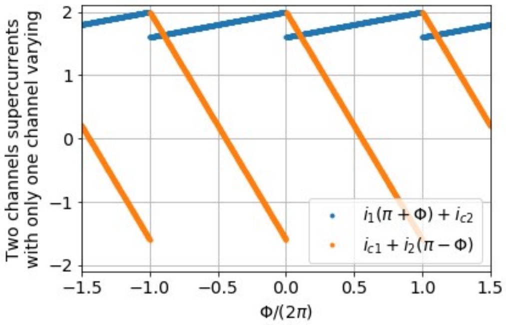

Figure 1.28 – Computation of the total supercurrent through an asymmetric DC SQUID with two long ballistic channels ($i_{c1} = 0.2$ and $i_{c2} = 1.8$) in two different configurations. The blue dots is the total current if the phase ϕ_1 across the channel 1 varies and $\phi_2 = \phi_2^{max}$ of the channel 2 is constant. The orange dots is the total current if the phase ϕ_2 across the channel 2 varies and $\phi_1 = \phi_1^{max}$ of the channel 1 is constant. Depending on the value of the flux Φ, one configuration yields a higher total current than the other. The critical current as a function of Φ is given by the maximum of these two curves.

1.6.2 . Other two channels junctions

After the analysis of the behavior of the DC SQUID with two channels with linear CPRs, which presents both the advantage of having simple analytical solutions and being relevant for modeling long ballistic topologically protected states, we now focus on more complex CPR that we may encounter in our experiments.

a) Short ballistic junctions

Fig. 1.29a shows $I_c(\Phi)$ computed patterns for DC SQUIDs with two short ballistic junctions with symmetric ($i_{c1} = i_{c1}$) and asymmetric ($i_{c1} \neq i_{c1}$) junctions, and the respective phases $\phi_{1,2}$ variations for both channels (Figs. 1.29b, 1.29c). The CPR of a short ballistic junction is plotted in Fig.1.18a.

The blue solid curve in Fig. 1.29a corresponds to a symmetric DC SQUID. Compared to the long ballistic case previously presented, the oscillations periodicity and amplitude are the same, with maximums at $\Phi = 0$ and with minimums of $I_c(0)/2$ at $\Phi = \pi$, but the shape is different. The pattern displays rounded peaks and sharp dips.

To better understand this, let us look at the corresponding phases $\phi_{1,2}$ in Fig. 1.29b. For $\Phi : -\pi \to 0$, we see that ϕ_1 increases linearly from 0 to π and $\phi_2 = \pi$. For $\Phi : 0 \to \pi$, ϕ_2 decreases linearly from π to 0 and $\phi_1 = \pi$. Thus, the phases' behavior is exactly the same as in the symmetric DC SQUID with long ballistic channels, and the difference in shape come from the differences between the linear long ballistic channel CPR and the doubled-period sinusoidal short ballistic channel CPR. They both are odd in phase and maximum at $\phi = \pi$, explaining their similarities at $\Phi = 0$ and $\Phi = \pi$, but the latter is curved with a negative second derivative in the $[0, \pi]$ range and has a 0 first derivative at its maximum at π.

This yields a curved shape between $\Phi = -\pi$ and $\Phi = \pi$, with a smooth transition with $\partial I_c/\partial\Phi = 0$ at $\Phi = 0$ when the junction swap between $I_c(\Phi) = i_1(\phi_1 = \pi + \Phi) + i_2(\phi_2 = \pi)$ and $I_c(\Phi) = i_1(\phi_1 = \pi) + i_2(\phi_2 = \pi - \Phi)$ (variations close to $\phi_{1,2} = \pi$), and a sharp transition when the junction swap between

$I_c(\Phi = \pi + \varepsilon) = i_1(\phi_1 = \varepsilon) + i_2(\phi_2 = \pi)$ and $I_c(\Phi) = i_1(\phi_1 = \pi) + i_2(\phi_2 = -\varepsilon)$ (variations close to $\phi_{1,2} = 0$).

The orange line in Fig. 1.29a results from a computation in the asymmetric junctions case, with $i_{c1} = 0.2$ and $i_{c2} = 1.8$. The corresponding phases $\phi_{1,2}$ variations are plotted in Fig.1.29c. One can understand this behavior the same way as the case in the previous subsection, with long ballistic junctions.

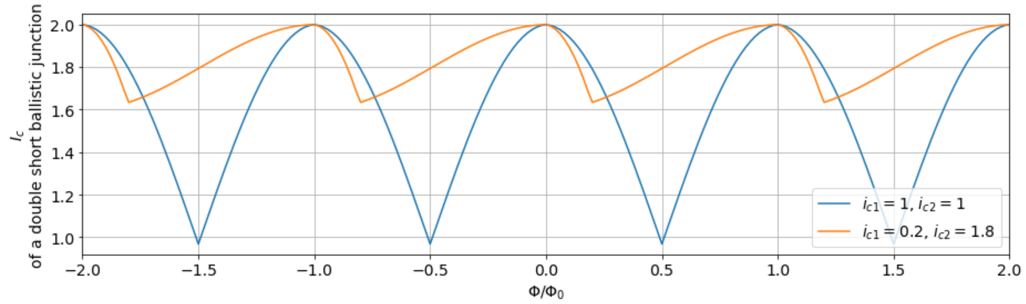

(a)

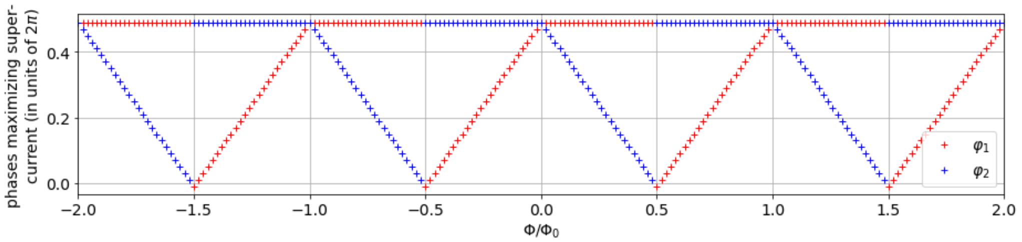

(b)

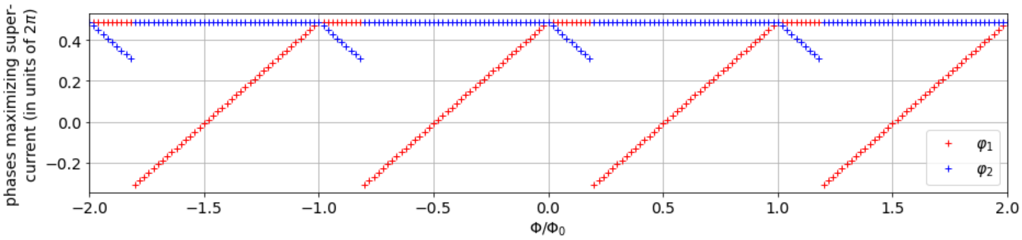

(c)

Figure 1.29 – (a) Critical current as a function of applied magnetic field for a junction featuring two short ballistic subjunctions, forming a DC SQUID. (b),(c) Corresponding phase differences of both junctions when $I = I_c$ in the symmetric case and in the asymmetric case, respectively.

b) Sinusoidal junctions

So far, we only considered ballistic channels with CPRs that present a discontinuity at $\phi = \pm\pi$. However, this type of CPR is only expected for ballistic channels, meaning very clean or topologically protected, at zero temperature. When taking into account scatterings or finite temperature, the discontinuity at $\phi = \pm\pi$ disappears and is replaced by a smooth transition between positive and negative current, the maximum current is reduced, and the phase of the maximum current $\phi^{max} < \pi$, see Fig.1.18. In the limit of low transmission (tunnel regime) or high temperature, the CPR is reduced to : $i(\phi) = i_c \sin\phi$, which is smooth everywhere, has a maximum at $\phi = \pi/2$, a minimum at $\phi = -\pi/2$, is antisymmetric with respect to $\phi = 0, \pm\pi$, and symmetric with respect to $\phi = \pm\pi/2$.

In Fig. 1.30a, we show the computed critical current for a DC SQUID composed of two sinusoidal junctions with symmetric ($i_{c1} = i_{c1}$) and asymmetric ($i_{c1} \neq i_{c1}$) junctions, and the respective phases $\phi_{1,2}$ variations for both channels (Figs. 1.30b, 1.30c). In the symmetric situation, the critical current represented by the blue solid line looks similar to the behavior of the DC SQUID with two short ballistic junctions in the same conditions, but here the oscillations goes down to a minimum of $I_c(\Phi = \pi) = I_c^{min} = 0$. However, looking at the asymmetric critical currents case (orange solid curve), we see a striking difference : the critical current oscillate with a sinusoidal pattern, displaying the CPR of the channel 1, and never following the CPR of the channel 2.

To clarify the situation, let us compare the individual phase differences of both channels in the two situations with the previously studied DC SQUID with short ballistic channels, see Figs. 1.30b, 1.30c. First, the variations of the phases in the symmetric situation (Fig. 1.30b) is different : they both vary simultaneously in opposite fashion. This is because there is no discontinuity in the CPRs close to their maximum current anymore, such that there is no very costly phase variations in one way compared to the other. For two channels with identical sinusoidal CPRs, the cost in current to increase the phase of channel 1 is equal to the cost in current to decrease the phase of channel 2.

To understand why the symmetric SQUID (blue curve in Fig. 1.30a) oscillations go to $I_c(\Phi = \pi) = 0$, let us have a closer look at Fig. 1.30b. At $\Phi = \pi$, $\phi_1 - \phi_2 = \pi$, meaning that the channels 1 and 2 must absorb together a phase π (absorb compared to $\Phi = 0$). Between $\Phi = 0$ and $\Phi = \pi$, $\phi_1 : \pi/2 \to \pi$ and $\phi_2 : \pi/2 \to 0$, such that the two channels share this phase π evenly, leading to $I_c(\Phi = \pi) = i_1(\pi/2 + \pi/2) + i_2(\pi/2 - \pi/2) = i_1(\pi) + i_2(0) = 0 + 0 = 0$. It contrasts with the ballistic channels SQUID, where the phase of only one channel varies to absorb $\phi_1 - \phi_2 = \pi$ while the other remains at its maximum current, leading to $I_c(\Phi = \pi) = i_1(\pi) + i_2(\pi - \pi) = i_1(\pi) + i_2(0) = i_{c1} + 0 = i_{c1}$.

In the asymmetric situations Fig. 1.30c, the difference between the costs in total current for a phase variation of the two channels ($\frac{\partial i_{1,2}}{\partial \Phi}$) is big enough to limit the variation of the phases to one channel at any value of the flux. This is not entirely true, as i_2 still has some leeway around its maximum value because $\frac{\partial i_2}{\partial \Phi} = 0$ for $\phi_2 = \pi/2$. More rigorously, one need to compare $\frac{\partial i_1}{\partial \phi_1}$ to $\frac{\partial i_2}{\partial \phi_2}$ at each $\phi_1 - \phi_2 = \Phi$.

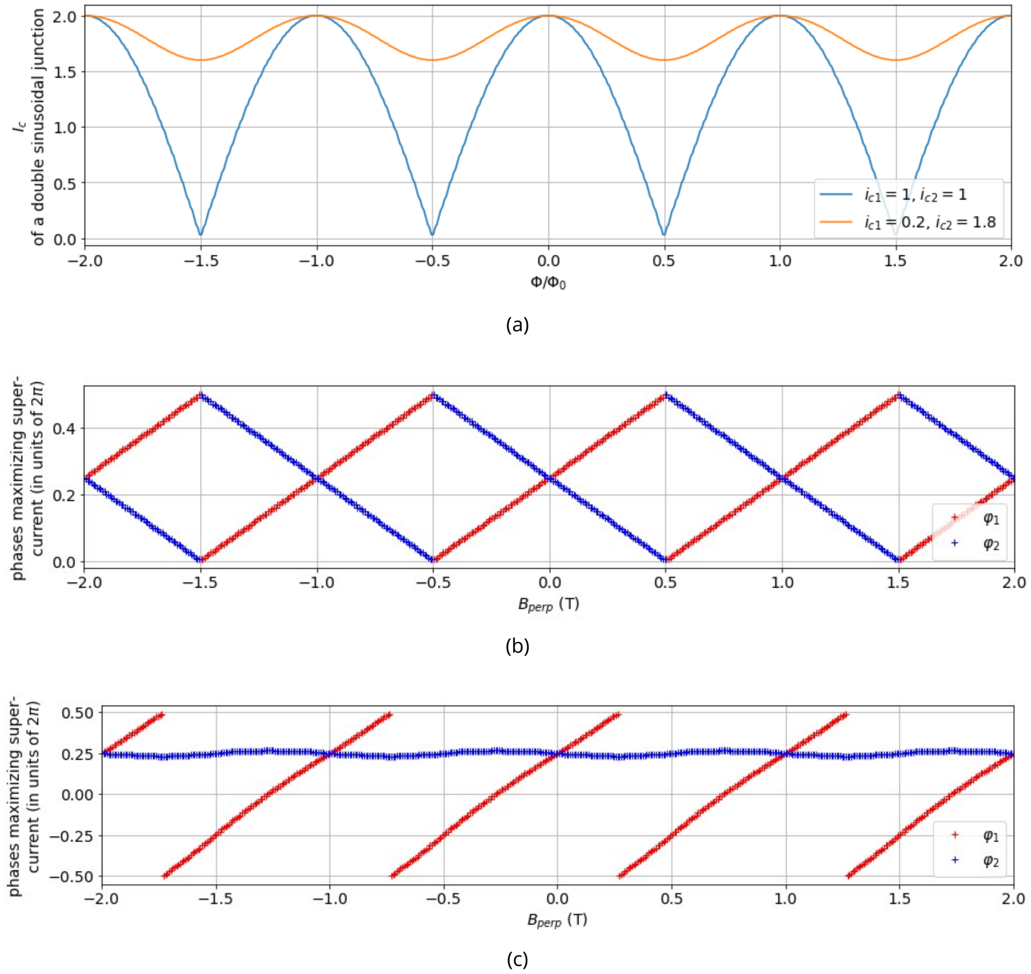

(a)

(b)

(c)

Figure 1.30 – (a) Computed critical current as a function of applied magnetic field for a junction featuring two sub-junctions with sinusoidal CPRs, forming a DC SQUID. (b),(c) Corresponding phase differences of both junctions when $I = I_c$ in the symmetric case and in the asymmetric case, respectively.

1.6.3 . Two 1d helical junctions with Zeeman energy

In this section, we now consider the effects on 1d helical channels of an energy term coming from a Zeeman interaction. In [73], the authors introduce a Zeeman term $\hat{H}_Z = -h\hat{\sigma_z}$ in the hamiltonian, where σ_z is the diagonal Pauli matrix. This term modifies the CPR as presented in part 1.4.3, following Eq. (1.29) for short topological junctions and Eq. (1.30) for long topological junctions.

The computed critical current of a DC SQUID with two short 1d helical channels is presented in Fig.1.31a with various parameters E_{Z1}/Δ and E_{Z2}/Δ, Δ being the superconducting energy of the superconducting leads, E_{Z1} the Zeeman energy for the channel 1, and E_{Z2} the Zeeman energy for the channel 2.

For the symmetric cases displayed as blue and orange solid lines, we see that they are both maximum at 0 field, but have very different shapes, maxima and minima. The blue solid curve is explained by the fact that both the maximum current of the CPR and the first order derivative of the current close to its maximum increases with E_Z/Δ_0 (see Fig.1.25a), leading to a behavior similar to the long ballistic junction.

On the other hand, the orange solid curve is explained by two factors. First, with decreasing E_Z/Δ_0, the maximum current of the CPR decreases, reducing the oscillations' amplitude. Second, with decreasing E_Z/Δ_0, the discontinuity in the CPR moves higher in phase, and the CPR extends its sinusoidal shape higher in phase, see Fig.1.25a. This leads to a smooth sinusoidal behavior in the vicinity of the maximum current of the CPR, explaining the similarity of the orange curve to the sinusoidal junction case.

The asymmetric situations lead to intermediate results, where a shift of the pattern can occur, and where the shape in the vicinity of the maxima is dictated by the CPR of the channel with the lowest first order derivative close to its maximum current phase. Fig.1.31b shows the same computations for long 1d helical junctions. Because the Zeeman energy only shifts the CPR for long 1d helical junctions (see Fig.1.25b), there is no effect of E_Z when the two junctions have identical $E_{Z1} = E_{Z2}$ (see blue and orange lines on top of each other), and the pattern is shifted for $E_{Z1} \neq E_{Z2}$ (see green line).

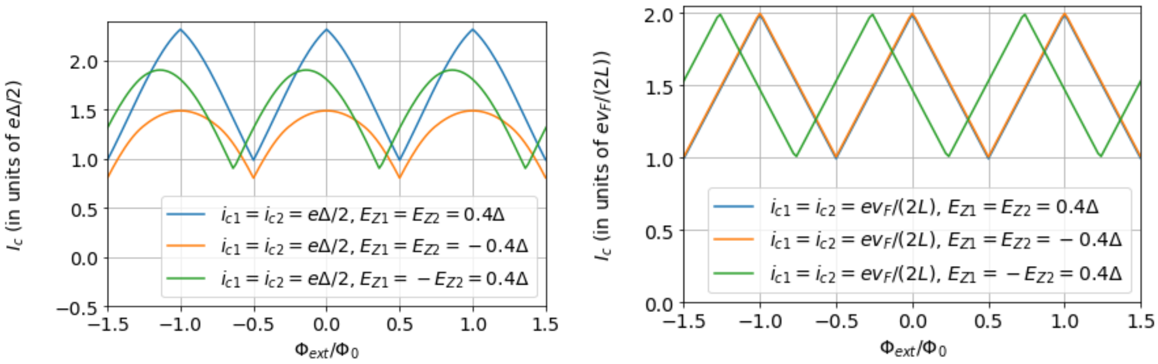

(a) (b)

Figure 1.31 – Critical current of a DC SQUID featuring two 1d helical channels/junctions, as a function of magnetic flux Φ_{ext} applied through the SQUID surface via an external magnetic field. (a) Junctions 1 and 2 are short 1d helical junctions with critical currents i_{c1} and i_{c2}, and Zeeman energies E_{Z1} and E_{Z2}, respectively. Blue line : $i_{c1} = i_{c2} = e\Delta/2$ and $E_{Z1} = E_{Z2} = 0.4\Delta$. Orange line : $i_{c1} = i_{c2} = e\Delta/2$ and $E_{Z1} = E_{Z2} = -0.4\Delta$. Green line : $i_{c1} = i_{c2} = e\Delta/2$ and $E_{Z1} = -E_{Z2} = 0.4\Delta$, showing a phase shift due to anomalous Josephson effect. (b) Junctions 1 and 2 are long 1d helical junctions with critical currents i_{c1} and i_{c2}, and Zeeman energies E_{Z1} and E_{Z2}, respectively. Blue line : $i_{c1} = i_{c2} = ev_F/(2L)$ and $E_{Z1} = E_{Z2} = 0.4\Delta$. Orange line : $i_{c1} = i_{c2} = ev_F/(2L)$ and $E_{Z1} = E_{Z2} = -0.4\Delta$. Green line : $i_{c1} = i_{c2} = ev_F/(2L)$ and $E_{Z1} = -E_{Z2} = 0.4\Delta$, showing a phase shift due to anomalous Josephson effect.

1.7 . Symmetries and inductances in superconducting junctions and SQUIDs

In this section, we discuss several effects that can influence the symmetries of the response in current of junctions in a superconducting circuit, as a function of magnetic field. The various sources of asymmetries depend on the circuit considered (single-junction critical current, AC SQUID, DC SQUID) as well as on the physical phenomenon considered (self-field effects, unknown junctions, asymmetric CPR content, anomalous Josephson effect). The asymmetry of the critical current versus magnetic field pattern induces Josephson Diode Effect (JDE), which is currently a trending topic in the community.

Among the possible origins of JDE, the Anomalous Josephson Effects (AJE) found in materials with SOC are very interesting and are attracting a growing attention from the scientific community. AJE can manifest as a form of Magneto-Chiral Anisotropy (MCA) yielding anisotropies of critical current depending on the geometry of the sample as well as the relative angle between the current vector and the magnetic field vector, see appendix 6.7.6. In part 1.6.3, we saw some effects of AJE in a DC SQUID, and in particular phase shift of the critical current pattern (see green lines in Figs.1.31a and 1.31b.

From a given asymmetric pattern, it may be hard to disentangle the contributions of the different phenomenons, especially in our Bi samples with a lot of uncontrolled/unknown parameters (geometry-dependent conduction modes). The various effects do not scale identically with the current, the magnetic field magnitude, the temperature, and the magnetic field orientation, as discussed in appendix 6.2.

This study is useful to understand the intermediate field scale behaviors of the samples analyzed in chapter 3. Moreover, we present in appendix 6.12 an analysis of the $I_c(\Phi_{ext})$ pattern of a DC SQUID made out of two segments of the same bismuth nanowire. It shows an important asymmetry varying with magnetic field orientation, that we quantify with a $B_{eff} = \beta I$ both in the superconducting state and the resistive state. A more thorough analysis is needed, but it may show experimental evidence for a link between the Edelstein effect in the resistive state and AJE in the superconducting state. Clever sample geometry and combinations of measurements at different field orientation and different temperatures may allow to isolate AJE.

First, we introduce the relations between time-reversal symmetry, inversion symmetry, and JDE. Then, we study the effects of inductive elements, with a focus on DC SQUID, which is the most relevant model for our experiments. Lastly, we discuss other sources of shifts in the critical current pattern.

1.7.1 . Time-reversal symmetry, inversion symmetry, and Josephson Diode Effect

We first consider a system that respects time-reversal symmetry (TRS) as a whole. Its response when excited one way is the time-reversed response when excited the time-reversed way. For a Josephson junction current response I, if there are no other TRS breaking elements than the phase difference φ between the two superconducting leads (e.g. no magnetic field, no trapped current loops), we can write this relation as :

$$I(\varphi) = \mathcal{T}[I(\varphi)] = -I(-\varphi) \tag{1.47}$$

So if the junction has TRS, its CPR is odd, with maxima and minima of opposite current values and at opposite phase values.

Defining the positive (I_c^+) and negative (I_c^-) critical current as the maximum current values for positive and negative current biases, respectively, we have :

$$I_c^+ = \max_\varphi[I(\varphi)] \tag{1.48}$$

$$I_c^- = |\min_\varphi[I(\varphi)]| \tag{1.49}$$

So if the junction has TRS, we have $I_c^+ = I_c^-$.

For the critical current measurement of a DC SQUID, with no other TRS breaking elements than the applied bias current and the applied magnetic field B, we write :

$$I_c^+(\boldsymbol{B}) = \mathcal{T}[I_c^+(\boldsymbol{B})] = I_c^-(-\boldsymbol{B}) \tag{1.50}$$

This relation involves I_c^+ and I_c^-, but does not guarantee the symmetry $I_c^\pm(\boldsymbol{B}) = I_c^\pm(-\boldsymbol{B})$ for a given current bias sign $\pm$. Actually, using Eq.(1.50), the symmetry in $\pm B$ for a given current bias sign $\pm$ can be rewritten :

$$I_c^\pm(\boldsymbol{B}) = I_c^\pm(-\boldsymbol{B}) \Longleftrightarrow I_c^\pm(\boldsymbol{B}) = I_c^\mp(\boldsymbol{B}) \tag{1.51}$$

where the two signs have been swapped. Hence, the $+B \longleftrightarrow -B$ symmetry of the critical current pattern is related to the symmetry of I_c^+ and I_c^- at a given field. Breaking the inversion symmetry of the junction, one can obtain $I_c^+(\boldsymbol{B}) \neq I_c^-(\boldsymbol{B})$, yielding the so-called Josephson Diode Effect or asymmetric Josephson effect (mind that I use AJE for anomalous Josephson effect, which is not always the case in the literature). Going back to Eq.(1.50), there is JDE whenever $I_c^\pm(\boldsymbol{B}) \neq I_c^\pm(-\boldsymbol{B})$.

However, still from Eq.(1.50) assuming only TRS, we get $I_c^+(0) = I_c^-(0)$ for $B = 0$, even when the inversion symmetry is broken. We conclude that in order to get JDE, one needs to break both TRS ($|B| > 0$) and inversion symmetry ($I_c^+(\boldsymbol{B}) \neq I_c^-(\boldsymbol{B})$).

Inductive elements can break TRS even at zero applied magnetic field by introducing an effective magnetic field or a superconducting phase difference induced by a current. But because the effective magnetic field is reversed when the current is reversed, it does not yield $I_c^+(0) \neq I_c^-(0)$. In a similar fashion, the (super)current in a material with SOC induces a polarization of the spins (Edelstein effect) that can play a similar role as the magnetic field, via the AJE, see part 1.3.9. However, the AJE only occurs in the presence of non-vanishing Zeeman energy, requiring a finite magnetic field, and do not yield $I_c^+(0) \neq I_c^-(0)$ too.

Even though $I_c^+(0) \neq I_c^-(0)$ can't be achieved, we saw that JDE is still possible by breaking TRS and inversion symmetry. Inductive elements and AJE can introduce effective magnetic fields that shift the critical current versus magnetic field patterns in opposite ways for positive and negative current bias. There are other mechanisms to introduce a shift in this pattern. The role of the different symmetries on the CPR and JDE are discussed in [107], for a 2d material with SOC.

In the following, we focus on the role of inductances, with an emphasis on their influence in a DC SQUID.

1.7.2 . Inductances

We refer to something as an inductance L if it generates an effective flux Φ that scales with $I : \Phi = LI$. This terminology is consistent with the classical electrodynamics geometric inductance. The inductance itself can depend on I. In SQUID measurements, the current depends on the flux through the surface of the SQUID. If inductive elements are present, the flux itself varies with the current. This kind of feedback effect can deform the response of the SQUID, shift its critical current versus magnetic field pattern, and even make some phase domain inaccessible or create hysteretic behavior in some cases. In appendix 6.2, we give the physical origin, the approximate expression, and comment the three types of inductive elements.

We identify three types of inductive elements :

- geometric self-inductance L_G of a current loop, with a typical value of $L_G \sim 0.2pH$ in the geometry of our experiments
- geometric self-inductance L_A of an asymmetric current distribution, with a typical value of $L_A \sim 4 \times 10^{-2}pH$ in the geometry of our experiments
- kinetic inductance L_K of unknown junctions in series with the known junctions, with $L_{K,W} \simeq 17pH$ per μm for the W compound superconducting leads, and $L_{K,u} \sim \frac{\Phi_0}{I_{c,u}}$ for a general unknown junction.

1.7.3 . Effects of inductances on an AC SQUID

Let us examine the influence of the three types of inductance for a Josephson junction in an AC SQUID. The working principle of the AC SQUID is presented in part 1.5.1. Fig.1.32a shows the sketch of the AC SQUID including the inductances. A current i runs through the SQUID, and an external magnetic field B_{ext} induces a magnetic flux $\Phi_{ext} = \boldsymbol{B}_{ext} \cdot \boldsymbol{S}$ in the surface S of the SQUID (of surface vector $\boldsymbol{S}$). The junction has a CPR $i(\phi)$, with ϕ the superconducting phase difference between its superconducting leads, and i_c its critical current.

Following the diamagnetic convention Eq.(6.12) for inductances and the AC SQUID phase-flux relation $\phi = \frac{2\pi}{\Phi_0}\Phi$, the current i circulating in the AC SQUID reads :

$$i(\phi) = i\left(\frac{2\pi}{\Phi_0}\Phi_{int}\right) = i\left(\frac{2\pi}{\Phi_0}(\Phi_{ext} - L.i)\right) \tag{1.52}$$

In this expression, both the self-field inductances, L_G and L_A, and the kinetic inductance(s) L_K contribute to ϕ, and we can simply add them up : $L = L_G + L_A + L_K$. In Eq.(1.52), we see that $L \neq 0 \Longrightarrow \Phi_{int} \neq \Phi_{ext}$,

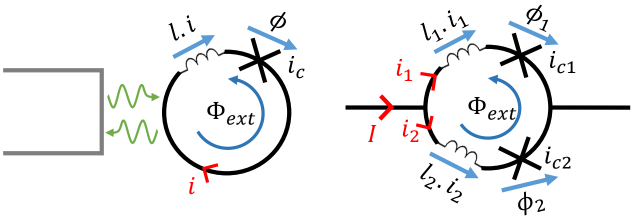

(a) (b)

Figure 1.32 – Sketches of superconducting circuits with Josephson junction(s) (cross symbol(s), superconducting phase difference ϕ, critical current i_c) and inductances (coil symbol(s), effective superconducting phase difference $l.i = \frac{2\pi L}{\Phi_0}.i$). (a) Sketch of an AC SQUID with one Josephson junction and inductances. (b) Sketch of a DC SQUID with two Josephson junctions in parallel, each in series with inductances.

and the phase ϕ of $i(\phi)$ is itself a function of i. It yields a deformation of the AC SQUID response, hysteresis and inaccessible $\phi = \frac{2\pi}{\Phi_0}\Phi_{int}$ regions in some cases.

Writing

$$\Phi_{ext} = \Phi_{int} + L.i\left(\frac{2\pi}{\Phi_0}\Phi_{int}\right) \tag{1.53}$$

, one can deduce Φ_{int} from Φ_{ext}. It is illustrated in Fig.1.33a for a junction with a sinusoidal $i(\phi)$, where one can see the different consequences of $L \neq 0$. Importantly, forbidden Φ_{int} (in red) appear near Φ_{int} values for which the current changes sign, at odd multiples of $\phi = \pi$ here, which may be detrimental to the experiment. For a junction with sinusoidal CPR, these forbidden values appear for $\beta_L = \frac{2\pi}{\Phi_0}Li_c \gtrsim 1$. Notice that at $\Phi_{ext} = 0$, $\Phi_{int} = 0$ too, even in the presence of inductances (if L is not too high such that $\Phi_{ext} = 0$ does not fall into an hysteretic region). This topic is further discussed in [108], including AJE.

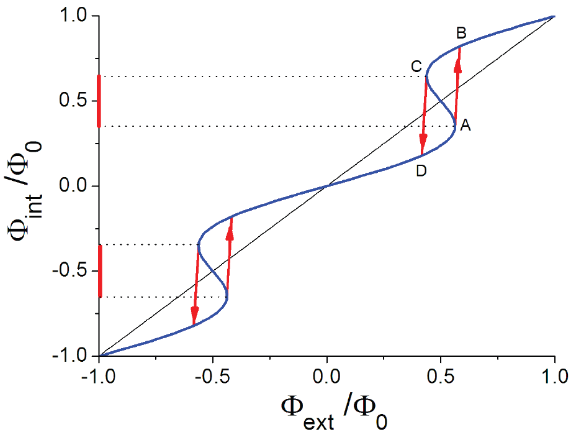

(a)

Figure 1.33 – Illustration of the effects of an inductance in an AC SQUID. The internal flux Φ_{int} differs from the bare external flux Φ_{ext}, related by $\Phi_{ext} = \Phi_{int} + L.i\left(\frac{2\pi}{\Phi_0}\Phi_{int}\right)$. In this graph, the inductance is supposed constant, the junction has a sinusoidal CPR, and $\beta_L = 1.65$. When increasing the external flux, the internal flux follows up to A, where it jumps to B. Decreasing the external flux, the internal flux only jumps back in C, creating an hysteresis cycle. The red lines mark the internal flux range not accessible. From [109].

1.7.4 . Effects of inductances on a DC SQUID

Let us examine the influence of inductive elements for two Josephson junctions in parallel, forming a DC SQUID. The principle of the DC SQUID is presented in part 1.5.3. Fig.1.32b shows the sketch of the DC SQUID including the inductances in series with each of the junctions, that is one global inductance L_1 in the top branch, and L_2 in the bottom branch. A total current I traverses the DC SQUID, with i_1 (i_2) in the top (bottom) branch. An external magnetic field B_{ext} applies a magnetic flux $\Phi_{ext} = \boldsymbol{B}_{ext} \cdot \boldsymbol{S}$ in the surface S of the SQUID (of surface vector $\boldsymbol{S}$). The top and bottom junctions have CPR $i_1(\phi_1)$ and $i_2(\phi_2)$, respectively, with $\phi_{1,2}$ the superconducting phase difference between their respective superconducting leads, and $i_{c1,c2}$ their critical currents.

Following the diamagnetic convention Eq.(6.12) for inductances and the DC SQUID phase-flux relation, the current I flowing through the DC SQUID writes :

$$I(\phi_1, \phi_2) = i_1(\phi_1) + i_2(\phi_2) \tag{1.54}$$

with

$$\phi_1 - \phi_2 = \frac{2\pi}{\Phi_0}\Phi_{int} = \frac{2\pi}{\Phi_0}(\Phi_{ext} - L_1 i_1 + L_2 i_2) \tag{1.55}$$

the constraint on the phases.

In contrast with the AC SQUID, in the DC SQUID the current I is imposed. Trying the same trick as for the inductances in the AC SQUID, we can rewrite Eq.(1.55) :

$$\phi_1 + \frac{2\pi}{\Phi_0}(L_1 + L_2)i_1(\phi_1) = \phi_2 + \frac{2\pi}{\Phi_0}(\Phi_{ext} + L_2 I) \tag{1.56}$$

where we see that the knowledge of Φ_{ext} and I is not enough to unequivocally determine the ϕ_1, due to the presence of ϕ_2. However, this is only the constraint on the phases, and the SQUID must also respect the constraint on the currents Eq.(1.54). The problem can be computed numerically.

In a DC SQUID, the quantity that is measured is the critical current of the full SQUID, expressed as $I_c^+ = \max_{\phi_1,\phi_2} I(\phi_1, \phi_2)$ and $I_c^- = |\min_{\phi_1,\phi_2} I(\phi_1, \phi_2)|$ for positive and negative bias current, respectively. In part 1.6, we saw that the critical current versus magnetic field pattern could be obtained by first considering the configuration giving the maximum supercurrent, and then varying the current in the two branches in a way that compensate the effect of the magnetic flux for a minimum loss of total supercurrent. Let us do this again including inductances.

Focusing first on positive current bias, the maximum critical current is obtained for $I_c^{+,max} = i_{c1}^+ + i_{c2}^+ = i_1(\phi_1^+) + i_2(\phi_2^+)$. This value is not affected by the inductances. However, $I_c^{+,max}$ is not at $\Phi_{ext} = 0$ anymore, but at :

$$\frac{2\pi}{\Phi_0}\Phi_{ext}^{max} = \phi_1^+ - \phi_2^+ + \frac{2\pi}{\Phi_0}(L_1 i_{c1}^+ - L_2 i_{c2}^+) \tag{1.57}$$

For two junctions with identical CPR shape, the shift of the maximum of the $I_c^+(\Phi_{ext})$ pattern is $\phi_1^+ = \phi_2^+ \implies \Phi_{ext}^{max} = L_1 i_{c1}^+ - L_2 i_{c2}^+$. The same reasoning can be applied for negative bias current.

Let us now try to understand better the influence of the inductances on the shape of the $I_c^+(\Phi_{ext})$ pattern. To do so, we focus on one branch, say the top branch, and we fix the current i_2. The current i_2 in the bottom branch produces a phase difference $L_2 i_2$ across the inductance and $\phi_2(i_2)$ across the junction, following its inverse CPR. Thus, the constraint between the phases impose that the total phase difference across the top branch, that we call ϕ_{t1}, is $\phi_{t1} = L_2 i_2 + \phi_2 + \frac{2\pi\Phi_{ext}}{\Phi_0}$. Without the inductance L_1, we simply have $\phi_1 = \phi_{t1}$ and $i_1 = i_1(\phi_{t1}(\Phi_{ext}, i_2))$. Introducing $L_1 \neq 0$, the inductance will absorb part of ϕ_{t1}, such that $\phi_1 + L_1 i_1 = \phi_{t1} \iff \phi_1 = \phi_{t1} - L_1 i_1$.

For $L_1 > 0$, ϕ_1 is reduced compared to the inductance-free situation. For a given variation of ϕ_{t1}, as induced by a magnetic flux, the current in the top branch, given by the CPR $i_1(\phi_1)$ of the junction, varies less as $i_1(\phi_1) = i_1(\phi_{t1} - L_1 i_1)$.

Hence, $L_1 > 0$ screens the magnetic flux variations, and the $I_c^+(\Phi_{ext})$ shows the result of screened CPRs. To understand it, one can apply the same reasoning as part 1.6 in the inductance-free case, but with $\phi_{1,2}$ variations upon flux variation of flux Φ_{ext} screened by the inductances :

- $\frac{\partial \phi_1}{\partial \Phi_{ext}} = 1 - l_1 \frac{\partial i_1}{\partial \phi_1} \frac{\partial \phi_1}{\partial \Phi_{ext}} \Longleftrightarrow \frac{\partial \phi_1}{\partial \Phi_{ext}} = \frac{1}{1+l_1 \frac{\partial i_1}{\partial \phi_1}} < 1$
- $\frac{\partial \phi_2}{\partial \Phi_{ext}} = -1 - l_2 \frac{\partial i_2}{\partial \phi_2} \frac{\partial \phi_2}{\partial \Phi_{ext}} \Longleftrightarrow \frac{\partial \phi_2}{\partial \Phi_{ext}} = -\frac{1}{1+l_2 \frac{\partial i_2}{\partial \phi_2}}$ and $|\frac{\partial \phi_2}{\partial \Phi_{ext}}| < 1$

The total accumulated phase can be written as $\Delta\phi_{1,2} = \int_{\Phi_{ext}^{max}}^{\Phi_{ext}} \frac{\partial \phi_{1,2}}{\partial \Phi'} d\Phi'$, yielding deformation compared to the inductance-free case. For a long ballistic channel, $\frac{\partial \phi_{1,2}}{\partial \Phi} = \frac{i_{c1,c2}}{\pi} \Longrightarrow \Delta\phi_{1,2} = \frac{1}{1+\frac{l_{1,2} i_{c1,c2}}{\pi}} \Phi_{ext}$.

Notice that the variations of I_c^+ close to $I_c^{+,max}$ reflect the CPR of the junctions close to their maximum at $i_{1,2}(\phi_{1,2}^+)$, whatever the value of the inductances. It is also true for negative current bias. This contrast with the AC SQUID and its β_L. In DC SQUID, the screening affects the lowest values of $i_{1,2}(\phi_{1,2})$, with low values of $\phi_{1,2}$ that may never be achieved.

Because inductances L_1 and L_2 change the "cost" in current i_1 and i_2 of varying the phase across top and bottom branches, respectively, their presence also changes the positions of the minima of $I_c^+(\Phi_{ext})$.

The different effects of inductances discussed here are illustrated in Fig.1.34 for two long ballistic (or helical) junctions. For comparison, the blue and orange lines correspond to situations without inductance, as introduced in part 1.6.1. The red line corresponds to junctions with equal critical currents and different inductances $L_1 = 1.78\ \Phi_0$ per unit of current and $L_2 = 0$. We see that it reproduces the modulation and the approximate skewness of the situation with asymmetric junctions without inductance, compare red line to orange line. In addition, its maximum critical current is shifted to $\Phi_{ext}^{max} \simeq -0.25\Phi_0$.

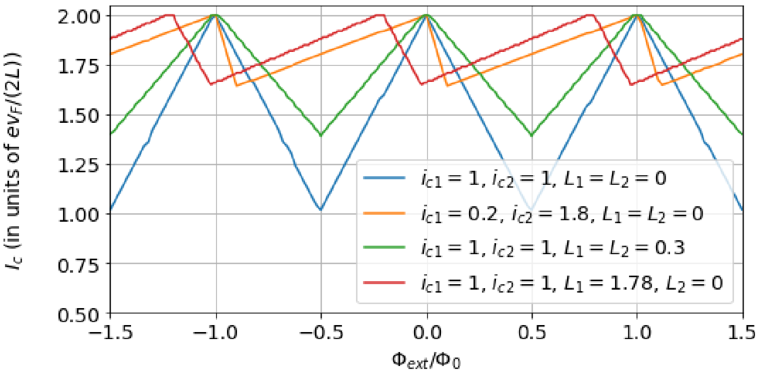

Figure 1.34 – Critical current of a DC SQUID with two long ballistic (or helical) junctions as a function of magnetic flux Φ_{ext} applied through the SQUID surface via an external magnetic field. The junctions are labelled 1 and 2, with critical currents i_{c1} and i_{c2}, and are in series with inductances L_1 and L_2, respectively. $i_{c1,c2}$ are expressed in units of $ev_F/(2L)$, and $L_{1,2}$ are expressed in Φ_0 per unit of current.

We conclude that inductances in a DC SQUID can be detrimental to our critical current pattern measurements in two ways. First, inductances can screen the variations of the phases with magnetic field, deforming the critical current pattern in a way that is indistinguishable from another critical current pattern. Second, inductances can shift the maximum critical current in field, making it hard to distinguish with MCA induced by AJE. However, close to the maximal critical current, the pattern always reflects the shape of the CPRs close to their maximum supercurrent, allowing us to distinguish long ballistic (or 1d helical) channels with sawtooth CPR.

1.7.5 . Inductances in a DC SQUID with two long ballistic junctions

In this subsection, we give analytical formulas for $I_c^+(\Phi_{ext})$ of a DC SQUID featuring two long ballistic Josephson junctions, including inductances in both branches. This system gives $I_c^+(\Phi_{ext})$ oscillating with periods corresponding to $\Delta\Phi_{ext} = \Phi_0$ in the surface of the SQUID, with a skewed triangular pattern. This corresponds to most of the situations encountered in our experiments.

We take the same conventions as the previous subsection, see Fig.1.32b. The full derivation of the formulas has been done by Dr. Yang Peng, and can be found in appendix 6.4, reproducing the supplementary materials of [5]. Appendix 6.4 also provides additional discussions for various limits.

Defining $l_{1,2} = \frac{2\pi L_{1,2}}{\Phi_0}$, $\Delta_{li} = l_1 i_{c1} - l_2 i_{c2}$, $\Delta\phi^+ = 2\pi\frac{i_{c1}(\pi+l_2 i_{c2})}{i_{c1}(\pi+l_2 i_{c2})+i_{c2}(\pi+l_1 i_{c1})}$ and $\Delta\phi^- = 2\pi\frac{i_{c2}(\pi+l_1 i_{c1})}{i_{c1}(\pi+l_2 i_{c2})+i_{c2}(\pi+l_1 i_{c1})}$, we can write the switching current as :

$$I_c(\Phi) = \begin{cases} i_{c1} + i_{c2} + i_{c2}\frac{\Delta_{li}-\Phi_{ext}}{\pi+l_2 i_{c2}} & \Phi_{ext} \geq \Delta_{li} \\ i_{c1} + i_{c2} + i_{c1}\frac{\Phi_{ext}-\Delta_{li}}{\pi+l_1 i_{c1}} & \Phi_{ext} \leq \Delta_{li} \end{cases} \tag{1.58}$$

The range of validity of this formula over a phase of 2π is given by :

$$-\Delta\phi^- + \Delta_{li} \leq \Phi \leq \Delta\phi^+ + \Delta_{li} \tag{1.59}$$

If Φ_{ext} is outside this interval, then the critical current can be obtained by applying periodic property $I_c(\Phi_{ext}) = I_c(\Phi_{ext} + 2\pi)$.

The modulation amplitude is :

$$\Delta I_c = 2\pi i_{c1} i_{c2}/[i_{c1}(\pi + l_2 i_{c2}) + i_{c2}(\pi + l_1 i_{c1})] = 2\pi i_{c1} i_{c2}/[\pi(i_{c1} + i_{c2}) + (l_1 + l_2) i_{c1} i_{c2}] \tag{1.60}$$

and one can define a skew coefficient as :

$$S = (\Delta\phi^- - \Delta\phi^+)/2\pi \tag{1.61}$$

$S = 1$ $(S = -1)$ when there is only a positive (negative) slope over the whole phase period. As defined, S does not depend on the modulation amplitude.

For symmetric branches with $i_{c2} = i_{c1} = i_c$ and $l_1 = l_2 = l$, Equation (6.47) yields :

$$I_c = i_c(2 - \mathrm{Saw}[\frac{|\Phi_{ext}|}{1 + l i_c/\pi}]). \tag{1.62}$$

This corresponds to a triangular flux dependence, with a modulation amplitude smaller than without inductances :

$$(I_c^{\max} - I_c^{\min})/2i_c = \Delta I_c/I_c^{\max} = \frac{1/2}{1 + 2L i_c/\Phi_0}. \tag{1.63}$$

1.7.6 . Other phase shifts contributing to SQUID measurements

Except inductances and AJE, other sources of phase shift can contribute to SQUID measurements. First, we ignored so far the effect on the local field of the diamagnetic superconducting contacts. Indeed, the superconductors have their own screening currents that induce flux focusing and add up to the magnetic flux through the SQUID surface. It can be caused by the "skin" currents, and induce spurious asymmetric responses as discussed in [110]. It can also be caused by the presence of Abrikosov vortices in the type-II superconductors [111], associated to discontinuities in the $I_c(\Phi_{ext})$ pattern when a new vortex is close to the SQUID surface, as observe for example in the supplementary material of [112] or in Fig.6.24a in the appendix.

Second, considering a DC SQUID, we saw that the maximum of the critical current is found when the two junctions reach their critical current, that is $i_1(\phi_1 = \phi_1^+) = i_{c1}^+$ and $i_2(\phi_2 = \phi_2^+) = i_{c2}^+$ (considering positive current bias). For this configuration, the constraint on the phases writes $\frac{2\pi}{\Phi_0}\Phi_{ext}^{max} = \phi_1^+ - \phi_2^+$ (Eq.(1.57)). Hence, for $\phi_1^+ \neq \phi_2^+$, the maximum critical current of the DC SQUID is shifted to :

$$\Phi_{ext}^{max} = \frac{\Phi_0}{2\pi}(\phi_1^+ - \phi_2^+) \tag{1.64}$$

For further discussion on this effect, see [113]. For example, this asymmetry in phase of maximum current can be realized by two junctions with different v_F, implying different E_T, and different i_c and harmonic content, see [114].Excluding AJE, this shift is independent of magnetic field. Moreover, it does not scale with $i_{c1,c2}$. It can be positive or negative, and it changes sign when the direction of the current is reversed.

Lastly, with or without SOC in the junctions, the magnetic field can induce π-junction transitions due to Zeeman energy. Such transitions have been observed in our DC SQUID devices with bismuth-based Josephson junctions. For an in-plane magnetic field, the regime of transition extends over $\sim 30G$, and $\sim 500G$ separate successive transitions [3].

1.8 . Beating between two channels

1.8.1 . Beating between two channels due to orbital dephasing

Previously in this manuscript, we studied the supercurrent of three types of Josephson junctions as a function of the phase difference between its superconducting leads. We have calculated the maximum supercurrent that can flow through a junction composed of two Josephson junctions (referred to as channels) separated in real space as a function of a magnetic field, that is the critical current $I_c(\Phi)$ of a DC SQUID enclosing a magnetic flux Φ. In particular, we saw that we could use a DC SQUID with asymmetric critical currents to probe the current-phase relation of the Josephson junction with the smallest critical current.

In this section, we will consider the total supercurrent of two channels with a dephasing that varies slightly with magnetic field. We will consider that the junction composed of the two channels is embedded in an annulus (like an AC SQUID or an asymmetric DC SQUID), such that the magnetic field also controls the phase difference Φ between the superconducting leads via the flux through the annulus. In this way, the applied magnetic field changes simultaneously the phase difference between the leads and the dephasing between the channels. In the rest of the manuscript, I will refer to this type of setup as current-flux relation(s), which is a current-phase plus dephasing relation.

The formula for such a system is :

$$I(\Phi) = i_1(\Phi - r\Phi/2) + i_2(\Phi + r\Phi/2) \tag{1.65}$$

with $i_1(\phi)$ the CPR of channel 1, $i_2(\phi)$ the CPR of channel 2, and r the ratio between the junction surface and the annulus surface.

This study is relevant both theoretically and experimentally for "large" junctions, "large" meaning that the magnetic flux through the junction of surface S has a sizable effect on the measurements performed up to a field B^{max}, that is $B^{max}S \simeq \Phi_0$ for orbital dephasing effects.

On the theoretical side, the current-flux relation is easy and fast to compute and gives a very good insight on the shape of the critical current as a function of magnetic field for large junctions. On the experimental side, this case is relevant as soon as there is one high current channel (or junction) in parallel to two lower current channels with a small dephasing that varies with the magnetic field. This situation can arise in a purposely asymmetric DC SQUID designed to measure the current-phase relation of a finite-size junction, or in a single-junction critical current measurement when there is an uncontrolled part of the junction that has a high current and forms an intrinsic asymmetric DC SQUID.

Fig. 1.35 shows the current-flux relations for three different types of junctions composed of two scattering-free channels with identical CPRs separated in real space. The phase difference between the two superconducting leads is Φ, the phase difference across channel 1 is 0.95Φ, and the phase difference across channel 2 is 1.05Φ. Thus, the dephasing between the two channels is 0.1Φ ($r = 0.1$), corresponding to an area between them of $1/10^{\text{th}}$ of the area of the annulus.

For the junction with two sinusoidal CPR channels, see Fig. 1.35a, we find the usual beating pattern of two sinusoidal signals of slightly different period, one with a period of $\Delta\phi_1 = 1/0.95 = 20/19$ and the other $\Delta\phi_2 = 1/1.05 = 20/21$. The main frequency of the signal is $(1/0.95 + 1/1.05)/2 \simeq 1$ and the envelope frequency is $(1/0.95 - 1/1.05)/2 \simeq 1/20$. The amplitude varnishes at $\Phi = 5 \times 2\pi$ $(+10n \times 2\pi)$. At this value, the flux between the two channels is $0.1\Phi = 0.1 \times 5 \times 2\pi = \pi$.

Looking at the envelope, we notice that we recover the pattern of the critical current of the symmetric DC SQUID with sinusoidal CPRs. This is not a surprise since the critical current of our two sinusoidal CPR channels junction is just the current-flux relation where we keep the dephasing between the channels but we release the constraint on the phase difference between the superconducting leads. The phases difference between the superconducting leads is given by the annulus large surface thus the high frequency, and the dephasing is due to the small junction surface thus the low frequency beating. By filtering out the high frequency and keeping only the envelope with a positive sign, we recover the critical current of the junction.

We further notice that in this first situation with sinusoidal CPRs, the frequency of the sinusoid is proportional to the surface of the annulus plus the surface between the considered channel and the channel 1. This additional surface is proportional to the transverse position of the considered channel, such that we have a direct relation between the transverse position of the channel and the frequency of the sinusoid. This can be generalized to any channels distribution and implies that the current-flux relation of a scattering-free junction with sinusoidal CPRs is simply the Fourier transform of its (critical) current density in the transverse direction. The Fourier transform relation can be used to determine the current density profile in junctions with a low aspect ratio $L/W \lesssim 1$ [115].

Fig. 1.35b displays the beating between two long ballistic channels. First, we recover the triangular envelope that goes down to $I_c^{max}/2 \neq 0$ when the dephasing between the two channels is $0.1\Phi = \pi \iff \Phi = 5 \times 2\pi$. Second, we see that a second period with a current close to 0 emerges as the dephasing between the two channels increases. This happens at flux values for which one channel has a positive current while the other one has a negative current. This is always the case when the dephasing is π, and leads to a doubling of the frequency of the current. We see a very similar behavior for two short ballistic junctions, see Fig. 1.35c.

1.8.2 . Beating between two channels due to Zeeman dephasing

So far, we have studied the influence of an orbital dephasing between the two channels. But there exist another source of dephasing that depends on the magnetic field : the Zeeman dephasing, as introduced in part 1.4.3.

For a junction featuring two identical helical pairs of channels with opposite helicities, like a symmetric QSHI with both edges or a trivial conductor with degenerate helicities, the contribution of both helical pairs of channels compensate exactly, see part 1.4.3. If their characteristics are different however (e.g. different v_F, L, g_{eff}, or initial phase due to a flux inside the junction area), they do not compensate exactly and can lead to various interference patterns.

More explicitly, for two long 1d helical junctions in parallel, Eq.(1.30) yields a Zeeman-induced phase difference :

$$\varphi_{h_1} - \varphi_{h_2} \simeq \left(\frac{L_1}{\hbar v_{F,1}} g_{eff,1} \cos\theta_1 - \frac{L_2}{\hbar v_{F,2}} g_{eff,2} \cos\theta_2 \right) \mu_B B \tag{1.66}$$

with $L_{1,2}$, $v_{F,1,2}$, $g_{eff,1,2}$ the respective lengths, Fermi velocities and effective g-factors of individual junctions 1 and 2. θ_1 and θ_2 are the angles between the spin quantization axes of junctions 1 and 2 and the magnetic field $\boldsymbol{B}$, respectively. This Zeeman dephasing is important whenever the Zeeman energy is comparable to the Thouless energy, that is $g_{eff}\mu_B BL/(\hbar v_F) \sim 1$.

Fig.1.36 shows the total current of two identical 1d helical channels with Zeeman energies that varies with the flux Φ through the annulus, and with different multiplication coefficients. In Figs.1.36a and 1.36b, we show the effect of equal Zeeman energies $E_{Z1}/\Delta_0 = E_{Z2}/\Delta_0 = 0.14\Phi/(2\pi)$ on two short 1d helical channels and two long 1d helical channels, respectively. We see that the Zeeman energy gradually change the current profile, which is just the sum of two CPRs in phase. For long ballistic channels (Fig.1.36b), it is a simple phase shift and it decreases the effective period.

On the other hand, in Figs.1.36c and 1.36d, we see the effect of opposite Zeeman energies $E_{Z1}/\Delta_0 = -E_{Z2}/\Delta_0 = 0.14\Phi/(2\pi)$. It differs from the previous situation, as it introduces a Zeeman-induced dephasing. For long 1d helical channels (Fig.1.36d), the pattern is exactly the same as the one obtained with an orbital dephasing (Fig.1.35b), further confirming that there is no difference between the two types of dephasing for those channels, except for the magnetic field scale.

In Fig.1.36c, the short 1d helical channels display a behavior that has some similarities with the orbital dephasing case (Fig. 1.35c), but with major qualitative differences. We see the same frequency-doubling phenomena and similar envelope, but the envelope dips lower than $I_c^{max}/2$, and the emerging period close to 0 current is now pinned at $I = 0$. To better understand it, let us focus on the region $\Phi \simeq 5 \times 2\pi$, where $E_{Z1}/\Delta_0 = -E_{Z2}/\Delta_0 = 0.14\Phi/(2\pi) \simeq 0.7$. In this situation, this current-flux relation is the sum of two CPRs that are very close to the sum of the CPRs represented by pink and yellow solid lines in Fig.1.25a, displaying regions of flux where the two CPR are opposite and give a flat $I = 0$ value.

Combining both orbital and Zeeman-induced effects yields complex supercurrent vs magnetic field patterns, studied in [116, 117].

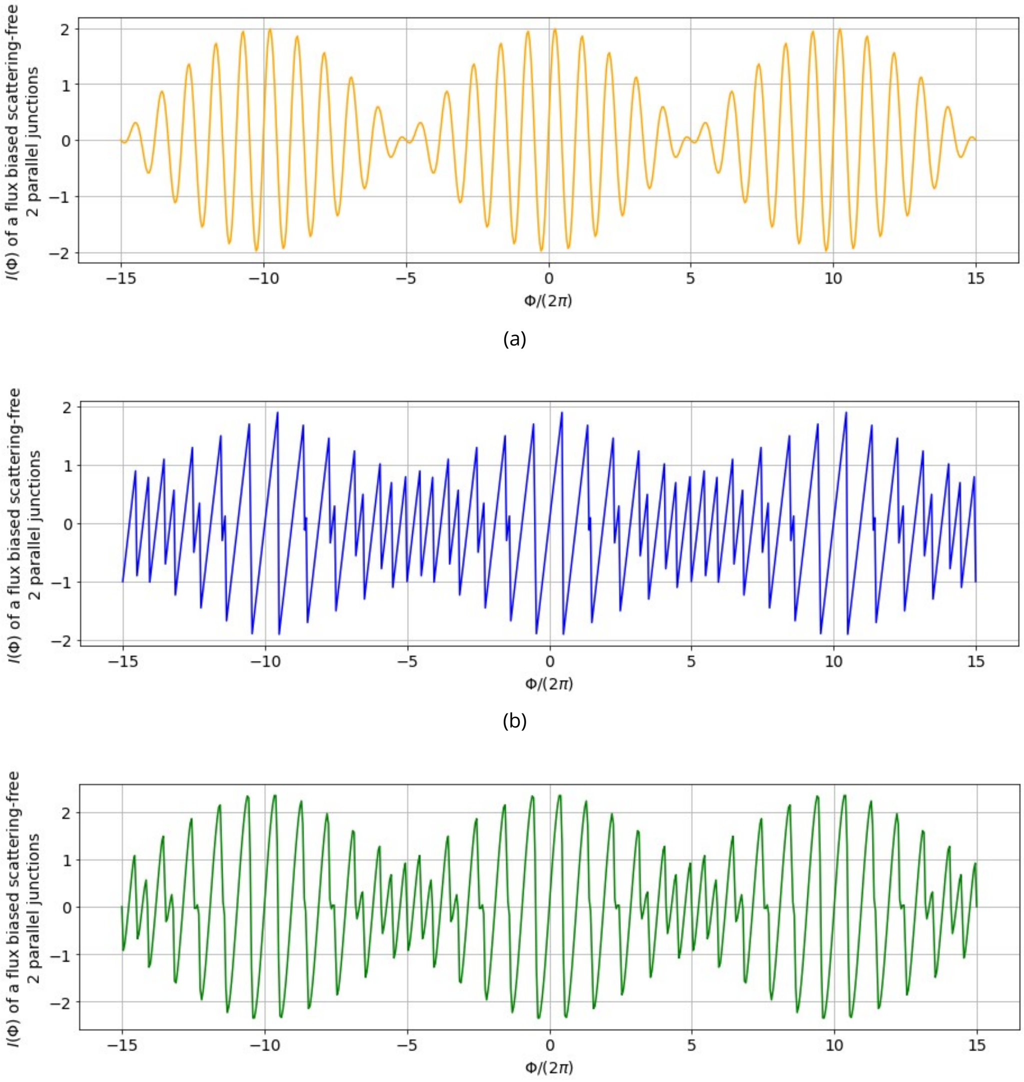

(a)

(b)

(c)

Figure 1.35 – Current-flux relations of junctions composed of two scattering-free channels with identical CPRs separated in real space. Here, the phase is considered to be imposed by a magnetic flux through an annulus, such that the magnetic field changes both the phase Φ across the junction and the dephasing between the two channels by a factor 0.1Φ. (a) Current-flux relation of a junction with two sinusoidal channels. (b) Current-flux relation of a junction with two long topological channels. (c) Current-flux relation of a junction with two short topological channels.

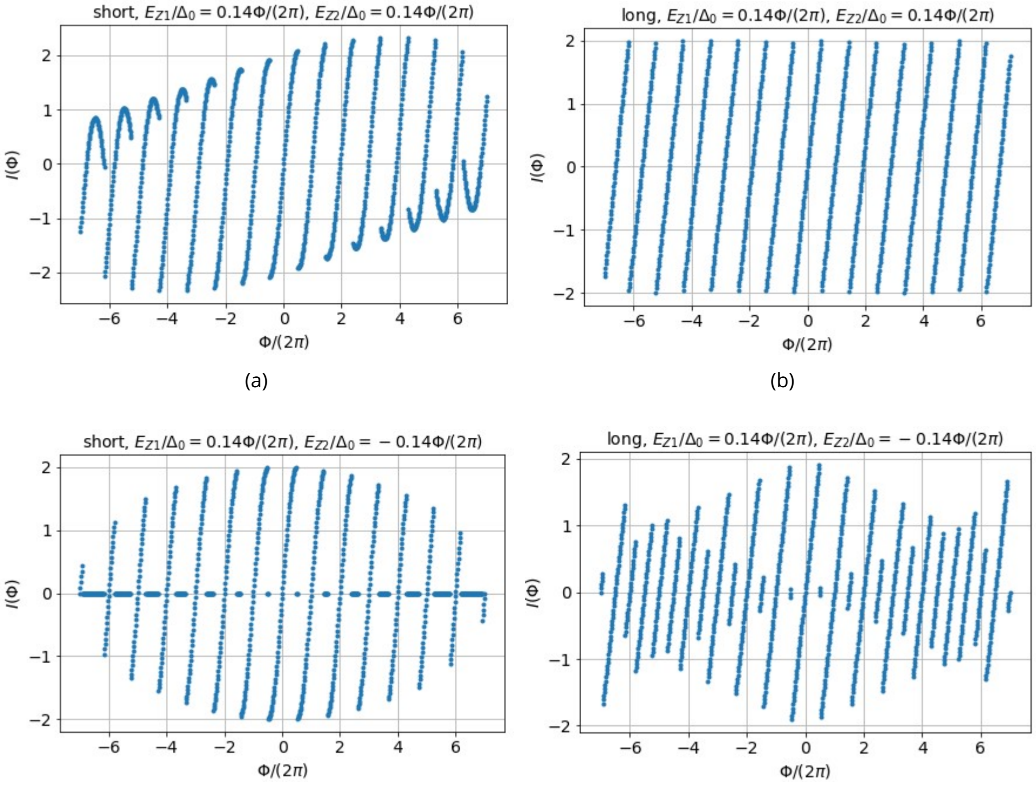

(a) (b)

(c) (d)

Figure 1.36 – Current-flux relations of junctions composed of two topological scattering-free channels with Zeeman energies. Here, the phase is considered to be imposed by a magnetic flux through an annulus, such that the magnetic field changes both the phase across the junction and the Zeeman energies. (a) Current-flux relation of a junction with two short topological channels with the same Zeeman energies. (b) Current-flux relation of a junction with two long topological channels with the same Zeeman energies. (c) Current-flux relation of a junction with two short topological channels with opposite Zeeman energies. (d) Current-flux relation of a junction with two long topological channels with opposite Zeeman energies.

1.9 . Critical current and Current-Flux Relations of many-channels junctions

In this section, we extend the analysis of supercurrent interference to junctions with a high number of channels, first in the ballistic case, and then in the diffusive case. We discuss the importance of the aspect ratio L/W of the junction, with L and W the length and width of the junction, respectively. Lastly, we present the critical current patterns generated by three specific transverse supercurrent density profiles.

1.9.1 . Wide and narrow ballistic junctions

In this subsection, we extend the analysis of current-flux relations to junctions with a large number of channels in parallel. We consider scattering-free channels evenly distributed along the transverse direction of the junction. Like in the previous section, the junction has a finite surface, and is embedded in an annulus with a larger surface. The magnetic field changes both the flux Φ through the annulus (hence the phase difference between the superconducting leads of the junction) and the flux $r\Phi$ through the junction, where r is the ratio between the two surfaces. The relevance of such a model is the same as in the previous section.

The formula for such a system is :

$$I(\Phi) = \sum_{n=0}^{N} i_n(\Phi + nr\Phi/N) \quad \text{with} \quad i_n(\phi) = i_{cn}.\mathrm{CPR}_n(\phi + \delta\phi_n) \tag{1.67}$$

with N the number of channels, $i_n(\phi)$ the CPR of channel n. This discrete sum of many channels allows us to model junctions with various critical currents and initial phases distributions, thanks to the terms i_{cn} and $\delta\phi_n$, respectively.

Fig.1.37 shows the current-flux relations obtained for 200 scattering-free channels with identical CPRs in parallel, with homogeneous critical currents and initial phases distributions. In Fig.1.37a, we see the results for sinusoidal CPRs. As explained in the previous section, it is the Fourier transform of a shifted gate, which is the product of a sinus of frequency $(1+r/2) = 1.05$ (high frequency) and a sinus cardinal (low frequency). The sinus cardinal forms the envelope, with $I = 0$ when $r\Phi = 0.1\Phi = 0.1 \times 10 \times 2p\pi = 2p\pi$, with p a non-zero integer.

Let us now look at the situation with 200 scattering-free ballistic channels in parallel. We saw in the previous section that the envelope never goes to $I = 0$ with two ballistic channels. Hence, one would naively guess that this behavior remains the same with a higher number of channels. The computations, see Fig.1.37b for long ballistic channels and Fig.1.37c for short ballistic ones, proves otherwise.

The envelopes display patterns very similar to the sinusoidal CPRs case, with $I = 0$ at $r\Phi = 2p\pi$, such that the Fourier transform argument seems to partly hold for non-sinusoidal signals, but we notice that the shape of the lobes are different, with a clear triangular shape of the central lobe in the long ballistic case (Fig. 1.37b).

Moreover, a closer look at the high frequency part of the current-flux relations in Figs .1.37b and 1.37c, shows a very peculiar and surprising effect : skew reversal ! From $\Phi \simeq 0$ to $\Phi \simeq 10 \times 2\pi$, the skew goes from positive to negative. And for every $r\Phi = 2p\pi$, the skew is reversed again, with a convex pattern for positive fields and concave pattern for negative ones. The same is true for negative Φ, the current-flux relation having the global time-reversal symmetry $(B, I) \longleftrightarrow (-B, -I)$.

In this analysis, we only considered the effect of orbital dephasing on plane waves with a wavevector along the longitudinal axis of the junction, and we completely ignored wavevectors with a component in the transverse direction. Such skewed trajectories participate to the interference pattern and can lead to "doubling" of the period of the Fraunhofer pattern for high L/W ratio, see [118]. Fig.1.38 shows their results for a ballistic junction in the limits of $L/W = 0$ and $L/W \longrightarrow \infty$, taking absorbing lateral boundaries. For specular lateral boundaries scattering, they find similar results. [119] further explore the interferences of ballistic trajectories in the wide junction limit.

For long ballistic junctions at low field, the authors of [118] find :

$$I_c(\nu) = \frac{W}{\lambda_F}\frac{ev_F}{L}\frac{(1-(\nu/2)^2)(\nu/2)^2}{|\nu/2|^2} \quad \text{with} \quad \nu = \Phi/\Phi_0 \tag{1.68}$$

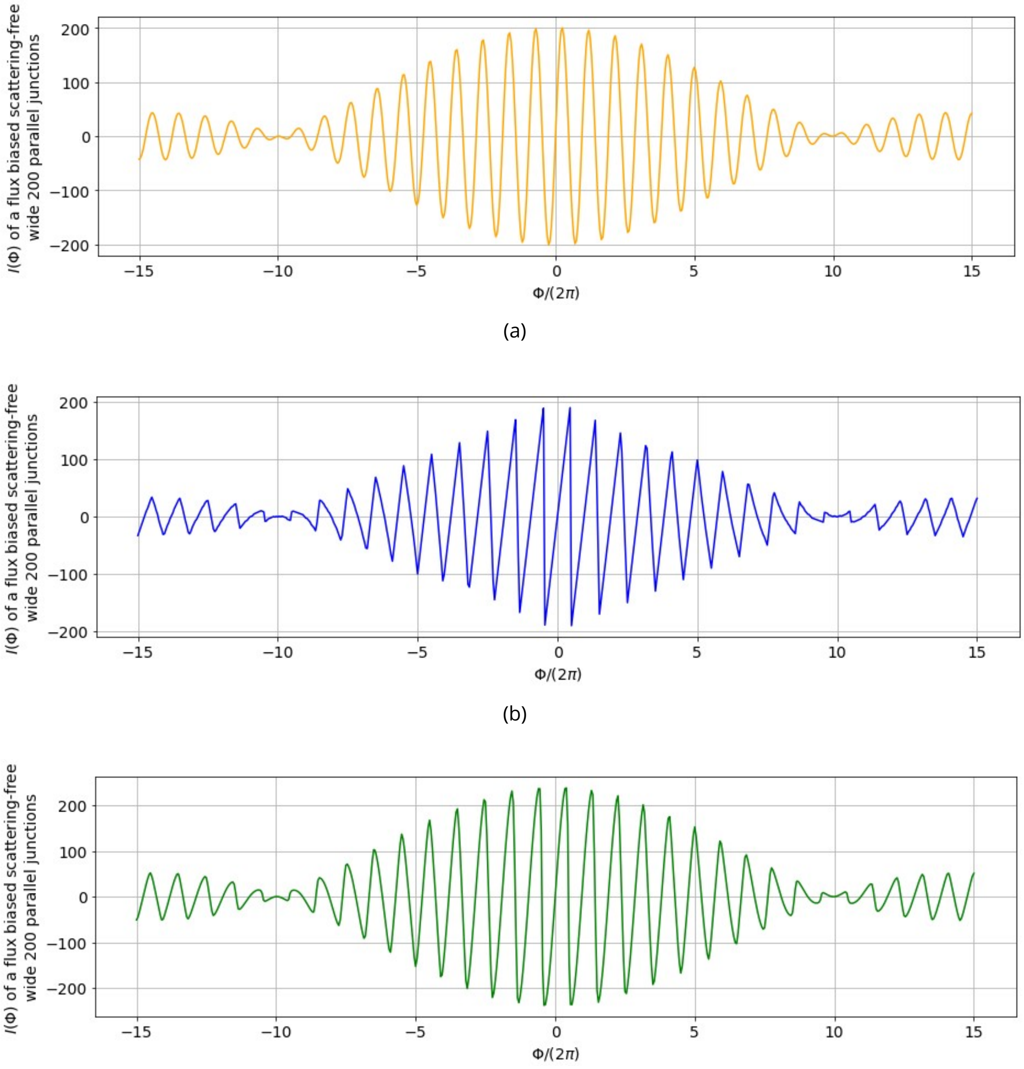

(a)

(b)

(c)

Figure 1.37 – Current-flux relations of junctions of finite areas composed of 200 topological scattering-free channels in parallel, with identical CPRs, and spread evenly across the junction transverse direction. Here the phase is considered to be imposed by a magnetic flux through an annulus, such that the magnetic field changes both the phase Φ across the junction and the dephasings between the 200 channels by a factor $0.1/200\Phi$. (a) Current-flux relation of a junction with 200 sinusoidal channels. (b) Current-flux relation of a junction with 200 long ballistic channels. (c) Current-flux relation of a junction with 200 short ballistic channels.

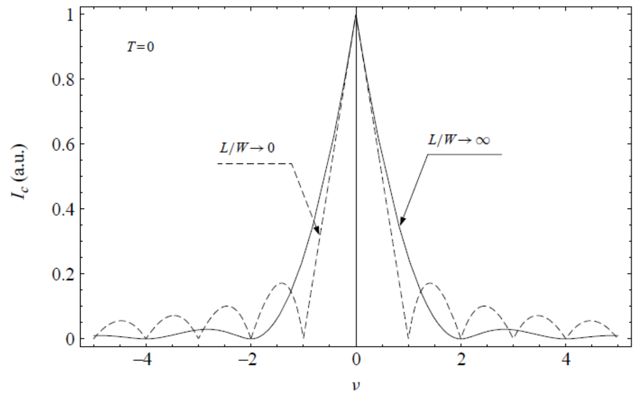

Figure 1.38 – Critical current of a 2d ballistic junction with many channels as a function of magnetic flux $\nu = \Phi_{ext}/\Phi_0$ in the junction, in the limits of $L/W = 0$ and $L/W \longrightarrow \infty$, taking absorbing lateral boundaries. L is the junction length and W the junction width. The pattern is similar for specular lateral boundaries scattering. From [118].

1.9.2 . Wide and narrow diffusive junctions

Now that we have an understanding of the behavior of scattering-free junctions, let us move on to the scattering-full case of diffusive junctions. In such systems, new parameters come into play.

In [120], the author treats the case of a long diffusive junction as a quasi-1d system, and solves a 1d diffusion equation $\left[\frac{\partial}{\partial t} - D\left(\frac{\partial}{\partial x} + i\frac{2\pi}{\Phi_0}By\right)\right] P(x,x',t) = \delta(x-x')\delta(t)$ with $P(x,x',t)$ the probability of diffusion between points x and x' at time t, D the diffusion constant, and By can be thought as the transverse component of the flux. Considering the magnetic field as a perturbation, it becomes :

$$\left(\frac{1}{\tau_B} + D\frac{\partial^2}{\partial x^2}\right) P(x,x') = \delta(t) \tag{1.69}$$

with $\tau_B = \frac{3\Phi_0^2}{\pi^2 D w^2 B^2}$ the characteristic time related to the magnetic field and w the total width of the junction. Note that this time can also include a typical coherence time τ_ϕ as $1/\tau = 1/\tau_B + 1/\tau_\phi$. The resolution of this equation leads to $I_c(B) = I_c(B=0)\frac{L/L^*}{\sinh L/L^*}$, with $L^* = \sqrt{D\tau} = \frac{\sqrt{3}\Phi_0}{\pi B w}$. This result is plotted as a black dashed line in the inset of Fig. 1.39d, with a shape very close to a gaussian curve.

In the diffusive limit of $\xi = \sqrt{\frac{\hbar D}{\Delta}} \gg l_e$, a more precise approach consist of using retarded Green functions, and solve Usadel equations. This has been done for example in [121] for 2d films with various widths and lengths. They showed that there is a competition between interference effects and depairing effects. To obtain large interference effects, the junction needs to be able to form "Josephson vortices". In the limits of this article, the characteristic variation scale of the Green functions in the transverse direction is $\xi_B = \sqrt{\Phi_0/B}$, with B the applied magnetic field.

If $W < \xi_B \Longleftrightarrow W/L < \sqrt{\Phi_0/\Phi}$, no Josephson vortex can form in the junction and the only effect left is the depairing one, yielding the quasi-1d behavior studied in [120]. On the other hand if $W \gg \xi_B \Longleftrightarrow W/L \gg \sqrt{\Phi_0/\Phi}$, the full interference effect dominate the critical current vs flux, and we recover the scattering-free limit. The results of the full computations are displayed in Fig. 1.39a, with various widths.

In Figs. 1.39c and 1.39d, we show experimental results of diffusive gold junctions with superconducting tungsten leads in the wide junction limit and in the narrow junction limit, see top and bottom Fig. 1.39b for respective sample images. These results come from [122]. For a more in-depth discussion, one can refer to [109] and [123]. However, the diffusive limit is not fulfilled in our bismuth junctions, where we have $\xi \sim l_e$.

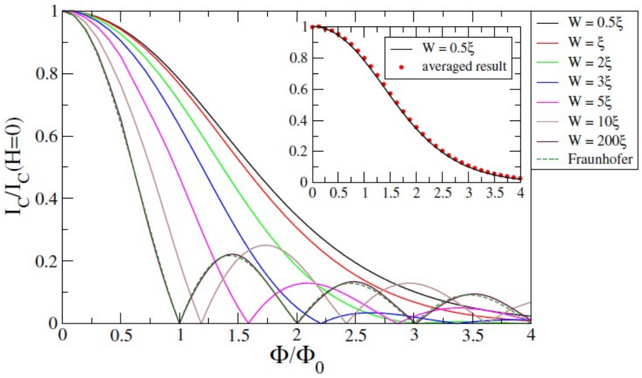

(a)

Figure protected by copyright

See original publication
or ask for complete version

(b)

Figure protected by copyright

See original publication
or ask for complete version

(c)

Figure protected by copyright

See original publication
or ask for complete version

(d)

Figure 1.39 – Critical current vs magnetic flux for diffusive junctions of finite areas. (a) Computations for a Usadel 2d model for various transverse lengths W, produced in [121]. Critical current normalized by the zero-field value vs magnetic flux for a wire length $L = 8\xi^d$, with $\xi^d = \sqrt{\hbar D/\Delta_0}$, perfect transparent interfaces, $k_B T = 0.01\Delta_0$, and different values of W. The inset shows for $W = 0.5\xi^d$ the comparison between the exact result and the approximation used for the narrow-junction limit.(b) Micrographs of a wide $L/W = 0.7$ (top) and a narrow $L/W = 4.5$ (bottom) W-Au-W junctions. See [122]. (c) Wide sample normalized critical current vs normalized flux at $T = 60\,mK$ (blue dots). Red line : numerical simulation of the 2d Usadel equation for a junction with aspect ratio $L/W = 0.7$ and W wires inductance $L = 11.5\,pH$. Inset : raw data for Ic(B), with $I_{c,max} = 38.8\,\mu A$. See [122]. (d) Main frame : long sample normalized critical current vs normalized flux at $T = 60\,mK$. Light blue line : numerical simulation of the 2D Usadel equations, where the flux has been rescaled by a factor of 2.5. Inset : theoretical predictions for the aspect ratio of the junction and perfect interfaces : the analytical result of the Usadel equation in the 1D limit $L \gg W$ (red line), the numerical simulation of the 2D Usadel equation (blue line), the semiclassical model for a 1D diffusive normal wire (dotted line), and a Gaussian curve (dashed line). See [122].

1.9.3 . Transverse supercurrent density profiles of boundary state

In this subsection, we study the patterns of the critical current of a junction with three different supercurrent density profiles as a function of magnetic field. We write $\rho(y)$ the supercurrent density as a function of transverse position y. The magnetic field B induces orbital dephasing $\exp^{-i2\pi BLy/\Phi_0}$ proportional to B and $L \times y$, with L the junction length. The relation between B and y is the same as the relation between frequency f and time t in Fourier analysis.

Following the analysis [2], let us consider an asymmetric ($y \geq 0$ only) decreasing exponential profile with a density of states of the form $\rho(y) \propto e^{-2\pi y/\lambda}$, with λ the transverse characteristic length. The resulting interference pattern reads :

$$I_c(B) = \frac{I_0}{\sqrt{1+(BL\lambda/\Phi_0)^2}} = \frac{I_0}{\sqrt{1+(B/B_1)^2}} \quad \text{with} \quad B_1 = \Phi_0/(\lambda L) \tag{1.70}$$

giving a $I_c(B) \propto |B|^{-1}$ at high fields. It decreases similarly to the height of the lobes of a Fraunhofer pattern, but slower than a gaussian function.

Considering a symmetric decreasing exponential profile with a density of states of the form $\rho(y) \propto e^{-2\pi|y|/\lambda}$, the resulting interference pattern reads :

$$I_c(B) = \frac{I_0}{1+(BL\lambda/\Phi_0)^2} = \frac{I_0}{1+(B/B_1)^2} \quad \text{with} \quad B_1 = \Phi_0/(\lambda L) \tag{1.71}$$

giving a lorentzian function with $I_c(B) \propto |B|^{-2}$ at high fields. It decreases similarly to the theoretical pattern generated by ballistic junctions with long aspect ratio $L/W \gg 1$ at low field [118], but still slower than a gaussian function.

Considering a gaussian profile with a density of states of the form $\rho(y) \propto e^{-\pi(y/\lambda)^2}$, the resulting interference pattern reads :

$$I_c(B) = I_0 e^{-\pi(BL\lambda/\Phi_0)^2} = I_0 e^{-\pi(B/B_1)^2} \quad \text{with} \quad B_1 = \Phi_0/\lambda L \tag{1.72}$$

giving a gaussian function that decreases faster than the two critical current patterns studied above.

All these patterns can be generated either by individual states with this type of supercurrent density profile, or by a dense array of independent 1d ballistic states whose critical currents depend on their positions according to the same profile. The latter is plausible in the case of interfaces whose quality depends on the penetration depth. If the critical current associated to these patterns implies a high number of channels, it suggests that they are separated in space, by a distance $d \gtrsim \lambda_F$. This spreading can occur over different spatial dimension, affecting the interference pattern depending on the direction and the sources of the dephasings. If the λ found is larger than the typical λ_F, one might as well consider the dense array of independent 1d ballistic states' hypothesis.

1.10 . Modelisation of the switching dynamics

In this section, we present basic notions to model the switching dynamics of a superconducting circuit. First, we introduce the standard RCSJ model to understand the switching out of one superconducting state with a current biased experiment. Then, we study the occupation dynamics at a fixed superconducting phase difference when multiple superconducting states are involved, introducing the rate equations. Lastly, based on the previous two subsections, we discuss the switching out of multiple states with a current biased experiment. In relation with our experiment analyzed in chapter 4, we introduce a dynamical phase-biased model based on a current biased asymmetric DC SQUID. Thanks to this last model, elaborated with the theoretical physicists Yang Peng, Yuval Oreg and Felix von Oppen after several online meetings, we managed to extract both pair relaxation times τ_p and quasi-particle poisoning times $\tau_{1,2}$ from the comparison between the experimental and theoretical switching distributions as a function of magnetic field.

1.10.1 . Switching from one state with a current bias : RCSJ model

To understand the switching from a (proximity induced) superconducting state to a resistive state in a current biased experiment, let us introduce the standard Resistively and Capacitively Shunted Josephson junction (RCSJ) model. In this model, the Josephson junction is in parallel with a resistor R and a capacitor C, see inset of Fig.1.40. The total current reads :

$$I_b = I_J + I_R + I_C = I_c.\mathrm{CPR}(\varphi) + \frac{\mathrm{V}}{\mathrm{R}} + \mathrm{C}\frac{\partial \mathrm{V}}{\partial \mathrm{t}} \tag{1.73}$$

with I_b the current bias, V the voltage across the junction, φ the superconducting phase difference between the two superconducting contacts of the junction, and $I_c.\mathrm{CPR}(\varphi)$ the current-phase relation of the junction.

Using the energy-phase relation $V = \frac{\hbar}{2e}\frac{\dot{\varphi}}{2\pi}$, we have [109] :

$$I_b = I_c.\mathrm{CPR}(\varphi) + \frac{\hbar}{2\mathrm{eR}}\dot{\varphi} + \frac{\hbar\mathrm{C}}{2\mathrm{e}}\ddot{\varphi} \Longleftrightarrow \mathrm{C}\left(\frac{\hbar}{2\mathrm{e}}\right)^2\ddot{\varphi} + \frac{1}{\mathrm{R}}\left(\frac{\hbar}{2\mathrm{e}}\right)^2\dot{\varphi} + \frac{\partial \mathrm{U}}{\partial \varphi} = 0 \tag{1.74}$$

with

$$U(\varphi) = -E_J(\mathrm{C\tilde{P}R}(\varphi) + \frac{I_b}{I_c}\varphi) \quad E_J = \frac{\hbar}{2e}I_c \quad \mathrm{C\tilde{P}R}(\varphi) = \int_0^{\varphi}\mathrm{CPR}(\varphi')\mathrm{d}\varphi' \tag{1.75}$$

Eq.(1.74) has the form of a motion equation for a particle of position φ, with a mass $\propto C$, a friction term $\propto 1/R$, in a potential $U(\varphi)$ with an average slope $\propto I_b$. The mechanical analogy is illustrated in Fig.1.40, with a sinusoidal CPR. Inductive elements, not included in this model, have been found to influence the switching dynamics, filtering the supercurrent fluctuations [124]. Depending on C, R, U and how I_b varies with time, the "position" φ varies with time. φ is related to the voltage by $V = \frac{\hbar}{2e}\dot{\varphi}$, such that variations of φ result in variations of V. With a finite $I_b(t)$ pulse one can achieve phase slips, where φ escapes from its local potential well and is retraped in another one, producing a finite $\int V(t)dt$. With a periodic $I_b(t) = I_b\sin(\omega t)$ of period T, one can move φ across multiple wells in one period, resulting in quantized average voltage response $\frac{1}{T}\int_t^{t+T}V(t')dt' = n\frac{\hbar\omega}{2e}$ $(n \in \mathbb{Z})$, called Shapiro steps (see part 1.5.4).

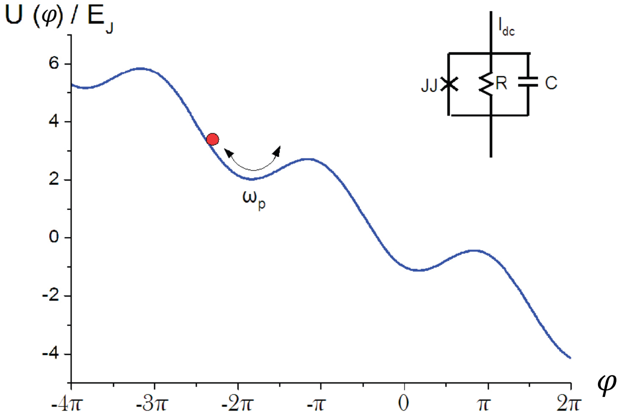

Figure 1.40 – "Washboard" potential of the RCSJ model with a Josephson junction with sinusoidal CPR $I_J(\varphi) = I_c\sin\varphi$. The dynamics of the superconducting phase difference φ follows Eq.(1.74), which is analogous to the equation of motion of a particle of position φ in a potential $U(\varphi) = -E_J(\mathrm{C\tilde{P}R}(\varphi) + \frac{I_b}{I_c}\varphi)$, with $\mathrm{C\tilde{P}R}(\varphi)$ the integrated CPR of the junction and I_b the current bias. Hence, the shape of the potential depends on the CPR of the junction and on the current bias, while the phase inertia and friction depends on its environment. Inset : electrical circuit corresponding to the RCSJ model. From [109].

For $I_b \gg I_c$, there is no potential barrier and φ falls continuously producing an average voltage $\langle V\rangle \neq 0$, and the junction is resistive. For a small capacitance, $I_b > I_c \Longrightarrow \langle V\rangle = R\sqrt{I_b^2 - I_c^2}$. For $I_b \simeq I_c$, φ can overcome the potential barrier by three ways : by inertia, by thermal fluctuations (see Fig.1.42a), or by macroscopic quantum tunneling (see Fig.1.42b). The thermal fluctuations can be included as a Langevin force [125]. If φ manages to escape its local minimum, it results in a finite average voltage $\langle V\rangle \neq 0$ and the junction switches to a resistive state.

Hence, the bias current I_b at which the junction switches, that we name the switching current, depends on the CPR of the junction (via $U(\varphi)$), on its environment (via R, C, and also $\mathcal{L}$), and on the shape of $I_b(t)$ as seen in Eq.(1.74). A standard switching current measurement method relies on sending short current impulses of a set amplitude I_0 and recording if a voltage has developed, yielding a probability of switching $P(I_0)$ [126, 127, 66]. In our experiments, we used a periodic current ramp such that $I_b(t) = a.t$, recording at which I_b the junction becomes resistive, see part 2.8.2 for more details. For a sinusoidal CPR, it leads to an asymmetric switching current distribution close to $I_b = I_c$ [128].

1.10.2 . Switching from multiple states with a phase bias : rate equation

In the previous subsection, we used the RCSJ model to study the probability of switching out of one (proximity induced) superconducting state, as a function of current bias I_b. In this subsection, we extend the problematic to multiple possible superconducting states (or configurations). Let us consider a conventional short Josephson junction with a fixed superconducting phase difference φ. The junction can be in four different states (see part 1.3.3) : a low energy spinless state with an even number of fermions (noted $|-\rangle$), two degenerate zero energy states with opposite spins and odd numbers of fermions (noted $|\uparrow\rangle$ and $|\downarrow\rangle$), and a high energy spinless state with an even number of fermions (noted $|+\rangle$).

The junction can exchange energy and fermionic quasiparticles with its environment, yielding transitions between its four accessible states. These transitions are modeled by rates Γ_{in}, Γ_{out} and Γ_{+-}, as illustrated in Fig.1.41 [126, 66, 129]. Γ_{in} and Γ_{out} involve the exchange of one quasiparticle with the environment (often referred to as "poisoning"), while Γ_{+-} involves only energy (allowing for microwave-induced transitions) or pairs of quasiparticles.

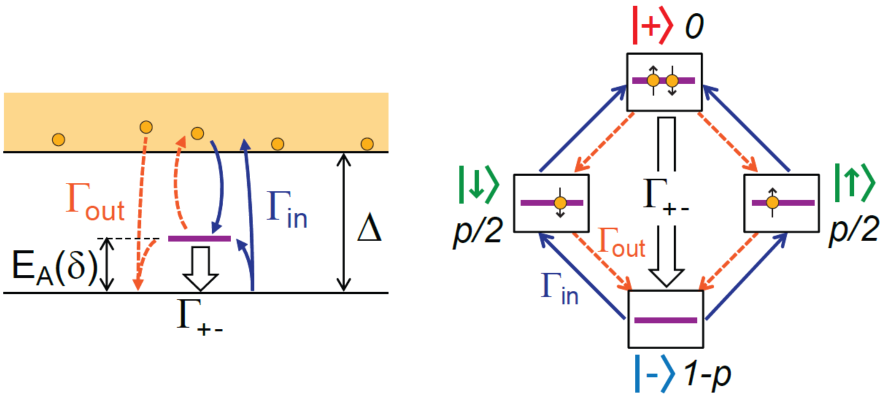

Figure 1.41 – Model for the dynamics of the population of the Andreev configurations of a conventional Josephson junction at fixed superconducting phase difference φ, in the excitation representation (left), and in the configurations space (right). Quasiparticles can jump in and out of the Andreev levels at rates Γ_{in} and Γ_{out}. If both levels of the Andreev doublet are occupied, the system can decay directly to the ground state (rate Γ_{+-}, much faster than all other rates). From [66].

Typically, the junction contacts act as a reservoir of quasiparticles with a bath temperature T_b and a characteristic time τ_{qp} which, combined with the Fermi golden rule, give rates [130] :

$$\Gamma_{in,out} \propto f_{FD}(\pm\delta_E/(k_B T_b))/\tau_{qp} \tag{1.76}$$

with $f_{FD}(x) = 1/(1+e^x)$ the Fermi-Dirac distribution and δ_E the difference in the junction energy before and after the transition. Notice that $\Gamma_{in,out}$ depends on φ through $\delta_E(\varphi)$ (at least). Depending on the environment, the characteristic time τ_{qp} can range from tens of μs to hundreds of ms [126, 131, 129, 77]. On the other hand, the characteristic time τ_p associated to Γ_{+-} is always much smaller than τ_{qp} in conventional junctions, of the order of $\sim 1\mu s$, as the junction can easily relax to its ground state by releasing a pair of quasiparticles to the Cooper pair condensate in the contacts (see works cited above and the associated relaxation time T1 of the Andreev Qubit [132]).

Given the transitions between states i and j, with their respective rates $\Gamma_{i\rightleftharpoons j}$, the probability p_i of the junction to be in the state i follows the rate equation :

$$\frac{dp_i}{dt} = \sum_{j\neq i} \Gamma_{i\leftarrow j} p_j - \sum_{j\neq i} \Gamma_{j\leftarrow i} p_i \tag{1.77}$$

For the transition illustrated in Fig.1.41, it yields the set of coupled equation :

$$\begin{aligned} \frac{dp_\uparrow}{dt} = \frac{dp_\downarrow}{dt} &= \Gamma_{in} p_- + \Gamma_{out} p_+ - (\Gamma_{in} + \Gamma_{out}) p_\uparrow \\ \frac{dp_+}{dt} &= \Gamma_{in} p_\uparrow + \Gamma_{in} p_\downarrow - (\Gamma_{+-} + 2\Gamma_{out}) p_+ \\ \frac{dp_-}{dt} &= \Gamma_{out} p_\uparrow + \Gamma_{out} p_\downarrow + \Gamma_{+-} p_+ - 2\Gamma_{in} p_- \end{aligned} \tag{1.78}$$

where we ignored the transition $\Gamma_{-+} \ll \Gamma_{in}, \Gamma_{out}, \Gamma_{+-}$.

Again, notice that this set of equations depends on φ via the $\delta_E(\varphi)$ in the rates Γ. At fixed φ, the probabilities p_i for a junction at equilibrium are found by solving all Eq.(1.77) with $dp_i/dt = 0$. For a φ varying with time, one needs to solve the equation by integration, including the dynamics of φ and the initial values of p_i. For the initial values $p_i(t=0)$, one can take the equilibrium values at fixed initial $\varphi(t=0)$.

1.10.3 . Switching from multiple states with a current bias

In this subsection, we connect the theoretical model to our experimental problematic. We aim to understand the switching dynamics of our topological bismuth Josephson junctions, with a current biased experiment. Such a junction is predicted to host several helical Andreev bound states protected by parity-conservation, see part 1.4. In addition, the junction studied in chapter 4 is made from a bismuth nanoring, forming two bismuth junctions in parallel, which realizes a (intrinsic) DC SQUID configuration. We combine the ideas introduced in the two previous subsections to understand the switching to a resistive state of a Josephson junction with multiple possible superconducting states, with a current biased experiment.

On the one hand, the switching dynamics of a DC SQUID with conventional junctions has been analyzed in [124]. In this situation, the 1d motion equation Eq.(1.74) and its associated tilted washboard potential become 2d, with phases $\phi_{1,2}$ for the two junctions. For an inductive DC SQUID with sinusoidal junctions, depending on the parameters of the SQUID, it has been shown that there is a privileged escape direction that rescales both the plasma frequency ω_p and the barrier potential ΔU. In general, the dispersion of the switching current depends on the flux inside the SQUID Φ/Φ_0, affected by the inductance(s).

On the other hand, in [133], the authors used a RCSJ model (with $C = 0$) to predict the current-voltage relation of a 1d helical junction in various limits (DC voltage response to a DC current bias). The junction has two superconducting states of opposite energy and different parity, yielding different potential $U_i(\varphi)$. The junction can switch from one state to the other by exchanging one quasiparticle with its environment, changing its parity. This process enables a new escape route and modifies the I-V curve. This process is illustrated in Figs.1.42c and 1.42d for short and long topological junctions, respectively, with $x = I_b/I_c$. A new dimensionless parameter appears, $\gamma = \Gamma_{qp}\tau_J$, with Γ_{qp} the quasiparticle exchange transition rate and $\tau_J = \frac{\hbar}{2e}\frac{1}{RI_c}$ the characteristic time of the junction. τ_J corresponds to the time it takes for φ to increase by 2π when the junction is biased by a current $I_b = I_c$. $\gamma = 1$ corresponds to on average one quasiparticle exchange every 2π when $I_b \simeq I_c$. This new escape route reduces the switching current in the limits of high temperature $k_BT_b \gg \Delta$ or $\gamma > 0$. If one consider two 1d helical junctions in parallel, spatially separated, a magnetic flux can dephase the two junctions and leads to a new field-dependent switching current [133, 130].

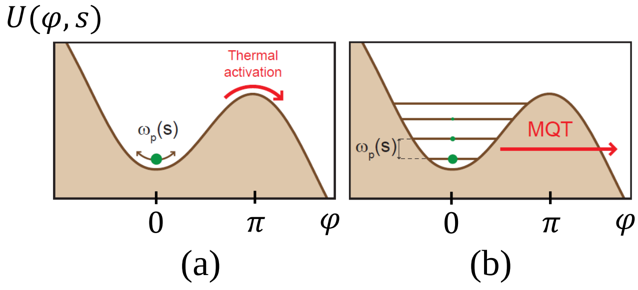

Figure protected by copyright

See original publication
or ask for complete version

(c)

Figure protected by copyright

See original publication
or ask for complete version

(d)

Figure 1.42 – Illustration of the different processes for the superconducting phase difference φ of a Josephson junction to escape its local potential well $U(\varphi, I_b/I_c)$, see Eq.(1.74). (a) and (b) : Escape by thermal and macroscopic quantum tunneling, respectively, for a conventional junction with a 2π-periodic sinusoidal CPR. From [66]. (c) and (d) : Escape by transition to another superconducting state, for a short and a long 1d topological junction, respectively. $x = I_b/I_c$. $\gamma = \Gamma_{qp}\tau_J$, with Γ_{qp} the quasiparticle exchange transition rate and $\tau_J = \frac{\hbar}{2e}\frac{1}{RI_c}$ the characteristic time of the junction. The black vertical arrows symbolize a change of state. From [133].

In the next subsection, we discuss the case of an asymmetric DC SQUID with 1d topological junction(s).

1.10.4 . Switching from multiple states of an asymmetric DC SQUID

The junction studied in chapter 4 is made from a bismuth nanoring, forming two bismuth junctions in parallel, which realizes a (intrinsic) DC SQUID configuration with a surface $\simeq 1.2\mu m^2$ normal to the vertical direction. We measure periodic $\simeq 200nA$ variations of the switching current as a function of vertical magnetic field, on top of a $\simeq 2.5\mu A$ background. The small variations have a sharp sawtooth shape, a period of $17G$ corresponding to Φ_0 inside the nanoring area, and are still visible at fields as high as $7T$. This behavior is typical of an asymmetric DC SQUID with the weakest junction being long and ballistic, with narrow supercurrent-carrying states, as expected for topologically protected helical hinge states (see parts 1.4 and 1.6.1). Moreover, the analysis of the switching statistics revealed the presence of additional superconducting states/configurations.

Hence, to model the experiment, we introduce a dynamical phase-biased model based on a current biased asymmetric DC SQUID. Thanks to this last model, elaborated with the theoretical physicists Yang Peng, Yuval Oreg and Felix von Oppen after several online meetings, we managed to extract both pair relaxation times τ_p and quasi-particle poisoning times $\tau_{1,2}$ from the comparison between the experimental and the theoretical switching distribution as a function of magnetic field.

In the following, the model used by the group of theoreticians in [125], to discuss the differences between the switching statistics of a conventional (see also [127]) and a topological short Josephson junction as a function of superconducting phase difference, is adapted for a current ramp biased asymmetric DC SQUID.

The situation is illustrated in Fig.1.43a. To leading order, the current ramp $\mathcal{I}(t)$ controls the phase difference $\gamma(t)$ across the strong junction branch. Thus, γ increases from zero to the phase $\gamma_{\max}$ at which the Josephson current is maximal as $\mathcal{I}$ increases from zero to values close to the critical current of the strong junction. In principle, $\gamma_{\max}$ is given by the current-phase relation of the strong junction but may have an additional inductive contribution. Depending on the inductive contribution, $\gamma_{\max}$ can take any value.

Unless otherwise specified, we choose $\gamma_{\max} = \pi/2$ which fits the experimental data the best. However we also give an example of the good agreement obtained with $\gamma_{\max} = \pi$ in Fig. 4.11. Due to the flux threading the SQUID Φ (measured in units of the $\hbar/(2e)$), the phase difference across the weak junction is given by

$$\phi(t) = \Phi + \gamma(t). \tag{1.79}$$

The additional current flowing through the weak junction with current-phase relation $i_n(\phi)$ modulates the critical current

$$I_c \simeq I_{c,\text{strong}} + i_n(\Phi + \gamma_{\max}), \tag{1.80}$$

at which the SQUID switches to a resistive state. Thus, measuring the switching current of the SQUID provides a direct measurement of the current-phase relation of the weak junction, see part 1.5.3. Since the results do not depend sensitively on the precise current-phase relation of the strong junction, we make the simplifying assumption that $\gamma(t)$ increases linearly in time, $\gamma(t) = \omega t$, from zero to $\gamma_{\max}$ as the current $\mathcal{I}(t)$ ramps up from zero to the critical current.

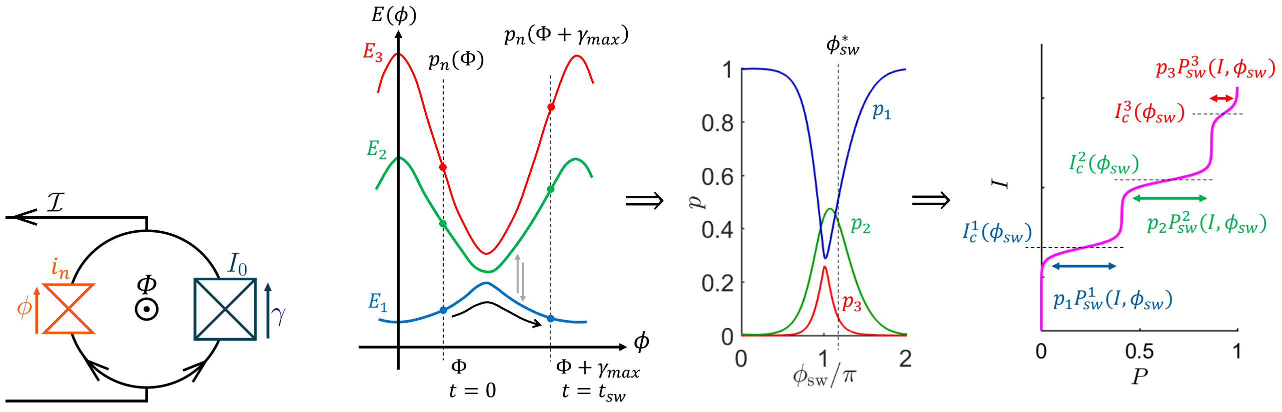

(a) (b)

Figure 1.43 – (a) Asymmetric DC SQUID consisting of two arms. The right arm has a critical current I_0 much larger than the critical current $i_{n,c}$ of the left arm. Together with the magnetic flux Φ_{ext} inside the SQUID surface, the right arm junction imposes its superconducting phase difference γ to the left arm junction (with $\phi = \frac{2\pi}{\Phi_0}\Phi_{ext} + \gamma$). $i_n(\phi)$ depends on the state n of the junction. (b) Process of the asymmetric SQUID dynamics model. From left to right : computation of states occupation probabilities by integration of rate equations between $\phi = \Phi$ and $\phi_{sw} = \Phi + \gamma_{max}$, computed occupation probabilities has a function of ϕ_{sw}, resulting total switching probability of the SQUID at a given $\phi_{sw} = \phi^*_{sw}$. See text for more details.

We can therefore substitute d/dt by $\omega d/d\phi$ in the rate equations Eq.(1.77). The probabilities p_n can be obtained by numerically integrating from $\phi = \Phi$ to $\phi = \phi_{\rm sw} = \Phi + \gamma_{\max}$, see Fig.1.43b left and center for an illustration.

From the probabilities of occupying the different states, we compute the probability to switch to a resistive state for those occupation probabilities, thereby generating the switching current statistical distribution. To this end, we take into account that, for a given state, switching is a stochastic event characterized by a current probability distribution for repeated current ramps. To simulate the corresponding switching histograms, we introduce a state-dependent switching probability $P^n_{sw}(I, \phi_{sw})$, which is the probability of finding the SQUID in the resistive state at bias current I and switching superconducting phase difference $\phi_{\rm sw}$, for a given occupied state n. We approximate $P^n_{\rm sw}(I, \phi_{\rm sw})$ by a smoothed step function of width δI centered around the SQUID's critical current $I^n_c(\phi_{\rm sw}) \simeq I_{c,\text{strong}} + i_n(\phi_{\rm sw})$.

$$P_{\mathrm{sw}}^{n}(I,\phi_{\mathrm{sw}}) = \frac{1}{2}\left[\tanh\left(\frac{I - I_c^n}{\delta I}\right) + 1\right], \tag{1.81}$$

where have neglected the well-known asymmetry of the switching current probability distribution [128].

The total switching probability is then expressed as :

$$P(I,\phi_{sw}) = \sum_{n} p_n(\phi_{sw}) P_{sw}^{n}(I,\phi_{sw}) \tag{1.82}$$

The whole process is illustrated in Fig.1.43b. The specific transitions and rate equations used to model the dynamics of the bismuth nanoring junction are detailed in part 4.2.1, and the resulting computed probabilities are detailed in parts 4.2.2 and 4.2.4.

2 - Samples' preparation and measurement methods

2.1 . Growth of the nanowires

There are many different methods to synthesize bismuth nanowires. They fall into two categories [134] :
- template-based growth (AAO templates, Taylor-Ulitovsky, quartz template, Bi(NO$_3$)$_3$·5H$_2$0 chemical synthesis, etc.)
- template-free growth (PVD, OFF-ON)

To facilitate the measurement of the topological helical hinge states of single-crystal bismuth (see parts 1.2 and 1.3.6), the ideal characteristics that we are looking for are the following :
- single-crystal bismuth with low defects and impurities
- clean oxide layer-bismuth interface, the thinner the better
- diameter $\lesssim 50\ nm$ to reduce bulk and surface conduction contributions
- length $> 6\ \mu m$, the longer the better
- crystal axis and facets that lead to distinct hinge channels

The group first experimented with nanowires produced by the template-based growth using electrodeposition from a Bi(NO$_3$)$_3$·5H$_2$0 solution through a polycarbonate template with pores of diameter $\lesssim 100nm$ [40, 1, 2], based on the work [135]. This method produces thin nanowire ($\lesssim 90nm$ diameter) of controllable diameter, but the nanowires are hard to isolate properly, show surface irregularities, and are often coated with polycarbonate residues.

The group then moved on to template-free methods with Physical Vapor Deposition (PVD). In PVD, high-purity bismuth is deposited by sputtering at a small rate in a high vacuum chamber, at a temperature lower than the melting temperature of bismuth ($T < 271.3°C$). To control the characteristics of the grown nanowires, an active buffer layer can be used. During my PhD, we used sample fabricated using PVD with iron buffer layer [136] and with vanadium buffer layer [137]. The growth mechanism is still debated but is suspected to be a tip growth for Fe buffer layer and a root growth for V buffer layer.

The PVD on Fe deposition is done in a plasma sputtering high vacuum chamber ($P \lesssim 10^{-6}mbar$). A $30\ nm$ of Fe is first deposited at $0.3nm.s^{-1}$ on a Si substrate. After that, $150\ nm$ of high purity Bi (99.9999% purity) are sputtered at $0.9\ nm.s^{-1}$. The substrate is kept between 160 and $230°C$ during the whole process. This method produces nice single-crystal wires of width $100-400\ nm$ and length $4-60\ \mu m$ of various crystalline orientation. Transmission electron microscopy revealed a low number of defects and a small oxide layer of $\lesssim 3nm$ after long exposure to air, see Figs.2.1a and 2.1c. The density of nanowires is in the good range to provide both large enough statistics and isolated nanowires when transferred on a host substrate, with variations depending on the transfer method. However, the average nanowire diameter is rather large compared to the desired $\lesssim 50nm$.

The main results of my PhD, that are presented in the main text of this thesis, have used PVD on vanadium rather than Fe used previously. The Fe layer is replaced by $30\ nm$ of vanadium, and the substrate is kept at $T < 70°C$ during the deposition. This method produces thinner wires, the smallest one we spotted being $40\ nm$ wide.

Both PVD on Fe and on V were done by A. Kasumov (also in our group), Yu.A. Kasumov, and V.T. Volkov in the Institute of Microelectronics Technology and High Purity Materials RAS, Chernogolovka, Russia.

Thanks to a recent purchase of a Korvus Technology sputtering machine specific for bismuth deposition,

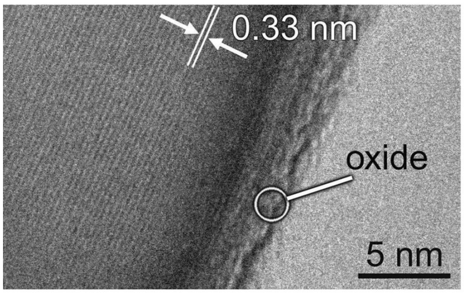

Figure protected by copyright

See original publication
or ask for complete version

Figure protected by copyright

See original publication
or ask for complete version

(a) (b) (c)

Figure 2.1 – (a) Transmission Electron Microscope image of the edge of a bismuth nanowire grown with PVD. We distinguish well organized atomic layers with inter-layer distance of $0.33nm$. A thin oxide layer of $\lesssim 3nm$ covers the surface. (b) Electron diffraction pattern of a $1\mu m$ long area of a bismuth nanowire grown with PVD. We see well defined intense Bragg peaks, attesting the crystalline structure over a $1\mu m$ area. (c) Other TEM image of the edge of a bismuth nanowire grown with PVD. For this nanowire, there is no oxide layer at all even though the nanowire has been exposed to air. From [136].

we were able to produce similar nanowires in Laboratoire de Physique des Solides d'Orsay (LPS), Orsay, France, and to test variations and other growth methods. For the nanowires grown in LPS, we used Bi with a purity of 99.999% instead of the 99.9999% used in Chernogolovka. Purity is an important factor, especially for conductors with low carrier densities like Bi, where impurities can change the carrier densities a lot. Moreover, the distribution of impurities is not homogeneous and the concentration is much higher around defects, including surfaces. However, the measurements we performed on nanowires grown in LPS show signatures of 1d ballistic hinge transport in the superconducting state (see sample Bi_1^{squid} in chapter 3) and elastic mean free path $l_e \sim 100nm$ in the resistive state (see appendix 6.9.2), similar to the sample with 99.9999% purity grown in Chernogolovka. Thus, the loss of a factor 10 in purity does not seem detrimental to our experiments.

Tested in LPS, On-Film-Formation Of Nanowires method (OFF-ON) [138, 139], relying on mechanical stress-induced preferential diffusion process, produced thin $(100 - 300\ nm)$ and very long nanowires $(10 - 100\ \mu m)$ with a lower but reasonable density. With a thinner initial Bi layer and a shorter diffusion phase time, $\sim 200nm$ wide and $\lesssim 40nm$ thick crystalline islands with $[111]$ axis perpendicular to the substrate were produced.

2.2 . Deposition of the nanowires

Once the nanowires are grown, we need to transfer them onto a clean insulating substrate. The host insulating substrate has regularly spaced indexed prepatterned $9\mu m$ Au/Ti crosses to help for nanowire localization. Since none of the previous experiments showed any gate effects, we use undoped SiO_2 host substrates. The transfers are done using three different techniques.

First, rubbing a piece of clean tissue onto the growth substrate then the host substrate proved efficient. It leaves clusters of nanowires on the host substrate where the tissue has been rubbed. The density among the clusters depends on how many consecutive times it is rubbed on the host substrate. The transferred nanowires are shorter than one could expect looking at the growth substrate. For nanowires grown with the PVD-Fe method, we find a maximum length of $\simeq 10\mu m$. For nanowires grown with the PVD-V method, it fails to transfer nanowires with smaller diameter.

Another method consists in shooting $10\ ns$ UV LASER pulses on the growth substrate. The pulses generate mechanical shockwaves that shake off the nanowires on the edge of the growth substrate (already used in [140]). The host substrate is placed underneath the edge to collect the falling nanowires, see Fig.2.3a. With this technique, the Chernogolovka team managed to transfer the thinner nanowires grown with PVD-V, with diameters down to $\simeq 40nm$. In addition to the usual straight nanowires, it leaves some very curved nanowires, still highly crystalline, some of them even forming closed loops. This curvature may be a sign of stress release. The main results of my PhD, that are presented in the main text of this thesis, have used this transfer technique.

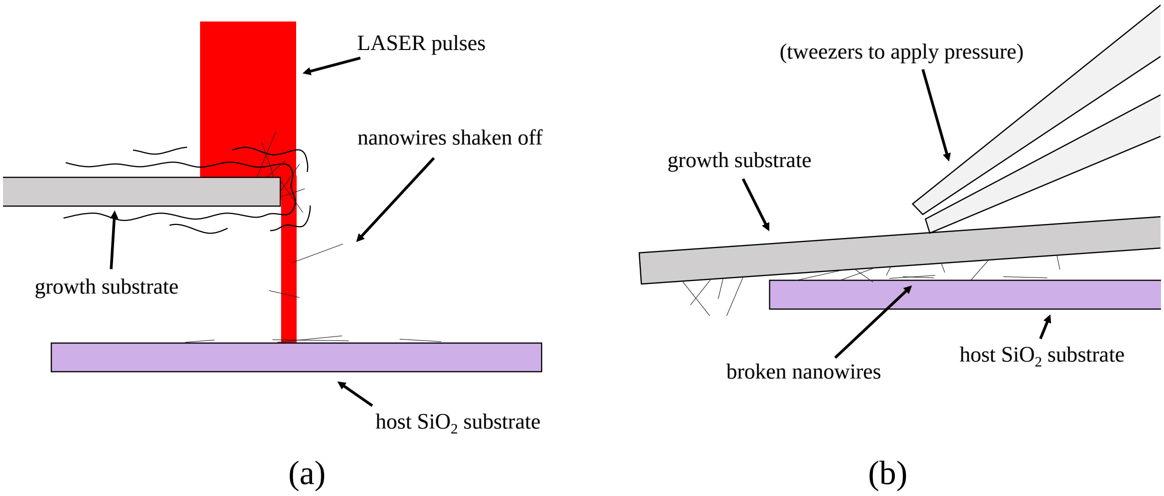

Figure 2.2 – (a) Principle of the LASER pulses shockwave transfer method. (b) Principle of the surface contact transfer method.

Lastly, I tested putting the growth substrate and the host substrate surfaces in contact, by resting one on top of the other, sometime applying pressure on it, see Fig.2.3b. Doing this with a PVD-Fe growth substrate, I managed to transfer nanowires with a reasonable density. This method, without pressure, seems more appropriate to prevent long nanowires from breaking into small parts before arriving on the host substrate, as I managed to transfer $60\mu m$ long and $110nm$ wide nanowires, which was not observed with the tissu rubbing method. This method was used to transfer the nanowires analyzed in appendix 6.9. Applying pressure yields a higher density but shorter nanowires, with dimensions $\sim 6 \times 0.1 \times 0.1 \mu m^3$.

2.3 . Selection of the nanowires

To characterize and select interesting bismuth nanowires among all the nanowires transferred to the host substrate, we used two complementary electron imaging techniques. After a preliminary characterization with an optical microscope, we used the Zeiss Supra55VP Scanning Electron Microscope (SEM) of the laboratory to spot isolated thin (diameter $< 200nm$) and long ($L > 6\mu m$) bismuth nanowires with no surface irregularities, and ideally well defined visible facets, as displayed in Fig.2.3a. It also allows to spot interesting structures such as the nanoring analyzed in chapters 3 and 4, close parallel nanowires that can be used to form a DC SQUID such as sample Bi$_1^{squid}$ analyzed in chapter 3, or overlapping nanowires as measured during my visit in Advanced Device Laboratory, RIKEN, Japan (not shown in this thesis).

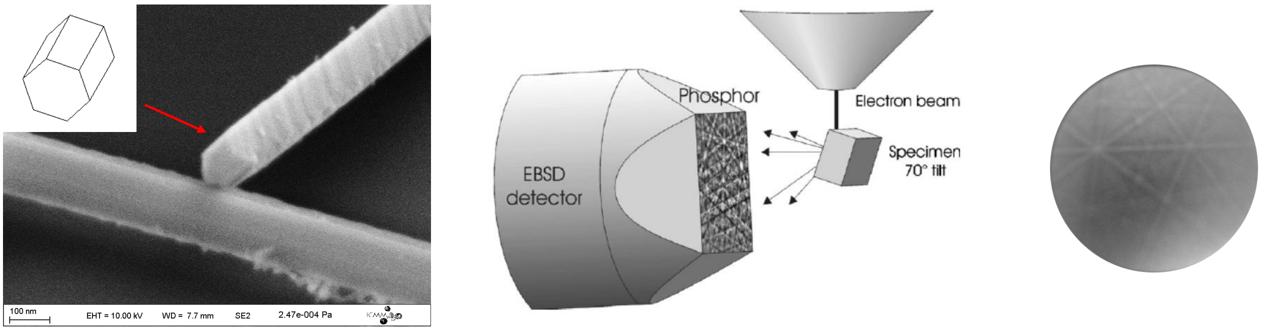

(a) (b) (c)

Figure 2.3 – (a) Scanning electron microscope image of a $\simeq 100nm$ large bismuth nanowire at a $\simeq 70^\circ$ angle. Inset : cell of the bismuth crystal reconstructed from the EBSD pattern (hexagonal representation). (b) Principle of the EBSD technique. From [2]. (c) Typical diffraction pattern obtained from electron waves interference backscattered by a bismuth nanowire single-crystal.

The other technique is Electron BackScatter Diffraction (EBSD). Similar to X-ray diffraction, it exploits the wave nature of the electrons to reveal the crystalline structure of the bismuth nanowires. The electrons backscattered by the bismuth crystal form (interference) diffraction patterns that can be analyzed to deduce the orientation of the bismuth crystal unit cell. The principle is sketched in Fig.2.3b, together with a typical diffraction pattern in Fig.2.3c. The orientation of the cell displayed corresponds to the $[001]$ crystal orientation in the hexagonal basis, or $[111]$ in the rhombohedral basis. With the diffraction analysis, we are able to confirm the single-crystalline nature of our bismuth nanowires, to determine the approximate orientation of its facets, and to follow its structure along the nanowire length. The size of the electron-beam spot is $\lesssim 100nm$. The EBSD analysis were done with François Brisset in Institut de Chimie Moléculaire et des Matériaux d'Orsay, Orsay, France.

2.4 . Superconducting contacts

During this PhD work, the bismuth nanowires were contacted by two different types of contacts. For the main results of this thesis, we used superconducting contacts to induce superconducting correlations inside our bismuth nanowires by proximity effect.

Motivated by its efficiency in previous works done in the group [141, 3, 2], the superconducting contacts were realized by Ga$^+$ Focused-Ion-Beam (FIB) assisted deposition of a tungsten compound. In this technique, gallium is ionized at a narrow tip, accelerated to $30kV$, and focused toward the deposition area using magnetic lenses similar to those used in scanning electron microscopes, producing a current of $10pA$. Close to the deposition area, a heated nozzle releases a W(CO)$_6$ gas that is decomposed by the incident Ga$^+$ and a W-C-Ga compound is deposited on the surface of the sample, in the region scanned by the FIB, see Fig.2.4a. The designed superconducting contacts have a width of $220nm$ and an approximate thickness of $200nm$, see Fig.2.4b. Such contacts are made of approximately 40% of W and C and 20% of Ga, resulting in a disordered tungsten compound that is a type II superconductor of exceptional robustness [142, 143, 141], with a critical temperature $T_c \simeq 5K$, an upper critical field $B_{c2} > 10T$, and a superconducting coherence length $\xi \lesssim 5nm$. The FIB deposition was done with Cédric Baumier and Frank Fortuna in Centre de Sciences Nucléaires et de Sciences de la Matière, Orsay, France.

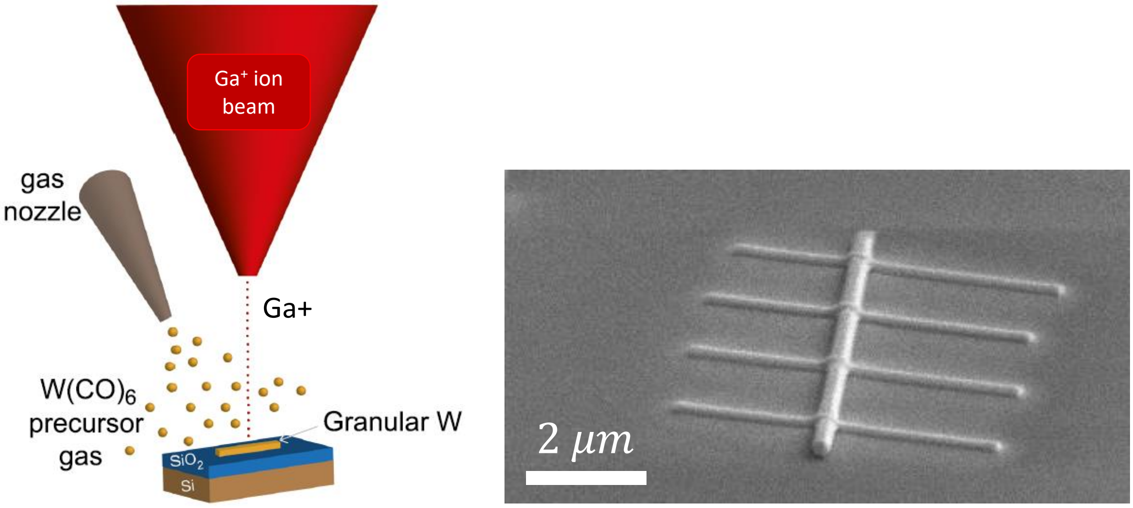

(a) (b)

Figure 2.4 – (a) Principle of the Ga$^+$ FIB assisted deposition of the superconducting W compound contacts. Adapted from [144]. (b) Scanning electron microscope image (with a $\simeq 70°$ tilt angle) of a bismuth nanowire with four superconducting W compound contacts deposited with the FIB technique.

Because the contacts can't be realized in-situ, an important fabrication step is the removal of the few nanometers thick oxide layer at the surface of the Bi nanowires. With the FIB, the few second delay between the beginning of the exposure to ions and the increase in W(CO)$_6$ pressure is enough to etch the nanowires before the deposition, ensuring good contact.

During the FIB deposition process, the decomposed gas can diffuse out of the designed FIB writing region. Citing [2] : "This can lead to a layer of aggregated materials such as W, C, Ga, O, which is termed contamination. If this contamination is conducting, there is a chance that it can become superconducting at low temperatures either intrinsically or by proximity effect. A previous characterization study done by Alik Kasumov shows that this can be the case if the distance between the FIB deposited W contacts is smaller than 200 nm. Away from this distance the contamination contains mainly C, and is of similar nature than the contamination that can be induced by the electron beam of a SEM. It is therefore highly resistive and does not short the connected device [...]."

To complete this contamination study, we performed a careful analysis of several samples using a combination of Energy Dispersive Spectroscopy and etching. We can assert that tungsten contamination extends less than $300nm$ around the deposition regions, see appendix 6.3. This analysis was done with the expertise of Frank Fortuna, now in Institut des Sciences Moléculaires d'Orsay, Orsay, France.

2.5 . Metallic contacts

After deposition of the superconducting disordered W contacts with FIB Ga$^+$, one needs a way to connect them to the macroscopic measurement system. To do so, we realize on-chip metallic contacts with low resistance that connects to the superconducting contacts with a precision of $\simeq 100nm$ on one end, and conduce the current to a large $\simeq 200 \times 200\mu m^2$ area. The large area is then connected to the sample holder pins using ultrasound precision bonding machine with AlSi wires.

To realize the metallic contacts, we use standard electron-beam lithography and vacuum evaporation, realized in three steps :

- (lithography) a mask is designed and produced using a Scanning Electron Microscope-Focused Electron

Gun (SEMFEG)
- (deposition) layers of metallic materials are deposited on the entire surface of the chip
- (lift-off) the mask is removed

The various steps are illustrated in Fig.2.5.

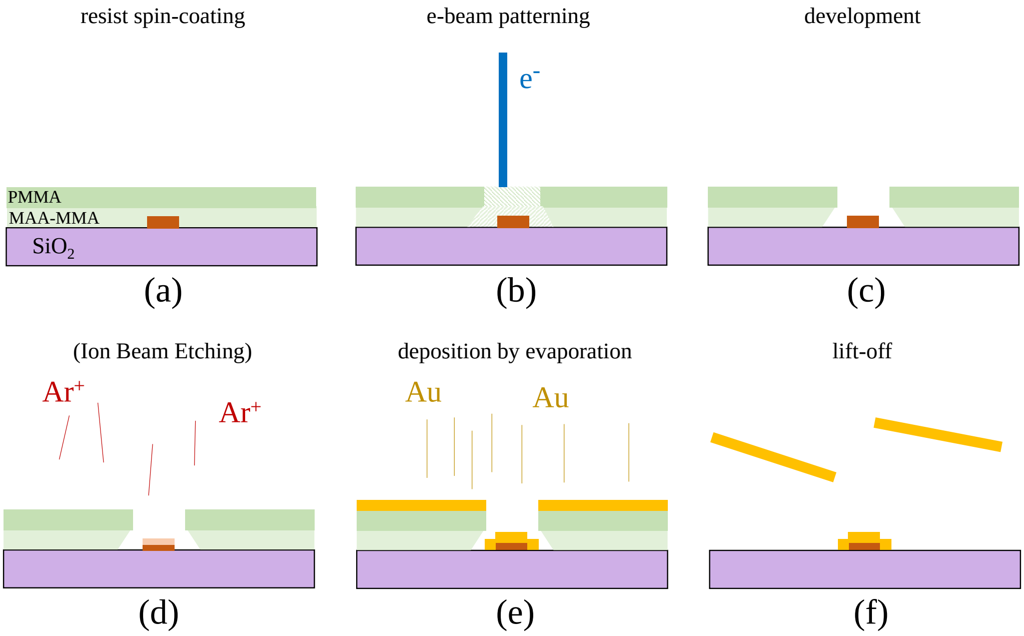

Figure 2.5 – Principle of the metallic contacts deposition process.

The mask itself is realized in three steps. First, the chip hosting the sample is spin-coated with an electron-sensitive co-polymer resist of methacrylic acid-methyl methacrylate (MAA-MMA EL10) spun at $2000rpm$ during $1min$, covering the whole chip. After a baking phase of $3min$ at $180°C$, a second layer of poly(meth)acrylates (PMMA A3) resist is spun at $4000rpm$ during $1min$, with a second baking phase of $5min$ at $180°C$. This bilayer resist helps to avoid side-walls accumulation effect and eases the lift-off process. This recipe was working fine for our contacts design, but is not ideal to realize homogeneous and sharply defined structures like superconducting planar resonators. Second, the resist is exposed to a $320\mu C.cm^{-2}$ dose of electrons on regions defined by the experimentator and drawn by a SEMFEG Zeiss Supra55VP located in the laboratory. The resist damaged by the electron beam is then removed by a "development" phase, where the chip is submerged in a methyl isobutyl ketone (MIBK) solution at room temperature during $40s$ (and quickly dried afterward).

Once the resist has been selectively removed, layers of pure metals are deposited over the whole chip. The deposition process is done under high vacuum ($P \lesssim 2 \times 10^{-7}mbar$) in an electron-beam evaporator with multiple targets allowing evaporation of different high purity materials. It was realized in the laboratory. A first layer of $5nm$ of titanium is deposited at a rate of $0.2nm.s^{-1}$ for adhesion. Then, a thick layer of $150nm$ of gold is deposited at $0.4nm.s^{-1}$ in 3 step with 15 minutes breaks to avoid overheating the chip. Lastly, the chip is submerged in an acetone solution at $50°C$ during several tens of minutes, dissolving the resist mask, until all the metallic layers over undesired regions are lifted off the chip, leaving metal on desired regions only.

To realize metallic (non-superconducting) contact directly on bismuth nanowires, in order to remove the thin oxide layer on their surface, we performed an additional Ion Beam Etching step of $30s$ with an argon plasma accelerated to $195V$, etching $\simeq 60nm$ of the bismuth. This etching step was realized right before the deposition step, in a vacuum chamber connected to the deposition chamber, such that the bismuth nanowire was not re-exposed to air. It yielded good contacts with $\simeq 25\Omega$ resistance, see the measurements performed in the normal state in appendix 6.9. However, we know that bismuth can become a superconductor when alloying with metals, as reported in [2] for Pd. The measurements in the normal state show no resistance drop at low temperature. In a series of tests, we managed to contact $\simeq 200nm$ island with the same method (albeit a shorter etching time) and measured no resistance drop at low temperature either, confirming the metallic character of the Bi-Ti/Au contact.

2.6 . A word on superconducting bismuth

Under certain conditions, bismuth materials can be superconducting at temperatures relevant to our experiments. This possibility has been discussed by my predecessor in [2]. First, bismuth can become a superconductor when forming a non-magnetic metallic alloy with other materials. Second, amorphous bismuth is superconducting for $T \lesssim 6K$ and crystalline bismuth is predicted to be superconducting at $T_c \simeq 1.3mK$. The size of the bismuth sample also plays a role. For decreasing size, it first shows an enhancement of superconductivity due to increasing electron-phonon coupling, then shows a decrease of superconductivity as quantum size effects arise. In particular, amorphous Bi films of thickness $\lesssim 0.5nm$ aren't superconducting [145].

In our experiments, bismuth isn't an intrinsic superconductor. On the fabrication side, the samples are single-crystals (with large crystalline patchs), and the surface irregularities are limited to a few atomic layers at the interface with the thin oxide layer. On the measurement side, at $T \simeq 70mK$, we see no evidence of weak residual intrinsic superconductivity that would be killed by a magnetic field of a few Gauss. Moreover, we measured several bismuth samples that were not superconducting at $T \simeq 70mK$, see the bismuth nanoring with W compound contacts during a second cooldown (see appendix 6.10), the long nanowires with metallic contacts (see appendix 6.9), and the bismuth $\simeq 200nm$ island with metallic contacts (not shown here).

2.7 . Dilution refrigerators

To reach the superconducting state of the tungsten compound contacts, and the proximity induced regime of the bismuth Josephson junctions, as well as to reduce thermal noise in general, our measurements are performed at temperatures below $1K$. This is achieved thanks to a liquid helium cryostat (to get to $T_{eb}(He) \simeq 4.2\ K$) in which a He$_3$/He$_4$ dilution refrigeration is inserted. The external part of the dilution system as well as the top of the cryostat are visible in Fig.2.6a. The sample is thermally connected to the mixing chamber of the dilution system. This way, the samples can be cooled down to $\simeq 70\ mK$.

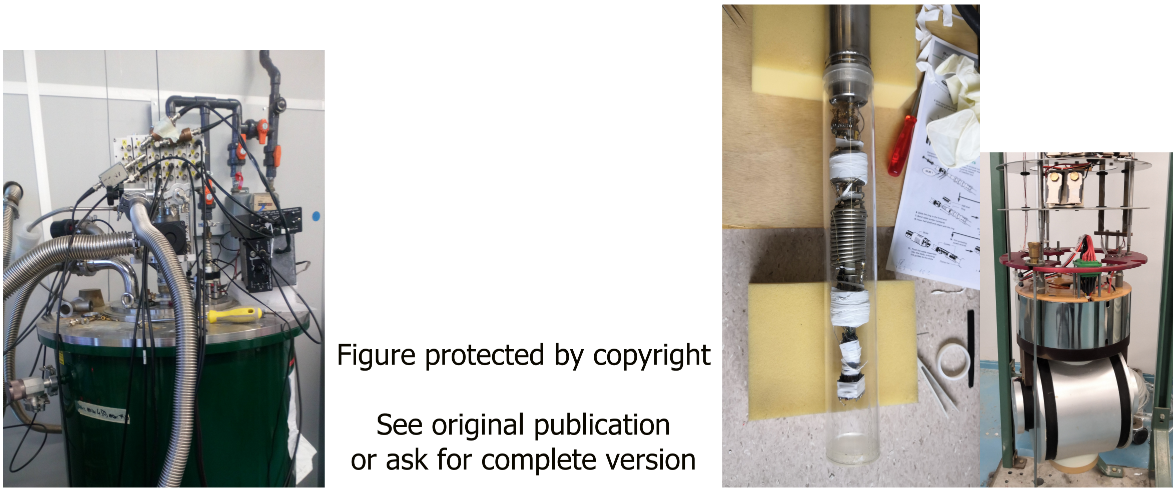

Figure protected by copyright

See original publication
or ask for complete version

(a) (b) (c) (d)

Figure 2.6 – (a) Picture of the top of the refrigeration system. The He$_3$/He$_4$ dilution system on the top, with coaxial connectors and pipes for helium mixture re-injection, is plunged into the liquid helium cryostat. (b) Principle of the He$_3$/He$_4$ dilution. The heat is absorbed in the mixing chamber region, to which the sample is thermally connected. From [146, 147]. (c) Picture of the actual dilution system. The transparent shell is to temporarily protect it, and is replaced by a proper airtight shell robust to low temperature before insertion into the cryostat. (d) Picture of the insert of the cryostat, showing the vertical and horizontal coils used to produce the magnetic field.

The cooling power of the He$_3$/He$_4$ dilution system comes from the peculiar negative enthalpy of mixing of the two isotopes under the right conditions, where mixing them absorbs heat [146, 147]. The concentration imbalance is maintained by pumping He$_3$ on one side and re-injecting it on the other side, away from the sample. The sketch of the dilution principle is shown in Fig.2.6b, and a picture of the real apparatus is shown in Fig.2.6c. The dilution system hosts conducting lines connecting electrically the low-temperature sample holder at the bottom to the room temperature connectors at the top. The lines are thermalized along the way and feature Π-filters at room temperature.

During my PhD, we used two different liquid helium cryostats. In the first one, a superconducting coil oriented along the vertical axis, submerged into liquid helium, allows us to apply a homogeneous (over the $\simeq 1cm^2$ chip) external vertical magnetic field up to $12T$. In the second cryostat, together with a $8T$ vertical coil, a second coil oriented along a fixed horizontal direction allows us to apply a $0.7T$ horizontal magnetic field. A picture of the interior of this second cryostat is shown in Fig.2.6d. By rotating the whole dilution system, we can change the relative angle between the horizontal magnetic field and the sample. However, this system is not ideal as it can't be automated and only allows for certain angles, as several elements on the top of the cryostat block certain orientations. Moreover, the horizontal coil exhibit a $\simeq 100G$ hysteresis that needs to be taken into account. By combining vertical and horizontal fields, one can achieve oblique magnetic fields.

In addition, thanks to a new Bluefors dry refrigerator with vectorial 911 magnetic field, we were able to perform a more precise and extensive analysis of the response of sample Bi$_1^{squid}$ as a function of magnetic field orientation, see chapter 3.

2.8 . Measurement setups

In this section, we present the different experimental setups used to measure our samples. For our analyses, we used lock-in techniques to measure differential resistances and second harmonic responses with either current bias or voltage bias. For switching current measurements, we coupled it to a current ramp waveform generator synchronized with a counter.

2.8.1 . Differential resistances

The voltage response of the sample to a current bias excitation $I = I_{DC} + \delta I$ can be written as :

$$V(I) \simeq V(I_{DC}) + \frac{\partial V}{\partial I}\delta I + \frac{1}{2}\frac{\partial^2 V}{\partial I^2}\delta I^2 + ... \tag{2.1}$$

with $\frac{\partial V}{\partial I} = R$ the (differential) resistance.

Using standard Stanford Research Systems SR830 lock-in instruments, we can measure individually $\frac{\partial V}{\partial I}$ and $\frac{\partial^2 V}{\partial I^2}$. It is done by introducing a small varying bias current $\delta I = I_{AC}\sin\omega t$, multiplying the measured voltage by the n-th harmonic $\sin(n\omega t)$ (and $\cos(n\omega t)$), and integrating the resulting signal over a time $\tau_i \gg 2\pi/(n\omega)$. To first approximation, this process yields $R = \frac{\partial V}{\partial I}$ for the first harmonic $n = 1$, and $\frac{1}{2}\frac{\partial^2 V}{\partial I^2}$ for the second harmonic $n = 2$, and filters out the signal outside a $1/\tau_i$ frequency window around $n\omega/(2\pi)$. The working principle is the same for conductance with a voltage bias. We used typical lock-in frequencies between $60Hz$ and a few kHz, avoiding noisy frequencies, and $\tau_i \sim 300ms$. Before multiplication by the lock-in, the voltage response of the sample is amplified by a low-noise $(2nV/\sqrt{Hz})$ amplifier at room temperature.

To current bias our sample, we use a voltage source and place a high value resistor $R_{bias} \gg R_{samp}$ in series with our sample, such that $I = V/(R_{bias} + R_{samp}) \simeq V/R_{bias}$. Typically, we have $R_{samp} < 10k\Omega$ and $R_{bias} > 1M\Omega$. Using this method, we can add up a DC current $I_{DC}/R_{bias,DC}$ from a DC voltage source and the AC current $I_{AC}/R_{bias,AC}$ from the lock-in. The full circuit is sketched in Fig.2.7a.

To measure the long nanowires with high resistance studied in appendix 6.9, we used a voltage bias with a voltage divider and adder circuit, sketched in Fig.2.7b. Following the notations of Fig.2.7b, if $r \ll R_A, R_B, R_{samp}$, we have :

$$V = \frac{1}{1 + r/R_A + r/R_B + r/R_{samp}}\left(\frac{r}{R_A}U_A + \frac{r}{R_B}U_B\right) \simeq \frac{r}{R_A}U_A + \frac{r}{R_B}U_B \tag{2.2}$$

Typically, we used $r = 25\Omega$, $R_A = 25k\Omega$ and $R_B = 250k\Omega$.

2.8.2 . Switching current

To measure a switching current, that is the maximum supercurrent that can be carried by the Josephson junction before becoming dissipative, we use the setup sketched in Fig.2.8a. A waveform generator produces a skewed triangular voltage bias with a given amplitude and frequency f. The skewness of the triangular signal is quantified by the asymmetry coefficient A_{asym}, where $A_{asym} = 0.5$ is a symmetric triangular signal and $A_{asym} = 1$ is a sawtooth signal with value increasing linearly with time. It is converted into a current bias thanks to a high $(1M\Omega)$ resistance in series with the sample, and yields a peak bias current of I_{max}. When the current reaches the sample's switching current, close to the critical current, the sample becomes dissipative, which causes a jump in resistance and a voltage drop. A counter is synchronized with the waveform generator with a TTL signal. Triggering on the TTL signal and a fixed jump in the voltage drop at the sample, the counter records the delays between the start of the current ramp t_A (zero current) and the instant at which the voltage drop exceeds the preset value t_B. The current ramp is repeated at frequency f, yielding a distribution of switching current values. This switching delay is then converted into

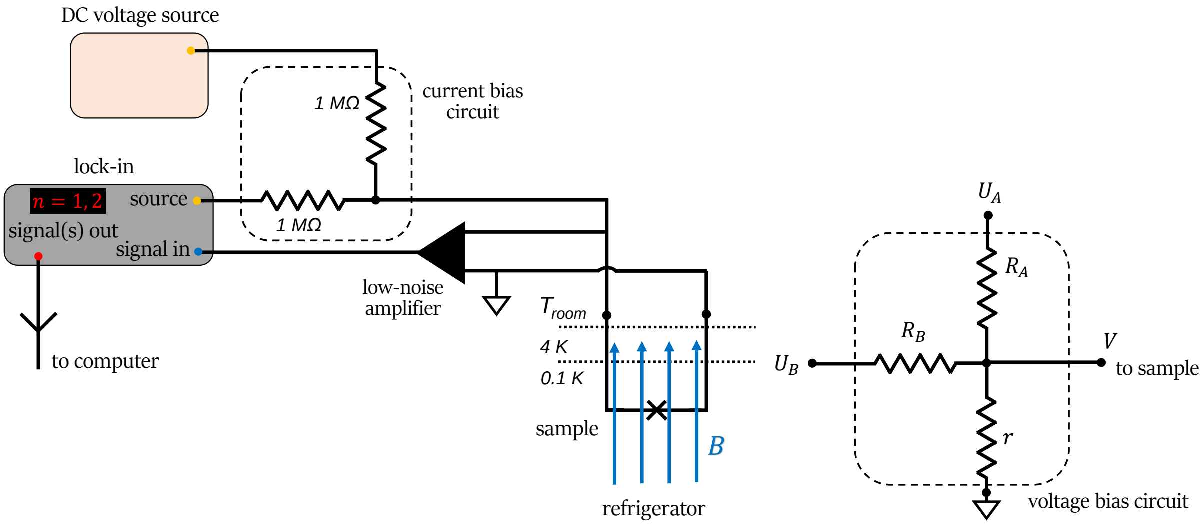

(a) (b)

Figure 2.7 – (a) Sketch of the lock-in based measurement setup of the voltage response of the sample to a current bias. Measuring the first harmonic response $n = 1$ yields the (differential) resistance. (b) Replacing the current bias circuit by this circuit yields a voltage bias $V \simeq \frac{r}{R_A}U_A + \frac{r}{R_B}U_B$.

a switching current using the formula $I_{sw} = I_{max} f(t_B - t_A)/A_{asym}$, see the sketch of Fig.2.8b. The typical values we used are $I_{max} \sim 5\mu A$ (I_{max} must be greater than the I_{sw} of the sample), $f \sim 17Hz$, and $A_{asym} = 0.8$.

For the measurements reported in chapter 3, the event t_B was triggered by a voltage drop in the differential resistance measured by a lock-in. The use of a lock-in together with the current ramp generator requires a tuning of the frequencies and the integration time τ_i, and optionally an additional filter. The resulting voltage signal can deform slightly the switching current distribution at a given magnetic field. To avoid any deformation of the full switching distribution measurements presented in chapter 4, we changed the circuit to trigger directly on the V-I curve, without the lock-in.

At a fixed magnetic field, we record N switching events (typically $N = 200$). The process is then repeated over different fixed magnetic field values. Notice that for every period of the waveform generator, the junction is guaranteed to switch to its dissipative state, thus resetting its initial (proximity induced) superconducting state, although the W compound contacts remain superconducting. This process helps to prevent memory effects that could affect the dynamics of the junction, removing the necessity of a pre-pulse step [66]. The current ramp changes the switching probability distribution, as discussed in section 1.10.

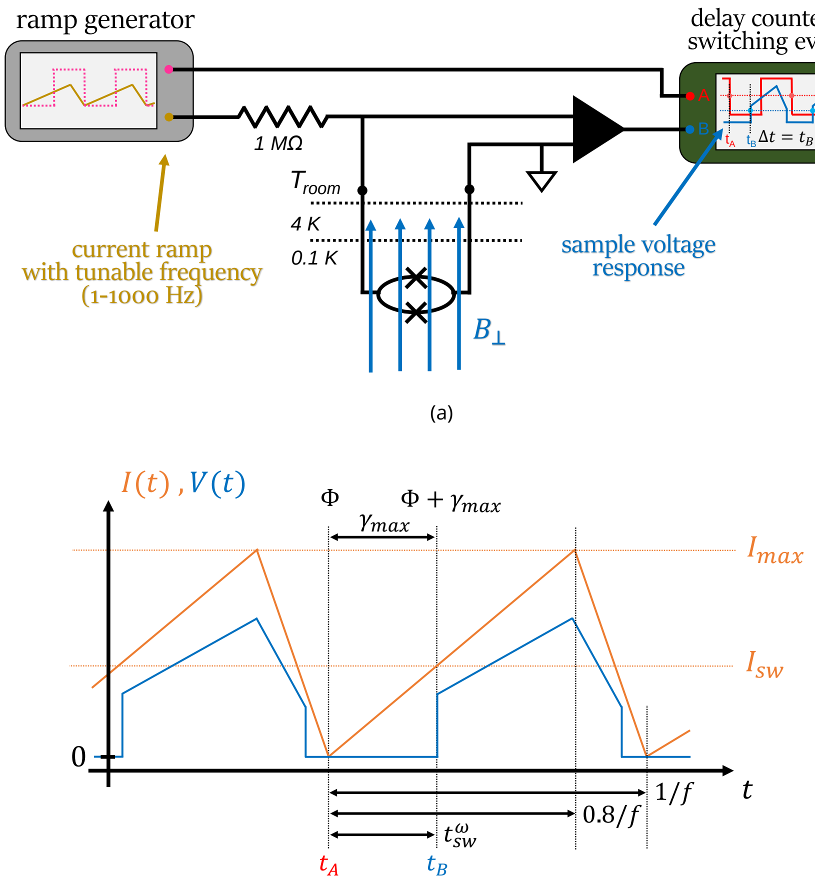

(a)

(b)

Figure 2.8 – (a) Sketch of the experimental setup (see text). (b) Sketch of the link between time and current. For the asymmetric DC SQUID model used in chapter 4, also shows the link with the phase sweep between Φ and $\Phi + \gamma_{max}$ (see text).

3 - Magnetic field-induced supercurrent interferences as evidence of helical hinge channels in Bi nanowires Josephson junctions

During this PhD work, we performed measurements of switching supercurrent on 20 segments of varying characteristics from 11 different Bi wires fabricated by three different methods. The goal of this section is to present the main common features we identified in eight of them by varying the magnetic field magnitude and orientation.

Based on theoretical and experimental works (see part 1.2), we expect the presence of bulk (3d) and surface (2d) diffusive modes and, the focus of our investigation, ballistic 1d helical modes on specific hinges of the nanowires. The former comes from the semi-metallic behavior of bismuth (bulk) single-crystal, and the latter from its second-order topological nature. Their differences in effective dimensionality, size and location in the nanowires (that depends on wire geometry and crystalline orientation) translate into distinctive supercurrent versus magnetic field patterns. To limit the contribution of bulk and surface modes, we chose to work with nanometric-size wires, with transverse dimensions close to their Fermi wavelengths ($\lambda_F^{\text{surface}} \simeq 5\ nm$, $\lambda_F^{\text{bulk}} \simeq 50\ nm$), thus lowering the number of modes.

The magnetic field dependence of the supercurrent in SNS junctions is determined by two different physical effects : an orbital effect due to the geometry-dependent (orbital) dephasing of Cooper pairs by the vector potential (see part 1.6), and a Zeeman effect due to the interaction of the magnetic field with the electron spin (see parts 1.3.8, 1.3.9, 1.4.3). The Zeeman effect is also geometry dependent in crystalline systems with strong spin-orbit interactions. It is not easy to disentangle the two effects since both lead to field-dependent interference patterns of the critical current in spatially extended Josephson junctions.

If the various modes carrying the supercurrent, of various nature, do not interfere or interact, one expect a simple sum of the specific interference sub-patterns. Varying the magnetic field direction would rescale differently the sub-patterns if the modes they originate from are not embedded in the same surface. However, as we will see on some measurements we performed, this is only an approximation. Given that superconductivity of the contacts provides macroscopic phase coherence, we can expect that channels of different nature indeed interfere and lead to more complex interference (sub-)patterns if the channels' geographic distribution is not simple. One way to circumvent this complexity is to invoke a large inductance somewhere in the orbital loops, most probably in the contact region, that decouple the phases of the channels. Another way is to focus on a smaller field ranges, if parasitic interferences or interactions have very different magnetic field scales.

In our analysis, we used this independent magnetic field sub-patterns analysis over different magnetic scales to decompose, identify and locate the supercurrent carrying channels, sometimes invoking inductances when appropriate.

That is why the magnetic field dependence of the critical current in Bi nanowires based Josephson junctions varies from sample to sample and presents a complex behavior, characterized by several salient features :

- Variations of critical current with different field scales.
- Variations of critical current which depend on the orientation of the magnetic field.
- Asymmetric field dependence. The maximum critical current can be reached at non-zero magnetic field, sometimes as high as a few thousands Gauss, and the measured pattern can be asymmetric with respect to its "central" value.

We understand this complex behavior as related to several factors :
1 - Geometry of the wires, number and orientation of the facets.
2 - Supercurrent carried by both hinge and surface states.
3 - Strong spin orbit interactions giving rise to spin momentum locking both on surface states and hinge states.
4 - Existence of several Josephson junctions in the contact regions, giving rise to an inductance in series with the wire.
5 - Decreasing of the superconducting gap of tungsten at very high magnetic field.

1 and 2 - Orbital effect and geometry of supercurrent-carrying paths
The geometry of the sections carrying the supercurrent can be determined via the field scale with which the critical current decays, as a function of field direction, see parts 1.9.1, 1.9.2 and 1.9.3. Thus, in some samples we find a supercurrent that persists to fields of up to a several thousand Gauss in all field directions, which indicates that the supercurrent is carried by a small number of strongly confined channels (within one nanometer). In other samples, a faster decay of the critical current in one direction indicates that the current is carried by a more extended region (a few tens of nanometers). In contrast with the rather smooth decay, sharp sawtooth oscillations with a fixed period are indicative of an isolated (hinge) state which interferes with either other hinge states or a more delocalized surface states.

3 - Zeeman effect
In addition to these orbital effects, the magnetic field couples to the spin of the Cooper pairs and contributes to the interference pattern by introducing a phase shift, especially in materials with SOC, see part 1.8.2.

4 - Inductances in series
As shown in appendix 6.2, inductances in series give rise to a phase shift through the Josephson junction which is also proportional to the current. It is in general difficult to discriminate this effect from the one generated by spin-orbit interactions, except in very specific geometries.

5 - Tungsten contacts
The decrease of the superconducting gap of tungsten with magnetic field can explain in some samples the rather smooth decay of the Josephson current at very large magnetic field (the low temperature critical field of the W wires exceeds $10\ T$).

In this subsection, we focus on the average bias current at which the bismuth part of the Josephson junction switches to a resistive state, hence the name of "average switching current". This measurement is performed at low temperature (in the $10 - 1000\ mK$ range) using the method shown in parts 2.7, 2.8.1 and 2.8.2. Unless specified otherwise, the measurement temperature is in approximately $T \simeq 100mK$. The analysis led to the identification of three magnetic field scales. We split our analysis into four subsections. First, we present five of the samples we analyzed, leaving the remaining three samples to simply figure in summarizing tables or to analysis in a later chapter. Second, we analyze the large field scale decrease due to orbital dephasing of narrow (1d ballistic) channels. Then, we discuss the short field scale oscillations due to orbital periodic dephasing between long ballistic channels with sawtooth CPR. Lastly, we present intermediate field scale variations and propose several hypotheses based on Zeeman or orbital dephasing, together with Josephson diode effects found in the five samples. All these observations are consistent with the hinge modes expected in Higher-Order Topological Insulators.

3.1 . The samples and their zero-field characteristics

In this subsection, we present the used fabrication, the geometry, and the zero-field superconducting behavior of the different samples. From comparison between the expected theoretical values (see part 1.3.7) and the measured values of the product $R_N I_c$, we obtain information on the nature of the Josephson junctions.

The results of this analysis are summarized in Tab.3.1. To support the analysis, we included Bi nanowire junction Bi$_3^{wire}$ fabricated by the Advanced Device Laboratory, RIKEN, Wako, Japan. It is a single-crystal with a [111] axis perpendicular to the nanowire axis and with a lot of strips on the surface, looking like a bundle of wires. We also included the asymmetric DC SQUID Bi$_2^{squid}$ made of two segments of the same Bi nanowire, that we analyze further in appendix 6.12. Its resistance at low temperature is overestimated, probably because of a weak part of the superconducting contacts which is resistive at $T \simeq 100mK$ and current bias $\simeq 8\mu A$. From their zero-field superconducting behavior, we conclude that all junctions exhibit a ballistic long regime behavior, except for sample Bi$_{11}^{wire}$ that may be closer to a ballistic regime of intermediate length.

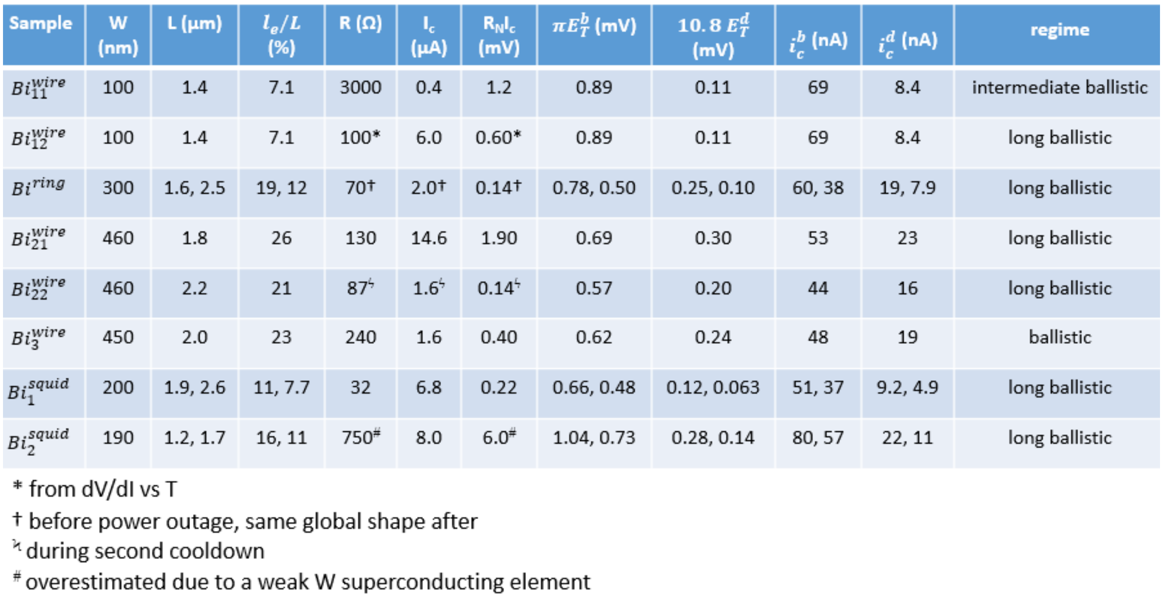

Sample	W (nm)	L (µm)	l_e/L (%)	R (Ω)	I$_c$ (µA)	R$_N$I$_c$ (mV)	πE_T^b (mV)	$10.8\ E_T^d$ (mV)	i_c^b (nA)	i_c^d (nA)	regime
Bi_{11}^{wire}	100	1.4	7.1	3000	0.4	1.2	0.89	0.11	69	8.4	intermediate ballistic
Bi_{12}^{wire}	100	1.4	7.1	100*	6.0	0.60*	0.89	0.11	69	8.4	long ballistic
Bi^{ring}	300	1.6, 2.5	19, 12	70†	2.0†	0.14†	0.78, 0.50	0.25, 0.10	60, 38	19, 7.9	long ballistic
Bi_{21}^{wire}	460	1.8	26	130	14.6	1.90	0.69	0.30	53	23	long ballistic
Bi_{22}^{wire}	460	2.2	21	87ϟ	1.6ϟ	0.14ϟ	0.57	0.20	44	16	long ballistic
Bi_3^{wire}	450	2.0	23	240	1.6	0.40	0.62	0.24	48	19	ballistic
Bi_1^{squid}	200	1.9, 2.6	11, 7.7	32	6.8	0.22	0.66, 0.48	0.12, 0.063	51, 37	9.2, 4.9	long ballistic
Bi_2^{squid}	190	1.2, 1.7	16, 11	750#	8.0	6.0#	1.04, 0.73	0.28, 0.14	80, 57	22, 11	long ballistic

* from dV/dI vs T

† before power outage, same global shape after

ϟ during second cooldown

\# overestimated due to a weak W superconducting element

Figure 3.1 – General characteristics of a selection of samples that have been measured. Because every sample have W compound contacts that have been deposited the same way, they all share the same theoretical values for the ballistic short junctions regime, with $eR_NI_c = \pi\Delta \simeq 3.8\ meV$, superconducting coherence length $\xi_S^b = \hbar v_F/\Delta \simeq 329\ nm$, and single channel critical current $i_c^{s,b} = \pi\Delta/\Phi_0 \simeq 294\ nA$. $\pi E_T^b = \pi\hbar v_F/L$ is the theoretical value of eR_NI_c for a long ballistic junction, with v_F the Fermi velocity and L the length of the junction. $10.8E_T^d = 10.8\hbar v_F l_e/(mL^2)$ is the theoretical value of eR_NI_c for a long diffusive junction, with l_e the elastic mean free path and m the number of dimensions for the diffusive states. $i_c^b = \pi E_T^b/\Phi_0$ and $i_c^d = 10.8E_T^d/\Phi_0$ are the critical currents of a single ballistic and diffusive channel, respectively. Based on previous works [2], we took $v_F = 6 \times 10^5\ m.s^{-1}$, l_e equals to the width of the junction, and $m = 2$ for diffusive surface transport.

a) Nanowire segment Bi$_{11}^{wire}$

The Bi$_{11}^{wire}$ sample is a $1.4\ \mu m$ long segment of a $100\ nm$ wide bismuth nanowire grown by PVD on vanadium, deposited with LASER pulses, and contacted with W compound superconducting contacts, see part **??** for more details. Fig.3.2a shows an optical image of the sample, where Bi$_{11}^{wire}$ corresponds to the segment between contacts labeled F and E. Its [111] crystalline orientation was measured by EBSD and found to form a $\sim 30°$ angle with the wire axis, see Fig. 3.2a inset. Its surfaces clearly present facets, and the wire is probably cleaved along its axis, leaving only half a section of the naturally grown wire, see Fig. 3.2c. This segment changed after a power outage while another segment of the same wire was being measured, changing its critical current from $I_c > 3.4\ \mu A$ to $I_c \simeq 0.4\ \mu A$. Here, we show the results after the power outage. We did not measure the new V-I (or dV/dI-I curve), but measurements at $4\ K$ suggest $R_N \simeq 3000\ \Omega$, giving a $eR_NI_c \simeq 1.2\ meV$. The comparison between the theoretical and experimental values of eR_NI_c points toward a ballistic junction of intermediate length. Analysis of the switching current as a function of magnetic field shows intermediate behavior.

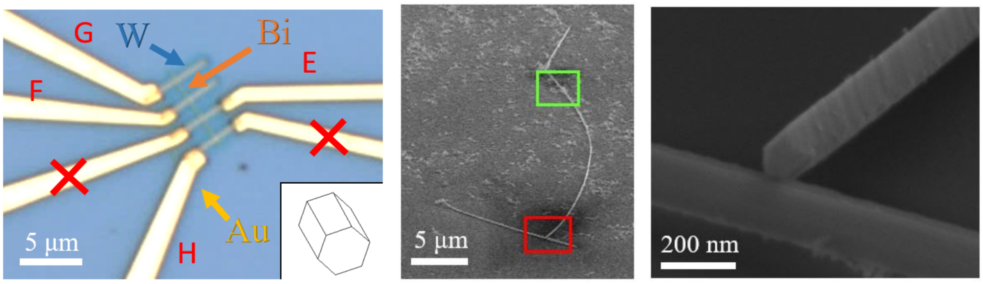

(a) (b) (c)

Figure 3.2 – (a) Optical image of the bismuth-nanowire-based Josephson junction, with segments Bi$_{11}^{wire}$ (FE) and Bi$_{12}^{wire}$ (EH). It is a bismuth single-crystal nanowire proximitized by Ga^{+} FIB-deposited W compound and connected to the measurement circuit by Au/Ti leads. Inset : EBSD determination of the unit cell of the bismuth crystal. The Bi nanowire originates from a longer wire, see the green rectangle in (b). (b) SEM image of the original long nanowire used for the Bi$_{11}^{wire}$ and Bi$_{12}^{wire}$ junctions. The sample was tilted by a $60°$ angle around the left↔right axis for this image. The lower part of the wire was lost during a brief exposure to the FIB. The green rectangle corresponds to the part contacted for the measurements. The red rectangle corresponds to the part shown in the zoomed SEM image (c). (c) SEM image of the lower part of the original nanowire.

b) Nanowire segment Bi$_{12}^{wire}$

Sample Bi$_{12}^{wire}$ is right next to the sample Bi$_{11}^{wire}$, from the same nanowire and with the same geometry $w = 100\ nm$ wide and $L = 1.4\ \mu m$, see contacts E and H in Fig.3.2a and see Fig.3.2c. Its superconducting behavior is quite different however, as shown in the differential resistance versus DC current bias Fig. 3.3a and in the average switching current versus out-of-plane magnetic field analyzed after. From Fig. 3.3a, we have $eR_NI_c \simeq 3000 \times 6 \times 10^{-6} \simeq 18\ meV$ which is superior to its maximum theoretical value in the short junction limit $3.8\ meV$. This can happen if part of the W wires in series with the junction also switches at $6\ \mu A$, resulting in an overestimation of $R_N \simeq 3000\Omega$.

To circumvent this issue, we can look at the differential resistance versus temperature of Bi$_{12}^{wire}$ as it cooled down, as shown in Fig. 3.3b. We find the $\sim 3000\Omega$ jump at $T \simeq 5K$, corresponding to the critical temperature of the disordered W compound, and another $\sim 100\Omega$ jump at $T \simeq 3.5K$ that most likely correspond to the Bi part of the Bi$_{12}^{wire}$ junction, dissipating less heat this time thanks to a lower current excitation (no DC current bias), see part 1.3.7 for more details. Taking $R_N = 100\Omega$, we get $eR_NI_c \simeq 0.6\ meV$. We find that the measured eR_NI_c is close to the long ballistic theoretical one, as confirmed in the switching current versus magnetic field data.

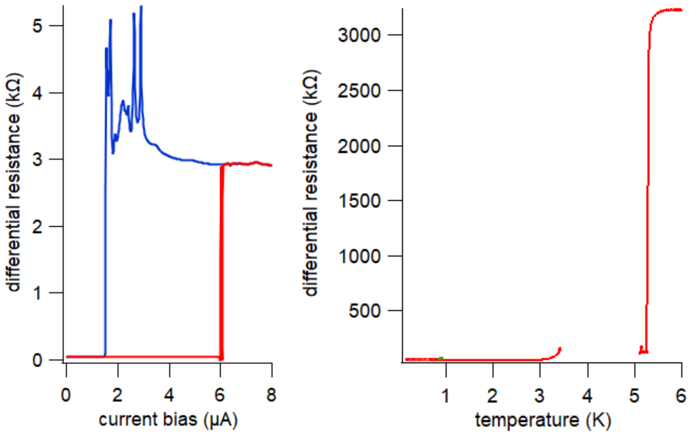

(a) (b)

Figure 3.3 – (a) Differential resistance of junction Bi$_{12}^{wire}$ as a function of current bias. (b) Differential resistance of Bi$_{12}^{wire}$ as a function of temperature as the sample was cooled down, with a low AC current excitation and no DC current bias.

c) Nanoring Bi^{ring}

Let us now consider the sample Bi^{ring}. It was part of the same batch of samples as Bi$_{11}^{wire}$ and Bi$_{12}^{wire}$, with the same fabrication method. A false color scanning electron microscope image is visible in Fig. 3.4a. The particularity of this sample is its ring shape. It is a curved nanowire of width $w \simeq 300\ nm$, with no clear facets on its surface. An EBSD analysis at multiple points along the nanowire showed a clear crystalline structure and a [111] crystal axis forming a $60-90°$ angle with the nanowire axis, pointing almost in the radial direction at any point of the ring. We deposited two superconducting disordered W contacts with the same FIB technique, closing the loop, with two branches of lengths $L_1 \simeq 1.6\ \mu m$ and $L_2 \simeq 2.5\ \mu m$.

The V-I characteristic of Bi^{ring} sample yields $eR_NI_c \simeq 70 \times 2 \times 10^{-6} \simeq 0.14\ meV$, see Fig.3.4b. The value of I_c changed to $I_c = 2.8\ \mu A$ after a power outage, but the overall $I_c(B)$ behavior of the junction remained the same in spite of the higher switching current. The two branches of different length have different theoretical eR_NI_c values. From the eR_NI_c alone, we can't conclude if the junction is long ballistic or long diffusive, but later analysis as a function of magnetic field proves that it is in the long ballistic regime.

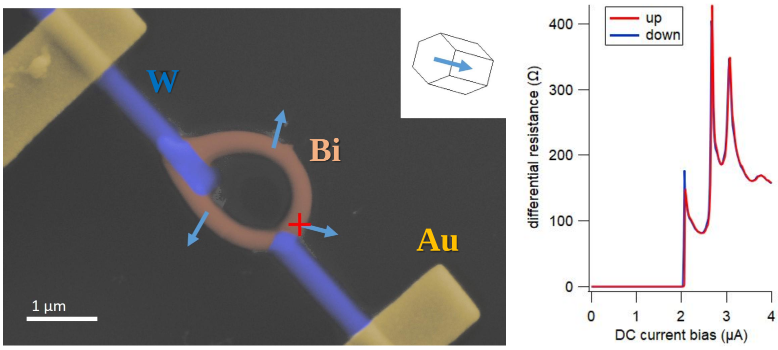

(a) (b)

Figure 3.4 – (a) SEM image with false colors of the Bi^{ring} sample. It is a Bi ring (brown) with superconducting W compound contacts (blue) and Au leads (yellow). The crystalline [111] axis, represented as blue arrows, was determined by EBSD at several points, and found to rotate along with the wire, maintaining its radial orientation. Inset : EBSD determination of the unit cell of the bismuth crystal at the red cross location. The blue arrows indicate the direction of the [111] crystal axis. (b) Differential resistance of Bi^{ring} as a function of DC current bias, before power outage.

d) Nanowire segment Bi$_{21}^{wire}$

Sample Bi$_{21}^{wire}$ is a pure Bi nanowire grown with PVD on Fe, deposited with the rubbing technique, see part 2. A scanning electron microscope image is displayed in Fig. 3.5a. Sample Bi$_{21}^{wire}$ corresponds to the segment between contacts labeled X and M. It shows clear facets as well as a series of strips on one of its side surfaces. Its width is $w \simeq 0.46\ \mu m$ and its length is $L \simeq 1.80\ \mu m$. The inset shows a crystalline axis forming a $\sim 30°$ angle with the wire axis, measured by EBSD.

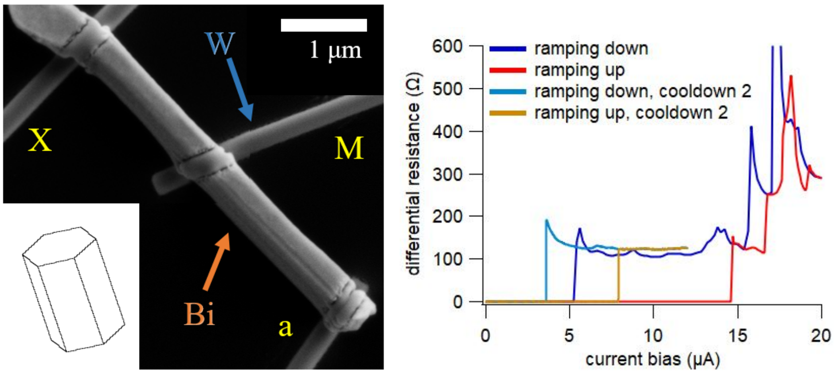

(a) (b)

Figure 3.5 – (a) Scanning electron microscope image of the bismuth-nanowire-based Josephson junction, with segments Bi$_{21}^{wire}$ (XM) and Bi$_{22}^{wire}$ (aM). It is a bismuth single-crystal nanowire proximitized by Ga+ FIB deposited W compound and connected to the measurement circuit by Au/Ti leads. Inset : EBSD determined orientation of the crystal unit cell. (b) Differential resistance of Bi$_{21}^{wire}$ at $T \simeq 60\, mK$, with increasing and decreasing bias current magnitude, and for the first and the second experiment.

The differential resistance as a function of the bias current can be seen in Fig. 3.5b. The blue and red curves are the results of the first experiment done with this sample, whereas the light blue and the gold curves have been recorded after a second cooldown months later. We see that the sample evolved between the two experiments, with a nearly unchanged resistance (first plateau) but a reduction of the switching current for the second cooldown. Because we have much more data from the first experiment, we will focus on it.

As often, there are multiple jumps in the differential resistance curve, indicating successive switches of some parts of the junction, the weakest part switching at the lowest current bias. The first jump occurs at $I_{bias} = I_c = 14.6\ \mu A$ and the following plateau show a differential resistance $R_N = 130\ \Omega$, giving $eR_NI_c = 1.90\ meV$.

Approximate theoretical characteristic values of the junctions in the different regimes are displayed in Tab.3.1. We recall that for a short ballistic junction, we expect $eR_NI_c = \pi\Delta \simeq 3.8\ meV$, which is twice the measured value. Because L is not so large compared to ξ_S^b and ξ_S^d, the junction may be in an intermediate regime which would have higher single channel critical current i_c. The magnetic field response shows a long ballistic junction behavior.

e) Asymmetric DC SQUID Bi$_1^{squid}$

Sample Bi$_1^{squid}$ is an asymmetric SQUID based on two parallel bismuth nanowires of width $w \simeq 200\ nm$ and lengths $\sim 1.9\ \mu m$ and $2.6\ \mu m$, displayed in Fig. 3.6a. The Bi wires were grown at the LPS with PVD on Fe, and transferred on the host substrate with the surface contact technique, see part 2.

This sample was designed to reproduce and collect more data on the switching statistics measured on ring sample Bi^{ring}. Unfortunately, we did not manage to reproduce it, but it provided more insights on the variations with magnetic field orientation. The two wires differential resistance measurement between the "T9" and "T7" contacts showed multiple jumps. The following measurements of switching current as a function of magnetic field magnitude and orientation were done on the lowest current resistance jump at a temperature of $\sim 10\ mK$. This jump of $\sim 32\ \Omega$ occurred at a current $\sim 6.8\ \mu A$, giving a $eR_NI_c \simeq 0.22\ meV$, see Fig. 3.6b. From the eR_NI_c analysis alone, we can't conclude on the junction regime, but later measurements as a function of magnetic field prove it is a long ballistic junction (see Fig.3.17).

To get rid of the leads' resistance in series with the sample, we changed the wiring to a four wires measurement : the supercurrent was sent from the "T9" contact to the "T7" contact, and the voltage jump measured between the "19" and "T8" contacts. With this four wires measurements, we managed to get rid of the series resistances, see Fig. 3.6c.

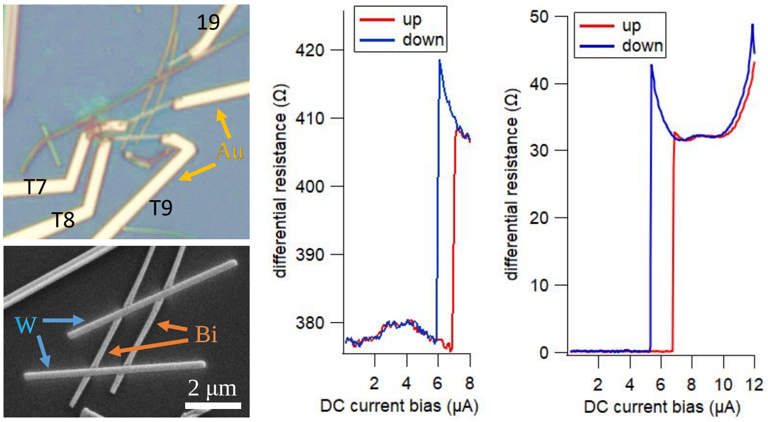

(a) (b) (c)

Figure 3.6 – (a) Top : optical image of the Bi$_1^{squid}$ sample. Bottom : SEM image of the Bi$_1^{squid}$ sample before the Au/Ti leads deposition. It is composed of two Bi segments in parallel, closed and proximitized with Ga+ FIB assisted deposed W compound, and connected to the measurement apparatus with Au/Ti leads. (b) Two wires differential resistance of Bi$_1^{squid}$ as a function of DC bias current. (c) Four wires differential resistance of Bi$_1^{squid}$ as a function of DC bias current.

3.2 . High magnetic field behavior : narrow channels

In this subsection, we show that all samples feature a switching current decreasing unusually slowly with increasing vertical field magnitude, on a scale of a few Tesla. It corresponds to a large portion of the supercurrent being carried by narrow channels of transverse size $\sim 1nm$, consistent with ballistic transport in our $\sim 100nm$ nanowires. For the nanowire segments, we find that it decreases as B^{-1} or B^{-2} along certain field directions, but with additional complexity for other directions of field. Such experiments involving ballistic junctions with high aspect ratio $L/W > 10$ have been little explored by the community, especially for high number of channels. Apart from nanotubes, one can cite the work of our own group on Bi [40, 3, 2], [148] for a graphene-based junction with $L/W \simeq 1$ and [149] for InSb nanowires with $L/W \simeq 6$, both exhibiting an anomalous Fraunhofer pattern.

We first present the similar large field scale behavior of the two nanowire segments Bi$_{11}^{wire}$ and Bi$_{12}^{wire}$. Then we study the more intricate response of segments of another nanowire with various field directions : Bi$_{21}^{wire}$ and Bi$_{22}^{wire}$. Next, we briefly present the field orientation dependence of the Bi DC SQUID Bi$_1^{squid}$. Lastly, we show the large field scale response of the nanoring Bi^{ring} as a function of out-of-plane field. The characteristic field scales we found are summarized in Tab.3.21.

a) Nanowire segments Bi$_{11}^{wire}$ and Bi$_{12}^{wire}$

Figs. 3.7a shows the average switching current of the junction Bi$_{11}^{wire}$ as a function of vertical magnetic field, perpendicular to the wire and the substrate. The curves plotted on the positive and negative magnetic field side have been both obtained with a positive and increasing magnetic field, but one with a positive bias current and the other with a negative bias current, where we used time-reversal symmetry of the whole system. It displays both regular small scale modulations as well as higher scale dampings.

Fig. 3.7b shows the average switching current of sample Bi$_{12}^{wire}$as a function of vertical magnetic field. On the $\sim 4\ T$ scale, there is a $\sim 6\ \mu A$ background supercurrent slowly decreasing to $\sim 2\ \mu A$ at $8\ T$.

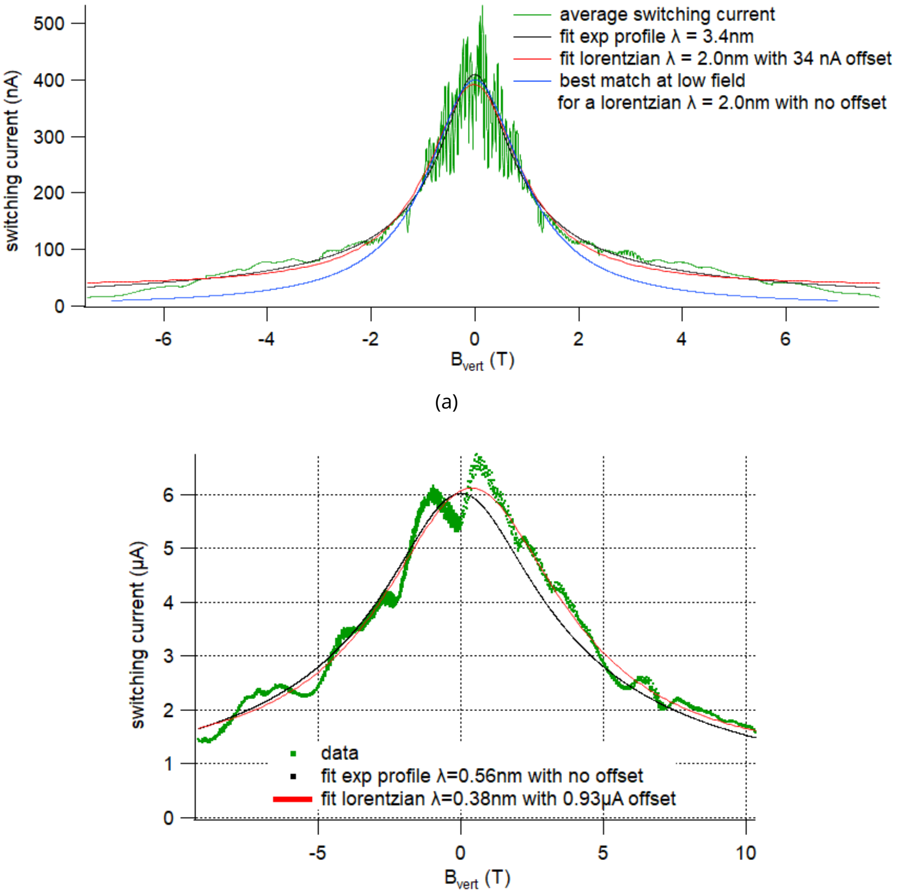

(a)

(b)

Figure 3.7 – (a) Green curve : average switching current of the junction Bi$_{11}^{wire}$ as a function of vertical magnetic field perpendicular to the wire. Black curve : fit with an asymmetric exponential current density profile model function $y = 409/\sqrt{1+(x/0.62)^2}\,(nA)$. Red curve : fit with a symmetric exponential current density profile model function $y = 375/(1+(x/1.1)^2) + 34\,(nA)$. (b) Green curve : average switching current of junction Bi$_{12}^{wire}$ as a function of vertical magnetic field perpendicular to the wire axis. Black curve : fit with $y = 6.02/\sqrt{1+(x/2.63)^2}\,(\mu A)$. Red curve : fit with $y = 5.18/(1+(x/3.9)^2) + 0.93\,(\mu A)$.

Following the analysis in part 1.9.3, we consider a ballistic mode with an exponential current density profile in the transverse direction, with a characteristic length-scale λ. This type of profile yields different switching current patterns : one decreasing as $|B|^{-1}$ at large fields for an asymmetric profile, the other as $|B|^{-2}$ (lorentzian function) for a symmetric profile.

The black and red solid lines displayed in Fig.3.7a result from a fit with either models with $\lambda = 3.4\ nm$ and $\lambda = 2.0\ nm$, respectively, where we took an effective junction length of $L = 1.0\ \mu m$. Apart from their difference in λ, both fits match well the data. However, the fit with the asymmetric exponential model yields a zero field switching current of $I_0 = 409nA$ without current offset, while it yields $I_0 = 375nA$ and a $34nA$ current offset for the other model. Matching the low field behavior with the second model without current offset yields the blue solid line in Fig.3.7a, which deviates from the data at large fields. Lastly, fitting the data with a gaussian function with or without current offset yields large deviations from the data and is not satisfying.

Following the results on Bi$_{11}^{wire}$, Fig. 3.7b displays two different numerical fits. The black curve fit is for the asymmetric exponential model with $I_0 = 6.02\ (\pm 0.01)\ \mu A$ and $B_1 = 2.63\ (\pm 0.01)\ T \iff \lambda = 0.56\ nm$, taking $L = 1.4\ \mu m$ (see Eq. 1.70), and without current offset. This fit is quite convincing, much more than a fit with a gaussian function. Alternatively, the red solid line results from a fit with the symmetric exponential model with $B_1 = 3.9\ T \iff \lambda = 0.38\ nm$ and a $0.93\mu A$ current offset.

Consistent with the analysis of previous works [2], these two segments from the same Bi nanowire show a large field scale switching current pattern consistent with narrow ballistic channels with an asymmetric (transverse) current density profile, carrying most of the supercurrent in the junction. This behavior is expected for transport dominated by 1d helical channels, as can be found in HOTI.

b) Nanowire segments Bi$_{21}^{wire}$ and Bi$_{22}^{wire}$

Fig. 3.8a shows the average switching current of sample Bi$_{21}^{wire}$ over 100 switching events for a vertical magnetic field varying from $-4\ T$ to $4\ T$. The green curve was obtained during the first experiment, and the gold curve during a second cooldown months later (with a 1.4 rescaling on the y axis). Proceeding to the same analysis as the previous subsection, we compare the data with the patterns resulting from an asymmetric (black solid line) and a symmetric (red dashed line) exponential current density profile. For this junction and for this magnetic field orientation, these models deviate significantly from the data. The pink solid curve is the result of a fit with a gaussian function with a characteristic field $B_1 = 4.4T$.

This gaussian decrease can have multiple explanations. First, it can result from narrow channels with a gaussian transverse current density profile of characteristic length $\lambda = 0.26nm$, as introduced in part 1.9.3. Second, the gaussian function is characteristic of sums of random processes with identical random variable distributions. Hence, for these channels and this field orientation, there might be phase fluctuation processes that dominate over orbital dephasing according to $\langle e^{i\phi} \rangle = \langle e^{-\phi^2/2} \rangle$ (where the average is over the trajectories) with characteristic field $B_1 = 4.4T$. Lastly, this specific sample have been measured in different experimental circumstances, and we cannot exclude that it comes from a failure of the trigger of the switching current measurement setup. At low switching current ($\lesssim 6\mu A$ here, for $|B| \gtrsim 2.5T$), the instrument may not trigger on the voltage jump from the switching anymore, but on the dissipative part of the $dV/dI - I_{DC}$ curve. However, usually the transition from a valid trigger to a wrong one is much more visible in the data.

For sample Bi$_{21}^{wire}$, the measurement apparatus allowed us to probe the response of the average switching current as a function of the magnetic field direction, see Fig.3.8b. The magnetic field is described with three parameters in spherical coordinates : a magnitude B_ρ, a polar angle φ corresponding to an angle in the horizontal plane between the horizontal coil axis and a reference line on the dilution head (with anti-trigonometric convention looking from the top-side of the chip), and an azimuthal angle θ corresponding to an angle away from the vertical axis. This is sketched in Fig.3.9.

First, let us focus on the $\theta = 90°$, $\varphi = 315°$ down curve in red in Fig. 3.8b. This will be our reference throughout the whole large scale pattern variations analysis, and correspond to a field orientation in the plane of the chip and nearly perpendicular to the wire. The width of the pattern is one order of magnitude smaller than the vertical field case (see the rescaled green curve) and is clearly different from a gaussian shape (see pink dashed line). The black dashed curve is the result of a fit with a single exponentially localized channel model function $y = 12.84/\sqrt{1 + ((x + 517)/556)^2}$ (μA, fields in G) with an additional constant current of $3.65\ \mu A$. The fit is very convincing and corresponds to a ballistic channel of dimensions $L = 1.8\ \mu m$ and $\lambda \simeq 21\ nm$. Alternatively, we can fit this curve with a lorentzian function $y = 11.1/(1 + ((x + 521)/973)^2)$ with a current offset of $4.7 \mu A$.

This characteristic length $\lambda \simeq 21\ nm$ measured in horizontal field is much larger than $\lambda \simeq 1\ nm$ measured in vertical field. This surprising result points toward anisotropic confinement for the ballistic channels carrying the supercurrent. This may result from an exceptional penetration of topological hinge modes in the bulk for specific crystalline orientations, as discussed in part 1.2.2 for the Bi(111) surface states. We also suspect that the geometry of the nanowire may play a role, with side surfaces showing clear strips that could host several ballistic hinge channels. Moreover, notice that the pattern is shifted by a field of $\sim -517\ G$ which can't be explained by the small hysteretic behavior of the horizontal coil. We will come back to this last point later on. We further notice that these variations as a function of horizontal field direction involve a supercurrent of $12.8\ \mu A$, while a $3.65\ \mu A$ remains unaffected by the magnetic field on a scale of $\sim 7000\ G$.

Let us now analyze the variations of the large scale pattern as a function of in-plane magnetic field angle. The light blue curve in Fig. 3.8b has been obtained at an angle $\varphi = 45°$, away from the plane perpendicular to the wire axis. Its magnetic field magnitude can be rescaled by a factor of $-1/7$ such that it matches perfectly with the $\varphi = 315°$ up curve.

In appendix 6.6.1, we analyze the large magnetic field scale switching current decrease as a function of polar and azimuthal angles. We find that for $\theta = 90°$ (horizontal field), the rescaling of the field with φ is consistent with orbital dephasing of channels embedded in a vertical surface on the side of the nanowire, with a nanowire oriented along $\varphi = 36°$ and a surface vector oriented along $\varphi_S = 306°$. For a field perpendicular to the nanowire with $\varphi \simeq 306°$ and $\theta = 45°$, we find that a simple orbital dephasing by a flux within a single surface is inconsistent with the measurement with a field along the vertical direction.

These results show that, in the horizontal plane, the large scale pattern is very well modelized by an asymmetric exponential current density profile on a surface of the wire. There is a qualitative difference between the ballistic interference pattern for a horizontal magnetic field and the gaussian pattern for a vertical magnetic field. This may be caused by an anisotropy in the transverse confinement profile of the modes, or by a transition between a random-dephasing-dominated (vertical field) and an orbital dephasing dominated (horizontal field) interference pattern. From the switching current as a function of magnetic field at large field scale, we found that the characteristic size of the ballistic channels is $h \times w \simeq 21 \times 0.3 nm^2$.

During this first cooldown of the sample, the contact "a" was not properly connected. For the second cooldown, we were able to measure both the segments XM (Bi$_{21}^{wire}$) and aM (Bi$_{22}^{wire}$), see Fig.3.5a. Unfortunately, the switching current of Bi$_{21}^{wire}$ was changed during this cycle, and we can't exclude that Bi$_{22}^{wire}$ changed too. This weakens the comparison between the Bi$_{21}^{wire}$ data shown here and the Bi$_{22}^{wire}$ data available. Nevertheless, let us quickly discuss what we found for Bi$_{22}^{wire}$.

The main characteristics of Bi$_{22}^{wire}$ for the second cooldown are noted in table 3.1. The average switching current of segment Bi$_{22}^{wire}$ as a function of vertical magnetic field shows a $\sim 1.6\ \mu A$ maximum close to $B = 0$, see red line in Fig.3.10 (rescaled). It decreases with a B^{-1} or B^{-2} law just like the others segments of nanowires, with a characteristic field scale $\sim 1.25T$, see the fit with the asymmetric exponential current density profile in Fig.3.10 (black line). It is consistent with a collection of ballistic channels embedded in a single surface of effective dimensions $2.2\mu m \times 0.8nm$, $2.2\mu m$ being the segment length. In addition, one can see some $\sim 100\ nA$ variations, but with no clear periodicity.

Now considering the average switching current of segment Bi$_{22}^{wire}$ as a function of horizontal magnetic field perpendicular to the nanowire ($\theta = 90°$, $\varphi \simeq 315°$), the background is rescaled by a field factor ~ 5.6, decreasing on a scale $\sim 2250\ G$, corresponding to an effective surface of $2.2\mu m \times 4.2nm$ for the collection of ballistic channels. On top of that, there is now a clear oscillation pattern of amplitude $\sim 200\ nA$ and a quite regular period of $\sim 270\ G$, corresponding to orbital dephasing through an effective surface $2.2\mu m \times 35nm$. The shape of the oscillations is triangular, characteristic of interference between long ballistic channels.

We conclude that both segments Bi$_{21}^{wire}$ and Bi$_{22}^{wire}$ show a behavior consistent with supercurrent carried by a ballistic channels of transverse characteristic size $h \times w \simeq 10 \times 1nm^2$. The Bi$_{21}^{wire}$ segment also show an average switching current pattern that does not rescale like a simple $\vec{B}.\vec{S}$ as a function of magnetic direction.

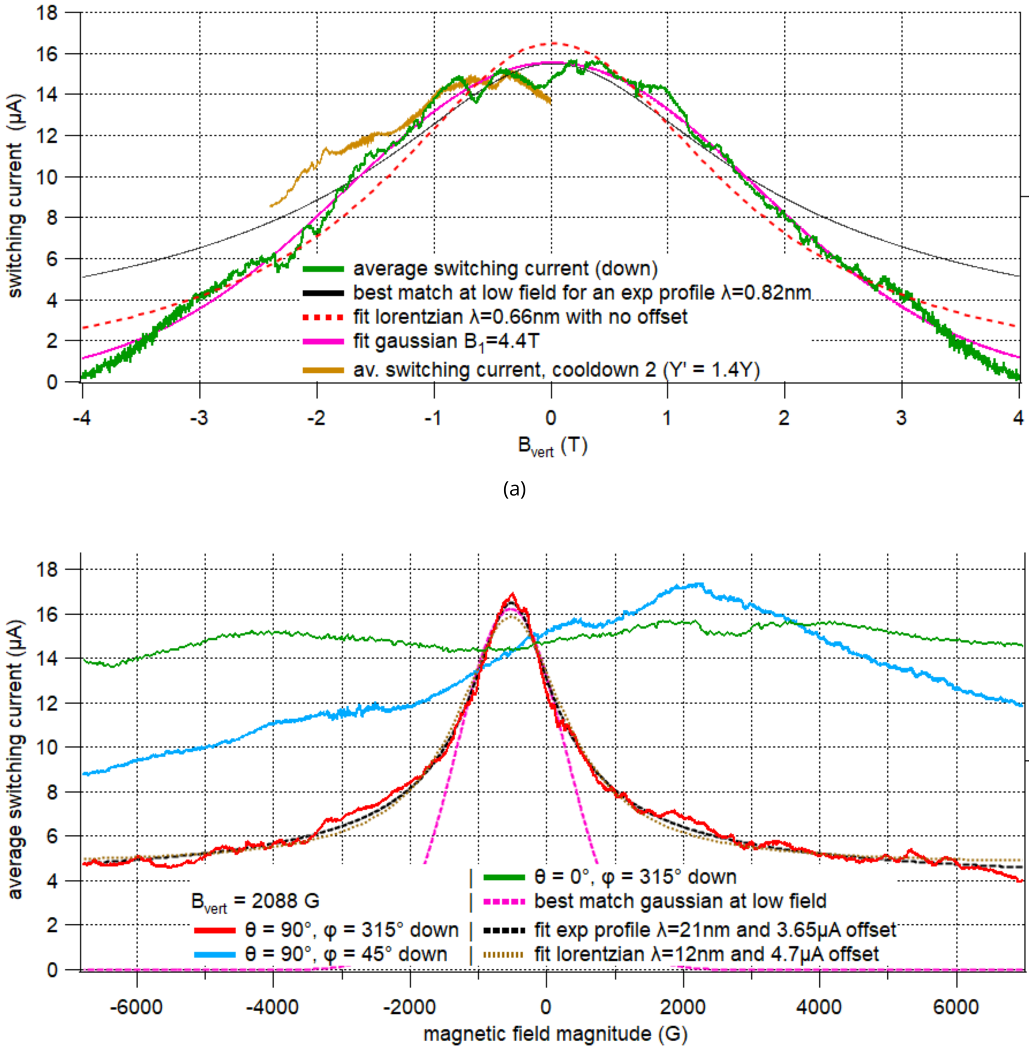

(a)

(b)

Figure 3.8 – Average switching current of Bi$_{21}^{wire}$ as a function of magnetic field magnitude in various direction. θ is the azimuthal angle, with $\theta = 0°$ the vertical direction. φ is the polar angle between the horizontal coil axis and a reference line on the dilution head, with $\varphi = 36°$ the nanowire direction. (a) Dependence on vertical magnetic field up to $4T$, for the first and the second experiment. Black solid line : qualitative comparison at low field with an asymmetric exponential profile model function $y = 15.5/\sqrt{1+(x/1.4)^2}$ (μA). Red dashed line : fit with a symmetric exponential profile model function $y = 16.5/(1+(x/1.8)^2)$ (μA). Pink solid line : fit with a gaussian function $y = 15.5\exp(-\pi(x/4.4)^2)$ (μA). (b) Dependence on horizontal magnetic field up to $7000G$. For the two measurements at angles $\theta = 90°$, $\varphi = 315°$ (red curve) and $\theta = 90°$, $\varphi = 45°$ (blue curve), there was a constant vertical field $B_z = 2088\,G$. Black dashed line : fit with $y = 12.84/\sqrt{1+((x+517)/556)^2} + 3.65$ (μA, fields in G). Brown dashed line : fit with $y = 11.1/(1+((x+521)/973)^2) + 4.7$ (μA, fields in G). Pink dashed line : fit at low field with a gaussian function $y = 16.21\exp(-\pi((x+523)/2e+3)^2)$ (μA, fields in G).

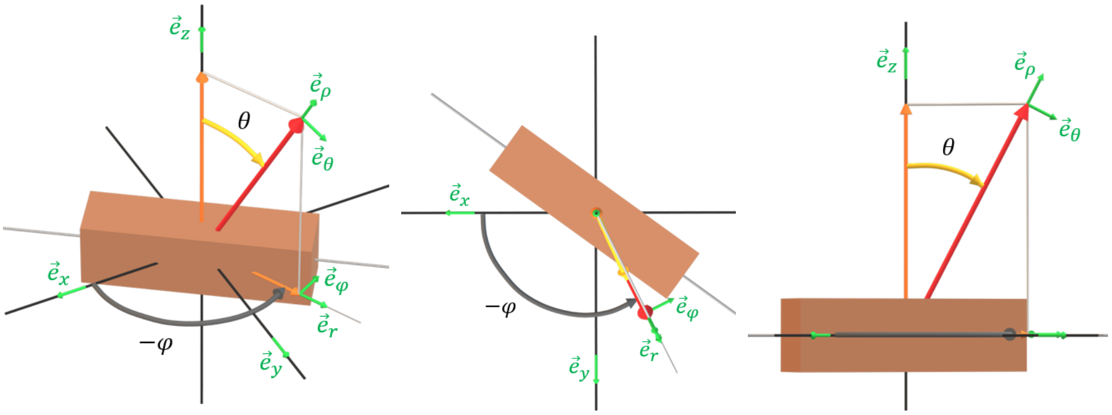

(a) (b) (c)

Figure 3.9 – Sketch to illustrate the decomposition of a vector in the cartesian, cylindrical, and spherical basis. The red arrow is the vector to decompose. The orange arrows are the projection of the vector on the vertical axis and the horizontal plane. The small green arrows are unit vectors of the three basis. The dark gray curved arrow represents the polar angle $-\varphi$ between the reference 0° axis and the projection of the vector on the horizontal plane. The yellow curved arrow represents the azimuthal angle θ between the vertical axis and the vector. (a) 3d view. (b) Top view of the x-y plane. (c) Side view of the plane parallel to the vertical axis and to the vector.

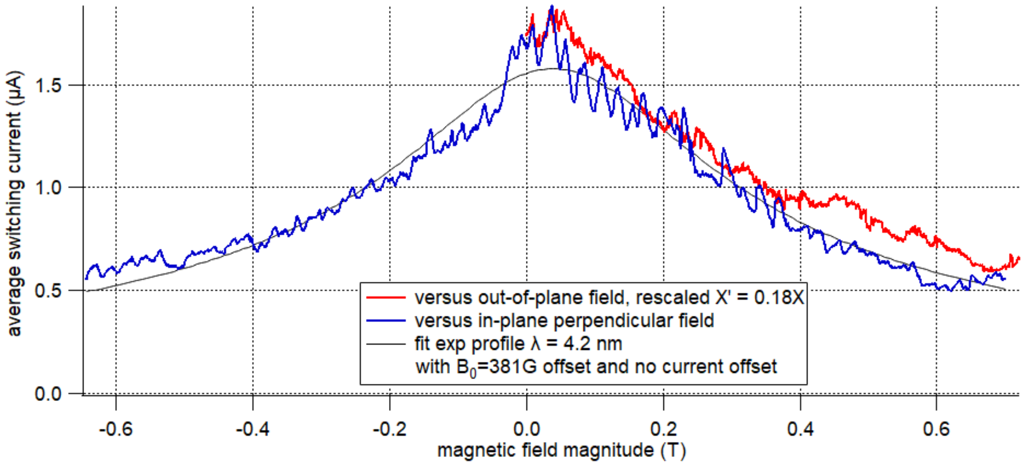

Figure 3.10 – Average switching current of the bismuth-nanowire-based Josephson junction Bi$_{22}^{wire}$ as a function of vertical (red line) and horizontal (blue line) magnetic field perpendicular to the nanowire. Black line : fit of the blue line data with an asymmetric exponential current density profile model function $y = 1.58/\sqrt{1+((x-381)/0.225)^2}$ (μA) corresponding to $\lambda \simeq 4.2nm$.

c) Asymmetric DC SQUID Bi$_1^{squid}$

We analyzed the average switching current of a proximitized bismuth nanowire Bi$_{21}^{wire}$ as a function of magnetic field magnitude and direction, and we found surprising results. We ran a similar series of experiment on the following DC SQUID sample Bi$_1^{squid}$, with a new dilution cryostat allowing us to control the magnetic field in 3d up to $1\ T$ with good precision. The following set of measurements provides more data and confirmed the presence of a dephasing mechanism more complex than orbital dephasing.

The average switching current as a function of magnetic field magnitude and orientation in the horizontal plane is plotted in Fig. 3.11a. The conventions for azimuthal angle θ' and polar angle φ' are the same as θ and φ sketched in Fig.3.9, respectively. Each curve magnetic field magnitude has been rescaled such that they all fall to a unique curve. The rescaling factors are plotted in Fig. 6.23a in the appendix, and clearly follow a cosine rule as expected for a standard orbital flux scalar product $\vec{B}.\vec{S}$ for a $\vec{S}$ at a polar angle $\varphi' = 148°$ (perpendicular to the wire axis). The rescaling factor is $0.311\ kG^{-1}$ for at $\varphi' = 148°$. The characteristic field scale of the $\varphi' \simeq 148°$ curve is $\sim 4000\ G$, corresponding to a $2.6\mu m \times 2nm$ effective surface.

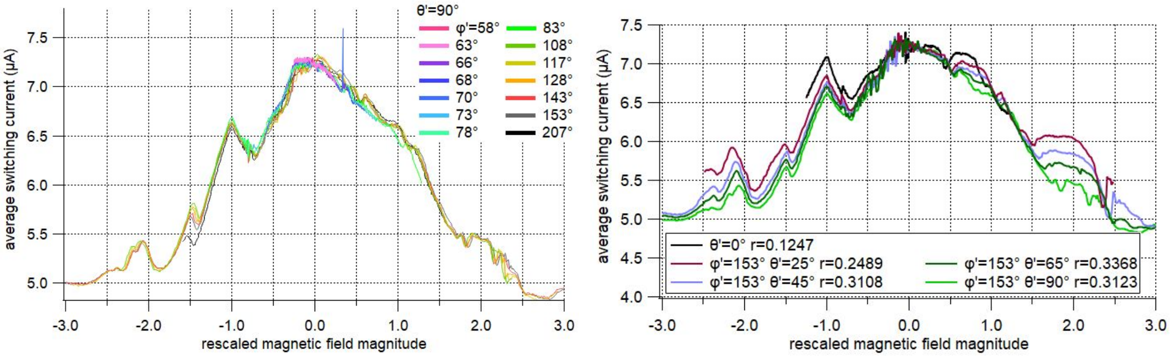

(a) (b)

Figure 3.11 – Average switching current of Bi$_1^{squid}$ as a function of magnetic field magnitude for various horizontal polar angles φ' and azimuthal angles θ'. Each curve magnetic field magnitude has been rescaled to fall to a unique curve. (a) Horizontal field with variable φ' and fixed $\theta' = 90°$. (b) Perpendicular field with variable θ' and fixed $\varphi' = 153°$. The field rescaling factors in (a) and (b) match with $\vec{B}.\vec{S}$ with $\vec{S}$ perpendicular to $\varphi' = 148°, \theta' = 68°$, but it fails to account for the amplitude differences in (b).

Fig. 3.11b shows the average switching current as a function of rescaled magnetic field magnitude for various field azimuthal angle θ' and fixed polar angle $\varphi' = 153°$, close to perpendicular to the nanowire axis. In Fig. 3.11b, we notice that in contrast with the polar angle variations, the switching current pattern does no fall into a single curve. For example, there is a net difference in switching current for features at $X \simeq -2$, -1, or 2.

The height of the $X = -1$ peak and the field rescaling factors r are plotted as a function of azimuthal angle θ' on Fig. 6.23b in the appendix. The field rescaling factors fit with a cosine function which maximum is at $\theta' = 68°$, matching with a surface vector $\vec{S}$ oriented along $\varphi' = 148°$ and $\theta' = 68°$. We see a sharp contrast between the field rescaling factors that match very well with the orbital dephasing by a flux through a surface oriented along $\varphi' = 148°$, $\theta' = 68°$, and the variations of the current values of some features (like the peaks at $X = -1$) that indicate an additional mechanism, with potentially Zeeman-induced effects.

d) Nanoring Bi^{ring}

Looking at the high field scale average switching current versus vertical magnetic field curves of Bi^{ring} displayed in Fig. 3.12, we see regular $\sim 0.5\ \mu A$ dips at the $\sim 1\ T$ scale (discussed in the next subsection 3.4), and a background current slowly decreasing from $\sim 2.8\ \mu A$ at $B = 0T$ to $\sim 0.5\ \mu A$ at $B \sim 4T$. To provide a rough estimate, the red solid line in Fig. 3.12 shows a fit with a lorentzian function with $\lambda \simeq 0.44nm$ for the branch $L = 1.6\mu m$ or $\lambda \simeq 0.28nm$ for the branch $L = 2.5\mu m$, and no current offset. Additionally, the decrease at low field (first lobe in Fig. 3.12) may have a contribution from more spatially extended. The characteristic field scale is $\sim 0.2T$ corresponding to a surface $\sim 2\mu m \times 5nm$.

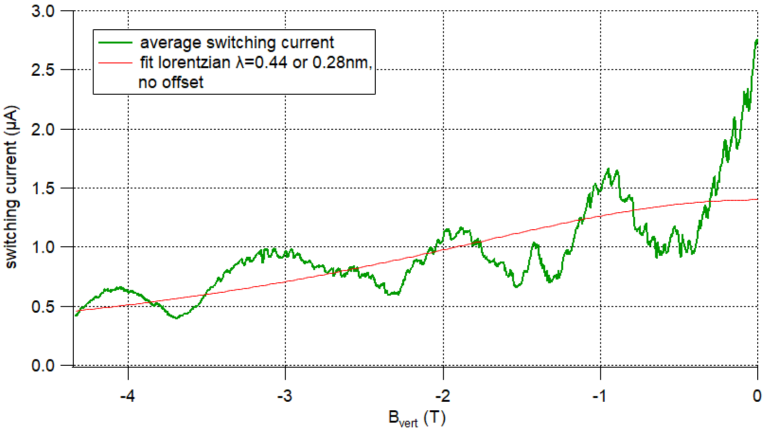

Figure 3.12 – Large scale average switching current of the nanoring Bi^{ring} as a function of vertical magnetic field perpendicular to the ring plane (green line), and fit with a lorentzian function corresponding to $\lambda \simeq 0.44nm$ for the branch $L = 1.6\mu m$ or $\lambda \simeq 0.28nm$ for the branch $L = 2.5\mu m$.

In this subsection, the variations of the switching currents on large magnetic field scale and for various field orientation showed that all samples exhibit supercurrents surviving up to very high fields, of the order of $B \sim 1T$. This indicates that there is always a large part of the supercurrent that is carried by modes with a narrow transverse extension, of the order of $\lambda \sim 1nm$, consistent with 1d ballistic hinge mode transport expected in HOTI. We found that the vertical field dependence of nanowire segments Bi$^{wire}_{11}$ and Bi$^{wire}_{12}$, as well as the horizontal field dependence of nanowire Bi$^{wire}_{21}$, are well modelized by a exponential (transverse) current density profile producing either a $|B|^{-1}$ or a $|B|^{-2}$ behavior at high fields. In nanowire Bi$^{wire}_{21}$ and Bi DC SQUID Bi$^{squid}_{1}$, the study of the variations of the switching current pattern as a function of magnetic field direction revealed a standard orbital flux scalar product relation for horizontal fields but a more complex behavior as a function of azimuthal angle. Segments Bi$^{wire}_{21}$ and Bi$^{wire}_{22}$ of a nanowire showed a large anisotropy between vertical and horizontal fields, with a confinement of $\lambda \simeq 0.3nm$ and $\simeq 21nm$, respectively.

In this subsection, we focused on the field scale of the decrease of the switching current, and did not discuss its amplitude. We can estimate the critical current of a single long ballistic channel to $i^b_c = \pi E^b_T/\Phi_0 = ev_F/L \simeq 50nA$ (see Tab.3.1), giving an estimate of ~ 100 channels carrying a typical maximum supercurrent of $\sim 5\mu A$. To fit these ~ 100 channels in the bismuth junction, they must be separated by a distance corresponding to their transverse confinement of $\sim 1nm$. But such a spacing could produce a visible interference pattern due to significant orbital dephasing, see part 1.9.1. This leads us to believe that the $\lambda_h \simeq 21nm$ and $\simeq 4.2nm$ found in horizontal field dependence in Bi$^{wire}_{21}$ and Bi$^{wire}_{22}$ might be caused by tens of channels interfering, consistent with the strips visible on the sides of the nanowire (see Fig.3.5a). Moreover, we note that the orbital dephasing can be blurred out if the distributions of critical currents and initial phases of the individual channels have a random components (e.g. with random lengths or interface quality).

3.3 . Low magnetic field behavior : CPR of long ballistic junctions

In this subsection, we study the variations of the switching currents on small magnetic field scale of our five samples. In the nanowire segments Bi$_{12}^{wire}$ and Bi$_{21}^{wire}$, and to a lesser extent in Bi$_{11}^{wire}$, we found skewed triangular oscillations with a period corresponding approximately to Φ_0 through the surface of the junction. In the bismuth-based DC SQUID Bi$_{1}^{squid}$ and Bi^{ring}, we also found skewed triangular oscillations, but with a period corresponding to Φ_0 through the surface defined by the two branches of the SQUID. These oscillation patterns are specific to interference between long ballistic channels with sawtooth CPR, confirming the presence of 1d protected channels that are found in HOTI. The oscillations are robust up to magnetic fields $|B| > 1T$, as expected for interference between narrow channels.

We first analyze the oscillations of nanowire segments Bi$_{11}^{wire}$ and Bi$_{12}^{wire}$ as a function of vertical magnetic field. Then, we study the variations of the oscillations pattern of nanowire Bi$_{21}^{wire}$ with magnetic field direction and temperature. Lastly, we analyze the oscillations of Bi DC SQUID Bi$_{1}^{squid}$ and Bi^{ring} with vertical magnetic field.

a) Nanowire segment Bi$_{11}^{wire}$

Fig. 3.13b displays the oscillations of the average switching current of the nanowire segment Bi$_{11}^{wire}$ as a function of vertical magnetic field, with smooth background removed. We see regular modulations of amplitude $\sim 150\ nA$ and period $\sim 710\ G$ that look like a symmetric SQUID pattern ($|\cos(\varphi)|$) with both junctions in the rather short-junction limit, see part 1.6.2. We also notice a damped sinusoid of amplitude $\sim 100\ nA$ and period $\sim 3300\ G$, dying off at $|B| \simeq 1.1\ T$, that will be discussed in the next subsection 3.4. On this plot, we clearly see that the short-period oscillations amplitude never vanishes and monotonously decreases as $|B|$ increases. Given the length of the junction Bi$_{11}^{wire}$, a long-junction behavior is expected. We recall that a power outage occurred and obviously changed the characteristics of the junction, probably changing its NS interfaces, thereby changing the relative contributions of the various transport channels and their effective lengths.

The $\sim 710G$ oscillation period corresponds to a superconducting quantum of flux $\Phi_0 \simeq 2.068 \times 10^{-15}\ Wb$ in an area of $\sim 2.95 \times 10^{-2}\ \mu m^2$. Considering a rectangular surface of length of $1\mu m$ (a little bit shorter that the $1.4\ \mu m$ of the junction) perpendicular to the magnetic field direction, it corresponds to a (minimum) surface width of $\sim 30\ nm$. These modulations become less symmetric for $|B| \gtrsim 0.2\ T$ and are drastically reduced at $|B| > 1.1\ T$.

The fact that all the modulations vanish quickly at $|B| \simeq 1.1\ T$, on the same field scale as the background current, suggests that the extinction of one channel at $|B| \simeq 1.1\ T$ ends the interferences. Fig. 3.13c shows the results of a numerical computation for two ballistic channels in parallel in the short junction limit and no inductance, with critical currents $i_{c1} = 0.1$ and $i_{c2} = 0.3$ and damping field scales $B_1 = 0.4\ T$ and $B_2 = 0.618\ T$, such that $i_{c1,c2}(B) = 1/\sqrt{1 + (B/B_{1,2})^2}$. Comparing with Fig.3.13a, this model reproduces qualitatively the oscillations and their decreasing amplitude, correlated with the decrease of the background amplitude. However, it ignores the $\sim 3300G$ variations and the transition at $|B| \simeq 1.1\ T$ seems too smooth compared to the data, such that there might be an additional phenomenon involved at the $1T$ field scale.

We can compare these critical current values to the ones expected in various limits : $i_c^{s,b} = \pi\Delta/\Phi_0 \simeq 294\ nA$ in the short ballistic case, $i_c^b = \pi E_T^b/\Phi_0 = ev_F/L \simeq 68.7\ nA$ in the long ballistic case, and $i_c^d = 10.8 E_T^d/\Phi_0 \simeq 8.4\ nA$ in the long diffusive case. We see that the $0.1 - 0.3\ \mu A$ critical currents we estimate match with the ballistic regimes.

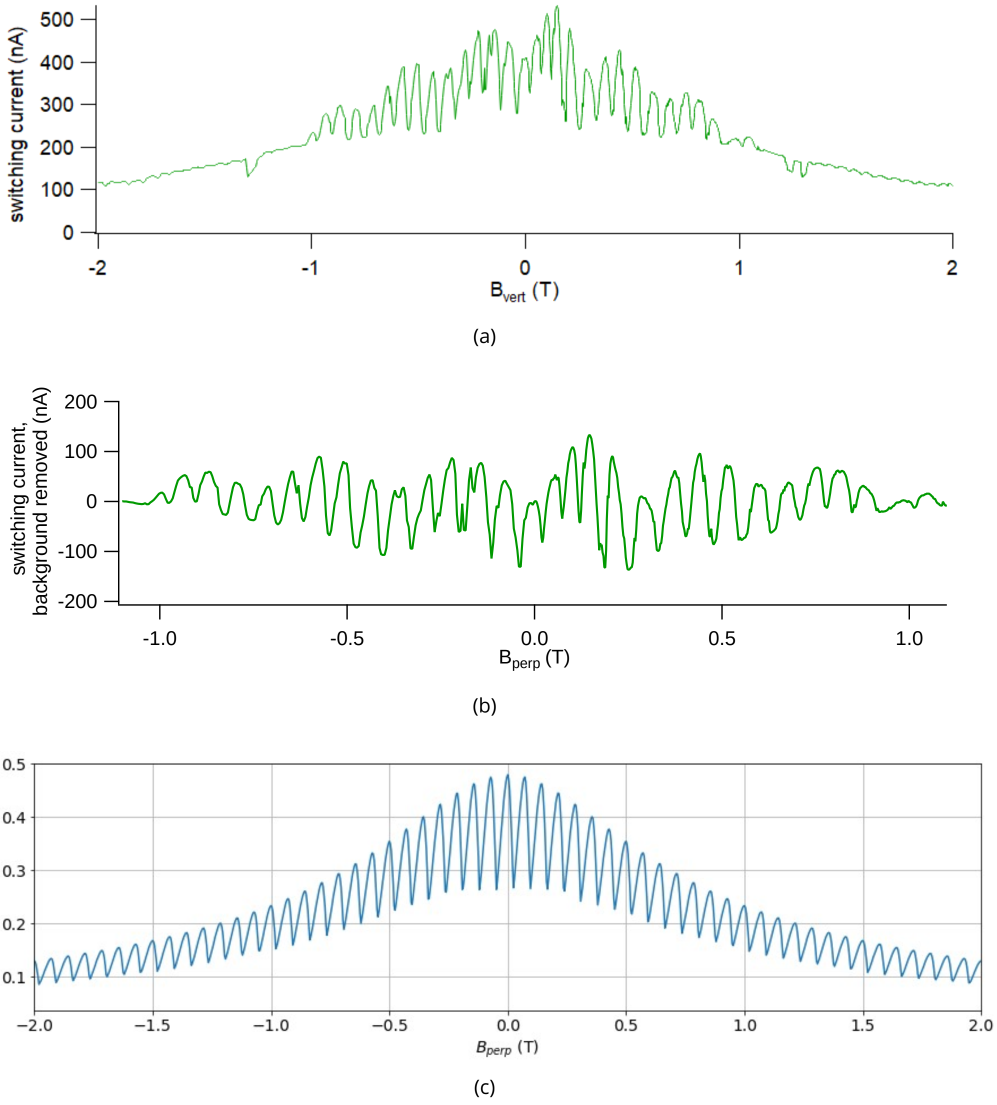

(a)

(b)

(c)

Figure 3.13 – (a) Average switching current of sample Bi$_{11}^{wire}$ as a function of vertical magnetic field perpendicular to the wire, on a $2T$ range. The $\sim\ 710G$ period corresponds to ballistic channels separated by $\sim\ 30\ nm$. (b) Same as (a) with smooth background current subtracted. (c) Results of a numerical computation for two ballistic channels in parallel in the short junction limit and no inductance, with critical currents $i_{c1} = 0.1$ and $i_{c2} = 0.3$ and damping field scales $B_1 = 0.4\,T$ and $B_2 = 0.618\,T$ ($i_{c1,c2}(B) = 1/\sqrt{1 + (B/B_{1,2})^2}$). This simple model reproduces the oscillation period and amplitude variations, but ignores the $\sim\ 3300G$ sinusoidal contribution that requires a third channel in series with an inductance.

b) Nanowire segment Bi$_{12}^{wire}$

Figs. 3.14a and 3.14b show the average switching current of the nanowire segment Bi$_{12}^{wire}$ on the small field scale, with background current removed by subtraction of a 300 points smoothed version of the data. There is a $\sim 416\ G$ periodic variation of amplitude $\sim 300\ nA$, with a symmetric triangular pattern (see Fig. 3.14b for a zoom with background removed). The amplitude of this short-scale oscillations survives up to $\sim 6\ T$ but vanishes over a few periods every $\sim 1\ T$, correlated with the $\sim 1\ T$ scale $\sim 1\ \mu A$ variations of the background supercurrent, as discussed in the next subsection 3.4. We further notice that the oscillations envelope does not decrease a lot between consecutive bumps. Looking closer at the $\sim -4.3\ T$ region, we see an interesting change : the oscillations seem to split and rearrange to give three different periods, see appendix 6.6.5 for more details. Consistent with the analysis at large field scale, the resilience of the oscillations up to high field is associated to very narrow states. Consistent with the eR_NI_c analysis, the observed symmetric triangular oscillations are expected in the case of two similar long ballistic supercurrent-carrying channels, with sawtooth current-phase relations. The $\sim 416\ G$ period corresponds to one superconducting flux quantum in a $4.97 \times 10^{-2}\ \mu m^2$ area, and a minimum distance of $36\ nm$ between the two interfering supercurrents for $L = 1.4\ \mu m$.

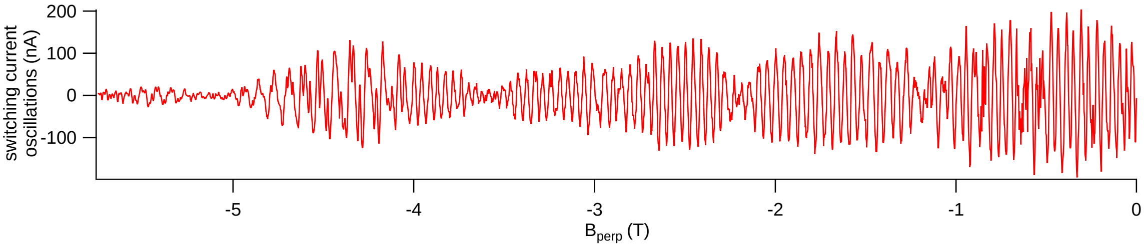

(a)

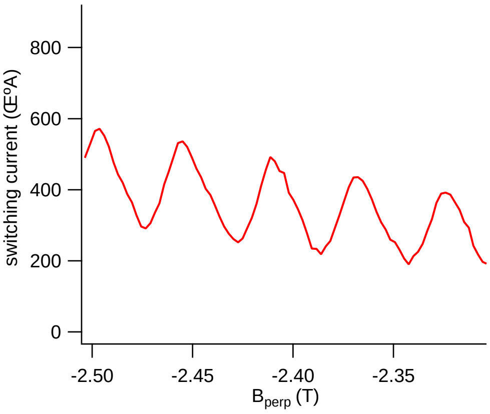

(b)

Figure 3.14 – (a) Average switching current oscillations of sample Bi$_{12}^{wire}$ as a function of vertical magnetic field, where a 300 points smoothed version of the data has been subtracted. The oscillation amplitude vanishes regularly on $\sim 1T$ and is correlated to the background current amplitude. (b) Zoom on the curve displayed in (a). The $\sim 416G$ period corresponds to long ballistic channels separated by $\sim 36\ nm$.

c) Nanowire segment Bi$_{21}^{wire}$

Figs. 3.15a and 3.15b show the average switching current of the nanowire segment Bi$_{21}^{wire}$ as a function of vertical magnetic field on small scales, with smooth background current removed. We see $\sim 400\ nA$ regular triangular oscillations with a short-period of $\sim 25\ G$ (see Fig. 3.15). The oscillations survive up to $\sim 1\ T$, on the same field scale as the background variations, consistent with interfering narrow channels. Again, this type of oscillation pattern corresponds to the case of two symmetric narrow ballistic long channels enclosing a surface of dimensions $1.8 \times 0.46\ \mu m^2$. This is consistent with topological hinge channels running along the junction on opposite sides, as the width of the surface $0.46\ \mu m$ is basically the width of the nanowire seen from the vertical direction.

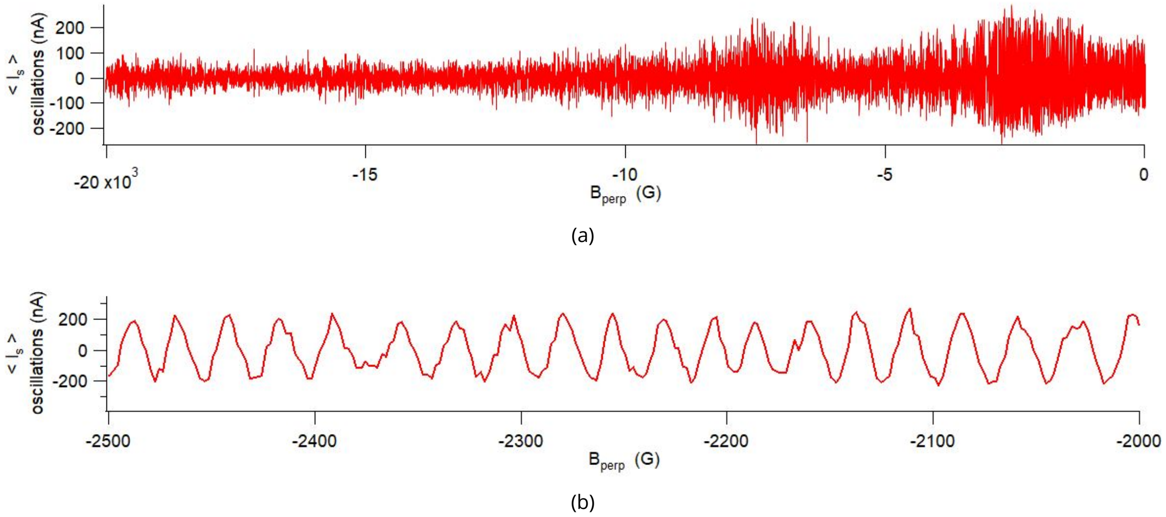

Figure 3.15 – Oscillations of the average switching current of sample Bi$_{21}^{wire}$ as a function of vertical magnetic field. The large-scale background current variations have been subtracted out. (a) Oscillations over a $2\ T$ field range. (b) Oscillations over a $500\ G$ field range. The $\sim\ 25G$ period corresponds to long ballistic channels separated by $\sim 460\,nm$.

The measurement of the oscillation period as a function of magnetic field orientation is discussed in the appendix 6.6.1. For an orientation $\varphi = 320°$ ($14°$ off the plane perpendicular to the wire direction) and $\theta = 45°$ the oscillations have a period of $22\ G$ and an amplitude $\sim 400\ nA$. Together with the oscillation along the vertical axis, it suggests that the two interfering channels define a surface oriented along $\theta_S = 31.2°$ and $\varphi_S = 320°$. However, once again the analysis of the period over other orientations deviate from this hypothesis. The most realistic hypothesis to explain this discrepancy is that the supercurrent responsible for the oscillations involves more than the orbital dephasing between two structures embedded in a single plane.

Fig. 3.16a shows the evolution of the oscillation pattern for temperature between $0.28\ K$ and $0.93\ K$, and for a vertical magnetic field varying from $-720\ G$ to $-695\ G$. We notice a clear change of the skewness of the triangular pattern, with a positive skewness for $T > 0.69\ K$ and a negative skewness for $T < 0.51\ K$. This demonstrates a change of the channels carrying the supercurrent on an energy scale of $k_B T \simeq 50\ \mu eV$. Fig. 3.16b shows the amplitudes of the oscillations and the background supercurrent as a function of T from two other measurements. Between $65\ mK$ and $1.0\ K$, the oscillations' amplitude is reduced by a factor ~ 0.54, whereas the background supercurrent is reduced by a factor ~ 0.9. Such a decrease corresponds to a $eR_N I_c(T=0) \simeq 0.28\ meV$ for the channels conducting the supercurrent responsible for the oscillations, and $eR_N I_c(T=0) \simeq 0.59\ meV$ for the channels carrying the background current.

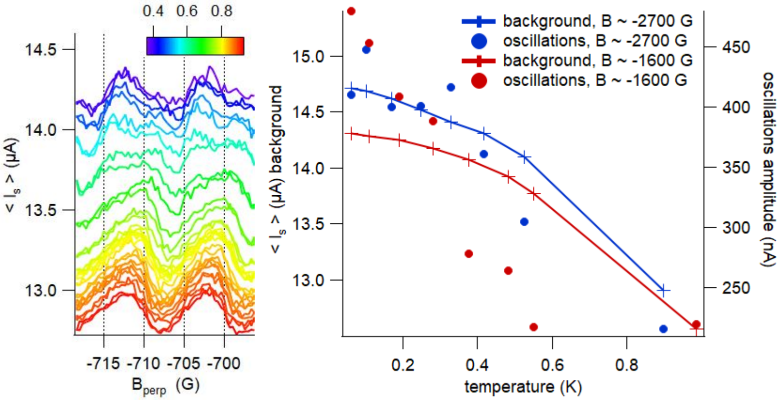

(a) (b)

Figure 3.16 – Variation with temperature of Bi$_{21}^{wire}$ average switching current oscillations amplitude and background value. The magnetic field is oriented along the vertical axis. (a) Continuous recording over two periods while cooling down from $0.93\ K$ to $0.38\ K$ over 90 minutes. It demonstrates a change of the channels carrying the supercurrent on an energy scale of $k_BT \simeq 50\ \mu eV$. (b) Oscillation amplitude (dots, left axis) and background value (lines, right axis) as a function of temperature for two measurements set, one for one period close to $-1700\ G$ and the other one for one period close to $-2700\ G$. It yields $eR_NI_c(T=0) \simeq 0.28\ meV$ for the oscillations, and $eR_NI_c(T=0) \simeq 0.59\ meV$ for the background current.

For this, we used the formula $eR_NI_c(T) = x(1 - 1.3\exp^{-x/(3.2k_BT)})$ with $x = eR_NI_c(T=0)$, see part 3.3.1 of [71]. It translates into :
$eR_NI_c(T=0) = 3.2k_BT\ln(1.3/(1 - I_c(T)/I_c(T=0)))$.

Compared with the previous $eR_NI_c(T=0) \simeq 1.9\ meV$ estimated by differential resistance measurements, the new values are more consistent with a long junction regime. However, the new values are close to the geometric estimation for ballistic channels for the background current and for diffusive channels for the oscillations current, which is the opposite of what we expect. However, $eR_NI_c(T=0) \simeq 0.28\ meV$ yields a Thouless energy $E_T \simeq eR_NI_c/\pi \simeq 89\mu eV$ and a Fermi velocity $v_F = E_TL/\hbar \simeq 2.4 \times 10^5 m.s^{-1}$, which corresponds to a typical value for v_F. This short analysis does not include the effects of imperfect interfaces.

d) Asymmetric DC SQUID Bi$_1^{squid}$

Figs. 3.17a and 3.17b show the low field behavior of the Bi DC SQUID Bi$_1^{squid}$ for various magnetic field direction θ' and φ'. The $\sim 60\ nA$ oscillations of shorter $\sim 7\ G$ period (black solid lines) for vertical field correspond to interference between supercurrent going through separate branches of the SQUID. The oscillations form an asymmetric triangular pattern, consistent with long ballistic channels, and survives up to $B_z > 3000\ G$. In addition, we see $\sim 200nA \sim 70G$ sinusoidal oscillations that develop close to $B_z \simeq -200\ G$ (the hysteresis of the vertical magnetic coil is $\sim 20\ G$). The later correspond to orbital dephasing with a flux in an effective surface of $2.6\mu m \times 114nm$, that is supercurrent interference in a single nanowire. Moreover, we notice on the $\varphi' = 148°\ \theta' = -45°$ an unusual switching current plateau behavior, that extends over a field range that vary with θ'. The asymmetry between positive and negative magnetic fields is discussed in the next subsection.

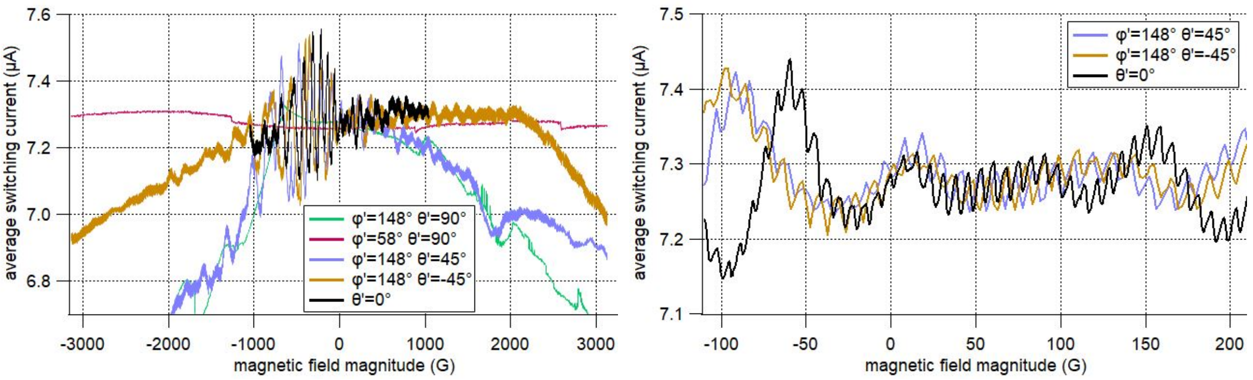

(a) (b)

Figure 3.17 – (a) Low field average switching current of sample Bi$_1^{squid}$ as a function of magnetic field magnitude for various orientations $\varphi'\ \theta'$. (b) Zoom at lower fields. The $\sim 7G$ period corresponds to long ballistic channels located in different branches of the DC SQUID. The $\sim 70G$ period corresponds to long ballistic channels in the same branch, separated by $\sim 114\,nm$.

e) Nanoring Bi^{ring}

Looking at the average switching current versus vertical magnetic field curves of the nanoring Bi^{ring} displayed in Figs.3.18a, 3.18b, and 3.18c, we distinguish patterns with two field scales again. We see $\sim 0.3\ \mu A$ variations on the $\sim 700\ G$ scale, and $100 - 300\ nA$ oscillations with a constant $\sim 17\ G$ period. Fig.6.24a in the appendix displays both the data taken with the field swept up and down, where the down curve is shown in Fig.3.18a. Even though they show the same kind of features, the two curves differ at high fields, but they are reproducible (except for some glitches due to flux trapping in the contacts). Focusing on a smaller range, Fig.3.18c show the switching current for both bias current directions. After reversing the sign of the magnetic field, the two curves coincide, confirming that the system does not break time-reversal symmetry on this scale.

Focusing on the smaller field scale close to 0 field (Fig. 3.18c), we see a very regular $\sim 17\ G$ periodic pattern. The $\sim 17\ G$ period corresponds to a superconducting flux quantum through an area of $\sim 1.2\ \mu m^2$, which is consistent with the area of the ring. We notice three distinct behaviors : a sawtooth shape in the negative field region, a symmetrical rounded shape around 0 field, and a reversed sawtooth shape with higher amplitude in the positive field region. This behavior corresponds to an asymmetric DC SQUID with at least two long ballistic channels, where the role of the strong and weak junctions switches from one channel to the other at 0 field, and the oscillations of the critical current versus flux curve can be interpreted as the CPR of the weaker channel, see part 1.6.1. Scenarios for the variations of the role of the two channels are discussed in the next subsection 3.4.

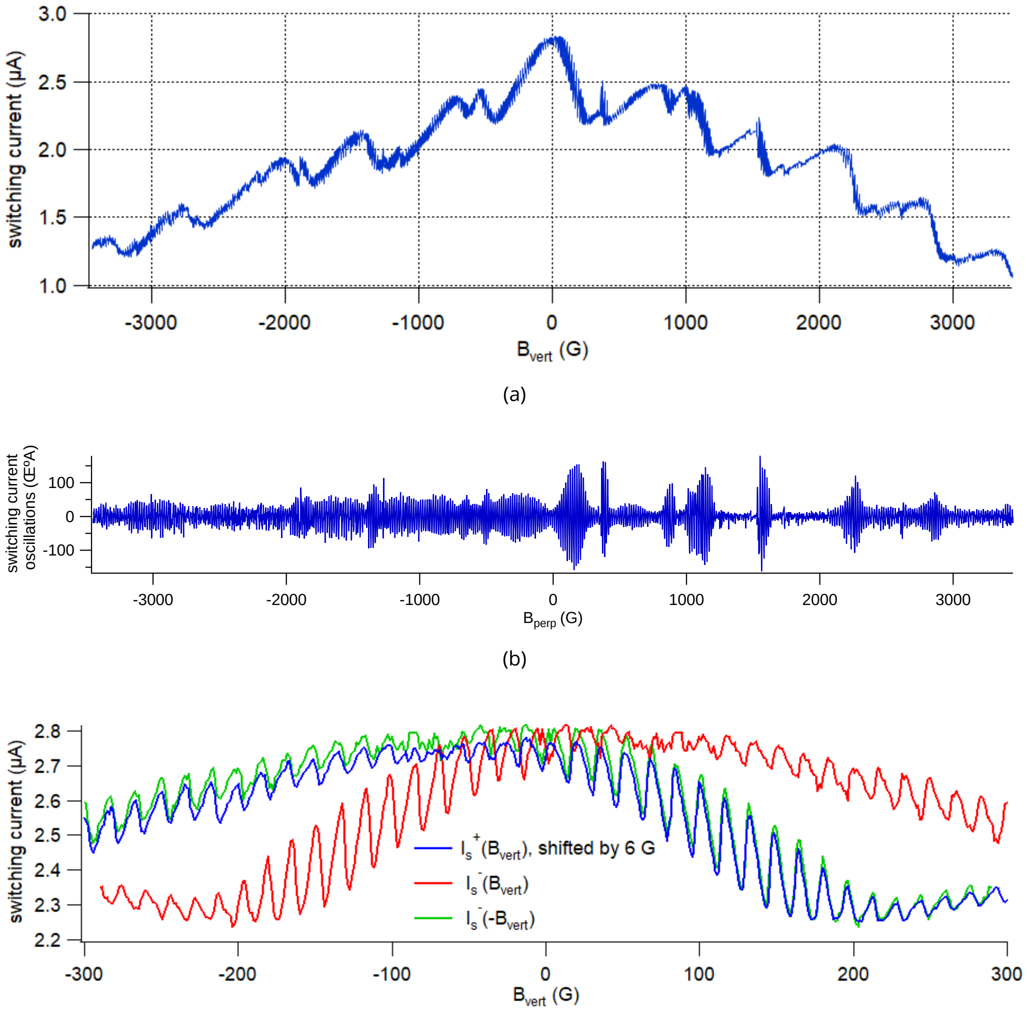

Figure 3.18 – (a) Small scale average switching current of the Bi^{ring} sample as a function of vertical magnetic field perpendicular to the ring plane. (b) Average switching current oscillations as a function of vertical magnetic field, where a 100 points smoothed version of the data has been subtracted. (c) Low-field average switching current, with positive bias current $I_s^+(B_{vert})$ (blue line), with negative bias current $I_s^-(B_{vert})$ (red line), and with reversed field negative bias current $I_s^-(-B_{vert})$ (green line). The $\sim 17G$ period corresponds to long ballistic channels located in different branches of the nanoring.

In this subsection, the variations of the switching currents over small vertical magnetic fields revealed regular oscillations typical of interference between long ballistic channels with sawtooth CPR in four of the presented samples (Bi$_{12}^{wire}$, Bi$_{21}^{wire}$, Bi^{ring}, Bi$_{1}^{squid}$), and interference between narrow channels of intermediate length in nanowire segment Bi$_{11}^{wire}$. The oscillations amplitude survives up to fields of $\sim 1T$, just like the background supercurrent, indicating that both the interfering channels are narrow. This behavior is one of the signatures of transport through 1d topological helical hinges expected in HOTI. Zooming on a smaller field scale revealed the existence of an intermediate field scale, with intricate switching current patterns. The intermediate field scale behaviors are discussed in the next subsection.

3.4 . Intermediate magnetic field scale behavior : other phase shifts

In this subsection, we present the response of the different samples for intermediate field scales, between the decrease of switching current on a $\sim 1T$ scale and the regular triangular oscillations on the $\sim 10-100G$ scale. On this scale, the $I_s(B_z)$ pattern is less regular and can be attributed to :

- interference between channels separated by a small distance $d \sim 10nm$, such that orbital dephasing scale is $B = \Phi_0/(dL) \sim 0.1T$, taking $L = 2\mu m$ (see part 1.6 for the theory)
- Zeeman-induced dephasing between spin-polarized channels with different Zeeman energies (different spin components or different g_{eff}), such that $\Delta g_{eff}\mu_B B/2 \sim E_T^b \iff B \sim 1T$, with $E_T^b \sim 0.2meV$ and $g_{eff} \sim 7$ (see part 1.8.2 for the theory)
- sample asymmetries in the channels' critical currents or in the CPR (see part 1.6 for the theory)

This is also the field scale that display the most important Josephson diode effect, with asymmetry $I_s(B) \neq I_s(-B)$. Moreover, all samples show a maximum of $I_s(B)$ shifted away from $B = 0$, except sample Bi^{ring}. We give an estimate of the inductance L' or the effective magnetic field $B_{eff} = \beta_S I$ needed to obtain such a shift.

We first discuss the cases of the $\sim 1T$ variations of sample Bi^{ring} and the $\sim 3300G$ oscillations of sample Bi$_{11}^{wire}$, before proposing several hypotheses for more complex common features for the periodic amplitude modulation of the oscillations of samples Bi^{ring} and Bi$_{12}^{wire}$. We discuss the Josephson diode effect found in every sample in the next subsection 3.5.

a) $\sim 1T$ variations of sample Bi^{ring}

For the nanoring Bi^{ring}, Fig. 3.12 shows regular $\sim 0.5\ \mu A$ dips at the $\sim 1\ T$ scale. The $\sim 1\ T$ dips are most likely due to a Zeeman-induced dephasing, as reported in earlier work in Bi [40] and in WTe$_2$ [150].

$1\ T$ corresponds to a Zeeman-induced dephasing between spin-polarized channels with a difference of Zeeman energy corresponding to $g_{eff} \simeq 7$, which is very reasonable for a Bi crystal. Alternatively, a $1T$ oscillation period corresponds to orbital dephasing between two channels separated by $d \simeq 1nm$.

b) $\sim 3300G$ oscillations of sample Bi$_{11}^{wire}$

In Fig. 3.13b, the small period oscillations of sample Bi$_{11}^{wire}$ are plotted, where the smooth background has been removed. We notice that it looks like a sum of a SQUID pattern ($|\cos(\varphi)|$) of period $\Delta B_1 \sim 710\ G$ and a damped sinusoid of period $\Delta B_2 \sim 3300\ G$.

It is not clear what causes the $\sim 3300\ G$ periodic sub-pattern. Its clear periodicity tends to favor an interpretation in terms of orbital dephasing, and would involve a third channel carrying a maximum supercurrent of $\sim 100\ nA$. But its amplitude is close to the one of the SQUID pattern and its phase dependence would change the observed SQUID pattern on the $\sim 710\ G$ scale, forming a triple branch DC SQUID. We see no influence of the modulations on the ΔB_2 scale on the modulations on the ΔB_1, and conversely.

The only way to obtain this pattern with orbital dephasing is to consider an inductance L_3 that "screens" most of the phase variations. Such an inductance in series with the branch responsible for the background current should verify $L_3 i_{c3} \gg \Phi_0 \iff L_3 \gg 21nH$, with $i_{c3} \simeq 100nA$ corresponding to the background current (total current minus currents responsible for the $\sim 710\ G$ SQUID pattern). Such $L_3 \gg 21nH$ is high and would require additional junctions of critical currents $\sim 100nA$ in the contact regions. But such a high L_3 is incompatible with this third junction with $i_{c3} \simeq 100nA$ that would modulate by $\sim 50\%$ on a $\sim 3300\ G$ period, as it should reduce drastically the modulation amplitude. Thus, the orbital dephasing scenario is unrealistic.

A $\sim 3300\ G$ period corresponds to a minimum loop surface of $\sim 6.27 \times 10^{-3}\ \mu m^2$, i.e. a surface width of $\sim 6\ nm$ for an effective surface length $L = 1\ \mu m$. More realistically, this could correspond to a Zeeman-induced dephasing with $g_{eff} \simeq 30$, which is in the range expected in Bi.

c) Periodic amplitude modulation of the oscillations of samples Bi^{ring} and Bi$^{wire}_{12}$

The nanoring Bi^{ring} and the nanowire segment Bi$^{wire}_{12}$ show very similar intermediate field behavior, on a scale of $\sim 700G$ for Bi^{ring} (see Figs.3.18a and 3.18b) and $\sim 1T$ for Bi$^{wire}_{12}$ (see Fig.3.14a). They exhibit variations of the amplitude of the short-scale oscillations, where the amplitude vanishes regularly over a few periods. Moreover, the period of this amplitude modulation is correlated with the background current, with a low amplitude associated to the peaks and dips of the background current. Additionally, the skewness of the short-scale oscillation pattern of Bi^{ring} changes between two amplitude extinctions. To this day, we don't have a fully satisfying explanation for this behavior. In the following, we present two candidates that could partly explain it.

The first hypothesis relies on a dense array of individual 1d ballistic channels, as discussed in part 1.9.1. For "clean" arrays with similar ballistic channels, it generates a Fraunhofer-like beating pattern on a scale $B.S = \Phi_0$ in the surface of the array. In some situations, it also exhibits skewness reversal.

For nanowire Bi$^{wire}_{12}$, the $\sim 1\ T$ scales corresponds to a surface width $d \simeq \Phi_0/\Delta BL \simeq 1.5\ nm$. Together with its oscillation period, it corresponds to two main supercurrent-carrying structures, a clean array of 1d ballistic channels of width $\sim 1.5\ nm$ and another channel or similar structure $36 - 100\ nm$ away. For nanoring Bi^{ring}, the $\sim 700\ G$ modulation period corresponds to a surface width $d \simeq 18\ nm$ for the $1.6\ \mu m$ long branch, and $d \simeq 12\ nm$ for the $2.5\ \mu m$ long branch. It means that the array is in one of the two branches and another channel or similar structure in the other branch. We recall that only the dependence on vertical magnetic field was explored for these two samples, implying that the true surfaces may be greater than the estimated ones. Moreover, the estimated width is only an approximation (corresponding to a symmetric DC SQUID) and can differ by a factor ~ 5 compared to the realistic models fitting the experiments. This hypothesis introduces other problems, and does not explain the correlation with the background current variations.

The other hypothesis relies on Zeeman-induced dephasing. For nanowire Bi$^{wire}_{12}$, this would correspond to Zeeman dephasing between two channels with $g_{eff} \simeq 10$, which is reasonable for bismuth crystals. But as seen in parts 1.8.1 and 1.8.2, the envelope of a beating between two similar sawtooth CPR doesn't modulate by 100%, whereas it is the case in the experiment. Similar to the response of a dense array of ballistic channels with orbital dephasing, 100% modulation with Zeeman-induced dephasing would involve many channels.

The Zeeman dephasing hypothesis brings more concurring behavior for nanoring Bi^{ring}. As shown in Fig. 1.25a, a Zeeman interaction changes the shape of the CPR of a short ballistic junction. This depends on the Zeeman energy term h in the CPR formula (1.29). Fig. 3.19 displays the results of a calculation of the critical current of a DC SQUID model with two ballistic short channels of constant $i_{c1} = 0.1\ \mu A$ and $i_{c2} = 2.5\ \mu A$, but varying Zeeman energy terms $h_1/\Delta_0 = -39.2B$ and $h_2/\Delta_0 = +7B$ (B in T). Taking $\Delta_0 = 1meV$, we can write $h_1 = -g_{eff}\mu_B \times 1/2 \times B$, giving an effective gyromagnetic factor of $g_{eff} = 1625$ which is one order of magnitude larger than the maximum g_{eff} we expect for a bismuth crystal. On this field range, this hypothesis explains both the background variations and the change of skewness of the oscillation pattern in Bi^{ring}.

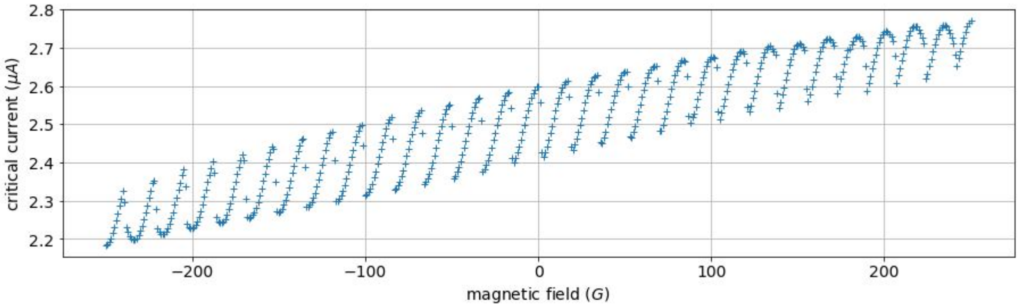

Figure 3.19 – Critical current as a function of magnetic field, for two ballistic short channels of constant $i_{c1} = 0.1\,\mu A$ and $i_{c2} = 2.5\ \mu A$, but varying Zeeman energy terms $h_1/\Delta_0 = -39.2B$ and $h_2/\Delta_0 = +7B$ (B in T). It reproduces the oscillation period and change of skewness as well as the variations of the background current, but fails in other aspects.

In addition to the very high g_{eff}, this later hypothesis also comes with its own problems. Two of which are the absence of visible curvature in the experimental CPR away from $B = 0$ and the inconsistency with the junction length to conclude to a short junction behavior rather than a long junction one. Another problem is the limit range of field for the formula (1.29) to be valid. Indeed, it is only valid for $|h_1/\Delta_0| < 1$, but the data would fit very well the Zeeman hypothesis if the junction behaved periodically in h_1/Δ_0 instead. Other hypotheses involving channel's critical currents or inductances varying with magnetic field are discussed in appendix 6.4.

3.5 . Josephson diode effect due to inductance ? Magneto-Chiral Anisotropy ?

The switching current as a function of magnetic field $I_s(B)$ of all samples studied in this chapter are asymmetric with respect to a change of the sign of B, keeping the same current bias direction $+I$, that is : $I_s^+(B) \neq I_s^+(-B)$. By time-reversal symmetry, it means that they also exhibit Josephson Diode Effect (JDE), that is an asymmetry with respect to a change of the sign of I, keeping the same B : $I_s^+(B) \neq I_s^-(B)$.

All samples show JDE and all samples, except Bi^{ring}, show a shift of their maximum switching current away from $B = 0$. JDE zero-field shifts can be related to the interesting spin-orbit-induced Magneto-Chiral Anisotropy (MCA) predicted in material with SOC. However, MCA is not the only phenomenon that can cause JDE, as discussed in part 1.7.

In this part, we evaluate various scenario for each sample. We associate the shift of the maximum switching current to three different scenarios :

- Scenario 1 (inductance) : the supercurrent I through a channel in series with an inductance L' causes an effective flux $\Phi_L = L'.I$ that dephases its interference with other channels by $\delta\phi = 2\pi\Phi_L/\Phi_0$, just like a

magnetic field $B_L = \Phi_L/S$ would. S is the surface defined by the interfering channels.
- Scenario 2 (MCA) : the current and the magnetic field are related by the spins via spin-orbit and Zeeman interactions. A supercurrent I through the junction has the same effect as a magnetic field $B_{eff} = \beta_S I$, with β_S that depends on the systems, e.g. its spin-orbit energy and its g_{eff}.
- Scenario 3 (asymmetric CPR) : like Scenario 1, but with a dephasing due to CPR that are maximum at different phases, for example a channel with sinusoidal CPR interfering with a channel with sawtooth CPR, producing a shift of $\pi/2$ at zero field. This mechanism can produce a shift between 0 and $\pi/2$, and is independent of the value of the supercurrent.

a) Sample Bi$_{11}^{wire}$

The critical current of sample Bi$_{11}^{wire}$ at zero magnetic field is not the highest one over all the magnetic field range, see Fig.3.13a. Over the lowest magnetic field period, the maximum is $I_s(B = 23G) \simeq 410\ nA$. The global maximum is $I_s(B^+) = 532\ nA$ at $B^+ = 1471\ G$, with a maximum $I_s(B^-) = 473\ nA$ at $B^- = -2207\ G$ in the negative field region, thereby exhibiting JDE.

To understand this shift, let us evaluate the scenario 1 with inductance. The shift of $B^+ = 1471\ G$ corresponds to a flux $\Phi_L \simeq \frac{1471}{3300}\Phi_0 \simeq 0.45\Phi_0$ in the surface defined by the interfering channels, as discussed in the previous subsection 3.4. It gives a $L' = \Phi_L/I_s^{max} \simeq 1.7nH$. This inductance is high compared to the typical values of self-field inductances ($< 1pH$) and kinetic inductance of the W contacts ($\sim 17pH.\mu m^{-1}$), see appendix 6.2. It would require a weak junction in the loop, with a critical current $\sim 1\mu A$.

Considering scenario 2 with MCA, the switching current at $B = 0$ corresponds approximately to the switching current $I_s(B^+) = 532\,nA$ with an extra effective magnetic field $B_{eff} = -B^+$. Assuming this B_{eff} is proportional to the current, we write $B_{eff} = \beta_S I$ with $\beta_S = \frac{B^+}{I_s(0)} \simeq 3.6\times10^3 G.\mu A^{-1} = 3.6\times10^5 T.A^{-1}$. This value of β_S is higher by a factor ~ 36 compared to the typical value of β_S we found during my PhD, see next samples and appendix 6.9 (in the resistive state) and 6.12 (in both resistive and superconducting states).

Alternatively in scenario 3, the $\sim 3300G$ modulation is due to a sinusoidal junction, with a maximum shifted by π due to a junction in parallel with a CPR not maximum at a phase $\pi/2$. This explanation is not very satisfying either, as we argued that the maximum possible phase-shift with asymmetric CPR is $\pi/2$.

b) Sample Bi$_{12}^{wire}$

Fig.3.20 displays the average switching current versus magnetic field pattern of sample Bi$_{12}^{wire}$, where the negative field response is reversed in field ($I_s^+(-B_z)$), such that it corresponds to switching current with opposite current bias direction ($I_s^-(B_z)$). It shows a clear asymmetry between positive and negative current bias. Focusing on the low field region, we see again that the overall maximum switching current is not at $0\ G$. On the contrary, we see a clear dip "centered" around $0\ G$, with $I_s(0) = 5.44\ \mu A$, and a higher switching current reached at higher field for both positive and negative current bias. The global maximum is $I_s(B^+) = 6.68\ \mu A$ at $B^+ = 0.64\ T$ in the positive field region (or positive bias current), and $I_s(B^-) = 5.95\ \mu A$ at $B^- = -1.7\ T$ is the maximum in the negative field region (or $B^- = 1.7\ T$ for negative bias current).

To understand this shift, let us evaluate the various scenario. Scenario 1 involves an inductance L' such that $\Phi_L \simeq L'.I_s^{max} \simeq \frac{0.64}{1}\Phi_0$, yielding $L' \simeq 0.2nH$. This value of inductance can be caused by a weaker junction of critical current $\sim 10\mu A$ in the contact region. Scenario 2 involves an effective current-induced magnetic field of $\frac{B_{eff}}{I} = \frac{0.64}{5.44\times10^{-6}} = 1.2\times10^5 T.A^{-1} = 1.2\times10^3 G.\mu A^{-1}$, which is higher by a factor 12 compared to the typical value found in other nanowires. Scenario 3 involves a shift by π, which can't be

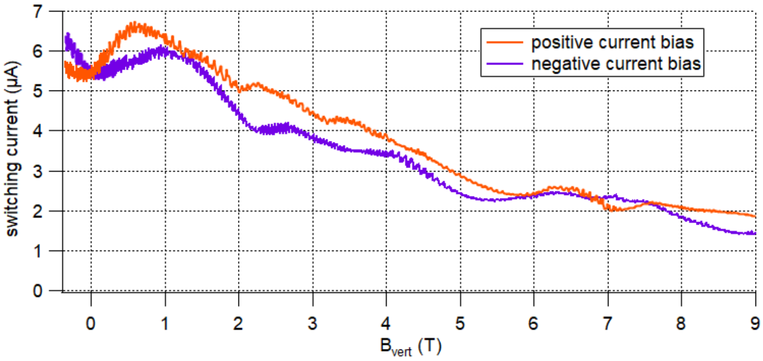

Figure 3.20 – Average switching current of nanowire Bi$_{12}^{wire}$ as a function of vertical magnetic field perpendicular to the wire, for positive (orange solid line) and negative (purple solid line) current bias. It shows clear Josephson diode effect, persisting to high fields.

achieved. Together with the analysis of sample Bi$_{11}^{wire}$, segment of the same nanowire, we conclude that the shift of the maximum switching current is caused by kinetic inductance from (very) weak junctions in the contact region or by high spin-orbit induced MCA.

c) Sample Bi$_{21}^{wire}$

For nanowire Bi$_{21}^{wire}$ (see Fig.3.8b), the shift of the whole pattern (see for example the maximum peak) in magnetic field depends on the field orientation, and scales exactly the same way has the effective flux $\vec{B}.\vec{S}$ for magnetic fields in the horizontal plane. The effective flux is maximum for $\vec{B} \parallel \vec{S}$, when $\vec{B}$ is oriented in the horizontal plane, perpendicular to the nanowire axis ($\theta \simeq 90°$, $\varphi \simeq 315°$). For this field orientation, the pattern is shifted by a field of $\sim -517\ G$ which can be only partially explained by the $\sim 200\ G$ hysteretic behavior of the horizontal coil, see Fig.6.22 in the appendix for up and down curves.

This shift can be explained by the presence of an inductance L', generating a constant screening flux $\Phi_L = L'.I_s^{max}$ that is more or less difficult to compensate depending on the magnetic field orientation. Φ_L is also equivalent to the magnetic flux of a field of $\sim -517\ G$ in the surface $S = 1.8\mu m \times 20.7nm$ defined by the interfering channels (see discussion of the response of Bi$_{21}^{wire}$ at high field, part 3.2). Thus, $L' = \Phi/I_s^{max} = 517 \times 10^{-4} \times 1.8 \times 10^{-6} \times 20.7 \times 10^{-9}/(12.84 \times 10^{-6}) = 150\ pH = 7.24 \times 10^{-2}\ \Phi_0/\mu A$. Once again, this value of inductance can be caused by a weaker junction of critical current $\sim 10\mu A$ in the contact region. For a field of $-517G$ in this direction perpendicular to the surface, $I_s^+(B) = 16.8\mu A$ and $I_s^-(B) = I_s^+(-B) = 9.78\mu A$, giving a very large JDE of $2\Delta I_s/(I_s^+ + I_s^-) = 53\%$.

Moreover, the switching current variations as a function of vertical field shows a dip close to $B_z \simeq 0$, see Fig.3.8a. The switching current increases with $|B_z|$, with asymmetric values between positive and negative fields, similar to the nanowire Bi$_{12}^{wire}$. As a function of vertical magnetic field, the global maximum value is $I_s^{max,z} = I_s(B_z^+) = 15.7\mu A$ for $B_z^+ = 0.18T$.

To evaluate an inductance L'' that could cause such a shift of the maximum, one needs to define a surface S', such that $\Phi_L = L''.I_s(B_z^+) = B_z^+.S'$. Looking at modulations of $I_s(B_z)$, one can guess a $\sim 0.6T$ period, that could correspond to orbital dephasing by the magnetic field in a surface $S' = \Phi_0/0.6 = 3.45 \times 10^{-3} \mu m^2$. This gives $L'' = \frac{\Phi_L}{I_s^{max,z}} = \frac{0.18S'}{15.7 \times 10^{-6}} = 40pH$, which is lower than the inductance found by looking at horizontal magnetic field response, that could be caused by similar elements.

Alternatively, scenario 2 for the shift of the $I_s(B_z)$ pattern involve a $B_{eff} = \beta_S I$ with $\beta_S \simeq \frac{B_z^+}{I_s(B_z=0)} \simeq \frac{0.18}{14.8 \times 10^{-6}} \simeq 1.2 \times 10^4 T.A^{-1} \simeq 1.2 \times 10^2 G.\mu A^{-1}$. This value is the typical value found in the other samples (except for Bi$_{11}^{wire}$ and Bi$_{12}^{wire}$, segments of the same nanowire). Again, scenario 3 seems unrealistic as it would require a shift $\simeq \pi$ which can't be achieved with asymmetric CPR.

d) Sample Bi$_1^{squid}$

The Bi DC SQUID Bi$_1^{squid}$ shows switching current asymmetries between positive and negative magnetic field, both on high and low field scales, as clearly visible in Figs.3.11b and 3.17, respectively. At low fields, we see that the global maximum switching current is close to $B_z^- = -208G \neq 0$ (much larger than the hysteresis intrinsic to the magnetic coil) and reaches $I_s(B_z^-) = 7.55\mu A$.

Again, let us evaluate the scenario 1 with inductance. The shift of $B_z^- = -208G$ corresponds to three periods of the $\sim 70G$ oscillations, that is a flux $\Phi_L \simeq 3\Phi_0$ in the surface defined by the interfering channels, as discussed in the previous subsection 3.3. It gives a $L' = \Phi_L / I_s^{max} \simeq 0.3nH$. Again, it would require a weak junction in the loop, with a critical current $\sim 10\mu A$.

Alternatively, scenario 2 for the shift of the $I_s(B_z)$ pattern involve a $B_{eff} = \beta_S I$ with $\beta_S \simeq \frac{B_z^-}{I_s(B_z=0)} \simeq \frac{0.02}{7.3\times10^{-6}} \simeq 2.8 \times 10^3 T.A^{-1} \simeq 28G.\mu A^{-1}$. This value is the typical value found in the other samples (except for Bi$_{11}^{wire}$ and Bi$_{12}^{wire}$, segments of the same nanowire).

Because the junction explicitly breaks inversion symmetry, scenario 3 with asymmetric CPR seems more reasonable. However, if we interpret the dephasing in terms of interfering channels enclosing a surface $S = \frac{\Phi_0}{70\times10^{-4}} = 0.295\mu m^2$ like above, it would require a dephasing of 6π, which again can't be achieved with asymmetric CPR. We note that the values of shift we considered here would have been different if we had chosen another oscillation period, e.g. one on a larger scale.

e) Sample Bi^{ring}

In contrast with the other samples, Bi^{ring} switching current at zero magnetic field is the overall maximum switching current, see Fig.3.18a. But it is still asymmetric with respect to a change of sign of the magnetic field, and all the bumps at the $\sim 700\ G$ scale are skewed in the same direction. Focusing on the zero field lobe, we can symmetrize it by considering a supercurrent-induced screening field of $\alpha = 150\ G.\mu A^{-1}$, that is an inductance of $L = 430\ pH = 0.21\ \Phi_0/\mu A$. However, such an inductance should shift the field value of the maximum switching current by $\simeq 150 \times 2.8 = 420G$. That is not the case here, suggesting that this asymmetry is due to asymmetric current amplitudes.

3.6 . Conclusion

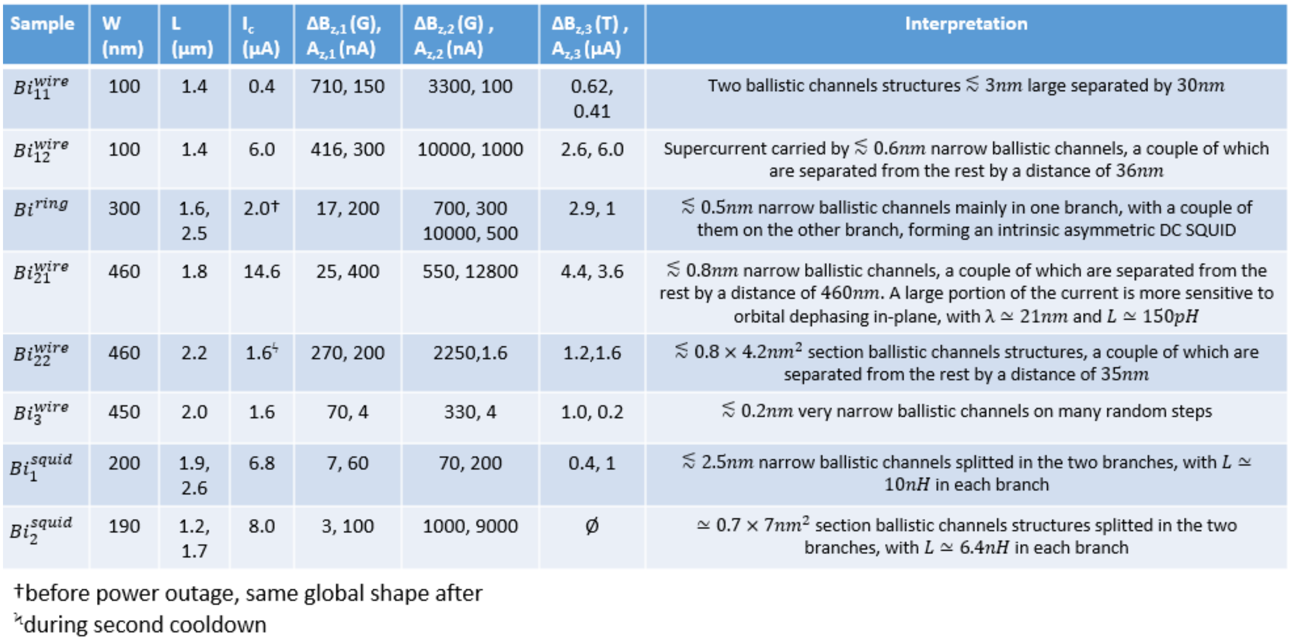

Sample	W (nm)	L (µm)	I_c (µA)	$\Delta B_{z,1}$ (G), $A_{z,1}$ (nA)	$\Delta B_{z,2}$ (G) , $A_{z,2}$ (nA)	$\Delta B_{z,3}$ (T) , $A_{z,3}$ (µA)	Interpretation
Bi_{11}^{wire}	100	1.4	0.4	710, 150	3300, 100	0.62, 0.41	Two ballistic channels structures $\lesssim 3nm$ large separated by $30nm$
Bi_{12}^{wire}	100	1.4	6.0	416, 300	10000, 1000	2.6, 6.0	Supercurrent carried by $\lesssim 0.6nm$ narrow ballistic channels, a couple of which are separated from the rest by a distance of $36nm$
Bi^{ring}	300	1.6, 2.5	2.0†	17, 200	700, 300 10000, 500	2.9, 1	$\lesssim 0.5nm$ narrow ballistic channels mainly in one branch, with a couple of them on the other branch, forming an intrinsic asymmetric DC SQUID
Bi_{21}^{wire}	460	1.8	14.6	25, 400	550, 12800	4.4, 3.6	$\lesssim 0.8nm$ narrow ballistic channels, a couple of which are separated from the rest by a distance of $460nm$. A large portion of the current is more sensitive to orbital dephasing in-plane, with $\lambda \simeq 21nm$ and $L \simeq 150pH$
Bi_{22}^{wire}	460	2.2	1.6↯	270, 200	2250,1.6	1.2,1.6	$\lesssim 0.8 \times 4.2nm^2$ section ballistic channels structures, a couple of which are separated from the rest by a distance of $35nm$
Bi_{3}^{wire}	450	2.0	1.6	70, 4	330, 4	1.0, 0.2	$\lesssim 0.2nm$ very narrow ballistic channels on many random steps
Bi_{1}^{squid}	200	1.9, 2.6	6.8	7, 60	70, 200	0.4, 1	$\lesssim 2.5nm$ narrow ballistic channels splitted in the two branches, with $L \simeq 10nH$ in each branch
Bi_{2}^{squid}	190	1.2, 1.7	8.0	3, 100	1000, 9000	∅	$\simeq 0.7 \times 7nm^2$ section ballistic channels structures splitted in the two branches, with $L \simeq 6.4nH$ in each branch

†before power outage, same global shape after

↯during second cooldown

Figure 3.21 – Geometry and characteristic magnetic field scales variations of the average switching current of a selection of samples that have been measured. We generally find three typical field scales, noted as $\Delta B_{z,1}$, $\Delta B_{z,2}$, $\Delta B_{z,3}$, with associated switching current variations noted $A_{z,1}$, $A_{z,2}$, $A_{z,3}$. $\Delta B_{z,1}$ corresponds to small field scale, with regular triangular oscillations of the switching current indicating interference between long ballistic channels. $\Delta B_{z,3}$ corresponds to large field scale, with a monotonous decrease of the background current associated to supercurrent carried mainly by narrow (1d ballistic) channels. $\Delta B_{z,2}$ corresponds to intermediate field scale, where orbital dephasing between nearby channels and Zeeman-induced dephasing induce more complex patterns.

The analysis of the average switching current of eight Josephson junction samples based on bismuth nanowires as a function of magnetic field magnitude and direction revealed interesting common behaviors on three field scales. The field scales and the interpretation of the supercurrent transport specific to each sample is summarized in Tab3.21. On the Bi$_{12}^{wire}$-Bi^{ring}-Bi$_{21}^{wire}$-Bi$_{22}^{wire}$-Bi$_{1}^{squid}$ samples, we measured skewed triangular oscillations that correspond to interferences between long ballistic channels dephased by an orbital flux in the nanowire or in the DC SQUID, as expected for topologically protected hinge channels. On the Bi$_{11}^{wire}$-Bi$_{12}^{wire}$-Bi$_{21}^{wire}$-Bi$_{22}^{wire}$-Bi^{ring} samples, we measured a $|B|^{-1}$ (or $|B|^{-2}$) decrease at high fields consistent with the presence of narrow (1d ballistic) channels with an exponential transverse current density profile. On the Bi$_{11}^{wire}$-Bi$_{12}^{wire}$-Bi$_{21}^{wire}$-Bi$_{1}^{squid}$, we found clear evidence of dephasing mechanisms at zero magnetic field, that may be caused by inductive elements or induced by SOC. On the Bi$_{12}^{wire}$ and Bi^{ring} samples, we found a correlation between the short-scale oscillation pattern and the larger-scale background current variations. Finally, on the Bi$_{21}^{wire}$ and Bi$_{1}^{squid}$ sample, we found that the average switching current pattern does not scale like a simple scalar product $\vec{B}.\vec{S}$ as a function of field direction. This could be a sign of the influence of the SOC on the supercurrent carried by the surface and hinge channels.

4 - Andreev bound states occupation dynamics as evidence of helical hinge channels in a Bi nanoring Josephson junction

Soon after the discovery of one-dimensional (1D) helical states in two-dimensional TIs (2DTI) [151, 152] or three-dimensional Second Order TIs (SOTI) [153, 154, 155], it was realized that Josephson junctions containing helical modes as their weak link should display remarkable features. Indeed, the spin-momentum locking which characterizes the helical states translates into a fixed helicity for the Andreev states shuttling the supercurrent along each edge, in contrast to the spin degeneracy of conventional Josephson junctions. Among the predicted consequences are 4π [91, 78] and 8π [156, 157] periodicities of the supercurrent-versus-phase relation (CPR) of a Josephson junction formed with a single helical edge state. Originating from fermion-parity protected crossings of Andreev levels at phase difference π, these periodicities are contingent on the absence of fermion-parity-breaking processes. The necessity to beat such relaxation processes motivated the initial search for topological signatures at finite frequencies.

Past measurements have relied on the ac Josephson effect, via Shapiro steps [79] and Josephson emission of voltage-biased junctions [80], or, as suggested in [78], on the high-frequency response of a phase-biased topological junction [4]. Recent theoretical predictions suggest that signatures of topological superconductivity can also be found in switching current experiments conducted at frequencies comparable to the relaxation rate [130, 125, 133, 102]. The idea is that the current at which the junction switches to its resistive state depends on the number and occupation of the current-carrying Andreev states. This implies that detailed information about the Andreev states and relaxation processes can be extracted from phase-dependent statistical distributions of switching currents [126, 125]. The particular sawtooth-like shape of the CPR makes long Josephson junctions with multiple subgap Andreev levels especially well suited for such investigations [99, 133].

In this chapter, we report measurements of the switching current distribution of a micrometer-size, ring-shaped bismuth single-crystal with superconducting contacts, whose general characteristics have been described in chapter 3 already (see Figs.3.4, 3.12 and 3.18). We find that in our device, the Bi ring acts as an intrinsically asymmetric DC SQUID whose average switching current yields the characteristic sawtooth CPR of a long ballistic junction. Using a phenomenological model of two helical Andreev hinge modes, we find that pairs relax at a rate comparable to individual quasiparticles, in striking contrast with non-topological systems. This constitutes a unique telltale sign of the spatial separation of topological helical hinges, corroborating the existence of helical hinge modes in Bi. Our analysis leads to the identification of single-particle and two-particle relaxation times, both of the order of milliseconds, consistent with well-separated topological hinge modes.

The analysis presented in this chapter is the fruit of a collaboration between members of our mesoscopic physics group at Laboratoire de Physique des Solides and theoreticians Dr. Yang Peng, Prof. Yuval Oreg and Prof. Felix von Oppen, authors of the article [125] that we used as a reference to build our model of two helical Andreev hinge modes. Yang Peng calculated the analytical formulas with inputs from Yuval Oreg and Felix von Oppen, and made the MATLAB program that computes the occupation probabilities and the resulting switching current distributions. Together with Yang Peng, we ran the program to analyze the influence of each parameter on the occupation probabilities, and to find the set of parameters that fits best our data. The final model is the result of many inputs and improvements done over our numerous meetings. This work motivated the writing of an article, just published in Nature Physics [5].

In this chapter, I reorganize and develop the work presented in this article [5]. First, we present the experimental data and their peculiar features. Second, we introduce the theoretical model of the asymmetric DC SQUID used to understand the results of our experiments, together with computations showing the influence of the various parameters of the model. This model is a special case of the one presented in part 1.10.4. Then, we describe how to make the connection between the experimental data and the theoretical computations. Lastly, we confront the data to the model, and use it to extract the characteristic transition times.

4.1 . Measurement : full switching current distribution varying with magnetic field and current ramping rate

The average switching current at low fields, shown in Fig.3.18c, displays periodic oscillations superimposed on a slowly varying baseline. The $17G$ period, corresponding to one superconducting flux quantum $\Phi_0 = h/2e$ through an area of $1.2\ \mu m^2$, is consistent with the ring area. The oscillations have a (somewhat rounded) sawtooth shape, reminiscent of switching experiments on asymmetric DC SQUIDs designed to measure the CPR of small Bi nanowire junctions [3]. In [3], the sawtooth modulation corresponded to the CPR of a long ballistic Josephson junction, and thus demonstrated the higher order topological nature of the Bi nanowire [69, 99, 3, 13]. In the present experiment, the sawtooth modulation suggests that the bismuth ring, with its two superconducting contacts, acts *intrinsically* as an asymmetric DC SQUID, yielding a ballistic CPR for the "weak" branch of the ring with the smaller critical current.

Fig. 4.1 presents the average switching current and the standard deviation, up to $4500G$. Oscillations with the $17G$ period corresponding to one flux quantum through the bismuth ring diameter are visible over the entire range. The period also appears in the standard deviation, with a higher value when the superconducting phase difference φ across the weak branch is $\varphi \simeq \pi$. These variations of the standard deviation are still present at 7 T (not shown). In addition to the small $17G$ period, oscillations of the average current (and of the standard deviation magnitude) with a 600 to $1000G$ scale are also clearly visible. We attribute those oscillations to interference effects caused by the magnetic field, see part 3.4.

Rather than the average switching current, this chapter focuses on the switching current distribution, arguably a much more powerful (and underexploited) tool. We show that the distribution reveals the phase-dependence of the ground and excited states of the Andreev spectrum, their occupation probability and spatial separation, and hence their topological character. Two such distributions, recorded in two magnetic field regions, are displayed in Fig.4.3a and 4.3c, with distributions on the full $-500G$ to $500G$ scale on Fig.4.2.

In contrast to the average (red solid lines), the switching current distributions are not rounded as a function of field. In the first magnetic field region, around $B = 450\ G$, a notable feature of the sawtooth jump region are the two well separated peaks in the histogram, see the red circle in Fig.4.3a at $B = 433\ G$, and the green curves in Figs.4.3a and 4.3b. This indicates that the weak junction can be in two different states on the timescale of the current ramp.

In a second field region, see green circle in Fig.4.3c near $B = -187\ G$ and green curves in Figs.4.3c and 4.3d, an additional intermediate, fainter branch develops around the sawtooth jump, so that there are three well separated peaks in the switching histograms.

Figs 4.2 and 4.4 display the switching current distribution at two different current ramp frequencies, 17 and $187Hz$. The main sawtooth-shaped branches are visible over most of the field sweep, with smaller field regions (e.g. around 0 field) where the switching current shape is symmetric. Fainter branches that are shifted with respect to the main branches also are visible in some magnetic field regions (most clearly between -100 and -400 G).

In Fig.4.5, we put side-to-side the switching current distributions obtained close to $B = -170G$ both at

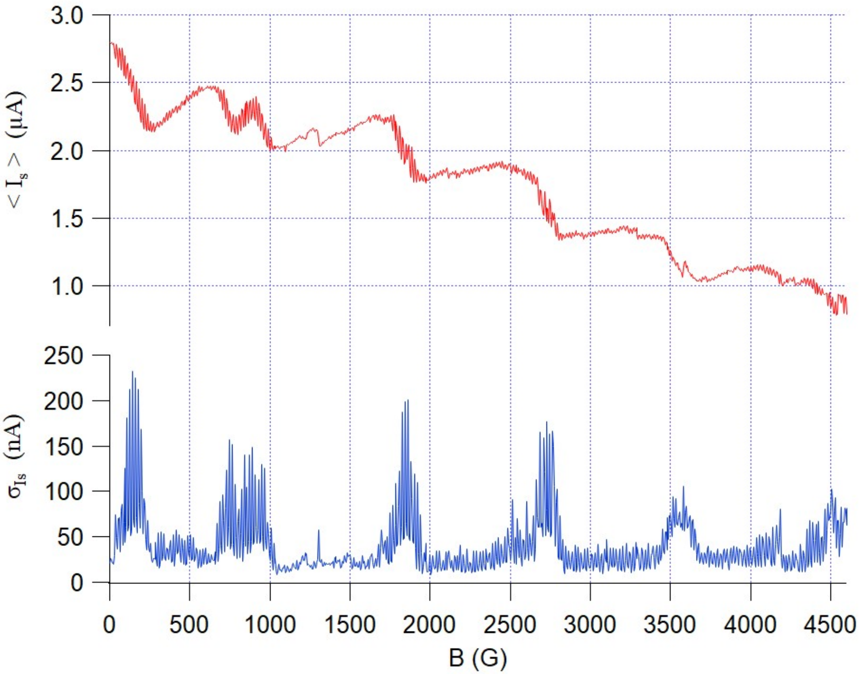

Figure 4.1 – Upper panel : Switching current averaged over 200 switching events as a function of out-of-plane magnetic field, with bias ramp at 17 Hz. Lower panel : corresponding standard deviation of 200 switching events distribution, as a function of out-of-plane magnetic field. The counter can provide the full histogram, or the average and the standard deviation. Both the average and the standard deviation display the $17G$ period.

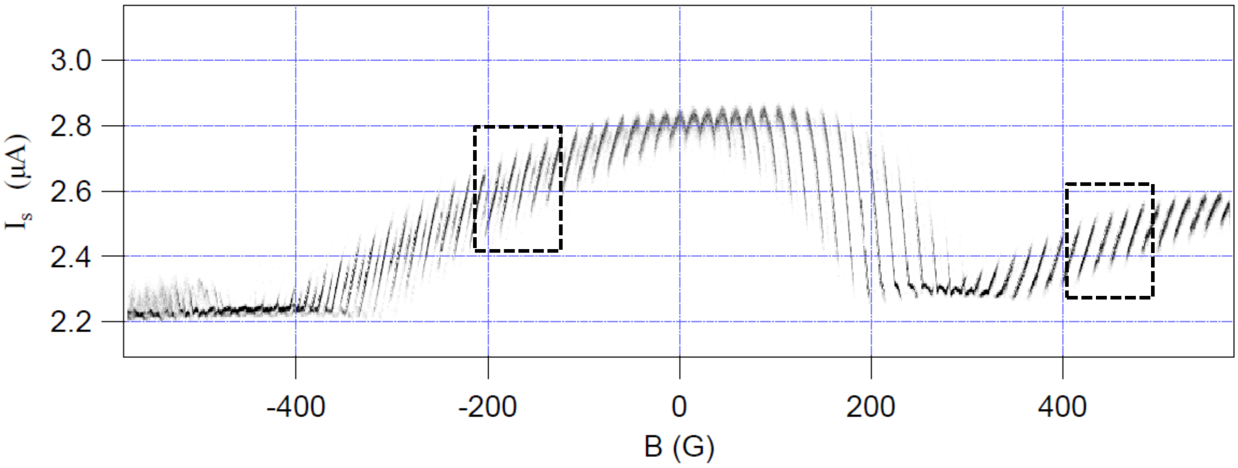

Figure 4.2 – Switching current events as a function of out-of-plane magnetic field, with 200 switching events per histogram and a current ramp of 17 Hz. The number of switching events is coded in shades of grey. The flat horizontal signal, when the switching current is lower than $\sim 2.3\,\mu A$, is due to an experimental limitation.

$17Hz$ and $187Hz$. It clearly shows that the visibility of the intermediate current branch varies significantly on a time scale of $\sim 10ms$, which is long for the dynamics of a Josephson junction. At higher frequency, the intermediate branch extends over a larger range of field.

To properly model the system, one needs to be able to reproduce the various effects identified. Namely, the model needs to account for the presence of an intermediate switching current value close to $\varphi \simeq \pi$, linear in field, in the middle of the two main switching values close to $\varphi \simeq \pi$. It forms an intermediate

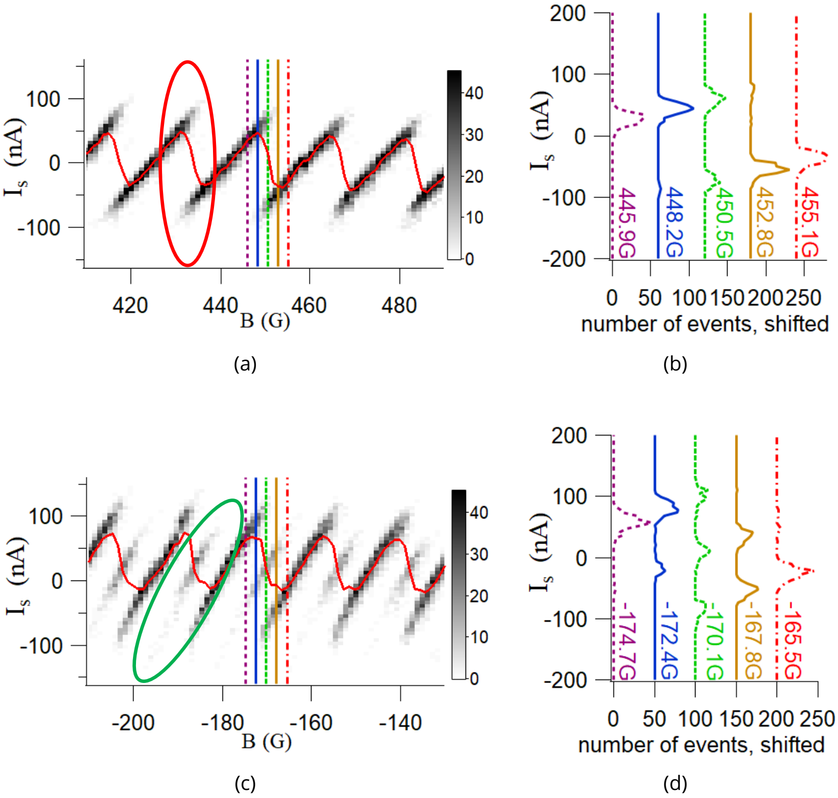

Figure 4.3 – Switching current distributions (histograms) as a function of out-of-plane magnetic field of the bismuth-nanoring based Josephson junction, in the $B \simeq 450G$ (a) and $B \simeq -170G$ (c) regions. The slowly varying current background has been removed by a first order polynomial. The current bias is ramped at a frequency of $17Hz$. The number of events is color-coded in shades of grey. The red solid line is the switching current averaged over the whole distribution at each field. (b) and (d) are histograms at specific values of fields in (a) and (c), respectively, see colors. Curves are shifted for clarity.

branch that extends asymmetrically in field (see Fig.4.5c), and whose visibility depends on the magnetic field (see Figs.4.3a and 4.3c), and increases with increasing current bias ramp frequency (see Figs.4.5a and 4.5c). Moreover, notice that there exist no field value for which the intermediate branch is the only switching current value. It is always accompanied by another switching current value. The combination of these behaviors rules out a lot of potential models.

In the following we argue that each peak in the histogram corresponds to a different occupation of the Andreev spectrum of a Josephson junction made of two helical hinges. Our analysis then yields the relative relaxation rates of the Andreev states, providing information about the topological character of these hinges.

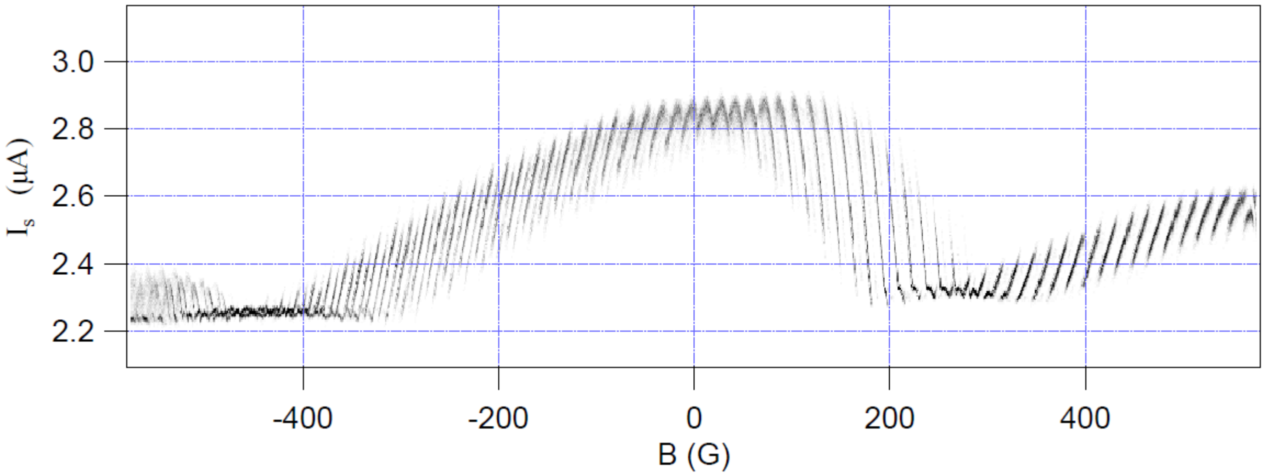

Figure 4.4 – Switching current events as a function of out-of-plane magnetic field, with 200 switching events per magnetic field value and a current ramp at 187 Hz. The number of switching events is coded in shades of grey. The flat horizontal signal, when the switching current is lower than $\sim 2.3\ \mu A$, is due to an experimental limitation.

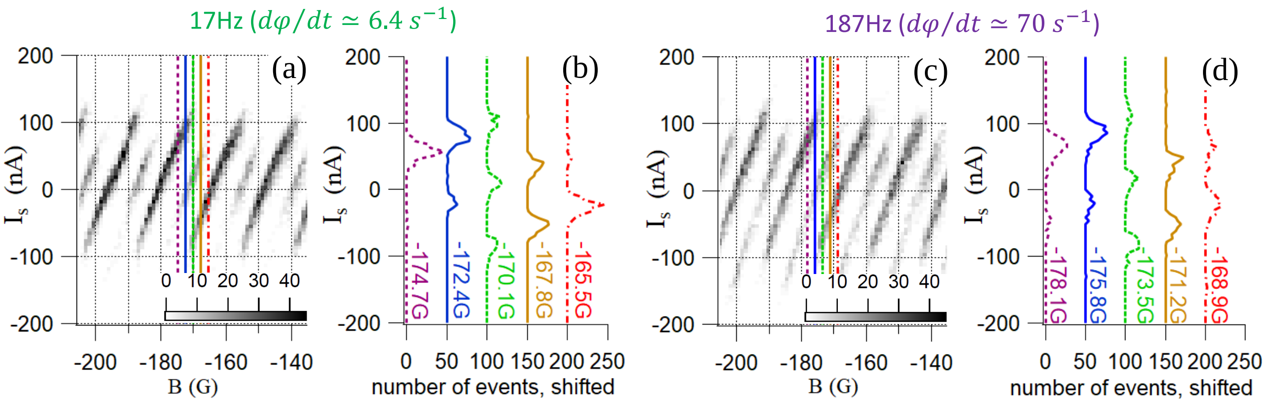

Figure 4.5 – Switching current distributions (histograms) as a function of out-of-plane magnetic field of the bismuth-nanoring based Josephson junction, with $17Hz$ (a) and $187Hz$ (c) current bias ramp frequencies. The slowly varying current background has been removed by a first order polynomial. The number of events is color-coded in shades of grey. (b) and (d) are histograms at specific values of fields in (a) and (c), respectively, see colors. Curves are shifted for clarity.

4.2 . Model : two 1d helical Andreev states embedded in an asymmetric DC SQUID

4.2.1 . Introduction of the model

The analysis is based on a model of the Bi ring connected to two superconducting contacts, as a SOTI-based asymmetric SQUID. In the model, the weak Josephson junction consists of two helical supercurrent-carrying hinges located in one branch of the ring, and the strong junction, with higher critical current, is formed by the other branch (see Fig.4.6). To leading order, the current bias ramp $\mathcal{I}(t)$ controls the phase difference $\gamma(t)$ across the strong junction : as $\mathcal{I}$ increases from zero to values close to the strong junction's critical current $I_{c,\text{strong}}$, γ increases from zero to $\gamma_{\max}$. Due to the flux threading the SQUID Φ (in units of $\hbar/(2e)$), the phase difference across the weak junction is $\phi(t) = \Phi + \gamma(t)$. The additional current through the weak junction with CPR $i(\phi)$ modulates the critical current at which the SQUID switches to a resistive state : $I_c \simeq I_{c,\text{strong}} + i(\Phi + \gamma_{\max})$. The SQUID's switching current thus provides a direct measurement of the current-phase relation (CPR) of the weak junction [126, 125, 158].

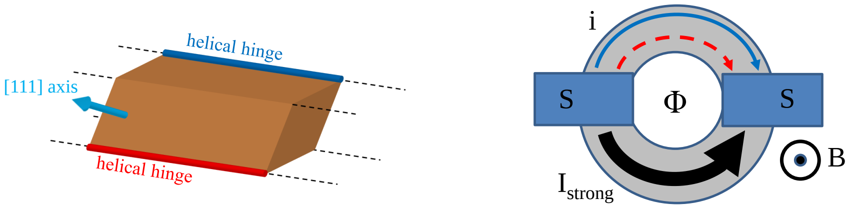

(a) (b)

Figure 4.6 – (a) Sketch of an idealized segment of the ring with a radial [111] axis (light blue arrow) and two helical hinge channels of opposite helicities (red and blue lines). (b) Simplified sketch of the bismuth nanoring connected to two superconducting contacts (S), constituting an intrinsic Superconducting Quantum Interference Device (SQUID). In the model (see text), the total supercurrent is carried by two helical channels (solid blue and dashed red), with a supercurrent i, in parallel with a large junction of supercurrent I_{strong}. The out-of-plane magnetic field B induces a flux Φ through the ring loop.

The CPR $i(\phi)$ reflects the Andreev spectrum and, importantly, its occupations as a function of the phase difference ϕ [99], see part 1.10.4 for more details on the model. The case of a junction made of a single hinge has been discussed in part 1.4.2. The transitions between its ground $(I_g(\phi))$ and excited $(I_e(\phi))$ state requires the exchange of a quasiparticle with its environment. Its CPR for ground and excited states are displayed in Fig.4.7a. Both are piecewise linear and 2π-periodic functions [99, 159, 102].

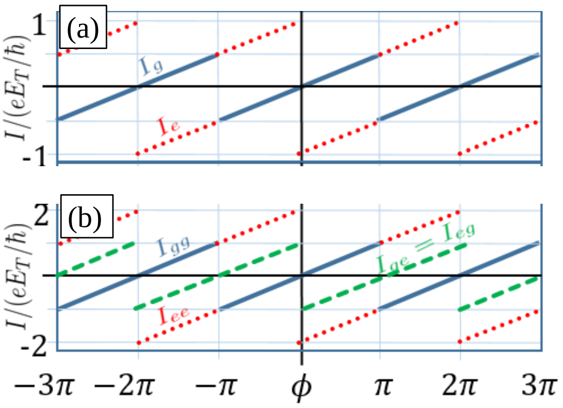

Figure 4.7 – (a) Corresponding Josephson currents $i_g(\phi)$ in the ground state (solid blue line) and $i_e(\phi)$ in the first excited state (dashed red line), obtained by taking a derivative of the many-body energies with respect to ϕ. i_g is linear between $-\pi$ and π, with downward jumps by $ev_F/L \equiv \frac{e}{\hbar}E_T$, with $E_T = \hbar v_F/L$ the Thouless energy, at $\phi = \pi + 2\pi n \, (n \in \mathbb{Z})$, with v_F the velocity of the hinge mode and L the distance between the two superconducting leads. For the excited state, i_e is also linear, with downward jumps by $2ev_F/L$ at $\phi = 2\pi n$ and upward jumps by ev_F/L at $\phi = \pi + 2\pi n$. (b) Josephson currents of a junction with two (identical) hinge modes. The current equals $i_{gg}(\phi) = 2i_g(\phi)$ when both hinges are in their ground states, $i_{eg}(\phi) = i_{ge}(\phi) = i_g(\phi) + i_e(\phi)$ when one hinge is in the excited state, and $i_{ee}(\phi) = 2i_e(\phi)$ when both are excited.

We now consider the case of two hinges. Given that each hinge can be either in the ground (g) or excited

(e) state, there are four possible Andreev states, gg,ee and eg/ge, whose CPR is $i_{ll'} = i_l(\phi) + i_{l'}(\phi)$, with l, l' (g) or (e). In the case of two hinge channels in the long junction regime, with same critical currents, $i_{gg} = 2i_g$, $i_{ee} = 2i_e$, and $i_{ge}(\phi) = i_{eg}(\phi) = i_g(\phi) + i_e(\phi) = i_{gg}(\phi + \pi)$, which is the sawtooth-shaped CPR of the ground state shifted by π. The three different CPRs are sketched in Fig.4.7b. The one-hinge spectrum is recalled in Fig.4.8b, where one can obtain the two-hinge energy by summing the energy over two identical one-hinge spectrums.

Following part 1.10.4, the next step is to compute the probability of occupying each of the four states, by solving the rate equations for the occupation probabilities. The equations read :

$$\begin{aligned}\frac{dp_{gg}}{dt} &= -2\Gamma_{eg\leftarrow gg}p_{gg} + 2\Gamma_{gg\leftarrow eg}p_{eg} - \Gamma_{ee\leftarrow gg}p_{gg} + \Gamma_{gg\leftarrow ee}p_{ee} \\ \frac{dp_{eg}}{dt} &= -\Gamma_{gg\leftarrow eg}p_{eg} + \Gamma_{eg\leftarrow gg}p_{gg} - \Gamma_{ee\leftarrow eg}p_{eg} + \Gamma_{eg\leftarrow ee}p_{ee},\end{aligned} \tag{4.1}$$

with $p_{ee} = 1 - 2p_{eg} - p_{gg}$. They include two types of relaxation processes, sketched in Figs.4.8a and 4.8c :
- (1) the intra-hinge, or poisoning processes, cause one hinge to be excited or relax with a rate $\Gamma_{ee\rightleftarrows ge}$, involving a relaxation time τ_2, or $\Gamma_{eg\rightleftarrows gg}$, involving a relaxation time τ_1
- (2) the inter-hinge or pair processes with rates $\Gamma_{gg\rightleftarrows ee}$, in which two quasiparticles from different hinges condense into one Cooper pair (or a Cooper pair splits to populate the two hinges), involving a pair relaxation time τ_p. We note that such inter-hinge, or pair relaxation processes do not require external particles from the fermionic bath, but only energy. These processes are suppressed for hinge modes that are far apart in real space on the scale of the superconducting coherence length.

Following [130], we assume that the intra-hinge transition rates involve a fermionic bath at a temperature $T_{\rm qp}$:

$$\begin{aligned}\Gamma_{ee\leftarrow eg}(\phi) &= f(\delta_E(\phi)/k_B T_{\rm qp})/\tau_2 \\ \Gamma_{eg\leftarrow ee}(\phi) &= f(-\delta_E(\phi)/k_B T_{\rm qp})/\tau_2,\end{aligned} \tag{4.2}$$

where τ_2 denotes a relaxation time, f is the Fermi distribution function, and $\delta_E(\phi) = E_e(\phi) - E_g(\phi)$ is the gap between the ground and excited states. Similarly,

$$\begin{aligned}\Gamma_{eg\leftarrow gg}(\phi) &= f(\delta_E(\phi)/k_B T_{\rm qp})/\tau_1 \\ \Gamma_{gg\leftarrow eg}(\phi) &= f(-\delta_E(\phi)/k_B T_{\rm qp})/\tau_1,\end{aligned} \tag{4.3}$$

The interhinge or pair rates also involve a fermionic bath, at a temperature $T_{\rm b}$ (that can be different from $T_{\rm qp}$), but contain the Bose-Einstein function and twice the excitation energy $\delta_E(\phi)$:

$$\begin{aligned}\Gamma_{ee\leftarrow gg} &= \frac{1}{E_T\tau_p}\int dE f\left(\frac{E}{k_B T_b}\right)\left[1 - f\left(\frac{E + 2\delta_E(\phi)}{k_B T_b}\right)\right] \\ &= \frac{2\delta_E(\phi)}{E_T\tau_p} n_B\left(\frac{2\delta_E(\phi)}{k_B T_b}\right),\end{aligned} \tag{4.4}$$

where $E_T = \hbar v_F/L$ is the Thouless energy, τ_p is the relaxation time for this process, and $n_B(x) = (e^x - 1)^{-1}$ is the Bose function. Similarly,

$$\Gamma_{gg\leftarrow ee} = \frac{2\delta_E(\phi)}{E_T\tau_p}\left[1 + n_B\left(\frac{2\delta_E(\phi)}{k_B T_b}\right)\right]. \tag{4.5}$$

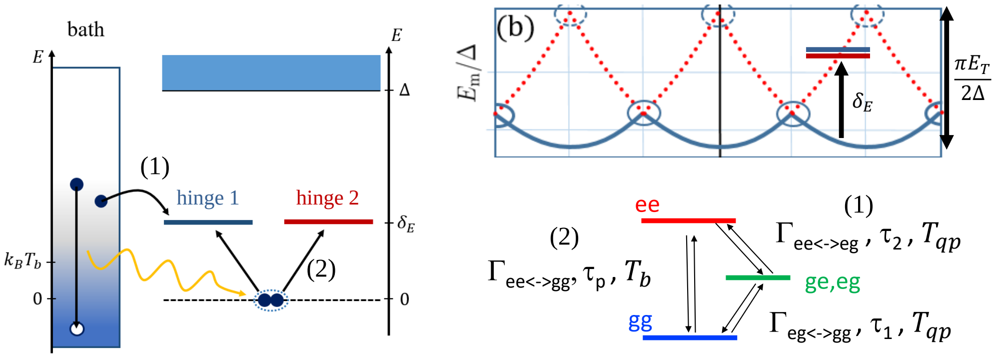

(a)

(c)

Figure 4.8 – (a) Quasiparticle and pair excitation processes. The dashed horizontal lines at zero energy represent the superconducting ground state, that acts as a Cooper pair reservoir. The blue region above energy Δ represent the quasiparticle continuum. The dark blue and red horizontal lines represent in-gap non-spin-degenerate helical Andreev bound states energy levels at a fixed ϕ and energy $\delta_E(\phi)$, each associated to a single helical (hinge) mode, see (b). Arrows represent processes that transfer one-particle occupation between two states. The intra-hinge or poisoning process (1) involves only one hinge and the quasiparticle bath, and the exchange of a quasiparticle that changes the parity of the hinge [131, 129, 126]. The inter-hinge or pair process (2) involves two hinges, an energy $2\delta_E$ from the bath, and a Cooper pair from the superconducting condensate. It does not change the global parity of the two-hinge system. (b) Spectrum of one helical hinge, including the ground state $E_g(\phi)$ (solid blue line) and the first excited state $E_e(\phi)$ (dashed red line). The excitation energy $\delta_E(\phi) = E_e(\phi) - E_g(\phi)$ is indicated by an arrow. Level crossings at odd multiples of π (full-line circles) are protected by fermion parity, while level crossings at even multiples of π (dashed circles) are protected by time reversal symmetry (strictly speaking broken by the magnetic field in the experiment). (c) ABS energy levels of the two-hinge junction and corresponding transition rates.

Notice that the energy difference between the "ee" and "gg" states appearing in the Fermi function is $2\delta_E(\phi)$.

Still following part 1.10.4, we substitute d/dt by $\omega d/d\phi$ in the rate equations. The probabilities are obtained from numerically integrating Eq.(4.1) from $\phi = \Phi$ to $\phi_{\mathrm{sw}} = \Phi + \gamma_{\mathrm{max}}$. For the curves presented in the main text, we have chosen $\gamma_{\mathrm{max}} = \pi/2$ which best fits the experimental data. But in Fig. 4.11 we present similar curves computed with $\gamma_{\mathrm{max}} = \pi$. The initial conditions of the rate equation (4.1) at $\phi = \Phi$ are computed from the stationary conditions $dp_i/dt = 0$.

4.2.2 . Cases with visible poisoning

Some examples of probabilities p_{gg}, p_{eg} and p_{ee} obtained by solving these equations are plotted in Fig. 4.9, 4.10 and 4.11. Here we have taken $\tau_1 = \tau_2 = \tau_{qp}$.

Figure 4.9 considers two extreme cases for the interhinge pair relaxation time τ_p. When $\omega\tau_p \gg 1$ (Fig. 4.9 left), no co-relaxation or co-excitation occur : the two channels are independent, and $p_{ee} \propto p_{eg}$ for all Φ, such that p_{ee} and p_{eg} are always peaked at the same flux. In the other limit of extremely correlated channels $\omega\tau_p \ll 1$ (Fig. 4.9 right), p_{ee} is always peaked at $\phi_{\mathrm{sw}} = \Phi + \gamma_{\mathrm{max}} = \pi$ and the p_{ee} peak always touches the p_{gg} dip, that is $p_{ee} = p_{gg}$ and $p_{ee} = (1 - p_{eg})/2$ at that point.

Figure 4.10 illustrates the precision with which the parameters can be determined. To this end, we present results of the two hinge model computed with sets of parameters close to the ones that reproduce best the experimental data presented in later Figs.4.17 and 4.18 for the $-170\ G$ region. As shown in Fig. 4.10(a) and Fig. 4.10(c), in which the different curves correspond to computations with the same $\omega\tau_{qp}$ but different $\omega\tau_p$, the variation of $\omega\tau_p$ is almost invisible on the $p_{eg}+p_{ge}$ peak, and is best seen on the height of the p_{ee} peak of 4.10(c). On the other hand, the curves shown on Fig. 4.10(b) and Fig. 4.10(d) are the results of computations at fixed $\omega\tau_p$ and different $\omega\tau_{qp}$. The variation with $\omega\tau_{qp}$ is weak on the p_{ee} peak, and is best seen on the $p_{eg}+p_{ge}$ peak(s) both in Fig. 4.10(b) and 4.10(d). Thus, Fig. 4.10(c) suggests that for a given $\omega\tau_{qp}$, $\omega\tau_p$ can be estimated within a factor ~ 5 by looking at the p_{ee} peak, which is not very sensitive to the chosen $\omega\tau_{qp}$. The parameter $\omega\tau_{qp}$ can be estimated within a factor ~ 2 on the $p_{eg}+p_{ge}$ peak on Fig. 4.10(b) and Fig. 4.10(d). This leads to an overall error of a factor ~ 7 on the ratio τ_{qp}/τ_p.

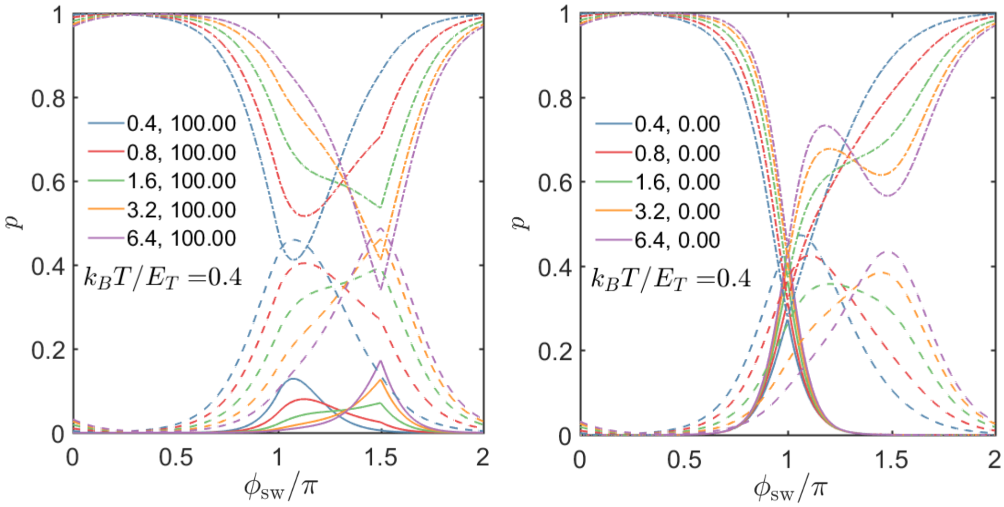

Figure 4.9 – Computed probabilities of the junction to be in its doubly-excited state (p_{ee}, solid lines), singly-excited state ($p_{eg} + p_{ge}$, dashed lines), or ground state (p_{gg}, dashed-dotted lines), as a function of $\phi_{sw} = \Phi + \gamma_{max}$, with $\gamma_{max} = \pi/2$, for various dynamics parameters $\omega\tau_{qp}$ (first number in the legends) and $\omega\tau_p$ (second number in the legends). ω is the phase ramping frequency, τ_{qp} is the intra-hinge relaxation time, τ_p is the pair or inter-hinge co-relaxation time, $T = T_b = T_qp$ is the bath temperatures, and E_T denotes the Thouless energy of the hinge junction.

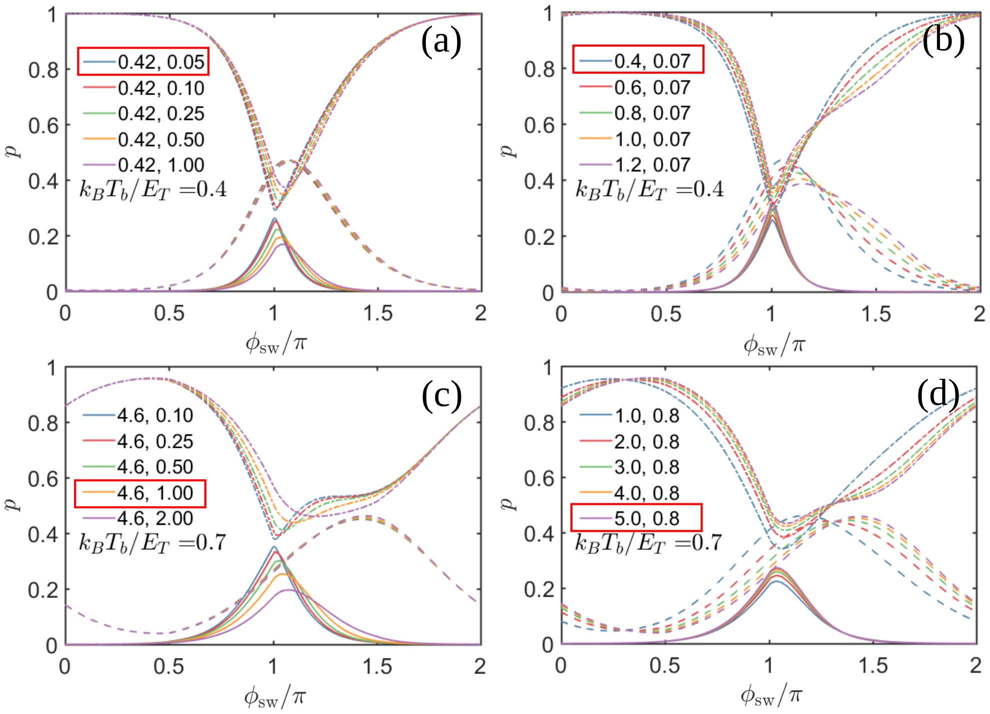

Figure 4.10 – Computed probabilities of the junction to be in its doubly-excited state (p_{ee}, solid lines), singly-excited state ($p_{eg} + p_{ge}$, dashed lines), or ground state (p_{gg}, dashed-dotted lines), as a function of $\phi_{sw} = \Phi + \gamma_{max}$, with $\gamma_{max} = \pi/2$, for two different bath temperatures $T_b (= T_q p)$ and varying parameters $\omega\tau_{qp}$ (first number in the legends) and $\omega\tau_p$ (second number in the legends). ω is the phase ramping frequency, τ_{qp} is the intra-hinge relaxation time, τ_p is the pair or inter-hinge co-relaxation time, and E_T denotes the Thouless energy of the hinge junction.

4.2.3 . $\gamma_{max} = \pi$ instead of $\pi/2$

Figure 4.11 displays computed probabilities that reproduce the qualitative features of the experimental occupation probabilities measured around -170 G, using a phase range $\gamma_{\max} = \pi$ instead of $\gamma_{\max} = \pi/2$ (used in the rest of the analysis). Compare later Fig.4.17d with Fig. 4.11a for the $17Hz$ current ramp frequency, and Fig.4.18d with Fig. 4.11b for the $187Hz$ current ramp frequency.

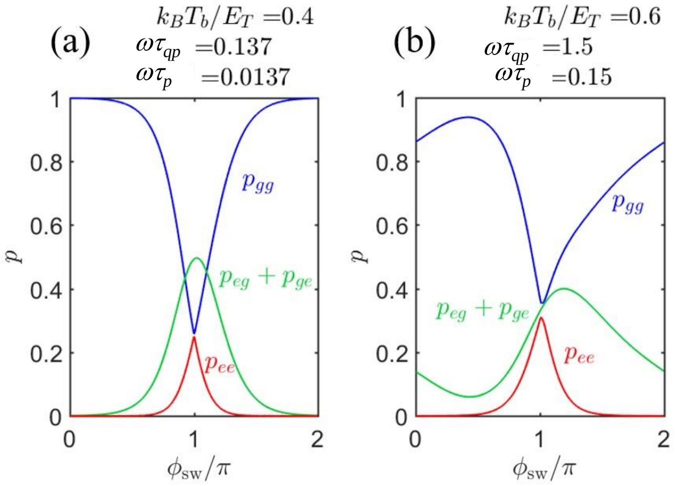

Figure 4.11 – Computed probabilities of the junction to be in the doubly-excited state (p_{ee}, red line), singly-excited state ($p_{eg} + p_{ge}$, green line), or ground state (p_{gg}, blue line), as a function of $\phi_{sw} = \Phi + \gamma_{max}$. For the results presented here, the range of the phase over one current ramp period is $\gamma_{max} = \pi$ rather than $\pi/2$ used in the rest of the analysis. ω is the phase ramp frequency, τ_{qp} the single-hinge relaxation time, τ_p the pair or inter-hinge relaxation time, $T_b = T_qp$ is the bath temperatures, and E_T denotes the Thouless energy of the junction.

4.2.4 . Cases with very little visible poisoning

Interestingly, the fact that there are two hinge channels is not easily seen in the switching current distribution around $420G$: the intermediate branch is almost invisible, see Figs.4.2, 4.4, 4.3a and b. However, a non-zero probability of the intermediate state (with one hinge in the excited state and the other in the ground state, noted 'eg') is seen, even though it can be quite small, less than five percent, in the reconstructed occupation probability (and is displayed in later Fig.4.15).

We have therefore extended our model in order to reproduce the type of occupation probability measured in that field region, which is characterized by a much greater probability to be in the doubly excited state than to be in eg state. To this end, we have found that we need to include a small gap in the Andreev spectrum, and we need to consider that the quasiparticles leading to the poisoning are very few (which we translate as a very small quasiparticle temperature). In addition, parity switching transitions require two different rates $\Gamma_{ee \rightleftarrows eg}$ and $\Gamma_{eg \rightleftarrows gg}$, depending on whether they involve the doubly excited state or the ground state, respectively. Of course, this larger number of parameters precludes claiming a quantitative fit to the experiment in that region.

Figs.4.12 and 4.13 illustrate the key ingredients to observing very little poisoning in the system. Fig. 4.12 focuses on the relaxation times, and clearly displays how a small and shifted poisoning probability p_{eg} (as seen in the experiment) requires a much faster relaxation from the poisoned state to the ground state than the relaxation from excited to poisoned (compare (a), (b) and (c)). A high maximum of the excited probability p_{ee} also requires a fast pair relaxation time (compare (a) and (d)). Fig. 4.13 focuses on the quasiparticle and pair temperatures, and shows that a small poisoning requires a very small quasiparticle temperature compared to the gap in the spectrum.

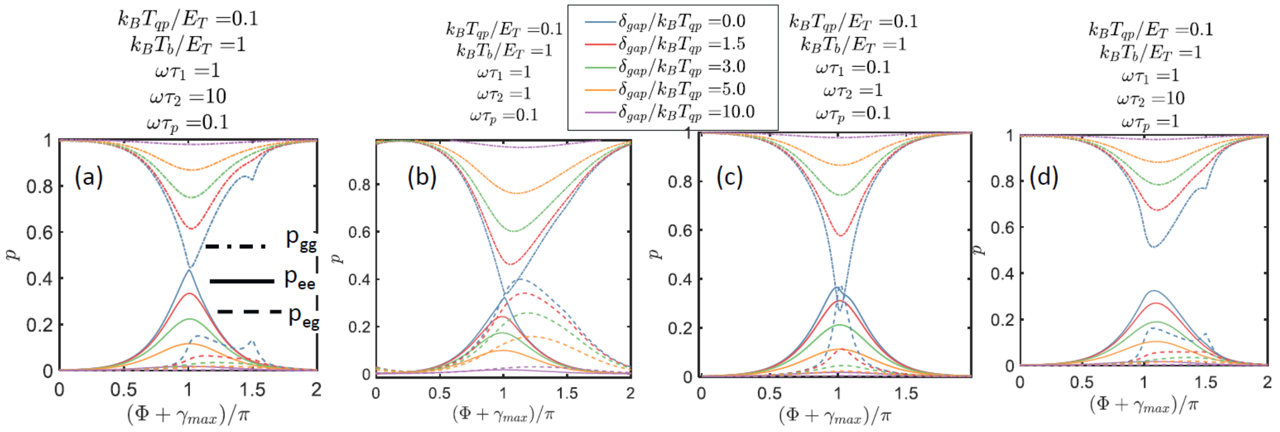

Figure 4.12 – Role of the relative relaxation times in the poisoning probability. Probability of the two-hinge junction to be in the excited excited, ground ground or poisoned Andreev state respectively (p_{ee}, continuous lines, p_{gg}, dashed dotted lines, and p_{eg}, dashed lines), for several values of the gap (0 to $10\ k_BT_{qp}$), and changing the respective quasiparticle relaxation times τ_1 and τ_2 in (a), (b) and (c). It is seen that a poisoning probability p_{eg} smaller than the excited probability p_{ee}, and shifted with respect to the extrema of p_{ee} and p_{gg} is obtained only with $\tau_p \ll \tau_1 \ll \tau_2$. Panel (d) displays the effect of a longer pair relaxation time.

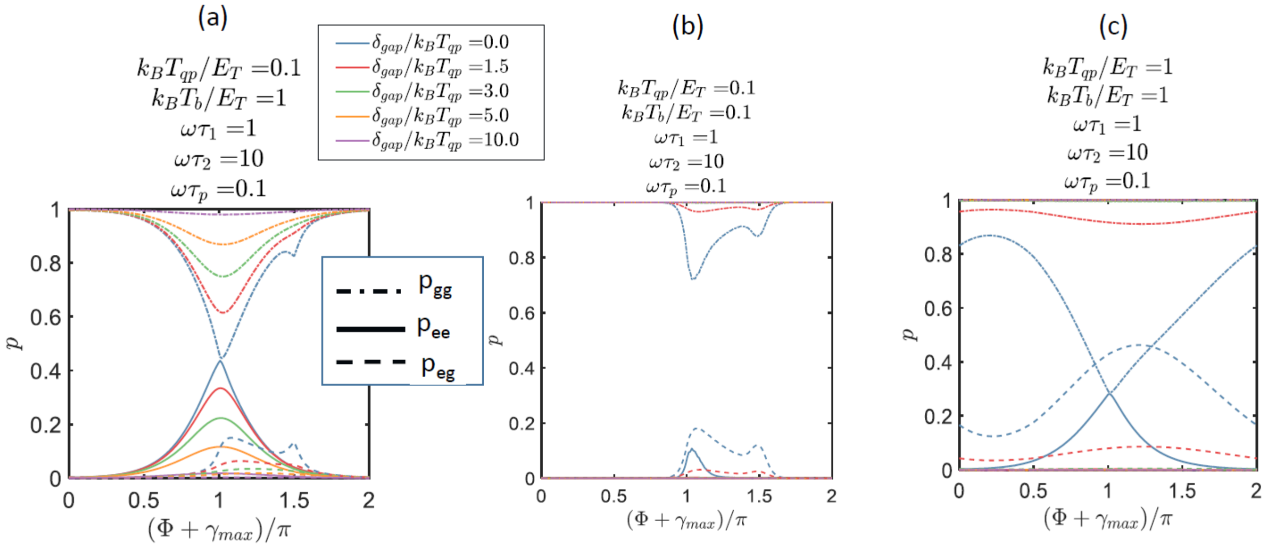

Figure 4.13 – Role of the relative quasiparticle and pair temperature on the poisoning probability. Only a quasiparticle temperature T_{qp} smaller than the gap, combined with a pair bath temperature T_b larger than the gap (situation of panel (a) produces the small poisoning probabilities p_{eg} relative to the p_{ee}, as seen in the experiment near $450G$).

4.3 . Relations between the experiment and the model

4.3.1 . From switching current histograms to probabilities

The occupation probabilities are extracted from the integrated switching current distributions (see e.g. later Fig.4.17c) by noting that each step in the integrated distribution corresponds to a transition out of a specific supercurrent-carrying state. The height of the step from one plateau to the next therefore counts the number of switching events from that state, and is normalized to yield the occupation probability of that state just before the switching event. The integrated switching current distribution corresponds to the total switching probability of the junction, as defined in Eq.(1.82) in part 1.10.4. The probabilities are associated to the steps by comparison between the experimental distributions (e.g. Figs.4.3 and 4.5) and the CPR of the two-helical-hinges model Fig.4.7b, assuming that the most visible branch in the data corresponds to the (most probable) ground-ground state. By construction, p_{ee} can't exceed p_{gg}, as we attributed the state with the lowest probability between the two to the doubly-excited state. From the theoretical analysis, we associate $p_{ge}+p_{eg}$ to the "poisoned state" eg, p_{ee} to the "doubly-excited state" ee, and p_{gg} to the "ground state" gg. In the following figures showing the experimental probabilities, mind that the data for $17Hz$ and $187Hz$ current bias ramp frequencies have been taken during two series of measurements, and a shift in magnetic field may have happened between the two.

Fig.4.14 displays the occupation probabilities deduced from the experiment over four periods of modulation around $-170\ G$, at both $17\ Hz$ and $187\ Hz$ current bias ramp frequencies. At $17Hz$, peaks and dips in the probabilities of states ee and gg have close values $p_{ee} \lesssim p_{gg} \simeq 0.35$, and the probability of poisoned state eg is higher, with a maximum slightly shifted toward positive field. Their eights vary a bit over the four periods, but their widths seem constant. At $187Hz$, the gap between p_{ee} and p_{gg} grows, p_{gg} is globally lower compared to its $17Hz$ value, and $p_{ge}+p_{eg}$ is globally higher compared to its $17Hz$ value. The width of the $p_{ge}+p_{eg}$ peak (and conjointly of the p_{gg} dip) increased. Lastly, the $p_{ge}+p_{eg}$ shift toward positive field increased. In this region of field, there is an extra state (p_s, grey lines) that is not accounted for in our model, corresponding to one hinge in its ground state and the other hinge in its second excited state.

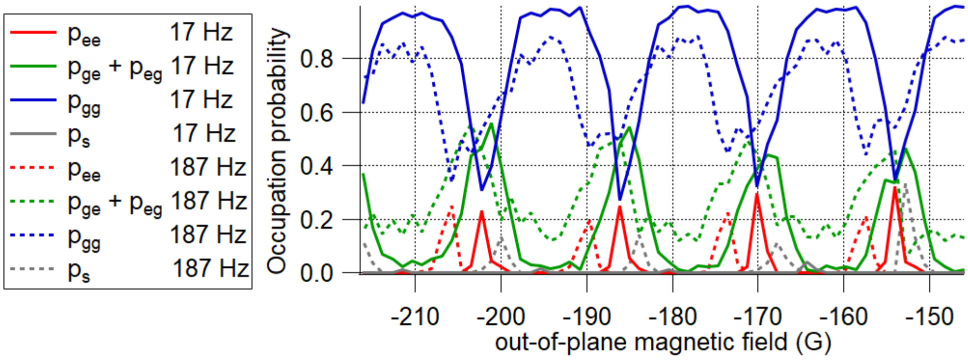

Figure 4.14 – Occupation probabilities extracted from the integrated experimental switching current distributions at bias ramp frequency of 17 Hz (solid lines) and 187 Hz (dashed lines). In addition to the ground (p_{gg}, blue lines) and doubly-excited (p_{ee}, red lines) state probabilities of the two-hinge model, the $p_{eg}+p_{ge}$ probability of the poisoned state (green lines) is large, and shifted with respect to the p_{ee} peak. In this region of field, there is an extra state (p_s, grey lines) that is not accounted for in our model, corresponding to one hinge in its ground state and the other hinge in its second excited state.

Fig.4.15 displays the occupation probabilities deduced from the experiment over six periods of modulation around $420\ G$, at both $17\ Hz$ and $187\ Hz$ current bias ramp frequencies. We see that the widths of the peaks (dips) of the occupation probability of the doubly-excited (ground) state do not vary substantially over this range, but their heights do. Close to $400G$ and $420G$, they barely touch each other, but otherwise the values at their dip/peak is $p_{gg} \simeq 0.6 > p_{ee} \simeq 0.4$. We also see how the small shoulder of the poisoned state probability (green lines) is larger at $187\ Hz$ than at $17\ Hz$. It is striking that in the case of very little poisoning, the higher energy ee level has a higher probability than the lower energy eg level.

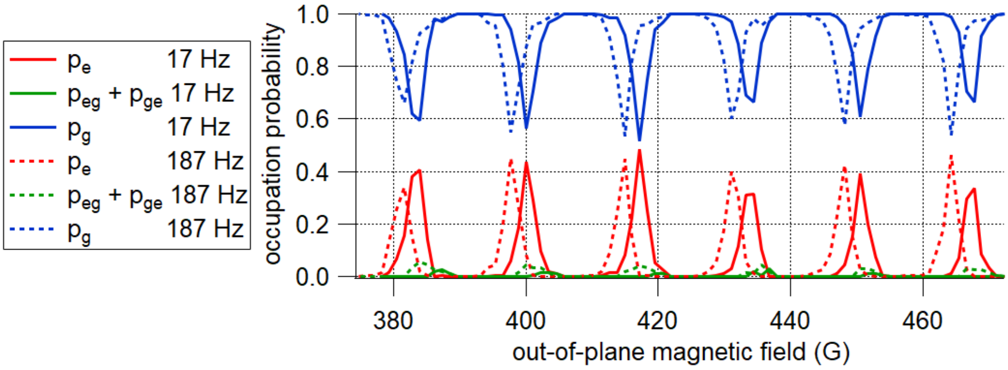

Figure 4.15 – Occupation probabilities extracted from the integrated experimental switching current distributions at bias ramp frequency of 17 Hz (solid lines) and 187 Hz (dashed lines). In addition to the ground (p_{gg}, blue lines) and excited (p_{ee}, red lines) state probabilities of the two-hinge model, the $p_{eg} + p_{ge}$ probability of the poisoned state (green lines) is extremely small, and shifted with respect to the p_{ee} peak.

4.3.2 . From current ramp signal to relaxation times

We choose a bias current ramp that is an asymmetric triangular periodic signal from 0 to $3\ \mu A$ with a $0.8/f$ rise time, where f is the sweep frequency refereed as the current bias ramp frequency. In our analysis, we suppose that the current sweep from 0 to the switching current corresponds to a linear evolution with time of the weak junction's superconducting phase difference, from Φ to $\Phi + \gamma_{\text{max}} = \Phi + \omega.t^{\omega}_{\text{sw}}$, with $\gamma_{\text{max}} = \pi/2$. Here ω is the phase sweep pulsation and t^{ω}_{sw} is the time it takes to switch. To relate ω to the current sweep frequency f we use the fact that the switching current for the low magnetic field values studied here is $I_{sw} \sim 2.5\ \mu A$, and the current is swept up to $I_{max} \simeq 3\ \mu A$. Therefore $t^{\omega}_{\text{sw}} = 2.5/3 * 0.8/f$. It is illustrated in Fig.4.16.

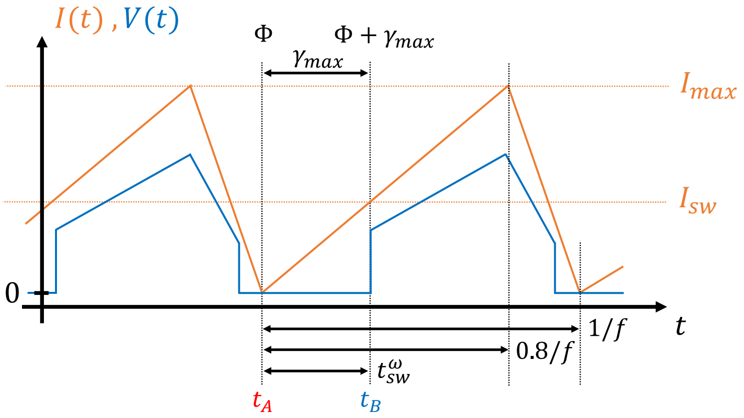

Figure 4.16 – Sketch of the link between time t, current I and superconducting phase difference across the weak two-helical-hinges junction of our asymmetric DC SQUID model. V is the voltage across the sample, Φ is the flux through the DC SQUID, and γ_{max} is the phase at which the current in the strong junction of the asymmetric DC SQUID is maximum.

Since $\omega t^{\omega}_{\text{sw}} = \gamma_{\text{max}}$ we find $\omega_{17} \simeq 40\ rad.s^{-1}$ for $f = 17Hz$ and $\omega_{187} \simeq 441\ rad.s^{-1}$ for $f = 187Hz$. The theoretical model which reproduce best the experimental data provides the parameters $\omega\tau_1$, $\omega\tau_2$, and $\omega\tau_{qp}$. We then use ω_{17} and ω_{187} to calculate τ_1, τ_2, and τ_{qp}.

4.4 . Comparison : exceptionally long-lived ABS

To compare experiment and theory, we extract from the experimental switching current distributions the field-dependent histograms and integrated histograms, from which we derive the state-dependent experimental occupation probabilities. The theoretical occupation probabilities are then computed using the parameters $\omega\tau_1$, $\omega\tau_2$, $\omega\tau_p$, T_b and T_{qp} which best reproduce the experimental occupation probabilities. $P^l_{\rm sw}(I,\phi_{\rm sw})$, $dP(I,\phi_{\rm sw})/dI$ and the full switching distribution as a function of flux are subsequently generated with those parameters.

Figs.4.17 and 4.18 display how well the experimental switching current distribution around -170 G are reproduced by theory. Two current ramp frequencies, 17 and 187 Hz, were investigated. The model reproduces the extent over which the fainter intermediate (poisoning) branch extends, and how it extends further in the case of the higher current ramp frequency. The model also reproduces remarkably well the shape, height, and relative positions of the three probability distributions p_{gg}, $p_{eg}+p_{ge}$ and p_{ee} extracted from the integrated experimental histogram (compare Fig.4.17d with 4.17h and Fig.4.18d with 4.18h). In the regions with three possible switching currents, there are three non-negligible occupation probabilities of the states gg, ee and eg. For the slowest ramp, p_{gg} and p_{ee} are extremal at π, whereas $p_{eg}+p_{ge}$ is maximal slightly above π (Fig.4.17d). The corresponding plot at a ramp frequency eleven times greater, Fig.4.18d, displays a much greater shift of the maximum of $p_{eg}+p_{ge}$. This shift is the signature of the inter-hinge pair relaxation processes of typical time τ_p. The parameters used to match the experimental data are $\tau_{qp}=\tau_1=\tau_2=10.5\ \rm ms$ and $\tau_p=1.82\ \rm ms$ for both the slow and fast ramp. Only $T_b=T_{qp}$ was allowed to change, yielding $k_BT_{\rm b}/E_T\simeq 0.4$ for 17 Hz and $k_BT_{\rm b}/E_T\simeq 0.7$ for 187 Hz, reflecting the smaller time available for quasiparticle thermalization in the reservoirs.

The asymmetry of the switching current distribution, reflecting the finite relaxation times, is visible in Figs.4.17a and 4.18a thanks to the intermediate distribution. Correspondingly, the asymmetric shapes of the occupation probability peaks (or dips) are clearly visible both in experiment (Figs.4.17d and 4.18d) and theory (Figs.4.17h and 4.18h). The model fails, however, to capture some of the experimental features at $187\ \rm Hz$: in experiment Fig.4.18a, the main branch is asymmetric towards positive current, whereas the intermediate, fainter branch is asymmetric towards negative current. The switching statistics generated in the theory, by contrast Fig.4.18e, displays a main branch that extends further, for both positive and negative current, than the intermediate branch. This discrepancy may be attributed to the fact that the model is restricted to only the first excited state, see Fig.1.24 in part 1.4.2.

We now turn to modeling the experimental switching current distribution around 450 G, see Figs.4.19 and 4.20. Interestingly, in this field region hardly any intermediate switching branch is visible (Figs.4.19a and 4.20a). This means that the ee and gg states are much more populated than the eg state, as clearly seen in the extracted occupation probabilities, Figs.4.19d and 4.20d : the poisoned state probability p_{eg} is less than 5%, with a maximum shifted with respect to the p_{ee} and p_{gg} extrema. This situation, with very little poisoning, is unexpected since it corresponds to a higher probability of the more energetic ee state than the eg state. It can be reproduced using a slow pair relaxation time and a relaxation time τ_2 out of the ee state and into the eg state that is ten time longer than the relaxation time τ_1 out of eg and into gg (see 2(g)). In addition, a much smaller quasiparticle temperature is required compared to the pair bath temperature, along with a small gap in the Andreev spectrum (too small to be detected in the experiment). The parameters are the same $\tau_p=1.82\ ms$ pair relaxation time as previously, but $\tau_1=25\ ms$ and $\tau_2=250\ ms$. Given the larger number of parameters involved, we consider the description of this low poisoning regime qualitative rather than quantitative.

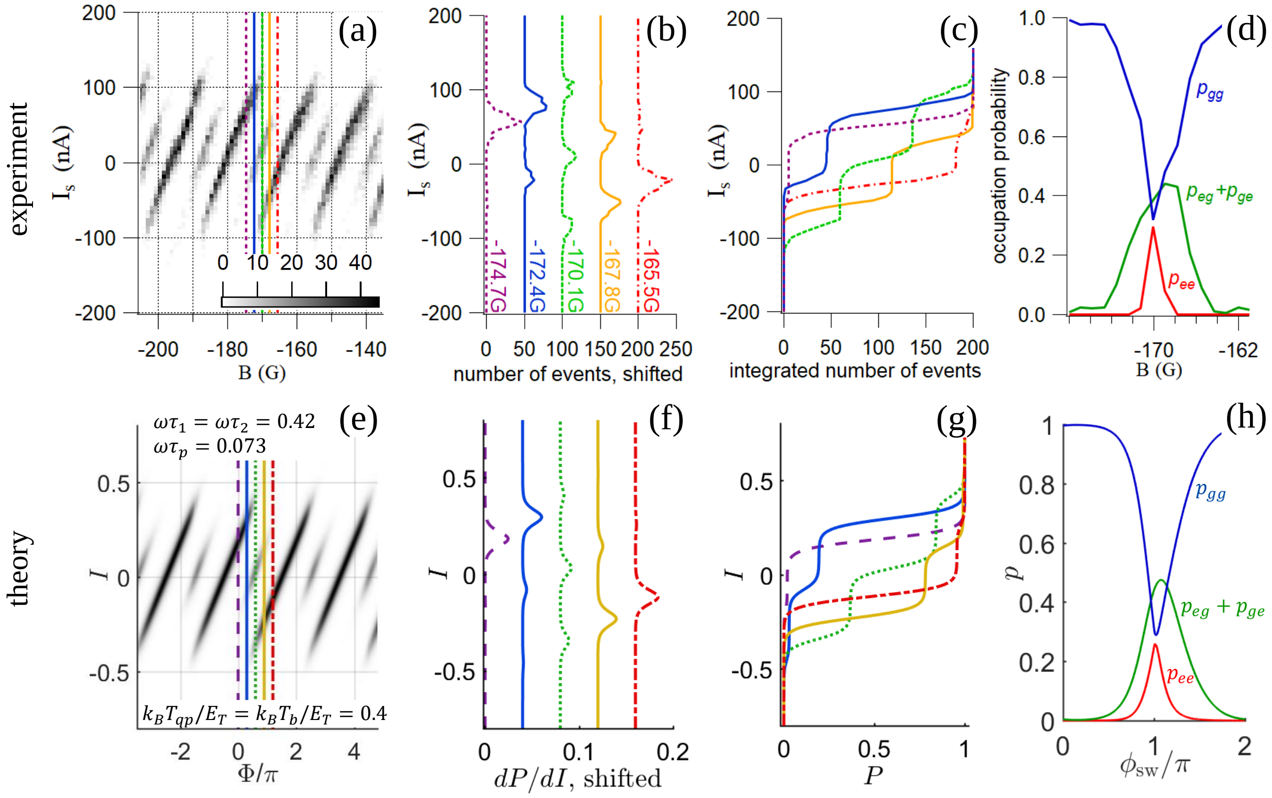

Figure 4.17 – Measured switching current distributions and extracted probabilities of Andreev hinge states occupations in a field region where an additional switching branch develops, for a current ramp frequency of 17 Hz. Comparison to theory with two current-carrying hinge modes. (a) Switching current histograms over four flux periods around -170 G. The number of switching events is coded in shades of grey. The background has been removed with a first order polynomial. (b) Histograms at magnetic fields around the jump at B = -170 G where $\phi = \pi$, see the corresponding colored lines in (a). (c) Integrated histograms close to the jump at B = -170 G. (d) Field-dependence of the occupation probability of three supercurrent-carrying Andreev states, corresponding respectively to both hinges in the ground state (p_{gg}, blue curve), both hinges in the excited state (p_{ee},red curve), or one hinge in the ground state and the other in the excited state ($p_{eg} + p_{ge}$, green curve). The corresponding theoretical curves (e),(f),(g),(h) are computed using the parameters $k_BT_b/E_T = k_BT_{qp}/E_T = 0.4$, $\omega\tau_{qp} = 0.42$, $\omega\tau_p = 0.073$, yielding $\tau_{qp} = 10.5ms$ and $\tau_p = 1.82ms$. $\phi_{sw} = \Phi + \gamma_{max}$ with $\gamma_{max} = \pi/2$. The theoretical curves (e) resolve the fainter intermediate distribution seen in the experiment (a). This leads to a range of flux where three values of switching current are possible. This corresponds to regions with three peaks in the histogram (see, e.g., the green curve at -170.1 G in the experimental panel (b)), which are qualitatively reproduced in (f), albeit with a less equally distributed peak height. The integrated histograms with two intermediate plateaus ((c)) are also qualitatively reproduced in the theory ((g)). Finally, the theory ((h)) with these parameters, captures the shape, height, and relative positions of the three probability distributions $p_{gg}, p_{eg} + p_{ge}$ and p_{ee} shown (d).

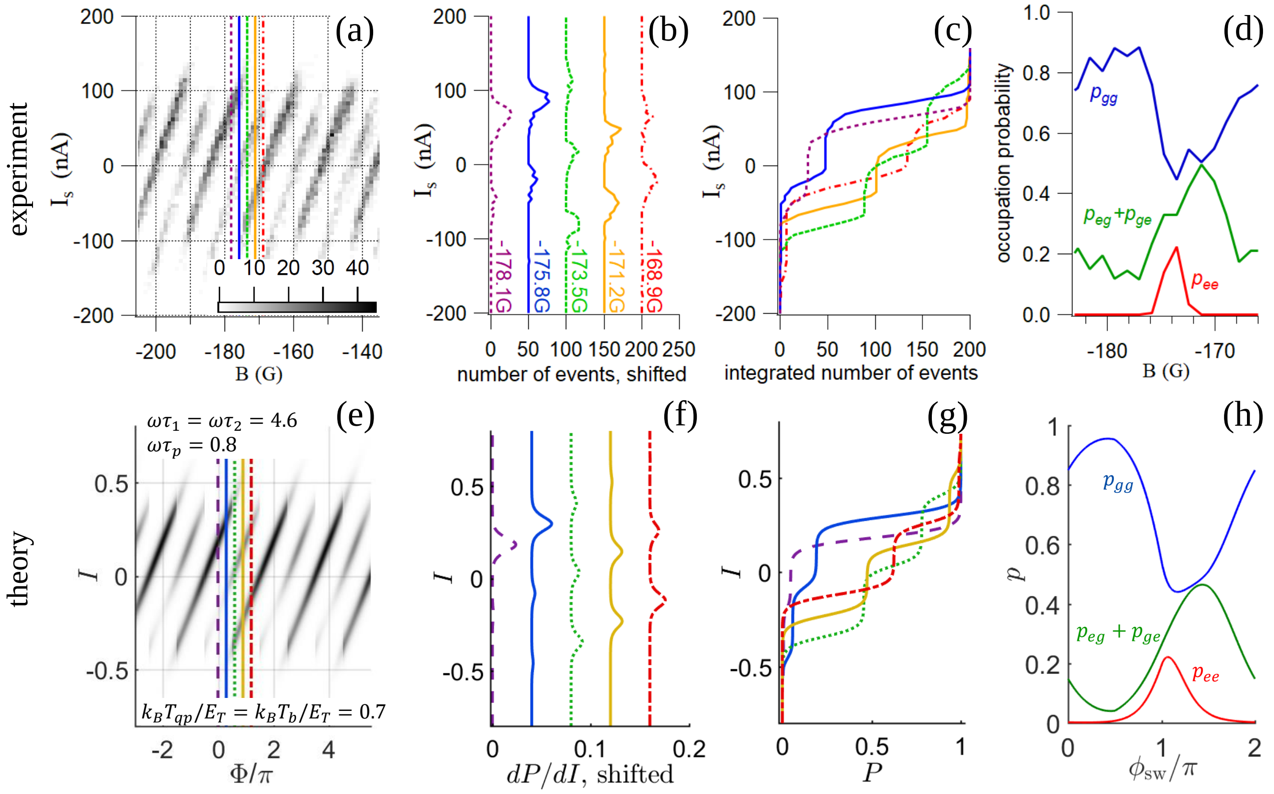

Figure 4.18 – Measured switching current distribution and extracted probability of Andreev hinge state occupation in the same field region as Fig. 4.17, for a faster current ramp frequency of 187 Hz. Comparison to theory with two current-carrying hinge states. (a) Switching current histograms over four flux periods around -170 G. The number of switching events is coded in shades of grey. The background has been removed with a first order polynomial. (b) Histogram curves at magnetic fields around the jump at B = -170 G where $\phi = \pi$, see the corresponding colored lines in (a). (c) Integrated histograms close to the jump at B = -170 G. (d) Field-dependence of the occupation probability of three supercurrent-carrying Andreev states, corresponding respectively to both hinges in the ground state (p_{gg}, blue curve), both hinges in the excited state (p_{ee}, red curve), or one hinge in the ground state and the other in the excited state ($p_{eg} + p_{ge}$, green curve). The corresponding theoretical curves (e),(f),(g),(h) are computed using the parameters $k_BT_b/E_T = k_BT_{qp}/E_T = 0.7$, $\omega\tau_{qp} = 4.6$, $\omega\tau_p = 0.8$, yielding $\tau_{qp} = 10.5ms$ and $\tau_p = 1.82ms$. $\phi_{sw} = \Phi + \gamma_{max}$ with $\gamma_{max} = \pi/2$. The theory reproduces the main features of the experiment : number of histogram peaks ((b) and (f)), number of intermediate plateaus ((c) and (g)), broadened occupation probabilities, and increased shift in $p_{eg} + p_{ge}$ ((d) and (h)).

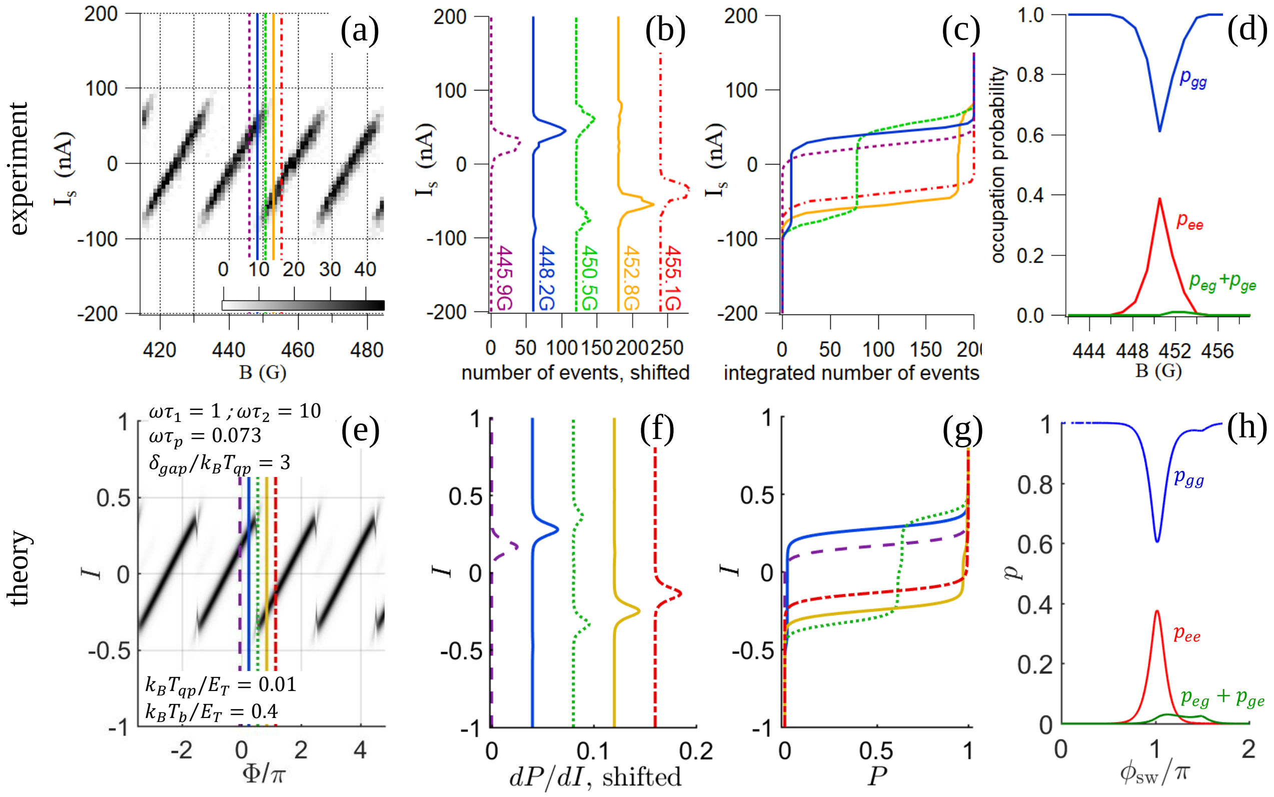

Figure 4.19 – Measured switching current distribution and extracted probability of Andreev hinge state occupation in the case with very little visible poisoning (faint intermediate branch, very small p_{eg} probability) (a) Switching current histograms over four flux periods around 450 G, with a 17 Hz current ramp. The number of switching events is coded in shades of grey. (b) Histogram curves at magnetic fields around the discontinuity in the sawtooth at B = 450 G where $\phi = \pi$, see the corresponding colored lines in (a). (c) Integrated histograms over the same field range. (d) Field-dependence of the occupation probability (p_{gg} blue curve), excited (p_{ee}, red curve) and poisoned (p_{eg}, green curve) states. The corresponding theoretical curves (e),(f),(g),(h) are computed using the parameters $k_BT_b/E_T = 0.4$, $k_BT_{qp}/E_T = 0.01$, $\omega\tau_p = 0.073$, $\omega\tau_1 = 1$ and $\omega\tau_2 = 10$, yielding the relaxation times $\tau_p = 1.82\,\mathrm{ms}$, $\tau_1 = 25\,\mathrm{ms}$ and $\tau_2 = 250\,\mathrm{ms}$. The gap in the spectrum is $3k_BT_{qp}$. $\phi_{\rm sw} = \Phi + \gamma_{\rm max}$ with $\gamma_{\rm max} = \pi/2$.

Our analysis has led to the identification of three times, describing respectively the intra-hinge relaxation from the excited to the ground state within a single hinge (single-quasiparticle or poisoning process, with times τ_1 and τ_2), and the inter-hinge or pair relaxation involving a two-particle process in which two hinges simultaneously acquire or release a quasiparticle over a time τ_p. This process is impeded if the hinges are far apart, and correspondingly the time τ_p should increase with the separation between hinges.

Let us compare the values of τ_p and τ_{qp} we have found (albeit overestimated because of possible inductance effects, see appendix 6.2), in the $\sim 10-100\ \mathrm{ms}$ range, to the values obtained in nontopological junctions in similar environments. The poisoning relaxation times we find are similar to the ones measured in Josephson junctions based on atomic contacts [126, 129] and semiconducting nanowires [131, 77], which vary between a few hundred μs and ms. In striking contrast, the pair relaxation times τ_p estimated in those works, and associated to the T_1 relaxation time of the Andreev qubit [132] are two to three orders of magnitude shorter, in the μs range, than what we find in the bismuth nanowire.

We interpret this as demonstrating the strong decoupling between hinges, confirming the topological character of bismuth. Indeed, while in a nontopological Josephson junction, every helical channel locally coexists with its opposite helicity counterpart, in a topological system, the two helical channels are spatially separated, typically by one hundred nanometers or more. This separation is roughly one hundred times greater than the transverse extension of the helical Andreev states at the Bi nanowire hinges (which is in the nanometer range, as shown by the extraordinary field range over which the supercurrent persists, see Figs.4.1 and 3.12 as well as [3, 40]), and ten times greater than the superconducting coherence length of the disordered W contacts (typically a few nanometers).

A remaining puzzle is why the degree of poisoning depends on magnetic field, so that poisoning is clear in one field range and practically undetectable in another. One possibility is that the Zeeman field, by tilting the spins, can remove the orthogonality between states of a given hinge, thereby allowing spin-conserving, backscattering relaxation/poisoning transitions within one hinge. Whereas when the states are orthogonal, backscattering relaxation must occur through a change of hinge, which is very slow if the hinges are separated. A second possibility, mentioned in [130], explains the change in effective temperature of the poisoning quasiparticles T_{qp} by a change in the nature and number of quasiparticles that can couple to Andreev bound states. Depending on magnetic field, the Andreev bound states, whose energy shifts with Zeeman field, could be alternately coupled to the quasiparticle continuum above the superconducting gap (yielding a rather large temperature), or coupled only to rarer localized states (corresponding to a very small temperature). We believe that both the number of available quasiparticles and the selection rules given by the helical nature of the hinges could explain the two very different regimes we see.

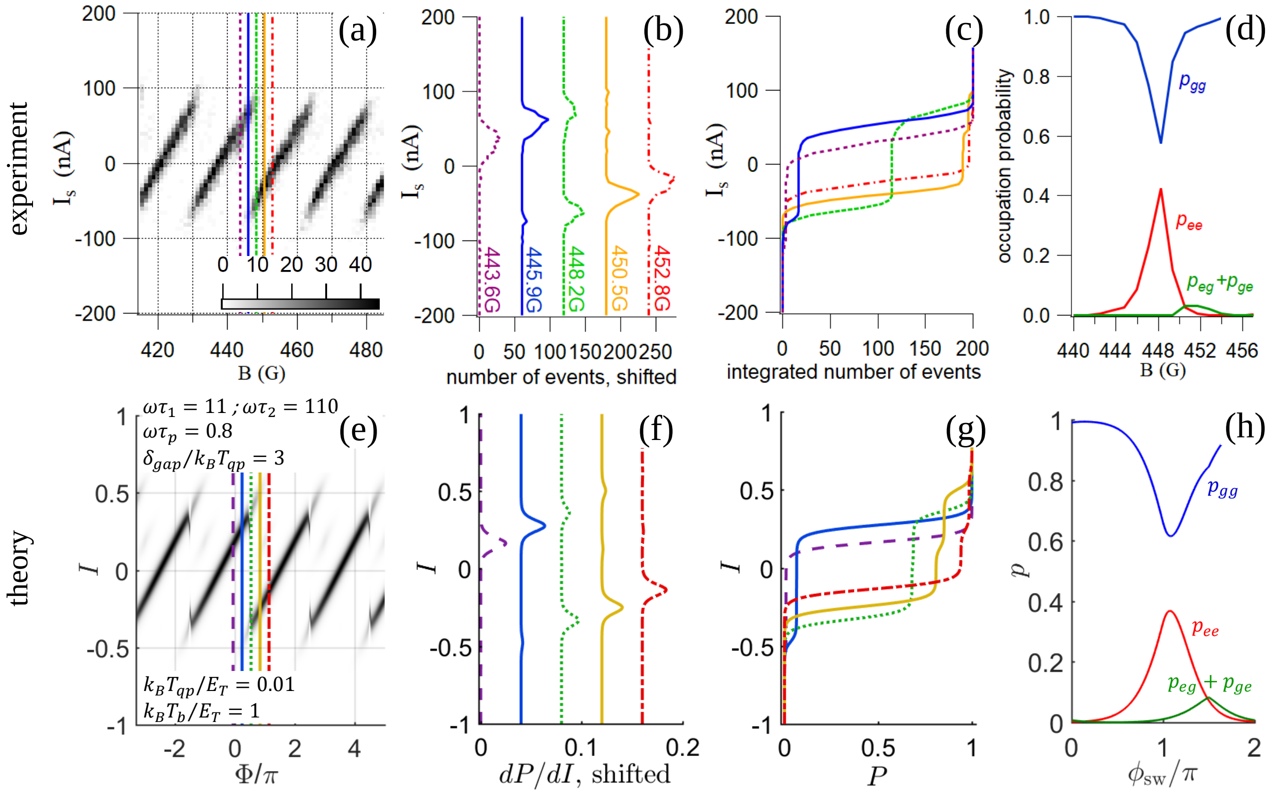

Figure 4.20 – Measured switching current distribution and extracted probability of Andreev hinge state occupation in the case with very little visible poisoning (faint intermediate branch, very small p_{eg} probability) (a) Switching current histograms over four flux periods around 450 G, with a 187 Hz current ramp. The number of switching events is coded in shades of grey. (b) Histogram curves at magnetic fields around the discontinuity in the sawtooth at B = 450 G where $\phi = \pi$, see the corresponding colored lines in (a). (c) Integrated histograms over the same field range. (d) Field-dependence of the occupation probability (p_{gg} blue curve), excited (p_{ee}, red curve) and poisoned (p_{eg}, green curve) states. The corresponding theoretical curves (e),(f),(g),(h) are computed using the parameters $k_BT_b/E_T = 1$, $k_BT_{qp}/E_T = 0.01$, $\omega\tau_p = 0.8$, $\omega\tau_1 = 11$ and $\omega\tau_2 = 110$, yielding the relaxation times $\tau_p = 1.82\,\mathrm{ms}$, $\tau_1 = 25\,\mathrm{ms}$ and $\tau_2 = 250\,\mathrm{ms}$. The gap in the spectrum is $3k_BT_{qp}$. $\phi_{\rm sw} = \Phi + \gamma_{\rm max}$ with $\gamma_{\rm max} = \pi/2$.

4.5 . Conclusion

In conclusion, our investigation of the full switching current statistics of a bismuth nanoring Josephson junction provides an unprecedented look into Second Order Topological Insulators and the helical Andreev Bound States that are predicted to carry the supercurrent along spatially separated 1D hinges. Our detection around phase π, of switching events originating from both excited and ground states, on millisecond timescales, is a demonstration of slow relaxation of quasiparticles and, more spectacularly, of pairs. These features are an unambiguous signature of the topological protection provided by parity conservation in Quantum Spin Hall state-based Josephson junctions. In addition, the SOTI hypothesis of transport occurring through two Andreev hinge states of opposite helicities situated at two separate hinges is confirmed by the unusually long pair relaxation time as compared to the ones found in non-topological materials. We believe the full statistical measurement of the switching current is a simple yet powerful technique that will prove useful to investigate topology and correlations between current-carrying paths in a vast range of Josephson junctions, in particular based on 2DTI and other SOTI materials, such as WTe2 [150] and $\mathrm{Cd_3As_2}$ [160].

5 - General conclusion

My PhD work confirms and strengthens the claim of the existence of topologically protected 1d helical states in bismuth nanostructures, as predicted for a higher-order topological insulator. It gives new insights into the boundary states of Josephson junctions based on 2d TIs and 3d SOTIs, in particular on the role of helicity in the variations of the supercurrent with magnetic field as well as in the occupation dynamics of the junction.

With supercurrent interferometry, we confirmed the presence of three field scales corresponding to orbital dephasing between 1d ballistic states at small fields, to orbital dephasing within individual narrow states at large fields, and to both orbital and Zeeman dephasing at intermediate fields. Further analysis led to the identification of several mechanisms to explain the observed Josephson diode effects, including spin-orbit-coupling-induced anomalous Josephson effects.

With the analysis of the statistical distribution of the switching current, using a model of the occupation dynamics of a system with two helical hinge states developed in collaboration with theorists, we revealed a pair relaxation time $\tau_p \simeq 2ms$, two to three orders of magnitude larger than conventional Josephson junctions. We interpret this result as a proof of spatial separation between the two non-spin-degenerate helical Andreev state partners.

Lastly, with second harmonic transport response and switching current variations with magnetic field, we estimated a spin-orbit-coupling-induced magneto-chiral anisotropy both in the resistive and superconducting states of several samples, that we quantify with a (super)current-induced effective magnetic field $B_{eff}/I = \beta \sim 10 - 100G.\mu A^{-1}$.

The measurement and analysis methods developed during my PhD opened new experimental possibilities. These methods are currently used in the group for transport measurement of other predicted second-order TIs, such as WTe_2 and Bi_4Br_4, and start to bear their fruits. In addition to the experimental techniques developed in my PhD, other methods using contact-free detection schemes can be used. These contact-free measurements can be achieved by forming AC SQUIDs coupled to a microwave resonator [109, 70, 4, 106] or by detection of the small magnetization of the sample (embedded or not in an AC SQUID) in response to a magnetic field, using giant magnetoresistance sensors [105]. The insights from my PhD work are also useful for these different experiments.

6 - Appendix

6.1 . Topological insulators

In the Landau theory of phase transitions, the phases of matter are identified by an order parameter that can vary continuously. The topological phases are different, they are characterized by topological invariants, calculated from the structure of the ground state of the system, that can only take discrete values. This discrete character of topological invariants is an essential element of topological phases. Indeed, the physical properties in relation with a topological invariant are robust against perturbations that can't change its discrete value. Topological phases of matter feature general physics notions like the Berry curvature, deep quantum physics phenomenon like Majorana fermions and parity anomaly, as well as very practical applications like more efficient transduction processes and topological protection against perturbations.

For example, the integer quantum Hall effect arises when a 2d electron gas is put in a high magnetic field. It manifests by an insulating 2d bulk and an integer number of chiral states at the boundaries of the 2d system, propagating in one direction. These edge states conduct perfectly the current, resulting in a quantized conductance $G = n\frac{e^2}{h}$, $n \in \mathbb{Z}$. This conductance is topologically protected against perturbations like scattering on an impurity, and can't be changed without closing an energy gap in the bulk of the material. These properties justify its denomination as a topological insulator. This topological protection is used in metrology, as the quantized conductance relates the voltage to the current by fundamental physical constants.

In this section, I present key ideas to understand the topological nature of bismuth crystals and its implications on electronic transport. First, I introduce the most fundamental element of practical interest for transport : chiral edge modes. It will be done using the Dirac lattice picture. Second, I make the link between band inversion(s), topology and chiral edge modes by presenting the standard TKNN-Chern bulk-boundary correspondence. This part justifies the denomination of Topological Insulators (TI). Third, I extend this analysis to symmetry protected topological modes, among which are the time-reversal symmetric TI and the Topological Crystalline Insulators (TCI). Finally, I further extend it to Higher-Order Topological Insulators (HOTI), which include pure bismuth crystal, featuring topologically protected 1d helical states propagating on certain of its hinges.

6.1.1 . Lattice Dirac model and band inversion

Let us consider the simplest tight binding system that can exhibit Dirac equations and band inversion, that is the 1d Dirac chain with a unit cell featuring two states (referred to as atoms, orbitals, or bands depending on the context). For any two states model, the Bloch hamiltonian can be written as :

$$\hat{h}(\mathbf{k}) = \epsilon_0(\mathbf{k})\hat{1} + \mathbf{d}(\mathbf{k}).\hat{\boldsymbol{\tau}} \tag{6.1}$$

with $\hat{\boldsymbol{\tau}} = (\tau_x, \tau_x, \tau_z)$ and $\tau_{x,y,z}$ the Pauli matrices acting on the orbitals degree of freedom, and $\mathbf{d}(\mathbf{k})$ the Bloch vector.

For now, let us focus on the boundary between two regions with 1d Dirac cones gaped by a "mass" parameter m that changes sign. We consider a set of parallel 1d Dirac chains with linear dispersion along the x direction and varying parameter $m(y)$ along the y direction. We impose that $m(y)$ goes continuously and monotonously from a constant negative value at large negative y to a constant positive value at large positive y, as sketched in Fig.6.1a. The Bloch hamiltonian is :

$$\hat{h}(k_x, y) = \nu k_x \tau_y - i\hbar\eta\tau_x\partial_y + m(y)\tau_z \tag{6.2}$$

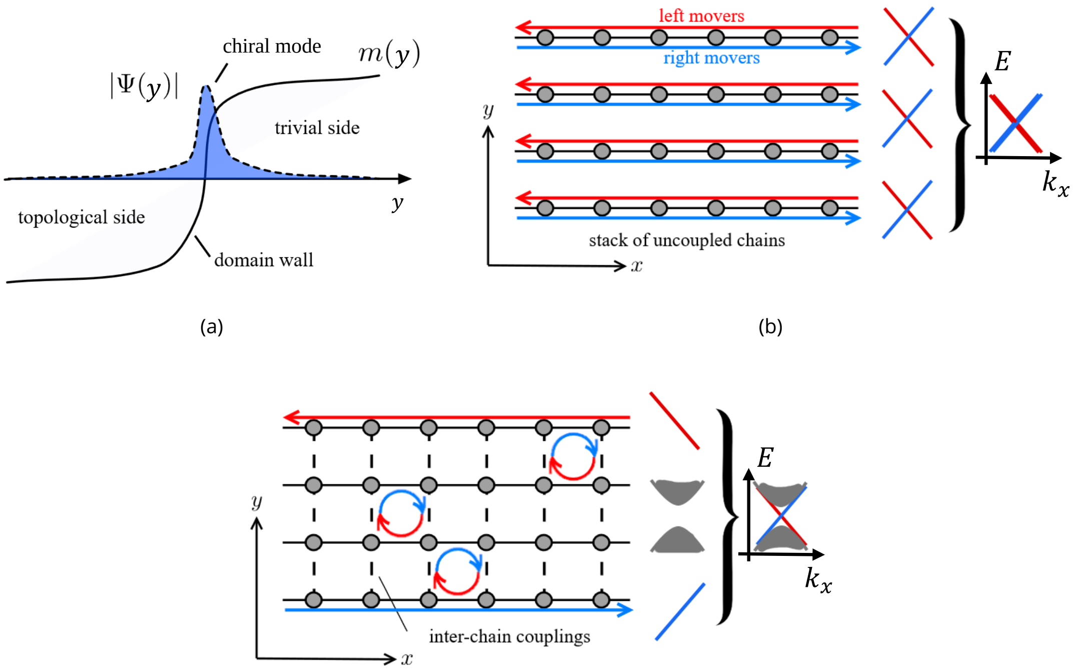

(a)

(b)

(c)

Figure 6.1 – Illustration of chiral edge states governed by a Dirac equation arising from time-reversal symmetry breaking in the bulk. (a) Sketch of a chiral edge state profile living at the boundary between two topologically unequivalent phases with band inversion. (b), (c) Sketches illustrating the emergence of chiral edge states from a lattice Dirac model with (c) and without (b) bulk chiral coupling terms between infinite 1d Dirac chains. The grey circles represent the atoms and the lines between them represent the hopping terms, in the tight binding approach. The arrows represent the propagation of an electron, as allowed by the hoppings between neighbors. The local and global spectrums are sketched in the right hand side, with gapless states with linear dispersion represented in blue (right movers) and red (left movers), and gaped bulk states represented in grey. Adapted from [161].

Considering first $k_x = 0$, this equation admits a solution at zero energy that writes :

$$|\psi(y)\rangle = \exp\left[\pm\frac{1}{\hbar\eta}\int_0^y m(y')dy'\right]\begin{pmatrix}1\\ \pm i\end{pmatrix} \tag{6.3}$$

where the $\pm$ sign relate to the sign of the $m(y)$ transition ($+$ from negative to positive with increasing y, and $-$ in the opposite situation). Introducing back $\nu k_x \tau_y$ as a perturbation, the first order correction to the energy of these solutions yields $E = \pm\nu k_x$.

It is a chiral mode localized at the boundary between $m(y) > 0$ and $m(y) < 0$, vanishing exponentially for large $|y|$, and whose propagation direction is determined by the sign of the $m(y)$ transition (from negative to positive in the present case). It has a linear dispersion relation and its energy can take any value, contrasting with the gaped spectrum of the chains with finite values of $m(y)$ at larger $|y|$. This chiral edge mode is protected against impurity scattering (disorder), as there exist no other mode to scatter with at the same energy, neither in the gaped bulk nor in the edge which propagates in one direction only. This chiral edge mode is the most fundamental element of practical interest for transport and is at the basis of every topologically protected boundary modes that propagates in TI.

This hamiltonian has the same form as a set of 1d Kitaev chains close to $k_x = k_y = 0$, with a chiral inter-chain coupling $\frac{\eta}{2}|n_y\rangle\langle n_y+1|(\tau_z + i\tau_x)$, where only chiral modes of opposite propagation direction are coupled [161]. Such a coupling breaks time-reversal symmetry and can be achieved by external or internal magnetic fields.

Fig.6.1b illustrates the situation of a set of parallel 1d Dirac chains without any inter-chain coupling ($\eta = 0$) and $m = 0$. In this case the spectrum is a massless (gapless) Dirac cone with a degeneracy corresponding to the number of chiral modes propagating in one or the other direction. It corresponds to $m(y) = 0$ everywhere in the material and the propagation isn't protected against backscattering at an impurity.

On the other hand, Fig.6.1c illustrates the same Dirac lattice but with chiral inter-chain coupling. It gaps out the bulk of the material (massive Dirac cones) but leaves one gapless chiral mode on each of the two edges, with opposite propagation directions. We recover the case of isolated chiral modes on the edge discussed before, and its protection against scattering. This type of behavior is very peculiar, with an insulating bulk and perfect conduction on the edges. We will see in the following that it is a common feature of topological insulator. This corresponds to $m(y) < 0$ everywhere in the bulk and $m(y) > 0$ outside the material. Because the mass term m characterizes the bulk gap and has a reversed sign compared to the exterior of the material, it is often thought of as a "band inversion". To complete the picture, a term $m(y) > 0$ in the bulk would yield a gaped bulk and gaped edge modes, referred as "trivial" insulator.

In this subsection, we found a tight binding model that exhibits very peculiar behavior, with an insulating bulk and chiral edge modes protected against disorder. This model requires the opening of a gap in a Dirac hamiltonian by a mass term that breaks time-reversal symmetry and introduces chirality. We found a connection between the sign of this mass term and the presence of the chiral edge modes. In the next subsection, we will clarify this connection and relate it to the topological Chern number.

6.1.2 . Bulk-boundary correspondence

We saw in the previous subsection how a Dirac mass term, a property of the bulk hamiltonian of a system, can dictate if the boundaries of a finite version of the system host a chiral state. In this part, we give the basic ideas to generalize this bulk-boundary correspondence. To do so, we restrict ourselves to system breaking time-reversal symmetry and insulating in the bulk, like the one discuss in the previous subsection or like in the Integer Quantum Hall Effect (IQHE).

There are two parts to establish bulk-boundary correspondence :
- spectral flow : relating a number computed from the knowledge of the bulk only to the edge states pro-

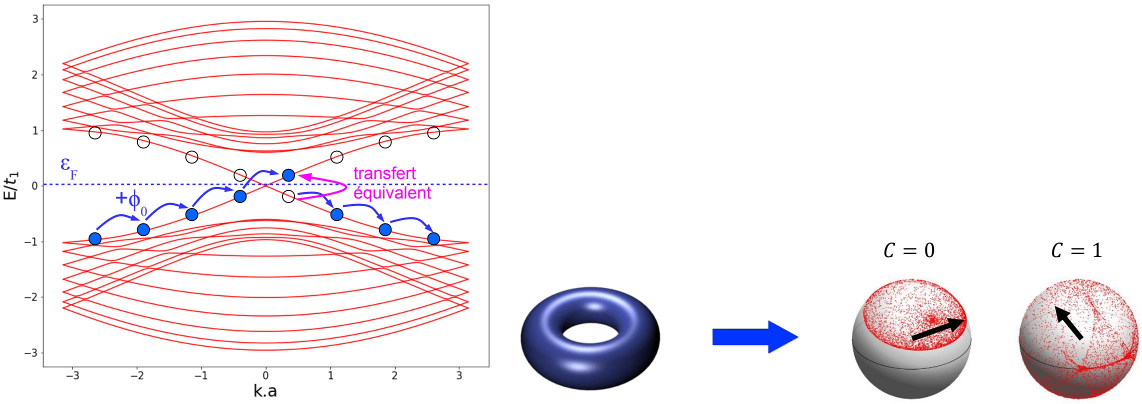

(a)

(b)

Figure 6.2 – (a) Illustration of the concept of spectral flow. Spectrum of an infinite ribbon in the x-direction with a topological TKNN-Chern invariant $\mathcal{C} = 1$ (background red lines). It features $2n = 2$ states crossing the bulk gap, corresponding to two counter-propagating topologically protected chiral states, $n = \mathcal{C} = 1$ on each edge. Wrapping the ribbon on itself along x yields quantized wavevectors (circles). Inserting a quantum of magnetic flux $\phi_0 = h/e$ move each state to its neighbor, effectively pumping n electrons (blue circles) from one edge to the other. (b) For a 2-band 2d system, illustration of the relation between the wavevector $\boldsymbol{k}$ living on the 2d surface of a torus (Brillouin zone) (left), and the 3d unit Bloch vector $\mathbf{s}(\mathbf{k}) = \frac{\mathbf{d}(\mathbf{k})}{||\mathbf{d}(\mathbf{k})||}$ living on the 2d surface of a sphere (right). The TKNN-Chern topological invariant $\mathcal{C}$ counts the number of wrapping of the sphere when $\boldsymbol{k}$ explores the whole torus. Adapted from [164].

tected against perturbations that do not close the gap
- Chern number : relating a number computed from the knowledge of the bulk only to a topological quantity (invariant under weak perturbation by disorder)

a) Spectral flow : Laughlin argument

First, the relation between the boundary states and a quantity computed from the bulk can be understood with the Laughlin argument [162], which is a special case of Thouless pump [163]. It goes as follows. We want to know, from a quantity calculated in the bulk, if a given 2d insulating material has topologically protected chiral states propagating on its edges. Take the 2d material you want to study, and wrap it on itself in one direction, say x, while living it with open boundaries in the other direction, say y. This forms a finite cylinder along y with two independent edges. Along x, the periodic boundary conditions result in a quantization of k_x.

By adding adiabatically exactly one quantum of magnetic flux $\Phi_0 = h/e$ inside the cylinder, all the occupied states at various k_x are moved to their neighbor at $k_x + 2\pi/L_x$, where L_x is the perimeter of the cylinder. The hamiltonian of the system $\hat{H}(\phi = 0) = \hat{H}(\phi = \Phi_0)$ is unchanged, but charges have been pumped between the states. If the system has n topologically protected chiral states propagating on its edges, there necessarily will be n states going up (one edge) in energy and n states going down (other edge). This is illustrated in Fig.6.2a with $n = 1$. So one edge gained n electrons while the other lost n electrons, which amounts to a transfer of n electrons between the two edges, through the insulating bulk. This is an illustration of the concept of spectral flow.

Now, can we relate this integer n to a property of the bulk ? The answer is yes. The n charges transferred between the two edges can be expressed as a current I_y along y generated by the electric field response

E_x along x to the insertion of the flux Φ. We can write $E_x = \frac{1}{L_x}\frac{d\Phi}{dt}$ and the current density $j_y = I_y/L_x$, yielding $j_y/E_x = \sigma_{xy} = I_y/\dot{\Phi}$, with σ_{xy} the Hall conductivity. In one cycle $\Delta\Phi = \Phi_0$ realized in a time ΔT, n charges have been transferred, thus $ne = I_y\Delta T = \sigma_{xy}\dot{\Phi}\Delta T = \sigma_{xy}\Phi_0$. Finally, we get :

$$\sigma_{xy} = n\frac{e^2}{h} \tag{6.4}$$

which relates a property of the bulk σ_{xy} to the number of topologically protected chiral states propagating on its edges. But how does it relate to a topological invariant ?

b) TKNN-Chern topological invariant

Now we want to calculate σ_{xy} in the bulk of our 2d material, which will give us the number of topologically protected chiral states propagating on its edges. Studying an infinite translation-invariant material, the eigenstates can be expressed as eigenstates of the Bloch hamiltonian labeled by a band index m and a wave vector $\boldsymbol{k} = (k_x, k_y)$: $|u_{\mathbf{k}}^{(m)}\rangle$

In Heisenberg representation, it is possible to show that the equation of evolution of the position of $|u_{\mathbf{k}}^{(m)}\rangle$ in the presence of an electric force $\mathbf{F} = q\mathbf{E}$ writes, at first order in $\mathbf{F}$ [164] :

$$\hbar\frac{d\mathbf{r}}{dt} = \hbar\mathbf{v}(\mathbf{k}) = \nabla_{\mathbf{k}}\mathcal{E}_{\mathbf{k}}^{(m)} + \mathbf{\Omega_m}(\mathbf{k}) \times \mathbf{F} \tag{6.5}$$

where $\mathbf{\Omega_m}(\mathbf{k}) = \nabla_{\mathbf{k}} \times \mathcal{A}_{\mathbf{m}}$ is the Berry curvature of band m, equivalent of a magnetic field in $\boldsymbol{k}$-space. $\mathcal{A}_{\mathbf{m}}(\mathbf{k}) = i\,\langle u_{\mathbf{k}}^{(m)}|\nabla_{\mathbf{k}}|u_{\mathbf{k}}^{(m)}\rangle$ is the Berry connection associated to the evolution of $|u_{\mathbf{k}}^{(m)}\rangle$ with $\boldsymbol{k}$ in the band m. $\nabla_{\mathbf{k}}\mathcal{E}_{\mathbf{k}}^{(m)}$ is the standard group velocity.

For a fully occupied band m with $\mathbf{F} = qE_x\hat{\boldsymbol{x}}$, the current $\boldsymbol{j}$ is oriented along y, and we have :

$$\frac{j_y}{E_x} = \sigma_{yx} = \frac{e^2}{h}\mathcal{C} \text{ with } \mathcal{C} = \frac{1}{2\pi}\iint_{BZ}\Omega_m(\mathbf{k})dk_x dk_y \tag{6.6}$$

where $\mathcal{C}$ is the TKNN-Chern number, introduced in [165]. The integral is over the full 2d Brillouin zone. Thus $\mathcal{C} = n$ by identification with Eq.(6.4).

The Brillouin zone is a torus, which is a closed surface. If $|u_{\mathbf{k}}^{(m)}\rangle$ can be defined using a single smooth gauge, then Green-Ostrogradski integral formula applies and $\nabla_{\mathbf{k}} \cdot (\nabla_{\mathbf{k}} \times \mathcal{A}_{\mathbf{m}}) = \mathbf{0} \implies \mathcal{C} = \mathbf{0}$ and $n = 0$, meaning that there is no topologically protected chiral states propagating on its edges. $\mathcal{C} \neq 0$ is an obstruction to finding continuous gauge throughout the surface of a 2d torus.

For a 2-band system, there is a nice visualization of the problem [166]. Eq.(6.1) implies that for each 2d wavevector $\boldsymbol{k}$ of the Brillouin zone (torus), there is an associated 3d Bloch vector $\mathbf{s}(\mathbf{k}) = \frac{\mathbf{d}(\mathbf{k})}{||\mathbf{d}(\mathbf{k})||}$ of unit length (Bloch sphere) and an eigenstate $|u_{\mathbf{k}}^{(m)}\rangle$ (SU(2)). It is illustrated in Fig.6.2b. If $\mathbf{s}(\mathbf{k})$ covers the whole sphere at least once when $\boldsymbol{k}$ explores the whole Brillouin zone, then the "hairy ball" theorem implies that there is at least one point in $\boldsymbol{k}$ (and on the sphere) where $|u_{\mathbf{k}}^{(m)}\rangle$ is ill-defined. In such a case, the integral operation requires the use of multiple gauges patched together, yielding $\mathcal{C} \neq 0$.

Actually, for a 2-band system, $\mathcal{C}$ has an alternative formula, well known by the mathematician as the number of wrapping of the Bloch sphere when $\boldsymbol{k}$ explores the whole Brillouin zone :

$$\mathcal{C} = \frac{1}{4\pi}\iint_{BZ}\mathbf{s}.[(\partial_{k_x}\mathbf{s}) \times (\partial_{k_y}\mathbf{s})]dk_x dk_y \tag{6.7}$$

This wrapping number is an integer number defining a topological invariant, making clear the connection between the number of topologically protected chiral states propagating on the edges n, the bulk Hall conductivity $n = \sigma_{xy}\frac{h}{e^2}$, and the topological TKNN-Chern invariant $n = \mathcal{C}$.

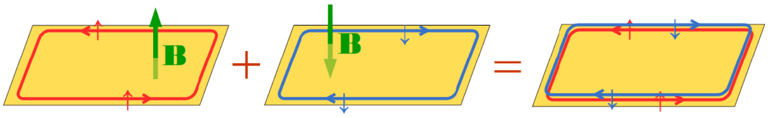

Figure 6.3 – Illustration of the process used to build a time-reversal symmetric topological insulator from two time-reversed conjugate copies of a Chern insulator with IQHE. Being spin-$\frac{1}{2}$ particle states and time-reversed version of each other, the two counter-propagating edge states can't couple to each other as long as TRS is preserved, thanks to Kramers' theorem. They form a helical pair of time-reversed states, called Kramers' pair. From [2].

6.1.3 . $\mathbb{Z}_2$ time-reversal invariant topological insulators

In the previous subsection, we introduced key ideas to relate the topology of the occupied states of the bulk, characterized by a topological invariant, to the number of chiral modes living on the boundary between two materials with different topological invariants. But because the topological invariant is proportional to the integral of the Berry curvature of the Brillouin zone, and the latter vanishes for time-reversal symmetric systems, it was long believed that such topological phases were limited to systems that break TRS.

However, in 2005, Kane and Mele [151] proposed the following idea : what if we build a system from two copies of spinfull TRS breaking TI which are the time-reversal conjugate of each others ? In that case, we have a TRS system with helical edge modes protected by TRS and Kramer's theorem. The situation is sketched in Fig.6.3, with a spin up chiral mode propagating in one direction and a spin down chiral mode propagating in the opposite direction.

To do so, they introduced in graphene a term $\lambda_I \kappa \tau_z \sigma_z$ ($\kappa = \pm 1$ for K or K' valleys, τ_z acting on orbital space, s_z acting on electron spin space) which respects all symmetries but breaks TRS for individual spin species. It yields two Chern numbers, one for spin up states $C_\uparrow$ and one for spin down states $C_\downarrow$, related by TRS such that $C_\uparrow = -C_\downarrow$. What makes it very interesting is that adding TRS terms that mix spin up and spin down components do not remove the helical edge mode (if the bulk gap did not close). This is a consequence of anti-unitary operators, and more specifically Kramer's theorem for spin-$\frac{1}{2}$ particles under time-reversal conjugation.

For a spin-$\frac{1}{2}$ particle, taking the time-reversal conjugation of its state can be written as the operator : $\mathcal{T}\left|\psi\right\rangle = -i\sigma_y \mathcal{K}\left|\psi\right\rangle$, with $\mathcal{K}$ the complex conjugation operation. Doing the operation twice yields $\mathcal{T}^2 = -1$. It is the key to Kramer's theorem, and we will present its meaning and consequences in two steps.

1 - If the system has TRS, it implies that if a state $\left|\psi\right\rangle$ is an eigenstate of the hamiltonian $H\left|\psi\right\rangle = E\left|\psi\right\rangle$, then $\mathcal{T}\left|\psi\right\rangle$ is also an eigenstate $H(\mathcal{T}\left|\psi\right\rangle) = E(\mathcal{T}\left|\psi\right\rangle)$. For the Bloch hamiltonian $h(\boldsymbol{k})$, it translates into $\mathcal{T}h(\boldsymbol{k})\mathcal{T}^{-1} = h(-\boldsymbol{k})$, so for an eigenstate $h(\boldsymbol{k})\left|\psi(\boldsymbol{k})\right\rangle = \mathcal{E}(\boldsymbol{k})\left|\psi(\boldsymbol{k})\right\rangle$ we also have $h(-\boldsymbol{k})(\mathcal{T}\left|\psi(\boldsymbol{k})\right\rangle) = \mathcal{E}(\boldsymbol{k})(\mathcal{T}\left|\psi(\boldsymbol{k})\right\rangle)$, that is $\mathcal{T}\left|\psi(\boldsymbol{k})\right\rangle$ is also an eigenstate of $h(-\boldsymbol{k})$ with the same energy $\mathcal{E}(\boldsymbol{k})$. For most of the spectrum, this implies a 2-fold degeneracy, where $\left|\psi(\boldsymbol{k})\right\rangle$ and $\mathcal{T}\left|\psi(\boldsymbol{k})\right\rangle$ are two different states.
But is it still true for time-reversal invariant momenta (TRIM), mapping a momentum to its itself by time-reversal operation $\boldsymbol{k} \longrightarrow -\boldsymbol{k}$? There are four TRIM in a 2d square lattice Brillouin zone.

2 - Kramer's theorem states that : for a TRS system with spin-$\frac{1}{2}$ particles, all states are at least 2-fold degenerate. It implies that as long as TRS is respected, no perturbation can lift the 2-fold degeneracy, even at TRIM.

Going back to the uncoupled spins picture illustrated in Fig.6.3, we see that Kramers theorem ensures that backscattering can't occur in the helical edge as long as TRS is preserved, because the two chiral modes composing the helical edge mode are TRS conjugate of each others (called Kramers partners, together forming a Kramers pair). We recover the topological protection of the chiral edge modes, but requiring the preservation of TRS.

As discussed by the authors [151], electron-electron interaction could break the protection against backs-

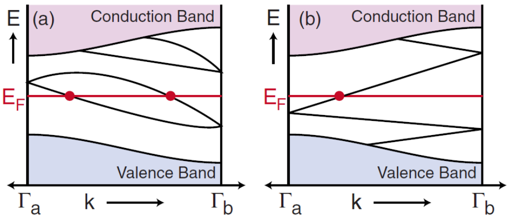

Figure 6.4 – Band structure of a bulk TRS system with a boundary parallel to $\boldsymbol{k}$ with edge states, between two TRIM points Γ_a and Γ_b. In (a) the number of edge states crossing the Fermi energy E_F is even, whereas in (b) it is odd. An odd number of crossings leads to a topologically protected Kramers pair of boundary states. From [168].

cattering in principle, but for weak interaction it is irrelevant under the renormalization group. Thus it does not lead to an energy gap or localization, in contrast with ordinary 1d wires. Nonetheless, electron-electron interaction allows inelastic scattering, yielding a reduced conductance $G < e^2/h$ for each edge. A more in depth discussion can be found in [167], together with a review on the advances on this type of topological insulators.

There are only two ways of connecting Kramers pairs from one TRIM to another TRIM, as illustrated in Fig.6.4 [168]. In Fig.6.4 left, they connect pairwise, crossing the Fermi energy an even number of times. These crossings aren't protected and can be removed by a change of parameters that do not close the bulk gap. In contrast in Fig.6.4 right, they cross the Fermi energy an odd number of times, in a way that cannot be eliminated. Coming back to the simple model of Kane and Mele with uncoupled spin up and down, the number of crossing is the difference between the number of states going up and down in energy, divided by 2 because we only consider one of the two Kramers partners :

$$\nu = \frac{C_\uparrow - C_\downarrow}{2} \quad mod\ 2 \tag{6.8}$$

The $mod\ 2$ in the above equation appears as a result of the Kramers theorem ultimately only protecting one Kramers pair. It defines a $\mathbb{Z}_2$ topological invariant. Even if a TRS term that couples up and down spins is added, it doesn't change the value of the topological invariant, unless a gap is closed in the process. For the specific situation of helical edge modes with spins quantized along a single direction, the introduction of a magnetic field parallel to this spin quantization axis does not break the topological protection as long as no bulk gap closes [169].

For TRS systems that can't be splitted into two time-reversed copies like this one, one has to find a way of counting the number of band inversion over the different TRIM. The general formula involves products of Pfaffian over all the TRIM, but Fu and Kane [58] proposed a simpler one for inversion symmetric systems :

$$(-1)^\nu = \prod_{\boldsymbol{k} \in TRIM} \prod_{n \in occ.} \xi_{\boldsymbol{k},n} \tag{6.9}$$

where ν is the topological invariant, and $\xi_{\boldsymbol{k},n}$ is the parity operator eigenvalue of the occupied band n at the TRIM $\boldsymbol{k}$. $\nu = 1\ mod\ 2$ corresponds to a topological insulator while $\nu = 0\ mod\ 2$ to a trivial insulator.

It is found that the topological $\mathbb{Z}_2$ classification of 2d TRS systems can be extended to 3d TRS systems, featuring 2d surface states with single (helical) Dirac cones protected by TRS. One way to do so is to deform the system into a set of Su-Schrieffer-Heeger chains, see [170] for more details. For an inversion-symmetric system, the Fu-Kane index Eq.(6.9) can be extended to 3d systems, where the product includes the additional TRIMs in the third dimension. One band inversion yields one Dirac cone at the surfaces, protected by TRS, while two band inversions yields two Dirac cones that can hybridize and gap out, thus not protected even with TRS.

In this subsection, we briefly showed how topological insulators with an integer number of chiral edge modes, characterized by a $\mathbb{Z}$ topological invariants, could be extended to time-reversal symmetric systems. This forms a new class of topological insulators, characterized by a $\mathbb{Z}_2$ invariant. For 2d systems, it is called Quantum Spin Hall Insulators (QSHI), with one helical pair of edge mode protected by TRS. For 3d systems, it is simply referred to as strong 3d Topological Insulators (3DTI), with 2d surface states with single (helical) Dirac cones protected by TRS. In the next subsection, we discuss the extension of these symmetry arguments to other symmetry protected topological insulators.

6.1.4 . Extension to other symmetry protected topological insulators

We saw in the previous subsection an example of a symmetry that plays a crucial role in the topological classification of materials. The symmetries of a crystalline system can be divided into two categories : exceptional symmetries and spatial symmetries [170, 171].

a) Exceptional symmetries : the 10-fold way

There are three exceptional symmetries, restricting the system, in particular the form of the Bloch hamiltonian $h(\boldsymbol{k})$:
- time-reversal symmetry (operator $\mathcal{T}$) : imposing $\mathcal{T}h(\boldsymbol{k})\mathcal{T}^{-1} = h(-\boldsymbol{k})$, relating states of identical energy and opposite momenta, it is an anti-unitary operator with $\mathcal{T}^2 = -1$
- particle-hole symmetry (operator $\mathcal{C}$) : imposing $\mathcal{C}h(\boldsymbol{k})\mathcal{C}^{-1} = -h(-\boldsymbol{k})$, relating states of opposite energies and opposite momenta, it is an anti-unitary operator with $\mathcal{C}^2 = -1$
- chiral symmetry (operator $\mathcal{S}$) : product $\mathcal{C}.\mathcal{T}$, relating states of opposite energies and identical momentum, it is unitary with $\mathcal{S}^2 = +1$

The three exceptional symmetries lead to the "10-fold way" classification of topological matter, that we do not develop further, as we focus in details on specific cases.

b) Spatial symmetries : Topological Crystalline Insulators

The spatial symmetries, among which mirror, n-fold rotational (C_n), and inversion symmetries, involve space groups. The spatial symmetries yield additional complexity, with specific protected boundary modes. Citing [172] : "[...] since a crystalline symmetry acts non-locally in space, it also maps different parts of the Brillouin zone onto each other. However, when there are submanifolds of the Brillouin zone which are left invariant by the action of the symmetry considered, we may evaluate a non-crystalline invariant on them, suited for the dimension and symmetry class of the corresponding submanifold, as long as we restrict ourselves to one of the symmetry's eigenspaces." This point deserves some attention as it is a key element to the understanding of Higher Order Topological Insulators.

In Topological Crystalline Insulators (TCI), the crystalline symmetry of a surface is needed to get massless Dirac cones, and is identical to the crystalline symmetry of the bulk crystal. Let us consider for example a lattice that is mirror symmetric along the y-direction, illustrated in Fig.6.5a. Its Brillouin zone has two (k_x, k_z) planes that are their own mirror symmetric image, at $k_y = 0, \pi$, see Fig.6.5b. In each of these planes, the eigenstates of the Bloch hamiltonian are also eigenstates of the mirror operator (with eigenvalues $\pm i$), defining two "mirror subspaces" of mirror-symmetric and mirror-antisymmetric eigenstates. At each of these special k_y slices, playing the same game as Kane and Mele for QSHI, we can define Chern numbers $C_\pm$ for the two mirror subspaces $\pm i$, with $C_\pm \neq 0$ even though the total Chern number $C = 0$ by TRS. A 2d system with this 2d bulk characteristic, parametrized by k_y, exhibits a $n_M(k_y) = \frac{C_+(k_y)-C_-(k_y)}{2}$ ("mirror Chern number") pairs of chiral states at its 1d boundaries, which is exactly the same formula as the Kane-Mele

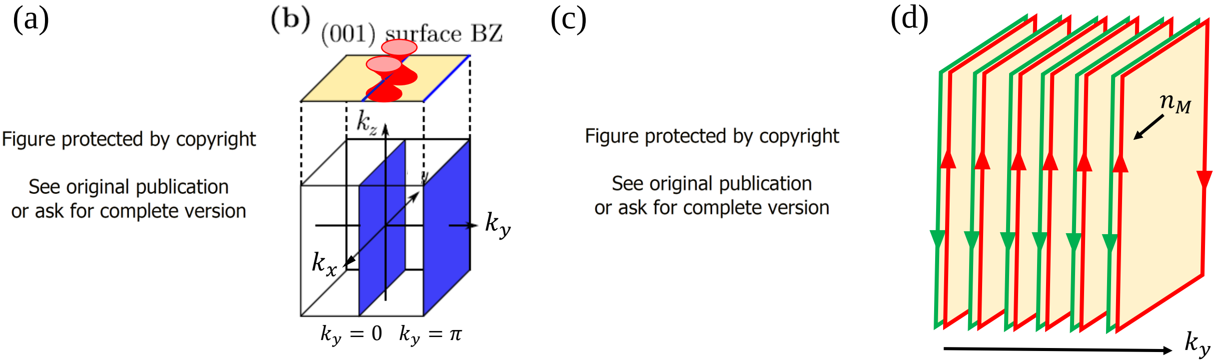

Figure 6.5 – Illustration of a TCI with mirror-symmetry-protection along y. (a)-(c) Adapted from [174]. (a) Simple cubic lattice with a mirror plane highlighted in turquoise. (b) Corresponding bulk Brillouin zone with the two mirror-invariant planes highlighted in blue. The (001) surface Brillouin zone is shown on top including the projections of the mirror-invariant planes. The spectrum close to $k_y = 0$ shows two Dirac cones if $n_M(k_y = 0) = 2$, see text. (c) Sketch of a nontrivial surface band structure along the projection of the $k_y = 0$ mirror-invariant plane, corresponding to a 2d system with the Bloch hamiltonian $h_{\text{bulk}}(k_x, k_y = 0, k_z)$, $n_M(k_y = 0) = 2$, and a boundary perpendicular to z, see text. (d) Stacking of finite 2d systems with the Bloch hamiltonian $h_{\text{bulk}}(k_x, k_y = 0, k_z)$ with $n_M(k_y = 0) = 2$. The so-built system has mirror symmetric surfaces along y and is translation-invariant in the same direction.

index (see Eq.(6.8)), but with mirror symmetry protection instead of time-reversal symmetry [173, 174, 172]. The spectrum of such a 2d system is sketched in Fig.6.5c for $k_y = 0$ and $n_M(k_y = 0) = 2$.

If you now consider a stack of such 2d systems along the y-direction, as illustrated in Fig.6.5d, the so-built system has mirror symmetric surfaces along y and is translation-invariant in the same direction. Thus, both the bulk and the surfaces acquire a quantum number k_y, allowing to make the connection with the 3d Brillouin zone discussion. At $k_y = 0$, the system is described as independent 2d slices with $n_M(k_y = 0) = 2$ chiral pairs circulating on the surface. Away from $k_y = 0$ however, the states do not map onto themselves in momentum-space anymore, and the symmetry protection is not guaranteed, analogous to the absence of protection by TRS away from the TRIMs in QSHI. Thus, the crossings at the Dirac points along x (see red and green lines in Fig.6.5c) are most likely lifted when $k_y \neq 0$, yielding $n_M(k_y = 0) \in \mathbb{Z}$ surface Dirac cones of states related by mirror-symmetry along y (analogous to the helicity in strong 3DTI), as illustrated in Fig.6.5b for the (001) surface Brillouin zone.

For the TCI with mirror symmetry described above (see Fig.6.5), it follows a $\mathbb{Z}$ classification, with (at least) $n_M(k_y = 0)$ Dirac cones on mirror-symmetric surfaces. For body-centered systems and face-centered systems, $k_y = 0$ is the only mirror symmetric plane, and there is only one mirror Chern number $n_M = n_M(k_y = 0)$ [175]. Considering now instead a surface $(0, \alpha, 1)$, the bulk maintains its mirror symmetric planes illustrated in Fig.6.5b, but their projections on the 2d surface Brillouin zone does not map on the 1d mirror-symmetric lines of the latter, resulting in no mirror-symmetry protection for the surface states, and possible hybridization. Thus, the topological protection is limited to mirror-symmetric surfaces.

6.1.5 . Higher-order topological insulators

Higher-Order Topological Insulators (HOTI(s)) are a new class of topological materials, that emerged between 2017 and 2018 [155, 176, 153, 177]. In fact, HOTIs are a special type of TCI with lower symmetry requirement for the surfaces [178], making them potentially more common than TCI with gapless surface states [179]. First-order topological insulators are n-dimensional systems with topologically protected $n-1$-dimensional boundary states in the bulk energy gap. HOTIs go beyond this picture, with boundary states of lower dimensionality. For a second-order TI (SOTI) of dimension n, it hosts topologically protected boundary

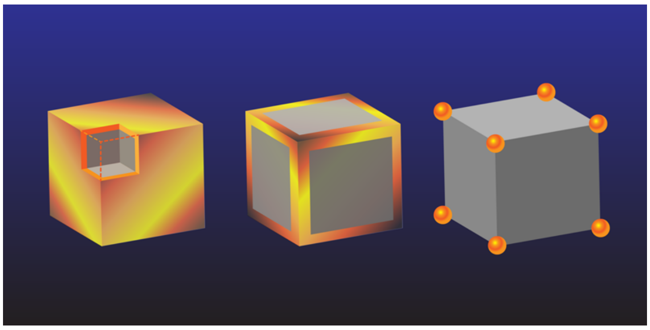

Figure 6.6 – (a) First-order strong 3d TI with insulating 3d bulk, and 2d surface states with one (helical) gapless Dirac cone. (b) Second-order TI with insulating 3d bulk, insulating 2d surfaces, and 1d hinge states with one helical pair of gapless states. (c) Third-order TI insulating everywhere, and 0d corner states in the gap. From Alan Stonebraker (APS).

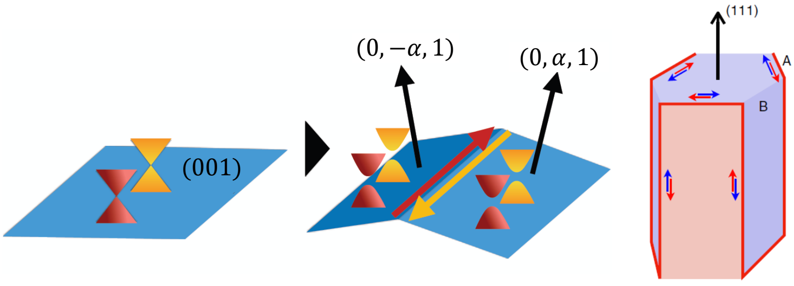

(a)

(b)

Figure 6.7 – Illustrations of the surfaces of a 3d HOTI. (a) Roof picture of a (001) surface with two Dirac cones protected by a spatial symmetry from hybridization (left), and resulting states when this symmetry is broken except at one hinge (right). It can represent either the surface of a TCI protected by mirror symmetry along y, or the surface of TRS 3d HOTI with double band inversion. The hinge hosts $n_M \in \mathbb{Z}$ pairs of counter-propagating states in the former, and $1 \in \mathbb{Z}_2$ helical pair of states in the latter. Adapted from [172]. (b) Schematic of the hinge states of a hexagonally shaped HOTI oriented along the trigonal [111] axis, with C_3 and inversion symmetry (such as bismuth). Red lines represent a single one-dimensional Kramers pair of gapless protected (helical) modes. In the Dirac picture of a HOTI surface, red and blue surfaces correspond to opposite signs of the unique TRS surface mass term m. From [13].

states of dimension $n-2$, that is corner states for a 2d SOTI and 1d propagating hinge states for a 3d SOTI, see Fig.6.6.

To understand HOTIs, let us consider again the TCI with mirror symmetry along y discussed in the previous subsection, illustrated in Fig.6.5. We saw that the mirror Chern number $n_M = \frac{C_+ - C_-}{2} = 2$ ensures the presence of two Dirac cones on the (001) surface, illustrated in Fig.6.5b top and Fig.6.7a left. If we consider a tilted surface $(0\alpha1)$, it breaks mirror symmetry on the surface and the Dirac cones are not protected anymore. But if we introduce a kink that locally preserves the mirror symmetry along y, as illustrated in Fig.6.7a right, n_M 1d Dirac cones survive on the hinge thus formed. To understand its protection(s) and its topological invariant, one can examine the effects of a minimal perturbation respecting the proper symmetries by stacking specific systems on top of each surface, as in [153]. This example shows how symmetry-protected boundary states two dimensions lower than the bulk can emerge.

This approach can be generalized to other symmetries. For inversion-symmetric systems (with TRS), the $\mathbb{Z}_2$ Fu-Kane index ν for strong first-order TIs (Eq.(6.9)) can be promoted to a $\mathbb{Z}_4$ topological index κ [175, 172] :

$$\kappa = \frac{1}{2} \sum_{\boldsymbol{k} \in \mathrm{TRIM}} (n_{\boldsymbol{k}}^{(+)} - n_{\boldsymbol{k}}^{(-)}) \;\; mod \;\; 4 \tag{6.10}$$

where $n_{\boldsymbol{k}}^{(\pm)}$ are the numbers of occupied bands with even $(+)$ and odd $(-)$ parity at each TRIM $\boldsymbol{k}$, counting only one of the two spin-degenerate bands. We have $\kappa \;\; mod \;\; 2 = \nu$. κ has four possible values :
- $\kappa = 0 \implies \nu = 0$ corresponds to a topologically trivial insulator
- $\kappa = 1, 3 \implies \nu = 1$ corresponds to a strong TI
- $\kappa = 2 \implies \nu = 0$ corresponds to a HOTI

To understand the case of a HOTI with $\kappa = 2$, let us consider an inversion and time-reversal symmetric 3d system with a double band inversion. This double band inversion is not captured by ν but results in $\kappa = 2$. Let us take a strong TI with $\nu = 1$ and one band inversion, and a copy of it. If the two TIs are not coupled, the whole system exhibit two Dirac cones on its 2d boundaries, for example on its (001) surface. These two Dirac cones are not protected against hybridization, reflecting the $\mathbb{Z}_2$ character of ν. If we now couple the two TIs, introducing a "mass" term m in the Dirac equation (there is actually only one way to do it given the Dirac hamiltonian and TRS [175], the surface states can be gaped out. Between two surfaces with masses of opposite sign however, there will be propagating 1d helical boundary modes at the hinge, just like the edge modes of a QSHI. For illustration, one can look at Fig.6.7a again, although the nature of the hinge states is different. The sign of the mass term of the surfaces depends on the system (as the bulk) and its symmetries. For bismuth with C_3, inversion, and time-reversal symmetries, the sign of the mass term is represented by the alternating colors of the crystal surfaces in Fig.6.7b. If two surfaces are related by inversion symmetry, inversion symmetry of the bulk imposes $m(-\boldsymbol{r}) = -m(\boldsymbol{r})$, guarantying the presence of at least one hinge mode somewhere, separating the two surfaces.

Bismuth single-crystal is the first 3d higher order topological insulator discovered [13], but is not the best as it is a semi-metal rather than an insulator and because its small gap at L-points can be easily inverted, as we will see in depth in the next section dedicated to it. We discuss in part 1.2.4 how its topological nature is still debated, making the work of this PhD relevant.

Shortly after bismuth, γ-WTe$_2$ was also investigated for its HOTI character, with questions similar to bismuth, with a QSHI phase in its monolayer form and a semi-metallic plus HOTI phase in its bulk form [180, 181, 150]. There are other material candidates for being 3d HOTIs with helical hinge states, but stable ones with a full bulk gap are scarce. Among them, α-Bi$_4$Br$_4$ is promising, featuring Van der Waals-coupled 1d chains [182, 183, 184]. Our team is currently experimenting with both WTe$_2$ and Bi$_4$Br$_4$ in addition to Bi.

HOTIs may be particularly well suited for topological quantum computation designs [185, 92], and some first steps have been realized in this direction on a hinge state of Bi proximitized by superconducting Nb and magnetic Fe [53].

6.2 . Inductances

We refer to something as an inductance L if it generates an effective flux Φ that scales with I : $\Phi = LI$. This terminology is consistent with the classical electrodynamics geometric inductance, as we will see. The inductance itself can depend on I. In SQUID measurements, the current depends on the flux through the surface of the SQUID. If inductive elements are present, the flux itself varies with the current. This kind of feedback effect can deform the response of the SQUID, shift its critical current versus magnetic field pattern, and even make some phase domain inaccessible or create hysteretic behavior in some cases. We give the physical origin, the approximate expression, and comment three types of inductive elements. The two mechanisms yielding inductive behavior are illustrated in Fig.6.8.

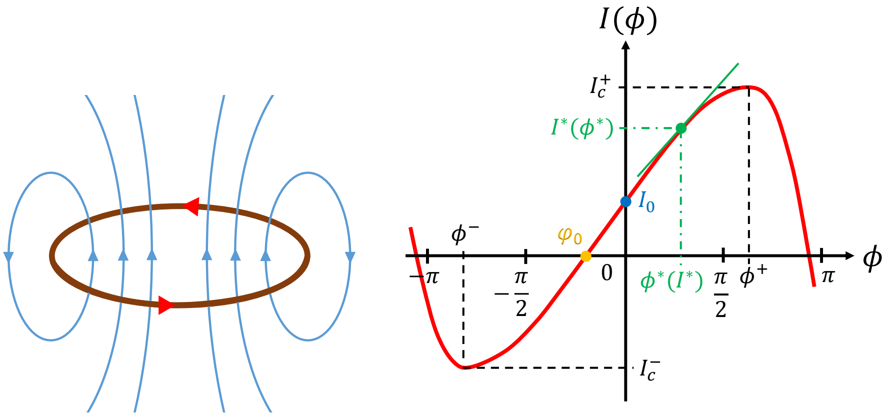

(a) (b)

Figure 6.8 – (a) Sketch of the magnetic field lines (blue lines) generated by a current circulating in a wire in a loop geometry (brown ring). The flux generated by the current add to the magnetic flux generated by an applied magnetic field through the surface of the ring. Illustrates self-field effect at the origin of geometric inductances. (b) CPR of a Josephson junction with the various conventions used to discuss phases shifts and critical current. The symmetry $I(\phi) = -I(-\phi)$ is broken when there is a magnetic field and AJE. Green solid line : derivative $dI/d\phi\rfloor_{\phi^*}$ of the CPR at the green point (I^*, ϕ^*). For a bias current I^*, the junction can be treated as a (kinetic) inductance $L_K(I^*) = \frac{\Phi_0}{2\pi}\frac{1}{dI/d\phi\rfloor_{\phi^*}}$.

a) Geometric self-inductance L_G of a current loop

Threading a current I through a wire generate of magnetic field B at point $\boldsymbol{r}$ via Ampere's law of magnetostatic : $\oint_{\boldsymbol{r}\in\partial\mathcal{S}} \boldsymbol{B}(\boldsymbol{r})\cdot d\boldsymbol{r} = \mu_0 I$, where the integral is over a closed loop $\partial\mathcal{S}$ encircling the wire section, and $\mu_0 = 4\pi\times 10^{-7}$ is the vacuum permeability. This effect is used to generate magnetic fields with coils. It is illustrated in Fig.6.8a. In the loop geometry, the magnetic field B_{ind} created is associated to a flux through the surface S of the loop : $\Phi_L = B_{ind}.S$. We can rewrite the flux in terms of the current through the wire :

$$\Phi_L = L_G I \tag{6.11}$$

with L_G called the geometric inductance. The flux generated by the current add with the flux generated by an external magnetic field $\Phi_{ext} = \boldsymbol{B}_{ext}\cdot\boldsymbol{S}$. This self-field effect do not need phase coherence and exists at the macroscopic scale. For loop geometries without contacts to impose a current, the response of the loop to a magnetic field is always diamagnetic and partially screens the magnetic field, such that we define the total flux :

$$\Phi_{tot} = \Phi_{ext} - LI \tag{6.12}$$

with L the total inductance, $L = L_G$ here.

Hence, L_G is always positive. Moreover, L_G only depends on the geometry of the system, and does not depend directly on current or magnetic field (there might be some situations where the geometry of the currents vary significatively with the current or the magnetic field). For a single cylindrical wire of radius r_w forming a ring of radius r_r, $L_G \sim \mu_0 r_r\left(\ln\frac{8r_r}{r_w} - 0.5\right)$ [186]. This give a typical value of $L_G \sim 0.2pH$ for

$r_r = 1\mu m$ (giving orbital dephasing oscillation period $\Delta B = \Phi_0/S \sim 7G$) and $r_w = 0.1\mu m.$

b) Geometric self-inductance L_A of an asymmetric current distribution

We saw in part 1.6 that introducing asymmetries in critical currents between two subjunctions with identical CPR can cause an asymmetric critical current versus magnetic field pattern of the full junction (DC SQUID). This type of asymmetry still leads to a maximum critical current at $B = 0$. But it does not include self-field effect. In [187], the authors calculate the self-field effect of a thin junction of thickness d and transverse dimension L and W under parallel magnetic field B_y with asymmetric local critical current profile $\mathcal{J}(x)$ (integrated along y) going from $\mathcal{J}(x) = 0$ to I, as shown in Fig.6.9.

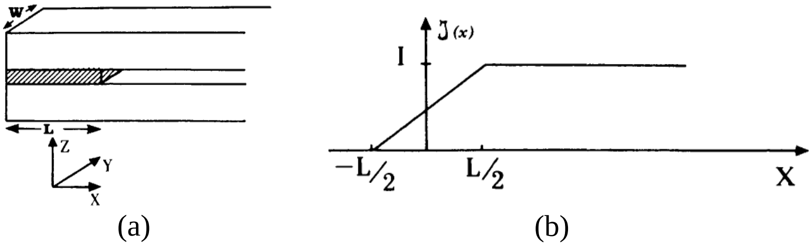

Figure 6.9 – Sketch of the junction geometry (a) used to estimate self-field effects under parallel magnetic field B_y with asymmetric critical current density profile $\mathcal{J}(x)$ (integrated along y) going from $\mathcal{J}(x) = 0$ to I (b). From [187].

They find a current-induced magnetic flux corresponding to an inductance $L_A \sim -\frac{2\pi L d}{cW}$. For a nanowire with $L = W$, $\frac{L_A}{d} \sim -\frac{2\pi}{c} \sim -2.1 \times 10^{-8} H.m^{-1}$. For a nanowire of length $d = 2\mu m$, we have $L_A \sim -4 \times 10^{-2} pH$. It results in an asymmetric critical current pattern, showing JDE, with a maximum shifted away from $B = 0$ by $B = -\frac{2\pi I_0}{cW}$, with I_0 the maximum critical current of the junction. Mind the various assumptions in [187]. Like the self-inductance L_G of a loop, L_A only depends on the geometry of the critical current through the junction. However, reversing the profile of $\mathcal{J}(x)$ also reverses the current-induced magnetic flux, yielding an L_A of opposite sign, explaining the negative inductance we found.

c) Kinetic inductance L_K

In classical electrodynamics, the inductance is defined as $L = \frac{V}{\frac{dI}{dt}}$. Combining it with the second Josephson equation (Eq.(1.18)), we write : $L = \frac{\frac{\Phi_0}{2\pi}\frac{d\phi}{dt}}{\frac{dI}{dt}}$, where ϕ is the superconducting phase difference. Finally, for a superconducting element with superconducting phase difference ϕ, we express it as :

$$L_K(I) = \frac{\Phi_0}{2\pi}\frac{1}{\frac{dI}{d\phi}} = \frac{\Phi_0}{2\pi}\frac{d}{dI}\phi(I) \tag{6.13}$$

where $\phi(I)$ is the inverse function of the CPR $I(\phi)$. We see that L_K scales as the inverse of the derivative of the CPR. Its sign follows $\frac{1}{\frac{dI}{d\phi}}$ close to $\phi(I)$ ($\simeq 0$ for low bias I compared to the maximum of the CPR), see Fig.6.8b. Considering the CPR of a Josephson junction, $L_K(I)$ is positive at zero magnetic field, but negative when it becomes a π-junction at higher field.

We identify the inductance effect related to the CPR of a junction as the "kinetic inductance". In a superconducting circuit, there are known junctions with known CPR, but there may also be unknown junctions with their own CPR playing a non-negligible role in the behavior of the circuit. The easiest way of including these unknown junctions in the analysis is to treat them as kinetic inductances. They introduce phase drops $\frac{2\pi}{\Phi_0} L_K(I)I$ in the circuit that can forbid some phase difference across the junctions of interest, as is discussed in parts 1.7.3 and 1.7.4. Notice that such kinetic inductances require phase coherence, which is greatly enhanced in superconducting materials. Contrasting with L_G and L_A, L_K depends on the shape of the CPR of the unknown junction, that may depend on both current, magnetic field magnitude, and magnetic field orientation. For example, the CPR of a tunnel junction is not linear, and is used as a non-linear inductance for QED and transmon Qbits.

The CPR of a superconductor is linear, giving a constant L, and a phase drop can occur if there is a supercurrent in the superconductor that we can't remove by a clever choice of loop (see Eq.(1.31) and part 1.5.1), like a constriction for example. More explicitly, the supercurrent density in a superconducting nanowire at zero temperature and zero field is $\boldsymbol{j}_S = \sigma \frac{\pi \Delta}{e} \boldsymbol{\nabla} \phi$. Writing $||\boldsymbol{\nabla}\phi|| \simeq \phi/l$ for a 1d wire, we get $I_S \simeq \frac{\pi\Delta}{eR_N}\phi$. Using Eq.(6.13), we get [188, 189, 124] :

$$L_{K,S} \simeq \frac{\hbar R_N}{2\pi\Delta} \tag{6.14}$$

For our W compound superconducting contacts, the typical resistance above T_c is $r \simeq 200\Omega.\mu m^{-1}$, and $\Delta \simeq 1.2meV$, yielding $L_{K,W} \simeq 17pH$ per μm.

On the other hand, a Josephson junction with critical current I_c corresponds to a kinetic inductance $L_{K,J} \sim \frac{\Phi_0}{I_c} = 207pH$ for $I_c = 10\mu A$. Lastly, many Josephson junctions in series can achieve very high inductance, as they can distribute the phase drop among all the junctions without changing much their current (phases add up while current is almost unchanged, just limited by the weakest junction), yielding a very low $dI/d\phi$, that is a very high $L_K(I) \propto \frac{1}{dI/d\phi}$.

Inductive elements change the response of a Josephson junction to a magnetic field, with self-field and superconducting phase drop effects. In the next subsections, we see how they influence differently AC and DC SQUID responses.

6.3 . Analysis of the W contamination range

In all the bismuth-based Josephson junctions studied during my PhD, the superconducting contacts are realized by Ga$^+$ Focused-Ions-Beam-assisted deposition (FIB) of a disordered tungsten compound, see part 2.4. During the FIB deposition process, the decomposed gas can diffuse out of the designed FIB writing region. Citing [2] : "This can lead to a layer of aggregated materials such as W, C, Ga, O, which is termed contamination. If this contamination is conducting, there is a chance that it can become superconducting at low temperatures either intrinsically or by proximity effect. A previous characterization study done by Alik Kasumov shows that this can be the case if the distance between the FIB deposited W contacts is smaller than 200 nm. Away from this distance the contamination contains mainly C, and is of similar nature than the contamination that can be induced by the electron beam of a SEM. It is therefore highly resistive and does not short the connected device [...]."

To complete this contamination study, we performed a careful analysis of several samples using a combination of Energy Dispersive Spectroscopy (EDS) and etching, both in Laboratoire de Physique des Solides d'Orsay (LPS) and with the expertise of Frank Fortuna in Institut des Sciences Moléculaires d'Orsay (ISMO).

EDS is an instrument that uses the scanning electron microscope to send high energy electrons (that is $\sim 10keV$ for low energy physics) with a few nm precision on a sample, and then collects secondary electrons. The difference in energy between the incident electron and the secondary electron corresponds to an energy absorbed by the sample. While energy absorption of the order of the eV can originate from various low-energy excitation processes near the Fermi energy (bands physics involving outer-electronic shells), energy absorption of the order of $1keV$ corresponds to transfer of energy with inner-electronic shells of the elements composing the sample. The energies of these inner-electronic shells are independent of the chemical bounding between the elements specific to each material, and are a signature of the different pure elements. Hence, EDS allows to estimate the chemical composition of a sample by looking at specific energy absorption peaks. However, the EDS data must be interpreted with caution, as our contamination range analysis shows.

At LPS, on the same chip as the nanoring :
1) With a spot on Bi with Ga+ FIB deposited W contacts, we found traces of W as far as $\simeq 1\mu m$ away from the W contact.
2) Comparing at equidistance of the same W nanowire, we found traces of W on Bi but not on substrate at $\simeq 300nm$, and traces of W on Bi and on substrate at $\simeq 110nm$.
Tests 1 and 2 suggest that there may be preferential deposition or diffusion of W contamination on Bi.

At LPS, on a different chip :
3) With a spot on Bi with He+ FIB deposited W contacts, we found traces of W $\simeq 500nm$ away from the W contact.
The He+ FIB, using helium ions instead of gallium ions, was designed to be much more precise than the Ga+ FIB, with a contamination range much smaller. The fact that we still detect W on Bi $\simeq 500nm$ away from the W contact suggests that it is not due to contamination.

At LPS, on the same chip as the nanoring :
4) With a spot on Bi with evaporated Au contacts, we found traces of Au $\simeq 600nm$ away from the Au contact.
Au contacts were deposited with the lithography technique described in part 2.5 and can't contaminate Bi on a distance of $\simeq 600nm$, also suggesting another explanation.

Thanks to these first test, and after discussions with specialists Franck Fortuna and Shamashis Sengupta, we concluded that it may be a manifestation of the diffusion of the electrons away from the illumination spot. Indeed, when measuring a spectrum from the illumination of a spot of bismuth, it excites and probes the chemical composition of the material much further away from the spot. The diffusion area depends on the atomic number of the elements of the sample and on the energy of the incident electrons. For heavy elements or low-energy incident electrons, the diffusion is shallower and broader compared to lighter elements or higher energy incident electrons. We tested this hypothesis as follows.

At LPS, on a chip from the same batch as the nanoring chip :
5) With a spot on substrate at $\simeq 300nm$ of a W wire, the W count was more important at incident electron energy of $13keV$ than $20keV$ (relative to a reference on W at both energies).
This test is consistent with the diffusion hypothesis, but does not exclude contamination at $\simeq 300nm$.

At ISMO, on the same chip as the nanoring, on a sample that melted :
6) At energy $13keV$, we measured W traces $\simeq 300nm$ away from a W nanowire contact at three spots, on Bi (close to point Pa R2 in Fig.6.10b), away from Bi on one side of the W nanowire (point Pa 1 in Fig.6.10b), and away from Bi on the opposite side of the W nanowire (mirror symmetric of point Pa 1 in Fig.6.10b with respect to the W nanowire axis). The traces of W on each side of the W nanowire, away from Bi, were identical. The traces of W at the Bi spot were higher.

After this reference step, we etched for a few seconds with the FIB on one side of the W nanowire, removing the surface layer on the Bi spot close to Pa R2 and on the spot Pa 1, but not on the mirror-symmetric spot of Pa 1, as visible in Fig.6.10a.

7) At energy $13keV$ again, we measured the same W traces $\simeq 300nm$ away from the W nanowire compared to test 6), at the same three spots.

If the W signal came from contamination of the surface $\simeq 300nm$ away from the W nanowire, the etching step would have removed this contamination and the W signals of test 6) and test 7) would have been different, as well as the W signals between spots on either sides of the W nanowire.

We conclude that the trace of W on the substrate $\simeq 300nm$ away from W and on Bi up to $\simeq 1\mu m$ away from the W contact are an artifact caused by diffusion of the electrons away from the spot. Moreover, we found that the contamination $\simeq 300nm$ away from W is negligible (i.e. undetectable with EDS) for the Ga+ FIB deposition conditions used for the chip with the nanoring. As we used the same Ga+ FIB deposition conditions for all our samples, we assume a W contamination range $< 300nm$ for all of them.

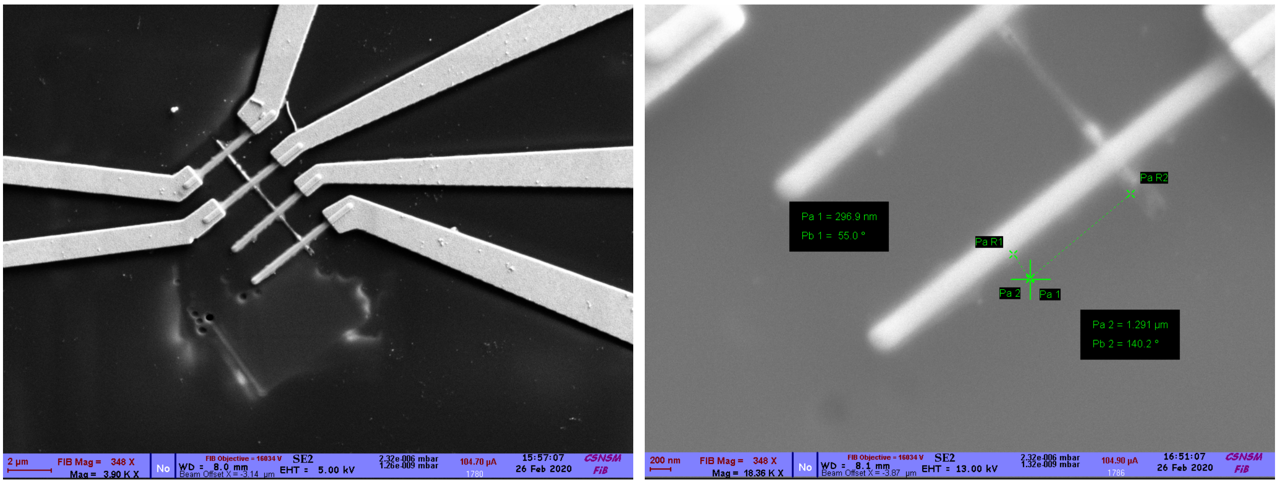

(a) (b)

Figure 6.10 – SEM image of a bismuth nanowire contacted with Ga+-FIB-deposited superconducting W compound and lithographed Au leads. The Bi nanowire melted during an experiment. It is on the same chip as the nanoring sample Bi^{ring}, and the W deposition was realized during the same session.

6.4 . Inductive DC SQUID calculations

The following sections present the complete analytical derivation of the interference pattern of two junctions with arbitrary values of critical current and inductances, as well as simple limits.

The analysis of the oscillation pattern is applied to the small field scale oscillations found in the bismuth-nanoring-based Josephson junction Bi^{ring}, which is introduced in chapter 3 and is the subject of an in-depth analysis in chapter 4. The goal is to find a set of parameters, possibly varying with the magnetic field, that reproduce the sawtooth modulations, their change of skewness, as well as the reduced amplitude around zero field.

The full derivation of the formulas has been done by Dr. Yang Peng, and reproduce the supplementary materials of our article [5], just published in Nature Physics.

6.4.1 . Analytical solution for two inductive branches

In this appendix, we provide the analytical solution of the critical current for the setup consisting of two branches, each containing a Josephson junction and an inductance (see Fig. 6.11(a)). Later on, we discuss the possibility of a highly inductive third branch in parallel, represented in Fig. 6.11(b).

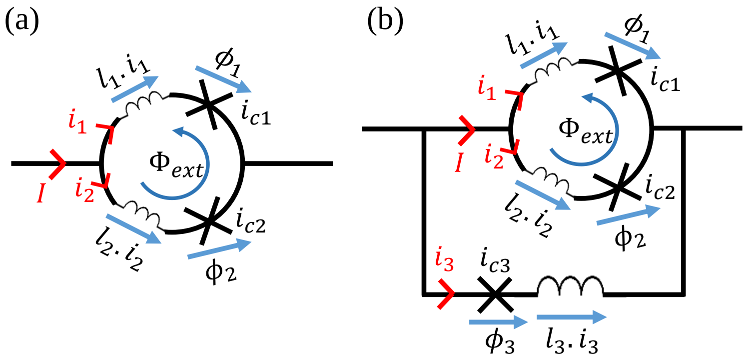

Figure 6.11 – (a) Sketch of the 2-branchs inductive SQUID model. (b) Sketch of the 3-branchs inductive SQUID model.

We write the total supercurrent as

$$I = i_{c1}\mathrm{Saw}(\phi_1) + i_{c2}\mathrm{Saw}(\phi_2), \tag{6.15}$$

where i_{c1} and i_{c2} are the critical currents of the two branches, and the superconducting phase differences at these two branches satisfy

$$\phi_1 - \phi_2 = \Phi + l_2 i_{c2}\mathrm{Saw}(\phi_2) - l_1 i_{c1}\mathrm{Saw}(\phi_1), \tag{6.16}$$

with $\Phi = 2\pi\Phi_{ext}/\Phi_0$, $l_{1,2} = 2\pi L_{1,2}/\Phi_0$. Here, Φ_{ext}, Φ_0 and $L_{1,2}$ are the external magnetic flux threaded between the two branches, the flux quantum $h/2e$, and the inductances in the two branches, respectively. The critical current is obtained by maximizing the total current in Eq. (6.15) given the constraint specified by Eq. (6.16). Note that the total current I is invariant if we simultaneously shift the two phases $\phi_{1,2} \to \phi_{1,2} + 2\pi$. Thus, without loss of generality, one can fix one of the phases, say ϕ_1 in the interval between $-\pi$ and π.

Using Eq. 6.16, one obtains the solution to ϕ_2 in terms of ϕ_1. However, such solutions are not unique, and can be expressed using an integer n, as

$$\begin{aligned} \phi_2 \equiv \phi_2^{(n)} &= \frac{\phi_1 + l_1 i_{c1}\mathrm{Saw}(\phi_1) - \Phi - 2\pi n}{1 + l_2 i_{c2}/\pi} + 2n\pi \\ &= \phi_1 \frac{\pi + l_1 i_{c1}}{\pi + l_2 i_{c2}} - \frac{\Phi + 2n\pi}{1 + l_2 i_{c2}/\pi} + 2n\pi, \end{aligned} \tag{6.17}$$

where in the second line we have used the condition that ϕ_1 is between $-\pi$ and π. The integer n in the above equation must satisfy

$$-\pi < \frac{\pi + l_1 i_{c1}}{\pi + l_2 i_{c2}}\phi_1 - \frac{\Phi + 2n\pi}{1 + l_2 i_{c2}/\pi} \leq \pi. \tag{6.18}$$

Instead of writing the total current I in Eq. (6.15) as a function of ϕ_1 and ϕ_2, one can write it as a function of ϕ_1 and an integer n, with the latter constrained by the above inequality. Hence, to obtain the critical current, one can maximize

$$\begin{aligned} I(\phi_1, n) &= i_{c1}\mathrm{Saw}(\phi_1) + i_{c2}\mathrm{Saw}(\frac{\pi + l_1 i_{c1}}{\pi + l_2 i_{c2}}\phi_1 - \frac{\Phi + 2n\pi}{1 + l_2 i_{c2}/\pi}) \\ &= (i_{c1} + i_{c2}\frac{\pi + l_1 i_{c1}}{\pi + l_2 i_{c2}})\phi_1/\pi - i_{c2}\frac{\Phi + 2n\pi}{\pi + l_2 i_{c2}}. \end{aligned} \tag{6.19}$$

with respect to ϕ_1 and n.

To maximize the above equation at a given Φ, we can perform a two-step maximization. We first fix ϕ_1, and find the integer n that maximizes I. We repeat this procedure at every ϕ_1 between $-\pi$ and π, and then find the ϕ_1 which leads to the largest I.

Maximization with respect to n at a given ϕ_1

We first perform maximization with respect to n at a given ϕ_1. The integer n that maximizes I at a given ϕ_1 is given by the smallest integer n_{min} satisfying the inequality (6.18). We find that

$$\frac{\pi + l_1 i_{c1}}{\pi + l_2 i_{c2}} \phi_1/\pi - \frac{2\pi n_{min} + \Phi}{\pi + l_2 i_{c2}} = \frac{\mathrm{Saw}((1 + l_1 i_{c1}/\pi)\phi_1 - l_2 i_{c2} - \Phi) + l_2 i_{c2}/\pi}{1 + l_2 i_{c2}/\pi}, \tag{6.20}$$

which gives

$$I = i_{c1}\phi_1/\pi + i_{c2} \frac{\mathrm{Saw}((1 + l_1 i_{c1}/\pi)\phi_1 - l_2 i_{c2} - \Phi) + l_2 i_{c2}/\pi}{1 + l_2 i_{c2}/\pi} \tag{6.21}$$

Note that here n_{min} is actually ϕ_1 dependent.

Maximization with respect to ϕ_1

We now perform the second step, by finding the ϕ_1 between $-\pi$ and π that leads to the maximal total current I in Eq. (6.21). We realize that the argument in the sawtooth function satisfies

$$-\pi + l_1 i_{c1} - l_2 i_{c2} - \Phi < (1 + l_1 i_{c1}/\pi)\phi_1 - l_2 i_{c2} - \Phi \leq \pi + l_1 i_{c1} - l_2 i_{c2} - \Phi, \tag{6.22}$$

and thus we will consider the following different scenarios separately.

1. When the external flux satisfies $2\pi > \Phi + l_2 i_{c2} - l_1 i_{c1} > 0$. Let us divide $\phi_1 \in (-\pi, \pi]$ into two regions. In the first region,

$$\pi \geq \phi_1 > \frac{l_2 i_{c2} + \Phi - \pi}{1 + l_1 i_{c1}/\pi}, \tag{6.23}$$

we have

$$(1 + l_1 i_{c1}/\pi)\phi_1 - l_2 i_{c2} - \Phi > -\pi. \tag{6.24}$$

Thus, the current in Eq. (6.21) becomes

$$I = i_{c1}\phi_1/\pi + i_{c2} \frac{(1 + l_1 i_{c1}/\pi)\phi_1/\pi - \Phi/\pi}{1 + l_2 i_{c2}/\pi}, \tag{6.25}$$

which is maximized at $\phi_1 = \pi$. We denote this maximized current as

$$I^{(1)} = i_{c1} + i_{c2} \frac{1 + l_1 i_{c1}/\pi}{1 + l_2 i_{c2}/\pi} - i_{c2} \frac{\Phi/\pi}{1 + l_2 i_{c2}/\pi} \tag{6.26}$$

$$= i_{c1} + i_{c2} + i_{c2} \frac{l_1 i_{c1} - l_2 i_{c2} - \Phi}{\pi + l_2 i_{c2}} \tag{6.27}$$

In the second region,

$$-\pi < \phi_1 \leq \frac{l_2 i_{c2} + \Phi - \pi}{1 + l_1 i_{c1}/\pi}, \tag{6.28}$$

we have

$$-3\pi < -\pi + l_1 i_{c1} - l_2 i_{c2} - \Phi < (1 + l_1 i_{c1}/\pi)\phi_1 - l_2 i_{c2} - \Phi \leq -\pi, \tag{6.29}$$

and thus the current in Eq. (6.21) becomes

$$I = i_{c1}\phi_1/\pi + i_{c2}\frac{(1 + l_1 i_{c1}/\pi)\phi_1/\pi - \Phi/\pi + 2}{1 + l_2 i_{c2}/\pi}, \tag{6.30}$$

which is maximized at

$$\phi_1 = \frac{l_2 i_{c2} + \Phi - \pi}{1 + l_1 i_{c1}/\pi}. \tag{6.31}$$

In this case, the maximized current is

$$\begin{aligned} I^{(2)} &= i_{c1}\frac{l_2 i_{c2} + \Phi - \pi}{\pi + l_1 i_{c1}} + i_{c2}\frac{(l_2 i_{c2} + \Phi - \pi)/\pi - \Phi/\pi + 2}{1 + l_2 i_{c2}/\pi} \\ &= i_{c2} + i_{c1} + i_{c1}\frac{i_2 i_{c2} - l_1 i_{c1} + \Phi - 2\pi}{\pi + l_1 i_{c1}}. \end{aligned} \tag{6.32}$$

Thus, the condition for $I^{(1)} \geq I^{(2)}$ is

$$i_{c2}\frac{l_1 i_{c1} - l_2 i_{c2} - \Phi}{\pi + l_2 i_{c2}} \geq i_{c1}\frac{l_2 i_{c2} - l_1 i_{c1} + \Phi - 2\pi}{\pi + l_1 i_{c1}} \tag{6.33}$$

which is

$$\Phi + l_2 i_{c2} - l_1 i_{c1} \leq \frac{2\pi i_{c1}(\pi + l_2 i_{c2})}{[i_{c2}(\pi + l_1 i_{c1}) + i_{c1}(\pi + l_2 i_{c2})]}. \tag{6.34}$$

2. When $-2\pi < \Phi + l_2 i_{c2} - l_1 i_{c1} < 0$, and if $\phi_1 \in (-\pi, \pi]$, we can again divide ϕ_1 into two regions. In the first region,

$$-\pi < \phi_1 \leq \frac{\pi + l_2 i_{c2} + \Phi}{1 + l_1 i_{c1}/\pi} \leq \pi, \tag{6.35}$$

we have

$$(1 + l_1 i_{c1}/\pi)\phi_1 - l_2 i_{c2} - \Phi \leq \pi. \tag{6.36}$$

In this case, we have

$$I = i_{c1}\phi_1/\pi + i_{c2}\frac{(1 + l_1 i_{c1}/\pi)\phi_1/\pi - \Phi/\pi}{1 + l_2 i_{c2}/\pi}, \tag{6.37}$$

which is maximized at

$$\phi_1 = \frac{\pi + l_2 i_{c2} + \Phi}{1 + l_1 i_{c1}/\pi}. \tag{6.38}$$

This leads to the maximal current

$$I^{(3)} = i_{c1}\frac{\pi + i_2 i_{c2} + \Phi}{\pi + l_1 i_{c1}} + i_{c2}\frac{(\pi + l_2 i_{c2} + \Phi) - \Phi}{\pi + l_2 i_{c2}} \tag{6.39}$$

$$= i_{c1} + i_{c2} + i_{c1}\frac{\Phi + l_2 i_{c2} - l_1 i_{c1}}{\pi + l_1 i_{c1}} \tag{6.40}$$

In the other region, if

$$\pi \geq \phi_1 \geq \frac{\pi + l_2 i_{c2} + \Phi}{1 + l_1 i_{c1}/\pi}, \tag{6.41}$$

we have

$$3\pi > (1 + l_1 i_{c1}/\pi)\phi_1 - l_2 i_{c2} - \Phi > \pi. \tag{6.42}$$

Hence, we have the total current

$$I = i_{c1}\phi_1/\pi + i_{c2}\frac{(1 + l_1 i_{c1}/\pi)\phi_1/\pi - \Phi/\pi - 2}{1 + l_2 i_{c2}/\pi}, \tag{6.43}$$

which is maximized at $\phi_1 = \pi$, giving rise to

$$I^{(4)} = i_{c1} + i_{c2} + i_{c2}\frac{l_1 i_{c1} - \Phi - l_2 i_{c2} - 2\pi}{\pi + l_2 i_{c2}}.$$

Thus, $I^{(3)} \geq I^{(4)}$ if

$$\Phi + l_2 i_{c2} - l_1 i_{c1} \geq \frac{-2\pi i_{c2}(\pi + l_1 i_{c1})}{[i_{c1}(\pi + l_2 i_{c2}) + i_{c2}(\pi + l_1 i_{c1})]}. \tag{6.44}$$

3. Without a surprise, we have

$$I^{(4)}(\Phi) = I^{(1)}(\Phi - 2\pi) \tag{6.45}$$

$$I^{(3)}(\Phi) = I^{(2)}(\Phi + 2\pi), \tag{6.46}$$

since the critical current should be 2π-periodic in Φ.

4. Defining $\Delta_{li} = l_1 i_{c1} - l_2 i_{c2}$, $\Delta\phi^+ = 2\pi \frac{i_{c1}(\pi + l_2 i_{c2})}{i_{c1}(\pi + l_2 i_{c2}) + i_{c2}(\pi + l_1 i_{c1})}$ and $\Delta\phi^- = 2\pi \frac{i_{c2}(\pi + l_1 i_{c1})}{i_{c1}(\pi + l_2 i_{c2}) + i_{c2}(\pi + l_1 i_{c1})}$, we can write the switching current as :

$$\boxed{I_c(\Phi) = \begin{cases} i_{c1} + i_{c2} + i_{c2}\frac{\Delta_{li} - \Phi}{\pi + l_2 i_{c2}} & \Phi \geq \Delta_{li} \\ i_{c1} + i_{c2} + i_{c1}\frac{\Phi - \Delta_{li}}{\pi + l_1 i_{c1}} & \Phi \leq \Delta_{li} \end{cases}} \tag{6.47}$$

The range of validity of this formula over a phase of 2π is given by :

$$\boxed{-\Delta\phi^- + \Delta_{li} \leq \Phi \leq \Delta\phi^+ + \Delta_{li}} \tag{6.48}$$

If Φ is outside this interval, then the critical current can be obtained by applying periodic property $I_c(\Phi) = I_c(\Phi + 2\pi)$.

For $\Phi = \Delta_{li}$

We simply get $I_c(\Phi) = i_{c1} + i_{c2}$ which is the maximum value of I_c over the 2π period. Without inductances, that is $l_1 = l_2 = 0$, the maximum of I_c is at $\Phi = 0$. Δ_{li} quantify the flux shift due to the screening in this inductive loop.

For $\Phi = \Delta_{li} + \Delta\phi^+ = \Delta_{li} - \Delta\phi^- + 2\pi$

$I_c(\Delta_{li} + \Delta\phi^+) = i_{c1} + i_{c2} - i_{c2}\Delta\phi^+/(\pi + l_2 i_{c2}) = i_{c1} + i_{c2} - 2\pi i_{c1} i_{c2}/[i_{c1}(\pi + l_2 i_{c2}) + i_{c2}(\pi + l_1 i_{c1})]$ which is the minimum value of I_c over the 2π period. Thus, the modulation amplitude is :

$$\Delta I = 2\pi i_{c1} i_{c2}/[i_{c1}(\pi + l_2 i_{c2}) + i_{c2}(\pi + l_1 i_{c1})] \tag{6.49}$$

For $\Delta_{li} \leq \Phi \leq \Delta\phi^+ + \Delta_{li}$

$I_c(\Phi) = i_{c1} + i_{c2} + i_{c2}\frac{\Delta_{li} - \Phi}{\pi + l_2 i_{c2}}$ which decreases with increasing Φ with a negative slope $-\alpha_2 = -i_{c2}/(\pi + l_2 i_{c2})$. This behavior occurs on a range of phase $\Delta\phi^+$.

For $-\Delta\phi^- + \Delta_{li} \leq \Phi \leq \Delta_{li}$

$I_c(\Phi) = i_{c1} + i_{c2} + i_{c1}\frac{\Phi - \Delta_{li}}{\pi + l_1 i_{c1}}$ which increases with increasing Φ with a positive slope $\alpha_1 = i_{c1}/(\pi + l_1 i_{c1})$. This behavior occurs on a range of phase $\Delta\phi^-$.

Using these observations, one can define a skewness coefficient as

$$S = (\Delta\phi^- - \Delta\phi^+)/2\pi \tag{6.50}$$

$S = 1$ ($S = -1$) when there is only a positive (negative) slope over the whole phase period. As defined, S does not depend on the modulation amplitude.

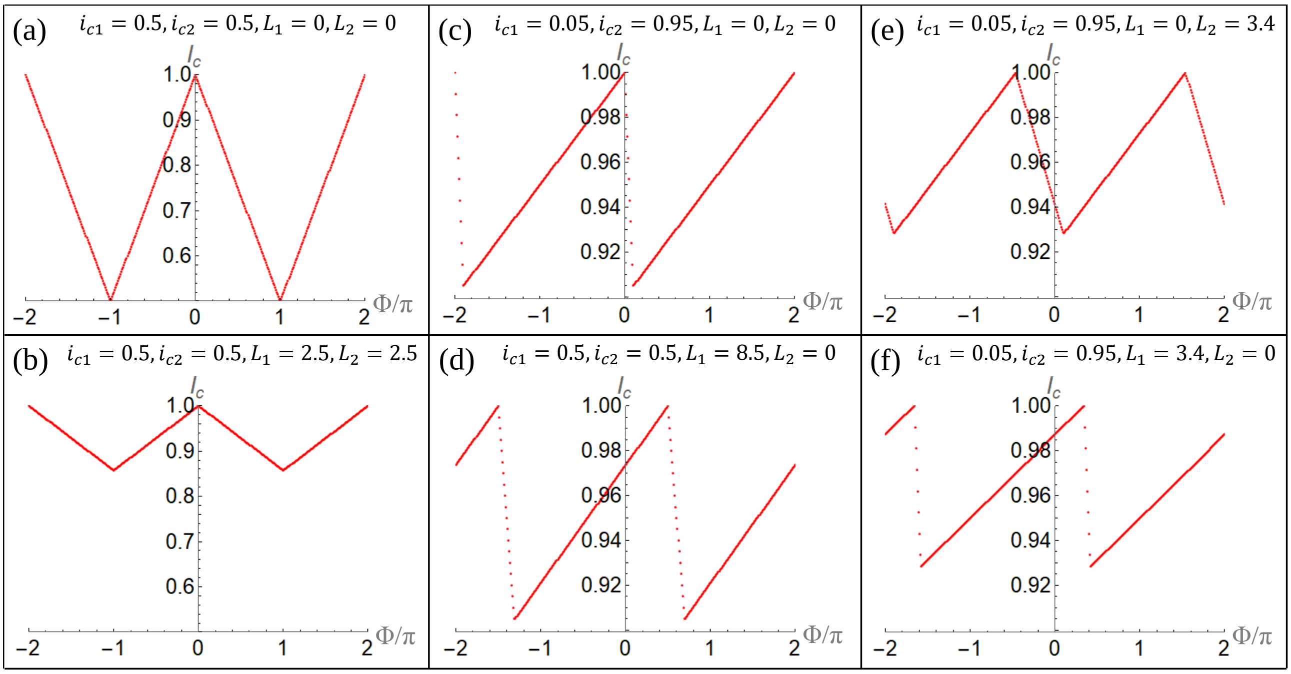

Figure 6.12 – Modulation of the switching current in several scenarios. Self-inductances are expressed in units of Φ_0 over one unit of current. (a) Symmetric case with no self-inductance. (b) Symmetric case with self-inductances. (c) Asymmetric case with $i_{c1} << i_{c2}$, no self-inductance. (d) Equal switching currents but self-inductance in one branch. (e) Asymmetric case with $i_{c1} << i_{c2}$, with self-inductance L_2 in the strongest branch. (f) Asymmetric case with $i_{c1} << i_{c2}$, with self-inductance L_1 in the weakest branch.

6.4.2 . Analytical solution for two inductive branches with equal critical current and equal inductance

When the critical currents of both branches are similar, $i_{c2} \simeq i_{c1} \simeq i_c$, and the inductances are equal, $l_1 \simeq l_2 \simeq l$, Equation (6.47) yields

$$I_c = i_c(2 - \mathrm{Saw}[\frac{|\Phi|}{1 + l i_c/\pi}]). \tag{6.51}$$

This corresponds to a triangular flux dependence, with a modulation amplitude smaller than without inductances :

$$(I_c^{\max} - I_c^{\max})/2i_c = \frac{1/2}{1 + 2Li_c/\Phi_0}. \tag{6.52}$$

This is illustrated in Fig. 6.12(a) and Fig. 6.12(b), without and with self-inductances, respectively.

The experimental variations plotted in Fig. 4.2 yield a critical current i_c given by $I_{c\max} = 2i_c = 2.8\ \mu A$. The symmetric modulation around zero field has an amplitude of 100 nA, yielding a ratio $Li_c/\Phi_0 \simeq 6.5$, and an inductance of $10\ nH$. Such a high inductance cannot be attributed to a mere geometrical inductance, but is probably caused by the high kinetic inductance of the W compound used as the superconducting contacts to the bismuth ring.

6.4.3 . Analytical solution in the limit of different critical currents, no inductances

In the asymmetric case of two very different critical currents in the two branches, to first approximation,

$$I_c = i_{c2} + i_{c1}\mathrm{Saw}[\Phi + \gamma_{max,2}], i_{c2} \gg i_{c1} \tag{6.53}$$

and

$$I_c = i_{c1} + i_{c2}\mathrm{Saw}[-\Phi - \gamma_{max,1}], i_{c1} \gg i_{c2}. \tag{6.54}$$

Thus, the critical current of the ring in this case is the CPR of the branch with the smallest critical current, shifted by a phase factor, added to a constant current given by the critical current of the branch with the highest critical current. This is illustrated if Fig. 6.12(c) in the case $i_{c2} \gg i_{c1}$. With sawtooth CPRs and no self-inductances, the skewness is $S = (i_{c2} - i_{c1})/(i_{c1} + i_{c2})$. Two sawtooth curves of opposite skewness are found for $i_{c2} \gg i_{c1}$ and $i_{c1} \gg i_{c2}$ respectively, since the two solutions correspond to indices 1 and 2 interchanged, and the opposite sign of the external flux.

Experimentally, we find in the positive skewness region $I_c^{max} = i_{c1} + i_{c1} \simeq 2.8\ \mu A$ and $\Delta I \simeq 0.18\ \mu A$. Eq. (6.49) with $l_1 = l_2 = 0$ leads to $2i_{c1}^2 - 2I_c^{max} i_{c1} + I_c^{max}\Delta I = 0$, where the solution with positive skewness is $i_{c1} \simeq 0.093\ \mu A$ and $i_{c2} \simeq 2.707\ \mu A$.

6.4.4 . Analytical solution in the limit of equal critical currents and different inductances

Inductance affects both the amplitude of the modulation and its skew. Let us consider the positive skewness condition : $S \gg 0$. Following Eq. (6.50), this means $\Delta\phi^- \gg \Delta\phi^+$, or $i_{c2}(\pi + l_1 i_{c1}) \gg i_{c1}(\pi + l_2 i_{c2})$. We can rewrite it $\pi(i_{c2} - i_{c1})/i_{c1}i_{c2} \gg l_2 - l_1$. In the case of $i_{c1} = i_{c2} = i_c$, then $S \gg 0$ when $l_1 \gg l_2$, and $\Delta I = \frac{i_c}{1+(l_1+l_2)i_c/2\pi}$. In Fig. 6.12(d), we illustrate a situation with asymmetric inductances that reproduce the skewness and the modulation amplitude of the asymmetric critical currents case shown in 6.12(c).

Experimentally, we find in the positive skewness region $I_c^{max} = i_{c1} + i_{c1} \simeq 2.8\ \mu A$ and $\Delta I \simeq 0.18\ \mu A$. The equation of ΔI with $i_{c1} = i_{c2} = i_c \simeq 1.4\ \mu A$ leads to $l_1 + l_2 = 2\pi(i_c - \Delta I)/i_c\Delta I \simeq 30.42$, that translate into $L \simeq 4.84\ \Phi_0/\mu A$.

6.4.5 . Effects of the inductance in the limit of strongly asymmetric critical currents

Taking again the positive skewness condition $S \gg 0$, we have $l_1 + \pi(1 - i_{c1}/i_{c2})/i_{c1} \gg l_2$. In the limit $i_{c2} \gg i_{c1}$, it can be approximated to $l_1 i_{c1} + \pi \gg l_2 i_{c1}$. Notice here that this inequality does not involve $l_2 i_{c2}$ but $l_2 i_{c1}$. Thus, in the present limit $i_{c2} \gg i_{c1}$, an inductance l_2 in the strong branch tends to symmetrize the modulations but its effect is weighted by i_{c1}. On the other hand, an inductance l_1 in the weak branch tends to increase the asymmetry of the modulations and its effect is also weighted by i_{c1}.

For the modulation amplitude, the role of the inductance is the same whether it is in the strong (l_2) or the weak (l_1) branch. Indeed, one can write : $\Delta I = 2\pi i_{c1}i_{c2}/[\pi(i_{c1} + i_{c2}) + (l_1 + l_2)i_{c1}i_{c2}]$.

Finally, inductance also induces a phase shift $\Delta_{li} = l_1 i_{c1} - l_2 i_{c2}$. In the limit $i_{c2} \gg i_{c1}$, the influence of l_2 is more striking compared to l_1.

These effects are illustrated in Fig. 6.12(e) and 6.12(f).

6.4.6 . Inclusion of variations with magnetic field of the critical currents or the inductances

To reproduce the experimental variations of the switching current, we need to include variations of the critical currents of both branches with magnetic field. This variation could stem from two interfering hinge states in each branch rather than a single one, for instance because they are laterally separated, and therefore the superconducting phase differs at the interface with the superconducting contact (see Fig.6.13 for an illustration of simple varying critical currents). The justification of such a field variation of the critical current is discussed in the sections 6.6.4 and 6.6.4. To obtain a smaller modulation amplitude around zero

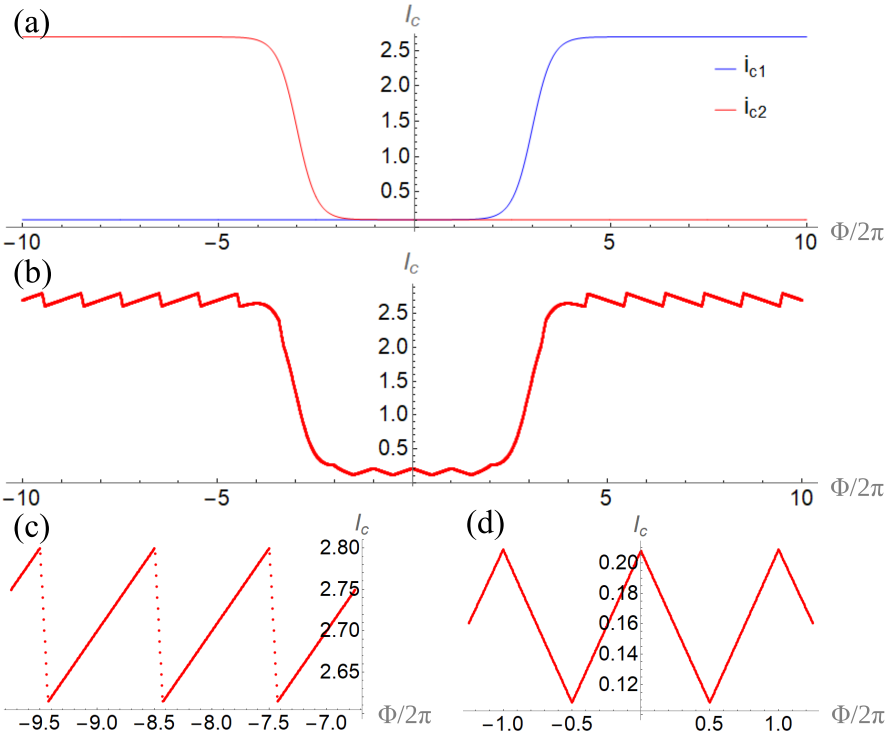

Figure 6.13 – Calculation that reproduce the observed short-range modulations, with i_{c1} and i_{c2} varying in field as displayed in (a), and constant $L_1 = L_2 = 0.192\,\Phi_0/\mu A$. $i_{c1}(0) = i_{c2}(0) = 0.104\,\mu A$ (b) Critical current of the 2-branches model with these parameters. (c) Zoom in the negative field region. (d) Zoom in the 0-field region.

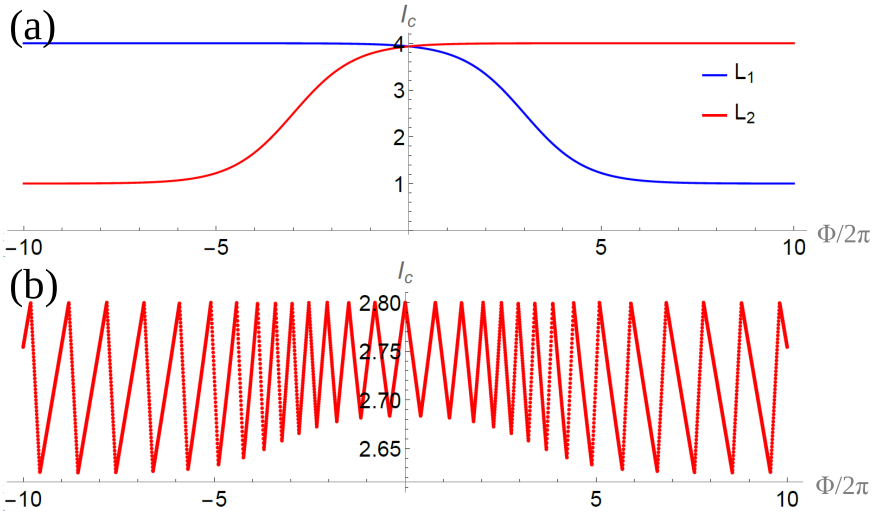

Figure 6.14 – (a) Sub-junctions inductances L_1 and L_2 (in units of $\Phi_0/\mu A$) as a function of magnetic flux. (b) Junction total critical current as a function of magnetic flux, with magnetic field dependent sub-junctions inductances as displayed in (a). $I_{c1} = I_{c2} = 1.4\mu A$.

field, one need to include a decrease of total critical current or an increase of inductance in this region of field.

The variations seen in the experiment could also be reproduced qualitatively if one supposes that the inductances, rather than the critical currents, vary in each branch with magnetic field. The result with this hypothesis is displayed in Fig. 6.14.

6.4.7 . Conclusion for the small field scale oscillations of the switching current of Bi^{ring}

In conclusion, the experiment can be interpreted by assuming that the ring's critical current is due to interference between the supercurrent in the two branches of the ring, given the three following conditions : i) The hinge states in each branch have a sawtooth supercurrent-versus-phase relation, as expected for topologically protected hinge states. ii) The critical current in each branch varies with magnetic field on a field scale much greater than one flux quantum through the ring area. iii) At least one of the branch of the ring contain a high inductance L. Inductive sections in the ring are required to explain the partial (5 to 30 percent, depending on magnetic field) rather than full modulation of the ring's critical current. We suggest that the contact region may be responsible for the inductive sections. Indeed, it is known that a granular, discontinuous W deposit extends roughly 100 nm on either side of the W wire. This contact region can be modeled by a one-dimensional array of Josephson junctions in series, each junction having a size of order ξ_W, the superconducting coherence length of W. This array of Josephson junctions contributes a kinetic inductance L_K in series with the Bi ring, of the order of $L_K = 2\pi N\Phi_0/i_c$ where N is the number of Josephson junctions in the array and i_c the typical critical current of a W grain. A typical i_c, as estimated by resistance jumps observed in several junctions well above the critical current of bismuth nanowires, but below the critical current of the W wires themselves (which is in the hundred μA range), is of the order of i_c= 10 μA. Taking N=30 could explain an inductance L of the order of $10\ nH$ in each branch of the ring, which is what is needed to explain our findings. In addition, the strong spin-orbit interaction in bismuth could also play a role, but further theoretical investigations are needed to ascertain this point.

6.5 . Calculations in 3d with different coordinate systems

Depending on what is the most suitable to analyze the experiment, we will use three different coordinate systems (see Fig.6.15 for illustration and conventions) :

- the cartesian system, with the orthonormal basis ($\vec{e}_x$,$\vec{e}_y$,$\vec{e}_z$) ($\vec{e}_x$ is the unit vector parallel to the horizontal plane, parallel to the $0°$ axis. $\vec{e}_y$ is the unit vector parallel to the horizontal plane, perpendicular to $\vec{e}_x$. $\vec{e}_z$ is the unit vector parallel to the vertical axis, perpendicular to both $\vec{e}_x$ and $\vec{e}_y$.)
- the cylindrical system, with the orthonormal basis ($\vec{e}_r$,$\vec{e}_\varphi$,$\vec{e}_z$) ($\vec{e}_r$ is the unit vector parallel to the projection of the vector in the horizontal plane. $\vec{e}_\varphi$ is the unit vector parallel to the horizontal plane, perpendicular to $\vec{e}_r$. $\vec{e}_z$ is the unit vector parallel to the vertical axis, perpendicular to both $\vec{e}_r$ and $\vec{e}_\varphi$.)
- the spherical system, with the orthonormal basis ($\vec{e}_\rho$,$\vec{e}_\theta$,$\vec{e}_\varphi$) ($\vec{e}_\rho$ is the unit vector parallel to the vector. $\vec{e}_\varphi$ is the unit vector parallel to the horizontal plane, perpendicular to $\vec{e}_r$. $\vec{e}_\theta$ is the unit vector perpendicular to both $\vec{e}_r$ and $\vec{e}_\varphi$.)

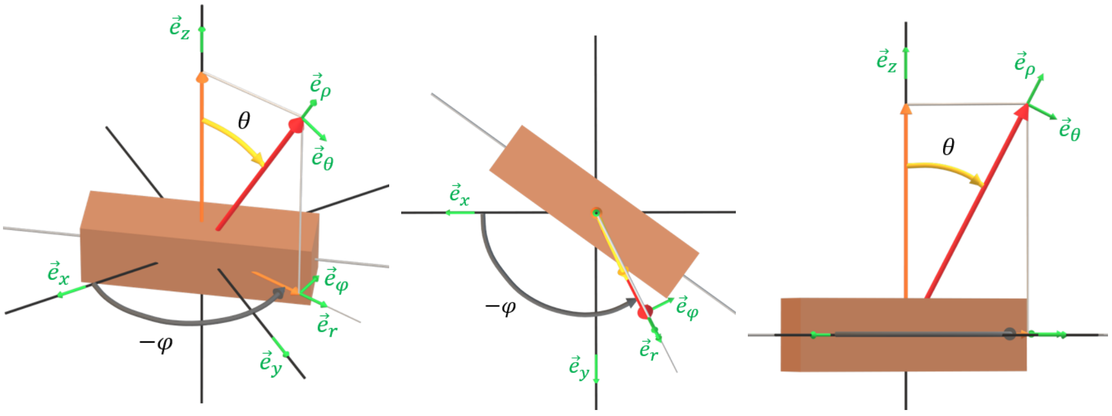

(a) (b) (c)

Figure 6.15 – Sketch to illustrate the decomposition of a vector in the cartesian, cylindrical, and spherical basis. The red arrow is the vector to decompose. The orange arrows are the projection of the vector on the vertical axis and the horizontal plane. The small green arrows are unit vectors of the three basis. The dark grey curved arrow represents the polar angle $-\varphi$ between the reference $0°$ axis and the projection of the vector on the horizontal plane. The yellow curved arrow represents the azimuthal angle θ between the vertical axis and the vector. (a) 3d view. (b) Top view of the x-y plane. (c) Side view of the plane parallel to the vertical axis and to the vector.

A given vector $\vec{V}_{\{\rho,\theta,\varphi\}}$ expressed in spherical coordinates can be written in cartesian coordinates using the matrix $R_{C\leftarrow S}(\theta,\varphi)$, such that :

$$\vec{V}_{\{x,y,z\}} = R_{C\leftarrow S}(\theta,\varphi).\vec{V}_{\{\rho,\theta,\varphi\}} = \begin{bmatrix} \vec{e}_\rho.\vec{e}_x & \vec{e}_\theta.\vec{e}_x & \vec{e}_\varphi.\vec{e}_x \\ \vec{e}_\rho.\vec{e}_y & \vec{e}_\theta.\vec{e}_y & \vec{e}_\varphi.\vec{e}_y \\ \vec{e}_\rho.\vec{e}_z & \vec{e}_\theta.\vec{e}_z & \vec{e}_\varphi.\vec{e}_z \end{bmatrix}.\vec{V}_{\{\rho,\theta,\varphi\}}$$

$$\vec{V}_{\{x,y,z\}} = \begin{bmatrix} \sin\theta\cos\varphi & \cos\theta\cos\varphi & -\sin\varphi \\ \sin\theta\sin\varphi & \cos\theta\sin\varphi & \cos\varphi \\ \cos\theta & -\sin\theta & 0 \end{bmatrix}.\vec{V}_{\{\rho,\theta,\varphi\}}$$

Similarly, a given vector $\vec{V}_{\{r,\varphi,z\}}$ expressed in cylindrical coordinates can be written in cartesian coordinates using the matrix $R_{C\leftarrow P}(\varphi)$, such that :

$$\vec{V}_{\{x,y,z\}} = R_{C\leftarrow P}(\varphi).\vec{V}_{\{r,\varphi,z\}} = \begin{bmatrix} \vec{e}_r.\vec{e}_x & \vec{e}_\varphi.\vec{e}_x & \vec{e}_z.\vec{e}_x \\ \vec{e}_r.\vec{e}_y & \vec{e}_\varphi.\vec{e}_y & \vec{e}_z.\vec{e}_y \\ \vec{e}_r.\vec{e}_z & \vec{e}_\varphi.\vec{e}_z & \vec{e}_z.\vec{e}_z \end{bmatrix}.\vec{V}_{\{r,\varphi,z\}} = \begin{bmatrix} \cos\varphi & -\sin\varphi & 0 \\ \sin\varphi & \cos\varphi & 0 \\ 0 & 0 & 1 \end{bmatrix}.\vec{V}_{\{r,\varphi,z\}}$$

The magnetic field is described with three parameters in spherical coordinates : a magnitude B_ρ, a polar angle φ corresponding to an angle in the horizontal plane between the horizontal coil axis and a reference line on the dilution head (with anti-trigonometric convention looking from the top-side of the chip), and an azimuthal angle θ corresponding to an angle away from the vertical axis ($\vec{e_z}$). Varying the proportion between vertical and horizontal field changes the azimuthal angle θ of the magnetic field vector $\vec{B}$, and rotating the sample by rotating the dilution changes its polar angle φ.

The magnetic field vector $\vec{B}$ is first expressed with spherical coordinates $\vec{B}_{\{\rho,\theta,\varphi\}} = B_\rho \vec{e}_\rho + 0\vec{e}_\theta + 0\vec{e}_\varphi = \begin{bmatrix} B_\rho & 0 & 0 \end{bmatrix}$ and then decomposed in the cartesian basis $\vec{B}_{x,y,z} = R_{C\leftarrow S}(\theta,\varphi).\vec{B}_{\{\rho,\theta,\varphi\}} = B_\rho \sin\theta\cos\varphi \vec{e}_x + B_\rho \sin\theta \sin\varphi \vec{e}_y + B_\rho \cos\theta \vec{e}_z$.

Doing the same for the surface vector $\vec{S}$, the scalar product can be written :

$$\vec{B}.\vec{S} = B_\rho S_\rho \left[\sin\theta\cos\varphi\sin\theta_S\cos\varphi_S + \sin\theta\sin\varphi\sin\theta_S\sin\varphi_S + \cos\theta\cos\theta_S\right] \tag{6.55}$$

Writing $\varphi = \varphi_S + \varphi'$, we get :

$$\vec{B}.\vec{S} = B_\rho S_\rho \sin\theta\sin\theta_S\cos\varphi' + B_\rho S_\rho \cos\theta\cos\theta_S \tag{6.56}$$

where φ' is the angle between the projections of $\vec{B}$ and $\vec{S}$ in the horizontal plane.

With $\vec{B}$ in cylindrical coordinates, it is : $\vec{B}.\vec{S} = B_r S_\rho \sin\theta_S \cos\varphi' + B_z S_\rho \cos\theta_S$.

6.6 . Supplementary sample information

6.6.1 . Switching current of nanowire Bi$_{21}^{wire}$ as a function of field direction

In this appendix, we give more details on the switching current of the bismuth-nanowire-based Josephson junction Bi$_{21}^{wire}$ as a function of field direction.

The fixed $B_z = 2270\ G$ measurements shown in Fig. 6.16a provides additional data for the rescaling behavior. Indeed, orbital dephasing involves the effective flux $\vec{B}.\vec{S}$ which can be written as :
$\vec{B}.\vec{S} = B_r S_\rho \sin\theta_S \cos\varphi' + B_z S_\rho \cos\theta_S$, with $\varphi' = \varphi - \varphi_S$. See appendix 6.5 for conventions.

In this set of measurements, we vary only B_r and φ'. $B_z S_\rho \cos\theta_S$ acts as a constant shift in the switching current vs magnetic field patterns, that is the same for every horizontal angle φ'. On the other hand, $S_\rho \sin\theta_S \cos\varphi'$ acts as a rescaling factor and makes for a simple way to determine if there is indeed an orbital dephasing effect and to know what is the orientation of the interfering surface vector φ_S.

The rescaled curves are plotted in Fig. 6.16b, and the raw ones in Fig. 6.16a. The rescaling factors are plotted in Fig. 6.16c as a function of the (horizontal) polar angle φ. The few angles available match very well the $\cos$ function displayed as a black curve, with a shift of $-54°$, yielding $\varphi_S = 306°$ and a $\varphi = 36°$ angle for vanishing flux. Therefore, $\varphi = 36°$ correspond to the wire axis, consistent with its approximate orientation on the sample holder.

Now that we know the angle φ_S of the surface vector $\vec{S}$ in the horizontal plane, we can repeat the process by fixing the polar angle $\varphi \simeq \varphi_S = 306°$ and vary the azimuthal angle θ. The formula for the effective flux becomes :
$\vec{B}.\vec{S} = B_\rho S_\rho (\sin\theta\sin\theta_S + \cos\theta\cos\theta_S) = B_\rho S_\rho \cos(\theta - \theta_S)$,
with B_ρ the magnetic field magnitude, and $S_\rho \cos\alpha$ the new total rescaling factor with $\alpha = \theta - \theta_S$ the angle between $\vec{S}$ and $\vec{B}$ in the plane perpendicular to the wire axis.

We already have the $\theta = 0°$ curve shown in green in Fig. 3.8a that we can rescale such that the slopes close to $|B| \simeq 1000\ G$ are similar, but we already know that its low field behavior and its gaussian large field decrease deviate from the wide ballistic model described above. Another measurement at $\theta = 45°$, $\varphi = 320°$ is shown as a grey curve Fig. 6.17. It displays clear $\sim 22\ G$ oscillations (see Fig. 6.19) and a

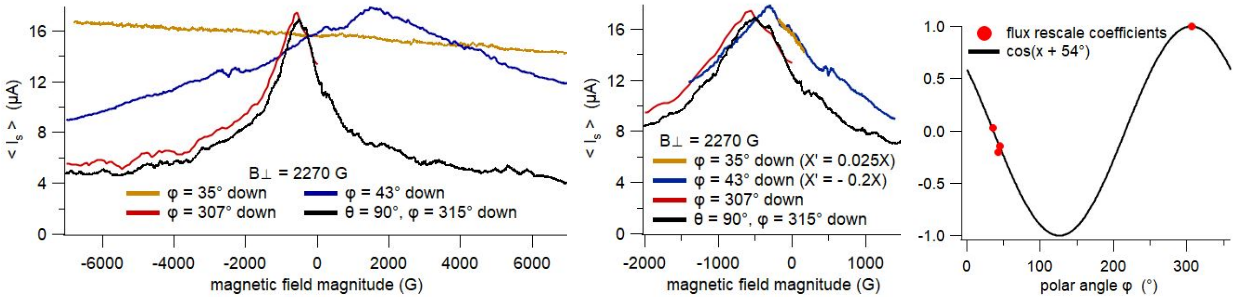

Figure 6.16 – (a) Average switching current of Bi$_{21}^{wire}$ as a function of magnetic field magnitude up to $7000\ G$ for various horizontal field directions, and a constant vertical field $B_z = 2270\ G$. (b) Curves with rescaled field. The rescaling factor has been chosen such that the rescaled curve matches the $\theta = 90°$, $\varphi = 315°$ reference black curve. (c) Rescaling coefficients as a function of polar angle φ, together with a $\cos(x + 54°)$ function.

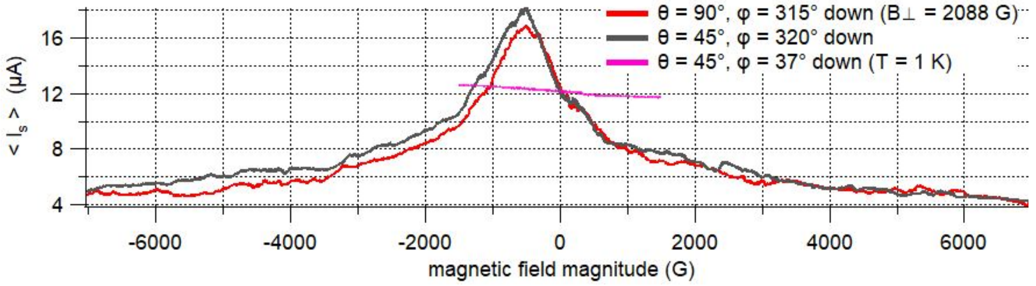

Figure 6.17 – Average switching current of Bi$_{21}^{wire}$ as a function of oblique magnetic field. Grey line : $\theta = 45°$, $\varphi = 320°$ (close to the perpendicular to the wire axis). Pink line : $\theta = 45°$, $\varphi = 37°$ (horizontal component along the wire axis). Red line : $\theta = 90°$, $\varphi = 315°$ with a constant $B_z = 2088\ G$, for comparison.

large scale pattern that matches the $\theta = 90°$, $\varphi = 315°$ with a magnetic field rescaling factor of 1.2. This observation alone would suggest that the $\vec{S}$ is closer to $\theta = 45°$ than $\theta = 90°$, but we saw that the large field scale of $I_c(B_z)$ contradicts it. These observations are gathered in Fig. 6.18, and are difficult to fit with a 2π-periodic function $\cos$ function (red curve), indicating that the supercurrent carrying states responsible for the oscillations involve more than orbital dephasing in a single plane.

Let us now look for oscillations of the switching current with other magnetic field orientations. On the $\theta = 90°$, $\varphi = 45°$ response (blue curves in Fig. 3.8b, close to wire axis), one can guess a $\sim 100 - 200\ G$ periodic pattern of amplitude $\sim 200\ nA$, but only on a few periods and not very regular. The same kind of unclear pattern is found on the $\theta = 90°$, $\varphi = 315°$ (red curves in Fig. 3.8b, close to perpendicular to the wire in the horizontal plane), with a $\sim 70\ G$ period and a $\sim 200\ nA$ amplitude.

On the other hand, measurements done at $\theta = 45°$ show clear symmetric triangular oscillations. For a horizontal angle $\varphi = 37°$, along the wire direction, the oscillations have a period of $26\ G$ and an amplitude $\sim 200\ nA$, see Fig. 6.19c. In contrast with the other measurements, this one has been done at $T \simeq 1\ K$, explaining why the amplitude is $< 400\ nA$.

For an angle $\varphi = 320°$, $14°$ off the perpendicular to the wire direction, the oscillations have a period of $22\ G$ and an amplitude $\sim 400\ nA$, see Figs. 6.19a and 6.19b for the short-scale oscillating part, and Fig **??** for its Discrete Fourier Transform. Fig. 6.17 show the same measurements on the $7000\ G$ scale.

The $22\ G$ period for $\varphi = 320°$ corresponds to Φ_0 in a surface $1.8 \times 0.523\ \mu m^2$. Compared to the $25\ G$

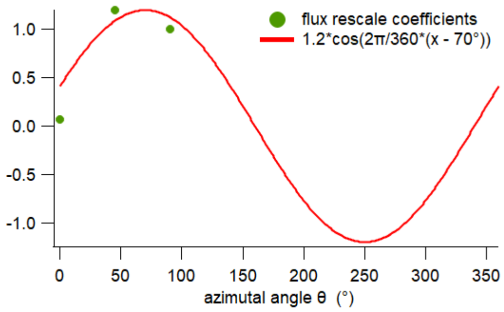

Figure 6.18 – Field rescaling coefficients as a function of azimuthal angle θ. The coefficients are chosen such that the rescaled curves visually match the large-scale variations of the $\theta = 90°$, $\varphi = 315°$ curve used as a reference (see light red curve in Fig. 3.8b). The red curve is an attempt to match the data points with a simple single-plane orbital dephasing $\cos$ function, but seems significantly off.

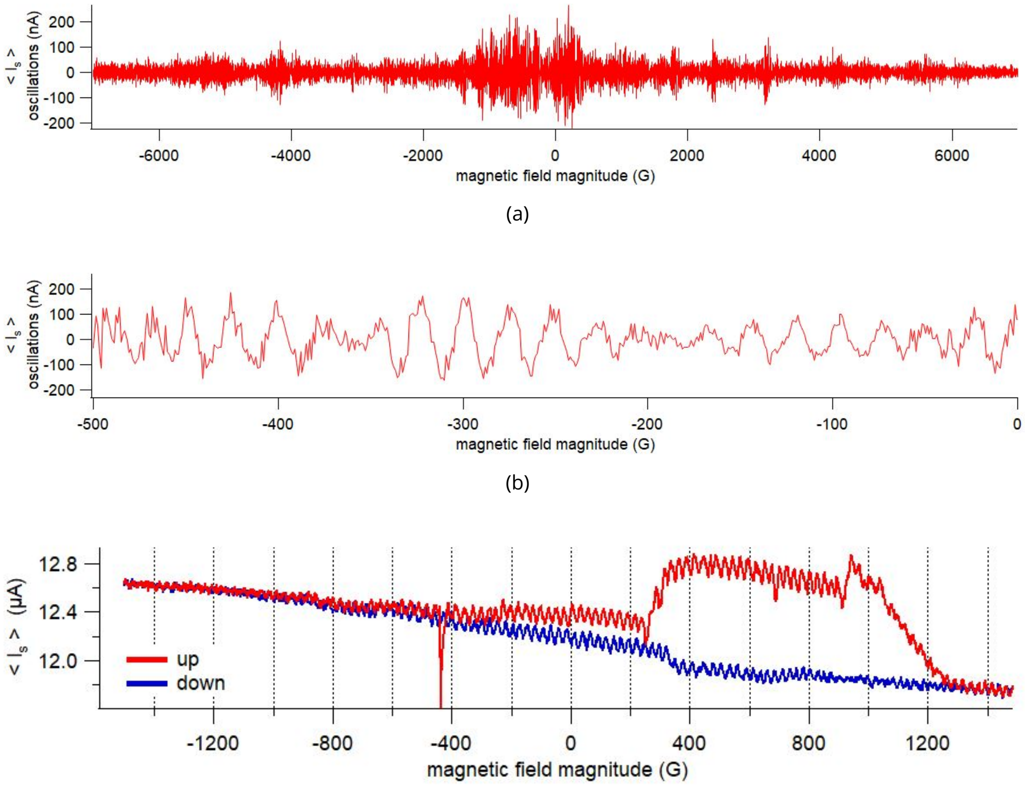

(a)

(b)

(c)

Figure 6.19 – Oscillations of the average switching current of Bi$_{21}^{wire}$ as a function of oblique magnetic field. (a),(b) $\theta = 45°$, $\varphi = 320°$ (close to the perpendicular to the wire axis). The large-scale background current variations have been subtracted out. $T = 60\,mK$.(c) $\theta = 45°$, $\varphi = 37°$ (horizontal component along the wire axis). $T \simeq 1\,K$.

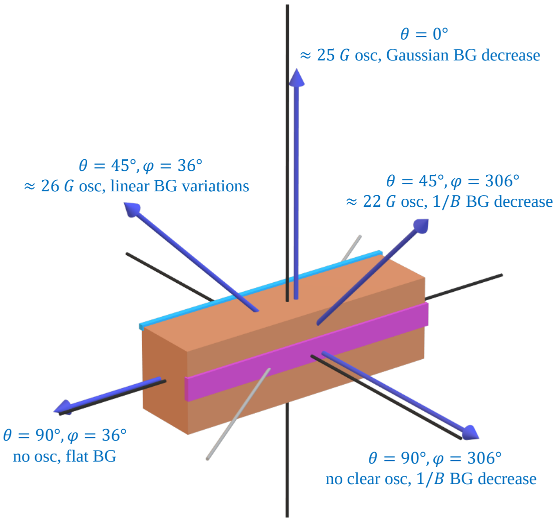

Figure 6.20 – Summary of the main information on the nanowire sample Bi$_{21}^{wire}$. The dark blue arrows show specific magnetic field orientations θ and φ, with the information on the associated switching current oscillations periods and background (BG) behaviors. The bismuth nanowire is also sketched in this figure as a brown block, with two colored zones on its surface to illustrate a 1d ballistic hinge channel (light blue zone) and a set of 1d ballistic channels on the opposite surface (pink zone).

period measured at $\theta = 0°$ and its $1.8 \times 0.46\ \mu m^2$ surface, from simple geometric arguments, it suggests that the surface responsible for the oscillations is tilted by an angle $\alpha = \arccos(0.46/w^*) = 31.2°$ with respect to the vertical axis, in the direction of $\varphi = 320°$, with $w^* = 0.538$ such that $45° = \arccos(0.46/w^*) + \arccos(0.523/w^*)$.

Let us now find out what are the oscillation periods expected with such a surface vector $\vec{S}_{osc}$ (enclosed by the states responsible for the oscillations) oriented along $\theta_S = 31.2°$ and $\varphi_S = 320°$. We have :
$\vec{B}.\vec{S}_{osc} = B_\rho S_{osc,\rho} \sin\theta \sin\theta_S \cos\varphi'' + B_\rho S_{osc,\rho} \cos\theta \cos\theta_S$, with $\varphi'' = \varphi - \varphi_S$.
For $\theta = 0°$, $\varphi = 315°$: $\vec{B}.\vec{S}_{osc} = B_\rho S_{osc,\rho} \cos\theta_S = 0.855 B_\rho S_{osc,\rho}$, producing a period of $\sim 25\ G$.
For $\theta = 45°$, $\varphi = 320°$: $\vec{B}.\vec{S}_{osc} = B_\rho S_{osc,\rho} 1/\sqrt{2}(\sin\theta_S + \cos\theta_S) = 0.971 B_\rho S_\rho$, producing a period of $\sim 22\ G$.
For $\theta = 45°$, $\varphi = 37°$: $\vec{B}.\vec{S}_{osc} \simeq B_\rho S_{osc,\rho} \cos\theta \cos\theta_S \simeq 0.605 B_\rho S_{osc,\rho}$, producing a period of $\sim 35\ G$.
For $\theta = 90°$, $\varphi = 315°$: $\vec{B}.\vec{S}_{osc} \simeq B_\rho S_{osc,\rho} \sin\theta_S \simeq 0.518 B_\rho S_{osc,\rho}$, producing a period of $\sim 41\ G$.

With this two-channels model defining a surface vector $\vec{S}_{osc}$ oriented along $\theta_S = 31.2°$ and $\varphi_S = 320°$, we find an expected oscillations period of $\sim 35\ G$ for $\vec{B}$ at $\theta = 45°$, $\varphi = 37°$. This is in sharp contrast with the measured $\sim 26\ G$. The most realistic hypothesis to explain this discrepancy is that the supercurrent responsible for the oscillations involves more than the orbital dephasing between two channels embedded in a single plane.

Fig.6.20 summarized our findings on sample Bi$_{21}^{wire}$.

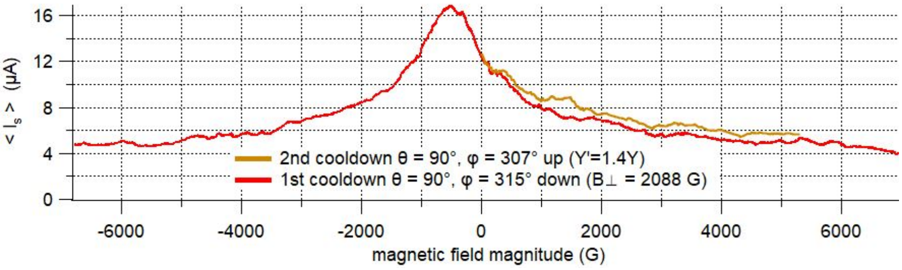

Figure 6.21 – Average switching current of Bi$_{21}^{wire}$ as a function of horizontal magnetic field magnitude up to $7000\,G$, perpendicular to the wire axis : $\theta = 90°$, $\varphi = 315°$. The gold curve has been obtained during the second experiment for a field direction close to the one used for the red curve, and shows good correspondence upon rescaling the current value by a factor 1.4.

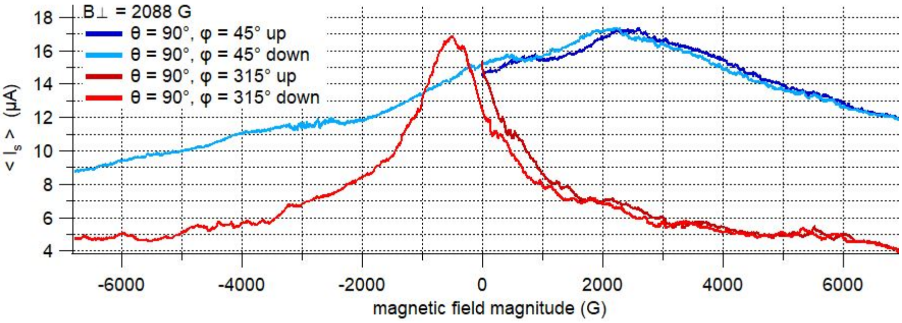

Figure 6.22 – Average switching current of Bi$_{21}^{wire}$ as a function of magnetic field magnitude up to $7000\,G$ for two horizontal field directions, and a constant vertical field $B_\perp = 2088\,G$, for an increasing and decreasing magnetic field magnitude. The horizontal coil shows a hysteresis of $\sim 250 - 300\,G$.

6.6.2 . Supplementary information on nanowire Bi$_{21}^{wire}$

6.6.3 . Switching current of asymmetric DC SQUID Bi$_1^{squid}$ as a function of field direction

The average switching current of the bismuth-nanowire-based DC SQUID Bi$_1^{squid}$ as a function of magnetic field magnitude and orientation in the horizontal plane is plotted in Fig. 3.11a in the main text. The conventions for azimuthal angle θ' and polar angle φ' are the same as θ and φ sketched in Fig.6.15, respectively. Each curve magnetic field magnitude has been rescaled such that they all fall to a unique curve. The rescaling factors are plotted in Fig. 6.23a, and clearly follow a cosine rule as expected for a standard orbital flux scalar product $\vec{B}.\vec{S}$ for a $\vec{S}$ at a polar angle $\varphi' = 148°$ (perpendicular to the wire axis). The rescaling factor is $0.311\ kG^{-1}$ for at $\varphi' = 148°$. The characteristic field scale of the $\varphi' \simeq 148°$ curve is $\sim 4000\ G$, corresponding to a $2.6\mu m \times 2nm$ effective surface.

Fig. 3.11b shows the average switching current as a function of rescaled magnetic field magnitude for various field azimuthal angle θ' and fixed polar angle $\varphi' = 153°$, close to perpendicular to the nanowire axis. The height of the $X = -1$ peak and the field rescaling factors r are plotted as a function of azimuthal angle θ' on Fig. 6.23b. The field rescaling factors fit with a cosine function which maximum is at $\theta' = 68°$, matching with a surface vector $\vec{S}$ oriented along $\varphi' = 148°$ and $\theta' = 68°$.

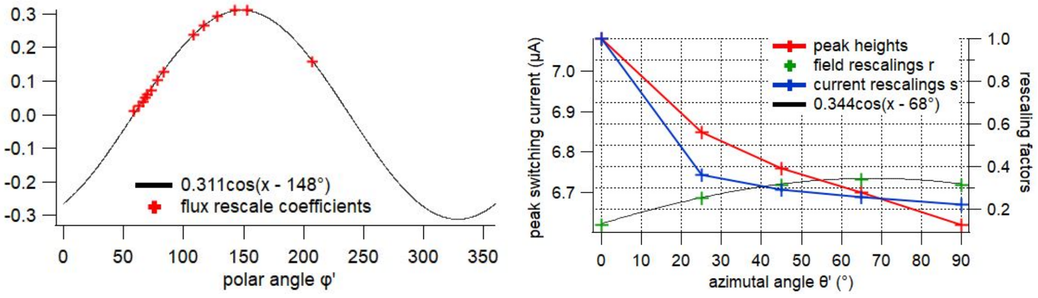

(a)

(b)

Figure 6.23 – (a) Red crosses : rescaling factors of Bi$_1^{squid}$ as a function of magnetic field polar angle φ' (fixed $\theta' = 90°$). The values have been chosen such that all the average switching current of Bi$_1^{squid}$ versus magnetic field magnitude curves fall into a unique curve. They follow a cosine law, as shown by the cosine fit black line. (b) Characteristic features of the average switching current of Bi$_1^{squid}$ versus magnetic field magnitude curves for various azimuthal angle θ' (fixed $\varphi' = 153°$). Red crosses : heights of the $X = -1$ peak. Blue crosses : current rescaling factors s. Green crosses : field rescaling factors r. Black line : cosine fit of the field rescaling factors r.

6.6.4 . Intermediate field scale variations of the switching current of the nanoring sample Bi^{ring}

In this appendix, we show additional data on the bismuth-nanoring-based Josephson junction Bi^{ring}. We also provide an alternate scenario for the small amplitude of the small field scale oscillations and for the background current variations.

a) Background current : intermediate field scale variations

See Fig.6.24.

b) Background current : three channels scenario

In the following we discuss an alternate scenario, in which the ring is modeled by three parallel junctions of critical currents i_{c1}, i_{c2}, i_{c3}. Junction 1 is in the upper branch whereas 2 and 3 are in the lower branch of the ring. We assume that $i_{c3} \gg i_{c1}, i_{c2}$. We also assume a high inductance L_3 in series with junction 3 such that $l_3 i_{c3}$, $l_3 i_{c1}$ and $l_3 i_{c2}$ are all much greater than 2π (here $l_i = 2\pi L_i/\Phi_0$). In the following, we show that the variations of the critical currents with flux Φ is determined by junctions 1 and 2, while junction 3 gives a constant (i.e. flux-independent) contribution i_{c3} to the total critical current.

Given $\phi_{1,2,3}$ the respective phases across junctions 1,2 and 3 (see Fig. 6.11), and assuming that $l_2 i_2 \ll 1$ and $l_1 i_1 \ll 1$, one has

$$\phi_2 \equiv \phi_1 - \Phi \equiv \phi_3 + l_3 i_3 \mod 2\pi. \tag{6.57}$$

The critical current is obtained as the maximum of :

$$F(\phi_1) = |i_{c1} Saw(\phi_1) + i_{c2} Saw(\phi_1 + \Phi) + i_{c3} Saw(\pi(1 - \epsilon(\phi_1, \Phi)))|, \tag{6.58}$$

where we have written $\phi_3 \equiv \pi(1 - \epsilon(\Phi, \phi_1)) \mod 2\pi$. Eq. (6.57) yields $\epsilon(\phi_1, \Phi) = 2\pi((\Phi - \phi_1 - \alpha - \pi) \mod 2\pi)/l_3 i_{c3}$, where $\alpha \equiv l_3 i_{c3} \mod 2\pi$. ϵ is thus very small for a highly inductive third branch. In the limit where both $l_3 i_{c1}$ and $l_3 i_{c2} \gg 2\pi$, the maximization of $F(\phi_1)$ can therefore be performed assuming that

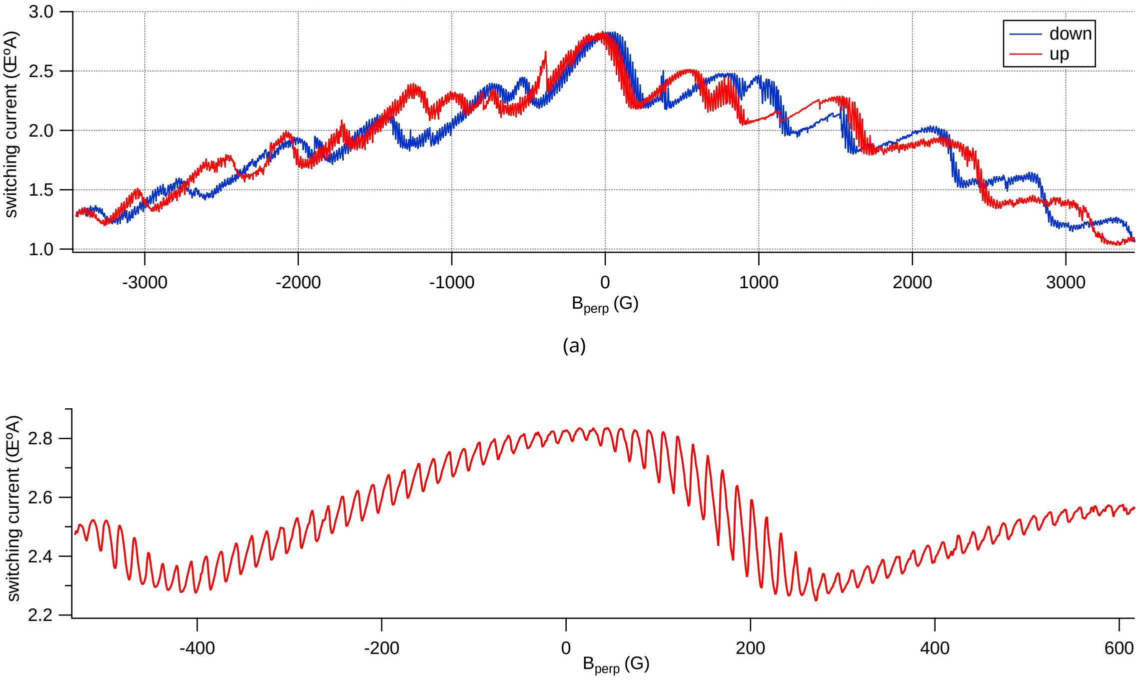

(a)

(b)

Figure 6.24 – (a) Intermediate field scale average switching current of the Bi^{ring} sample as a function of vertical magnetic field perpendicular to the ring plane. The red and blue lines correspond to data obtained with an increasing and a decreasing field, respectively. For $|B| \lesssim 400G$, the data is simply shifted by the hysteresis of the horizontal coil. For $|B| \gtrsim 400G$, there are important difference between the up and down curves, with some sharp jumps that correspond to the apparition/disappearance of a vortex in the superconducting contacts. (b) Low-field zoom on the curve displayed in (a).

$\epsilon(\phi_1, \Phi)$ is equal to zero within $1/l_3$, which is very small compared to the flux variation of I_c determined by the minimum value of i_{c1} and i_{c2}. We therefore find that junction 3 does not lead to any flux-dependent interference pattern : the interference is solely determined by junctions 1 and 2. We can then easily reproduce the experimentally observed interference, including skewness reversals, taking as above that i_{c1} and i_{c2} vary with field on large field scales due to the Zeeman effect or flux oscillations through the Bi wires. We could generalize this result to the case where the supercurrent in each branch 1 and 2 is carried by several 1D channels labeled by indexes j1 and j2. These channels being characterized by their critical currents $i_{c,j1}$, $i_{c,j2}$ and inductances L_{j1}, L_{j2}. The highly inductive channels give rise to a contribution to the supercurrent which is nearly independent of the flux through the ring, whereas the observed flux oscillations result from the interference between the channels whose inductance is negligible.

c) Background current : slow modulation by orbital dephasing

We demonstrate that a slow (i.e. on a scale much greater than one flux quantum through the ring area) variation with field of the critical current in one branch of the ring can be explained by interference between two supercurrent-carrying edge states in one branch. This interference depends on the magnetic flux between the two edges, giving a typical period in the range of a thousand Gauss if the edges are spaced a few tens of nanometers apart.

The interplay between the flux through the ring and the smaller flux through the interfering channels within each branch appears when considering the critical current of each branch, in a model, sketched in Fig. 6.25 in which each branch is placed between superconducting contacts with phases $\pm\delta/2$.

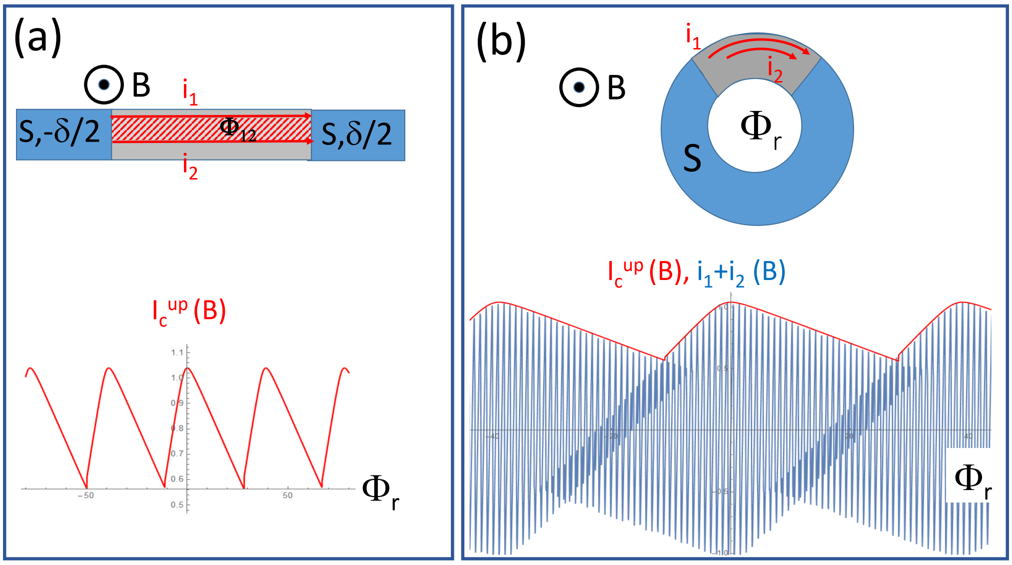

Figure 6.25 – Illustration of how the interference between the supercurrent carried by two hinge states (i_1 and i_2) in a given branch of the ring can cause a field-dependent critical current $I_c^{up}(B)$ of that branch. We have plotted equation (2) and (3) with $i_{c2} = 0.357 i_{c1}$ and $\Phi_{12} = BS_{12} = 0.0257 BS_r = 0.0257\Phi_r$, with S_r the area of the ring and S_{12} the lateral area between hinges 1 and 2. (a), Field-dependence of the critical current of a wire containing two hinges, connected to two superconductors with a phase difference δ. (b), interpretation of this critical current as due to interference between the supercurrent through the two hinges carrying the supercurrent in an ac SQUID configuration with a flux Φ_r through the ring, expressed in units of $\hbar/2e$, $\phi_r = 2\pi\Phi_r/\Phi_0$.

The current through each branch is then the sum of the current carried by the two hinge channels. The phase difference for each hinge channel depends, in addition to the phase difference δ between the superconducting contacts, on the vector potential along the hinge . (It can also depend on the field, via an additional field-dependent Zeeman phase $g_{eff}\mu_B BL/(hv_F)$, where $g_{eff} \gg 1$).

$$I^{up}(B) = i_{c1} Saw[\delta + \frac{2e}{\hbar}\int_1 Adl] + i_{c2} Saw[\delta + \frac{2e}{\hbar}\int_2 Adl], \mathrm{and} I_c^{up}(B) = \max_\delta [I^{up}(B)] \tag{6.59}$$

in the upper branch.

Since the flux encircled by the two edges is, in units of $\hbar/2e$, $\phi_{12} = 2\pi\Phi_{12}/\Phi_0 = 2\pi/\Phi_0(\int_1 Adl - \int_2 Adl)$, the critical current of the top branch is given by

$$I_c^{up}(B) = \max_\delta [i_{c1} Saw[\delta + \phi_{12}/2] + i_{c2} Saw[\delta - \phi_{12}/2]]\,, \tag{6.60}$$

with $\Phi_{12} = S_{12}B$ and $\Phi_0 = h/2e$, S_{12} is the surface between paths 1 and 2, and B is the magnetic field.

As seen in Fig. 6.25, this critical current of one branch has a period $S_{ring}/S_{12} = 25$ times larger than the period corresponding to one flux quantum through the ring area. This critical current can also be viewed as the envelope (or amplitude modulation) of the beating pattern between two hinges of a wire that would be embedded in an ac SQUID configuration, as sketched in Fig. 6.25b. The total current in such a ring would read

$$i_1 + i_2 = i_{c1} Saw[\phi_r + \phi_{12}/2] + i_{c2} Saw[\phi_r - \phi_{12}/2] = i_{c1} Saw[\frac{2\pi}{\Phi_0}(S_r + S_{12}/2)B] + i_{c2} Saw[\frac{2\pi}{\Phi_0}(S_r - S_{12}/2)B] \tag{6.61}$$

with $\phi_r = 2\pi\Phi_r/\Phi_0$, and is displayed in Fig. 6.25b.

These considerations therefore justify our assumption that each branch of the ring can be described as having a sawtooth-shaped CPR with a critical current whose amplitude has a slow and asymmetric variation with magnetic field. In addition, considering two branches (top and bottom) with such field dependent critical current also explains how, depending on the magnetic field, one or the other branch of the ring can carry the largest critical current. This alternation in branch carrying the greatest critical current cause the alternation in sign of the skewness observed. This interference also explains that if the hinges have different transmissions, lengths or even different effective g factors, the field-modulation may be asymmetrical with respect to zero field. What is important here is the absence of spatial inversion symmetry in each branch.

6.6.5 . Change of periodicity of the switching current oscillations of nanowire Bi$_{12}^{wire}$

Fig.6.26 shows the change of periodicity of the average switching current of the bismuth-nanowire-based Josephson junction Bi$_{12}^{wire}$ as a function of vertical magnetic field around $4.3T$. Close to $-3.9\ T$ the period is $\sim 426\ G$, close to $-4.8\ T$ it is doubled $\sim 852\ G$, and in the middle a pattern with three peaks repeating with a period $\sim 896\ G \simeq 852\ G$. The black lines are $\sim 426\ G$ apart and and the grey lines are shifted by half a period.

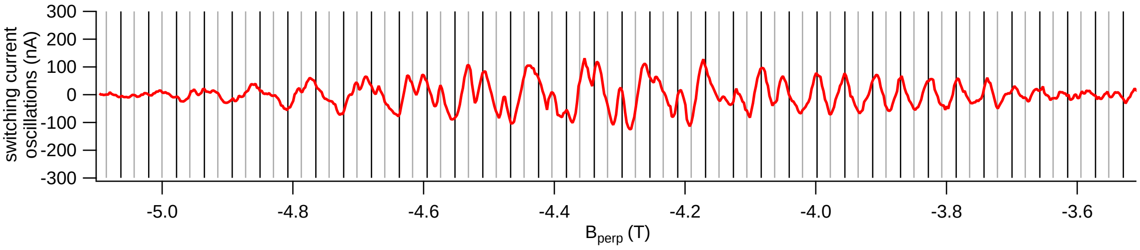

Figure 6.26 – Change of periodicity of the average switching current of the bismuth-nanowire-based Josephson junction Bi$_{12}^{wire}$ as a function of vertical magnetic field around $4.3T$. The slowly varying background has been subtracted.

6.6.6 . More information on resistive state measurements

Figs.6.27 and 6.28 provide additional information on the magnetoresistance of the long bismuth nanowire samples Bi$_{21}^{long}$, Bi$_{22}^{long}$ and Bi$_{4}^{long}$.

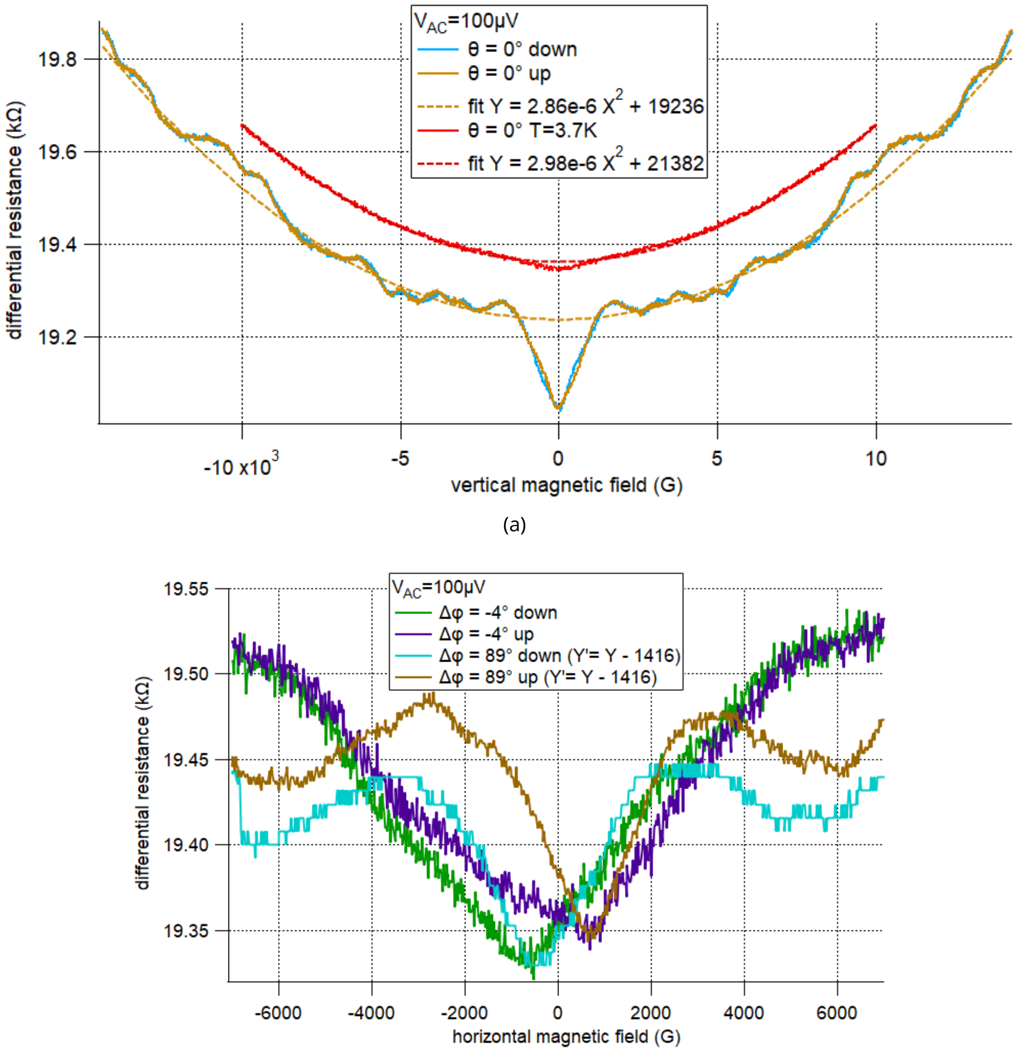

(a)

(b)

Figure 6.27 – Resistance of the long nanowire sample Bi$_{21}^{long}$ as a function of vertical (a) and horizontal (b) magnetic fields. In (a), the orange and blue curves have been obtained with $T \simeq 0.1K$. In (b), $\Delta\varphi$ is the angle between the horizontal magnetic field and the approximate axis of the nanowire.

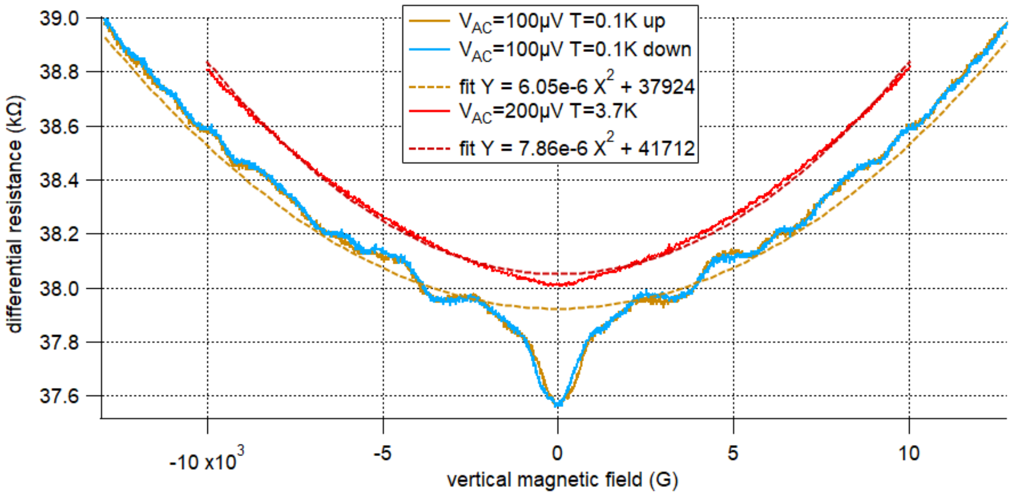

(a)

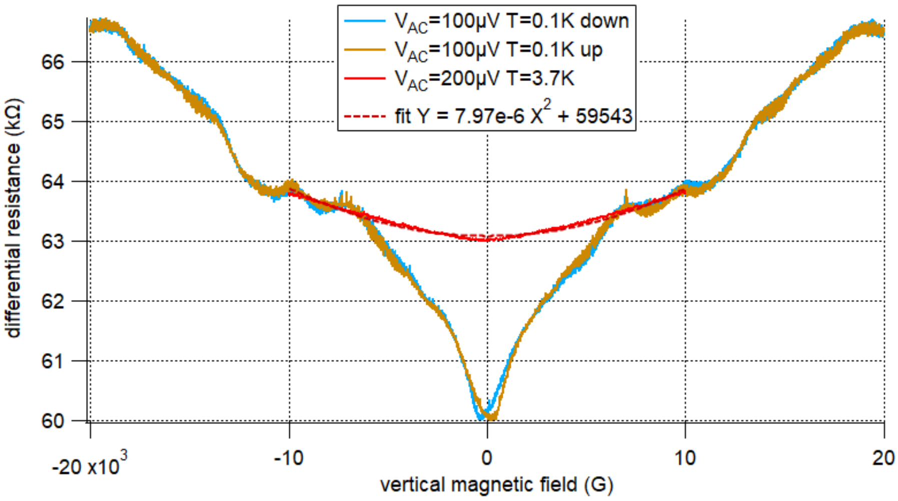

(b)

Figure 6.28 – Resistance of the long nanowire samples Bi$_{22}^{long}$ (a) and Bi$_{4}^{long}$ (b) as a function of vertical magnetic field, for different excitation amplitudes and different temperatures.

6.7 . Magneto-Chiral Anisotropy

In this appendix, we discuss spin-orbit-induced Magneto-Chiral Anisotropy (MCA) in both the resistive and the superconducting states of samples with SOC. In particular, we argue that the Edelstein effect causes a current-induced effective magnetic field $B_{eff} \simeq \beta I$ in both states, with a current-to-field coefficient β. β can be measured via the second harmonic voltage (or current) response of the samples to a current (or voltage) excitation in the resistive state, and via a deformation and a shift of the critical current versus Zeeman field pattern of the samples in the superconducting states. The phenomenological models introduced in this appendix are used in the analysis of MCA in the experiments reported in appendix 6.9 and 6.12.

6.7.1 . Edelstein effects

We consider a 2DEG in its resistive state with Rashba SOC. Its spin-texture is derived in part 1.1. Using the semiclassical Boltzmann transport theory, applying an electric field $\boldsymbol{E} = E_x\hat{\boldsymbol{x}}$ parallel to the $\hat{\boldsymbol{x}}$ direction can be interpreted as a shift of the Fermi lines in $\boldsymbol{k}$-space by [10] :

$$\delta\boldsymbol{k} = -\frac{|e|\tau_e}{\hbar}\boldsymbol{E} \tag{6.62}$$

where e is the elementary charge and τ_e is the elastic scattering time. The situation is illustrated in Fig.6.29. Moreover, Ohm's law writes $\boldsymbol{j} = \sigma_D\boldsymbol{E} = ne^2\tau_e\boldsymbol{E}/m^*$ for the current density $\boldsymbol{j}$, with σ_D the Drude conductivity, m^* the effective mass, and n the 2d density of states. Together, it gives :

$$\delta\boldsymbol{k} = -\frac{k_F}{n|e|v_F}\boldsymbol{E} \tag{6.63}$$

with k_F the Fermi wavevector and v_F the Fermi velocity.

Now we consider the effect of this electric field on the polarization of the spins. The expectation value of the spin at a given $\boldsymbol{k}$ is $\boldsymbol{s}(\boldsymbol{k})$, as introduced in part 1.1. For Rashba SOC, $\boldsymbol{s}(\boldsymbol{k}) \perp \boldsymbol{k}$. Let us focus on the expectation value of the total spin $\langle\boldsymbol{\sigma}\rangle$, calculated by summation of $\boldsymbol{s}(\boldsymbol{k})$ over all occupied states. At equilibrium, there is a perfect compensation of $\boldsymbol{s}(\boldsymbol{k})$ at opposite $\boldsymbol{k}$, that is $\boldsymbol{s}(\boldsymbol{k}) + \boldsymbol{s}(-\boldsymbol{k}) = 0$, yielding $\langle\boldsymbol{\sigma}\rangle = 0$. Introducing the shift $\delta\boldsymbol{k} \propto \boldsymbol{E}$ breaks it.

For Rashba SOC, there still exists a partial compensation due to the other band with opposite chirality, but they don't cancel exactly anymore. Due to the larger radius of the outer circle, a non-vanishing in-plane spin density remains, perpendicular to the applied electric field $\boldsymbol{E}$, proportional to α and E, and independent

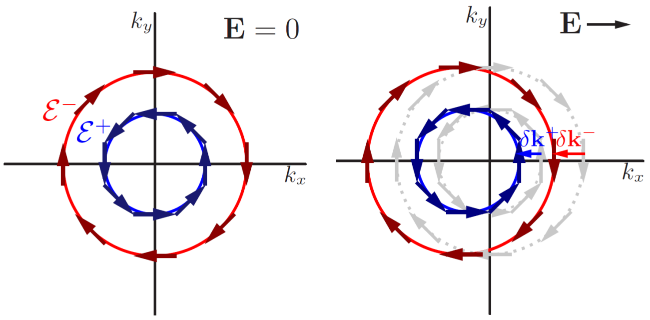

(a) (b)

Figure 6.29 – Fermi lines with corresponding spin expectation values (arrows) of a 2DEG with Rashba SOC with (b) and without (a) external in-plane electric field. From [10].

of $\mathcal{E}_F$. This effect is referred to as the Edelstein effect from [9] or as Current-Induced Spin Polarization (CISP) and is a magnetoelectric effect. It is the generation of an out-of-equilibrium spin polarization from an applied constant electric field (or DC current).

For Rashba SOC, in the diffusive limit, the total spin density writes [9, 10] :

$$\frac{\langle \boldsymbol{\sigma} \rangle}{A} = \frac{\alpha m^* \hbar}{|e|(\alpha^2 m^* + \hbar^2 \mathcal{E}_F)} (\hat{\boldsymbol{z}} \times \boldsymbol{j}) \tag{6.64}$$

with A the area of the whole system, $\boldsymbol{j} = ne^2\tau_e \boldsymbol{E}/m^*$ the current density provided by Ohm's law. For $\boldsymbol{j} = j_x \hat{\boldsymbol{x}}$, the only non-zero component of $\langle \boldsymbol{\sigma} \rangle$ is along $\hat{\boldsymbol{y}}$. One can look at [8] for the other types of SOC, and [190] for TMD.

For a single Fermi circle with Rashba SOC and linear dispersion relation, like the surface states of 3d topological insulators (see part 1.1), we have [10] :

$$\frac{\langle \boldsymbol{\sigma} \rangle}{A} = \frac{-|e|\tau_e k_F}{4\pi\hbar} (\hat{\boldsymbol{z}} \times \boldsymbol{E}) \tag{6.65}$$

which is larger than the Rashba SOC expression by a factor $\hbar v_F/\alpha$ (typically a ~ 10). Adding disorder, [191] found $\langle \boldsymbol{\sigma} \rangle \propto \hbar/(ev_F)(\hat{\boldsymbol{z}} \times \boldsymbol{j})$ with a prefactor that only depends on v_F but not on disorder.

There exists an Onsager reciprocal effect called inverse Edelstein effect or spin-galvanic effect. Because the Edelstein effect is an out-of-equilibrium effect, a static Zeeman field can't produce the inverse effect, as it generates an equilibrium spin polarization. To get the inverse Edelstein effect, one need to inject spins in out-of-equilibrium [192].

As we will see in part 6.7.3, the Edelstein effect is a source of electrical Magneto-Chiral Anisotropy, a behavior that is promoted by SOC and induce non-linear non-reciprocal dissipative transport. We measured such an effect in long bismuth nanowires, see part 6.9.4. The Edelstein effect has a counterpart in the superconducting state, where this time the induced spin polarization is at equilibrium. In addition, in the superconducting state there is a deep connection between the inverse Edelstein effect and the anomalous Josephson effect [85]. A finite magnetization can induce a supercurrent even if the superconducting phase difference is null. We use the analysis of the later effect in part 6.7.6 to interpret our results on a DC SQUID composed of two bismuth-based Josephson junction in part 6.12.4.

6.7.2 . Resistive state non-reciprocal charge transport and Magneto-Chiral Anisotropy in the literature

In this part of the appendix, we introduce non-reciprocal charge transport and Magneto-Chiral Anisotropy (MCA) in the resistive state. We also discuss non-linear resistance and the various sources of non-linearity. This part is a lightened version of the discussion found in [193].

Based on Onsager's reciprocity relation for the symmetry properties of diffusive transport, any two-contacts electrical transport property can only have an even magnetic field dependence, that is for a generalized transport coefficient σ_{ij} between contacts i and j that only depends on magnetic field $\boldsymbol{B}$:

$$\sigma_{ij}(\boldsymbol{B}) = [\sigma_{ji}(\boldsymbol{B})]^\dagger = \sigma_{ji}(-\boldsymbol{B}) \Longrightarrow \sigma_{xx}(\boldsymbol{B}) = \sigma_{xx}(-\boldsymbol{B}) \tag{6.66}$$

where $\dagger$ denotes time reversal operation. However, this relation implies transport properties even in field only in the linear response.

In fact, any transport term that is TRS does not violate Onsager's reciprocity relation. As such, any term $\propto j^{2p+1}B^{2q+1}$ featuring a product of current j and magnetic field B is allowed by the Onsager reciprocity relation, where p and q are integers. For such a term, Onsager's reciprocity relation reads :

$$\begin{aligned}
&\sigma_{ij}(\boldsymbol{j}, \boldsymbol{B}) = \sigma_{ij}(\boldsymbol{j}^{2p+1} \cdot \boldsymbol{B}^{2q+1}) = \left[\sigma_{ji}(\boldsymbol{j}^{2p+1} \cdot \boldsymbol{B}^{2q+1})\right]^{\dagger} \\
&\iff \sigma_{ij}(\boldsymbol{j}^{2p+1} \cdot \boldsymbol{B}^{2q+1}) = \sigma_{ji}((-\boldsymbol{j})^{2p+1} \cdot (-\boldsymbol{B})^{2q+1}) = \sigma_{ji}((-1)^{2(p+q)}\boldsymbol{j}^{2p+1} \cdot \boldsymbol{B}^{2q+1}) = \sigma_{ji}(\boldsymbol{j}^{2p+1} \cdot \boldsymbol{B}^{2q+1}) \\
&\implies \sigma_{xx}(\boldsymbol{j}^{2p+1} \cdot \boldsymbol{B}^{2q+1}) = \sigma_{xx}(\boldsymbol{j}^{2p+1} \cdot \boldsymbol{B}^{2q+1})
\end{aligned}$$

meaning that this relation imposes no further constrains on the symmetries of σ_{xx}, contrasting with Eq.(6.66). We see that, by introducing a product between two quantities that change sign under time reversal, σ_{xx} can now be odd in magnetic field.

Such a term $\propto j^{2p+1}B^{2q+1}$ only appears in non-linear transport. For example, if σ_{xx} is the resistance, such a term involves a resistance that depends on the current j, which corresponds to non-linear voltage response to a current excitation. Notice that because $\boldsymbol{j}$ is odd under inversion operation while $\boldsymbol{B}$ isn't, this type of term breaks inversion symmetry and thus only exists in systems with broken inversion symmetry.

In [194], inspired by the developing field of spin-orbit materials and by recent discoveries at that time, G.L.J.A.Rikken and P.Wyder introduced in 2005 a minimal model that allowed for an anisotropy in the two-contacts resistance in the direction perpendicular to the crossed electric and magnetic fields, and the magnitude of which depends linearly on the electric and the magnetic field :

$$\sigma_{ij}(\boldsymbol{j} \cdot \boldsymbol{E} \times \boldsymbol{B}) = [\sigma_{ji}(\boldsymbol{j} \cdot \boldsymbol{E} \times \boldsymbol{B})]^{\dagger} = \sigma_{ji}((-\boldsymbol{j}) \cdot \boldsymbol{E} \times (-\boldsymbol{B})) \implies \sigma_{xx}(\boldsymbol{j} \cdot \boldsymbol{E} \times \boldsymbol{B}) = \sigma_{xx}(\boldsymbol{j} \cdot \boldsymbol{E} \times \boldsymbol{B}) \tag{6.67}$$

where once again this relation imposes no further constrains on the symmetries of σ_{xx}. The term $\boldsymbol{j} \cdot \boldsymbol{E} \times \boldsymbol{B}$ is even under parity (inversion), charge conjugation, and time-reversal, and can exist in any system with non-zero crossed electric and magnetic fields. Again, if σ_{xx} is a resistance, it is linear in j, and therefor contributes to the second-order voltage response to a current excitation.

The electric and magnetic fields can be applied externally or be caused by internal polarizations of the system. An interesting feature is that the sheer presence of an electrical polarization on moving particles creates such a term, where special relativity generate, in the reference frame of the particle, a magnetic field perpendicular to both the particle velocity and the electric field. Owing to the same special relativity argument, spin-orbit coupling can also be the origin of a non-linear resistance term with the same symmetries, without any externally applied electric field. In this case, the non-zero electric field is caused by local inversion symmetry breaking in the crystalline structure of the material, in its bulk or at its boundaries, see part 1.1.

In general, this crossed term applies to all diffusive transport phenomena and is referred to as Magneto-Electric Anisotropy (MEA) and is a form of Magneto-Chiral Anisotropy (MCA).

The precise mechanisms that link the spin-orbit coupling to the non-linear resistance depends on the system. A general semiclassical derivation on non-linear charge transport can be found in [195], and a focus on non-linear Hall effect in [196]. [197] provides a review of various effects that can cause non-reciprocal response from non-centrosymmetric materials. The main contribution to the (non-linear) magneto-chiral anisotropy (MCA) depends on the system, and its name can change accordingly. To name a few :
- MCA in 3d TI Bi_2Se_3 films [198] is explained by the combined effect, considering a topological surface state with hexagonal warping, of second order pure spin current and spin imbalance caused by an applied $\boldsymbol{B}_{ext}$ [199], and is called Bilinear Magneto-Electric Resistance (BMER).
- MCA in WTe_2 films [200] is explained by computing the second-order current response of the system to an electric and a magnetic field with a Wannier tight-binding Hamiltonian model that reproduces the complex Fermi surface topology, spin-texture and convexity, and is called Non-Linear Magnetoresistance (NLMR)
- MCA in materials with isotropic spin-momentum locked Fermi surface can arise from the interplay of current-induced spin-polarization ($\boldsymbol{B} = \boldsymbol{B}_{ext} + a\boldsymbol{j}$) (Edelstein effect) and scattering processes due to inhomogeneities of spin-momentum locking [201], potentially much stronger that the effect discussed in

[198, 199], and called Bilinear Magnetoresistance (BMR).
- giant MCA in $(\mathrm{Bi}_{1-x}\mathrm{Sb}_x)_2\mathrm{Te}_3$ nanoribbons under gate voltage [202] is explained by the tailoring of the band structure, splitting and Zeeman shifting them by the applied gate voltage and magnetic field.
All these manifestations of MCA require inversion symmetry breaking by external or internal electric field (e.g. SOC) and finite magnetic field.

Interestingly, MCA was also found in various non-centrosymmetric superconducting systems, see [203] in MoS_2 monolayer, [204] in WS_2 nanotube, [205] in $\mathrm{Bi}_2\mathrm{Te}_3$/FeTe TI/SC heterostructure, etc.

Other effects can contribute to the non-linear transport response of the system. Asymmetries of the contacts, the conductor, or the diffusion centers inside the conductor can contribute to the non-linear response. From [206], one can derive variations of the conductance G with voltage V via the chemical potential μ : $\frac{\partial G}{\partial \mu}\delta\mu \simeq \frac{\partial G}{\partial \mu}(1-2a)e\delta V$ ($a = 1/2$ for symmetric contacts). This term relies on variations of the density of states as a function of voltage. These variations are even in field [207], and the resulting non-linear response is even in field too.

However, combining voltage-induced LDOS asymmetries and electron-electron interactions can produce a non-linear response odd in field. As an illustration, [193] considered the asymmetric electric potential energy created around an impurity in the presence of both a non-equilibrium current and electron-electron interactions. These so-called Landauer dipoles change the potential landscape and contribute to the quantum interference conductance fluctuations, responsible for non-linear response even in field. But in contrast with the situation without electron-electron interactions, the potential landscape is not necessarily even in field, and can contribute to a non-linear response odd in field.

Considering other sources of non-linear response, we note that heating is only in non-linear conductance corresponding to odd powers of V [189], and does not contribute to second order response. Considering the classical Hall effect, the Hall electrical field in finite conductors can't lead to measurable MEA as it changes sign with the magnetic field or the current.

6.7.3 . Phenomenological model of MCA in the resistive state

Rather than using detailed and complex models that can be found in the literature, we chose to follow the spirit of [208] and to use a very simple model to analyze MCA in this first round of measurements in this type of system. This phenomenological model is probably over-simplistic but it will allow us to gain some insight on the physics of our bismuth samples. The analysis of the data will show some successes and limits of this model.

Inversion-breaking SOC in a 2d surface creates a spin texture in the Fermi lines. With a voltage bias or a current bias, the electrons close to the Fermi lines will acquire an extra momentum $\delta\boldsymbol{k} \propto \boldsymbol{j}$ and the Fermi lines will shift accordingly. Because of the spin-texture, this shift can induce a net non-equilibrium spin polarization. This effect is called current-induced spin polarization (CISP) or Edelstein effect, see part 6.7.1. The approximation we make is the following : this $\delta\boldsymbol{k}$ has the same effect on spins as an effective magnetic field $B_{\text{ext}} = \beta I$ in the spin polarization direction for this specific direction (I is the total current between the two contacts and β is a "current-to-field" factor). Including this extra effective magnetic field in the part of the magnetoresistance that is quadratic in the spin polarization, we add a new term in the magnetoresistance :

$$\delta R \simeq A_Z.B_{Z,eff}^2 \simeq A_Z.(B_{\text{ext}} + \beta I)^2 \simeq A_Z B_{\text{ext}}^2 + 2A_Z\beta I B_{\text{ext}} + A_Z\beta^2 I^2 \tag{6.68}$$

where A_Z is the coefficient associated to this quadratic term, that depends on the system, and B_{ext} is the magnitude of the externally applied magnetic field. With this mechanism, we introduced an electrical MCA in the resistance that is linear (thus odd) in both the current bias I and the external magnetic field B_{ext}. This term gives rise to a voltage response that is quadratic in I, and a contribution of the second harmonic response that is linear in B_{ext}.

This approach was successfully used in [208] to interpret the resistance MCA (that they call Unidirectional Magneto-Resistance) in Ge(111) films with a Rashba SOC hamiltonian $\mathcal{H}_R = \alpha(\boldsymbol{k} \times \boldsymbol{\sigma}) \cdot \hat{\boldsymbol{z}}$, $\hat{\boldsymbol{z}}$ being the unit vector perpendicular to the surface.

Applying a current $\boldsymbol{j}$ in a material with such a spin-orbit coupling induces an effective magnetic field $\boldsymbol{B}_{eff} = \alpha\lambda/(g_{eff}\mu_B)\hat{\boldsymbol{z}} \times \boldsymbol{j}$, such that the SOC energy term derived from $\mathcal{H}_R$ can be written as :

$$\alpha((\boldsymbol{k} + \delta\boldsymbol{k}) \times \boldsymbol{\sigma}) \cdot \hat{\boldsymbol{z}} = \alpha(\boldsymbol{k} \times \boldsymbol{\sigma}) \cdot \hat{\boldsymbol{z}} + \alpha\lambda(\hat{\boldsymbol{z}} \times \boldsymbol{j}) \cdot \boldsymbol{\sigma} = \alpha(\boldsymbol{k} \times \boldsymbol{\sigma}) \cdot \hat{\boldsymbol{z}} + g_{eff}\mu_B \boldsymbol{B}_{eff} \cdot \boldsymbol{\sigma} \tag{6.69}$$

with $\delta\boldsymbol{k} = \lambda\boldsymbol{j}$, g_{eff} the effective g-factor, and $\mu_B = e\hbar/(2m_e)$ the Bohr magneton, see part 6.7.1 for a more precise discussion.

This $\boldsymbol{B}_{eff}$ adds to the externally applied magnetic field and affect the standard magnetoresistance $R(\boldsymbol{B}) = R(\boldsymbol{B}_{ext} + \boldsymbol{B}_{eff}) = R(\boldsymbol{B}_{ext}, \boldsymbol{j})$, causing Unidirectional Magnetoresistance (UMR) or Bilinear Magneto-Electric Resistance (BMER) depending on its origin, as in Eq.(6.68).

We see that with such a current-to-field conversion mechanism present in material with spin-momentum locking, by introducing a current along a particular crystallographic direction and measuring the UMR as a function of magnetic field direction, we can probe the orientation of the spins of the Fermi surface in this crystallographic direction. This technique allows for a mapping of the spin texture of the Fermi surface, albeit partial for complex Fermi surfaces.

6.7.4 . From current-induced effective magnetic field B_{eff} to second harmonic responses

Our simple model consist in introducing a "current-to-field" factor β, such that the effective Zeeman field $B_{Z,eff}$ will be modulated by the current I through the bismuth sample, following $B_{Z,eff} = B_{\text{ext}} + \beta I$. This will modulate the part of the magneto-resistance that depends on the Zeeman field and introduce a term $\beta B_Z I$ linear in $B_Z = g_{eff}\mu_B B_{\text{ext}}$ and I, among other terms, see Eq.(6.68).

Let us now write the resistance and its variations as a function of relevant experimental parameters. The variations of the resistance R have various contributions, as discussed in part 6.7.2. For now, let us focus on two major contributors, which are the magneto-resistances due to orbital effects induced by a magnetic field B_{orb}, and due to Zeeman effects induced by a magnetic field $B_{Z,eff}$. In this phenomenological model, we explicitly split the orbital and spin contributions of the magneto-resistance. What we do here is to reduce the spin-orbit induced coupling between the orbital and the Zeeman part precisely into this "current-to-field" conversion factor β. We write :

$$\begin{aligned} R(B_{orb}, B_{Z,eff}, I, \mu) + \delta R &= R(B_{orb}, B_{Z,eff}, I, \mu) + \left.\frac{\partial R}{\partial B_{orb}}\right|_{B_{orb}, B_{Z,eff}, I, \mu} \delta B_{orb} \\ &\quad + \left.\frac{\partial R}{\partial B_{Z,eff}}\right|_{B_{orb}, B_{Z,eff}, I, \mu} \delta B_{Z,eff} \\ &\simeq R(B_{orb}, B_{Z,eff}, I, \mu) + \frac{\partial R}{\partial B_{orb}} \delta B_{\text{ext}} + \frac{\partial R}{\partial B_{Z,eff}} (\delta B_{\text{ext}} + \beta \delta I) \end{aligned} \tag{6.70}$$

In appendix 6.11, to interpret some features in the data, we discuss another possible variation of resistance with current bias via the chemical potential μ, that is an additional term $\left.\frac{\partial R}{\partial \mu}\right|_{B_{orb}, B_{Z,eff}, I, \mu} \delta\mu \simeq \frac{\partial R}{\partial \mu} c_{\mu,I} \delta I$.

We further write :

$$\begin{aligned} R &\simeq A_{orb}.B_{orb}^2 + A_Z.B_{Z,eff}^2 + A_Z.B_0^2 \simeq A'_{orb}.B_{\text{ext}}^2 + A_Z.(B_{\text{ext}} + \beta I)^2 + A_Z B_0^2 \\ &\simeq A'_{orb}.B_{\text{ext}}^2 + A_Z B_{\text{ext}}^2 + 2A_Z \beta I B_{\text{ext}} + A_Z \beta^2 I^2 + A_Z B_0^2 \end{aligned} \tag{6.71}$$

where we introduced a quadratic term $A_{orb}.B_{orb}^2$ that describes the orbital part of the magneto-resistance, and a zero-field resistance written as $A_Z.B_0^2$ for convenience. Notice that written this way, g_{eff} in is included in the coefficient A_Z.

Notice that to extract β, we need to estimate A_Z. The simplest way is to measure the magneto-resistance with a magnetic field parallel to the nanowire axis, such that the orbital contribution $A_{orb}.B_{orb}^2$ is reduced. Of course, both A_Z and β most likely depends on the magnetic field orientation. In the analysis we present in the following, we extract A_Z at $T = 3.7\ K$ (where mesoscopic effects are reduced) along the nanowire axis, and extract β from second harmonic response measurement as a function of vertical (perpendicular) magnetic field.

In many works in the literature, MCA is quantified by a coefficient γ_N such that $R = R_1(1+\gamma_N B_{\text{ext}} I)$. From Eq.(6.71), ignoring the orbital part, we get $\gamma_N = \frac{2A_Z\beta}{A_Z B_{\text{ext}}^2 + A_Z B_0^2}$. As we will see later on, A_Z is of the order $\sim 100\Omega.T^{-2}$ whereas $R_0 = A_Z B_0^2 \sim 10\ k\Omega$, yielding $B_0 \sim 10\ T$. We performed the analysis of β at $|\tilde{B}_{\text{ext}}| < 0.2\ T \ll B_0$, such that we can consider $B_{\text{ext}}^2 + B_0^2 \simeq B_0^2$, yielding $\gamma_N = \frac{2A_Z\beta}{R_0}$. We see that the relation between γ_N and β involves A_Z and R_0, which depend on the particular magnetoresistance and geometry of the sample. We believe that β is a better hallmark of the spin-orbit-induced MCA.

We measure the magneto-resistance via Ohm's relation $V = R.I$ between the voltage V across the sample and the current I traversing it. But now with terms in the resistance that depends on I, there will be terms of higher order in I in the voltage response, leading to higher order harmonic responses to an AC current excitation.

More explicitly, let us write for a current biased measurement : $V = R(B_{\text{ext}}, I).I$ with $I = I_{\text{DC}} + I_{\text{AC}}\sin(\omega t)$

Ignoring the purely orbital part, we can write the following voltage response :

$$V/A_Z = (B_{\text{ext}}^2 + B_0^2)I_{\text{DC}} + 2\beta B_{\text{ext}} I_{\text{DC}}^2 + \beta^2 I_{\text{DC}}^3 \tag{6.72}$$

$$+ (B_{\text{ext}}^2 + B_0^2 + 4\beta B_{\text{ext}} I_{\text{DC}} + 3\beta^2 I_{\text{DC}}^2) I_{\text{AC}} \sin(\omega t) \tag{6.73}$$

$$+ (2\beta B_{\text{ext}} + 3\beta^2 I_{\text{DC}}) I_{\text{AC}}^2 \sin^2(\omega t) \tag{6.74}$$

$$+ \beta^2 I_{\text{AC}}^3 \sin^3(\omega t) \tag{6.75}$$

Writing $\sin^2(\omega t) = \frac{1}{2} - \frac{1}{2}\cos(2\omega t)$ and $\sin^3(\omega t) = \frac{1}{4}\sin(\omega t) - \frac{1}{4}\sin(3\omega t)$, we can rewrite it :

$$V/A_Z = (B_{\text{ext}}^2 + B_0^2)I_{\text{DC}} + \beta B_{\text{ext}}(2I_{\text{DC}}^2 + I_{\text{AC}}^2) + \beta^2 I_{\text{DC}}^3 + \frac{3}{2}\beta^2 I_{\text{DC}} I_{\text{AC}}^2 \tag{6.76}$$

$$+ ((B_{\text{ext}}^2 + B_0^2)I_{\text{AC}} + 4\beta B_{\text{ext}} I_{\text{DC}} I_{\text{AC}} + 3\beta^2 I_{\text{DC}}^2 I_{\text{AC}} + \frac{3}{4}\beta^2 I_{\text{AC}}^3)\sin(\omega t) \tag{6.77}$$

$$+ (-\beta B_{\text{ext}} I_{\text{AC}}^2 - \frac{3}{2}\beta^2 I_{\text{DC}} I_{\text{AC}}^2)\cos(2\omega t) \tag{6.78}$$

$$- \frac{1}{4}\beta^2 I_{\text{AC}}^3 \sin(3\omega t) \tag{6.79}$$

Because of experimental limitations of our setup involving high capacitances and our highly resistive long nanowires of $R \sim 10\ k\Omega$, current-biasing the samples at $\sim 100\ Hz$ was not possible. We had to rely on voltage bias for all our AC measurements, see part 2.8.1 for the electrical sketch.

For a voltage biased system, still considering a current-induced effective magnetic field, we need to solve :

$$\beta^2 I^3 + 2\beta B I^2 + (B^2 + B_0^2)I - \frac{V}{A_Z} = 0 \tag{6.80}$$

This leads to very cumbersome expressions and conditions for the harmonics of $I(B_{\text{ext}}, V_{DC}, V_{AC}, t)$.

To avoid this, we consider approximate solutions. In the appendix 6.8, we present two approaches that lead to the same types of terms that depend on powers of V_{DC}, V_{AC}, B_{ext}, as well as A_Z and G. However, the two approximations lead to different prefactors.

In the following, let us consider the Taylor expansion of the inverse of the current bias response. The expansion is done up to the second order in excitation amplitude $\delta V = V_{\mathrm{AC}} \sin(\omega t)$, and is valid for small high order variations of the conductance $G(B_{Z,eff})$ with variations of the effective Zeeman field $\delta B_{Z,eff}$, and small high order variations of the resulting current response $I(V, B_{ext})$ with variations of voltage bias V and applied external magnetic field B_{ext}.

With a voltage excitation $V_{\mathrm{DC}} + V_{\mathrm{AC}} \sin(\omega t)$, where we consider $\tilde{V} = V_{\mathrm{DC}}$ and $\delta V = V_{\mathrm{AC}} \sin(\omega t)$, and $B_{Z,eff} = \tilde{B} + \delta B_{Z,eff} = \tilde{B} + \beta \delta I \simeq \tilde{B} + \beta G(\tilde{B}_{ext}, \tilde{V}) \delta V + \beta I^{(2)} \delta V^2$, we have :

$$\begin{aligned}
I &= G(\tilde{B} + \delta B_{Z,eff}) \times (V_{\mathrm{DC}} + V_{\mathrm{AC}} \sin(\omega t)) \\
&= G(\tilde{B}) V_{\mathrm{DC}} \\
&+ \left(-2A_Z G^3(\tilde{B}) \beta \tilde{B} V_{\mathrm{DC}} + G(\tilde{B})\right) V_{\mathrm{AC}} \sin(\omega t) \\
&+ \left(-2A_Z G^2(\tilde{B}) \beta \tilde{B} I^{(2)} V_{\mathrm{DC}} - 2A_Z G^4(\tilde{B}) \left(1 - 4A_Z G(\tilde{B}) \tilde{B}^2\right) \beta^2 V_{\mathrm{DC}} - 2A_Z G^3(\tilde{B}) \beta \tilde{B}\right) V_{\mathrm{AC}}^2 \sin^2(\omega t) \\
&+ (...) V_{\mathrm{AC}}^3 \sin^3(\omega t)
\end{aligned}$$

With $\sin^2(\omega t) = \frac{1}{2} - \frac{1}{2}\cos(2\omega t)$, and ignoring terms in V_{AC}^3 ,we write :

$$I = G(\tilde{B}) V_{\mathrm{DC}} - \left(A_Z G^3(\tilde{B}) \beta \tilde{B} + A_Z G^4(\tilde{B}) \beta^2 V_{\mathrm{DC}} - 6A_Z^2 G^5(\tilde{B}) \beta^2 \tilde{B}^2 V_{\mathrm{DC}} + 12 A_Z^3 G^7(\tilde{B}) \beta^3 \tilde{B}^3 V_{\mathrm{DC}}^2 - 2A_Z^2 G^6(\tilde{B}) \beta^3 \tilde{B} V_{\mathrm{DC}}^2\right) V_{\mathrm{AC}}^2 \tag{6.81}$$

$$+ \left(G(\tilde{B}) - 2A_Z G^3(\tilde{B}) \beta \tilde{B} V_{\mathrm{DC}}\right) V_{\mathrm{AC}} \sin(\omega t) \tag{6.82}$$

$$+ \left(A_Z G^3(\tilde{B}) \beta \tilde{B} - 6A_Z^2 G^5(\tilde{B}) \beta^2 \tilde{B}^2 V_{\mathrm{DC}} + A_Z G^4(\tilde{B}) \beta^2 V_{\mathrm{DC}}\right) V_{\mathrm{AC}}^2 \cos(2\omega t) \tag{6.83}$$

$$\tag{6.84}$$

In theory, this formula is only valid for the response of I to a small excitation δV up to the second order in δV, close to $G(\tilde{B}) = G(B_{ext} = \tilde{B}_{ext}, V = V_{\mathrm{DC}})$. For each couple of value $(B_{ext} = \tilde{B}_{ext}, V = V_{\mathrm{DC}})$ that we apply to our system, we should measure the corresponding $G(\tilde{B}_{ext}, V_{\mathrm{DC}})$. In practice, we choose $V_{\mathrm{DC}} = 0$ and approximate $G(\tilde{B}_{ext}, V_{\mathrm{DC}} = 0)$ to :

$$G(\tilde{B}_{ext}, V_{\mathrm{DC}} = 0) \simeq \frac{1}{A_Z(\tilde{B}_{\mathrm{ext}}^2 + B_0^2)} \simeq \frac{1}{R(B_{Z,eff} = 0)} \tag{6.85}$$

We recall that $A_Z B_0^2 = R(B_{Z,eff} = 0)$ the resistance of the nanowire at zero magnetic field and infinitesimal excitation, and $A_Z B_0^2 \gg A_Z(\tilde{B}_{\mathrm{ext}}^2$ in our experimental range.

Let us now look at the relative contribution of the various terms. For the big picture, notice that the original terms in I^n induce a response at the n-th harmonic which is proportional to the n-th power of the excitation amplitude. But high powers of I also "trickle down" to lower harmonics, see for example the terms proportional to the second power of the excitation amplitude in the zero-th harmonic response.

What makes the high harmonics measurement interesting can be stated as follows :
for sufficiently low excitation amplitude, the main contribution to the n-th harmonic comes from the response of the term in the n-th power of the excitation. If we write $V = \Sigma_{n \in \mathbb{N}} c_n I^n$ and $V = \Sigma_{n \in \mathbb{N}} V^{(n\omega)} e^{in\omega t}$, then one can make the approximation that $V^{(n\omega)} \propto c_n$.

To illustrate this, we focus on the first harmonic response in Eq. (6.79) for a current biased experiment. In addition to the usual differential resistance term $A_Z(B_{\mathrm{ext}}^2 + B_0^2) I_{\mathrm{AC}}$, there are three other ones. First, there is $4A_Z \beta B_{\mathrm{ext}} I_{\mathrm{DC}} I_{\mathrm{AC}}$ that features β and is quadratic in I. The other terms are cubic in I and thus smaller.

Why not use the first harmonic response to extract β then?

Because, as we will see in the following measurements' analysis, we have $4A_Z\beta B_{\mathrm{ext}}I_{\mathrm{DC}}I_{\mathrm{AC}} \sim 4\times10^{-8}\ V$ whereas $A_Z(B_{\mathrm{ext}}^2+B_0^2)I_{\mathrm{AC}} \sim 10^{-2}\ V$, yielding $\frac{4A_Z\beta B_{\mathrm{ext}}I_{\mathrm{DC}}I_{\mathrm{AC}}}{A_Z(B_{\mathrm{ext}}^2+B_0^2)I_{\mathrm{AC}}} \sim 4\times10^{-6} \ll 1$. Furthermore, we recall that for out-of-plane magnetic field measurements we need to take into consideration $A_{orb}B_{\mathrm{ext}}^2I_{\mathrm{AC}} \sim 10^{-5}\ V$.

In [208], they measured a $\sim 5\times10^{-3}$ modulation of the first order resistance (with $R \sim 3\times10^4\Omega$) caused by UMR by applying $I_{\mathrm{DC}} = 10^{-5}\ A$ and $B_{\mathrm{ext}} = 1\ T$ on a micrometers-size sample. Reproducing it on our samples would lead to a $\sim 10^{-3}$ modulation of our first order resistance, that is if the current density does not burn them.

On the other hand, we see that the main contribution of the second harmonic response is $-A_Z\beta B_{\mathrm{ext}}I_{\mathrm{AC}}^2$, linear (thus odd) in applied magnetic field B_{ext} and quadratic in excitation amplitude I_{AC}^2. The following measurements show that $A_Z\beta B_{\mathrm{ext}}I_{\mathrm{AC}}^2 \sim 10^{-8}\ V$, which is still a small $\sim 10\ nV$ signal, but it is not polluted by bigger contributions to the signal, or by an uncontrolled I_{DC} contribution.

Let us now come back to the current response to a voltage biased sample (Eq. (6.84)). Focusing on the second harmonic response, there are two terms, both proportional to V_{AC}^2 and featuring powers of β. The first term, $A_ZG^3(\tilde{B})\beta\tilde{B}V_{AC}^2$, is linear in B_{ext}. The second term, $-6A_Z^2G^5(\tilde{B})\beta^2\tilde{B}^2V_{\mathrm{DC}}V_{AC}^2$, is quadratic in B_{ext} and linear in V_{DC}, and hence vanishes for $V_{\mathrm{DC}} = 0$.

As stated before, this toy model doesn't account for a lot of effects that could show in the second harmonic response, but if such a "current-to-field" conversion factor β exists, we expect to see it in the linear dependence of the second harmonic to the magnetic field. To see it clearly, we split the second harmonic response into two parts :

- a part that is odd in applied magnetic field : $f_{\mathrm{o}}(B_{\mathrm{ext}}) = 0.5(f(B_{\mathrm{ext}}) - f(-B_{\mathrm{ext}}))$
- a part that is even in applied magnetic field : $f_{\mathrm{e}}(B_{\mathrm{ext}}) = 0.5(f(B_{\mathrm{ext}}) + f(-B_{\mathrm{ext}}))$

As such, the presence of β should show as a linear dependence in the odd part of the second harmonic response at low field $f_{\mathrm{o}}(B_{\mathrm{ext}})$.

As shown in appendix 6.9.4, we find that the odd part have a linear dependence in B_{ext} up to $|B_{\mathrm{ext}}| \sim 0.2 - 2\ T$, depending on the sample. Moreover, we find that the general shape of the odd part does not vary much with V_{AC} in the $\sim 1 - 100\ mV$ range, and scales with V_{AC}^2. At higher magnetic field, we also find on some samples Shubnikov-de Haas-like variations that we discuss in appendix 6.11.

Considering the even part, it should scale as $B_{\mathrm{ext}}^2V_{\mathrm{DC}}V_{\mathrm{AC}}^2$ and vanish for $V_{\mathrm{DC}} = 0$. This is generally not what we see. At $V_{\mathrm{DC}} = 0$, we measure an even part of amplitude similar to the odd part, and not quadratic neither in B_{ext} or V_{AC}^2. Finally, the shape of the even part can change substantially with V_{AC}.

6.7.5 . Qualitative picture of the Anomalous Josephson Effects

In part 1.3.9, we presented the φ_0-junction effect that manifest in Josephson junctions with SOC and Zeeman energy. We saw that the Zeeman energy introduces a shift in the Fermi surface, inducing finite momentum pairing and a phase shift φ_0 at zero current. So far, we only examined the case of a 1d helical junction in part 1.4.3. In this appendix, we discuss the interplay of current, magnetic field, and phase shifts in a larger scope.

Let us start by a trivial observation : the supercurrent is affected by the magnetic field. Indeed, the magnetic field shifts the CPR by φ_0, and at a given phase difference φ the supercurrent $I(\varphi)$ has been changed. Embedding the junction in an AC SQUID would yield an anomalous supercurrent $I_0 = I(0)$ at zero flux, see the blue dot in Fig.6.30a, that depends on the Zeeman energy of the junction. This is the traditional formulation of the anomalous Josephson effect.

Conversely, applying a DC current bias I^* to the junction would yield a superconducting phase difference

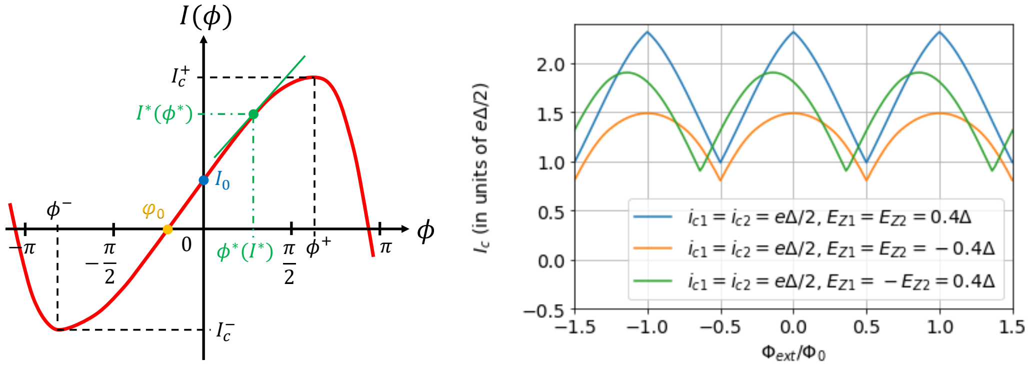

(a)

(b)

Figure 6.30 – (a) CPR of a Josephson junction with the various conventions used to discuss phases shifts and critical current. The symmetry $I(\phi) = -I(-\phi)$ is broken when there is a magnetic field and AJE. Gold dot : anomalous phase shift φ_0, for which $I(\varphi_0) = 0$. Blue dot : anomalous supercurrent $I_0 = I(\phi = 0) \neq 0$. Green solid line : derivative $dI/d\phi\rfloor_{\phi^*}$ of the CPR at the green point (I^*, ϕ^*). For a bias current I^*, the junction can be treated as a (kinetic) inductance $L_K(I^*) = \frac{\Phi_0}{2\pi}\frac{1}{dI/d\phi\rfloor_{\phi^*}}$. (b) Critical current of a DC SQUID featuring two short 1d helical channels/junctions, as a function of magnetic flux Φ_{ext} applied through the SQUID surface via an external magnetic field. Junctions 1 and 2 have critical currents $i_{c1} = i_{c2}$, and Zeeman energies E_{Z1} and E_{Z2}. Blue line : $E_{Z1} = E_{Z2} = 0.4\Delta$. Orange line : $E_{Z1} = E_{Z2} = -0.4\Delta$. Because of TRS and $\pm\Phi_{ext}$ symmetry, the blue and orange curves also correspond to identical E_{Z1} and identical E_{Z2} but opposite current bias $I_c^{\pm}$. In this situation, the AJE-induced phase shifts compensate while the AJE-induced current shifts add up, showing high JDE but no shift in flux. Green line : $E_{Z1} = -E_{Z2} = 0.4\Delta$. In this situation, the AJE-induced phase shifts add up while the AJE-induced current shifts compensate, showing low JDE but a shift in flux.

φ^* such that $I^* = I(\varphi^*)$. This φ^* is shifted by the field-induced φ_0, and there exists an I_0 such that $I_0 = I(0) \neq 0$, see the blue dot in Fig.6.30a. For this current bias I_0, the superconducting leads have the same phases, recovering the symmetry they had at zero current bias and without magnetic field. In other words, the current bias I_0 compensate exactly the finite momentum pairing induced by the magnetic field.

Indeed, carrying a supercurrent in a superconductor requires Cooper pairs with non-zero momentum, such that current bias creates finite momentum pairing. Just like the Zeeman-induced finite momentum pairing at zero current, the current bias induced one depends on the Fermi surface and its spin-texture. It is reminiscent of the Edelstein effect in the resistive state, where a DC current bias induces an out-of-equilibrium spin polarization, see part 6.7.1. In fact, the supercurrent I_0 at zero phase difference induces the same spin polarization as in the resistive state, except that it is now an equilibrium quantity [209].

So in a sense, one can say that it corresponds to the current-induced spin polarization necessary to produce the opposite of the applied magnetic field, such that the two effects cancel out. In this sense, applying a current bias is equivalent to applying a magnetic field. The rigorous connection, however, is between the inverse Edelstein effect and φ_0 [85]. In a superconductor with SOC, there is a relation between the phase gradient and spin polarization, such that $\varphi \neq 0$ induces a spin polarization, translating into a supercurrent via the inverse Edelstein effect. Conversely, a given Zeeman energy produces a spin polarization and a related φ. At $\varphi = \varphi_0$, the spin-induced supercurrent compensates exactly the supercurrent generated by the phase difference, such that $I_{tot} = I_{IEE} + I_p(\varphi = \varphi_0) = 0$, where $I_p(\varphi)$ is the CPR of the junction without the inverse Edelstein effect.

The supercurrent-momentum relation is affected by the Fermi surface and its spin-texture, that is modified by the Zeeman energy, just like the Zeeman energy-momentum relation is affected by the supercurrent.

So there is a deep connection between the supercurrent through the junction and the Zeeman energy, provided by the momentum of the Cooper pairs. For the simple case of 1d helical channels, the CPR can be calculated analytically within the Bogoliubov-de Gennes formalism [72, 73], as done in part 1.4.3. For more complex Fermi surfaces like 2d junctions with Rashba SOC, the most successful approach so far was to use the Ginzburg-Landau formalism, see [83] for general formulas and symmetries analysis and [84] for a focus on Rashba 2DEG.

Let us now discuss the implications of AJE for the $I_c^+(\Phi_{ext})$ patterns and for the JDE. For junctions with sinusoidal CPR, AJE only shifts the CPR in phase by φ_0. If the CPR has higher harmonics however, AJE can also induce an asymmetry between positive and negative currents, and in particular a difference in critical currents $I_c^\pm$ [72, 210, 211, 74, 86]. Indeed, the higher harmonics present in a CPR may not share the same phase shift φ_0 and can be shifted in an asynchronous way, such that the CPR is deformed by the magnetic field, as seen in part 1.4.3 for short ballistic helical junctions in a magnetic field.

Even if AJE only shifts a sinusoidal CPR by a phase φ_0, this effect can be detected in an AC SQUID geometry, as discussed in [108], or in a DC SQUID, as demonstrated in [112] in a geometry similar to the experiment showing MCA presented in appendix 6.12.

To illustrate the effects of both AJE-induced φ_0 phase-shifts and AJE-induced current-shifts (as opposed to pure φ_0 phase-shifts), let us look again at Fig.6.30b, reproduced from part 1.6.3. It shows the calculated critical current of a DC SQUID featuring two short 1d helical channels/junctions, as a function of magnetic flux Φ_{ext} applied through the SQUID surface via an external magnetic field. Junctions 1 and 2 have identical critical currents $i_{c1} = i_{c2}$, and Zeeman energies E_{Z1} and E_{Z2}. The particularity of a DC SQUID geometry is that the supercurrents from the two junctions add up to give the total supercurrent while their superconducting phase differences subtract in the total phase constrain, see part 1.5.3. Hence, if we approximate the effects of AJE as a combination of a pure phase-shift and a pure current-shift of the CPR, the DC SQUID geometry allows splitting both contributions of the AJE.

First, we recall that by TRS, for a critical current $I_c^+(E_Z, \Phi_{ext})$ with positive current bias, we have :

$$I_c^+(E_Z, \Phi_{ext}) = I_c^-(-E_Z, -\Phi_{ext}) \tag{6.86}$$

where the Zeeman energy E_Z corresponds to the Zeeman influence of the magnetic field, while Φ_{ext} corresponds to its orbital influence. This equation means that reversing the current bias is equivalent to reversing the magnetic field (both the Zeeman and the orbital contributions of the magnetic field), see part 1.7 for more details. Conversely, reversing both the current bias and E_Z is equivalent to reversing Φ_{ext}, and reversing both the current bias and Φ_{ext} is equivalent to reversing E_Z.

But now that multiple contributions of the magnetic field can be reversed, there are multiple definitions of JDE. Extrapolating from the discussion in part 1.7 with a single field contribution, one can be tempted to define JDE as $I_c^+(E_Z, \Phi_{ext}) \neq I_c^+(E_Z, -\Phi_{ext})$. However, this inequality does not yield $I_c^+(E_Z, \Phi_{ext}) \neq I_c^-(E_Z, \Phi_{ext})$ but $I_c^+(E_Z, \Phi_{ext}) \neq I_c^-(-E_Z, \Phi_{ext})$, which does not correspond to simply reversing the current bias, contrasting with the single field contribution situation. For the double field contribution situation, JDE writes $I_c^+(E_Z, \Phi_{ext}) \neq I_c^-(E_Z, \Phi_{ext}) \Longleftrightarrow I_c^+(E_Z, \Phi_{ext}) \neq I_c^+(-E_Z, -\Phi_{ext})$.

The green solid line in Fig.6.30b illustrate the case $E_{Z1} = -E_{Z2} = 0.4\Delta$, where Δ is the superconducting energy, see parts 1.4.3 and 1.6.3 for more details. In this situation, the main effect of AJE is to shift the SQUID interference pattern by $\simeq 2\varphi_0$, while the AJE-induced current-shifts do not contribute. Indeed, the subtraction of opposite phase shifts add up while the addition of opposite current shifts compensate each other. This situation corresponds to two junctions with opposite chiralities, either with identical current biases and magnetic fields but opposite helicities, or with identical magnetic field and helicities but opposite current biases (like samples studied in [112] and in appendix 6.12). Because of the orbital dephasing introduced by Φ_{ext}, reversing the current bias is equivalent to reversing not only both E_{Z1} and E_{Z2}, but also Φ_{ext}. As a result, because we have $I_c^+(E_{Z1}, E_{Z2}, \Phi_{ext}) \simeq I_c^+(-E_{Z1}, -E_{Z2}, -\Phi_{ext})$ (AJE essentially shift the pattern in the opposite direction when reversing both E_{Z1} and E_{Z2}), we have $I_c^+(E_{Z1}, E_{Z2}, \Phi_{ext}) \simeq I_c^-(E_{Z1}, E_{Z2}, \Phi_{ext})$ and JDE is negligible.

In contrast, the blue and orange solid lines in Fig.6.30b illustrate large JDE but no flux shift of the SQUID pattern. Indeed, these curves correspond to $E_{Z1} = E_{Z2} = 0.4\Delta$ and $E_{Z1} = E_{Z2} = -0.4\Delta$, respectively. Because both curves are symmetric in $\pm\Phi_{ext}$, we can write :

$$I_c^+(E_{Z1}, E_{Z2}, \Phi_{ext}) = I_c^+(E_{Z1}, E_{Z2}, -\Phi_{ext}) \Longleftrightarrow I_c^+(E_{Z1}, E_{Z2}, \Phi_{ext}) = I_c^-(-E_{Z1}, -E_{Z2}, \Phi_{ext}) \quad (6.87)$$

meaning that the two curves actually also correspond to identical E_{Z1} and identical E_{Z2} but opposite current bias. At any given set of field contributions $(E_{Z1}, E_{Z2}, \Phi_{ext})$, the blue and orange curves exhibit large I_c difference, yielding high JDE $I_c^+(E_{Z1}, E_{Z2}, \Phi_{ext}) \neq I_c^-(E_{Z1}, E_{Z2}, \Phi_{ext})$, even at $\Phi_{ext} = 0$. Here, the maximum is still at $\Phi_{ext} = 0$ and the patterns are symmetric in $\pm\Phi_{ext}$ because the φ_0-shifts compensate, and the only remaining effect is the AJE-induced current-shifts which add up.

6.7.6 . Phenomenological models of MCA in the superconducting state

As discussed in previous appendix 6.7.5), the spin-orbit-induced Anomalous Josephson Effects (AJE) can induce Josephson Diode Effect (JDE), where the maximum supercurrent depends on the orientation and magnitude of the magnetic field. This constitutes a form of Magneto-Chiral Anisotropy (MCA) in the superconducting state. In superconductors and Josephson junctions with SOC, MCA in the superconducting state is understood thanks to the finite Cooper pair momentum theory introduced in part 1.3.9. MCA can also be probed in the superconducting fluctuation regime, and is understood via the theory of paraconductivity [203]. While MCA is more easily probed in the superconducting fluctuation regime, it is harder to analyze as it is at the limit between the superconducting and the resistive states. In this appendix, we discuss the phenomenological models found in the recent literature, and we introduce our own very simple model that allows us to analyze and compare MCA of a bismuth-nanowire-based Josephson junction in both its resistive and superconducting states (see 6.12).

a) MCA in Josephson junctions

In [86], the authors use a simple two harmonics model to reproduce their experimental data. They write the CPR of their junction as :

$$I(\phi) = \frac{4e}{\hbar}\left(\Delta^2|\gamma_1|\sin\phi + \Delta^4|\gamma_2|\sin(2\phi+\delta)\right) \quad (6.88)$$

with Δ the superconducting energy. $|\gamma_1|$ and $|\gamma_2|$ are magnitudes of first- and second-order Cooper pair tunneling processes, respectively. δ is at the origin of the AJE-induced current-shift. $\delta = arg(\gamma_2) - 2arg(\gamma_1)$ is the phase shift associated with the interference between the first-order and second-order Cooper pair tunneling processes. In a superconductor with finite momentum q_x along x, induced by a magnetic field B_y along y (for Rashba SOC, see Fig.1.19d), the phase shift accumulated during the Cooper pair propagation across the junction is $\delta \simeq 2q_x d$, with d the length of the junction. At small values of field, q_x is linear in B_y and one can write :

$$\delta \simeq 2q_x d \simeq \pi\frac{B_y}{B_d} \quad (6.89)$$

where B_d is a characteristic of the junction.

Writing

$$I_c^{\pm} \simeq \left|I(\pm\frac{\pi}{2})\right| = \frac{4e}{\hbar}\left(\Delta^2|\gamma_1| \mp \Delta^4|\gamma_2|\sin\delta\right) \quad \text{the JDE is} \quad \Delta I_c = -\frac{8e}{\hbar}\Delta^4|\gamma_2|\sin\delta \quad (6.90)$$

with Δ that varies with temperature and magnetic field magnitude. This formula shows a form of MCA, with ΔI_c depending on $\boldsymbol{B}$ via $\delta \simeq \pi \frac{B_y}{B_d}$. For high field values, depairing reduces the value of Δ, following $\Delta(|\boldsymbol{B}|) \propto \sqrt{\left(1 - \left(\frac{|\boldsymbol{B}|}{B_c}\right)^2\right)}$, with B_c a critical field characteristic of the superconductor.

In [210, 211], they treat the AJE-induced current-shift by considering an entire array of planar junctions (perpendicular to $\hat{\boldsymbol{z}}$) with Rashba SOC as an inductance with MCA, $L = L_0(1 + \gamma_L \hat{\boldsymbol{z}} \cdot \boldsymbol{B} \times \boldsymbol{I})$, but it is an approximation only valid for low supercurrent and that ignores the φ_0-shift. For DC SQUID experiments, describing the junction with AJE-induced current-shift doesn't seem appropriate. The authors demonstrate both MCA of inductance L, JDE at $B_z = 0$ with $B_y = 750G$, and magnetoresistance MCA $R = R_0(1 + \gamma_F \hat{z} \cdot \boldsymbol{B} \times \boldsymbol{I})$ in the regime of thermal phase fluctuation at $T \lesssim T_c$. They find $\gamma_L \simeq 0.77 \times 10^6 T^{-1}.A^{-1}$ and $\gamma_F \simeq 4.1 \times 10^6 T^{-1}.A^{-1}$, with identical angular dependence for both MCA.

b) MCA in a non-centrosymmetric bulk superconductor

In [84], the authors found a $\boldsymbol{k}$-dependent $\Delta(\boldsymbol{k})$ for a 2d electron gas with Rashba SOC and bulk superconductivity ($|\Delta|$ homogeneous over the whole system), using BdG model. Moreover, they used Ginzburg-Landau theory to find the expression of the frontier between the superconducting and the resistive phases, valid when $T \lesssim T_c$ or $B \lesssim B_c$, expressed as a function of applied current $\boldsymbol{J}$ and magnetic field $\boldsymbol{B}$ as :

$$\left(\frac{|\boldsymbol{B}|}{B_c}\right)^2 + \left|\frac{\boldsymbol{J}}{J_c} - \nu \frac{\boldsymbol{B} \times \hat{\boldsymbol{z}}}{B_c}\left(1 - \frac{|\boldsymbol{B}|^2}{B_c^2}\right)^2\right|^{2/3} = 1 \tag{6.91}$$

with J_c the critical current at $\boldsymbol{B} = \boldsymbol{0}$, $\hat{\boldsymbol{z}}$ the unit vector perpendicular to the surface. $\nu = \nu(T) = \frac{\alpha_R}{v_F}\frac{B_c}{B_P}\sqrt{1 - \frac{T}{T_c}}$, with $B_P = 1.25 T_c$ the Pauli limit. For crystalline systems with reduced spatial symmetries, we expect this relation to also depend on the crystal orientation. The resulting asymmetry in $|\boldsymbol{B}|$ is illustrated in Fig.6.31a, for $\boldsymbol{B} \perp \boldsymbol{J} \perp \hat{\boldsymbol{z}}$, with $J_c^{\pm}$ critical currents at fixed $|\boldsymbol{B}|$ and $B_c^{\pm}$ the critical fields at fixed $|\boldsymbol{J}|$. They find :

$$\Delta B_c = B_c^+ - B_c^- = \frac{2}{3}\nu B_c \frac{J}{J_c} \text{ and } \Delta J_c = J_c^+ - J_c^- = 2\nu J_c \frac{B}{B_c} \tag{6.92}$$

They argue that, near T_c, $\Delta J_c \propto (T_c - T)^2$ and ΔB_c is independent of T, as $J_c \propto (T_c - T)^{3/2}$, $B_c \propto (T_c - T)^{1/2}$ and $\nu \propto (T_c - T)$. Thus, in addition to the dependence on magnetic field orientation, temperature might be useful to distinguish AJE from inductances, as its effects scale both with J_c and B_c, in contrast with inductive effects scaling only with J_c.

For a practical estimate, we can look at [212]. They express $\Delta I_c = \frac{4 e q_x v_F}{\hbar}$. For a spin-orbit energy much larger than the Zeeman energy E_Z, we have $q_x v_F = E_Z$. For small magnetic field B_y, it yields $\Delta I_c \simeq g_{eff} 1.8 \times 10^{-8} A.T^{-1} = g_{eff} 1.8 \times 10^{-6} \mu A.G^{-1}$.

c) B_{eff} extended to MCA in Josephson junctions

As seen in parts 6.7.3 and 6.7.6, Edelstein effects are sources of MCA both in the resistive and the superconducting states. In part 6.7.3, we introduced a phenomenological model of MCA in the resistive state which is based on a current-induced effective magnetic field proportional to the current $B_{eff} = \beta I$. In the same spirit, in part 6.7.6, we argue that one way to think about AJE is to consider a current-induced B_{eff} that adds to the Zeeman field. This approach is not rigorous but is fine for our analysis and to compare our results in both the resistive and superconducting states.

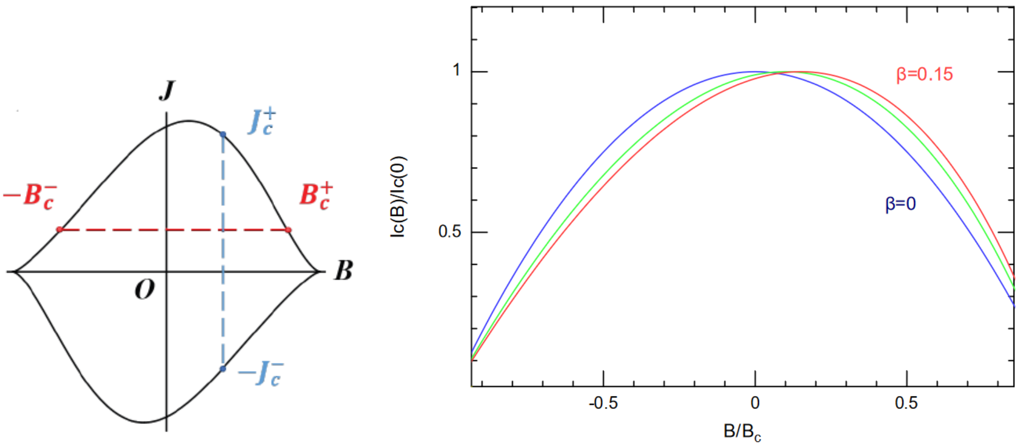

(a) (b)

Figure 6.31 – (a) Critical current of a junction made of a 2d electron gas with Rashba SOI and bulk superconductivity, as a function of in-plane magnetic field, perpendicular to the current. J_c^+ and J_c^- correspond to critical current for positive and negative current bias, respectively. No asymmetry in the junction. From [84]. (b) Critical current of a Josephson junction as a function of Zeeman field B, assuming a spin-orbit-induced current-induced effective Zeeman field $B_{Z,eff} = B + \beta I$. The blue solid line corresponds to a gaussian decay with characteristic Zeeman field B_c and $\beta = 0$. The green and red solid lines correspond to the same gaussian decay as the blue line, but with $\beta = TODO$ and $\beta = 0.15\frac{B_c}{I_c(0)}$, respectively.

In the case of Rashba SOI, a supercurrent-induced in-plane magnetization perpendicular to the current is predicted [209], which is identical to its value in the normal state in the long junction limit :

$$S_y = en\tau_e\alpha J/\sigma_D \tag{6.93}$$

in Bohr magneton units, with n the density of states , τ_e the elastic scattering time, σ_D the conductivity, and $J = I/W$ is the 2D current density assumed along the x axis.

Which can also be written as :

$$S_y = \frac{\alpha}{\hbar v_F}(I/I_0) \tag{6.94}$$

where $I_0 = ev_F/L$ is the critical current for a ballistic 1D channel in the long junction limit and I the current through the SNS junction

The maximum spin polarization is obtained when I is equal to the critical current I_c and reaches :

$$S_y^{max} \sim (\alpha/\hbar v_F)Ml_e/L \tag{6.95}$$

where $M = W/\lambda_F$ is the number of transverse channels of the junction. When the spin-orbit energy is of the order of the Fermi energy, this spin polarization corresponds to 1 Bohr magneton per effective conducting channels, which is the case for Bi based materials. It is much smaller for semiconductors where the spin orbit energy does not exceed few meV.

It is interesting to compare these relations with the case of a single helical ballistic edge state in the long junction limit whose spin polarization is expected to vary like : $S_y = I/I_0$ which corresponds to a unit spin polarization at the critical current.

In terms of energy, this spin polarization translates into an excess Zeeman magnetic energy $E_T I/I_0 = \Phi_0 I$ leading to the effective Zeeman field $g_{eff}\mu_B B_{eff}(I) = \Phi_0 I$ to be compared with Eq.(6.69) for Rashba

SOC. If one considers instead a Josephson junction with a large number N_h of helical states with a random distribution of helicities, these quantities are expected to scale as $N_h^{1/2}$

This effective Zeeman field B_{eff}, approximately proportional to I as $B_{eff} \simeq \beta I$, is expected to enter the Zeeman field dependence of the critical current varying as $I_c = I_c^{max}(B/B_c)$, where the magnetic field $B = B_Z + B_{eff}(I_c)$ gives rise to a field asymmetry of the critical current between positive and negative values of magnetic field, which depends on the sign of the current though the junction.

Depending on the ratio of B_{eff}/B_c different behaviors are expected. In particular, when $B_{eff} >> B_c$ the critical current is not maximum in zero field and first increase with magnetic field presenting a maximum at finite field.

This behavior was observed in a bismuth-nanowire-based Josephson junction with different field orientations, as shown in appendix 6.12. Fig.6.31b illustrates the effect of different coefficients β, assuming a gaussian decrease of the critical current with respect to the Zeeman field.

6.8 . Non-linear current response to a voltage bias

In this appendix, we detail two different calculation methods used to approximate the non-linear current response to a voltage bias, when including a current-induced effective magnetic field $B_{eff} = \beta I$.

For a voltage biased system, still considering a current-induced effective magnetic field, we need to solve :

$$\beta^2 I^3 + 2\beta B I^2 + (B^2 + B_0^2)I - \frac{V}{A_Z} = 0 \tag{6.96}$$

The solution is :

$$6I = -\frac{4B_{\text{ext}}}{\beta} + 2A_Z(B_{\text{ext}}^2 - 3B_0^2)\left(\frac{2}{\tilde{V}(B_{\text{ext}}, V)}\right)^{1/3} + \frac{1}{A_Z\beta^2}\left(4\tilde{V}(B_{\text{ext}}, V)\right)^{1/3} \tag{6.97}$$

with $\tilde{V}(B_{\text{ext}}, V) = A_Z^2\beta^3\left(2A_Z B_{\text{ext}}^3 + 18A_Z B_{\text{ext}} B_0^2 + 27\beta V + \sqrt{-4A_Z^2(B_{\text{ext}}^2 - 3B_0^2)^3 + (2A_Z(B_{\text{ext}}^3 + 9B_{\text{ext}}B_0^2) + 27\beta V)^2}\right)$.

Considering $V(t) = V_{DC} + V_{AC}\sin(\omega t)$, it becomes :

$$\begin{aligned}\frac{\tilde{V}(B_{\text{ext}}, V(t))}{A_Z^2\beta^3} &= 2A_Z B_{\text{ext}}^3 + 18A_Z B_{\text{ext}} B_0^2 + 27\beta V_{DC} + 27\beta V_{AC}\sin(\omega t) \\ &+ \sqrt{K + 54\beta(2A_Z(B_{\text{ext}}^3 + 9B_{\text{ext}}B_0^2) + 27\beta V_{DC})V_{AC}\sin(\omega t) + 729\beta^2 V_{AC}^2\sin^2(\omega t)}\end{aligned}$$

with $K = -4A_Z^2(B_{\text{ext}}^2 - 3B_0^2)^3 + \left(2A_Z(B_{\text{ext}}^3 + 9B_{\text{ext}}B_0^2) + 27\beta V_{DC}\right)^2$.

This leads to very cumbersome expressions and conditions for the harmonics of $I(B_{\text{ext}}, V_{DC}, V_{AC}, t)$.

To avoid this, let us find approximate solutions by two different methods.

6.8.1 . Taylor expansion in β of the solution of an approximate quadratic equation

Let us consider the following conditions : $\beta \ll 1$ and $\beta I \ll B_{\text{ext}}$. The equation for I thus becomes :

$$\cancel{\beta^2 I^3} + 2\beta B I^2 + (B^2 + B_0^2)I - \frac{V_{DC} + V_{AC}\sin(\omega t)}{A_Z} = 0 \tag{6.98}$$

and the solutions are : $I_\pm(t) = -\frac{B^2+B_0^2 \pm \sqrt{(B^2+B_0^2)^2 + 8B\beta(V_{DC}+V_{AC}\sin(\omega t))/A_Z}}{4B\beta}$

where the condition $(B^2 + B_0^2)^2 + 8B\beta(V_{DC} + V_{AC}\sin(\omega t))/A_Z > 0$ is always true for the small V applied.

The Taylor expansion of order two in β of the harmonic decomposition of $I_{\pm}(t)$ is :

$$I_{\pm} = \mp \frac{4\beta^2 B_{\mathrm{ext}}^2 \left(3V_{AC}^2 V_{DC} + 2V_{DC}^3\right)}{A^3\left(B_{\mathrm{ext}}^2 + B_0^2\right)^5} \pm \frac{\beta B_{\mathrm{ext}}\left(V_{AC}^2 + 2V_{DC}^2\right)}{A^2\left(B_{\mathrm{ext}}^2 + B_0^2\right)^3} \mp \frac{V_{DC}}{A\left(B_{\mathrm{ext}}^2 + B_0^2\right)} - \frac{B_{\mathrm{ext}}^2 + B_0^2}{2\beta B_{\mathrm{ext}}} \tag{6.99}$$

$$+ \left(\mp \frac{6\beta^2 B_{\mathrm{ext}}^2 V_{AC}\left(V_{AC}^2 + 4V_{DC}^2\right)}{A^3\left(B_{\mathrm{ext}}^2 + B_0^2\right)^5} \pm \frac{4\beta B_{\mathrm{ext}} V_{AC} V_{DC}}{A^2\left(B_{\mathrm{ext}}^2 + B_0^2\right)^3} \mp \frac{V_{AC}}{A\left(B_{\mathrm{ext}}^2 + B_0^2\right)}\right)\sin(\omega t) \tag{6.100}$$

$$+ \left(\mp \frac{\beta B_{\mathrm{ext}}}{A^2\left(B_{\mathrm{ext}}^2 + B_0^2\right)^3} V_{AC}^2 \pm \frac{12\beta^2 B_{\mathrm{ext}}^2 V_{DC}}{A^3\left(B_{\mathrm{ext}}^2 + B_0^2\right)^5} V_{AC}^2\right)\cos(2\omega t) \tag{6.101}$$

$$\pm \frac{2\beta^2 B_{\mathrm{ext}}^2}{A^3\left(B_{\mathrm{ext}}^2 + B_0^2\right)^5} V_{AC}^3 \sin(3\omega t) \tag{6.102}$$

6.8.2 . Taylor expansion of the inverse of the current bias response

Let us relate the second order response of the current to a voltage bias ($\frac{\delta^2 I}{\delta V^2}$) thanks to the previously calculated resistance. First, notice that in our toy model the resistance only depends on the current via the effective Zeeman field. Still leaving aside the orbital part, we have :

$$R(B_{Z,eff}) = R(B_{ext} + \beta I) = R(B_{ext}, I) \tag{6.103}$$

Conversely, we can write :

$$G(B_{Z,eff}) = \frac{1}{R(B_{Z,eff})} = G(B_{ext}, V) \tag{6.104}$$

For small high order variations of G with $\delta B_{Z,eff}$ ($\frac{\partial^n G}{\partial B_{Z,eff}^n}\Big|_{B_{Z,eff}=\tilde{B}} \delta B_{Z,eff}^n$), we can perform a first order Taylor expansion of G close to $B_{Z,eff} = \tilde{B}$:

$$G(\tilde{B} + \delta B_{Z,eff}) \simeq G(\tilde{B}) + \frac{\partial G}{\partial B_{Z,eff}}\Big|_{B_{Z,eff}=\tilde{B}} \delta B_{Z,eff} + \frac{1}{2}\frac{\partial^2 G}{\partial B_{Z,eff}^2}\Big|_{B_{Z,eff}=\tilde{B}} \delta B_{Z,eff}^2 \tag{6.105}$$

$$G(\tilde{B}+\delta B_{Z,eff}) \simeq G(\tilde{B}) - G^2(\tilde{B})\frac{\partial R}{\partial B_{Z,eff}}\Big|_{\tilde{B}} \delta B_{Z,eff} - G^2(\tilde{B})\left[\frac{\partial^2 R}{\partial B_{Z,eff}^2}\Big|_{\tilde{B}} - 2G(\tilde{B})\left(\frac{\partial R}{\partial B_{Z,eff}}\Big|_{\tilde{B}}\right)^2\right]\delta B_{Z,eff}^2 \tag{6.106}$$

From Eq. (6.71), we have $\frac{\partial R}{\partial B_{Z,eff}}\Big|_{\tilde{B}} = 2A_Z\tilde{B}$ and $\frac{\partial^2 R}{\partial B_{Z,eff}^2}\Big|_{\tilde{B}} = 2A_Z$. We write :

$$G(\tilde{B} + \delta B_{Z,eff}) \simeq G(\tilde{B}) - 2A_Z G^2(\tilde{B})\tilde{B}(\delta B_{ext} + \beta\delta I) - 2A_Z G^2(\tilde{B})\left(1 - 4A_Z G(\tilde{B})\tilde{B}^2\right)(\delta B_{ext} + \beta\delta I)^2 \tag{6.107}$$

So far, we have $G(\tilde{B} + \delta B_{Z,eff}) = G(B_{ext} = \tilde{B}_{ext} + \delta B_{ext}, I = \tilde{I} + \delta I)$. Now, we want to express $G(B_{ext}, I)$ in terms of variables B_{ext} and V. To do so, we need to relate δI to δV. Performing another Taylor expansion close to $B_{ext} = \tilde{B}_{ext}$ and $V = \tilde{V}$, we have :

$$\delta I = \frac{\partial I}{\partial V}\Big|_{\tilde{B}_{ext},\tilde{V}} \delta V + \frac{\partial I}{\partial B_{ext}}\Big|_{\tilde{B}_{ext},\tilde{V}} \delta B_{ext} + \frac{1}{2}\frac{\partial^2 I}{\partial V^2}\Big|_{\tilde{B}_{ext},\tilde{V}} \delta V^2 + \frac{1}{2}\frac{\partial^2 I}{\partial B_{ext}^2}\Big|_{\tilde{B}_{ext},\tilde{V}} \delta B_{ext}^2 + \ldots \tag{6.108}$$

Thus, for $\frac{\partial^3 I}{\partial V^3}\Big|_{\tilde{B}_{ext},\tilde{V}} \delta V \ll \frac{\partial^2 I}{\partial V^2}\Big|_{\tilde{B}_{ext},\tilde{V}}$ (and higher order terms), we can write $\delta I \simeq G(\tilde{B}_{ext}, \tilde{V})\delta V + I^{(2)}\delta V^2$, with $I^{(2)} = \frac{1}{2}\frac{\partial^2 I}{\partial V^2}\Big|_{\tilde{B}_{ext},\tilde{V}}$.

Finally, for small enough non-linear dependence of the current response δI on the effective Zeeman field $B_{Z,eff}$ and on the voltage bias V, and for $\delta B_{ext} = 0$, we can write :

$$\begin{aligned}G(\tilde{B} + \delta B_{Z,eff}) \simeq{}& G(\tilde{B}) - 2A_Z G^3(\tilde{B})\beta\tilde{B}\delta V \\ &- 2A_Z G^2(\tilde{B})\beta\tilde{B}I^{(2)}\delta V^2 - 2A_Z G^4(\tilde{B})\left(1 - 4A_Z G(\tilde{B})\tilde{B}^2\right)\beta^2\delta V^2\end{aligned}$$

With a voltage excitation $V_{\mathrm{DC}} + V_{\mathrm{AC}}\sin(\omega t)$, where we consider $\tilde{V} = V_{\mathrm{DC}}$ and $\delta V = V_{\mathrm{AC}}\sin(\omega t)$, we have :

$$\begin{aligned}I &= G(\tilde{B} + \delta B_{Z,eff}) \times (V_{\mathrm{DC}} + V_{\mathrm{AC}}\sin(\omega t)) \\ &= G(\tilde{B})V_{\mathrm{DC}} \\ &+ \left(-2A_Z G^3(\tilde{B})\beta\tilde{B}V_{\mathrm{DC}} + G(\tilde{B})\right)V_{\mathrm{AC}}\sin(\omega t) \\ &+ \left(-2A_Z G^2(\tilde{B})\beta\tilde{B}I^{(2)}V_{\mathrm{DC}} - 2A_Z G^4(\tilde{B})\left(1 - 4A_Z G(\tilde{B})\tilde{B}^2\right)\beta^2 V_{\mathrm{DC}} - 2A_Z G^3(\tilde{B})\beta\tilde{B}\right)V_{\mathrm{AC}}^2\sin^2(\omega t) \\ &+ (...)V_{\mathrm{AC}}^3\sin^3(\omega t)\end{aligned}$$

With $\sin^2(\omega t) = \frac{1}{2} - \frac{1}{2}\cos(2\omega t)$, and ignoring terms in V_{AC}^3, we write :

$$\begin{aligned}I = G(\tilde{B})V_{\mathrm{DC}} &- [A_Z G^3(\tilde{B})\beta\tilde{B} + A_Z G^4(\tilde{B})\beta^2 V_{\mathrm{DC}} - 6A_Z^2 G^5(\tilde{B})\beta^2\tilde{B}^2 V_{\mathrm{DC}} \\ &+ 12A_Z^3 G^7(\tilde{B})\beta^3\tilde{B}^3 V_{\mathrm{DC}}^2 - 2A_Z^2 G^6(\tilde{B})\beta^3\tilde{B}V_{\mathrm{DC}}^2]V_{\mathrm{AC}}^2 \\ &+ \left(G(\tilde{B}) - 2A_Z G^3(\tilde{B})\beta\tilde{B}V_{\mathrm{DC}}\right)V_{\mathrm{AC}}\sin(\omega t) \\ &+ \left(A_Z G^3(\tilde{B})\beta\tilde{B} - 6A_Z^2 G^5(\tilde{B})\beta^2\tilde{B}^2 V_{\mathrm{DC}} + A_Z G^4(\tilde{B})\beta^2 V_{\mathrm{DC}}\right)V_{\mathrm{AC}}^2\cos(2\omega t)\end{aligned}$$

To obtain this expression, we solved $I^{(2)}$ self-consistently, as :
$I^{(2)} = \frac{1}{2}\frac{\partial^2 I}{\partial V^2}\Big|_{\tilde{B}_{ext},\tilde{V}} \simeq -2A_Z G^2(\tilde{B})\beta\tilde{B}I^{(2)}V_{\mathrm{DC}} - 2A_Z G^4(\tilde{B})\left(1 - 4A_Z G(\tilde{B})\tilde{B}^2\right)\beta^2 V_{\mathrm{DC}} - 2A_Z G^3(\tilde{B})\beta\tilde{B}$.

6.9 . Resistive state behavior of long Bi nanowires

This appendix presents our results on long single-crystal bismuth nanowires with normal resistive contacts. We first present the samples and their geometry in part 6.9.1. In part 6.9.2, from their resistivities as a function of length and temperature, we determine the nature of transport. In part 6.9.3, we analyze the mesoscopic interference effects on their conductances, namely Weak Anti-localization (WAL), to determine their phase coherence length L_ϕ. In the last part 6.9.4, we analyze the magnetic field dependence of the second harmonic measurements, exhibiting Magneto-Chiral Anisotropy (MCA), using the current-induced effective field $B_{eff} = \beta I$ model introduced in appendix 6.7.3.

6.9.1 . The samples and their caracteristics

We present results on four long nanowires divided in seven different segments. The samples were grown by the Fe active buffer layer method with 99.999% pure bismuth, see part 2.1. The produced nanowires were then transferred from the growth substrate to the host substrate by surface contact between the two substrates. With this method, we managed to transfer very long nanowires, and in a selective way, as we found fewer short nanowires than with other techniques. Large contacts were then patterned using standard electron lithography techniques. After an IBE step of 30 seconds to remove the potential oxide layer on the

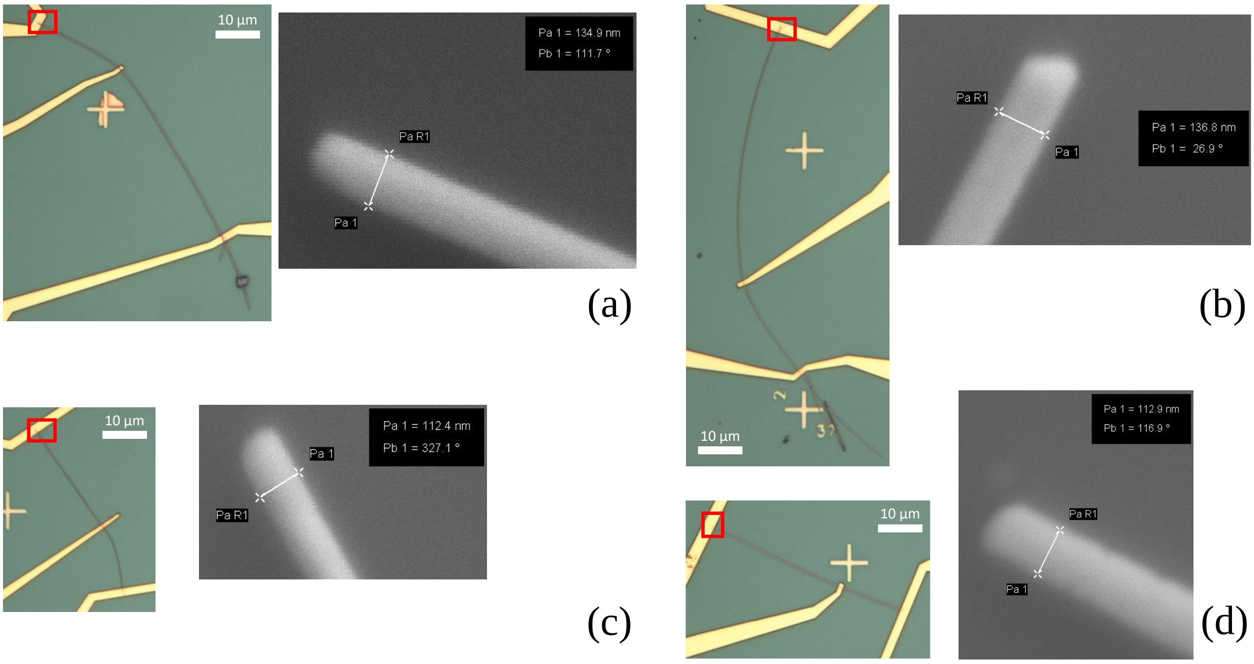

Figure 6.32 – Optical image (left) and scanning electron micrograph (right) of the four nanowires. We precise the name of each segment and its position on the optical image : (a) Segments Bi$_{12}^{long}$ (top) and Bi$_{11}^{long}$ (bottom). (b) Segments Bi$_{22}^{long}$ (top) and Bi$_{21}^{long}$ (bottom). (c) Segment Bi$_{4}^{long}$ (bottom). (d) Segments Bi$_{32}^{long}$ (left) and Bi$_{31}^{long}$ (right).

surface, $150\ nm$ thick Au contacts were deposited by low pressure evaporation in $3 \times 50\ nm$ steps, after deposition of a $5\ nm$ layer of Ti.

In Fig.6.32, we display both optical images and scanning electron micrograph of the four nanowires and their metallic contacts.

The main characteristics of the nanowires are summarized in Fig. 6.1, where the separation between different nanowires is represented by vertical lines. The methods leading to these results and their analysis are discussed in the following relevant subsections. Assuming similar leads and contacts resistances, combination of $300\ K$ measurements on segments of same nanowires gives a contact resistance $R_c \lesssim 25\ \Omega$.

segment	Bi$_{11}^{long}$	Bi$_{12}^{long}$	Bi$_{21}^{long}$	Bi$_{22}^{long}$	Bi$_{4}^{long}$	Bi$_{31}^{long}$	Bi$_{32}^{long}$
length (μm)	44.3	20.6	23.4	58.7	16.0	14.2	31.6
width (nm)	135		137		110	110	
R at $T \simeq 300\ K$ ($k\Omega$)	7.2	3.2	8.8	19.2	13.3	6.1	13.5
R at $T = 4.2\ K$ ($k\Omega$)	14.9	5.9	20.1	41.1	59.4	16.7	38.4
$R \times w/L$ at $T = 4.2\ K$ (Ω)	45.4	38.7	118	95.9	408	129	134
$R \times w^2/L$ at $T = 4.2\ K$ ($\Omega.\mu m$)	6.13	5.22	16.1	13.1	44.9	14.2	14.7
$R \times w^2/L$ at $T \simeq 300\ K$ ($\Omega.\mu m$)	2.96	2.83	7.06	6.14	10.06	5.20	5.17
$\varphi_{s/h}^{bot}$ (°)	120	162	~ 304	~ 263	~ 100	157	157
curved	no?	no?	yes	yes	yes	no	no
theo. L_T (μm) at $T = 0.2\ K$	3.60		3.63		3.25	3.25	
L_ϕ (μm) at $T \simeq 0.2\ K$	0.59	0.88	0.4	0.30	0.15	$\gtrsim 0.81$	0.71
A_{orb+Z} at $T = 3.7\ K$ ($\Omega.T^{-2}$)	1055	593	286	786	797	96.6	500
A_Z ($\Omega.T^{-2}$)	207?	207	?	?	?	292	292?
β ($G.\mu A^{-1}$)	$+166$?	-7.66	$> +321$	$> +106$	> 22.6	20.4	102?

Table 6.1 – Table summarizing geometric and transport characteristics of our four long nanowires divided in seven segments, with normal metal contacts. See the corresponding sections for the definitions and the analysis of the various quantities.

6.9.2 . Determination of the nature of transport

In this chapter, we will compare our resistance measurements to those found in the literature, and estimate what kind of conduction modes dominate our transport measurements. We recall here that crystalline bismuth is highly anisotropic with both bulk, surfaces and hinges transport, that the nanowires are subject to (potentially anisotropic) quantum confinement effects, and that the type of surface plays an important role when surface transport becomes dominant, see part 1.2. Hence, the transport properties depend on the crystalline orientation and the size and geometry of the section of the nanowire.

In our work, we find for all nanowires a monotonic increase of resistance with decreasing temperature, compare the $T = 300\ K$ and the $T = 4.2\ K$ values displayed in Tab. 6.1. In Fig. 6.33, the temperature dependence of the resistance of three segments, belonging to three different nanowires, are displayed. We see that the three segments have very similar behavior, with nearly a doubling of the resistance between $300\ K$ and $1\ K$, a large variation between 200 and $50\ K$, and a saturation plateau at low temperatures.

Fig. 6.33c shows the logarithm of the resistances of samples Bi$_{31}^{long}$ and Bi$_{11}^{long}$ on the left scale and the logarithm of the resistance of sample Bi$_{22}^{long}$ on the right scale as a function of temperature. For semiconductors, the resistivity can be approximated by $\rho(T) = \rho_0 e^{-\alpha T}$, decreasing with temperature, and should appear as a linear dependence on this semi-log graph as $\ln \rho(T) = \ln \rho_0 - \alpha T$.

For comparison, Fig. 6.33d shows the resistances of samples Bi$_{31}^{long}$, Bi$_{11}^{long}$ and Bi$_{22}^{long}$ as a function of temperature on a log-log scale. For metals, the resistivity varies as T^5 for phonon-phonon mediated scattering, as T^3 for s-d electron mediated scattering, and as T^2 for electron-electron mediated scattering. This should show in this log-log graph as linear dependence with coefficients between 2 and 5. We see here that it clearly doesn't match our data, as the resistivity of a metal should increase with temperature.

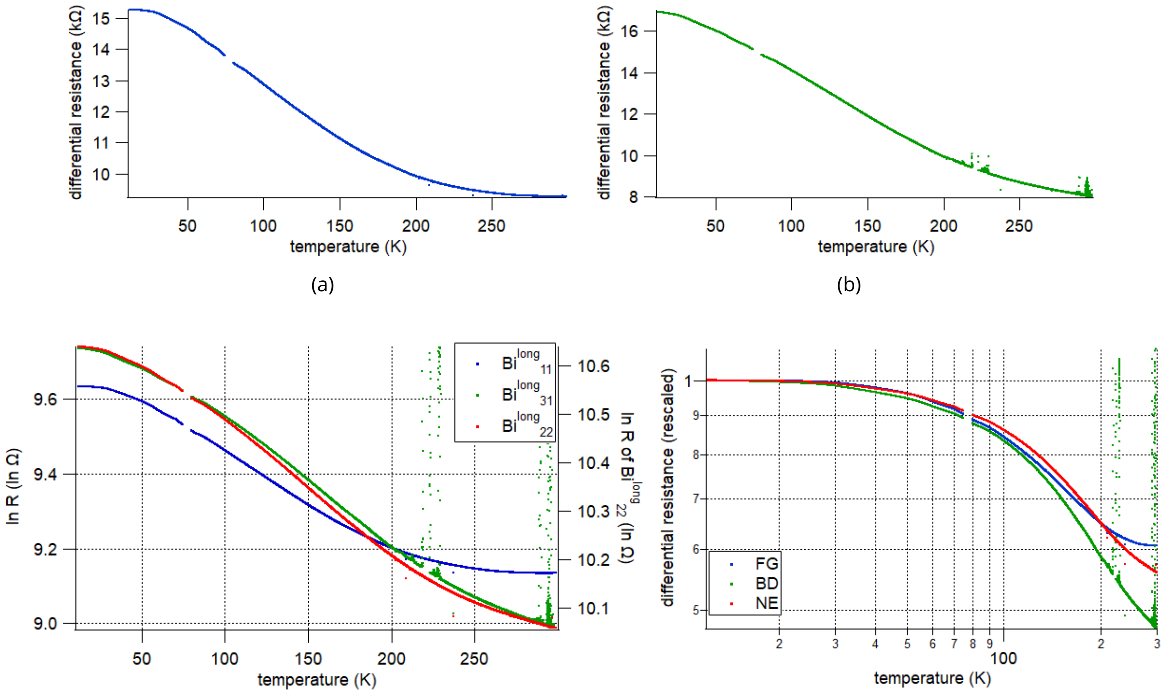

(a) (b)

(c) (d)

Figure 6.33 – (a) Differential resistance of segment Bi_{11}^{long} as a function of temperature. (b) Differential resistance of segment Bi_{31}^{long} as a function of temperature. (c) Log of differential resistance as a function of temperature for three segments of different nanowires. Notice the left and right axis. (d) Differential resistance as a function of temperature on a double log scale, for three segments of different nanowires.

To understand the terms used in the literature, let us recall that in the "large samples" community, the conductivity is expressed as :

$$\sigma = e(n_s\mu_{n,s} + n_b\mu_{n,b} - p_b\mu_{p,b}) = \frac{1}{\rho} \tag{6.109}$$

where we considered a three carriers model with e the electron charge, n_s, n_b, p_b, the carrier densities of surface electron states, of bulk electron states, and of bulk hole states, respectively. $\mu_{n,s}$, $\mu_{n,b}$ and $\mu_{p,b}$ are the carriers mobilities for the respective states. ρ is the resistivity.

The carriers mobilities can be further expressed as : $\mu = e\tau_e/m^*$
where τ_e is the elastic scattering time and m^* is the effective mass of the considered carrier.

In [213], the authors showed that, for diameters close to $\simeq 1\ \mu m$, the effective mean free path l_e is reduced by the scattering with the nanowire surface. This also reduces the carriers mobility and increases the resistivity of the electrons and holes from the bulk pockets. They modelized that, for diameters $< 500\ nm$, the resistivity increase monotonously with decreasing temperature, taking into account the change in bulk carriers mobilities only. However, this analysis does not include other quantum size effects appearing for diameters $\lesssim 300\ nm$.

For nanowires of smaller diameters, [39] ran an extensive study of longitudinal and transverse magnetoresistance of $7 - 200nm$ arrays of Bi nanowires with mainly $[0, 0.949, 0.315]$ crystalline orientation (in the binary, bisectrix, trigonal basis). They find a complex non-monotonic behavior as a function of NW width, even though it is averaged over the whole arrays. They found a similar doubling of the resistance between $300K$ and $1K$ for nanowires of diameter $30 < w < 70\ nm$. In [38], the authors measured individual nanowires of 50 and $75\ nm$ with similar temperature dependence. They explain the $T > 100\ K$ data with a semi-metallic model with reduced negative gap $\Delta \simeq 10\ meV$ compared to infinite bulk $\Delta \simeq 38\ meV$. With the same interpretation, we would find an intermediate $\Delta \simeq 20\ meV$.

Focusing on more recent results on similar individual nanowires of diameters from 21 to $178\ nm$, in [36], the authors identified three different transport regimes depending on nanowire diameter. For nanowires of diameter $\gtrsim 110\ nm$, they find a semi-metallic bulk-like behavior where the main effect of the finite diameter is to reduce the effective mean free path. For a diameter $40 < w < 110nm$, the increase of resistivity at low temperature is attributed to quantum size effects changing the band structure of the nanowire in a significant way, decreasing the bulk carriers densities, as well as an increase in carriers effective masses (decrease of mobilities) due to a strong coupling between electrons and holes. As the diameter is further reduced, the surface to volume ratio increases and for $w \lesssim 40\ nm$, the bulk becomes insulating [16] and the transport is dominated by the metallic surfaces, see also [37].

However, in order to explain the increase of resistance with decreasing temperature of intermediate diameter nanowires, all these interpretations rely on a similar contribution of bulk states and surface states on the resistance at high temperature. In light of the analysis of the contribution of both states at low temperature, done in [2] and in the following, it seems a bit unrealistic.

To better understand our transport, let us now look at the resistance of the samples as a function of sample lengths L. On Fig. 6.34, we plot with different colors the resistances of segments belonging to different nanowires as a function of segments lengths, both measured at $T = 300\ K$ (square marks) and $T = 4.2\ K$ (triangle marks). We see that both at $T = 300\ K$ and $T = 4.2\ K$, the resistances are consistent with a linear dependence on length, showing that we are in the diffusive regime where $L > l_e$.

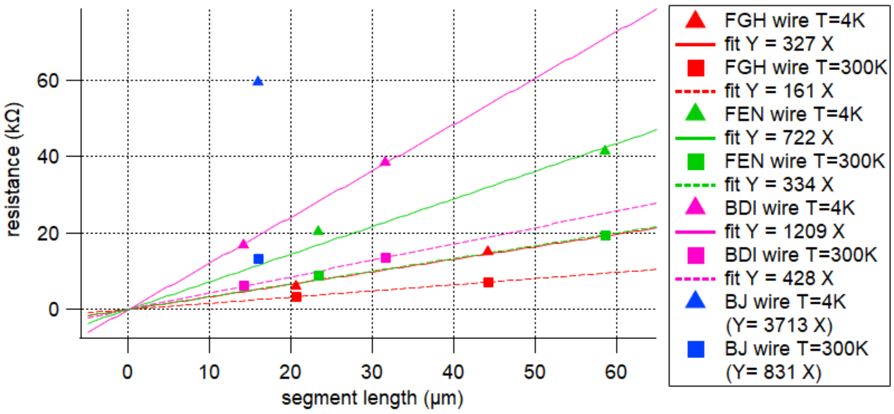

Figure 6.34 – Resistances of all the segments plotted as a function of segment length. Colors distinguish the nanowires. Triangular markers for data at $T = 4.2K$, square markers for data at $T \simeq 300K$. Solid lines for linear fits of $T = 4.2K$ data, dashed lines for linear fits of $T \simeq 300K$ data. See legend to know which nanowire and what value is given by the linear fits.

Bismuth nanowires are expected to support three types of conducting states : topological (ballistic) helical hinge states, (metallic) surfaces states with high spin-orbit coupling, and (semi-metallic) bulk states. Each topological helical hinge states should be ballistic and contribute to total conductance as half a quantum of conductance $\frac{1}{2}G_Q = e^2/h$, limited by its phase coherence length L_ϕ, and independent of the elastic mean free path l_e due to scattering. The number of topological hinge states depends on the geometry of the surface, and could range from 2 to ~ 100.

For non-protected surface states, conductance should roughly scale with the sample total surface width, i.e. the perimeter of the section, and with the inverse of the sample length, meaning that the resistance should scale as $R \propto L.w^{-1}$. For non-protected bulk states, conductance should scale with the sample section surface and with the inverse of the sample length, that is $R \propto L.w^{-2}$. In Tab. 6.1, we display $R \times w/L$ at $T = 4.2\ K$ for every nanowire segments, as well as $R \times w^2/L$ at $T = 4.2\ K$ and $T \simeq 300\ K$.

Let us now estimate our number of channels of Bi$_{12}^{long}$, the segment for which we have the most data.

From [6], depending on the effective dimensionality of the diffusion from between the contacts, the conductance G can be written as :

$$\begin{array}{ccc} quasi-1d & 2d & 3d \\ G = \frac{2e^2}{h}\frac{4}{3}M\frac{l_e}{L} & G = \frac{2e^2}{h}\frac{1}{2}k_F W\frac{l_e}{L} & G = \frac{2e^2}{h}\frac{1}{3\pi}k_F^2 S\frac{l_e}{L} \end{array} \tag{6.110}$$

where L is the sample length (in the direction of the current), W is the sample width (length of the long dimension transverse to the current for 2d), and S is the sample section (surface transverse to the current for 3d).

Given its measured Fermi wavelength (see appendix 6.11) $\lambda_{F,b} \simeq 51\ nm$, the section of the nanowires can host $M_b = \pi S/\lambda_{F,b} \simeq \pi(135/51)^2 \simeq 22$ bulk channels. From the quasi-1d formula for conductance, we get $M_{tot} = \frac{R_Q}{R}\frac{3L}{4l_e} \simeq 169 \gg M_b$, taking $l_e \simeq 200\ nm$, $R = 5.9\ k\Omega$, and $L = 20.6\ \mu m$. A possible explanation for this discrepancy is the presence of a large number of surface channels, not taken into account in M_b but included in M_{tot} via R, as found in [2].

More generally, the conductance for quasi-1d diffusion can be expressed as :

$$G = \frac{2e^2}{h}\frac{4}{3L}(M_b l_{e,b} + M_s l_{e,s}) = \frac{2e^2}{h}\frac{4}{3L}(\frac{\pi S}{\lambda_{F,b}^2}l_{e,b} + \frac{2W}{\lambda_{F,s}}l_{e,s}) \tag{6.111}$$

where we consider different number of channels for the bulk ($M_b = \frac{\pi S}{\lambda_{F,b}^2}$) and for the surfaces ($M_s = \frac{2W}{\lambda_{F,s}}$), as well as different mean free paths l_e. $\lambda_{F,b}$ and $\lambda_{F,s}$ are the Fermi wavelengths of the bulk and surface states, respectively. This is analogous to Eq.(6.109) in the small length scales and low temperature situations.

We find $M_b \simeq 22$ and $M_s \simeq \frac{2\times 4w}{(4\times 10^{-9})} \simeq 270$, and indeed $M_s \gg M_b$. With these values, considering $l_{e,b} = l_{e,s}$, we find at low temperature that $l_e \simeq 116\ nm \simeq w$, consistent with [213, 2].

Let us now compare the values at low temperature to the one at $T \simeq 300\ K$. The conductance gains a factor ~ 2 between low temperature and room temperature. This cannot be attributed to the surfaces, that are thought to be metallic (see part 1.2) and contribute to the conductance in the opposite way.

Looking again at Eq.(6.111) (approximation at low T), taking M_s independent of T, it suggests that the increase of conductance at high temperature is due to either an increase of the number of bulk states or an increase of $\frac{l_{e,b}}{l_{e,s}}$. However at first sight, a doubling of the conductance with a combination of both effects seems hard to achieve with reasonable numbers, which may indicate that couplings between the surface and bulk states are involved, as often discussed in ARPES experiments.

We also draw the reader attention to the fact that the quasi-1d surface (and bulk) channels should localize for a sample length ξ such that $\xi > Ml_e \simeq 34\ \mu m$, taking $M \simeq 292$ and $l_e = l_{e,b} = l_{e,s} \simeq 116\ nm$ previously found. This would filter out surface channels in long nanowires and leave out only the ballistic topological helical states. Unfortunately, as the next section will show, we can't observe it because the surface channels lose their phase coherence before localizing, that is $L_\phi \ll \xi$.

We conclude that, at low T, the transport is dominated by surface states with $l_e \simeq w \simeq 120\ nm$, consistent with previous analysis [2]. Between low and high T, the decrease of resistance is mainly due to an increasing contribution of bulk states, as reported in [39, 38, 36]. However, this type of behavior has been mainly reported for smaller nanowires of diameter $d \lesssim 70\ nm$ of various crystallographic orientations, and the change of resistance is hard to explain without invoking couplings between surface and bulk states.

The next section will be dedicated to the analysis of quantum interference effects in the resistance of the nanowires, and will provide an estimation of the phase coherence length L_ϕ for diffusive transport as well as a way to estimate l_e.

6.9.3 . Coherence length deduced from weak anti-localization peak

We now focus on the low temperature dependence of the resistance of our nanowires as a function of magnetic field magnitude and direction. In the following subsections, we analyze measurements done on two of the four nanowires, which have both two straight segments. Figs. 6.35a, 6.36a, 6.37a, 6.38 show the resistances of segments Bi$_{11}^{long}$, Bi$_{12}^{long}$, Bi$_{31}^{long}$ and Bi$_{32}^{long}$ as a function of transverse (vertical) magnetic field, at different temperatures. The higher temperature curves have been shifted in Y for clarity. The same graphs for the three remaining segments can be found in the appendix.

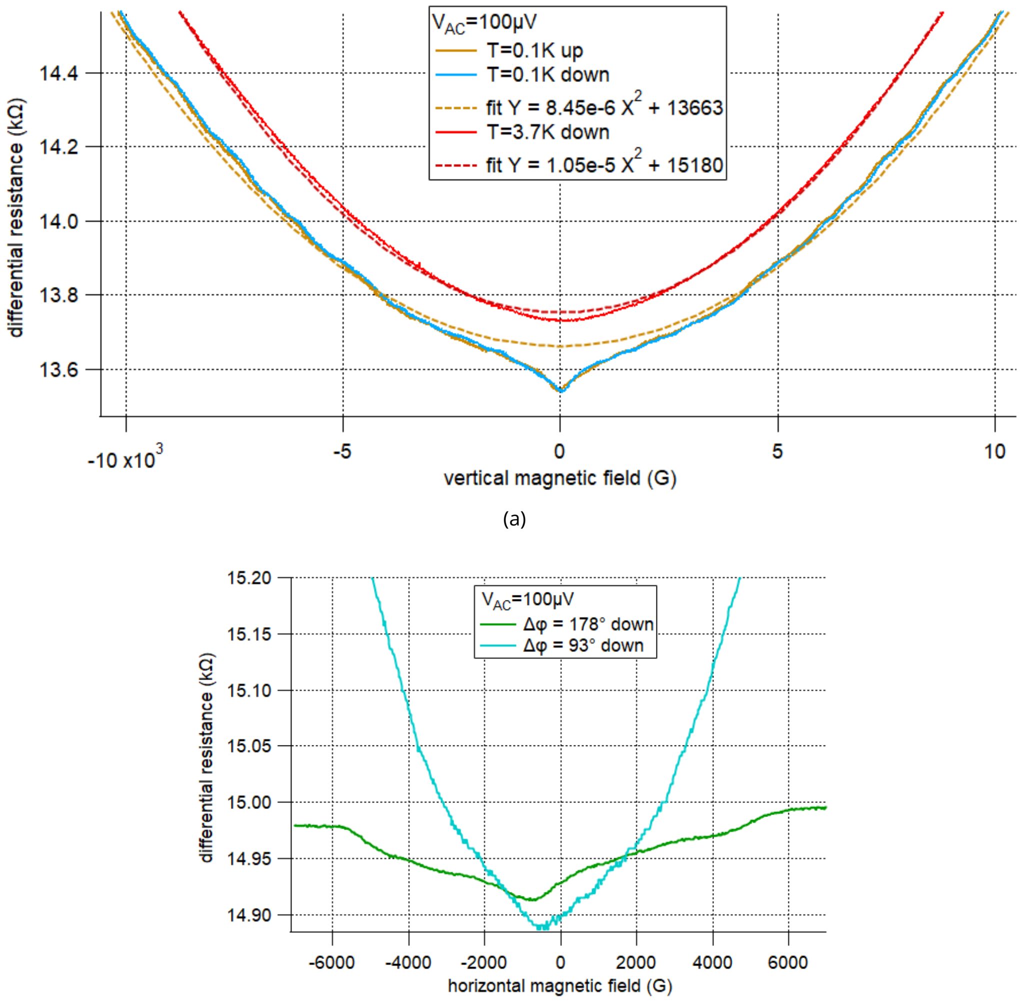

(a)

(b)

Figure 6.35 – Magnetoresistance of segment Bi$_{11}^{long}$. (a) Transverse (vertical) magnetic field, various temperatures. Higher temperature curves have been shifted in Y for clarity. (b) In-plane magnetic field with different angles $\Delta\varphi$, where $\Delta\varphi = 180°$ for a field parallel to the wire and in the direction of the current.

All segments show two clear corrections related to quantum coherence effects that decrease with increasing temperature : weak antilocalization (WAL) dips at low field, and universal conductance fluctuations (UCF) at higher field. The WAL dips at low magnetic fields come from destructive interference of counter-propagating closed trajectories in materials with spin-orbit coupling. These interferences are destroyed by a magnetic field, on a scale that depends on the phase coherence length L_ϕ. The UCF are due to the various diffusion trajectories from one end of the sample to the other, on a distance $\sim L_\phi$, and do not vanish at high magnetic field.

For the WAL correction, its amplitude depends on the effective dimensionality of the problem [6]. WAL is based on diffusion that produces closed trajectories. If the diffusion process is limited by L_ϕ only, the diffusion can be considered as 3d. If the diffusion process is limited by the sample edges in one direction, e.g. in a film of height $h < L_\phi$, the diffusion can be considered as 2d. If the diffusion process is limited by the sample edges in two direction, e.g. in a nanowire of width $w < L_\phi$, the diffusion can be considered as quasi-1d.

From [6], depending on the effective dimensionality of the diffusion between the contacts, the weak

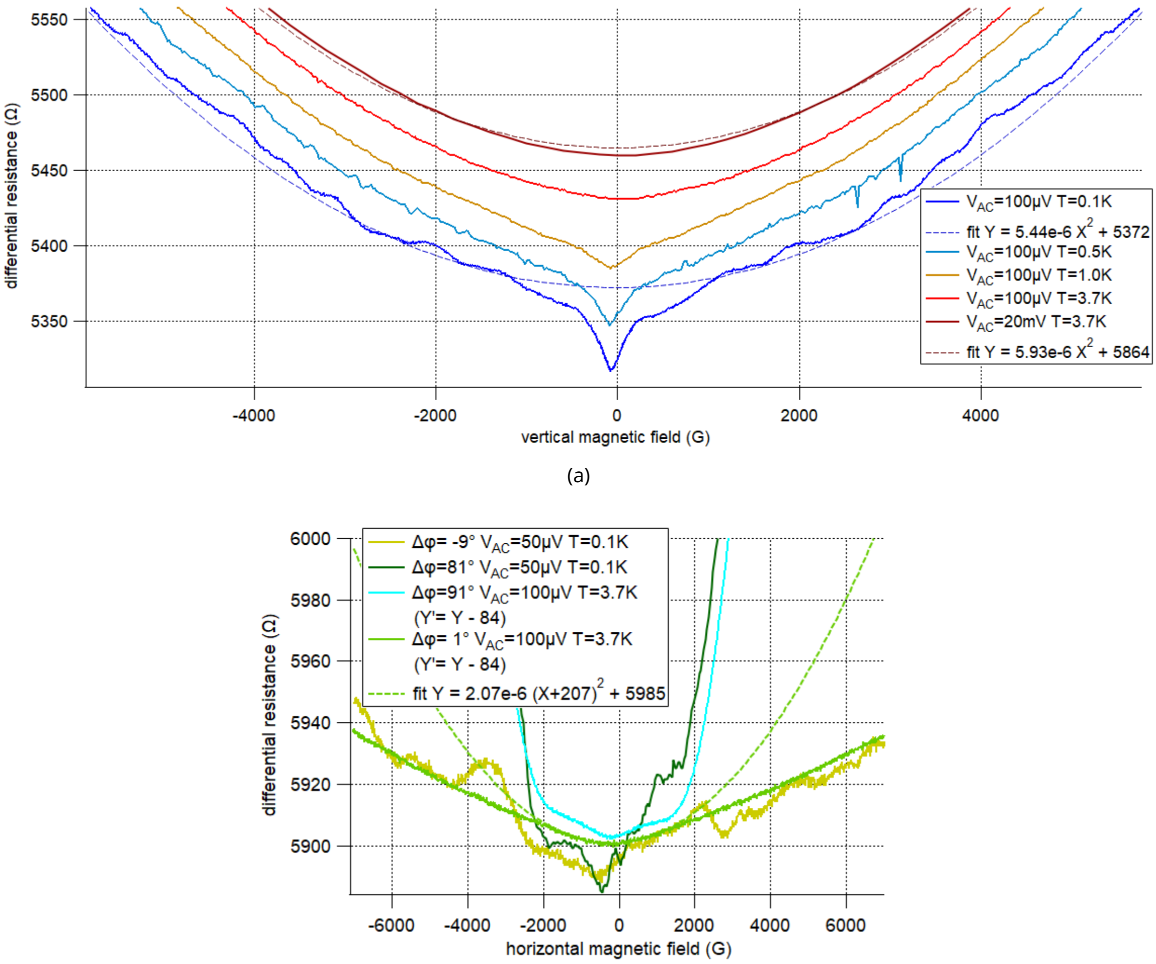

(a)

(b)

Figure 6.36 – Magnetoresistance of segment Bi$_{12}^{long}$. (a) Transverse (vertical) magnetic field, various temperatures. Higher temperature curves have been shifted in Y for clarity. (b) In-plane magnetic field with different angles $\Delta\varphi$, where $\Delta\varphi = 180°$ for a field parallel to the wire and in the direction of the current.

localization correction to the conductance ΔG can be written as :

$$\begin{array}{ccc} quasi-1d & 2d & 3d \\ \Delta G = -\frac{2e^2}{h}\frac{L_\phi}{L} & \Delta G = -\frac{2e^2}{h}\frac{1}{\pi}\frac{W}{L}\ln\left(\frac{L_\phi}{l_e}\right) & \Delta G = -\frac{2e^2}{h}\frac{1}{2\pi}\frac{S}{l_e L} \end{array} \tag{6.112}$$

The above formulas are valid for weak localization, that is the modification of the conductance by time reversed closed trajectories with no dephasing between them. The weak localization correction to conductance is affected by decoherence processes (irreversible) on one side, such as scattering with a magnetic impurity, and by SOC-induced dephasing (reversible) on the other side. We note the characteristic times τ_m and τ_{SO} for magnetic-scattering-induced decoherence and SOC-induced dephasing, respectively. These processes modify the average result of dephasing between time reversed trajectories by a factor [6]

$$\langle Q_{SO+m}(t)\rangle = \frac{1}{2}\left(3e^{-4t/3\tau_{SO}-2t/3\tau_m} - e^{-2t/\tau_m}\right) \tag{6.113}$$

where t is the travel time around the loop, with necessarily $t > \tau_e$ the elastic scattering time.

In the case of transport via bismuth surface, we consider a spin-orbit time $\tau_{\text{SO}} = \frac{h}{E_{\text{SO}}} \simeq 4\ fs$, taking

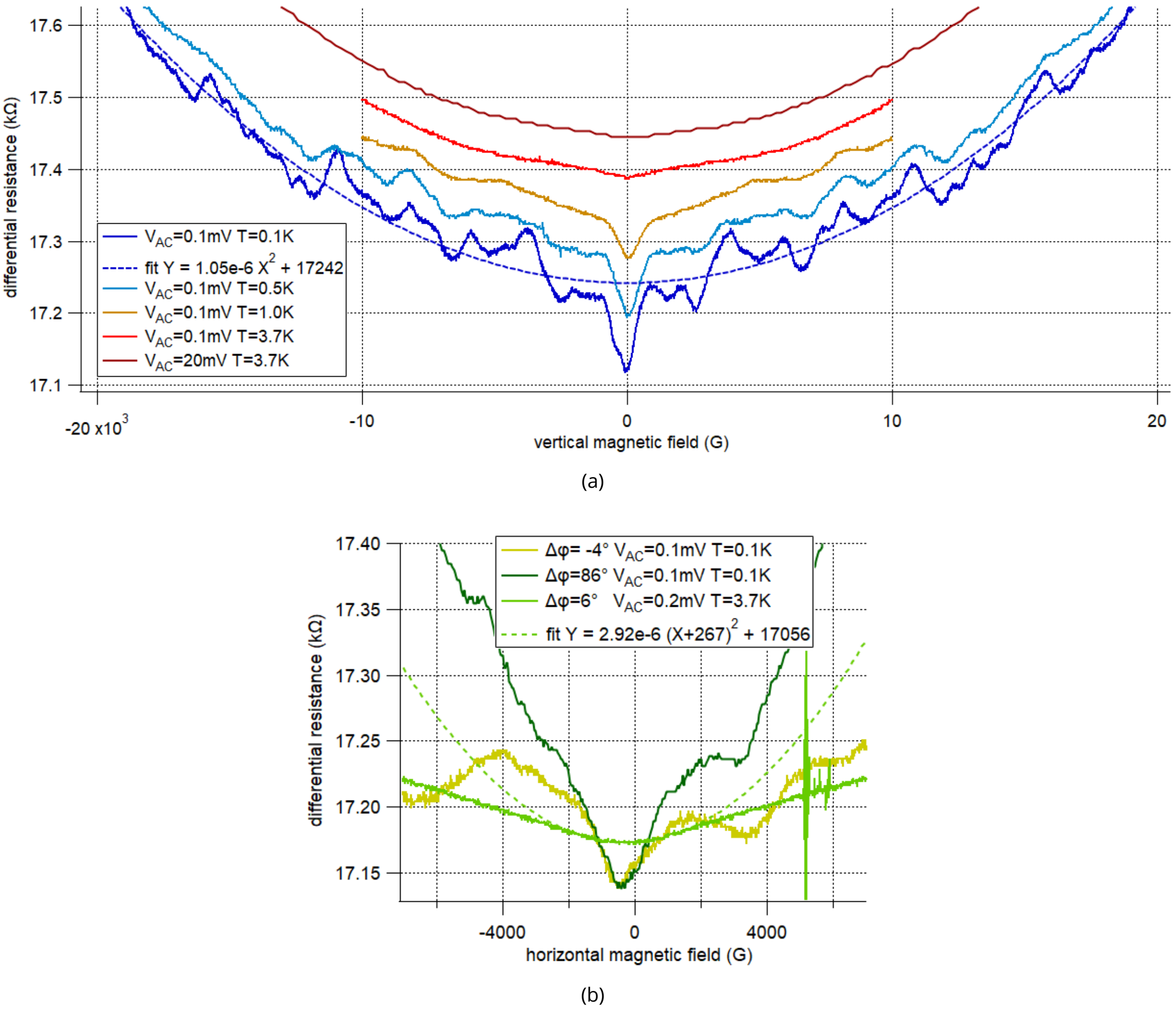

Figure 6.37 – Magnetoresistance of segment Bi_{31}^{long}. (a) Transverse (vertical) magnetic field, various temperatures. Higher temperature curves have been shifted in Y for clarity. (b) In-plane magnetic field with different angles $\Delta\varphi$, where $\Delta\varphi = 180°$ for a field parallel to the wire and in the direction of the current.

$E_{\text{SO}} \simeq 0.1\ eV$ (see [24] for example) much shorter than the elastic scattering time and thus $\tau_{\text{SO}} \ll t$. We also consider that there is no magnetic impurity ($\tau_m \gg t$).

In this limit, we obtain : $\langle Q_{SO+m}(t)\rangle = -\frac{1}{2}$ instead of $\langle Q(t)\rangle = 1$ of "bare" weak localization, becoming weak anti-localization with destructive interference.

Magnetic field can induce orbital dephasing. Again, the effect of the magnetic field depends on the effective dimensionality of the problem and the relative contributions of the dephasing processes. Assuming a phase coherence length $L_\phi > 137\ nm$, the maximum width of our nanowires, and dephasing processes of timescales very different compared to τ_ϕ and τ_e, we used the following simple formula for a quasi-1d system [6, 214] :

$$L_\phi(B) = \frac{L_\phi(0)}{\sqrt{1 + \left(\frac{2\pi}{\sqrt{3}\Phi_0} L_\phi(0) W_{eff} B\right)^2}} \qquad (6.114)$$

where $\Phi_0 = h/e$ is the quantum of flux, $L_\phi(0)$ the phase coherence length at zero magnetic field, and W_{eff}

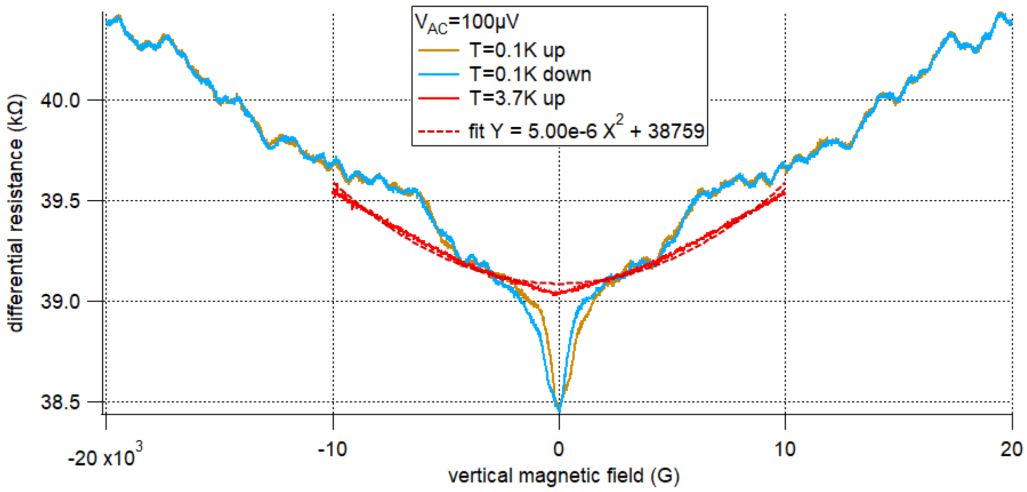

Figure 6.38 – Transverse (vertical) magnetoresistance of segment Bi$_{32}^{long}$.

the effective width of the nanowire.

The effective width of the nanowire W_{eff} is equal to the real nanowire width $W_{eff} = w$ if $w \gg l_e$. Previous analysis (see part 6.9.2 and [2]) led to the conclusion that l_e is close to the width of the nanowire, thus $w \simeq l_e$. In this situation, reflections on the boundaries play a major role and lead to flux cancellation effects, that can be translated to $W_{eff} < w$ [215]. [215] calculated that $W_{eff} = w\sqrt{\frac{3w}{9.5l_e}}$ for specular boundary reflection, and $W_{eff} = w\sqrt{\frac{3w}{4\pi l_e}}$ for diffusive boundary reflection. Notice that they calculated it analytically with a semiclassical treatment assuming $\lambda_F \ll l_e$ and $\lambda_F \ll w$, fulfilled for surface modes, but also in the limit $l_e \gg w$, hardly fulfilled here. Hence, W_{eff} is an interesting quantity to measure to test their formula in our $w \simeq l_e$ regime. If the formula holds, the rugosity of the boundaries of our samples being in the $1\ nm$ scale, we expect an intermediate W_{eff} for surface transport ($\lambda_F \sim 4\ nm$).

Putting everything together, we obtain the following weak antilocalization correction to the conductance for quasi-1d system with $L_\phi > w$ and $\tau_{SO} \ll \tau_e < \tau_\phi \ll \tau_m$:

$$\Delta g = \frac{\Delta G}{e^2/h} = \frac{L_\phi(B)}{L} = \frac{L_\phi/L}{\sqrt{1+\left(\frac{2\pi}{\sqrt{3}\Phi_0}L_\phi W_{eff}B\right)^2}} = \frac{A_1/L}{\sqrt{1+\left(\frac{2\pi}{\sqrt{3}\Phi_0}A_2B\right)^2}} \tag{6.115}$$

Fitting the conductance with the formula (6.115) with a parameter A_1 for the amplitude and a parameter A_2 for the width of the conductance peak, we extracted the phase coherence length of the various segments, see Tab. 6.1 for the measured values at $T \simeq 0.2\ K$ and Fig. 6.39 for the fits and the temperature dependence on segments Bi$_{31}^{long}$ and Bi$_{12}^{long}$. L_ϕ is expected to vary as $T^{-1/3}$, $T^{-1/2}$, and $T^{-3/4}$ for 1d, 2d, and 3d systems, respectively [37].

To be more specific, I first fitted the cleanest available data, that is the sample Bi$_{12}^{long}$ data between 0.24 and $0.48\ K$ (Fig.6.39a), and took $L_\phi = A_1$ and $W_{eff} = A_2/A_1$. The three fits gave the same $W_{eff} = A_2/A_1 \simeq 70\ nm$ and $L_\phi \simeq 0.8\ \mu m$, both of which that made sense.

Interestingly, the obtained W_{eff} has an intermediate value between specular and diffusive boundary reflections, i.e. $w\sqrt{\frac{3w}{4\pi l_e}} < W_{eff} < w\sqrt{\frac{3w}{9.5l_e}} \Longleftrightarrow 66 < 70 < 76\ nm$, taking $l_e = w = 135\ nm$. This value of l_e is consistent with the $106\ nm$ found with the conductance in part 6.9.2.

Fitting other data with the same interpretation led to suspicious values for W_{eff}, e.g. varying a lot with temperature or being close or larger than the nanowire width. Indeed, taking $L_\phi = A_1$ can be af-

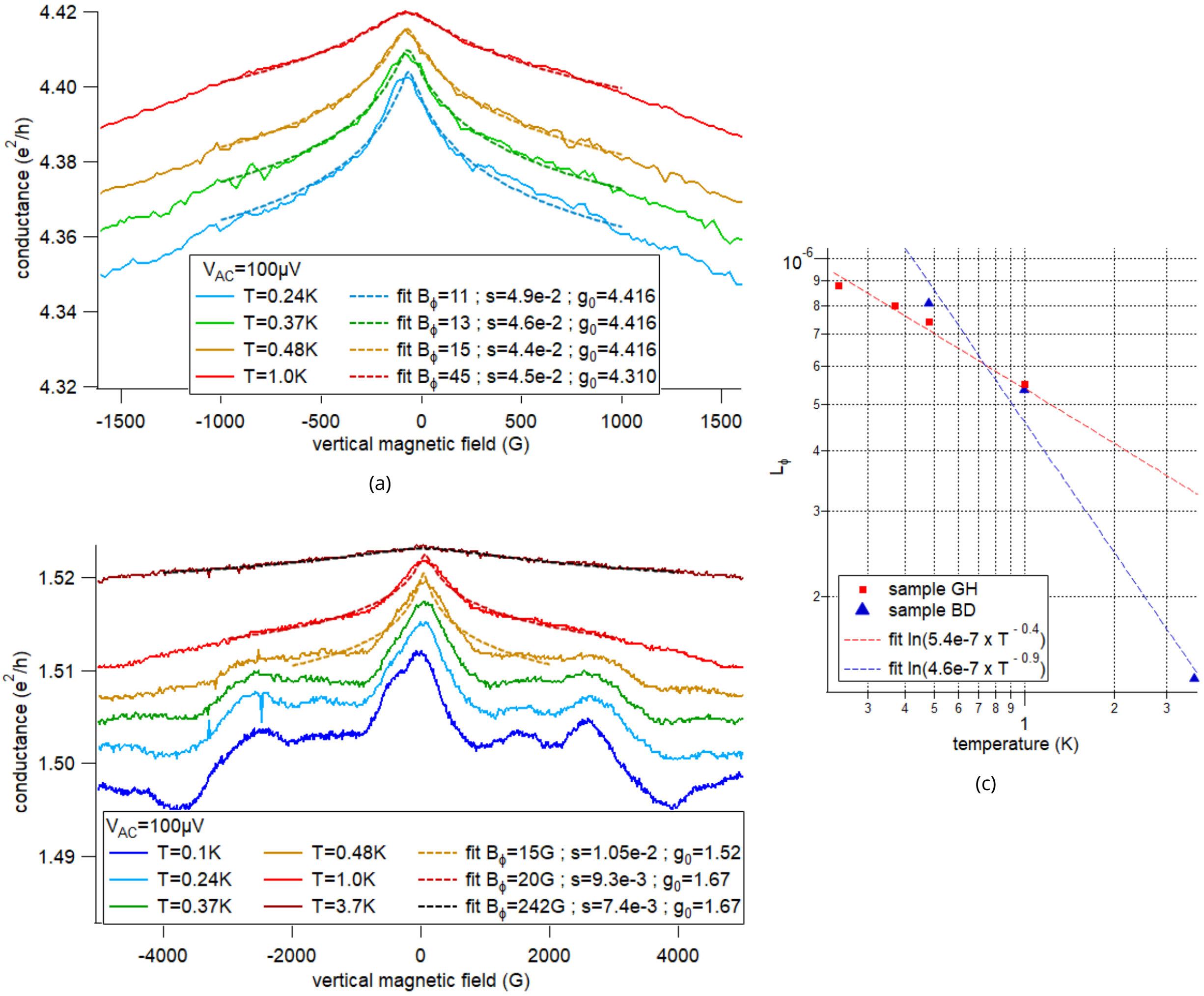

(a)

(b)

(c)

Figure 6.39 – (a) Solid lines : conductance of segment Bi$_{12}^{long}$ as a function of transverse (vertical) magnetic field, for various temperature. Dashed lines : fits of the conductance WAL peak with the formula Eq.(6.115). (b) Solid lines : conductance of segment Bi$_{31}^{long}$ as a function of transverse (vertical) magnetic field, for various temperature. Dashed lines : fits of the conductance WAL peak with the formula Eq.(6.115). (c) Phase coherence length L_ϕ in segments Bi$_{12}^{long}$ and Bi$_{31}^{long}$ as a function of temperature. The low number of data points as well as the errors on it makes for very approximate linear curve fits.

fected by an erroneous estimation of the baseline conductance of a few %. Thus, I decided to trust the $W_{eff} = A_2/A_1 \simeq 70\ nm$ of sample Bi_{12}^{long}, and used it to estimate the W_{eff}^{calc} of the other sample as follows : $W_{eff}^{calc} = \frac{W_{eff}^{\text{Bi}_{12}^{long}}}{(w^{\text{Bi}_{12}^{long}})^{3/2}} w^{3/2}$. I then used only A_2, more robust than A_1, to get $L_\phi = A_2/W_{eff}^{calc}$.

We find phase coherence lengths L_ϕ ranging from 0.15 to $0.88\ \mu m$ at $T \simeq 0.2\ K$, consistent with what can be found in the litterature [216, 217, 37]. These values are surprisingly short compared to the behavior measured on bismuth wires proximitized by superconducting contacts. Indeed, carrying a supercurrent through a non-superconducting piece of material by superconducting proximity effect requires full phase coherence to establish Andreev bound states (ABS).

The supercurrent carried by ABS should scale as e^{-2L/L_ϕ}, and would lead to a minimum $\sim 10^{-2}$ reduction factor in the best case scenario. This could lead to a selection of the trajectories that have the shortest length, i.e. ballistic trajectories, but it would only increase the effective coherence length to $L_\phi^{bal} = v_F (L_\phi^{dif})^2/\sqrt{v_F l_e} \simeq 1.8\ \mu m$ at $T \simeq 0.2\ K$ in the best case scenario for the best nanowire segment, leading to a minimum reduction factor of < 0.2. On top of that, the amplitude of the n-th harmonic of the CPR should be reduced by a factor e^{-2nL/L_ϕ}. This is inconsistent with the sawtooth or triangular patterns we observed in the vast majority of the samples we studied, see part 3.3. Moreover, the reduction of L_ϕ with increasing temperature, by a minimum factor of 0.5 between $T \simeq 0.2\ K$ and $T \simeq 1.0\ K$ (see Fig. 6.39c), would have a very visible effect on the dependence of the supercurrent and the CPRs on temperature. This is not what we observe.

We also notice that the smallest L_ϕ correspond to curved nanowires, reduced by a factor $\lesssim 0.5$ compared to straight ones. This would be caused by an overestimation of $W_{eff} = w\sqrt{\frac{3w}{C_b l_e}}$ by a factor 2, which is hard to believe. Thus, we conclude that the curvature of nanowires seems to reduce L_ϕ.

For completeness, we include in Tab.6.1 the thermal length for quasi-1d system $L_T = \sqrt{\frac{h v_F l_e}{k_B T d}}$ at $T = 0.2\ K$, with k_B the Boltzmann constant, $d = 1$ the effective dimensionality, $v_F = 4 \times 10^5$, and $l_e = w$. We see that it is always larger than L_ϕ by a factor ~ 4, thus not influencing our measurement of L_ϕ.

We conclude that the phase coherence length $L_\phi \simeq 0.8\ \mu m$ measured at $T \simeq 0.2\ K$ in the resistive state is much smaller than the phase coherence length necessary to explain our results on proximitized bismuth nanowires. We make the hypothesis that this discrepancy can be attributed to a separate, stronger phase coherence for the ballistic channels we measure in the superconducting state, that do not participate to the WAL. The nuclear spins of Bi atoms have been found to affect WAL [218], and may also play a role in topological phase stabilization.

6.9.4 . Second harmonics analysis of the MCA induced by $B_{eff} = \beta I$

Following the analysis introduced in appendix 6.7.4, and in the same spirit of the analysis of the Bi-based Josephson junction in its resistive state in appendix 6.12 and the Bi nanoring in appendix 6.10, we write the conductance G as :

$$G \simeq G(B_{Z,eff}) \simeq G(B_{ext} + \beta I) \simeq G(B_{ext}, V) \tag{6.116}$$

where we left aside the orbital contribution of the magnetic field. $B_{Z,eff}$ is the effective magnetic field contributing to Zeeman effects. It is modeled by the addition of the external magnetic field B_{ext} and a current-induced effective Zeeman field βI, which originates from SOC and causes MCA of the resistance.

As G depends on the voltage variations δV via $\beta \delta I \simeq \beta G_0 \delta V + \beta I^{(2)} \delta V^2$, β is detectable in the non-linear components of G. For a small voltage excitation $\delta V = V_{\text{AC}} \sin(\omega t)$ plus a DC voltage bias V_{DC}, in second order of V_{AC}, the first harmonic current response reads (see Eq.(6.84)) :

$$I^{(1\omega)} \simeq \left(G_0 - 2A_Z G_0^3 \beta B_{ext} V_{\mathrm{DC}}\right) V_{\mathrm{AC}} \tag{6.117}$$

Within the same conditions, the second harmonic voltage response reads :

$$I^{(2\omega)} \equiv C^{2\omega} V_{\mathrm{AC}}^2 \simeq \left(A_Z G_0^3 \beta B_{ext} - 6A_Z^2 G_0^5 \beta^2 B_{ext}^2 V_{\mathrm{DC}} + A_Z G_0^4 \beta^2 V_{\mathrm{DC}}\right) V_{\mathrm{AC}}^2 \tag{6.118}$$

Hence, β can be extracted from the linear dependence of $I^{(2\omega)}$ on B_{ext}. To estimate β, the knowledge of A_Z and G_0 are required, which can be both extracted by a quadratic fit of the resistance as a function of B_{ext}, see 6.7.4.

We extracted β from the second harmonic current response of the nanowire segments to an AC voltage of amplitude $< 60\sqrt{2}\ mV$ with standard lock-in instruments at frequencies between 70 and $200\ Hz$. The measurements were done in the two-wires configuration. See part 2.8.1 for a sketch of the electronic setup.

Looking at Eq. (6.84), we expect to measure the main responses in the in-phase component of the first harmonic and in the in-quadrature component of the second harmonic. This is indeed the result we got.

a) First harmonic current response as a function of DC voltage V_{DC}

Fig.6.40 displays the first harmonic response $I^{(1\omega)}/V_{\mathrm{AC}}$ (conductance) as a function of DC voltage bias V_{DC} for four segment belonging to two different nanowires, at fixed $V_{\mathrm{AC}} = 10\mu V$. The variations are smaller than the noise level, that is less than 0.3%, and hence there is no big non-linearity induced by a finite V_{DC}.

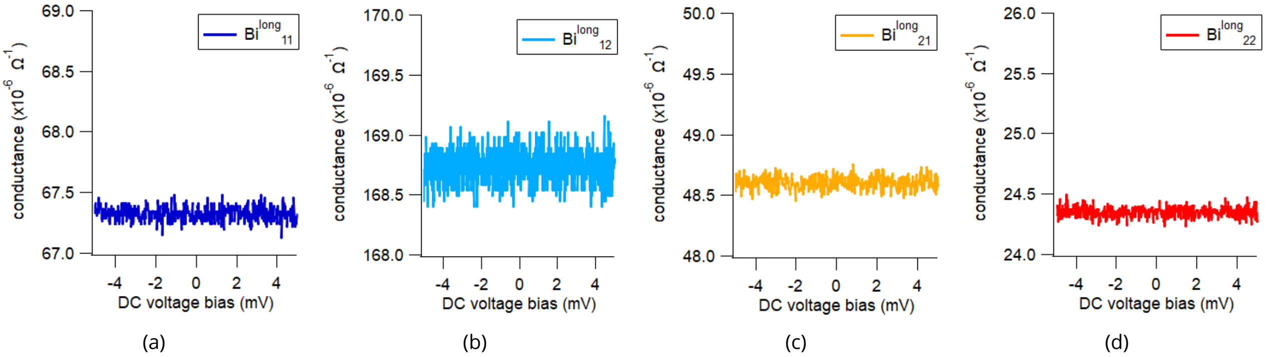

Figure 6.40 – Conductance dI/dV (first harmonic response $I^{(1\omega)}/V_{\mathrm{AC}}$) as a function of DC voltage bias V_{DC}, at fixed $V_{\mathrm{AC}} = 10\mu V$, no magnetic field, $T \simeq 100mK$. (a) Sample Bi$_{11}^{long}$. (b) Sample Bi$_{12}^{long}$. (c) Sample Bi$_{21}^{long}$. (d) Sample Bi$_{22}^{long}$.

b) Second harmonics current response as a function of excitation voltage V_{AC}

In Fig. 6.41, we show the second harmonic response of samples Bi$_{31}^{long}$, Bi$_{11}^{long}$, and Bi$_{12}^{long}$as a function of excitation amplitude V_{AC} and V_{AC}^2, for various magnetic fields. For all three of them, we notice two things :
- there are two visible low excitation regimes, with a peak and a crossover at $\sim 10\ mV$, that depends on the sample
- the second harmonic response variations with magnetic field are bigger in the higher excitation regime

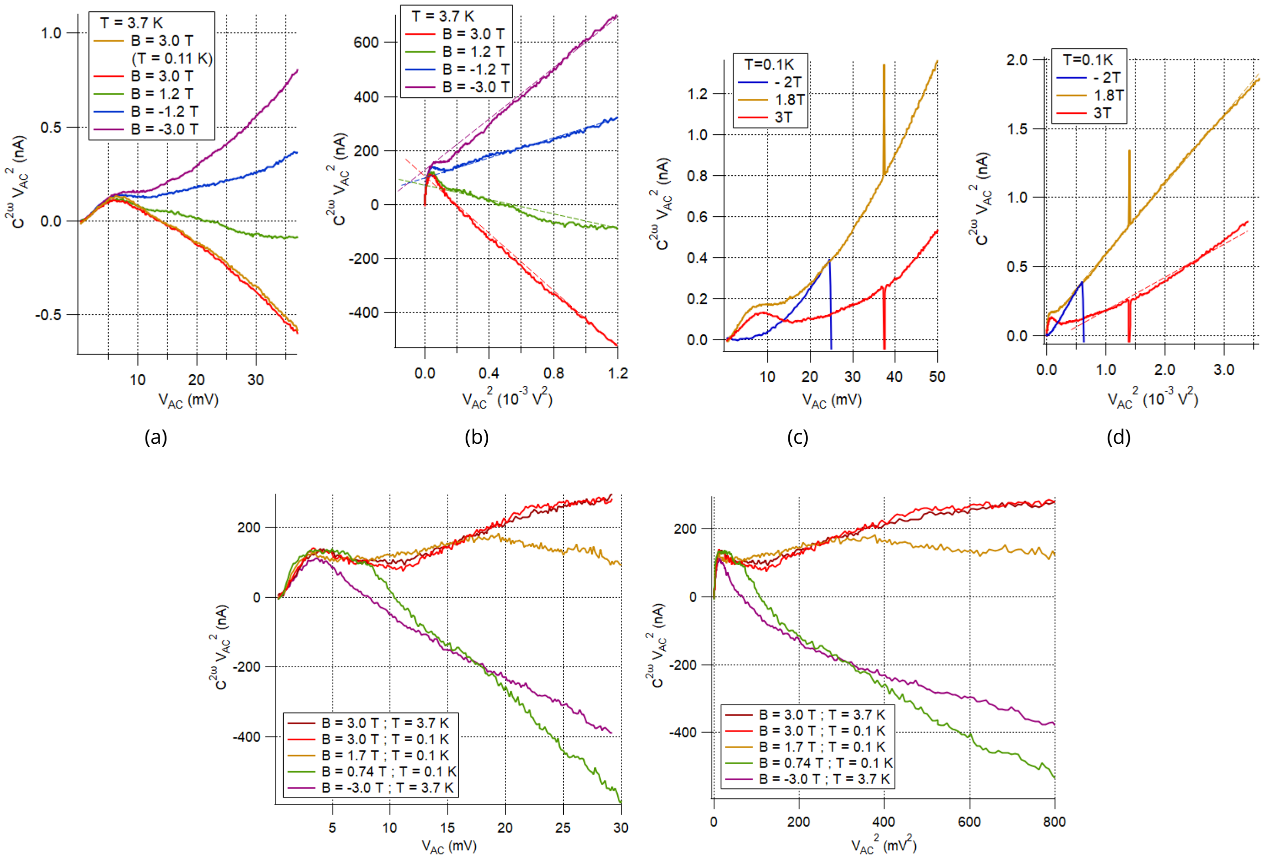

(a) (b) (c) (d)

(e) (f)

Figure 6.41 – Second harmonic current response as a function of voltage excitation amplitude V_{AC} and V_{AC}^2, with no DC voltage bias. (a),(b) Sample Bi$_{31}^{long}$. (c),(d) Sample Bi$_{11}^{long}$. (e),(f) Sample Bi$_{12}^{long}$

The crossover between the two excitation regimes correspond to $\sim 0.5\ \mu A$ for the three segments, that is close to $V_{\mathrm{AC}} \sim 5mV$ on the graphs. For segments Bi$_{31}^{long}$ and Bi$_{11}^{long}$, we see that the second harmonic response scales quite well with V_{AC}^2 as expected, but it is less clear for segment Bi$_{12}^{long}$. The following full measurement as a function of magnetic field will help us clarify this dependence.

c) Second harmonics current response as a function of magnetic field

In Figs. 6.42, 6.43, 6.44, we show the measured second harmonic current response as a function of vertical (perpendicular) magnetic field in the nanowire segments Bi$_{12}^{long}$, Bi$_{11}^{long}$, Bi$_{31}^{long}$, and Bi$_{32}^{long}$. All second harmonic responses have been rescaled by V_{AC}^2.

As explained in the previous part, we split the second harmonic signal into two parts, one even and the other one odd in magnetic field, and the presence of β should manifest itself as a linear dependence on the magnetic field in the odd part.

Sample Bi$_{12}^{long}$

In Fig. 6.42a, the raw second harmonic response of segment Bi$_{12}^{long}$ is represented with a solid black line, whereas the even and odd parts are represented in red and blue, respectively. We see that for $|B_{\mathrm{ext}}| \gtrsim 1\ T$ the second harmonic is dominated by its odd contribution, whereas for $|B_{\mathrm{ext}}| \lesssim 1\ T$ it is a mix of both even and odd.

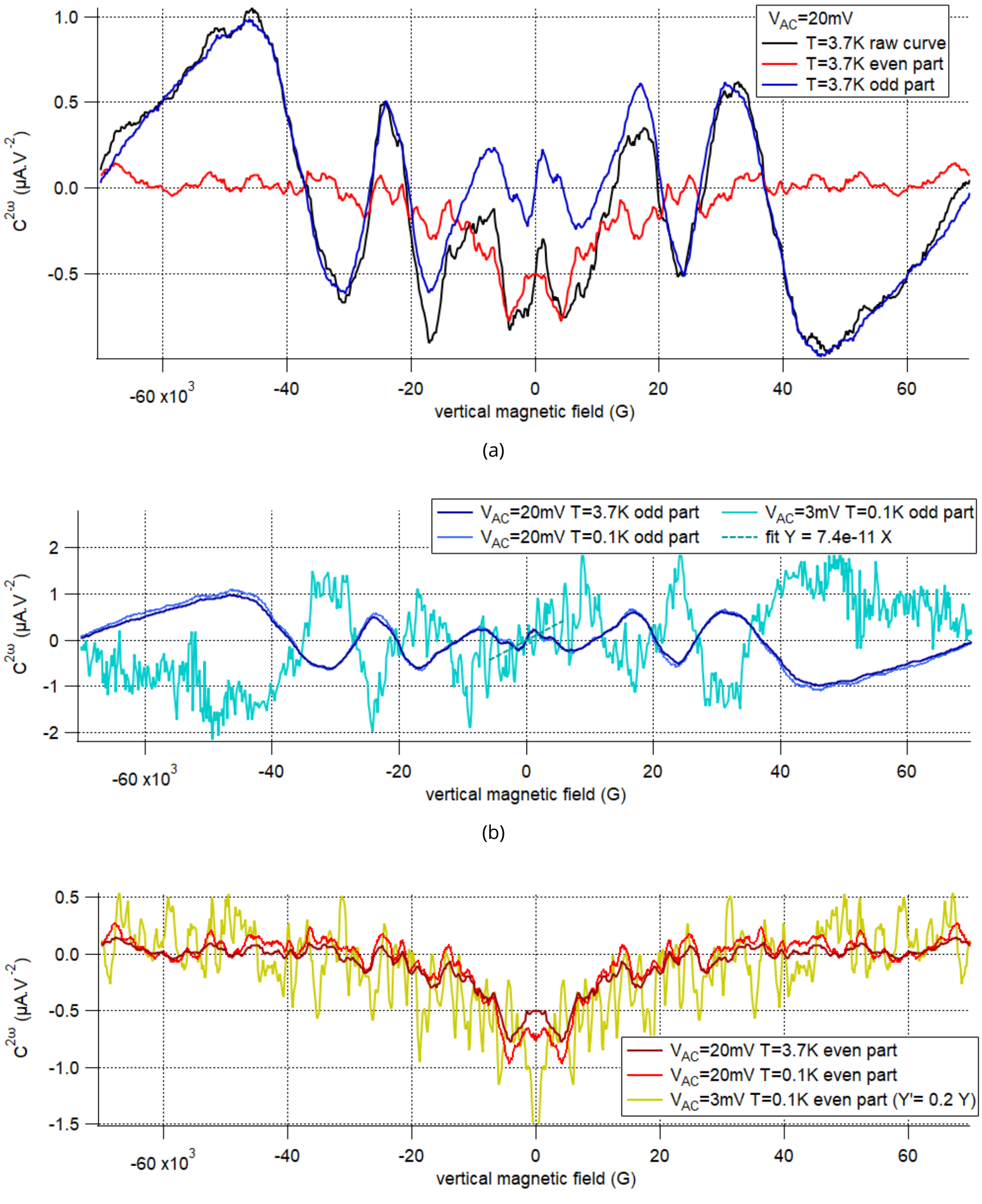

(a)

(b)

(c)

Figure 6.42 – Second harmonic current response of Bi$_{12}^{long}$ as a function of vertical (perpendicular, out-of-plane) magnetic field. (a) The raw signal (black line) is decomposed into a part even in field (red line) and odd in field (blue line). (b) Odd part for different temperatures and excitation amplitudes V_{AC}. The turquoise dashed line is the result of a linear fit at low field of the data shown as the turquoise solid line. The slope gives $|\beta| \simeq 7.66\, G.\mu A^{-1}$. (c) Even part for different temperatures and excitation amplitudes V_{AC}. The gold curve has been rescaled for easier visualization.

Fig. 6.42b focuses on the odd contribution to the second harmonic, with two different excitation amplitudes and two temperatures. We see that the two responses with the same $V_{\mathrm{AC}} = 20\ mV$ but different $T \simeq 0.1\ K$ and $T \simeq 3.7\ K$ are very close, with large and smooth variations for $|B_{\mathrm{ext}}| \gtrsim 1\ T$ and smaller features at low fields. The large scale variations are further analyzed in part 6.11.

The response of Bi$_{12}^{long}$ to a lower excitation $V_{\rm AC} = 3\ mV$, at the limit between the two excitation regimes identified in Fig. 6.41e, is shown as a light blue solid line in Fig. 6.42b. It is noisier and shows sharper peaks than the $V_{\rm AC} = 20\ mV$ response, but keep the same global shape, albeit a change of sign.

In [200], their change of sign of the second harmonic response is caused by a change of shape of the Fermi surface with the chemical potential. In our measurement however, we change the excitation $V_{\rm AC}$ of a voltage biased two-terminal setup. In [202], they also find changes of sign with the gate voltage, that coincide with first harmonic (resistance) variations. They interpret it as related to sub-band crossings.

Furthermore, the low field response features at $|B_{\rm ext}| \lesssim 0.5\ T$ disappear for $V_{\rm AC} = 3\ mV$. Except for this low field features, the linear dependence on $B_{\rm ext}$ is the same for $V_{\rm AC} = 3\ mV$ and $V_{\rm AC} = 20\ mV$. We conclude that the mechanism responsible for the change of sign doesn't affect the odd contribution to the second harmonic for $|B_{\rm ext}| \gtrsim 0.5\ T$.

A linear fit on the $V_{\rm AC} = 3\ mV$ $T \sim 0.1\ K$ odd part at low field is displayed as a dashed blue line in Fig. 6.42b, and gives $y = a.x$ with $a = 7.4 \times 10^{-11} A.V^{-2}.G^{-1}$. Looking at Eq. (6.84), we identify this coefficient as $A_Z G(\tilde{B})^3 \beta \tilde{B} \simeq A_Z G_0^3 \beta B_{\rm ext}$. To estimate the coefficient of the quadratic dependence of the resistance of Bi$_{12}^{long}$ on the Zeeman field A_Z, we do a low field quadratic fit on the resistance of Bi$_{12}^{long}$ as a function of magnetic field oriented along the nanowire axis, see the solid and dashed light green lines in Fig. 6.36b. Both the estimation of A_Z and the measurement of G_0 are done at $T \simeq 3.7\ K$ to reduce the contribution of the WAL on the magnetoresistance.

With $A_Z = 2.07 \times 10^{-6}\ \Omega.G^{-2} = 207\ \Omega.T^{-2}$, $G_0 = 1/5985 = 1.67 \times 10^{-4}\ \Omega^{-1}$ and a linear fit coefficient $a = 7.4 \times 10^{-11}\ A.V^{-2}.G^{-1}$, we obtain $|\beta| \simeq 7.66 \times 10^6\ G.A^{-1} = 766\ T.A^{-1} = 7.66\ G.\mu A^{-1}$. The sign and magnitude of β is analyzed at the end of this subsection.

With the measurements done on the nanowires with superconducting proximity effect (see part 3.4), this effective magnetic field (or flux) could be explained by geometric or kinetic inductances. With the present measurements that involve no superconductivity, it is clear that there are no such inductances.

Fig. 6.42c focuses on the even contribution to the second harmonic, with two different excitation amplitudes and two temperatures. First of all, the even contribution is not zero, even though $V_{\rm DC} = 20\ mV$. On the $V_{\rm AC} = 20\ mV$ curves, we see that they have smaller variations and on smaller field-scale than their odd counterpart.

Moreover, the $T \simeq 0.1\ K$ curve features slightly larger variations and additional small-scale patterns compared to the $T \simeq 3.7\ K$ curve. The field-scale of these variations is compatible with UCF, but notice on Fig. 6.36a that the UCF measured on the magnetoresistance of Bi$_{12}^{long}$ are drastically reduced for $V_{\rm AC} = 20\ mV$ and $T \simeq 3.7\ K$ (solid brown curve), unlike the variations measured on the even part of the second harmonic response.

To conclude with the even part of the second harmonic response, we find that the $V_{\rm AC} = 3\ mV$ and $T \simeq 0.1\ K$ response (solid gold curve) does not scale with $V_{\rm AC}^2$. To display it on the same scale as the two other curves, it has be been rescaled by a factor 0.2.

Sample Bi$_{11}^{long}$

In Figs. 6.43a and 6.43b are plotted the odd and even contributions to the second harmonic response of segment Bi$_{11}^{long}$ as a function of magnetic field, for various excitation amplitudes $V_{\rm AC}$. This segment is next to segment Bi$_{12}^{long}$, part of the same nanowire.

Compared to Fig. 6.42b, the odd part in Fig. 6.43a present the same linear dependence for fields $|B_{\rm ext}| \lesssim 0.3\ T$ and a sign reversal in the low excitation regime $V_{\rm AC} = 5mV$ (solid light blue line). We

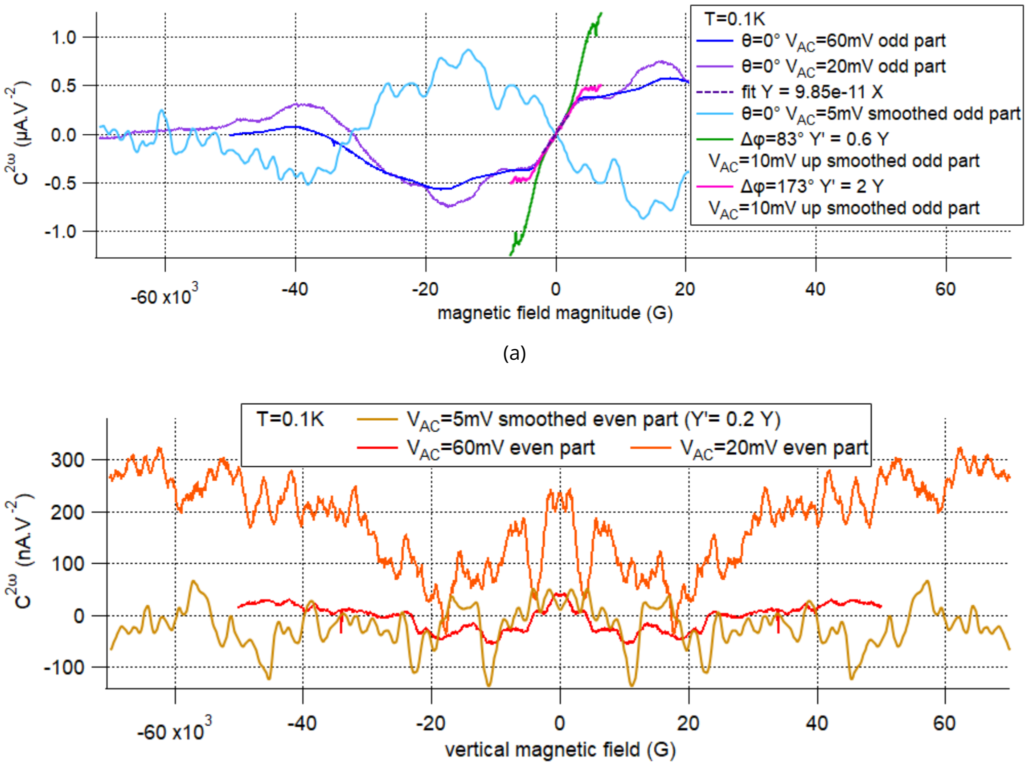

(a)

(b)

Figure 6.43 – Second harmonic current response of Bi$_{11}^{long}$ as a function of magnetic field in different orientations and for different excitation amplitudes V_{AC}. The raw signal is decomposed into a part even in field (b) and odd in field (a). $\theta = 0°$ corresponds to a field parallel to the vertical axis. $\Delta\varphi = 173°$ and $\Delta\varphi = 83°$ correspond to horizontal fields almost antiparallel and perpendicular to the nanowire axis, respectively. The green and pink curves have been rescaled to match the slope of the violet curve. The gold curve has been rescaled for easier visualization. The violet dashed line is the result of a linear fit at low field of the data shown as the violet solid line. The slope gives $|\beta| \simeq 166\,G.\mu A^{-1}$.

notice that the $V_{\mathrm{AC}} = 20mV$ response (solid purple line) presents thinner structures compared to the $V_{\mathrm{AC}} = 60mV$ response (solid dark blue line).

Following the same procedure as Bi$_{12}^{long}$, we extract a low field linear fit coefficient $y = a.x = -9.85 \times 10^{-11}x$ (dashed purple line). Assuming the same $A_Z = 2.07 \times 10^{-6}\ \Omega.G^{-2}$ as segment Bi$_{12}^{long}$ (same nanowire) and with $G_0 = 1/15180 = 6.59{\times}10^{-5}\ \Omega^{-1}$, we get $|\beta| \simeq 1.66{\times}10^{8}\ G.A^{-1} = 1.66{\times}10^{4}\ T.A^{-1} = 166\ G.\mu A^{-1}$. Despite being two segments of the same nanowire, segment Bi$_{11}^{long}$ has an $\beta \simeq 22$ times larger than segment Bi$_{12}^{long}$. This large discrepancy is commented at the end of this subsection.

For the nanowire segment Bi$_{11}^{long}$, we performed second harmonic response measurements as a function of in-plane (horizontal) magnetic field for two angles $\Delta\varphi$. $\Delta\varphi$ is the in-plane angle between the direction of the voltage gradient and the direction of the magnetic field. The solid pink and green lines shows the response to a magnetic field almost antiparallel ($\Delta\varphi = 173°$) and perpendicular ($\Delta\varphi = 83°$) to the nanowire axis, respectively.

The $\Delta\varphi = 173°$ response has been rescaled by a factor 2 and the $\Delta\varphi = 83°$ response by a factor 0.6. This indicates that the product $A_Z\beta$ in our toy model indeed depends on the magnetic field direction. In the present case, $A_Z\beta$ is the highest for a horizontal magnetic field perpendicular to the voltage gradient (or current propagation direction), and is the lowest for a magnetic field parallel to the voltage gradient. This type of behavior is expected for β for Rashba-type spin-orbit coupling, that is for spin locked perpendicular to the momentum. This type of spin-orbit is dominant on the surfaces of bismuth crystals.

Back to the even contribution to the second harmonic response of segment Bi$_{11}^{long}$(Fig. 6.43b), most of the general features discussed for the even part of Bi$_{12}^{long}$ also apply for Bi$_{11}^{long}$. We notice that in contrast to Bi$_{12}^{long}$, the even part of Bi$_{11}^{long}$does not vanish at high magnetic field.

Samples Bi$_{31}^{long}$ and Bi$_{32}^{long}$

In Figs. 6.44a and 6.44b are plotted the second harmonic responses of segments Bi$_{31}^{long}$ and Bi$_{32}^{long}$ as a function of vertical magnetic field, together with their contribution that are odd and even in magnetic field. The two segments are next to each other and are parts of the same nanowire.

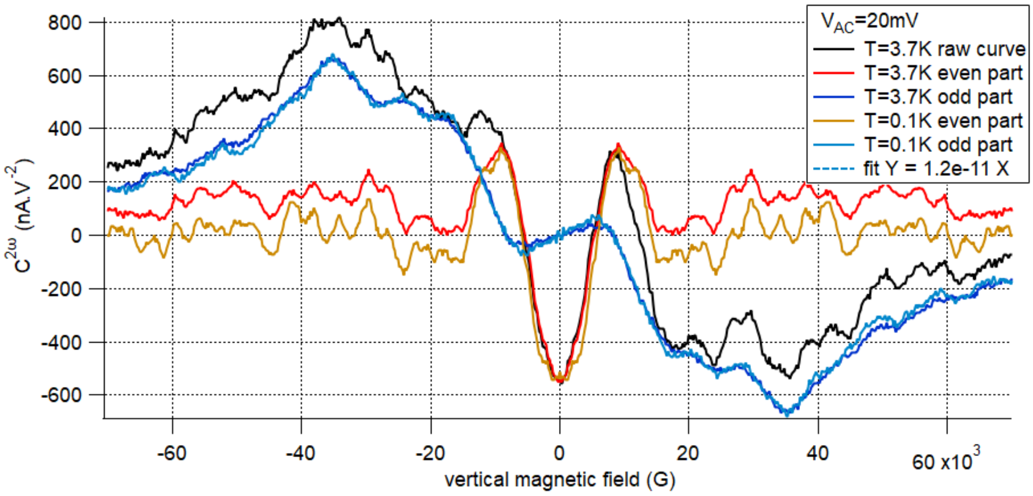

(a)

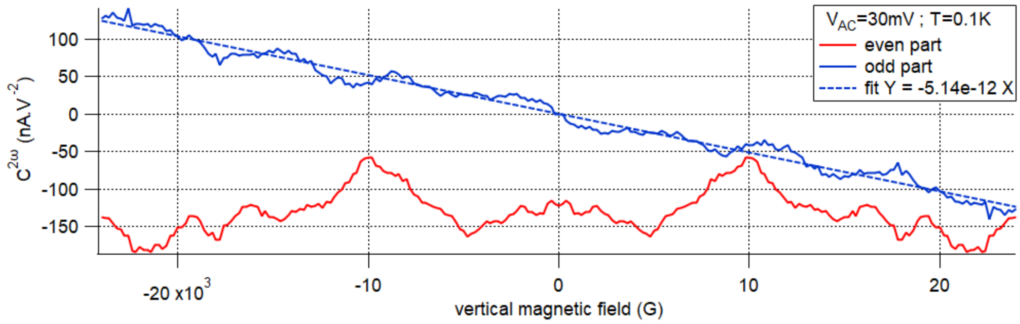

(b)

Figure 6.44 – Second harmonic current response as a function of vertical (perpendicular, out-of-plane) magnetic field, for different temperatures. The raw signal is decomposed into a part even in field and part odd in field. (a) Response of sample Bi$_{31}^{long}$. The light blue dashed line is the result of a linear fit at low field of the data shown as the light blue solid line. The slope gives $|\beta| \simeq 20.4\, G.\mu A^{-1}$. (b) Response of sample Bi$_{32}^{long}$. The blue dashed line is the result of a linear fit at low field of the data shown as the blue solid line. The slope gives $|\beta| \simeq -102\, G.\mu A^{-1}$.

In addition to the common behavior between all the second harmonic response measurements introduced above, we notice a clear change of regime for Bi$_{31}^{long}$ (Fig. 6.44a) happening close to $|B_{\text{ext}}| \simeq 1\, T$, and a linear dependence of the odd part of the response of Bi$_{32}^{long}$ (Fig. 6.44a) up to a field as high as $|B_{\text{ext}}| \simeq 2.3\, T$.

For segment Bi$_{31}^{long}$, we estimate $a = 1.2{\times}10^{-11}\ A.V^{-2}.G^{-1}$, $A_Z = 2.92{\times}10^{-6}\ \Omega.G^{-2}$ (see Fig. 6.37b), and $G_0 = 1/17056 = 5.86{\times}10^{-5}\ \Omega^{-1}$, giving $|\beta| \simeq 2.04{\times}10^{7}\ G.A^{-1} = 2.04{\times}10^{3}\ T.A^{-1} = 20.4\ G.\mu A^{-1}$.

For segment Bi$_{32}^{long}$, we estimate $a = -5.14 \times 10^{-12}\ A.V^{-2}.G^{-1}$, $A_Z = 2.92 \times 10^{-6}\ \Omega.G^{-2}$ identical to the one measured in segment Bi$_{31}^{long}$, and $G_0 = 1/38759 = 2.58 \times 10^{-5}\ \Omega^{-1}$, giving $|\beta| \simeq -1.02 \times 10^{8}\ G.A^{-1} = -1.02 \times 10^{4}\ T.A^{-1} = -102\ G.\mu A^{-1}$. Again, we see that even if they both are segments of a same nanowire, segments Bi$_{31}^{long}$ and Bi$_{32}^{long}$ have current-to-field conversion coefficients β differing by a factor 5.

d) Summary of the second harmonic response

To summarize the analysis of our measurements, we found that the second harmonic responses :
- features both contributions that are odd in magnetic field and contributions that are even in magnetic field
- features two excitation regimes with a crossover at $\sim 0.5\mu A$
- features a change of behavior on both the even and odd contributions when crossing a typical magnetic field of magnitude $|B_{\text{ext}}| \simeq 1\ T$
- have odd contributions that scale with V_{AC}^2
- have odd contributions that can reverse their sign depending on the excitation regime, but conserving their global shape
- have odd contributions that are linear up to magnetic fields $|B_{\text{ext}}| \simeq 0.2\ T$ to $|B_{\text{ext}}| \simeq 2.3\ T$
- have odd contributions that are not monotonous at high magnetic fields, and that can even oscillate with a $1/|B_{\text{ext}}|$ period between positive and negative values in some cases
- have odd contributions that can vary both in magnitude and shape with the magnetic field direction
- have even contributions that do not scale with V_{AC}^2, whose shapes change depending on V_{AC}, and that exist even for $V_{\text{DC}} = 0$
- have even contributions that feature variations on a smaller magnetic field scale than their odd counterparts, compatible with UCF yet much more resilient

When not explicit stated, the magnetic field in the above summary is vertical (out-of-plane).

From our toy model developed in the previous subpart, we related the low field linear dependence on B_{ext} of the odd contribution to β, i.e. $a.B_{\text{ext}} \simeq A_Z G_0^3 \beta B_{\text{ext}}$. From linear fits on the odd contributions to the second harmonic responses, we extracted the coefficients a. The coefficients A_Z of the quadratic dependence of the magnetoresistance on the Zeeman field have been extracted by low field fits of the magnetoresistance at $T \simeq 3.7K$ as a function of magnetic field parallel to the nanowire. The values of G_0 correspond to the inverse of the zero-field resistance at $T = 4.2K$.

In Fig.6.45, we plot the odd (in field) contribution of the second harmonic response of main long Bi nanowires as a function of vertical magnetic field. The curves obtained from the different samples have been rescaled by their respective values of $A_Z V_{\text{AC}}^2 / R_0^3$, such that their slope is directly β.

All the values of A_Z, $A_{\{orb+Z\}}$ (for the vertical field quadratic magnetoresistance coefficient) and β measured in the seven segments are displayed in Tab. 6.1.

The A_Z boxes completed with a value followed by a ? correspond to A_Z values estimated by a measure on their neighboring segment within the same nanowire. The β boxes featuring a ? follow from these questionable A_Z values. The β boxes completed by a value preceded by a $>$ or $<$ symbol indicate that β has been estimated taking a vertical field estimation of A_Z, that is $A_{\{orb+Z\}}$, by lack of available data. It is very clear that $A_{\{orb+Z\}} > A_Z$, such that the corresponding values of $|\beta|$ are underestimated. In the boxes containing estimations of β, we kept track of the sign taking into account the direction of the voltage gradient (or current propagation direction). When there is no $+$ or $-$ symbol, it means that there was no available data in the low excitation regime.

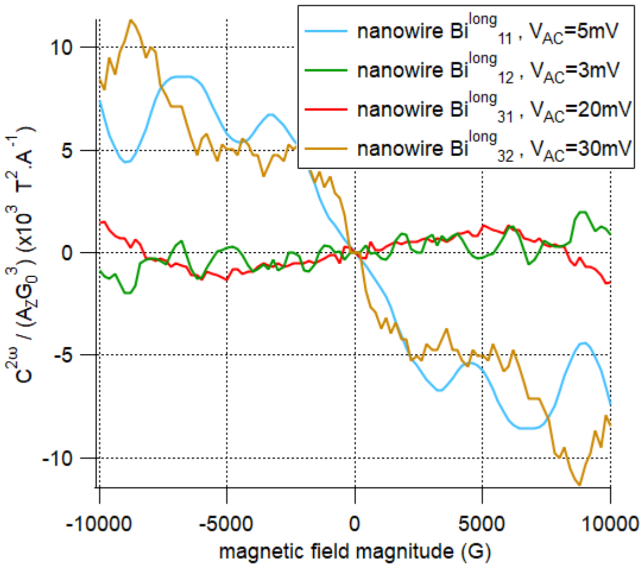

Figure 6.45 – Odd (in field) contribution of the second harmonic response of main long Bi nanowires as a function of vertical magnetic field. The curves obtained from the different samples have been rescaled by their respective values of $A_Z V_{\text{AC}}^2/R_0^3$, such that their slope is directly β.

We see that for the only straight nanowire with available data on the sign of β, the sign is opposite for segments Bi$_{12}^{long}$ and Bi$_{11}^{long}$. One possible, yet not very satisfying, explanation of this change of sign and magnitude is that the two segments have slightly different Fermi surface, but different enough to change β by a factor -22. This would explain why they have such different second harmonic shapes as a function of vertical magnetic field.

Depending on the segment, we find values of $|\beta|$ ranging from $8G.\mu A^{-1}$ to $321G.\mu A^{-1}$, with most trusted values in the $\sim 10G.\mu A^{-1}$ scale. In part 3.4, we found shifts in magnetic field of the critical current pattern of several proximity-induced superconducting bismuth nanowires, that would correspond to β ranging from 28 to 3600 $G.\mu A^{-1}$.

Compared to [208], translating our β into an asymmetry in the magnetoresistance (first harmonic response) leads to an MCA ~ 10 times weaker than what is found in Ge(111) films ($\frac{\Delta V_{UMR}}{V^{(1\omega)}} \simeq 2A_Z G_0 \beta B_{\text{ext}} I_{\text{DC}}$, yielding a 0.05 % and a 0.07 % modulation for segments Bi$_{12}^{long}$ and Bi$_{31}^{long}$assuming the same $I_{\text{DC}} = 10\mu A$ and $B_{\text{ext}} = 1T$).

In the supplementary materials of [202], they present a table with the MCA coefficient γ of many materials. γ is defined such that the correction to the resistance is $R = R_0(1 + \gamma BI)$, corresponding to $\gamma \simeq 2A_Z G_0 \beta$ (see Eq. (6.71)) in our experiments, yielding $\gamma \simeq 53$ $A^{-1}.T^{-1}$ for segment Bi$_{12}^{long}$ and $\gamma \simeq 70$ $A^{-1}.T^{-1}$ for segment Bi$_{31}^{long}$. According to [202], this place our samples in the rather high end of the MCA magnitude spectrum (although we notice that the Ge(111) sample of [208] is listed as $\gamma = 0.7$ whereas we estimate it to $\gamma \simeq 500$).

6.9.5 . Conclusion

Measurements of resistivity at low temperature are consistent with previous analysis, confirming that the transport is dominated by surface states with an elastic mean free path limited by the nanowires dimensions. The decrease of resistance at higher temperatures is attributed to a higher contribution of bulk states, but the variation of resistance is surprisingly large.

When varying magnetic field magnitude and orientation, we found a positive magnetoresistance that depends on relative orientation of field with respect to the wire axis. At low field, we measured a resistance dip, consistent with the expected weak anti-localization of 2d conducting surfaces with high spin-orbit coupling. At higher field, we saw universal conductance fluctuations. The amplitude of both quantum mesoscopic phenomenon decrease with increasing temperature. From the weak anti-localization (WAL) effect, we extracted a phase coherence length $L_\phi \simeq 0.8\ \mu m$ at $T \simeq 0.2\ K$, which is low compared to the lower limit given by the experiments on nanowires proximitized by superconducting contacts. This might be a sign of an L_ϕ reduction or enhancement mechanism between the resistive and proximity-induced superconducting states, that may be related to the spins of the Bi atoms.

In addition to the standard differential resistance analysis, we performed measurements of second harmonic response as a function of magnetic field. With a very simple model, we argued that we can estimate the strength of the spin-momentum locking of conducting states by extracting the part of the second harmonic signal that is odd in magnetic field. With our simplistic assumptions, we estimated this current-to-spin conversion, also referred to as Magneto-Chiral Anisotropy (MCA), to be $\beta \sim 10\ G.\mu A^{-1}$. This is consistent with the β values found in the experiments on the nanowire proximitized by superconducting contacts analyzed in appendix 6.12. According to the table found in the supplementary materials of [202], this place our samples in the rather high end of the MCA magnitude spectrum, with a $\gamma \sim 60\ A^{-1}.T^{-1}$.

6.10 . Second harmonic response of the ring sample Bi^{ring}

In chapters 3 and 4, we studied the low temperature transport characteristics of a bismuth nanoring. Its contacts were made of superconducting disordered tungsten of critical temperature $T \simeq 5\ K$. We measured a supercurrent $< 2.8\ \mu A$ with asymmetric triangular regular oscillations of period $\simeq 17\ G$, sign of proximity induced superconductivity in both branches of the ring and a Superconducting QUantum Interference Device (SQUID) behavior.

During a second cooldown one month later, we measured the low temperature transport characteristics of this bismuth nanoring as a function of in-plane magnetic field up to $7\ T$, in a two-terminals setup. In Fig. 6.46, we display the voltage response of the sample to an AC current excitation.

At $T \simeq 0.47\ K$, despite the contacts still being superconducting, there was no sign of supercurrent anymore and the total two-terminals resistance was $R_{tot,0.47} \simeq 300\ \Omega$. This yields $R_{ring,0.47} \simeq 250\ \Omega$ without the dilution refrigerator lines, which is larger than the resistance $R_{CD1} \simeq 160\ \Omega$ of the same ring for $T \simeq 0.1\ K$ during the first cooldown.

During the first and second cooldowns, we measured the resistance of a segment of the tungsten deposit contacting one side of the nanoring. It showed a resistance $\simeq 120\ \Omega$ at $T \simeq 5.5\ K$ for both cooldowns, with dilution lines resistances of $\simeq 60\ \Omega$.

Consequently, we can assume that the ring itself did not change a lot between the two cooldowns neither did the tungsten contacts, but their interfaces have changed in such a way that it suppressed the superconducting proximity effect.

In the following, we use the second harmonic response to estimate an effective current-to-field factor β induced by SOC, as introduced in appendix 6.7.4 and used in appendix 6.9.4 and 6.12.

Fig. 6.46a show the first harmonic response at $T \simeq 7.1\ K$ and for $I_{\mathrm{DC}} = 0$ and $I_{\mathrm{AC}} = 1\ \mu A$, that is the differential resistance of the nanoring in series with the tungsten contacts in their resistive state, with the interfacial contacts resistances, and with the dilution refrigerator lines.

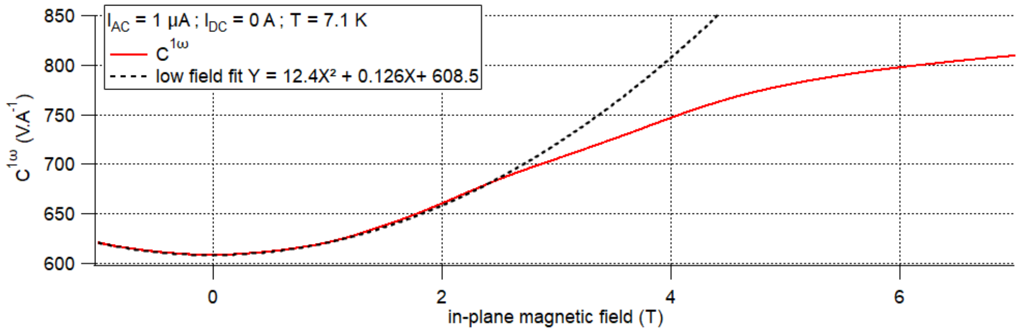

(a)

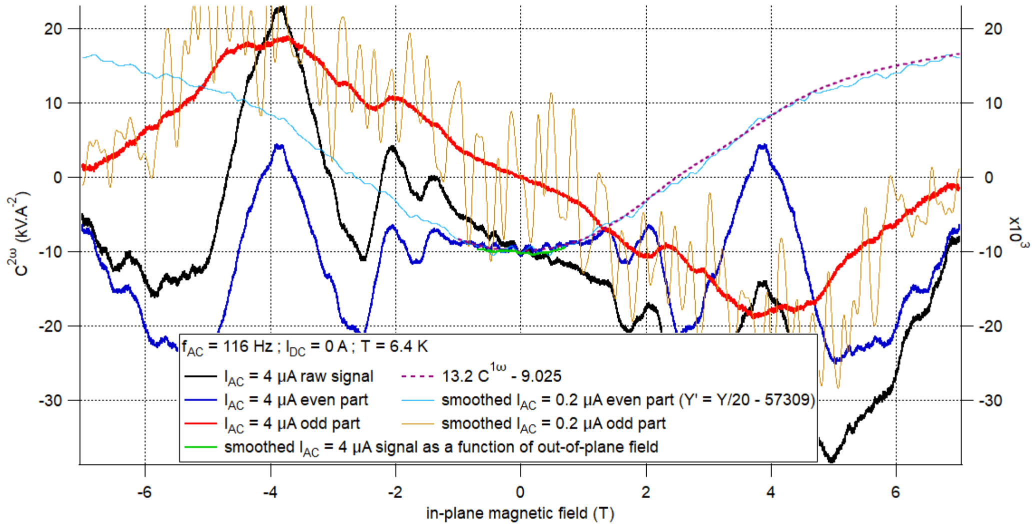

(b)

Figure 6.46 – (a) First harmonic voltage response (resistance) of the nanoring sample Bi^{ring} as a function of in-plane magnetic field, at $T \simeq 7.1\,K$ and for $I_{\rm DC} = 0$ and $I_{\rm AC} = 1\,\mu A$. (b) Second harmonic voltage response of the nanoring at $T \simeq 6.4\,K$ and $I_{\rm DC} = 0$ as a function of in-plane magnetic field, where we splitted the contributions that are even in magnetic field from the ones that are odd in magnetic field. The slope of the odd part at $I_{\rm AC} = 4\,\mu A$ (red line) gives us $\beta \simeq 2.77\,G.\mu A^{-1}$.

A low field quadratic fit gives $\tilde{A}_Z = 12.4\ \Omega.T^{-2} = 1.24 \times 10^{-7}\ \Omega.G^{-2}$, weaker than the measurements on voltage biased long nanowires by a factor ~ 10. Remember here that we measure the magnetoresistance of two curved segments in parallel of a nanowire, with approximate lengths of 1.6 and $2.5\ \mu m$, as a function of in-plane magnetic field, hence the $\tilde{A}_Z$ notation instead of A_Z.

In this setup, the sample itself is rotated. The in-plane field is applied by a large vertical coil which has a lower hysteretic behavior ($\lesssim 40\ G$) than the horizontal coil used in appendix 6.9 and 6.12. This could allow us to detect and quantify β in the first harmonic response. To this end, we also extract a linear coefficient $a^{(1)} = 0.126\ \Omega.T^{-1} = 1.26 \times 10^{-5}\ \Omega.G^{-1}$ from the fit. But notice that the term linear in B_{ext} in the first harmonic response in Eq. (6.79) is also linear in I_{DC}, and we did the measurement with an AC current bias of $1\ \mu A$ and no DC current. So, just like the even contribution to the second harmonic response, our phenomenological model fails to describe this behavior. To get an idea of the scales, we consider an $I_{\text{DC}} = 1\ \mu A$ and our $a^{(1)}$ and $\tilde{A}_Z$, giving us an $\beta \simeq 2540\ T.A^{-1} = 25,4\ G.\mu A^{-1}$, which is on the same typical scale as what we measured in the long nanowires.

The tungsten contacts at $T \simeq 7K$ showed a magnetoresistance much lower than the bismuth nanoring one.

In addition to its low field quadratic behavior, we managed to extract Shubnikov-de Haas oscillations from small high field variations of the magnetoresistance. To do so, we tried various numerical treatments and keep the most robust ones. We discuss and show the results in part 6.11.

Let us now consider the second harmonic voltage response of the nanoring sample in its normal state to a small current excitation.

In Fig. 6.47, we plot the second harmonic response as a function of AC (Figs. 6.47a,6.47b) and DC (Fig. 6.47c) excitation amplitude, at $T \simeq 6.3\ K$ and for various magnetic field values. Again, we find two excitation regimes delimited by a peak close to $I_{\text{AC}} \simeq 0.5\ \mu A$ in the second harmonic response, and a quadratic dependence on I_{AC} in the higher excitation regime.

In Fig. 6.47c, ignoring the Y offset caused by $I_{\text{AC}} = 3\ \mu A$, we find that the second harmonic response is mainly odd in I_{DC}, with an approximate linear dependence at low field, that varies with the magnetic field.

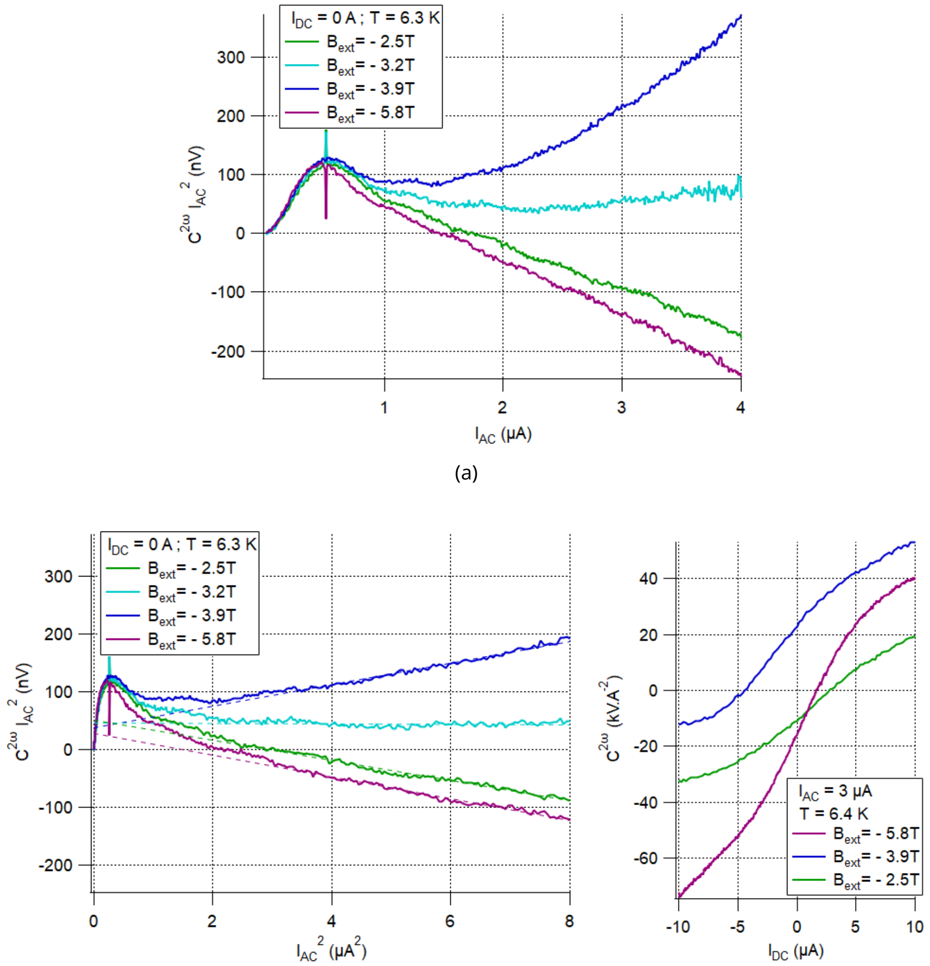

(a)

(b)

(c)

Figure 6.47 – Second harmonic voltage response of the nanoring sample Bi^{ring} as a function of AC and DC current excitations.

In Fig. 6.46b, we plot the second harmonic response of the nanoring at $T \simeq 6.4\ K$ and $I_{\mathrm{DC}} = 0$ as a function of in-plane magnetic field, where we splitted the contributions that are even in magnetic field from the ones that are odd in magnetic field.

The solid blue and red lines represent the even and odd contributions for an excitation amplitude of $I_{\mathrm{AC}} = 4\ \mu A$, respectively, in the higher excitation regime. The even contribution show two distinct behaviors. For $|B_{\mathrm{ext}}| \lesssim 1\ T$, we see small regular oscillations of period $\sim 2300\ G$ on top of a quadratic background and a constant offset $\sim -10\ kV.A^{-2}$. This would correspond to interference by orbital dephasing through a minimum surface $S = \Phi_0/\Delta B \simeq 9 \times 10^{-3}\ \mu m^2$, e.g. a circle of diameter $\sim 107\ nm$. This could be the surface of a section of the nanoring, although it is small considering the width of $\sim 300\ nm$ of the branches revealed by scanning electron microscope out-of-plane imaging. More realistically, it could be due to a $\sim 1\%$ misalignment of the magnetic field in the plane of the nanoring, leading to orbital dephasing through the all surface of the nanoring.

For $|B_{\mathrm{ext}}| \gtrsim 1\ T$, on top of the $\sim -10\ kV.A^{-2}$ offset, we see large variations with a period that increases with $|B_{\mathrm{ext}}|$. In appendix 6.11, we analyze it and find a $1/|B_{\mathrm{ext}}|$ periodicity corresponding to the same Shubnikov-de Haas oscillations as the ones found on the first harmonic response.

The solid light blue line represents the even contribution to an excitation $I_{\mathrm{AC}} = 0.2\ \mu A$ in the lower excitation regime, smoothed with a moving average over 1000 points to reduce the noise. We see that all the oscillations at low and high magnetic field disappeared and the signal is increasing smoothly with $|B_{\mathrm{ext}}|$. For comparison, it has been rescaled and shifted according to the formula $y' = y/20 - 57309$ and plotted alongside the first harmonic response (dashed purple line), rescaled and shifted according to $y' = 13.2y - 9.025$. With those manipulations, we notice that the two curves fall on top of each others, that is $C^{2\omega} = 264C^{1\omega} - 1.146 \times 10^6$. Like the measurements on individual nanowires, the even contribution does not scale as I_{AC}^2.

The solid red line shows the odd contribution to an excitation $I_{\mathrm{AC}} = 4\ \mu A$. For $|B_{\mathrm{ext}}| \lesssim 1\ T$, it is fully linear in B_{ext} and a linear fit in this field range (dashed red line) gives a coefficient $a = -3431\ V.A^{-2}.T^{-1}$. With $\tilde{A}_Z = 12.4\ \Omega.T^{-2}$ and using the expression in Eq. (6.79), we estimate $\beta \simeq 277\ T.A^{-1} = 2.77\ G.\mu A^{-1}$. This value is lower than the β found in individual nanowires, but remember here that a and $\tilde{A}_Z$ have been estimated with an in-plane field on a sample with two curved branches, and we know that both a and $\tilde{A}_Z$ vary with magnetic field direction. So this low value could be explained by an β of the same order as previous experiments, but with an averaged value over a wide range of direction and with partial compensation over the two branches. For $|B_{\mathrm{ext}}| \gtrsim 1\ T$, the odd contribution is still fairly linear up to $4\ T$ but shows bigger variations.

In the low excitation regime, the odd contribution scales with I_{AC}^2 and its global dependence on magnetic field is the same as in the higher excitation regime, see the solid orange line. In contrast with previously analyzed measurements on individual nanowires, we find Shubnikov-de Haas oscillations in the even contribution and not in the odd one.

In this appendix, we analyzed the second harmonic response of the nanoring in its resistive state to a small current excitation, as a function of in-plane magnetic field. We found many similarities, with an odd contribution giving $\beta \simeq 2.77\ G.\mu A^{-1}$ smaller but still consistent with the individual long nanowires measurements. The scalings of the even and odd contributions behave similarly. However, the even contribution show bigger and more regular variations than the UCF previously found. In particular, we found that the even contribution displays large Shubnikov-de Haas oscillations at high field, whereas we found Shubnikov-de Haas-like oscillations in the odd part of the second harmonic response of the long nanowire Bi$_{12}^{long}$.

6.11 . Discussion on the Shubnikov-de Haas-like variations at high field

In this appendix, we show large field scale variations of the second harmonic response of the long bismuth nanowire Bi$_{12}^{long}$ and the nanoring Bi^{ring}, that have an approximate $1/B_{\rm ext}$ periodicity. We discuss two physical processes that could induce such Shubnikov-de Haas (SdH)-like oscillations in the second harmonic response of our samples.

a) Mechanisms inducing SdH oscillations in the second harmonic response

Let us introduce here an attempt to explain these SdH-like variations. Let us first acknowledge that the SdH variations are usually best seen in the $\delta G/\delta B$ curve, filtering out the part of $G(B)$ that varies with B on larger scales. In our phenomenological model, we couple the effective Zeeman magnetic field $B_{Z,eff}$ to the current I through our sample with β. As the conductance only depends on the effective Zeeman field, we write :

$$\delta G = \frac{\partial G}{\partial B_{Z,eff}}\delta B_{Z,eff} = \frac{\partial G}{\partial B_{Z,eff}}(\delta B_{\rm ext} + \beta\delta I) \tag{6.119}$$

$$\implies \frac{\delta G}{\delta V} = \frac{\partial G}{\partial B_{Z,eff}}\frac{\delta B_{\rm ext}}{\delta V} + \beta\frac{\partial G}{\partial B_{Z,eff}}\frac{\delta I}{\delta V} = \beta G\frac{\partial G}{\partial B_{Z,eff}} \tag{6.120}$$

$$\iff \frac{\partial G}{\partial B_{Z,eff}} = \frac{1}{\beta G}\frac{\delta G}{\delta V} \tag{6.121}$$

Writing $I = \Sigma_{n\in\mathbb{N}}k_n V^n$, to the leading order for small V, we have : $\frac{\partial G}{\partial B_{Z,eff}} \propto k_2/k_1$. Rephrasing it, the variation of the conductance with the effective Zeeman magnetic field, very sensitive to SdH variations, is proportional to the ratio between the coefficient of the quadratic part of the current-voltage relation k_2V^2 and the coefficient of the linear part k_1V.

In terms of harmonic responses, this corresponds to the following approximation :

$$\frac{\partial G}{\partial B_{Z,eff}} \propto \frac{k_2}{k_1} \simeq \frac{C^{2\omega}}{C^{1\omega}} \tag{6.122}$$

where $C^{2\omega}$ is the coefficient of second harmonic response of I to an AC V excitation, and $C^{1\omega}$ is the coefficient of first harmonic response of I to an AC V excitation.

Notice here that we consider variation of the conductance caused by the effective Zeeman field only. This is much lower than the variation caused by the usual orbital contribution. We understand it like the orbital effects give rise to the Landau levels but we probe the SdH variations thanks to the small effective Zeeman field sensitive to variations of V.

Because $G(B_{Z,eff})$ is even, $\frac{\partial G}{\partial B_{Z,eff}}$ is odd. $C^{1\omega}$ is also mainly even in field, yielding SdH oscillations in $C^{2\omega} \propto \frac{\partial G}{\partial B_{Z,eff}}C^{1\omega}$ odd in field, that are visible in second harmonic response thanks to the existence of β, see Eq.(6.121).

For SdH oscillation, the periodicity corresponds to $\Delta_{\rm SdH}\left(\frac{1}{B}\right) = \frac{e\hbar}{\epsilon_F m*}$, with $m*$ the effective mass of the charge carriers [219]. Equivalently, one can write $1/B$ Shubnikov-de Haas periodicity as : $\Delta_{\rm SdH}\left(\frac{1}{B}\right) = \frac{2e}{\hbar k_F^2}$.

There exists another process yielding SdH in the second harmonic response. In appendix 6.7.2, we mentioned that an asymmetry in the contacts, the conductor, or the diffusion centers inside the conductor can contribute to the non-linear response. From [206], one can derive variations of the conductance G with voltage V via the chemical potential μ : $\frac{\partial G}{\partial \mu}\delta\mu \simeq \frac{\partial G}{\partial \mu}(1-2a)e\delta V$ ($a = 1/2$ for symmetric contacts). This term relies on variations of the density of states as a function of voltage. These variations of $\frac{\partial G}{\partial \mu}$ due to Landau levels, at the origin of SdH oscillations, are even in field. Thus, contrasting with the mechanism in

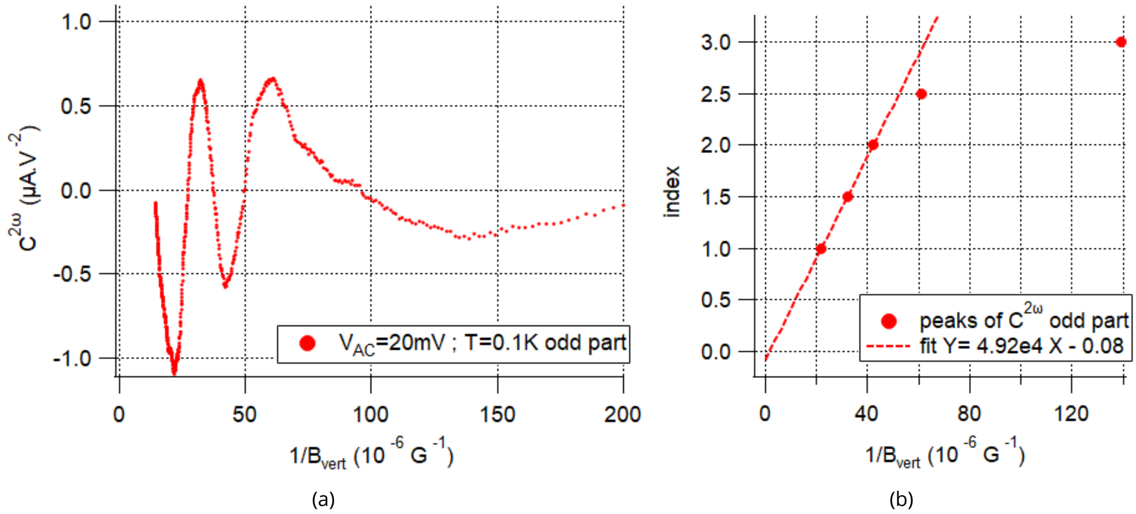

Figure 6.48 – Shubnikov-de Haas oscillations on the second harmonic current response of long nanowire sample Bi$_{12}^{long}$, yielding $\lambda_F \simeq 51\,nm$.

Eq.(6.121) exploiting β, the resulting SdH non-linear response is even in field.

b) Long nanowire Bi$_{12}^{long}$

In Fig. 6.48a, we plot the odd part of the second harmonic current response of segment Bi$_{12}^{long}$ to an AC voltage excitation, as a function of inverse out-of-plane magnetic field, int the positive B range. In Fig. 6.48b, we plot the indices of the oscillation peaks and dips as a function of their respective $1/B$ values. The first dip is indexed as 1 arbitrarily, as we have no theory and no other measurement to discriminate the peaks from the dips. The indices of the peaks are shifted by 0.5 and also plotted to provide more data. Looking closer at the curve, one can see other small structures that seem periodic in $1/B$. We don't analyze it further here, but other works have shown that smaller SdH oscillations can be attributed to holes pocket, see [37].

In Fig. 6.48b, we show a line fit of the first three points, corresponding to peaks and dips at higher magnetic fields, that are more reliable for an effect best shown at high field. From this, we extract a periodicity of $\Delta\left(\frac{1}{B}\right) = 1/(4.92 \times 10^4) \simeq 0.20 \times 10^{-4}\ G^{-1} \simeq 0.20\ T^{-1}$, similar to [220].

Interpreting it as standard SdH periodicity, it yields $\lambda_F \simeq 51\ nm$, which is the typical expected Fermi wavelength for bulk modes.

c) Nanoring Bi^{ring}

We repeat the same procedure for the even part of the second harmonic voltage response of the nanoring sample to an AC current excitation, as a function of in-plane magnetic field. In Fig. 6.49a, we plot if as a function of inverse magnetic field (solid red line) together with the small variations of the first harmonic response extracted with various methods. Indeed, we measured its first harmonic response up to high magnetic fields for this sample.

The red dots show the derivative of the first harmonic response where the slowly varying background has been subtracted thanks to a 4th order polynomial fit (which visually best fits the background). The peaks' positions matches with those of the second harmonic response, while the dips are quite off.

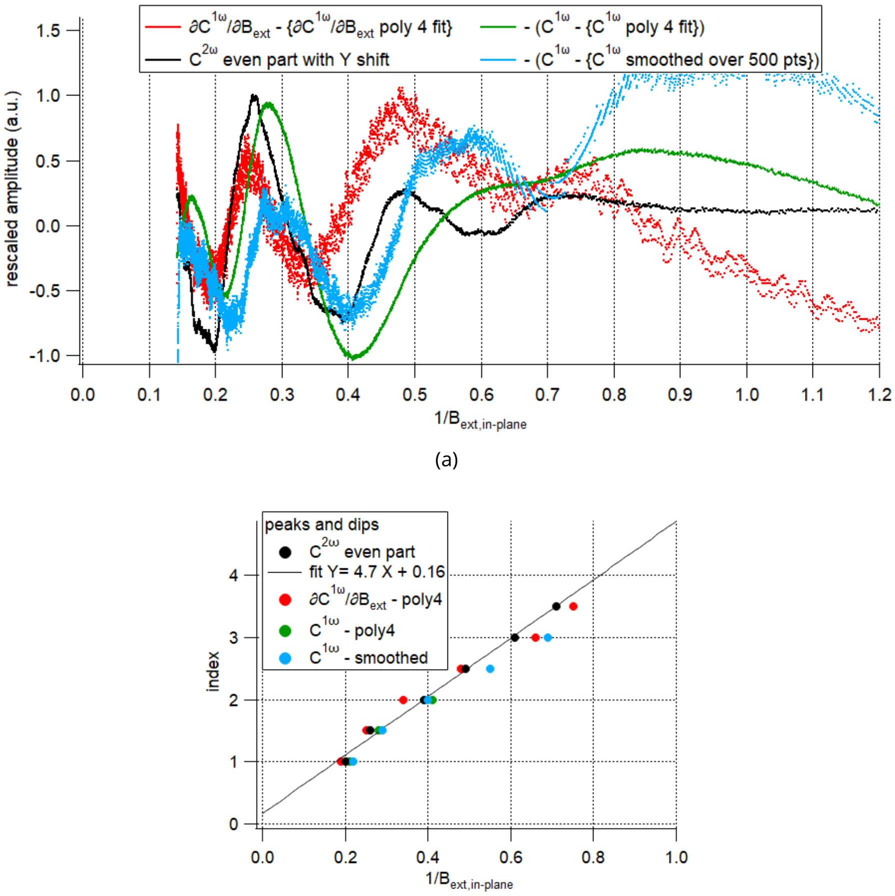

(a)

(b)

Figure 6.49 – Shubnikov-de Haas oscillations on the second harmonic voltage response of nanoring sample Bi^{ring}(black line) compared to various treatments on the first harmonic response, yielding $\lambda_F \simeq 52\,nm$.

The solid green line and the light blue dots show variations of the first harmonic response (no differential) where the slowly varying background has been subtracted thanks to a 4th order polynomial fit (shape robust up to a 6th order polynomial fit) and thanks to a smoothed version of the data (variations robust for different smoothing ranges), respectively. Their signs have been reversed for easier comparison with the other methods. We see that the peaks and dips of those two last methods are close, but they differ by $\simeq 20\%$ from the second harmonic and the derivative method.

These observations are visible in Fig. 6.49b, with the colors of the dots corresponding to the colors seen in Fig. 6.49a. We see that the periodicities that we can extract from all these methods are within $\lesssim 20\%$ of the periodicity of the second harmonic response, and that the second harmonic response gives the most regular periodicity.

Thus, we can say that within a 20% error, the second harmonic response of the nanoring has the same periodicity as its first harmonic response variations. This confirms that it is most likely standard SdH oscillations.

In Fig. 6.49b, we show the result of a line fit on the second harmonic data, see the solid black line. From it, we get $\Delta\left(\frac{1}{B}\right) = 1/4.7 \simeq 0.21\ T^{-1}$, and $\lambda_F \simeq 52\ nm$, as expected for bismuth bulk modes.

d) Conclusion

We found SdH oscillations in the second harmonic response of the long nanowire Bi$_{12}^{long}$ and the nanoring Bi^{ring}, corresponding to $\lambda_F \simeq 51\ nm$ and $52\ nm$ consistent with the bulk λ_F reported in the literature. These oscillations are odd in field for sample Bi$_{12}^{long}$but even in field for sample Bi^{ring}. For sample Bi$_{12}^{long}$, we attribute it to a consequence of the existence of β, yielding a contribution $\propto \frac{\partial G}{\partial B_{Z,eff}}$ to the second harmonic response. However, it is surprising that the large oscillations in the second harmonic have a periodicity corresponding to bulk states, whereas we expect it to be dominated by surface states of much shorter wavelength. For sample Bi^{ring}, we attribute it to a consequence of important asymmetries in the sample, yielding a contribution $\propto \frac{\partial G}{\partial \mu}$ to the second harmonic response.

6.12 . Magneto-Chiral Anisotropy of a Bi-nanowire-based sample with superconducting contacts

While Magneto-Chiral Anisotropy (MCA) in the proximity-induced superconducting state may not be caused by spin-orbit coupling but rather by inductive elements, this possibility is evicted in the resistive state. In this appendix, we report MCA of a bismuth-nanowire-based Josephson junction in both the resistive state and the superconducting state, showing common features, and ruling out the inductive scenario. For this, we introduce a current-to-field factor β in both states, see appendix 6.7 for more details.

The experiment presented in this appendix has been realized during the internship of the student Matthieu Bard, who actively participated in the measurements and who realized the numerical analysis of the data as well as the figures shown in this appendix. The data presented here are currently being further analyzed in preparation of an article (work in progress).

6.12.1 . Bi-nanowire-based DC SQUID

Fig.6.50 show a scanning electron micrograph of the studied sample. It is formed by a bismuth nanowire contacted by three superconducting disordered tungsten nanowires : a central contact (noted "A"), and two side contacts. The two side contacts are connected by a third tungsten nanowire, merging in a single contact (noted "B"). Contacts A and B are extended to the millimeter scale by resistive metallic gold leads, two on each contact.

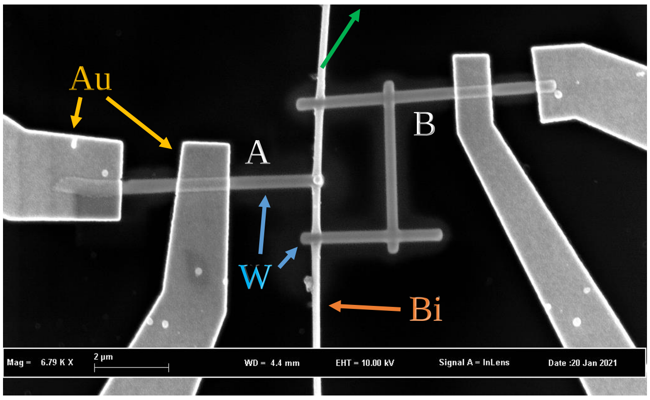

Figure 6.50 – Scanning electron micrograph of the DC SQUID sample, formed by two segments of the same bismuth nanowire with superconducting W compound contacts.

The nanowire has been grown by slow sputtering on a SiO$_2$ substrate with a thin active buffer layer of vanadium, as described in part 2.1. It comes from the same growth substrate as the nanoring studied in chapter 3 and 4. Its width is $w = 193\ nm$ and the lengths of the two segments are $\simeq 1.4\ \mu m$ and $\simeq 2.2\ \mu m$. The EBSD analysis revealed a crystalline structure with a trigonal axis forming a $\simeq 30°$ angle with the nanowire axis, see green arrow in Fig.6.50. The SEM analysis did not show reveal any clear facets, but a rather smooth surface. The superconducting disordered tungsten contact have been deposited with a FIB technique, see part 2. The larger contacts have been realized with standard electronic lithography and low pressure evaporation of $150\ nm$ of gold (in three steps of $50\ nm$) on top of $5\ nm$ of titanium. Each side of the SQUIDs is connected to two gold electrodes, linked to our BNC connections on the exterior of the cryostat, allowing us to measure them in both two and four wires configurations. This sample is referred as Bi$_2^{squid}$ in chapter 3.

With this configuration, the sample has two bismuth based Josephson junctions in parallel, forming a DC SQUID. The length of the two bismuth segments being different, the SQUID should be asymmetric.

Originally, this sample was designed to reproduce the measurements presented in chapter 4. Unfortunately, the conditions were not met to reproduce it, but we redirected its use for MCA analysis.

We measure the sample at low temperature thanks to a He_3/He_4 dilution system, in the second liquid helium cryostat described in part 2.7. The sketches of the configurations used to measure the resistance and the switching current of the sample can be found in parts 2.8.1 and 2.8.2.

6.12.2 . Zero-field characteristics in the proximity-induced superconducting state

Fig.6.51a shows the (differential) resistance $\frac{dV}{dI}$ of the SQUID sample at low temperature $(100\ mK)$. We see that at this temperature, the tungsten contacts are in a superconducting state and induce superconducting correlations in the bismuth nanowire segments by proximity effect. Thus, both the tungsten contacts and the bismuth segments are superconducting, giving a zero resistance at low current. At $I_{DC} \simeq 8\ \mu A$ a transition occurs, which is due to the Bismuth samples switching to a resistive state, see green line in Fig.6.51a. We note this switching current I_c. As we can see on fig 6.51a in order to keep a clear transition noticeable and measurable, everything regarding I_c will be done with a four-wire configuration. Fig.6.51b shows the variation of the resistance as a function of vertical magnetic field, in a four-wire configuration and for increasing DC bias current.

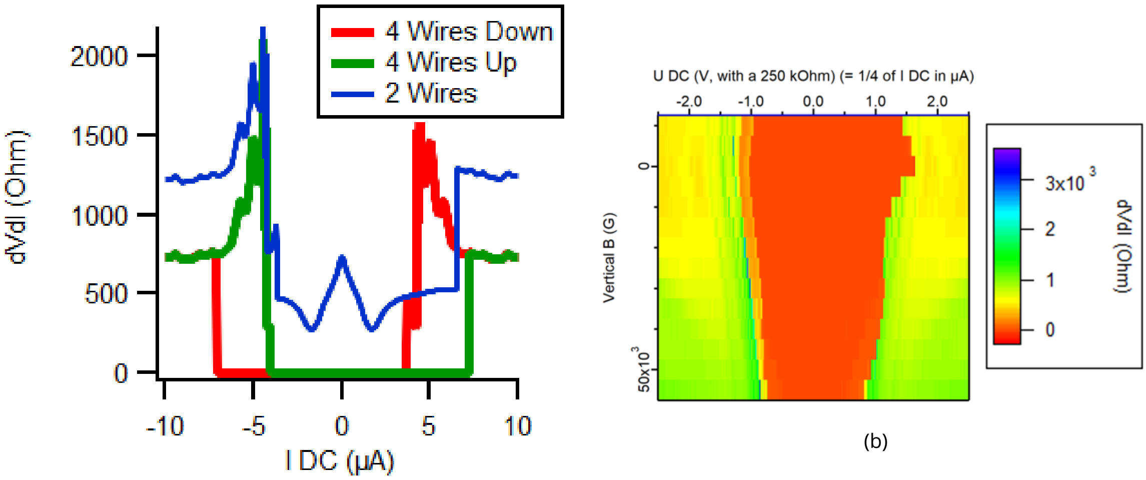

(b)

(a)

Figure 6.51 – (a) Resistance $\frac{dV}{dI}$ of the SQUID sample at low temperature $(100\ mK)$ as a function of DC current bias, in two and four wires configurations, up and down referring to the direction of variation of the DC bias current. (b) Variation of the resistance as a function of vertical magnetic field, in a four-wire configuration and for increasing DC bias current.

6.12.3 . Small field scale : periodic oscillations of the switching current induced by orbital dephasing

With the horizontal and vertical coils in our cryostat, we can measure the variations of the switching current I_c as a function of vertical magnetic field as well as magnetic field in the horizontal plane.

As in chapter 3, we can identify three field scales corresponding to different physical processes. In this appendix, we focus our analysis on the small and large field scales. The characteristics of $I_c(B)$ are sketched in Fig.6.52a. $I_c(B)$ shows small field scale periodic oscillations of amplitude $\delta I_c \simeq 100nA$ and period $\delta B \simeq 3G$, that are visible up to at least $0.5T$, with a characteristics triangular shape. This pattern corresponds to orbital dephasing between long 1d ballistic channels with sawtooth CPR in the two branches of the SQUID, caused by the magnetic flux through the surface of the SQUID $S \simeq 11\mu m^2$. This behavior is consistent with the HOTI nature of Bi, as shown in chapter 3.

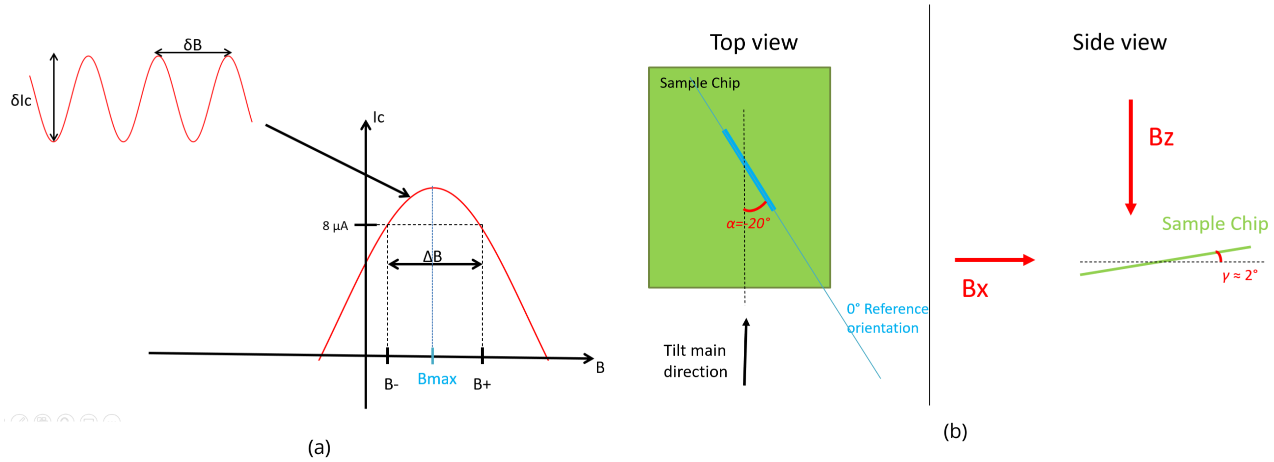

(a) (b)

Figure 6.52 – (a) Sketch of the characteristics of the switching current versus magnetic field curves $I_c(B)$. (b) Visualization of the spatial tilt of the sample.

Fig.6.53a displays the average (blue line) and standard deviation (red line) of the distributions of switching current as a function of vertical magnetic field (mind the two current scales). The standard deviation is also periodic in field, with the same period, and shifted by $\sim 1/4$th of a period. Looking at the full switching distributions plotted in Fig.6.53b, we see that the distribution for an upward slope is narrower than the distribution for a downward slope. In a DC SQUID with ballistic junctions, the two different slopes correspond to variations with field of the current in the two different branches, see part 1.6.1. The statistics of the switching current depends on the environment of the junction, see part 1.10, and further analysis may provide more information on the junctions.

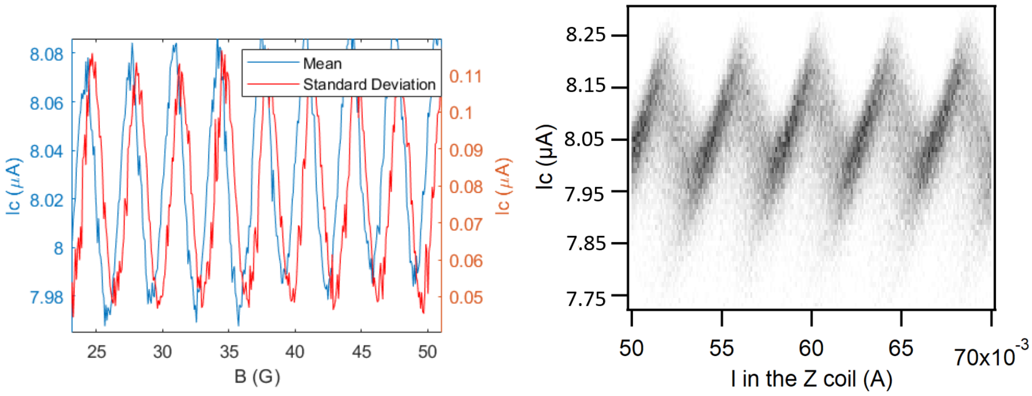

(a) (b)

Figure 6.53 – (a) Average (blue line) and standard deviation (red line) of the distributions of switching current as a function of vertical magnetic field (mind the two current scales). (b) Full switching distributions as a function of vertical magnetic field, for low field values. The number of events in each histogram bins are coded in shades of grey.

Such asymmetry is observed up to $\sim 1000\ G$, beyond which the oscillations are mostly symmetrical (see Fig.6.54a at $\sim 2000\ G$), until their disappearance at $\sim 5000\ G - 6000\ G$ (see Fig.6.54b) when the distribution width is larger than the oscillation amplitude.

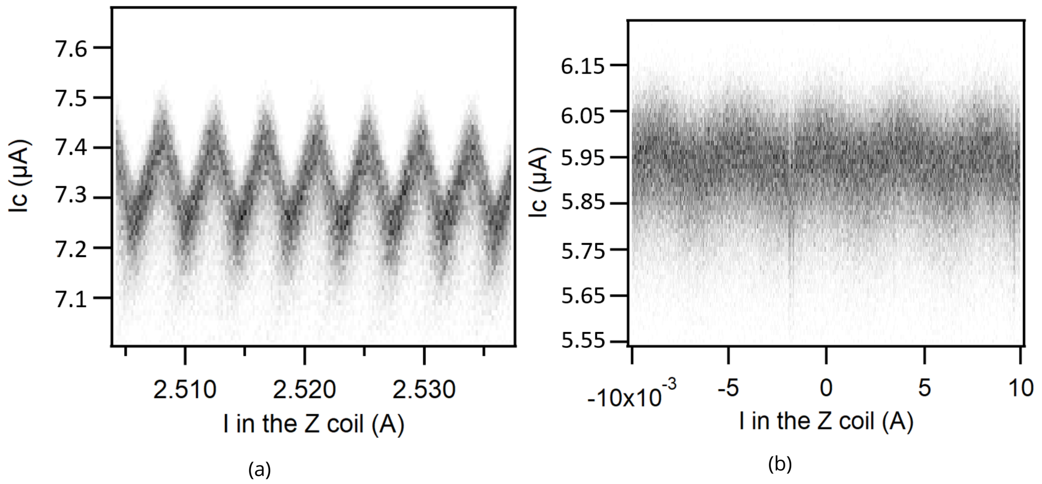

Figure 6.54 – Full switching distributions as a function of vertical magnetic field, close to $2000G$ (a) and $6000G$ (b). The number of events in each histogram bins are coded in shades of grey. In (b), the distribution deviation is of the same magnitude as the amplitude of the oscillations.

Let us now look at the small scale variations of I_c as a function of horizontal magnetic field. Fig.6.55b displays I_c as a function of horizontal magnetic field, parallel to the nanowire axis. The triangular oscillations are still present, with the same amplitude but a much larger period.

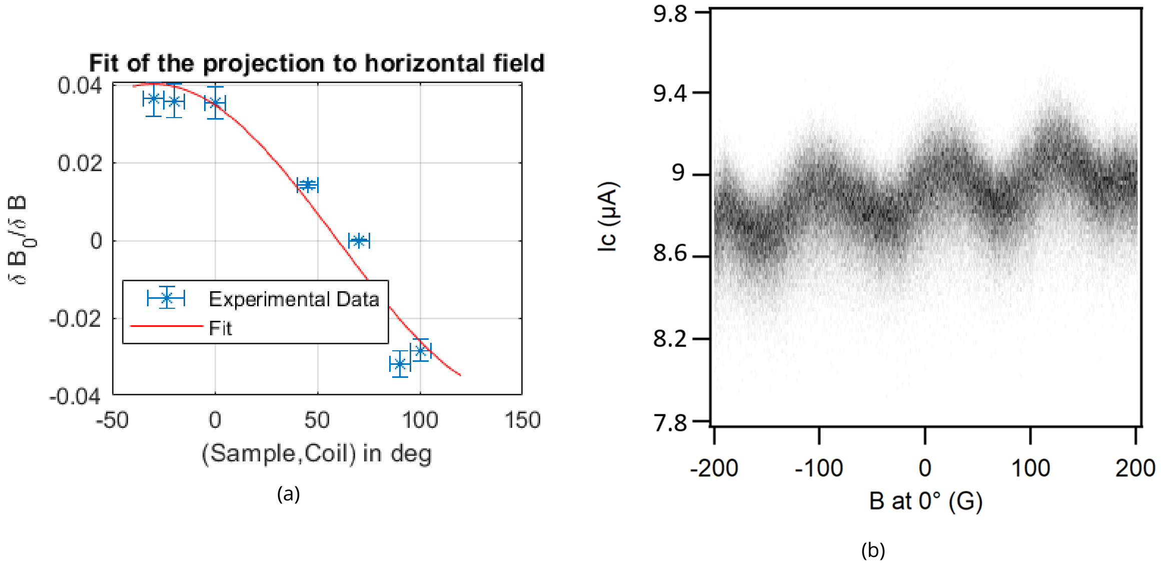

Figure 6.55 – (a) Blue crosses : experimental values of $\delta B_z/\delta B_r$ obtained by measuring the oscillation periods at horizontal fields with various angles φ. Red line : fit of the data with a cosine function corresponding to $\tan(2.3°)\cos(\varphi-(-30°))$. (b) Histogram obtained with a horizontal field at $\varphi = 0°$, parallel to the nanowire axis.

The presence of these oscillations even in horizontal field is explained by a residual flux in the surface of the SQUID, as the surface vector $\vec{S}$ of the SQUID is not perfectly perpendicular to the horizontal field $\vec{B_h}$. To evaluate how much the surface of the SQUID is tilted and in which direction, we write :

- $\vec{B} = B_r\vec{e}_r + B_z\vec{e}_z = \vec{B_h} + B_z\vec{e}_z$ in cylindrical coordinates

- $\vec{S} = S_\rho \vec{e}_\rho$ in spherical coordinates
See appendix 6.5 for more details on this calculation. Expressing both in cartesian coordinates, the flux in the surface of the SQUID is expressed as a scalar product :

$$\Phi = \vec{B}.\vec{S} = B_r S_\rho \sin\gamma \cos(\varphi - \alpha) + B_z S_\rho \cos\gamma \tag{6.123}$$

with φ the angle between $\vec{B}_h$ and the nanowire axis (more precisely its projection on the horizontal plane), α the angle between the projection of $\vec{S}$ on the horizontal plane and the nanowire axis, and γ the angle between $\vec{S}$ and the vertical axis. γ is the tilt of the SQUID surface $\vec{S}$ in the direction of α.

One oscillation period for a vertical magnetic field corresponds to $\delta B_z S_\rho \cos\gamma = \Phi_0$ $(B_r = 0)$, with $\delta B_z \simeq 3G$ the period in vertical field. One oscillation period for a horizontal magnetic field corresponds to $\delta B_r S_\rho \sin\gamma \cos(\varphi - \alpha) = \Phi_0$ $(B_z = 0)$, with δB_r the period in horizontal field at an angle φ. Equating the two, we have :

$$\delta B_z / \delta B_r = \tan\gamma \cos(\varphi - \alpha) \tag{6.124}$$

Fig.6.55a shows the experimental values of $\delta B_z/\delta B_r$ (blue crosses) obtained by measuring the oscillation periods at horizontal fields with various angles φ. The periods for field $\varphi > 60°$ are considered negative, and the period at $\varphi \simeq 60°$ is a rough estimate as the oscillations are barely visible. The red line is a fit of the data with a function $\tan(2.3°)\cos(\varphi - (-30°))$, giving a tilt $\gamma \simeq 2.3°$ in the direction $\alpha \simeq -30°$, illustrated in Fig.6.52b.

The DC SQUID can be modeled by two branches 1 and 2, both with a long ballistic junction with sawtooth CPR of critical current $i_{c1,c2}$ in series with an inductance $L_{1,2}$, see part 1.7.5 for the model. The junctions in each branches are most likely multiple 1d ballistic channels in parallel with individual critical currents $\sim 100nA$, adding up to $\simeq 4\mu A$. The modulation of $\sim 100nA$ of the period is much lower than the $\simeq 4\mu A$ expected for an inductance-less SQUID, suggesting high $L_{1,2}$.

Assuming $i_{c1} \simeq i_{c2} \simeq i_c$ and $L_1 \simeq L_2$, Eq.(1.63) gives a modulation amplitude :

$$\Delta I_c / I_c^{\max} = \frac{1/2}{1 + 2Li_c/\Phi_0}. \tag{6.125}$$

yielding $L_1 \simeq L_2 \simeq 6.2nH$, taking $i_{c1} \simeq i_{c2} \simeq 4\mu A$ and $\Delta I_c \simeq 160nA$.

We estimated that the kinetic inductance $L_{K,W} \simeq 17pH$ per μm of the W compound nanowires is the main source of inductance in the system. Given their length, it yields $L_1 \simeq 1\ nH$ for the short path and $L_2 \simeq 2\ nH$ for the long path. If the model with almost symmetric branches is correct, the inductance of the W nanowires is not enough to explain the amplitude of modulation. Note that if this missing inductance was related to MCA and the anomalous Josephson effects (AJE), we may expect a dependence of the modulation amplitude as a function of magnetic field orientation like in [210], which we don't see in first approximation. However the AJE does not change the modulation of a DC SQUID with long ballistic junctions (see part 1.6.3), and the DC SQUID configuration with $I = I_c$ is different from the AC SQUID with $0 \lesssim I < I_c$ of [210] (see appendix 6.7.6). Therefor, even if the modulation doesn't vary with magnetic field orientation, it doesn't exclude an AJE origin.

6.12.4 . Large field scale : MCA of the switching current induced by $B_{eff} = \beta_S I$

a) General shape at large scale

On the larger magnetic field scale, we can approximate the decrease of $I_c(B)$ by a "tilted" gaussian curve, which width ΔB, asymmetry, and maximum critical current field value B_{max} (such that $I_c^{max} = I_c(B_{max})$) depend on magnetic field orientation. The width ΔB is arbitrarily chosen at the point where the critical current is at $8\ \mu A$. These points are noted B_+ and B_-, where B_+ always has the same sign as B_{max}. These characteristics are sketched in Fig.6.52a.

The switching currents $I_c(B)$ of the sample as a function of magnetic field magnitude for various field orientations are plotted in Fig.6.56, for both positive bias current $+I$ and negative bias current $-I$. There is a clear "tilt" of the curve that depends on the magnetic field direction. In particular, we notice that :
- for $\varphi < -20°$: $-I \Rightarrow B_{max} > 0$ and $+I \Rightarrow B_{max} < 0$
- for $\varphi > -20°$: $-I \Rightarrow B_{max} < 0$ and $+I \Rightarrow B_{max} > 0$
- for $\varphi \simeq -20°$: $+I$ and $-I$ give similar curves, quite flat at $8.8\ \mu A$ and symmetric on a wide range of field, ΔB is maximum, and B_{max} is nearly $0\ G$.

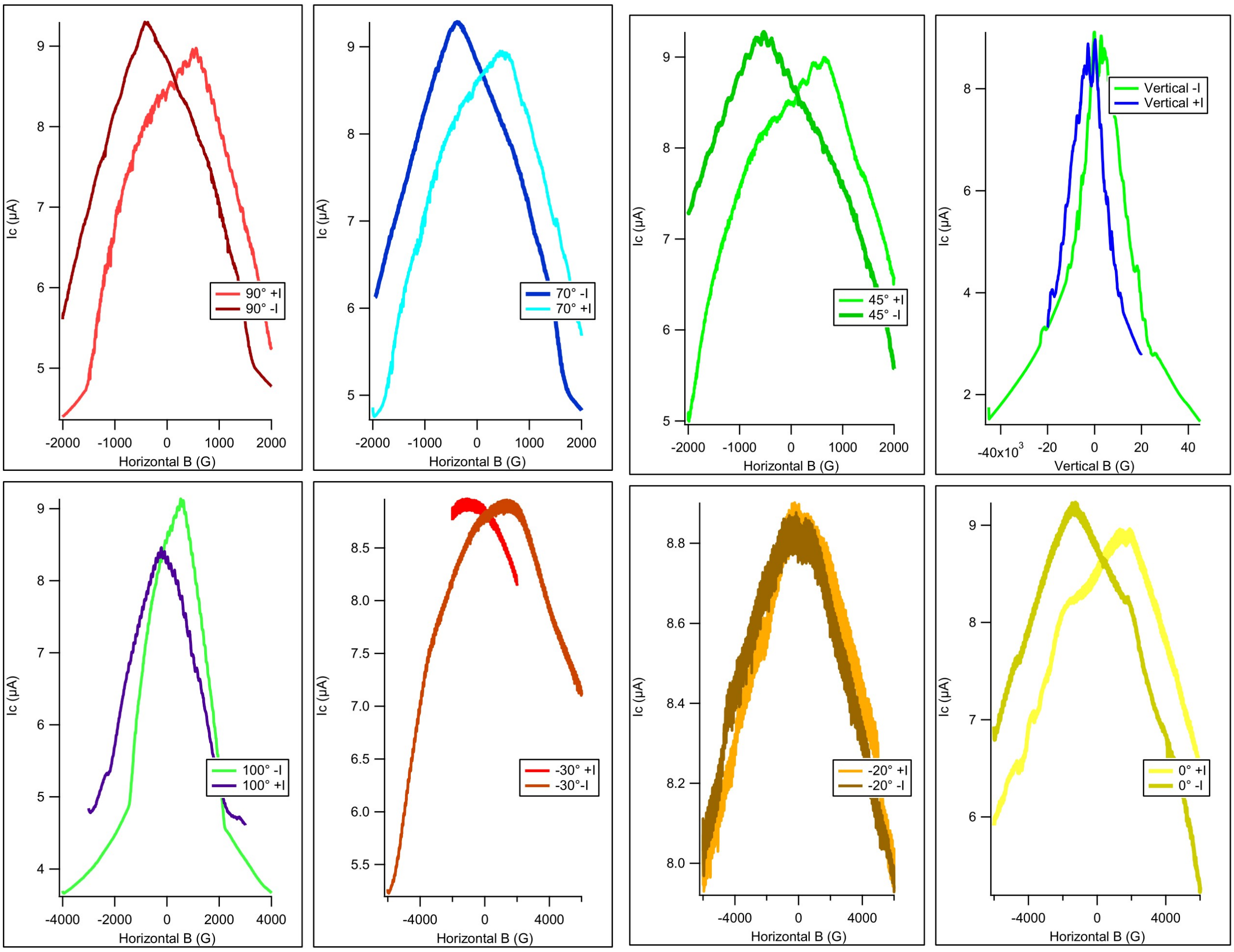

Figure 6.56 – Switching currents $I_c(B)$ of the sample as a function of magnetic field magnitude for various field orientations, for both positive and negative current bias $\pm I$. There is a clear "tilt" of the curve that depends on the magnetic field direction.

We notice that the maximum value of I_c varies with current bias direction, that may be due to a contact flaw heating the system under a certain value of magnetic field by superconducting transition.

To analyze the large field scale variations of I_c, we fit $I_c(B)$ with a gaussian function :

$$I_c(B) = I_0 \exp\left(-\frac{(B - B_{max})^2}{\Delta B_{fit}^2}\right) \tag{6.126}$$

This fit is used to quantify the shift B_{max} and the width ΔB_{fit}, but do not capture the asymmetry of the tilted curve with respect to its maximum I_c. This fit is used for this quick first analysis, and can be easily improved in the future using the phenomenological model discussed below.

b) Shift in field of the maximum critical current

We can extract from these fits a couple of important variables. Following the analysis introduced in appendix 6.7.6, and in the same spirit of the analysis of the resistive long Bi nanowires in appendix 6.9.4 and the Bi nanoring in its resistive state in appendix 6.10, we write :

$$B_{Z,eff} \simeq B_{ext} + \beta_S I \tag{6.127}$$

where the total magnetic field $B_{Z,eff}$ is the sum of the external field B_{ext} and a current-induced effective magnetic field $B_{eff} = \beta_S I$ originating from SOC in the Bi nanowire. In this expression, $B_{Z,eff}$ is the total Zeeman field, contributing to Zeeman-induced effects.

Assuming that the decrease of the experimental $I_c(B)$ is mainly of Zeeman origin, we write :

$$I_c(B) \simeq I_c(B_{Z,eff}) \simeq I_c(B_{ext} + \beta_S I_c(B_{Z,eff})) \tag{6.128}$$

The presence of $\beta_S I_c$ deforms the Zeeman-induced large field scale decrease, shifting its B_{max} away from $B_{ext} = 0$ and introducing an asymmetry with respect to the maximum of I_c. β_S can be approximated by

$$\boxed{\beta_S \simeq \frac{B_{max}}{I_c^{max}}} \tag{6.129}$$

Fig.6.57b displays the β_S obtained from the shift B_{max} of the switching current patterns as a function of various horizontal field angles φ, taking $I_c^{max} = 9\mu A$.

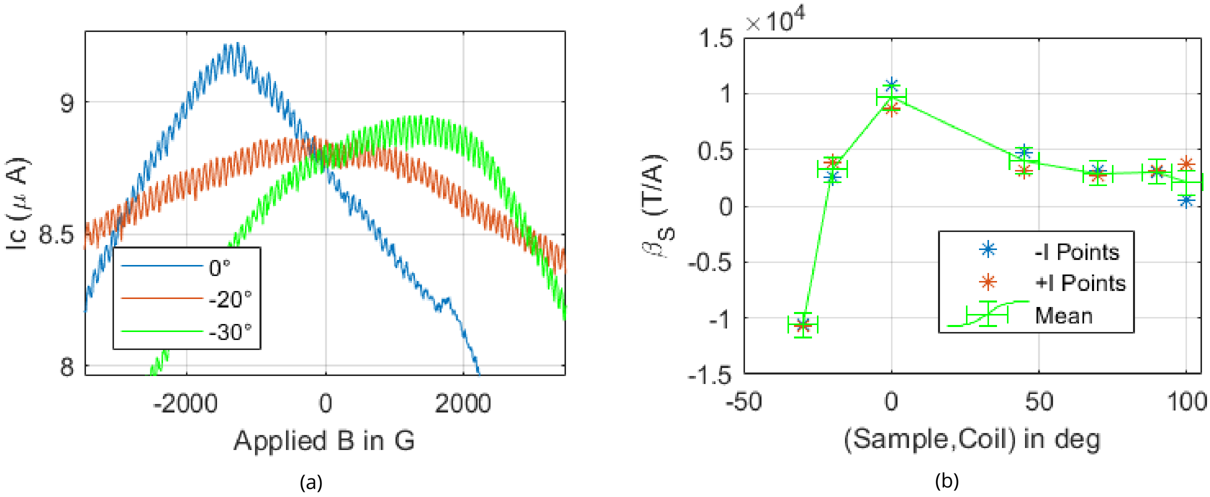

Figure 6.57 – (a) Switching current as a function of horizontal magnetic field at angles $\varphi \simeq 0°$ (blue line), $\varphi \simeq -20°$ (orange line) and $\varphi \simeq -30°$ (green line), all obtained with negative current bias ($-I$). (b) β_S for all the measured orientation in the horizontal plane.

As we can see β_S shows some interesting variation, particularly around $-20°$ where it gets close to 0 and changes its sign beyond this value. Fig.6.57a shows the three curves corresponding to a horizontal field at angles $\varphi \simeq 0°$ (blue line), $\varphi \simeq -20°$ (orange line) and $\varphi \simeq -30°$ (green line), all obtained with current bias

$-I$. On the $[50;100]^{\circ}$ interval, β_S is relatively constant. This orientation of -20° is interesting since it does not seem to coincide with the orientation of the wire (hence the current). This specific orientation comes back in other characteristic values both in the proximity-induced superconducting state and the resistive state, as shown in the following of this appendix.

c) Width and asymmetry of the large scale decrease

From the fits, we can also extract $S_{eff} = \Phi_0/\Delta B_{fit}$, varying between $\sim 0.1 \times 10^4$ and $\sim 1.2 \times 10^4 nm^2$, giving a better estimate of the width of the curve than the arbitrarily defined ΔB, see Fig.6.58a. If the large field scale decrease of the switching current was of orbital dephasing origin, S_{eff} would correspond to the effective surface of diffusive states carrying the supercurrent in the nanowire. While not being as well defined as the β_S estimated from the shift of B_{max}, we also find a change of behavior close to -20°.

The estimated width of the curve is greatly impacted by the choice of our fitting function. A better analysis would require to use the experimental $I_c(B_{ext})$ for which we estimate $\beta_S \simeq 0$ (most likely the data for $\varphi = -20^{\circ}$ in the present case), noted $I_c^{\beta_S \simeq 0}(B_{ext})$, and find for each field orientation for which value of β_S $I_c^{\beta_S \simeq 0}(B_{ext} + \beta_S I_c)$ fits the $I_c(B_{ext})$ data the best. This improved fitting method would allow to quantify the contributions of both the Zeeman-related β_S and the orbital-related decrease.

Even if the present fitting method is over-simplistic, we note that the effective surface S_{eff} doesn't scale as the inverse of β_S, that is $\Delta B_{fit} \not\propto B_{max}$. It contrasts with sample Bi$_{21}^{wire}$ exhibiting a field-orientation-dependent shift of its maximum, see part 3.2b) and Fig.3.8b. In the latter, we explained this shift by the presence of an inductance of $150pH$. In the sample studied in this appendix, $\Delta B_{fit} \not\propto B_{max}$ rules out this scenario.

With the present fitting method, we can also give a qualitative estimate of the asymmetry of the $I_c(B)$ curves relative to their maximum, thanks to the previously defined B_+ and B_-. We define the dimensionless parameter A :

$$A_{\pm} = \frac{|B_{max} - B_{\pm}|}{\Delta B} \tag{6.130}$$

Fig.6.58b shows $A_{\pm}$ obtained for different horizontal magnetic field orientations and for the two current bias directions $\pm I$. Once again -20° seems to be a key orientation.

Fig.6.59 shows the large scale variations of the switching current as a function of vertical magnetic field, for positive (blue line) and negative (orange line) current biases. For comparison, the green line corresponds to I_c as a function of horizontal field, oriented parallel to the nanowire axis ($\varphi = 0^{\circ}$). I_c as a function of vertical field exhibits a clear shift and asymmetry with respect to its maximum value, as well as intermediate scale variations on a scale $\sim 1000\ G$, reminiscent of what we found in part 3.4. At fields $|B| \gtrsim 1T$, the system is in another regime where we observe multiple switching current values at fixed field, giving for example the smooth $I_c(B)$ between -2 and $-1T$ seen on the orange line.

These intermediate field scale variations make the gaussian fit more difficult, but we can still extract a B_{max} and thus a β_S, yielding a $\beta_S \simeq -3.6 \times 10^4 T.A^{-1}$ three times higher than the maximum modulus of β_S with a horizontal field, as shown in Fig.6.67b.

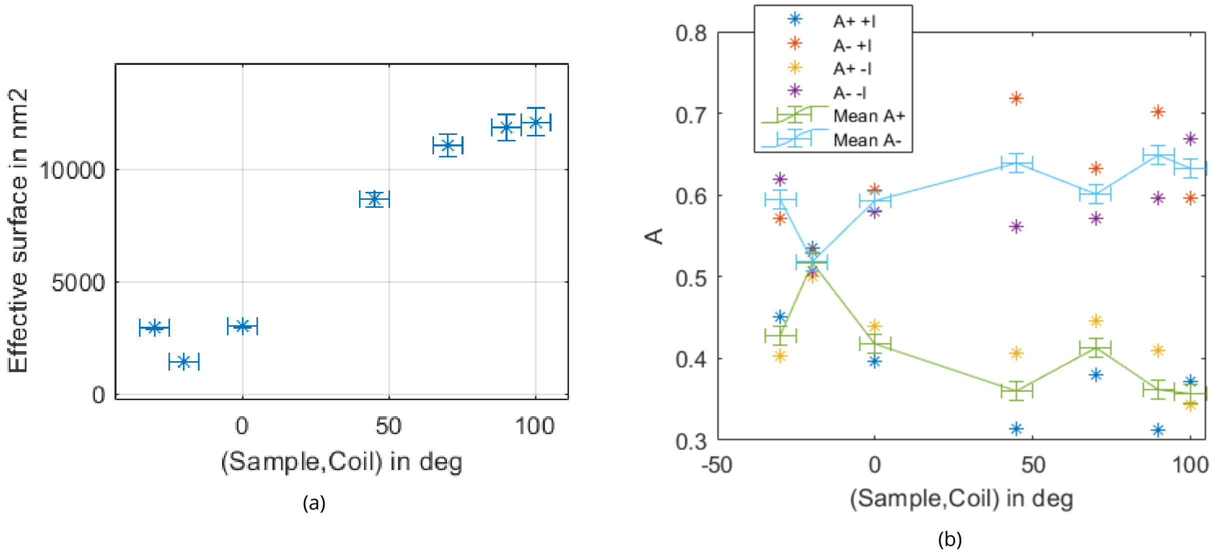

Figure 6.58 – (a) Effective surface $S_{eff} = \Phi_0/\Delta B_{fit}$ as a function of horizontal magnetic field orientation, with ΔB_{fit} the characteristic width of the $I_c(B)$ curves determined by a fit with a shifted gaussian. (b) Dimensionless parameter $A_{\pm}$ as a function of horizontal magnetic field orientation, used to describe qualitatively the asymmetry of the $I_c(B)$ curves with respect to their maximum values.

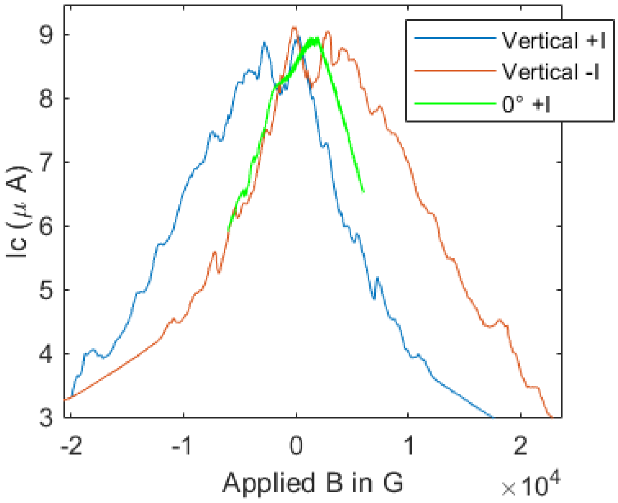

Figure 6.59 – Comparison of I_c as a function of vertical field with positive (blue line) and negative (orange line) current biases to result obtained with a horizontal field along $\varphi = 0^\circ$ (green line).

6.12.5 . Evolution of the switching current with temperature

Lastly, for the superconducting state, we examine how I_c evolves with temperature. All of the previous measurements were done between $100\ mK$ and $200\ mK$. But thanks to the multiple thermometer resistances on the dilution, we can warm up the sample to relatively precise temperature on the $100\ mK - 4\ K$ range.

Globally, temperature will decrease I_c as can be seen on Fig.6.60a, but it does not seem to affect the overall magnetic field behavior of I_c. As can be seen in Fig.6.60b, both the large scale shape and the oscillations seems relatively unchanged by a variation of temperature and are only reduced by a few μA up until $1.5\ K$. However, we can see at the boundaries of the curves that multi-switching (which are seen by a change of regime, beyond $-2000\ G$ for $1\ K$ and $-500\ G$ for $1.5\ K$) becomes much more accessible as temperature is increased. Fig.6.61 shows additional data for temperatures varying continuously between $\simeq 1.2$ and $\simeq 1.6K$.

Comparing the three curves in Fig.6.60b, we see that the shift B_{max} of the maximum I_c isn't directly proportional to the value of I_c^{max}. According to our model, this corresponds to a $\beta_S \simeq B_{max}/I_c^{max}$ that depends on the temperature, which is surprising in first approximation. This point needs further investigations.

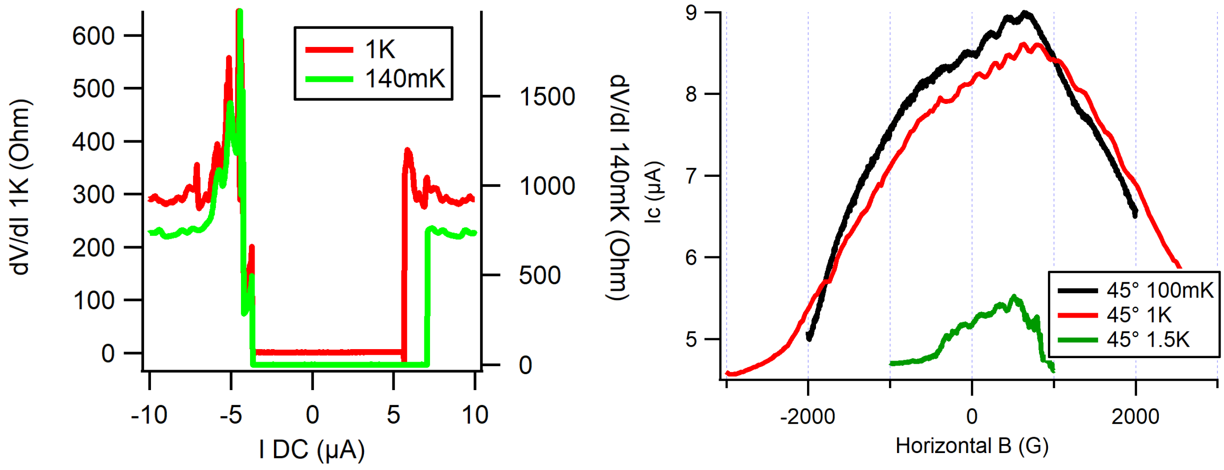

(a)

(b)

Figure 6.60 – (a) Resistance as a function of (increasing) DC current bias, at fixed magnetic field, for two temperatures. (b) Switching current as a function of horizontal magnetic field at 45° for three different temperatures.

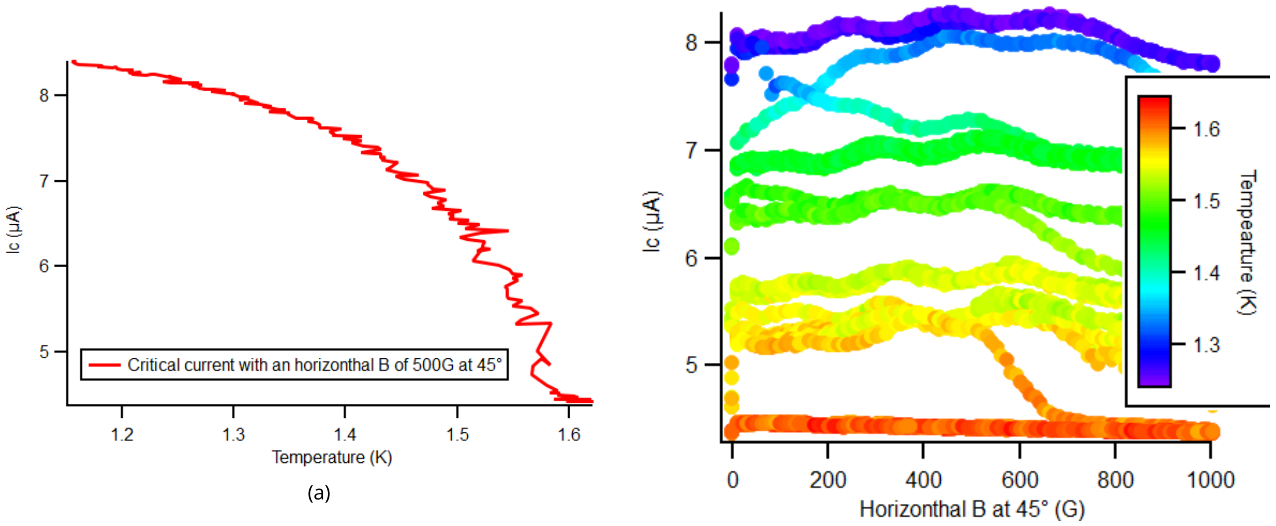

(a)

(b)

Figure 6.61 – (a) Switching current as a function of temperature, at fixed horizontal magnetic field of $500G$ at $45°$. (b) Switching current as a function of horizontal magnetic field at $45°$, with a varying temperature (see color scale).

6.12.6 . Resistive state : MCA of the resistance induced by $B_{eff} = \beta_N I$

In the following, we present magnetoresistance data of the same sample in the resistive state. For this purpose, the sample have been heated up to $5.2K$, which is well above the critical temperature of the proximitized Bi nanowire segments ($T_c \sim 1.5K$), see Fig.6.61. Moreover, this temperature is above the critical temperature of the W contacts, which also exhibit no field dependent contribution to the second harmonic voltage response to a current excitation, see Fig.6.62. This ensures that the variations of the second harmonic voltage response with magnetic field corresponds to a physical phenomenon in the Bi nanowire.

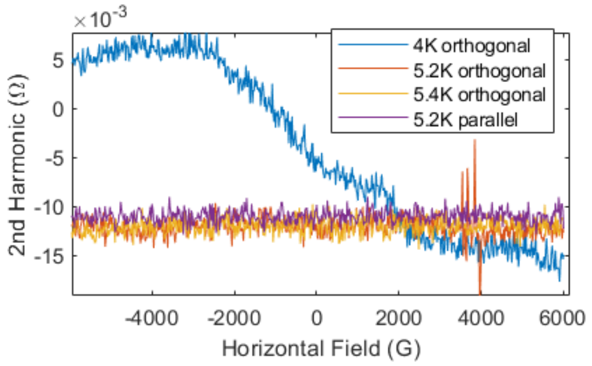

Figure 6.62 – Second harmonic voltage response of a segment of W nanowire, as a function of horizontal magnetic field, for different orientations and temperature.

Following the analysis introduced in appendix 6.7.4, and in the same spirit of the analysis of the resistive long Bi nanowires in appendix 6.9.4 and the Bi nanoring in appendix 6.10, we write the resistance R as :

$$R \simeq R(B_{Z,eff}) \simeq R(B_{ext} + \beta_N I) \simeq R(B_{ext}, I) \tag{6.131}$$

where we left aside the orbital contribution of the magnetic field. $B_{Z,eff}$ is the effective magnetic field contributing to Zeeman effects. It is modeled by the addition of the external magnetic field B_{ext} and a current-induced effective Zeeman field $\beta_N I$, which originates from SOC and causes MCA of the resistance.

As R depends on the current I via $\beta_N I$, β is detectable in the non-linear components of R. For a small current excitation $I = I_{\mathrm{AC}} \sin(\omega t)$, in second order of I_{AC}, the first harmonic voltage response reads (see Eq.(6.79)) :

$$V^{(1\omega)} \simeq (A_Z B_{ext}^2 + R_0) I_{\mathrm{AC}} \tag{6.132}$$

Within the same conditions, the second harmonic voltage response reads :

$$V^{(2\omega)} \simeq -A_Z \beta_N B_{ext} I_{\mathrm{AC}}^2 \tag{6.133}$$

Hence, β_N can be extracted from the linear dependence of $V^{(2\omega)}$ on B_{ext}. To estimate β_N, the knowledge of A_Z is required, which can be extracted by a quadratic fit of $V^{(1\omega)}$ as a function of B_{ext}. The quadratic fit of $V^{(1\omega)}$ also provides a measure of R_0.

Let us now proceed to the analysis of our sample under a magnetic field. The second and first harmonics voltage response of the sample as a function of vertical magnetic field are displayed in Figs.6.63a and 6.63b, respectively. As verified previously, we are in the normal state around $5.2\ K$. However, a strong enough magnetic field can cause other changes, as we can see on Fig.6.63. A change of regime seems to occur around $1-2\ T$, meaning that to stay consistent, our measurements will stay in the $[-1;1]\ T$ range, our horizontal coil being limited to $\sim 0.7\ T$ anyway.

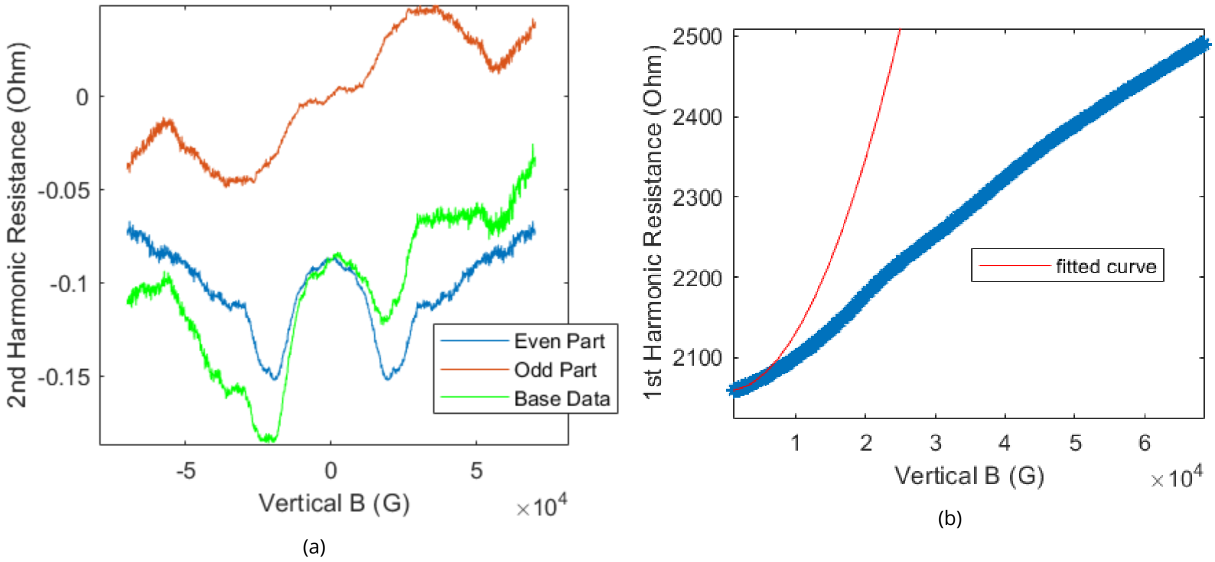

(a)

(b)

Figure 6.63 – Second (a) and first (b) harmonic voltage response as a function of vertical magnetic field. The second harmonic response in (a) (green line) is splitted into a component even in field (blue line) and odd in field (red line). The red line in (b) is a second-order polynomial fit of the low field magnetoresistance.

To analyze our data more easily, the second harmonic response in Fig.6.63a (green line) is splitted into a component even in field (blue line) and odd in field (red line), where β_N involves the odd component. However this splitting can't be done for horizontal field measurements, as there is an uncontrolled hysteresis of the horizontal coil. In Fig.6.63b, the red line is a second-order polynomial fit of the low field magnetoresistance.

In Fig.6.64a, we show the first harmonic as a function of horizontal magnetic field, oriented parallel to the wire $(0°)$, which minimizes the orbital contribution of the magnetic field. For the first harmonic, most of the curves obtained for different field orientations are approximately quadratic in field, although with much noise. We also get a linear term in the fit (in the range of $10^{-6}\ V/T$), which we decided to leave aside in our analysis.

Unfortunately the second harmonics aren't as clear, see Fig.6.64b. The signal over noise ratio is weak (given that our Bi segments are a bit short for this kind of experiment), but we will consider them as linear on the $[-0.6; 0.6]\ T$ interval.

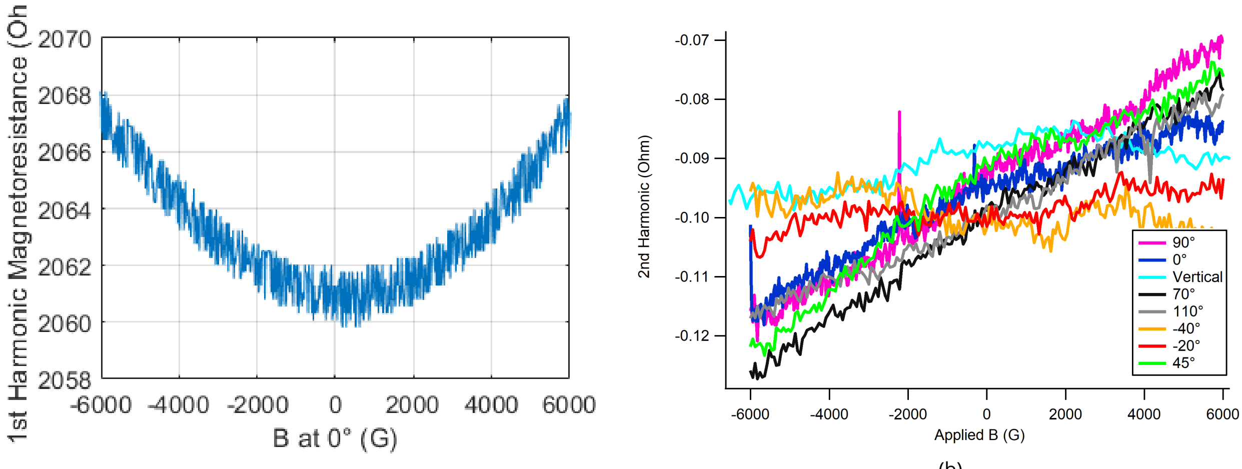

(a) (b)

Figure 6.64 – First (a) and second (b) harmonic voltage response as a function of horizontal magnetic field. In (a) the field is at angle 0°.

Fig.6.65a shows the zero-field resistance R_0 as a function of field orientation. As can be seen from its definition, R_0 should be constant as it does not depend on the field. However in our case we can see slight variations of a few tens of Ω. They can be explained by a slight variation of temperature, e.g. influenced by the helium level in the cryostat, which is different in every measurement.

In Fig.6.65b, we plot A_Z/R_0 as a function of magnetic field orientation. We note that the value obtained by application of a vertical field is particularly high compared to the others orientations.

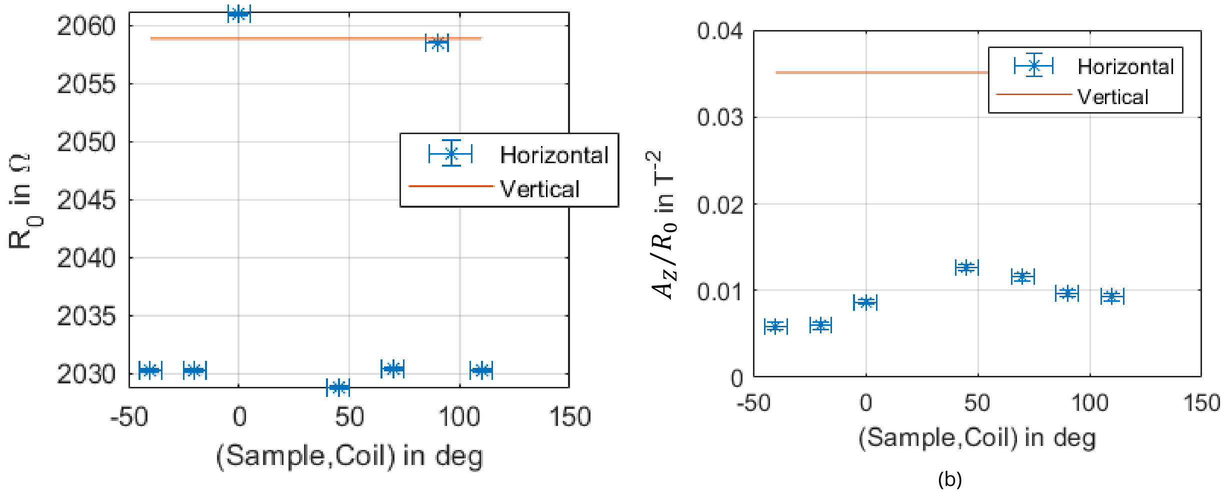

(a) (b)

Figure 6.65 – R_0 (a) and A_Z/R_0 (b) for various magnetic field orientations.

Fig.6.66a displays the current-to-field factor β_N of the sample in its resistive state, extracted from the linear part at low field of the data shown in Fig.6.64b and from the coefficients A_Z shown in Fig.6.65b.

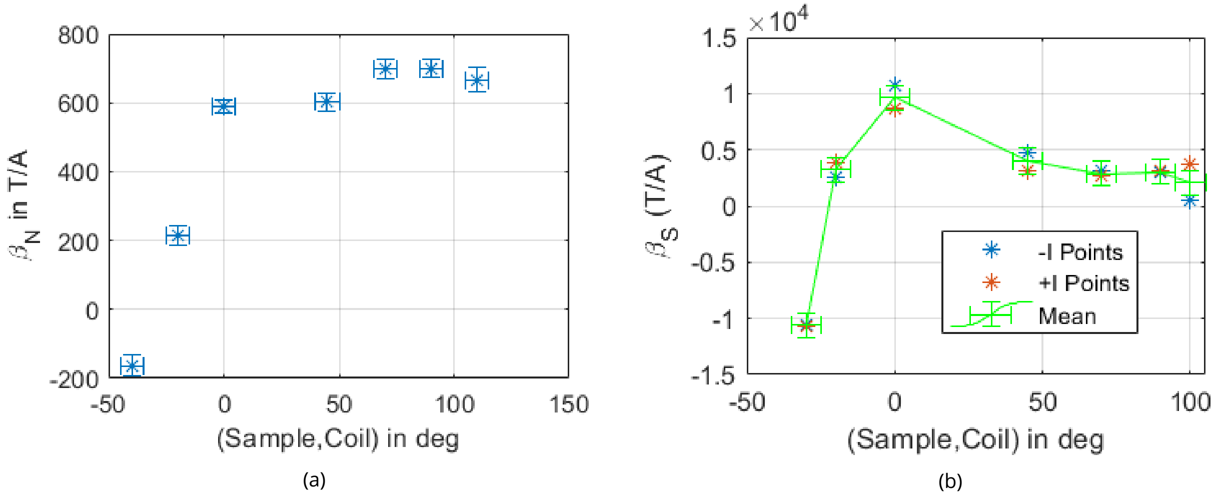

(a)

(b)

Figure 6.66 – β in the resisitve state (a) (β_N) and in the superconducting state (b) (β_S) as a function of horizontal magnetic field orientation.

Here we have a direct equivalent in the proximity-induced superconducting state, being the previously calculated β_S, plotted in Fig.6.66b. Comparing the two states side to side indicates a correlation : both are rather constant above $0°$, while changing their sign around $-20°$. This correlation might suggest a similar spin behavior between the two states.

The change of behavior at $-20°$ in both states differs from the highly symmetric axis of the system, that is the axis parallel to the nanowire $0°$ and perpendicular to the nanowire $90°$. Later EBSD analysis (see part 2.3 for the principle) revealed that the trigonal axis of the Bi crystal formed an approximate angle $|\theta| \simeq 30°$ with the nanowire axis, which is a hint that the crystallographic orientation may have a big impact on the spin-orbit-induced $\beta_{S,N}$ in both the resistive and the superconducting states. However, we recall that $\varphi \simeq -30°$ also corresponds to the angle with a maximum residual flux in the surface of the SQUID, with an estimated tilt of $\gamma \simeq 2°$. This flux may cause a residual orbital effect. More in-depth analysis is required to clarify the orbital and crystalline orientation contributions.

Furthermore, the values of β_N and β_S only differ by a factor ~ 2, which is surprisingly low as the transport properties in the resistive and the superconducting states are very different. Both states are subject to the Edelstein effects of identical magnitude and symmetries, but the pairing correlations induced by the superconductor are not trivial. This similarity in β_N and β_S is an interesting topic to explore, and may be different in intrinsic superconductors compared to SNS Josephson junctions.

Among the effects of the superconducting pairing correlations, the transverse current distribution is expected to be different in the two states, owing to the reduced relative contribution to transport of the diffusive surface states in the proximity-induced superconducting state, as discussed in parts 1.3.5 and 1.3.6. In the resistive state we expect a more uniform current distribution along the surface of the nanowire, whereas we expect the distribution to be more confined along particular hinges in the superconducting state.

Fig.6.67 shows the same plots but includes the β found for a vertical field. In the superconducting state, the data obtained with a vertical field is different from the ones obtained with a horizontal field, with a higher β_S. In contrast, β_N has a lower value, which is in the range of values obtained with a parallel field. However as we can see Fig.6.65b, the vertical value of A_Z/R_0 is abnormally high, which explains the low value of β_N.

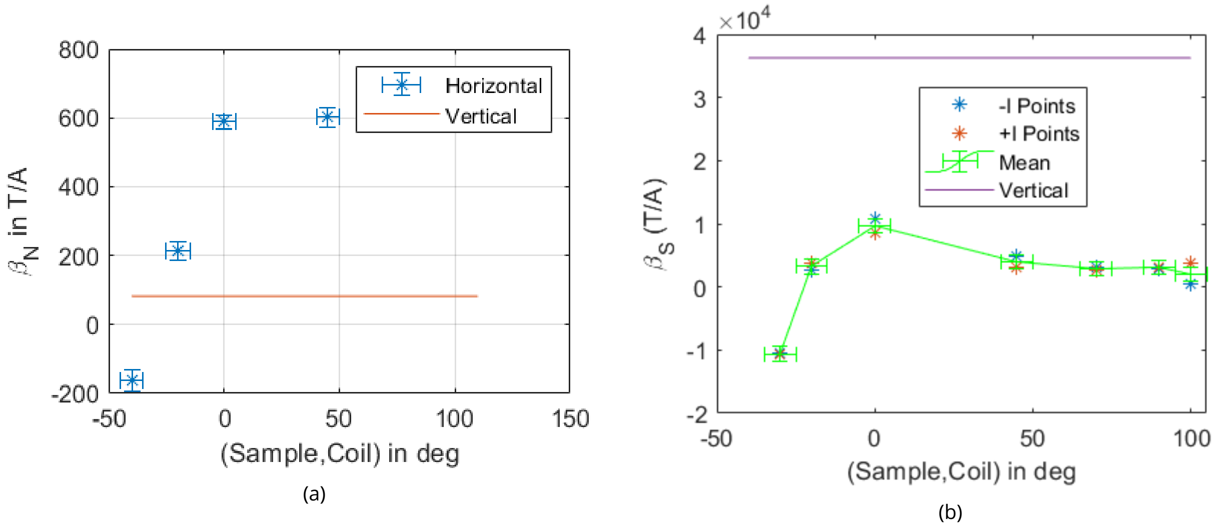

(a)

(b)

Figure 6.67 – Comparison between the vertical field value of β and the values of β obtained with a horizontal field, in the resistive state (a) and in the superconducting state (b).

6.12.7 . Conclusion

In conclusion, we managed to show a similarity in behavior between the proximity-induced superconducting and normal state of our bismuth-nanowire-based sample. With this first analysis, we showed that the MCA modeled by the finite momentum pairing theory in the superconducting state and the MCA modeled by the Unidirectional (or Bilinear) Magnetoresistance theory in the resistive state are captured by an effective (super)current-induced Zeeman field $B_{eff} = \beta I$ of the same order of magnitude in both states. However many points remains to be elucidated, especially in the superconducting state, among which the role of temperature and the contribution of orbital effects not captured by $\beta_S I$.

Bibliography

[1] Chuan Li. *Superconducting proximity effect in graphene and Bi nanowire based junctions*. PhD thesis, 2014.

[2] Anil Murani. *Superconducting proximity effect in monocrystalline bismuth nanowires*. PhD thesis, 2017.

[3] Anil Murani, Alik Kasumov, Shamashis Sengupta, Yu A. Kasumov, V. T. Volkov, I. I. Khodos, F. Brisset, Raphaëlle Delagrange, Alexei Chepelianskii, Richard Deblock, Hélène Bouchiat, and Sophie Guéron. Ballistic edge states in Bismuth nanowires revealed by SQUID interferometry. *Nature Communications*, 8 :15941, July 2017.

[4] A. Murani, B. Dassonneville, A. Kasumov, J. Basset, M. Ferrier, R. Deblock, S. Guéron, and H. Bouchiat. Microwave Signature of Topological Andreev level Crossings in a Bismuth-based Josephson Junction. *Physical Review Letters*, 122(7) :076802, February 2019.

[5] A. Bernard, Y. Peng, A. Kasumov, R. Deblock, M. Ferrier, F. Fortuna, V. T. Volkov, Yu. A. Kasumov, Y. Oreg, F. von Oppen, H. Bouchiat, and S. Guéron. Long-lived andreev states as evidence for protected hinge modes in a bismuth nanoring josephson junction. *Nature Physics*, January 2023.

[6] Eric Akkermans and Gilles Montambaux. *Mesoscopic physics of electrons and photons*. Cambridge university press, 2007.

[7] Emmanuel I. Rashba. Spin–orbit coupling and spin transport. *Physica E : Low-dimensional Systems and Nanostructures*, 34(1-2) :31–35, August 2006.

[8] L. L. Tao and Evgeny Y. Tsymbal. Spin-orbit dependence of anisotropic current-induced spin polarization. *Physical Review B*, 104(8) :085438, August 2021.

[9] V.M. Edelstein. Spin polarization of conduction electrons induced by electric current in two-dimensional asymmetric electron systems. *Solid State Communications*, 73(3) :233–235, January 1990.

[10] Annika Johansson, Jürgen Henk, and Ingrid Mertig. Theoretical aspects of the Edelstein effect for anisotropic two-dimensional electron gas and topological insulators. *Physical Review B*, 93(19) :195440, May 2016.

[11] Woun Kang, Felix Spathelf, Benoît Fauqué, Yuki Fuseya, and Kamran Behnia. Boundary conductance in macroscopic bismuth crystals. *Nature Communications*, 13(1) :189, December 2022.

[12] Yuki Fuseya, Masao Ogata, and Hidetoshi Fukuyama. Transport Properties and Diamagnetism of Dirac Electrons in Bismuth. *Journal of the Physical Society of Japan*, 84(1) :012001, January 2015.

[13] Frank Schindler, Zhijun Wang, Maia G. Vergniory, Ashley M. Cook, Anil Murani, Shamashis Sengupta, Alik Yu. Kasumov, Richard Deblock, Sangjun Jeon, Ilya Drozdov, Hélène Bouchiat, Sophie Guéron, Ali Yazdani, B. Andrei Bernevig, and Titus Neupert. Higher-order topology in bismuth. *Nature Physics*, 14(9) :918–924, September 2018.

[14] Yi Liu and Roland E. Allen. Electronic structure of the semimetals Bi and Sb. *Physical Review B*, 52(3) :1566–1577, July 1995.

[15] C. A. Hoffman, J. R. Meyer, F. J. Bartoli, A. Di Venere, X. J. Yi, C. L. Hou, H. C. Wang, J. B. Ketterson, and G. K. Wong. Semimetal-to-semiconductor transition in bismuth thin films. *Physical Review B*, 48(15) :11431–11434, October 1993.

[16] Yu-Ming Lin, Xiangzhong Sun, and M. S. Dresselhaus1, 2. Theoretical investigation of thermoelectric transport properties of cylindrical Bi nanowires. *Physical Review B*, 62(7) :4610–4623, August 2000.

[17] Ph. Hofmann. The surfaces of bismuth : Structural and electronic properties. *Progress in Surface Science*, 81(5) :191–245, January 2006.

[18] K Hricovini. Topological electronic structure and Rashba effect in Bi thin layers : theoretical predictions and experiments. *J. Phys.*, page 19, 2019.

[19] Shuichi Murakami. Quantum Spin Hall Effect and Enhanced Magnetic Response by Spin-Orbit Coupling. *Physical Review Letters*, 97(23), December 2006.

[20] M. Wada, S. Murakami, F. Freimuth, and G. Bihlmayer. Localized edge states in two-dimensional topological insulators : Ultrathin Bi films. *Physical Review B*, 83(12), March 2011.

[21] Shin Yaginuma, Katsumi Nagaoka, Tadaaki Nagao, Gustav Bihlmayer, Yury M. Koroteev, Eugene V. Chulkov, and Tomonobu Nakayama. Electronic Structure of Ultrathin Bismuth Films with A7 and Black-Phosphorus-like Structures. *Journal of the Physical Society of Japan*, 77(1) :014701, January 2008.

[22] Yu. M. Koroteev, G. Bihlmayer, E. V. Chulkov, and S. Blügel. First-principles investigation of structural and electronic properties of ultrathin Bi films. *Physical Review B*, 77(4) :045428, January 2008.

[23] T. Hirahara, K. Miyamoto, I. Matsuda, T. Kadono, A. Kimura, T. Nagao, G. Bihlmayer, E. V. Chulkov, S. Qiao, K. Shimada, H. Namatame, M. Taniguchi, and S. Hasegawa. Direct observation of spin splitting in bismuth surface states. *Physical Review B*, 76(15) :153305, October 2007.

[24] Toru Hirahara. The Rashba and quantum size effects in ultrathin Bi films. *Journal of Electron Spectroscopy and Related Phenomena*, 201 :98–104, May 2015.

[25] A. Takayama, T. Sato, S. Souma, and T. Takahashi. Giant Out-of-Plane Spin Component and the Asymmetry of Spin Polarization in Surface Rashba States of Bismuth Thin Film. *Physical Review Letters*, 106(16) :166401, April 2011.

[26] A. Takayama, T. Sato, S. Souma, and T. Takahashi. Rashba effect of bismuth thin film on silicon studied by spin-resolved ARPES. *Journal of Electron Spectroscopy and Related Phenomena*, 201 :105–109, May 2015.

[27] Yu. M. Koroteev, G. Bihlmayer, J. E. Gayone, E. V. Chulkov, S. Blügel, P. M. Echenique, and Ph. Hofmann. Strong Spin-Orbit Splitting on Bi Surfaces. *Physical Review Letters*, 93(4) :046403, July 2004.

[28] Christian R. Ast, Jürgen Henk, Arthur Ernst, Luca Moreschini, Mihaela C. Falub, Daniela Pacilé, Patrick Bruno, Klaus Kern, and Marco Grioni. Giant Spin Splitting through Surface Alloying. *Physical Review Letters*, 98(18) :186807, May 2007.

[29] Christian R. Ast and Hartmut Höchst. Fermi Surface of Bi(111) Measured by Photoemission Spectroscopy. *Physical Review Letters*, 87(17) :177602, October 2001.

[30] Ph. Hofmann, J. E. Gayone, G. Bihlmayer, Yu. M. Koroteev, and E. V. Chulkov. Electronic structure and Fermi surface of Bi(100). *Physical Review B*, 71(19) :195413, May 2005.

[31] Doaa Abdelbarey, Julian Koch, Zamin Mamiyev, Christoph Tegenkamp, and Herbert Pfnür. Thickness-dependent electronic transport through epitaxial nontrivial Bi quantum films. *Physical Review B*, 102(11) :115409, September 2020.

[32] Doaa Abdelbarey, Julian Koch, Philipp Kröger, Priyanka Yogi, Christoph Tegenkamp, and Herbert Pfnür. Magnetoconductance in epitaxial bismuth quantum films : Beyond weak (anti)localization. *Physical Review B*, 104(7) :075431, August 2021.

[33] Yuki Fuseya and Hidetoshi Fukuyama. Analytical Solutions for the Surface States of Bi $_{1}$ $_{x}$ Sb $_{x}$ (0 x \(\lesssim \) 0.1). *Journal of the Physical Society of Japan*, 87(4) :044710, April 2018.

[34] Irene Aguilera, Hyun-Jung Kim, Christoph Friedrich, Gustav Bihlmayer, and Stefan Blügel. Z 2 topology of bismuth. *Physical Review Materials*, 5(9) :L091201, September 2021.

[35] Jeongmin Kim, Wooyoung Shim, and Wooyoung Lee. Bismuth nanowire thermoelectrics. *Journal of Materials Chemistry C*, 3(46) :11999–12013, 2015.

[36] Jeongmin Kim, Seunghyun Lee, Yuri M. Brovman, Philip Kim, and Wooyoung Lee. Diameter-dependent thermoelectric figure of merit in single-crystalline Bi nanowires. *Nanoscale*, 7(11) :5053–5059, 2015.

[37] Jeongmin Kim, Seunghyun Lee, Yuri M. Brovman, MinGin Kim, Philip Kim, and Wooyoung Lee. Weak antilocalization and conductance fluctuation in a single crystalline Bi nanowire. *Applied Physics Letters*, 104(4) :043105, January 2014.

[38] A Nikolaeva, D Gitsu, L Konopko, M J Graf, and T E Huber. Quantum interference of surface states in bismuth nanowires probed by the Aharonov-Bohm oscillatory behavior of the magnetoresistance. *Physical Review B*, page 8, 2008.

[39] J. Heremans, C. M. Thrush, Yu-Ming Lin, S. Cronin, Z. Zhang, M. S. Dresselhaus, and J. F. Mansfield. Bismuth nanowire arrays : Synthesis and galvanomagnetic properties. *Physical Review B*, 61(4) :2921–2930, January 2000.

[40] Chuan Li, A. Kasumov, Anil Murani, Shamashis Sengupta, F. Fortuna, K. Napolskii, D. Koshkodaev, G. Tsirlina, Y. Kasumov, I. Khodos, R. Deblock, M. Ferrier, S. Guéron, and H. Bouchiat. Magnetic field resistant quantum interferences in Josephson junctions based on bismuth nanowires. *Physical Review B*, 90(24) :245427, December 2014.

[41] Zheng Liu, Chao-Xing Liu, Yong-Shi Wu, Wen-Hui Duan, Feng Liu, and Jian Wu. Stable Nontrivial Z 2 Topology in Ultrathin Bi (111) Films : A First-Principles Study. *Physical Review Letters*, 107(13) :136805, September 2011.

[42] Han Woong Yeom, Kyung-Hwan Jin, and Seung-Hoon Jhi. Topological fate of edge states of single Bi bilayer on Bi(111). *Physical Review B*, 93(7) :075435, February 2016.

[43] Jeffrey C. Y. Teo, Liang Fu, and C. L. Kane. Surface states and topological invariants in three-dimensional topological insulators : Application to Bi 1 x Sb x. *Physical Review B*, 78(4) :045426, July 2008.

[44] V. V. Enaldiev and V. A. Volkov. Quantum confinement and heavy surface states of Dirac fermions in bismuth (111) films : An analytical approach. *Physical Review B*, 97(11) :115305, March 2018.

[45] Irene Aguilera, Christoph Friedrich, and Stefan Blügel. Electronic phase transitions of bismuth under strain from relativistic self-consistent G W calculations. *Physical Review B*, 91(12) :125129, March 2015.

[46] Christian König, James C. Greer, and Stephen Fahy. Electronic properties of bismuth nanostructures. *Physical Review B*, 104(4) :045432, July 2021.

[47] C. Sabater, D. Gosálbez-Martínez, J. Fernández-Rossier, J. G. Rodrigo, C. Untiedt, and J. J. Palacios. Topologically Protected Quantum Transport in Locally Exfoliated Bismuth at Room Temperature. *Physical Review Letters*, 110(17) :176802, April 2013.

[48] Ilya K. Drozdov, A. Alexandradinata, Sangjun Jeon, Stevan Nadj-Perge, Huiwen Ji, R. J. Cava, B. Andrei Bernevig, and Ali Yazdani. One-dimensional topological edge states of bismuth bilayers. *Nature Physics*, 10(9) :664–669, September 2014.

[49] Naoya Kawakami, Chun-Liang Lin, Maki Kawai, Ryuichi Arafune, and Noriaki Takagi. One-dimensional edge state of Bi thin film grown on Si(111). *Applied Physics Letters*, 107(3) :031602, July 2015.

[50] Xiaogang Liu, Hongjian Du, Jufeng Wang, Mingyang Tian, Xia Sun, and Bing Wang. Resolving the one-dimensional singularity edge states of Bi(1 1 1) thin films. *Journal of Physics : Condensed Matter*, 29(18) :185002, May 2017.

[51] Lang Peng, Jing-Jing Xian, Peizhe Tang, Angel Rubio, Shou-Cheng Zhang, Wenhao Zhang, and Ying-Shuang Fu. Visualizing topological edge states of single and double bilayer Bi supported on multibilayer Bi(111) films. *Physical Review B*, 98(24) :245108, December 2018.

[52] A. Takayama, T. Sato, S. Souma, T. Oguchi, and T. Takahashi. One-Dimensional Edge States with Giant Spin Splitting in a Bismuth Thin Film. *Physical Review Letters*, 114(6) :066402, February 2015.

[53] Berthold Jäck, Yonglong Xie, Jian Li, Sangjun Jeon, B. Andrei Bernevig, and Ali Yazdani. Observation of a Majorana zero mode in a topologically protected edge channel. *Science*, 364(6447) :1255–1259, June 2019.

[54] Sheng-shi Li, Wei-xiao Ji, Ping Li, Shu-jun Hu, Li Cai, Chang-wen Zhang, and Shi-shen Yan. Tunability of the Quantum Spin Hall Effect in Bi(110) Films : Effects of Electric Field and Strain Engineering. *ACS Applied Materials & Interfaces*, 9(25) :21515–21523, June 2017.

[55] Yunhao Lu, Wentao Xu, Mingang Zeng, Guanggeng Yao, Lei Shen, Ming Yang, Ziyu Luo, Feng Pan, Ke Wu, Tanmoy Das, Pimo He, Jianzhong Jiang, Jens Martin, Yuan Ping Feng, Hsin Lin, and Xue-sen Wang. Topological Properties Determined by Atomic Buckling in Self-Assembled Ultrathin Bi(110). *Nano Letters*, 15(1) :80–87, January 2015.

[56] J. W. Wells, J. H. Dil, F. Meier, J. Lobo-Checa, V. N. Petrov, J. Osterwalder, M. M. Ugeda, I. Fernandez-Torrente, J. I. Pascual, E. D. L. Rienks, M. F. Jensen, and Ph. Hofmann. Nondegenerate Metallic States on Bi(114) : A One-Dimensional Topological Metal. *Physical Review Letters*, 102(9) :096802, March 2009.

[57] Leena Aggarwal, Penghao Zhu, Taylor L. Hughes, and Vidya Madhavan. Evidence for higher order topology in Bi and Bi0.92sb0.08. *Nature Communications*, 12(1) :4420, December 2021.

[58] Liang Fu and C. L. Kane. Topological insulators with inversion symmetry. *Physical Review B*, 76(4) :045302, July 2007.

[59] Wladimir A. Benalcazar and Alexander Cerjan. Bound states in the continuum of higher-order topological insulators. *Physical Review B*, 101(16) :161116, April 2020.

[60] Abhay Kumar Nayak, Jonathan Reiner, Raquel Queiroz, Huixia Fu, Chandra Shekhar, Binghai Yan, Claudia Felser, Nurit Avraham, and Haim Beidenkopf. Resolving the topological classification of bismuth with topological defects. *Science Advances*, 5(11) :eaax6996, November 2019.

[61] Fritz London. *Superfluids : Macroscopic theory of superconductivity*, volume 1. Dover publications, 1961.

[62] Gross R. Lecture notes on superconductivity and low temperature physics i (at walther meißner institut). 2022.

[63] LD Landau and VI Ginzburg. K teorii sverkhrovodimosti. *Zh. Eksp. Teor. Fiz*, 20(1064) :546–568, 1950.

[64] Lev Petrovich Gor'kov. Microscopic derivation of the ginzburg-landau equations in the theory of superconductivity. *Sov. Phys. JETP*, 9(6) :1364–1367, 1959.

[65] P.G. De Gennes. Superconductivity of metals and alloys. *WA Benjamin Inc., New York*, 1966.

[66] Landry Bretheau. *Localized Excitations in Superconducting Atomic Contacts : PROBING THE ANDREEV DOUBLET*. PhD thesis, 2013.

[67] Richard P Feynman, Robert B Leighton, and Matthew Sands. *The Feynman lectures on physics : volume III : quantum mechanics*. 1965.

[68] Cyril Metzger. *Effets de spin et de charge dans les états liés d'Andreev*. PhD thesis, 2022.

[69] Jérôme Cayssol, Takis Kontos, and Gilles Montambaux. Isolated hybrid normal/superconducting ring in a magnetic flux : From persistent current to Josephson current. *Physical Review B*, 67(18) :184508, May 2003.

[70] M. Ferrier, B. Dassonneville, S. Guéron, and H. Bouchiat. Phase-dependent Andreev spectrum in a diffusive SNS junction : Static and dynamic current response. *Physical Review B*, 88(17) :174505, November 2013.

[71] Pascal Dubos. *Transport électronique dans les nanojonctions supraconducteur - métal normal - supraconducteur*. PhD thesis, 2000.

[72] Margarita Davydova, Saranesh Prembabu, and Liang Fu. Universal josephson diode effect. *Science Advances*, 8(23) :eabo0309, 2022.

[73] Fabrizio Dolcini, Manuel Houzet, and Julia S. Meyer. Topological Josephson 0 junctions. *Physical Review B*, 92(3) :035428, July 2015.

[74] Tomohiro Yokoyama, Mikio Eto, and Yuli V Nazarov. Anomalous Josephson effect induced by spin-orbit interaction and Zeeman effect in semiconductor nanowires. *PHYSICAL REVIEW B*, page 14, 2014.

[75] Nikolai M. Chtchelkatchev and Yu. V. Nazarov. Andreev Quantum Dots for Spin Manipulation. *Physical Review Letters*, 90(22) :226806, June 2003.

[76] L. Tosi, C. Metzger, M.F. Goffman, C. Urbina, H. Pothier, Sunghun Park, A. Levy Yeyati, J. Nygård, and P. Krogstrup. Spin-Orbit Splitting of Andreev States Revealed by Microwave Spectroscopy. *Physical Review X*, 9(1) :011010, January 2019.

[77] M. Hays, V. Fatemi, D. Bouman, J. Cerrillo, S. Diamond, K. Serniak, T. Connolly, P. Krogstrup, J. Nygård, A. Levy Yeyati, A. Geresdi, and M. H. Devoret. Coherent manipulation of an Andreev spin qubit. *Science*, 373(6553) :430–433, July 2021.

[78] Liang Fu and C. L. Kane. Josephson current and noise at a superconductor/quantum-spin-Hall-insulator/superconductor junction. *Physical Review B*, 79(16) :161408, April 2009.

[79] Erwann Bocquillon, Russell S. Deacon, Jonas Wiedenmann, Philipp Leubner, Teunis M. Klapwijk, Christoph Brüne, Koji Ishibashi, Hartmut Buhmann, and Laurens W. Molenkamp. Gapless Andreev bound states in the quantum spin Hall insulator HgTe. *Nature Nanotechnology*, 12(2) :137–143, February 2017.

[80] R.S. Deacon, J. Wiedenmann, E. Bocquillon, F. Domínguez, T.M. Klapwijk, P. Leubner, C. Brüne, E.M. Hankiewicz, S. Tarucha, K. Ishibashi, H. Buhmann, and L.W. Molenkamp. Josephson Radiation from Gapless Andreev Bound States in HgTe-Based Topological Junctions. *Physical Review X*, 7(2) :021011, April 2017.

[81] A. I. Buzdin. Proximity effects in superconductor-ferromagnet heterostructures. *Reviews of Modern Physics*, 77(3) :935–976, September 2005.

[82] S. Ilić and F.S. Bergeret. Theory of the Supercurrent Diode Effect in Rashba Superconductors with Arbitrary Disorder. *Physical Review Letters*, 128(17) :177001, April 2022.

[83] James Jun He, Yukio Tanaka, and Naoto Nagaosa. A phenomenological theory of superconductor diodes. *New Journal of Physics*, 24(5) :053014, May 2022.

[84] Noah F. Q. Yuan and Liang Fu. Supercurrent diode effect and finite momentum superconductivity. *Proceedings of the National Academy of Sciences*, 119(15) :e2119548119, April 2022. arXiv : 2106.01909.

[85] François Konschelle, Ilya V. Tokatly, and F. Sebastián Bergeret. Theory of the spin-galvanic effect and the anomalous phase shift 0 in superconductors and Josephson junctions with intrinsic spin-orbit coupling. *Physical Review B*, 92(12) :125443, September 2015.

[86] Banabir Pal, Anirban Chakraborty, Pranava K. Sivakumar, Margarita Davydova, Ajesh K. Gopi, Avanindra K. Pandeya, Jonas A. Krieger, Yang Zhang, Mihir Date, Sailong Ju, Noah Yuan, Niels B. M. Schröter, Liang Fu, and Stuart S. P. Parkin. Josephson diode effect from Cooper pair momentum in a topological semimetal. *Nature Physics*, August 2022.

[87] F. S. Bergeret and I. V. Tokatly. Theory of diffusive $_0$ Josephson junctions in the presence of spin-orbit coupling. *EPL (Europhysics Letters)*, 110(5) :57005, June 2015.

[88] I. V. Tokatly. Usadel equation in the presence of intrinsic spin-orbit coupling : A unified theory of magnetoelectric effects in normal and superconducting systems. *Physical Review B*, 96(6) :060502, August 2017.

[89] N. Read and Dmitry Green. Paired states of fermions in two dimensions with breaking of parity and time-reversal symmetries and the fractional quantum Hall effect. *Physical Review B*, 61(15) :10267–10297, April 2000.

[90] A Yu Kitaev. Unpaired Majorana fermions in quantum wires. *Physics-Uspekhi*, 44(10S) :131–136, October 2001.

[91] H.-J. Kwon, K. Sengupta, and V. M. Yakovenko. Fractional ac Josephson effect in p- and d-wave superconductors. *The European Physical Journal B - Condensed Matter*, 37(3) :349–361, February 2003.

[92] Chetan Nayak, Steven H. Simon, Ady Stern, Michael Freedman, and Sankar Das Sarma. Non-Abelian anyons and topological quantum computation. *Reviews of Modern Physics*, 80(3) :1083–1159, September 2008.

[93] Xiao-Liang Qi and Shou-Cheng Zhang. Topological insulators and superconductors. *Reviews of Modern Physics*, 83(4) :1057–1110, October 2011.

[94] Liang Fu and C. L. Kane. Superconducting Proximity Effect and Majorana Fermions at the Surface of a Topological Insulator. *Physical Review Letters*, 100(9) :096407, March 2008.

[95] G. Tkachov and E. M. Hankiewicz. Spin-helical transport in normal and superconducting topological insulators. *physica status solidi (b)*, 250(2) :215–232, February 2013.

[96] Yuval Oreg, Gil Refael, and Felix von Oppen. Helical Liquids and Majorana Bound States in Quantum Wires. *Physical Review Letters*, 105(17) :177002, October 2010.

[97] B. van Heck, J. I. Väyrynen, and L. I. Glazman. Zeeman and spin-orbit effects in the Andreev spectra of nanowire junctions. *Physical Review B*, 96(7) :075404, August 2017.

[98] Elsa Prada, Pablo San-Jose, Michiel W. A. de Moor, Attila Geresdi, Eduardo J. H. Lee, Jelena Klinovaja, Daniel Loss, Jesper Nygård, Ramón Aguado, and Leo P. Kouwenhoven. From Andreev to Majorana bound states in hybrid superconductor–semiconductor nanowires. *Nature Reviews Physics*, 2(10) :575–594, October 2020.

[99] C. W. J. Beenakker, D. I. Pikulin, T. Hyart, H. Schomerus, and J. P. Dahlhaus. Fermion-Parity Anomaly of the Critical Supercurrent in the Quantum Spin-Hall Effect. *Physical Review Letters*, 110(1) :017003, January 2013.

[100] Dimitrie Culcer, Aydın Cem Keser, Yongqing Li, and Grigory Tkachov. Transport in two-dimensional topological materials : recent developments in experiment and theory. *2D Materials*, 7(2) :022007, April 2020.

[101] Kevin Le Calvez. *Signatures of a 4pi periodic Andreev bound state in topological Josephson junctions*. PhD thesis, 2017.

[102] F. Crépin and B. Trauzettel. Reprint of : Flux sensitivity of quantum spin Hall rings. *Physica E : Low-dimensional Systems and Nanostructures*, 82 :185–190, August 2016.

[103] G. Tkachov. Chiral current-phase relation of topological josephson junctions : A signature of the 4π-periodic josephson effect. *Phys. Rev. B*, 100 :035403, Jul 2019.

[104] M. Fuechsle, J. Bentner, D. A. Ryndyk, M. Reinwald, W. Wegscheider, and C. Strunk. Effect of Microwaves on the Current-Phase Relation of Superconductor–Normal-Metal–Superconductor Josephson Junctions. *Physical Review Letters*, 102(12) :127001, March 2009.

[105] J. Vallejo Bustamante, N. J. Wu, C. Fermon, M. Pannetier-Lecoeur, T. Wakamura, K. Watanabe, T. Taniguchi, T. Pellegrin, A. Bernard, S. Daddinounou, V. Bouchiat, S. Guéron, M. Ferrier, G. Montambaux, and H. Bouchiat. Detection of graphene’s divergent orbital diamagnetism at the Dirac point. *Science*, 374(6573) :1399–1402, 2021.

[106] Ziwei Dou, Taro Wakamura, Pauli Virtanen, Nian-Jheng Wu, Richard Deblock, Sandrine Autier-Laurent, Kenji Watanabe, Takashi Taniguchi, Sophie Guéron, Hélène Bouchiat, and Meydi Ferrier. Microwave photoassisted dissipation and supercurrent of a phase-biased graphene-superconductor ring. *Physical Review Research*, 3(3) :L032009, July 2021.

[107] Asbjørn Rasmussen, Jeroen Danon, Henri Suominen, Fabrizio Nichele, Morten Kjaergaard, and Karsten Flensberg. Effects of spin-orbit coupling and spatial symmetries on the Josephson current in SNS junctions. *Physical Review B*, 93(15) :155406, April 2016.

[108] C. Guarcello, R. Citro, O. Durante, F. S. Bergeret, A. Iorio, C. Sanz-Fernández, E. Strambini, F. Giazotto, and A. Braggio. rf-SQUID measurements of anomalous Josephson effect. *Physical Review Research*, 2(2) :023165, May 2020.

[109] Francesca Chiodi. *Dynamical effects in Superconductor/Normal metal/Superconductor long Josephson Junctions*. PhD thesis, 2010.

[110] H. J. Suominen, J. Danon, M. Kjaergaard, K. Flensberg, J. Shabani, C. J. Palmstrøm, F. Nichele, and C. M. Marcus. Anomalous Fraunhofer interference in epitaxial superconductor-semiconductor Josephson junctions. *Physical Review B*, 95(3) :035307, January 2017.

[111] T. Golod, A. Rydh, and V. M. Krasnov. Detection of the Phase Shift from a Single Abrikosov Vortex. *Physical Review Letters*, 104(22) :227003, June 2010.

[112] Elia Strambini, Andrea Iorio, Ofelia Durante, Roberta Citro, Cristina Sanz-Fernández, Claudio Guarcello, Ilya V. Tokatly, Alessandro Braggio, Mirko Rocci, Nadia Ligato, Valentina Zannier, Lucia Sorba, F. Sebastián Bergeret, and Francesco Giazotto. A Josephson phase battery. *Nature Nanotechnology*, 15(8) :656–660, August 2020.

[113] Rubén Seoane Souto, Martin Leijnse, and Constantin Schrade. The Josephson diode effect in supercurrent interferometers. *arXiv :2205.04469 [cond-mat, physics :quant-ph]*, May 2022. arXiv : 2205.04469.

[114] Chui-Zhen Chen, James Jun He, Mazhar N. Ali, Gil-Ho Lee, Kin Chung Fong, and K. T. Law. Asymmetric Josephson effect in inversion symmetry breaking topological materials. *Physical Review B*, 98(7) :075430, August 2018.

[115] R. C. Dynes and T. A. Fulton. Supercurrent Density Distribution in Josephson Junctions. *Physical Review B*, 3(9) :3015–3023, May 1971.

[116] S.V. Mironov, A.S. Mel'nikov, and A.I. Buzdin. Double Path Interference and Magnetic Oscillations in Cooper Pair Transport through a Single Nanowire. *Physical Review Letters*, 114(22) :227001, June 2015.

[117] G Tkachov. Giant spin splitting and 0- Josephson transitions from the Edelstein effect in quantum spin Hall insulators. *PHYSICAL REVIEW B*, page 5, 2017.

[118] Victor Barzykin and Alexandre M. Zagoskin. Coherent transport and nonlocality in mesoscopic SNS junctions : anomalous magnetic interference patterns. *Superlattices and Microstructures*, 25(5-6) :797–807, May 1999.

[119] Hendrik Meier, Vladimir I. Fal'ko, and Leonid I. Glazman. Edge effects in the magnetic interference pattern of a ballistic SNS junction. *Physical Review B*, 93(18) :184506, May 2016.

[120] Gilles Montambaux. Interference pattern of a long diffusive Josephson junction. *arXiv :0707.0411 [cond-mat]*, July 2007. arXiv : 0707.0411.

[121] J. C. Cuevas and F. S. Bergeret. Magnetic Interference Patterns and Vortices in Diffusive SNS Junctions. *Physical Review Letters*, 99(21) :217002, November 2007.

[122] F. Chiodi, M. Ferrier, S. Guéron, J. C. Cuevas, G. Montambaux, F. Fortuna, A. Kasumov, and H. Bouchiat. Geometry-related magnetic interference patterns in long SNS Josephson junctions. *Physical Review B*, 86(6) :064510, August 2012. arXiv : 1201.3509.

[123] F. S. Bergeret and J. C. Cuevas. The Vortex State and Josephson Critical Current of a Diffusive SNS Junction. *Journal of Low Temperature Physics*, 153(5-6) :304–324, December 2008.

[124] Franck Balestro. *Dynamique quantique d'un SQUID-DC*. PhD thesis, 2004.

[125] Yang Peng, Falko Pientka, Erez Berg, Yuval Oreg, and Felix von Oppen. Signatures of topological Josephson junctions. *Physical Review B*, 94(8) :085409, August 2016.

[126] M Zgirski, L Bretheau, Q Le Masne, H Pothier, D Esteve, and C Urbina. Evidence for Long-Lived Quasiparticles Trapped in Superconducting Point Contacts. *PHYSICAL REVIEW LETTERS*, page 4, 2011.

[127] L. Bretheau, Ç. Ö. Girit, C. Urbina, D. Esteve, and H. Pothier. Supercurrent Spectroscopy of Andreev States. *Physical Review X*, 3(4) :041034, December 2013.

[128] Anupam Garg. Escape-field distribution for escape from a metastable potential well subject to a steadily increasing bias field. *Physical Review B*, 51(21) :15592–15595, June 1995.

[129] D. G. Olivares, A. Levy Yeyati, L. Bretheau, Ç. Ö. Girit, H. Pothier, and C. Urbina. Dynamics of quasiparticle trapping in Andreev levels. *Physical Review B*, 89(10) :104504, March 2014.

[130] Shu-Ping Lee, Karen Michaeli, Jason Alicea, and Amir Yacoby. Revealing Topological Superconductivity in Extended Quantum Spin Hall Josephson Junctions. *Physical Review Letters*, 113(19) :197001, November 2014.

[131] M. Hays, G. de Lange, K. Serniak, D.J. van Woerkom, D. Bouman, P. Krogstrup, J. Nygård, A. Geresdi, and M.H. Devoret. Direct Microwave Measurement of Andreev-Bound-State Dynamics in a Semiconductor-Nanowire Josephson Junction. *Physical Review Letters*, 121(4) :047001, July 2018.

[132] C. Janvier, L. Tosi, L. Bretheau, Ç. Ö. Girit, M. Stern, P. Bertet, P. Joyez, D. Vion, D. Esteve, M. F. Goffman, H. Pothier, and C. Urbina. Coherent manipulation of andreev states in superconducting atomic contacts. *Science*, 349(6253) :1199–1202, 2015.

[133] Daniel Frombach and Patrik Recher. Quasiparticle poisoning effects on the dynamics of topological Josephson junctions. *Physical Review B*, 101(11) :115304, March 2020.

[134] Ye Tian and Johann Toudert. Nanobismuth : Fabrication, Optical, and Plasmonic Properties—Emerging Applications. *Journal of Nanotechnology*, 2018 :1–23, June 2018.

[135] C.C. Huang and K.Z. Fung. Effect of the surface configuration on the oxidation of bismuth nanowire. *Materials Research Bulletin*, 41(9) :1604–1611, September 2006.

[136] V. T. Volkov, A. Yu. Kasumov, Yu. A. Kasumov, and I. I. Khodos. Formation and possible growth mechanism of bismuth nanowires on various substrates. *Applied Physics A*, 123(8) :503, August 2017.

[137] Mingzhao Liu, Jing Tao, Chang-Yong Nam, Kim Kisslinger, Lihua Zhang, and Dong Su. Surface-Energy Induced Formation of Single Crystalline Bismuth Nanowires over Vanadium Thin Film at Room Temperature. *Nano Letters*, 14(10) :5630–5635, October 2014.

[138] Wooyoung Shim, Jinhee Ham, Kyoung-il Lee, Won Young Jeung, Mark Johnson, and Wooyoung Lee. On-Film Formation of Bi Nanowires with Extraordinary Electron Mobility. *Nano Letters*, 9(1) :18–22, January 2009.

[139] Wooyoung Shim, Dohun Kim, Kyoung-il Lee, Kye Jin Jeon, Jinhee Ham, Joonyeon Chang, Suk-Hee Han, Won Young Jeung, Mark Johnson, and Wooyoung Lee. Magnetotransport properties of an individual single-crystalline Bi nanowire grown by a stress induced method. *Journal of Applied Physics*, 104(7) :073715, 2008.

[140] A. Yu. Kasumov, R. Deblock, M. Kociak, B. Reulet, H. Bouchiat, I. I. Khodos, Yu. B. Gorbatov, V. T. Volkov, C. Journet, and M. Burghard. Supercurrents Through Single-Walled Carbon Nanotubes. *Science*, 284(5419) :1508–1511, May 1999.

[141] A. Yu. Kasumov, K. Tsukagoshi, M. Kawamura, T. Kobayashi, Y. Aoyagi, K. Senba, T. Kodama, H. Nishikawa, I. Ikemoto, K. Kikuchi, V. T. Volkov, Yu. A. Kasumov, R. Deblock, S. Guéron, and H. Bouchiat. Proximity effect in a superconductor-metallofullerene-superconductor molecular junction. *Physical Review B*, 72(3) :033414, July 2005.

[142] E. S. Sadki, S. Ooi, and K. Hirata. Focused-ion-beam-induced deposition of superconducting nanowires. *Applied Physics Letters*, 85(25) :6206–6208, December 2004.

[143] Wuxia Li, J. C. Fenton, Yiqian Wang, D. W. McComb, and P. A. Warburton. Tunability of the superconductivity of tungsten films grown by focused-ion-beam direct writing. *Journal of Applied Physics*, 104(9) :093913, November 2008.

[144] Shamashis Sengupta, Chuan Li, Cedric Baumier, Alik Kasumov, S. Guéron, H. Bouchiat, and F. Fortuna. Superconducting nanowires by electron-beam-induced deposition. *Applied Physics Letters*, 106(4) :042601, January 2015.

[145] Y. Liu, D. B. Haviland, B. Nease, and A. M. Goldman. Insulator-to-superconductor transition in ultrathin films. *Physical Review B*, 47(10) :5931–5946, March 1993.

[146] Frank Pobell. *Matter and methods at low temperatures*. Springer, Heidelberg, 1996.

[147] C. Enns and S. Hunklinger. *Low-Temperature Physics*. Springer, Heidelberg, 2005.

[148] V. E. Calado, S. Goswami, G. Nanda, M. Diez, A. R. Akhmerov, K. Watanabe, T. Taniguchi, T. M. Klapwijk, and L. M. K. Vandersypen. Ballistic Josephson junctions in edge-contacted graphene. *Nature Nanotechnology*, 10(9) :761–764, September 2015.

[149] Kun Zuo, Vincent Mourik, Daniel B. Szombati, Bas Nijholt, David J. van Woerkom, Attila Geresdi, Jun Chen, Viacheslav P. Ostroukh, Anton R. Akhmerov, Sebastién R. Plissard, Diana Car, Erik P.A.M. Bakkers, Dmitry I. Pikulin, Leo P. Kouwenhoven, and Sergey M. Frolov. Supercurrent Interference in Few-Mode Nanowire Josephson Junctions. *Physical Review Letters*, 119(18) :187704, November 2017.

[150] Artem Kononov, Gulibusitan Abulizi, Kejian Qu, Jiaqiang Yan, David Mandrus, Kenji Watanabe, Takashi Taniguchi, and Christian Schönenberger. One-Dimensional Edge Transport in Few-Layer WTe $_2$. *Nano Letters*, 20(6) :4228–4233, June 2020.

[151] C. L. Kane and E. J. Mele. Quantum Spin Hall Effect in Graphene. *Physical Review Letters*, 95(22) :226801, November 2005.

[152] B. Andrei Bernevig, Taylor L. Hughes, and Shou-Cheng Zhang. Quantum Spin Hall Effect and Topological Phase Transition in HgTe Quantum Wells. *Science*, 314(5806) :1757–1761, December 2006.

[153] Frank Schindler, Ashley M. Cook, Maia G. Vergniory, Zhijun Wang, Stuart S. P. Parkin, B. Andrei Bernevig, and Titus Neupert. Higher-order topological insulators. *Science Advances*, 4(6) :eaat0346, June 2018.

[154] Zhida Song, Zhong Fang, and Chen Fang. $(d-2)$-dimensional edge states of rotation symmetry protected topological states. *Phys. Rev. Lett.*, 119 :246402, Dec 2017.

[155] Josias Langbehn, Yang Peng, Luka Trifunovic, Felix von Oppen, and Piet W. Brouwer. Reflection-Symmetric Second-Order Topological Insulators and Superconductors. *Physical Review Letters*, 119(24) :246401, December 2017.

[156] Fan Zhang and C. L. Kane. Time-reversal-invariant Z_4 fractional josephson effect. *Phys. Rev. Lett.*, 113 :036401, Jul 2014.

[157] Yang Peng, Yuval Vinkler-Aviv, Piet W. Brouwer, Leonid I. Glazman, and Felix von Oppen. Parity Anomaly and Spin Transmutation in Quantum Spin Hall Josephson Junctions. *Physical Review Letters*, 117(26) :267001, December 2016.

[158] R. Delagrange, D. J. Luitz, R. Weil, A. Kasumov, V. Meden, H. Bouchiat, and R. Deblock. Manipulating the magnetic state of a carbon nanotube josephson junction using the superconducting phase. *Phys. Rev. B*, 91 :241401, Jun 2015.

[159] Fran çois Crépin and Björn Trauzettel. Parity measurement in topological josephson junctions. *Phys. Rev. Lett.*, 112 :077002, Feb 2014.

[160] Cai-Zhen Li, An-Qi Wang, Chuan Li, Wen-Zhuang Zheng, Alexander Brinkman, Da-Peng Yu, and Zhi-Min Liao. Reducing electronic transport dimension to topological hinge states by increasing geometry size of dirac semimetal josephson junctions. *Phys. Rev. Lett.*, 124 :156601, Apr 2020.

[161] Topocm online course on topology in condensed matter, https ://topocondmat.org/.

[162] R. B. Laughlin. Quantized hall conductivity in two dimensions. *Phys. Rev. B*, 23 :5632–5633, May 1981.

[163] D. J. Thouless. Quantization of particle transport. *Phys. Rev. B*, 27 :6083–6087, May 1983.

[164] Jean Dalibard. La matière topologique et son exploration avec les gaz quantiques. Cours donnée au Collège de France en 2018.

[165] D. J. Thouless, M. Kohmoto, M. P. Nightingale, and M. den Nijs. Quantized hall conductance in a two-dimensional periodic potential. *Phys. Rev. Lett.*, 49 :405–408, Aug 1982.

[166] J Cayssol and J N Fuchs. Topological and geometrical aspects of band theory. *Journal of Physics : Materials*, 4(3) :034007, July 2021.

[167] Michael S. Lodge, Shengyuan A. Yang, Shantanu Mukherjee, and Bent Weber. Atomically Thin Quantum Spin Hall Insulators. *Advanced Materials*, 33(22) :2008029, June 2021.

[168] M. Z. Hasan and C. L. Kane. *Colloquium* : Topological insulators. *Reviews of Modern Physics*, 82(4) :3045–3067, November 2010.

[169] Xiang-Long Yu, Pei-Hao Fu, and Jiansheng Wu. Response of quantum spin Hall insulators to Zeeman fields, and device design based on stanene. *Physical Review B*, 105(12) :125107, March 2022.

[170] Adolfo G Grushin. Introduction to topological Phases in Condensed Matter. page 28.

[171] Andreas W W Ludwig. Topological phases : classification of topological insulators and superconductors of non-interacting fermions, and beyond. *Physica Scripta*, T168 :014001, December 2016.

[172] Titus Neupert and Frank Schindler. Lecture Notes on Topological Crystalline Insulators. *arXiv :1810.03484 [cond-mat]*, 190 :31–61, 2018. arXiv : 1810.03484.

[173] Timothy H. Hsieh, Hsin Lin, Junwei Liu, Wenhui Duan, Arun Bansil, and Liang Fu. Topological crystalline insulators in the SnTe material class. *Nature Communications*, 3(1) :982, January 2012.

[174] Alexander Lau and Carmine Ortix. Novel topological insulators from crystalline symmetries. *The European Physical Journal Special Topics*, 227(12) :1309–1321, December 2018.

[175] Eslam Khalaf, Hoi Chun Po, Ashvin Vishwanath, and Haruki Watanabe. Symmetry Indicators and Anomalous Surface States of Topological Crystalline Insulators. *Physical Review X*, 8(3) :031070, September 2018.

[176] Max Geier, Luka Trifunovic, Max Hoskam, and Piet W. Brouwer. Second-order topological insulators and superconductors with an order-two crystalline symmetry. *Physical Review B*, 97(20) :205135, May 2018.

[177] Eslam Khalaf. Higher-order topological insulators and superconductors protected by inversion symmetry. *Physical Review B*, 97(20) :205136, May 2018.

[178] Biye Xie, Hai-Xiao Wang, Xiujuan Zhang, Peng Zhan, Jian-Hua Jiang, Minghui Lu, and Yanfeng Chen. Higher-order band topology. *Nature Reviews Physics*, 3(7) :520–532, July 2021.

[179] Feng Tang, Hoi Chun Po, Ashvin Vishwanath, and Xiangang Wan. Efficient topological materials discovery using symmetry indicators. *Nature Physics*, 15(5) :470–476, May 2019.

[180] Zhijun Wang, Benjamin J. Wieder, Jian Li, Binghai Yan, and B. Andrei Bernevig. Higher-Order Topology, Monopole Nodal Lines, and the Origin of Large Fermi Arcs in Transition Metal Dichalcogenides X Te 2 (X = Mo , W). *Physical Review Letters*, 123(18) :186401, October 2019.

[181] Yong-Bin Choi, Yingming Xie, Chui-Zhen Chen, Jinho Park, Su-Beom Song, Jiho Yoon, B. J. Kim, Takashi Taniguchi, Kenji Watanabe, Jonghwan Kim, Kin Chung Fong, Mazhar N. Ali, Kam Tuen Law, and Gil-Ho Lee. Evidence of higher-order topology in multilayer WTe2 from Josephson coupling through anisotropic hinge states. *Nature Materials*, 19(9) :974–979, September 2020.

[182] Chiho Yoon, Cheng-Cheng Liu, Hongki Min, and Fan Zhang. Quasi-One-Dimensional Higher-Order Topological Insulators. *arXiv :2005.14710 [cond-mat]*, May 2020. arXiv : 2005.14710.

[183] Ryo Noguchi, Masaru Kobayashi, Zhanzhi Jiang, Kenta Kuroda, Takanari Takahashi, Zifan Xu, Daehun Lee, Motoaki Hirayama, Masayuki Ochi, Tetsuroh Shirasawa, Peng Zhang, Chun Lin, Cédric Bareille, Shunsuke Sakuragi, Hiroaki Tanaka, So Kunisada, Kifu Kurokawa, Koichiro Yaji, Ayumi Harasawa, Viktor Kandyba, Alessio Giampietri, Alexei Barinov, Timur K. Kim, Cephise Cacho, Makoto

Hashimoto, Donghui Lu, Shik Shin, Ryotaro Arita, Keji Lai, Takao Sasagawa, and Takeshi Kondo. Evidence for a higher-order topological insulator in a three-dimensional material built from van der Waals stacking of bismuth-halide chains. *Nature Materials*, 20(4) :473–479, April 2021.

[184] Nana Shumiya, Md Shafayat Hossain, Jia-Xin Yin, Zhiwei Wang, Maksim Litskevich, Chiho Yoon, Yongkai Li, Ying Yang, Yu-Xiao Jiang, Guangming Cheng, Yen-Chuan Lin, Qi Zhang, Zi-Jia Cheng, Tyler A. Cochran, Daniel Multer, Xian P. Yang, Brian Casas, Tay-Rong Chang, Titus Neupert, Zhujun Yuan, Shuang Jia, Hsin Lin, Nan Yao, Luis Balicas, Fan Zhang, Yugui Yao, and M. Zahid Hasan. Evidence of a room-temperature quantum spin Hall edge state in a higher-order topological insulator. *Nature Materials*, July 2022.

[185] Chen-Hsuan Hsu, Peter Stano, Jelena Klinovaja, and Daniel Loss. Majorana Kramers Pairs in Higher-Order Topological Insulators. *Physical Review Letters*, 121(19), November 2018.

[186] Frederick W Grover. *Inductance calculations : working formulas and tables*. Instrument Society of America, Research Triangle Park, NC, 1981.

[187] Antonio Barone and Gianfranco Paterno. *Physics and applications of the Josephson effect*, volume 1. Wiley-Interscience Publication, 1982.

[188] R. Meservey and P. M. Tedrow. Measurements of the Kinetic Inductance of Superconducting Linear Structures. *Journal of Applied Physics*, 40(5) :2028–2034, April 1969.

[189] Sophie Gueron. *Superconducting proximity effect : from metals to molecules*. PhD thesis, 2009.

[190] Manuel Offidani, Mirco Milletarì, Roberto Raimondi, and Aires Ferreira. Optimal Charge-to-Spin Conversion in Graphene on Transition-Metal Dichalcogenides. *Physical Review Letters*, 119(19) :196801, November 2017.

[191] Wei Chen. Edelstein and inverse Edelstein effects caused by the pristine surface states of topological insulators. *Journal of Physics : Condensed Matter*, 32(3) :035809, January 2020.

[192] Ka Shen, G. Vignale, and R. Raimondi. Microscopic Theory of the Inverse Edelstein Effect. *Physical Review Letters*, 112(9) :096601, March 2014.

[193] Lionel Angers. *Rectification et supraconductivité de proximité dans des anneaux mésoscopiques*. PhD thesis, 2007.

[194] G. L. J. A. Rikken and P. Wyder. Magnetoelectric Anisotropy in Diffusive Transport. *Physical Review Letters*, 94(1) :016601, January 2005.

[195] Yang Gao. Semiclassical dynamics and nonlinear charge current. *Frontiers of Physics*, 14(3) :1–22, 2019.

[196] Carmine Ortix. Nonlinear Hall Effect with Time-Reversal Symmetry : Theory and Material Realizations. *Advanced Quantum Technologies*, 4(9) :2100056, September 2021.

[197] Yoshinori Tokura and Naoto Nagaosa. Nonreciprocal responses from non-centrosymmetric quantum materials. *Nature Communications*, 9(1) :3740, December 2018.

[198] Pan He, Steven S.-L. Zhang, Dapeng Zhu, Yang Liu, Yi Wang, Jiawei Yu, Giovanni Vignale, and Hyunsoo Yang. Bilinear magnetoelectric resistance as a probe of three-dimensional spin texture in topological surface states. *Nature Physics*, 14(5) :495–499, May 2018.

[199] Steven S.-L. Zhang and Giovanni Vignale. Theory of bilinear magneto-electric resistance from topological-insulator surface states. *Spintronics XI*, page 40, September 2018. arXiv : 1808.06339.

[200] Pan He, Chuang-Han Hsu, Shuyuan Shi, Kaiming Cai, Junyong Wang, Qisheng Wang, Goki Eda, Hsin Lin, Vitor M. Pereira, and Hyunsoo Yang. Nonlinear magnetotransport shaped by Fermi surface topology and convexity. *Nature Communications*, 10(1) :1290, December 2019.

[201] A. Dyrdał, J. Barnaś, and A. Fert. Spin-Momentum-Locking Inhomogeneities as a Source of Bilinear Magnetoresistance in Topological Insulators. *Physical Review Letters*, 124(4) :046802, January 2020.

[202] Henry F. Legg, Matthias Rößler, Felix Münning, Dingxun Fan, Oliver Breunig, Andrea Bliesener, Gertjan Lippertz, Anjana Uday, A. A. Taskin, Daniel Loss, Jelena Klinovaja, and Yoichi Ando. Giant magnetochiral anisotropy from quantum-confined surface states of topological insulator nanowires. *Nature Nanotechnology*, May 2022.

[203] Ryohei Wakatsuki, Yu Saito, Shintaro Hoshino, Yuki M. Itahashi, Toshiya Ideue, Motohiko Ezawa, Yoshihiro Iwasa, and Naoto Nagaosa. Nonreciprocal charge transport in noncentrosymmetric superconductors. *Science Advances*, 3(4) :e1602390, April 2017.

[204] F. Qin, W. Shi, T. Ideue, M. Yoshida, A. Zak, R. Tenne, T. Kikitsu, D. Inoue, D. Hashizume, and Y. Iwasa. Superconductivity in a chiral nanotube. *Nature Communications*, 8(1) :14465, April 2017.

[205] Kenji Yasuda, Hironori Yasuda, Tian Liang, Ryutaro Yoshimi, Atsushi Tsukazaki, Kei S. Takahashi, Naoto Nagaosa, Masashi Kawasaki, and Yoshinori Tokura. Nonreciprocal charge transport at topological insulator/superconductor interface. *Nature Communications*, 10(1) :2734, December 2019.

[206] H. Linke, W. D. Sheng, A. Svensson, A. Löfgren, L. Christensson, H. Q. Xu, P. Omling, and P. E. Lindelof. Asymmetric nonlinear conductance of quantum dots with broken inversion symmetry. *Physical Review B*, 61(23) :15914–15926, June 2000.

[207] V. Krstić, S. Roth, M. Burghard, K. Kern, and G. L. J. A. Rikken. Magneto-chiral anisotropy in charge transport through single-walled carbon nanotubes. *The Journal of Chemical Physics*, 117(24) :11315–11319, December 2002.

[208] T. Guillet, C. Zucchetti, Q. Barbedienne, A. Marty, G. Isella, L. Cagnon, C. Vergnaud, H. Jaffrès, N. Reyren, J.-M. George, A. Fert, and M. Jamet. Observation of Large Unidirectional Rashba Magnetoresistance in Ge(111). *Physical Review Letters*, 124(2) :027201, January 2020.

[209] A. G. Mal'shukov and C. S. Chu. Spin Hall effect in a Josephson contact. *Physical Review B*, 78(10) :104503, September 2008.

[210] Christian Baumgartner, Lorenz Fuchs, Andreas Costa, Simon Reinhardt, Sergei Gronin, Geoffrey C. Gardner, Tyler Lindemann, Michael J. Manfra, Paulo E. Faria Junior, Denis Kochan, Jaroslav Fabian, Nicola Paradiso, and Christoph Strunk. Supercurrent rectification and magnetochiral effects in symmetric Josephson junctions. *Nature Nanotechnology*, 17(1) :39–44, January 2022.

[211] C Baumgartner, L Fuchs, A Costa, Jordi Picó-Cortés, S Reinhardt, S Gronin, G C Gardner, T Lindemann, M J Manfra, P E Faria Junior, D Kochan, J Fabian, N Paradiso, and C Strunk. Effect of Rashba and Dresselhaus spin–orbit coupling on supercurrent rectification and magnetochiral anisotropy of ballistic Josephson junctions. *Journal of Physics : Condensed Matter*, 34(15) :154005, April 2022.

[212] Bianca Turini, Sedighe Salimian, Matteo Carrega, Andrea Iorio, Elia Strambini, Francesco Giazotto, Valentina Zannier, Lucia Sorba, and Stefan Heun. Josephson Diode Effect in High Mobility InSb Nanoflags. *arXiv :2207.08772 [cond-mat, physics :quant-ph]*, July 2022. arXiv : 2207.08772.

[213] Masayuki Murata, Daiki Nakamura, Yasuhiro Hasegawa, Takashi Komine, Takashi Taguchi, Shinichiro Nakamura, Christopher M. Jaworski, Vladimir Jovovic, and Joseph P. Heremans. Mean free path limitation of thermoelectric properties of bismuth nanowire. *Journal of Applied Physics*, 105(11) :113706, June 2009.

[214] Meydi Ferrier. *Transport électronique dans les fils quasi-unidimensionnels : cohérence de phase dans les réseaux de fils quantiques et supraconductivité des cordes de nanotubes de carbone*. PhD thesis, 2004. Thèse de doctorat dirigée par Bouchiat, Hélène Physique des solides Paris 11 2004.

[215] C. W. J. Beenakker and H. van Houten. Boundary scattering and weak localization of electrons in a magnetic field. *Physical Review B*, 38(5) :3232–3240, August 1988.

[216] M. Rudolph and J. J. Heremans. Spin-orbit interaction and phase coherence in lithographically defined bismuth wires. *Physical Review B*, 83(20) :205410, May 2011.

[217] B. Hackens, J. P. Minet, S. Faniel, G. Farhi, C. Gustin, J. P. Issi, J. P. Heremans, and V. Bayot. Quantum transport, anomalous dephasing, and spin-orbit coupling in an open ballistic bismuth nanocavity. *Physical Review B*, 67(12) :121403, March 2003.

[218] Zijian Jiang, V. Soghomonian, and J.J. Heremans. Dynamic Nuclear Spin Polarization Induced by the Edelstein Effect at Bi(111) Surfaces. *Physical Review Letters*, 125(10) :106802, September 2020.

[219] P. T. Coleridge, R. Stoner, and R. Fletcher. Low-field transport coefficients in gaas/$\mathrm{ga}_{1-\mathrm{x}}\mathrm{al}_{\mathrm{x}}$as heterostructures. *Phys. Rev. B*, 39 :1120–1124, Jan 1989.

[220] T. E. Huber, A. Nikolaeva, L. Konopko, and M. J. Graf. Observation of three-dimensional behavior in surface states of bismuth nanowires and the evidence for bulk-Bi surface quasiparticles. *Physical Review B*, 79(20) :201304, May 2009.

[221] A. Bernard, Y. Peng, A. Kasumov, R. Deblock, M. Ferrier, F. Fortuna, V. T. Volkov, Yu. A. Kasumov, Y. Oreg, F. von Oppen, H. Bouchiat, and S. Gueron. Evidence for topological hinge states in a bismuth nanoring josephson junction, 2021.

[222] F. D. M. Haldane. Model for a quantum hall effect without landau levels : Condensed-matter realization of the "parity anomaly". *Phys. Rev. Lett.*, 61 :2015–2018, Oct 1988.